STUDY OF FAR INFRARED CAVITIES AT 60 AND 100 MICRON INFRARED ASTRONOMICAL SATELLITE MAPS AROUND ASYMPTOTIC GIANT BRANCH STARS

A THESIS SUBMITTED TO THE

CENTRAL DEPARTMENT OF PHYSICS

INSTITUTE OF SCIENCE AND TECHNOLOGY

TRIBHUVAN UNIVERSITY

NEPAL

FOR THE AWARD OF

DOCTOR OF PHILOSOPHY

IN PHYSICS

By

ARJUN KUMAR GAUTAM

SEPTEMBER 2018

STUDY OF FAR INFRARED CAVITIES AT 60 AND 100 MICRON INFRARED ASTRONOMICAL SATELLITE MAPS AROUND ASYMPTOTIC GIANT BRANCH STARS

A THESIS SUBMITTED TO THE

CENTRAL DEPARTMENT OF PHYSICS

INSTITUTE OF SCIENCE AND TECHNOLOGY

TRIBHUVAN UNIVERSITY

NEPAL

FOR THE AWARD OF

DOCTOR OF PHILOSOPHY

IN PHYSICS

By

ARJUN KUMAR GAUTAM

SEPTEMBER 2018

RECOMMENDATION

This is recommended that **Mr. Arjun Kumar Gautam** has carried out research entitled **"STUDY OF FAR INFRARED CAVITIES AT 60 AND 100 MICRON INFRARED ASTRONOMICAL SATELLITE MAPS AROUND ASYMPTOTIC GIANT BRANCH STARS"** for the award of Doctor of Philosophy (Ph.D.) in **Physics** under my supervision. To my Knowledge, this work has not submitted for any other degree.

He has fulfilled all the requirements laid down by the Institute of Science and Technology (IOST), Tribhuvan University, Kirtipur for the submission of the thesis for the award of Ph.D. degree.

. . . . . .

Prof. Dr. Binil Aryal
Supervisor
Professor and Head Central Department of Physics
Tribhuvan University, Kirtipur
Kathmandu, Nepal

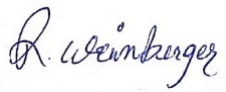

. . . . . .

Prof. Dr. Ronald Weinberger
Co-Supervisor
Innsbruck University,
Innsbruck, Austria

September 2018

LETTER OF APPROVAL

[Date:11/09/2018]

On the recommendation of **Prof. Dr. Binil Aryal** and **Prof. Dr. R. Weinberger**, this Ph.D. thesis submitted by "**Arjun Kumar Gautam**", entitled **"STUDY OF FAR INFRARED CAVITIES AT 60 AND 100 MICRON INFRARED ASTRONOMICAL SATELLITE MAPS AROUND ASYMPTOTIC GIANT BRANCH STARS"** is forwarded by Central Department Research Committee (CDRC) to the Dean, IOST, T.U..

. . . . . .

Dr. Binil Aryal
Professor
Head
Central Department of Physics
Tribhuvan University
Kirtipur, Kathmandu
Nepal

DECLARATION

Thesis entitled **"STUDY OF FAR INFRARED CAVITIES AT 60 AND 100 MICRON INFRARED ASTRONOMICAL SATELLITE MAPS AROUND ASYMPTOTIC GIANT BRANCH STARS"** which is being submitted to the Central Department of Physics, Institute of Science and Technology (IOST), Tribhuvan University, Nepal for the award of the degree of Doctor of Philosophy (Ph.D.), is a research work carried out by me under the supervision of Prof. Dr. Binil Aryal, Central Department of Physics, Tribhuvan University, Kirtipur, Kathmandu, Nepal and co supervised by Prof. Dr. Ronald Weinberger, Innsbruck University, Austria.

This research is original and has not been submitted earlier in part or full in this or any other form to any university or institute, here or elsewhere, for the award of any degree.

Arjun Kumar Gautam

ACKNOWLEDGMENTS

I became able to know the fundamentals of research in physics and saw the research world with third eye; this is only due to my supervisors. So, at first I would like to express my sincere gratitude to my supervisor Prof. Dr. Binil Aryal, HoD, CDP, TU, Kirtipur for the continuous scientific guidance, supports and parent-ship throughout my research work. I acknowledge to my co-supervisor Prof. Dr. Ronald Weinberger, Innsbruck University, Austria for his critical suggestion particularly in the interpretation of the results.

My sincere thank goes to Infrared Astronomical Satellite Survey (IRAS) and Far Infrared (FIR) loop catalog team for providing data. I heartedly remember Prof. Dr. Walter Saurer, Innsbruck University, Austria, Prof. Marat Gilfanov, Max Planck Institute fur Autrophysik, Germany, Prof. Andrzej Zdzarski, Copernicus Astronomical Center, Polland, Prof. Dr. Somak Ray Chaudhary, director, IUCAA, Dr. Prajwal Kafle, Sydney Institute for Astronomy, Australia, Dr. Rajan Chhetri, Curtin University, Australia for their encouraging comments and suggestions.

I would like to express my gratitude to Prof. Dr. Lok Narayan Jha, former HoD, CDP, TU, Kirtipur, Prof. Dr. Shekhar Gurung, Prof. Dr. Jeevan Jyoti Nakarmi, Prof. Dr. Om Prakash Niraula, Prof. Dr. Raju Khanal, Prof. Dr. Mukunda Mani Aryal, Prof. Dr. Udaya Raj Khanal, Prof. Dr. Narayan Prasad Adhikari, Prof. Dr. Ram Prasad Regmi for their support, help and encouragements during ups and downs of my journey of research work.

I would like to give thank to Associate Prof. Dr. Hari Prasad Lamichhane, Associate Prof. Dr. Bal Ram Ghimire, Associate Prof. Dr. Ishwar Koirala, Associate Prof. Dr. Gopi Chandra Kaphle, Assistant Prof. Dr. Sanju Shrestha and other faculty members of CDP for their constant support and encouragement during the research work.

My special thanks go to Associate Prof. Dr. Shiv Narayan Yadav, Associate Prof. Ajay Kumar Jha, Associate Prof. Bhanu Bhakta Sapkota, Associate Prof. Janak R. Malla, Mr. Rajesh Kumar Bachchan and Assistant Prof. Devendra Raj Upadhyay for the company. We learned a lot from each other.

Also, I am thankful to Librarian Mina Manandhar and other staffs of the CDP.

I would like to thank Department of Physics, Aggarwal P. G. College, Haryana, India for helping to present my research work in the international conference. I would like to thank Department of Physics, St. Xavier's College, Kathmandu, Nepal for providing me

an opportunity to present my research work in the national conference.

I am thankful to Institute of Science and technology, TU, Kirtipur and Central Department of Physics for providing me study leave to carry out my research work.

It is my great pleasure to thank Mahendra Multiple Campus, Nepalgunj and Bhaktapur Multiple Campus, Bhaktapur, for giving permissions to carry out Ph.D. research.

Finally, I would like to thank my parent, family members for their constant support, patience and encouragements. Special thank goes to Bina, Abisha and Abiral who always make me fresh and dynamic.

Arjun Kumar Gautam
September, 2018

ABSTRACT

Visible and ultraviolet light are absorbed by dust particles in the interstellar medium and re-emits infrared radiation. Infrared Astronomical Satellite (IRAS) is the first satellite which studied all-sky in the infrared region. We have systematically searched and studied cavity like structures around the carbon-rich Asymptotic Giant Branch (AGB) stars in the Milky Way. We made the following criteria for the selection of cavities: (i) the core region of the cavity or loop should have minimum flux at 100 μm IRAS maps, (ii) major diameter of the cavities or loops should be $> 0.3^\circ$, (iii) should be located within 1.5° of carbon-rich (c-rich) Asymptotic Giant Branch stars, (iv) should lie in the Galactic plane ($-20^\circ < b < 20^\circ$), and (v) no diffuse optical emission. Such low latitude cavities ($b < \pm 20^\circ$) are believed to be formed because of high pressure events occurred in the past (e.g., AGB wind, supernova explosion, etc.). We studied physical properties (dust color temperature, Planck function, dust mass, visual extinction, size, etc.) and kinematics (spectral distribution, etc.) of 18 far infrared cavities. We present our results in three chapters. In the first chapter, we describe the physical properties of 8 far infrared cavities, named CCRAS1, CCRAS2, CCRAS3, CCRAS4, CCRAS5, CCRAS6, CCRAS7 and CCRAS8, which are found to be located within 0.6° from C-rich AGB stars namely AGB0415+5441, AGB0609+1446, AGB0631+1606, AGB0633+1415, AGB0642+0053, AGB0651+0031, AGB0939-5249 and AGB1025-5933 respectively. The second chapter deals the physical properties of two far infrared cavities namely CCRPAS1 and CCRPAS2 around post-AGB stars located at R.A.(J2000) = $06^{\rm h}$ $51^{\rm m}$ $54.0^{\rm s}$, Dec.(J2000) = 01° 35' 25" ($l = 215.4^\circ$ and $b = 0.1^\circ$) and R.A.(J2000) = $08^{\rm h}$ 04 $^{\rm m}07.2^{\rm s}$, Dec.(J2000) = 37° 11' 48.0" ($l = 253.0^\circ$ and $b = 3.0^\circ$). The last chapter describes the physical properties of eight far infrared cavities namely CASKK1, CASKK2, CASKK3, CASKK4, CASKK5, CASKK6, CASKK7 and CASKK8 around C-rich AGB stars AGB0141+7104, AGB0409+6105, AGB0538+1216, AGB0555+2827, AGB0617-0634, AGB0619-0558, AGB0712-1720 and AGB1105-5451CAP1 respectively lying within the far infrared loops namely G125+09, G143+07, G195-11, G182+00, G212-11, G212-11, G229-03 and G287+04 respectively. The search limit of those cavities is found to be completed having major/minor diameter greater than $2.2/1.7$ arc deg. Most of the cavities except CASKK4, CCRPAS1 and CCRAS5 showed very good agreement with Gaussian distribution in both dust color temperature and dust mass. Range of minimum dust color temperature of all the cavities is found to (17.7 ± 1.4) K to (23.9 ± 0.3) K and of maximum dust color temperature is (19.5 ± 0.3) K to (25.0 ± 0.9) K. Minimum offset value of dust color temperature of the cavities is 0.3 K and maximum offset value

is 1.8 K. It means offset value of dust color temperature of all the cavities is < 1.8 K which suggests that most of the cavities may be in thermal equilibrium. But the linear fit between the Planck function and dust color temperature along extension and compression showed non uniform distribution and dust particles are oscillating in order to get dynamical equilibrium. It suggests that the dust particles along extension and compression might be affected by external factors possibly due to nearby AGB wind. Dust mass of the cavities ranges from 1.86×10^{28} kg to 2.47×10^{31} kg where as the average dust mass of each pixel of the cavities ranges from 4.93×10^{25} kg to 5.60×10^{28} kg. Visual extinction of the cavities ranges from 0.65×10^{-5} mag to 3.40×10^{-5} mag. It is found that the product of visual extinction and dust color temperature of all the cavities i.e., $A_V \times T_d$ is consistent and ranges from 0.6×10^{-4} to 4.0×10^{-4}. This result is also verified by their contour maps. Contour map of dust color temperature and dust mass of most of the cavities showed that lower temperature region is massive and vice-versa. It suggests that the distribution of dust mass with in the core region of the cavities follows cosmological principle i.e., their distribution is homogeneous and isotropic. Another important fact is the contour map of dust mass and visual extinction of all the cavities are nearly identical means they show linear relation. In certain cavities such as CCRAS7 and CCRAS8, dust color temperature and dust mass follow Gaussian distribution. Most of the cavities except CCRAS7 and CCRAS8 showed similar nature of the far infrared spectral distribution in all four bands. A significant decrease of flux density specially from 25 μm to 60 μm is noticed in most of the cavities except the cavities CCRAS7 and CCRAS8.

Key Words: ISM, IRAS, AGB stars, far infrared cavities, dust color temperature, dust mass, Planck function, visual extinction

LIST OF ACRONYMS AND ABBREVIATIONS

A&A	Astronomy and Astrophysics Journal
AGB	Asymptotic Giant Branch Star
AJ	Astronomical Journal
AKARI	Meaning 'light' in Japanese (Survey)
ApJ	Astrophysical Journal
ApJS	Astrophysical Journal Suppliment
Ap&SS	Astrophysics and Space Science
DEC	Declination
FIR	Far Infrared
FIRAS	Far Infrared Astronomical Satellite
FITS	Flexible Image Transport System
GIRL	Galactic Infrared Loop
HB	Horizontal Branch
HFI	High Frequency Instrument
HMOA	High Mass-Loss Rate 0-rich AGB Stars
H-R diagram	Hertzsprung-Russell diagram
HST	Hubble Space Telescope
IRAS PSC	Infrared Astronomical Satellite Point Source Catalog
IRIS	Infrared Image Sensor
IRTS	Infrared Telescope in Space Survey
ISCZ	Intershell Convection Zone
ISM	Interstellar Medium
ISO	Infrared Space Observatory
ISRF	Interstellar Radiation Field
ISSA	IRAS SKY Survey Atalas
JNPS	Journal of Nepal Physical Society
JPEG	Joint Photographic Experts Group
KK-loop	Kiss et al.(2004), Konyves et al.(2007)-loop
LOMA	Low Mass-Loss Rate 0-rich AGB Stars
LPVs	Long-Period Variables
LRS	Low Resolution Spectrograph
LTE	Local Thermal Equilibrium
LWS	Long Wave length Spectrometer
MNRAS	Monthly Notice of Royal Astronomical Society
MSX	Mid-Course Space Experiment

NASA	National Aeronautical Space Administration
NED	NASA Extragalactic Database
NIR	Near Infrared
NIRS	Near Infrared Spectrometer
OAJ	The Open Astronomy Journal
pAGB	post-Asymptotic Giant Branch Star
PAH	Polycyclic Aromatic Hydrocarbon
PASJ	Journal of Asia Pacific Society
PDCZ	Pulse Driven Convection Zone
PSC	Point Source Catalog
RA	Right Ascension
RAA	Research in Astronomy and Astrophysics
RGB	Red Giant Branch
RMxAA	Revista Mexicana de Astronomía y Astrofísica
SED	Spectral Energy Distribution
SIMBAD	Set of Identifications, Measurements, and Bibliography for Astronomical Data
SWS	Short Wave length Spectrometer
TP-AGB	Thermally Pulsating Asymptotic Giant Branch
WISE	Wide Field Infrared Survey Explorer
ZAMS	Zero Age Main Sequence Stars
2MASS	Two Micron All Sky Survey

LIST OF TABLES

LIST OF FIGURES

TABLE OF CONTENTS

CHAPTER 1

1. INTRODUCTION

1.1 Introduction

Interstellar matter are the most important particles which produce cool and dense molecular clouds in the interstellar medium. Such clouds merge gravitationally and produce giant molecular clouds. If such clouds overcome certain criteria specially Jean's criteria, they change in to stars. According to their mass, they are divided in to low, intermediate and massive stars which are in 1:1 000:10 000 ratio. For very low mass stars of masses < 0.08 $M_\odot$, no fusion takes place. Low and intermediate mass stars in the range 0.8 $M_\odot \geq M \leq 8\ M_\odot$ lie in the asymptotic giant branch stars (Herwig, 2005). Such AGB (asymptotic giant branch) stars are driven by nuclear burning which happens when the star has leaved the main sequence through red giant passed the horizontal branch.

According to Suh & Kwon (2009), AGB stars are classified into O-rich stars (M-type stars), C-rich stars (C-type stars or carbon stars), S (sulpher) stars, and silicate carbon stars. They presented the catalog of 2 193 O-rich stars, 1 167 C-rich stars, 287 S stars and 36 silicate carbon stars. The catalog of Galactic AGB stars based on reports of different IRAS resolution spectrographs. Data of Low Resolution Spectrograph (LRS: λ = 8 μm *to* 22 μm) are very useful to identify important features of O-rich and C-rich dust grains in AGB stars (Kwok et al., 1997). Infrared Space Observatory (ISO) has Short Wave Length Spectrometer (SWS: λ = 2.4 μm *to* 45.2 μm) and Long Wave Length Spectrometer (LWS: λ = 43 μm *to* 197 μm) which are useful to identify more detailed dust features (Suh, 2002). Near Infrared Spectrometer (NIRS: 1.4 μm *to* 4.0 μm; (Murakami et al., 1994) data are useful for identifying the molecular feature of AGB stars. The radio OH and SiO survey (Lewis et al., 1990) for IRAS color-selected objects have been very useful to identify AGB stars. The infrared astronomical satellite (IRAS) works at 12 μm, 25 μm, 60 μm and 100 μm wavelength band which lie in the infrared and far from infrared region. It is suitable to observe dust particles which absorbs ultraviolet radiation and emits infrared radiation. The Mid-course Space Experiment (MSX) (Egan et al., 2003) provided useful photometric data at 8.28 μm, 12.13 μm,

14.65 μm, 21.34 μm wavelength bands and the 2MASS data project (Skrutskie et al., 2006) provide the PSC that contains fluxes at J, H, and K bands. Suh & Kwon (2011) updated the catalog with SiO maser sources for O-rich AGB stars and additional sources for C-rich AGB stars. The updated catalog contains 3 003 O-rich and 1 168 C-rich AGB stars with their IRAS colors and has the largest confirmed AGB collection so far. So this catalog is most useful entry for the future study of AGB stars.

Far infrared Cavities are the dusty environment in the far infrared region in the interstellar medium. They provide so many informations about new processing stars and previously formed stars. If the cavities are stable then we can say that forming stars and formed stars have longer life. If their distribution of mass follow cosmological principle, they will be stable and have longer life and so on. The infrared astronomical satellite (IRAS) works at 12 μm, 25 μm, 60 μm and 100 μm wavelength band which lie in the infrared and far from infrared region. It is suitable to observe dust particles which absorbs ultraviolet radiation and emits infrared radiation. In this work, all these four bands and specially 60 μm and 100 μm bands are used.

Photographs of the milky way gives strong indications of large scale loop shaped dust & gas and big part of the interstellar medium is in the form of filaments (Brand & Zealey, 1975). These filaments may be related to the loop structures. It is shown that most of the interstellar medium is processed through supernova blast waves and winds of massive stars. It means galactic shells are formed by the supernova explosions and winds of the massive stars. Many examples of dust shells around regions of recent star formation are known in external galaxies. If dust shells extend out of the plane of the galaxy, they will fall back as streamers of material and will subject to Rayleigh Taylor instability (Brand & Zealey, 1975). They further suggested that diffusion process of dust to the cores of these streamers may preserve filamentary structure in the galactic plane.

There is a catalogue of far-infrared loops in the galaxy where Kiss et al. (2004) worked about features of far-infrared loops in the second galactic quadrant and catalogued 145 loops with investigation about their morphological and physical characteristics. Könyves et al. (2007) continued their work in the first, second and third galactic quadrants where 317 loops are catalogued. This combined work in all four galactic quadrants provide the catalogue of far- infrared loops in the galaxy. In their work, they used 60 μm and 100 μm ISSA (IRAS Sky Survey Atlas) plates in the $1^\circ \leq D \leq 40^\circ$ diameter range. In all sky survey, there are 462 far-infrared loops. Out of them for 137 loops, distances are provided in the catalogue which are useful to calculate dust mass of the cavity. In the catalogue name of the object is written as GIRLs which is stand as galactic infrared loops. There is a noticeable increase in loops towards the major spiral arms and the Perseus arms (Könyves et al., 2007). The database provided in the catalogue is a great opportunity to study large scale structure of the ISM in the galactic neighborhood of the

sun.

There is another on-line catalogue about galactic post-AGB stars referred as Torun catalogue developed by Szczerba et al. (2007). The catalogue contains 326 very likely post-AGB stars and 107 possible post-AGB star candidates. For very likely post-AGB stars, the catalog provides optical and infrared photometry, infrared spectroscopy and spectral types, etc. Later, the catalogue has been revised by the same author in 2010. In the newly revised catalogue, there are 391 very likely and 83 possible post-AGB stars. From this catalogue, we selected two far infrared cavities around two post-AGB star.

Jha et al. (2017) presented dust color temperature, dust mass and inclination angle of four far infrared loops namely G007+18, G143+07, G214-01 and G323-02 which are located within 1° from nearby pulsars PSR J1720-1633, PSR J0406+6138, PSR J0652-0142 and PSR J1535-5848, respectively. They found the dust color temperature of the core region which lie in the range (19.4 ± 1.2) K to (25.3 ± 1.7) K, whereas the range increased to 33 ± 2) K to (47 ± 3) K for the outer region. They measured average dust mass of each pixel of the four loops which lie in the range 2.96×10^{26} kg to 1822.2×10^{26} kg. The dust color temperature and dust mass distribution maps show that the low temperature region has greater density as expected. We have used similar method for calculation of dust color temperature and dust mass.

Again Jha & Aryal (2018) measured dust color temperature of two far infrared cavities lying nearly at the galactic plane ($-3°$) using IRIS and AKARI maps where IRIS is used at 60 μm and 100 μm where as AKARI is used at 90 μm and 140 μm. From IRIS, the measured dust color temperature of the two cavities are found to lie in the range (23.4 ± 1.3) K to (24.1 ± 1.4) K with an offset of only 0.7 K and (22.2 ± 1.2) K to (24.6 ± 1.3) K, with an offset of about 2.4 K respectively. Similarly from AKARI, the measured dust color temperature of the cavities lie in the range (26.0 ± 1.5) K to (28.1 ± 1.6) K, with an offset of 2.1 K and (25.4 ± 1.4) K to (29.7 ± 1.7) K, with a larger offset of 4.3 K respectively. At longer wavelengths (AKARI) dust color temperature is found larger than in the shorter wavelength (IRIS) region. We used similar method for calculation of dust color temperature but used 60 μm and 100 μm IRAS map.

1.2 Rational of the Study

Following two facts are the reasons or intentions that cause a particular actions to carry out this study:

1. The behavior of materials at low temperature is not well understood. The understanding of dynamics and kinematics of those materials in the sky lead modern science to know about the action of materials at low temperature.

2. The data taken from telescopes are obviously not the continuous and systematic data. Though those information keeps a record like fossils of the evolution of the nature. We believe to understand a few aspects of evolution in which a systematic behavior is seen. This is possible when we apply experimentally verified physical theory.

1.3 Objectives

Objectives are divided into two categories.

1.3.1 General Objectives

Following are the general objectives:

1. To perform a systematic search for new far infrared cavities at 60 μm and 100 μm IRAS Survey around AGB stars.
2. To study the physical properties of the far infrared cavities and discuss dynamics and kinematics of dust in their core region.

1.3.2 Specific Objectives

Following are the specific objectives:

1. To calculate and analyze dust color temperature, dust mass, visual extinction and size of the cavities.
2. To study and interpret the variation of Planck function and dust color temperature along the extension and compression of the cavities.
3. To study far infrared spectral distributions of cavities and compare with other published similar cavities.

1.4 Conceptual Research Hypothesis

They are as follows:

1. The ISM contains large number of far infrared cavities formed by the wind emitted from the AGB stars.
2. These cavities might not be in the thermal equilibrium with their surroundings.

3. The evolution of these cavities might influence the physical properties of the ISM and hence the star formation rate.

This thesis is organized as follows: a literature review regarding the statement of the problem is described in the chapter 2. The selection procedure of 18 far infrared cavities and the method of data reduction, calculation and analysis is given in the chapter 3. We present result and discussion in the chapter 4. Finally, we summarize conclusions in chapter 5 and summary in chapter 6.

CHAPTER 2

2. LITERATURE REVIEW

2.1 Interstellar Medium (ISM)

The space between the stars is not empty which contains matter and radiation. Thus the space between the star systems in a galaxy is called interstellar medium. It contains gas and dust in the form of both individual clouds and of a diffuse medium. Typically interstellar space contains about one gas atom per cubic centimeter and 100 dust particles per cubic kilometer. Cloud mainly contains neutral hydrogen (HI), ionized hydrogen (HII) and molecular hydrogen (H_2). Matter includes gas in ionic, atomic and molecular form, as well as dust and cosmic rays. ISM is diffuse so it doesn't radiate like a black body so continuous spectrum like stars cannot be seen.

At present, the most important observations of the interstellar medium are made at radio and infrared wavelengths, since the peak of the emission often lies at these wavelengths. But many forms of interstellar matter (such as solid bodies with diameters larger than 1mm) would be almost impossible to detect on the basis of their emission or absorption. An upper limit on the total mass of the interstellar matter, regardless of its form, can be derived on the basis of its gravitational effects. This is the Oort limit. The galactic gravitational field is determined by the distribution of matter. The interstellar medium (ISM) plays a central role in the evolution of galaxies. The formation of new stars slowly consumes the ISM, locking it up for millions to billions of year while stars, as they age, return much of their mass increased in metallicity, back to the ISM. Stars also inject radiative and kinetic energy into the ISM and this controls the physical characteristics (density, temperature and pressure) as well as the dynamics of the gas as revealed in observed spectra.

The interstellar medium (ISM) is the dust and gas between the stars. The interstellar medium is seen as the dark dust lanes in the Milky Way (or in other galaxies), or by its effects on starlight: reddening and extinction. It is also observed more directly as reflection or emission nebulae. Approximately 20% of the Galaxy's mass is ISM. The ISM absorbs visible light, but at the same time emits radio waves or infrared radiation.

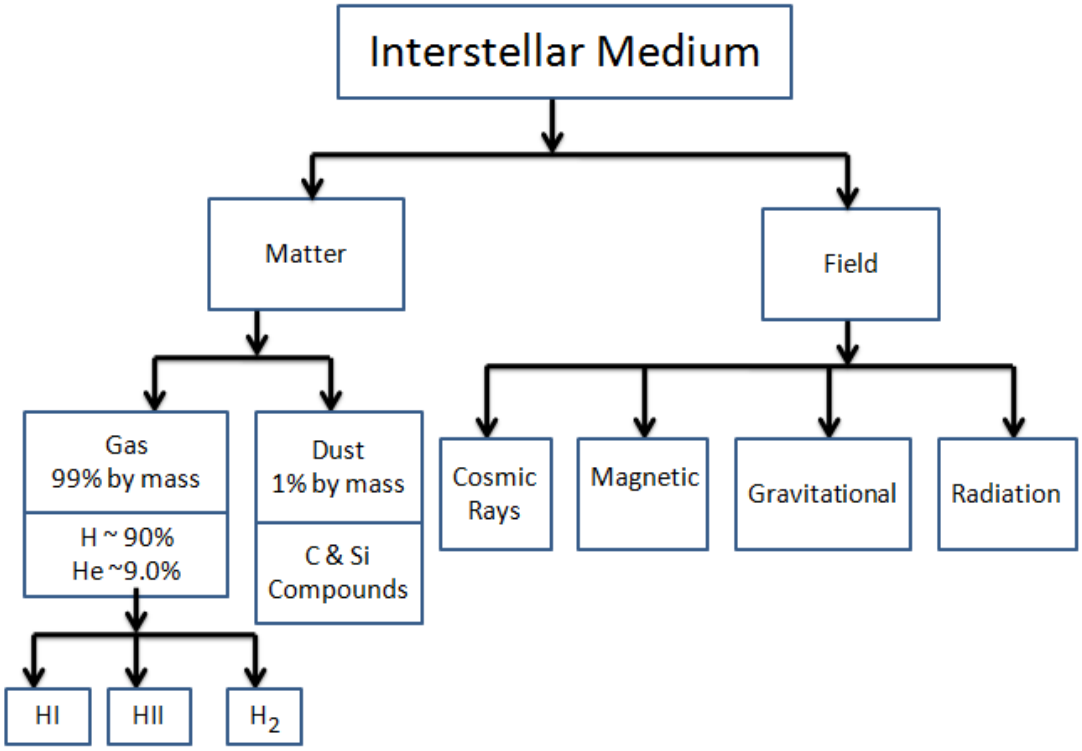

Figure 1: Flow chart of the ISM. ISM mainly contains matter and fields. Matter contains gas and dust where as fields contain cosmic rays, magnetic, gravitational and radiation (Karttunen et al., 2007).

Table 1: Four components of the interstellar medium where component, temperature, density and main constituents are shown in first, second, third and fourth column respectively (Cox, 2005)).

Component	Temperature [K]	Density [Atoms/cm^3]	Main Constituents
HI Clouds	50 - 150	1 - 1000	Neutral H, other atoms ionized
Inter Cloud Medium [HII]	10^3 - 10^4	0.01	Partially ionized H, other atoms fully ionized
Coronal Gas	10^5- 10^6	10^{-4} - 10^{-3}	All atoms highly ionized H
Molecular Clouds	20 - 50	10^3 - 10^5	Neutral gas: dust and molecules

So, while we can not make an accurate map of the distant Galaxy in visible light, we can see distant pockets of interstellar dust and gas quite easily. 99% of the ISM is gas, and only 1% of the mass is dust. Detail composition of the interstellar medium is shown in Figure 1.

Matter is the main component of the ISM which mainly contains gas and dust in neutral and ionized form.Its main four components are shown on Table 1.

2.2 Interstellar Dust

Infrared light does not get absorbed as easily as optical light, so infrared observations peer farther into the plane of the Milky Way than optical telescopes. Shorter wavelengths

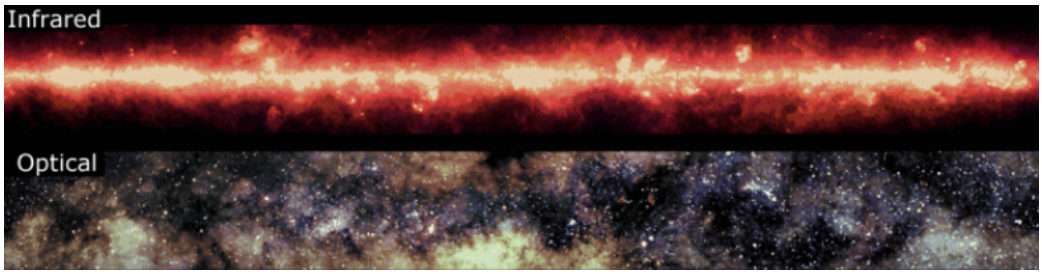

Figure 2: Milky Way in optical and infrared light. (Source: https://www.google.com/url?sa).

of infrared light reveal stars in the Milky Way while longer wavelengths show interstellar dust warmed by starlight. In Figure 2, there is a bright horizontal band in the infrared image where as the optical image looks dark. Since center of our galaxy contains numerous hidden clouds of gas and dust. Optical radiation is absorbed by gas and dust but infrared radiation can penetrate through them as a result image of our galaxy through infrared telescope is bright than optical telescope. The first evidence for the existence of interstellar dust was noticed during 1930s. Before that, it had been generally thought that space is completely transparent and light can propagate indefinitely without extinction (Trumpler, 1930a). There are three ways to detect the interstellar dust: infrared radiation from the warmed particles, extinction of visible light (dark patches), or reflection nebulae (Tielens, 2005).

(1) Dust is warmed by UV radiation, and therefore emits a blackbody spectrum that peaks in the infrared. Figure 2 shows the Milky Way Galaxy in the optical and the infrared. Dust emits in the infrared but blocks visible light. Therefore, the infrared image is bright whereas the optical image is dark, and vice versa.

(2) Dark nebulae: the dark patches in the Milky Way and dark clouds observed in other places (such as the Horsehead nebula). These dark nebulae are often called dust clouds even though they consist mostly of gas. These clouds range in size from less than 1 pc to more than 10 pc. Most nebulae absorb 75% of the starlight from background stars-a few absorb more, nearly 95% in some cases.

(3) Reflection nebulae: these shine by scattered starlight, in much the same way that the blue sky shines by scattered sunlight. These nebulae are always bluish in color, and so are easily distinguished from HII regions that are always reddish in color. The line spectrum of these nebulae resembles the spectrum of the stars whose light they scatter.

Diffuse interstellar dust is analogous to the diffuse interstellar gas. This dust is difficult to detect, and can only be found by looking at very distant clusters and comparing them to nearby clusters. The distant clusters will appear redder and fainter than they should at their distances. This is the result of two phenomena caused by the diffuse interstellar

dust: extinction and reddening (Tielens, 2005).

Extinction: The Milky Way is about 60 000 pc across, so most of the starlight from distant stars has been extincted before reaching the Earth. This extinction is caused by both scattering and absorption. Determining which effect is more important is impossible without a detailed knowledge of both the composition and the size of the dust grains. As most of the interstellar dust is in the plane of the Milky Way, we can only see the galaxies that are "above" or "below" the Milky Way. On average, the Milky Way is about 2 000 pc thick. It will be discussed in detail in next section.

Reddening: Dust scatters blue light more effectively than red light. As a result stars appear redder than they would if there were no dust in the line of sight. From a distance of 3 000 pc through the disk, only 2.5% of the blue light will reach us, whereas 6% of the red light will get through. The scattering efficiency decreases with decreasing frequency of light. This means that we can see deeply into the Milky Way using radio waves or infrared radiation, but not in ultraviolet radiation.

2.2.1 Interstellar Extinction

Virtually, all the information about a star comes from the electromagnetic radiation emitted by it. Photons from the deeper layers break free and stream outward into interstellar space at the photosphere. Luminosity and temperature at the photosphere are two basic properties of the star. Actually luminosity is the total energy emitted per unit time by the star. One may use the logarithmic quantity M_{V} , the absolute magnitude of the star in the V (for visual) band, a relatively narrow wavelength interval centered on 5500 Å. If we consider F_{V} is the flux received in this band, i.e., the energy in a unit wavelength interval per unit area per unit time. This flux is weaker for objects which are farther away. To measure the intrinsic brightness or absolute brightness of the star, we imagine the star of interest to be located at some fixed distance, conventionally taken to be 10 pc. Then M_{V} is defined as

$$M_{\mathrm{V}} = -2.5 \log F_{\mathrm{V}}(10 \text{ pc}) + m_{\mathrm{VO}} \tag{2.1}$$

where m_{VO} is a constant. By definition, fainter stars have numerically greater magnitudes. Here V band used as one of the standard Johnson-Morgan sequence of filters, which also include ultraviolet (U at 3650 Å) and blue (B at 4400 Å) wavebands.

For an arbitrary wavelength λ, equation (2.1) becomes

$$M_{\lambda} = -2.5 \log F_{\lambda}(10 \text{ pc}) + m_{\lambda \mathrm{O}} \tag{2.2}$$

This equation can further be generalized to cover the case where the star is not located at 10 pc, but is located at an arbitrary distance r. Thus the brightness of a star at a unknown distance r from the star is called apparent magnitude which is a distance-dependent quantity and is written as

$$m_\lambda = -2.5 \log F_\lambda(r) + m_{\lambda \mathrm{O}} \tag{2.3}$$

Since the flux depends as r^{-2}, then apparent and absolute magnitudes are related by

$$m_\lambda = M_\lambda + 5 \log \left(\frac{r}{10 \text{ pc}} \right) \tag{2.4}$$

where the term added to M_λ is the distance modulus. Let us first quantify the wavelength dependence of extinction which is the sum of absorption and scattering. Since the brightness of a star near any wavelength λ is measured either by m_λ or M_λ, its apparent and absolute magnitudes, respectively. Due to presence of dust between the star and the Earth, the relation between these two quantities is changed to

$$m_\lambda = M_\lambda + 5 \log \left(\frac{r}{10 \text{ pc}} \right) + A_\lambda \tag{2.5}$$

where A_λ is called extinction at wavelength λ which is a positive quantity measured in magnitudes. Note that, even at the fiducial distance i.e., 10 pc, the star now has $m_\lambda > M_\lambda$, i.e., apparent magnitude is dimmer than its absolute magnitude. The general tendency of dust to redden distant objects in the optical regime implies that A_λ must diminish with increasing λ (Karttunen et al., 2007).

2.2.2 Interstellar Extinction Curve

Another effect caused by the interstellar medium is the reddening of light: blue light is scattered and absorbed more than red. Detail description and derivation has given by Karttunen et al. (2007). The presence of dust in the interstellar medium was first recognized by its reddening effect on the light from distant stars. Reddening is due to the fact that the amount of extinction becomes larger for shorter wavelengths. Going from red to ultraviolet, the extinction is roughly inversely proportional to wavelength. For this reason the light of distant stars is redder than would be expected on the basis of their spectral class. The spectral class is defined on the basis of the relative strengths of the spectral lines which are not affected by extinction. Therefore color index (B - V) increases. The visual magnitude of a star is given by

$$V = M_\mathrm{V} + 5 \log \frac{r}{10 \text{ pc}} + A_\mathrm{V} \tag{2.6}$$

where M_{V} is the absolute visual magnitude and A_{V} is the extinction in the V pass band. Similarly for blue magnitudes

$$B = M_{\mathrm{B}} + 5\log\frac{r}{10\ \mathrm{pc}} + A_{\mathrm{B}} \tag{2.7}$$

The observed color index is obtained by subtracting equation (2.6) from (2.7).

$$B - V = M_B - M_{\mathrm{V}} + A_{\mathrm{B}} - A_{\mathrm{V}} \tag{2.8}$$

Since $A_{\mathrm{V}} = A_{\mathrm{B}} = 0$ at the surface of the star, so intrinsic color index is equal to M_{B} - M_{V}, thus, we get

$$B - V = (B - V)_0 + A_{\mathrm{B}} - A_{\mathrm{V}} \tag{2.9}$$

$$\text{or} \quad (B - V) - (B - V)_0 = A_{\mathrm{B}} - A_{\mathrm{V}} \tag{2.10}$$

$$\text{or} \quad E_{\mathrm{B\text{-}V}} = A_{\mathrm{B}} - A_{\mathrm{V}}\,, \tag{2.11}$$

where $(B - V)_0 = M_{\mathrm{B}} - M_V$ is the intrinsic color index of the star, A_B and A_V are the total extinctions in the photometric B (4400 Å) and V (5500 Å) bands respectively and $A_{\mathrm{B}} - A_{\mathrm{V}} = E_{\mathrm{B\text{-}V}} = (B - V) - (B - V)_0$ is the color excess. The most popular measure of extinction (reddening) is the color excess. The color excess may be determined even when the total extinction is not known in any of the photometric bands. As a rule, color excess grows with increasing absolute extinction.

When we consider third wave length λ , then equation (2.11) becomes

$$E_{\lambda - V} = A_\lambda - A_{\mathrm{V}} \tag{2.12}$$

Dividing equation (2.12) by (2.11), we get

$$\frac{E_{\lambda - V}}{E_{\mathrm{B\text{-}V}}} = \frac{A_\lambda - A_{\mathrm{V}}}{A_{\mathrm{B}} - A_{\mathrm{V}}} \tag{2.13}$$

$$\text{or} \quad \frac{E_{\lambda - \mathrm{V}}}{E_{\mathrm{B\text{-}V}}} = \frac{A_\lambda}{A_{\mathrm{B}} - A_{\mathrm{V}}} - \frac{A_{\mathrm{V}}}{A_{\mathrm{B}} - A_{\mathrm{V}}} \tag{2.14}$$

$$\text{or} \quad \frac{E_{\lambda - \mathrm{V}}}{E_{\mathrm{B\text{-}V}}} = \frac{A_\lambda}{A_{\mathrm{B}} - A_{\mathrm{V}}} - R\,, \tag{2.15}$$

where R is called the "fiducial ratio" , $E_{\lambda - \mathrm{V}}/E_{\mathrm{B\text{-}V}}$ is called normalized selective extinction and $A_\lambda/(A_{\mathrm{B}} - A_{\mathrm{V}})$ is called normalized total extinction.

Studies of the interstellar medium show that the ratio of the visual extinction A_V to the color excess $(A_{\mathrm{B}} - A_{\mathrm{V}})$ is almost constant for all stars.

$$R = \frac{A_{\mathrm{V}}}{A_{\mathrm{B}} - A_{\mathrm{V}}} \approx 3.1 \tag{2.16}$$

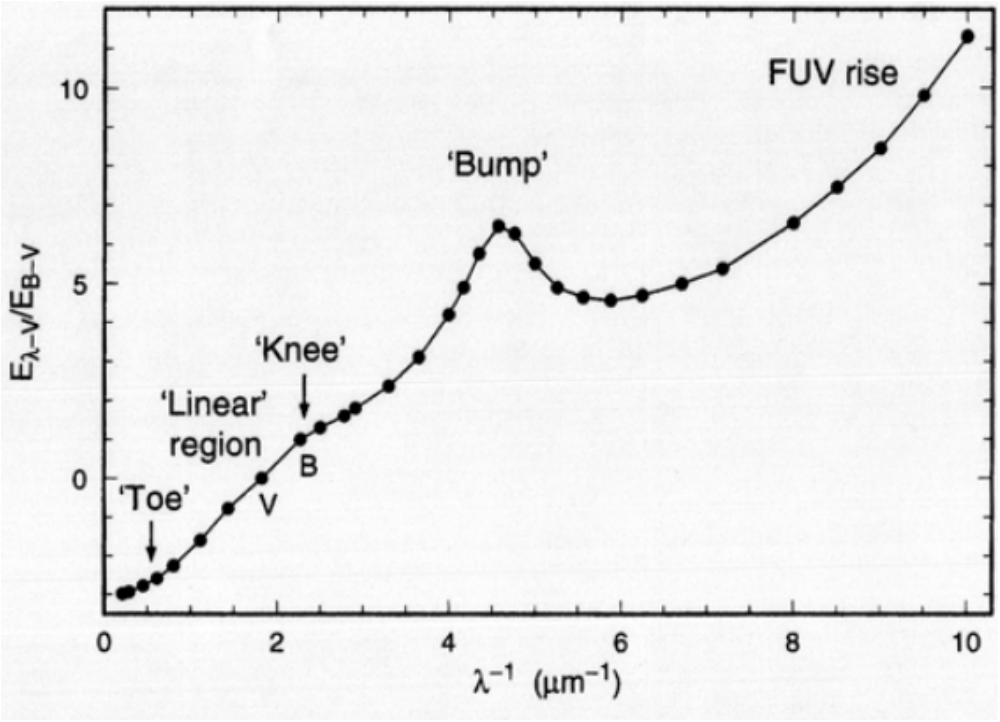

Figure 3: The interstellar extinction curve $E_{\lambda-\mathrm{V}}/E_{\mathrm{B-V}}$ verses λ^{-1} in the spectral range 0 to 10 $(\mu\mathrm{m})^{-1}$. Various features of the curves and positions of the B and V pass bands selected for normalization described in the text are indicated. (Source:http://people.virginia.edu/).

It means visual extinction can be calculated when color excess is known.

When V, A_{V} and M_{V} are known, distance r can be calculated from equation (2.6). Trumpler (1930b) proved that extinction depends on the wavelength approximately as λ^{-1}. This is why extinction curves are still plotted as a function of reciprocal wavelength following Trumpler's rule. Thus a graph between normalized selective extinction $E_{\lambda-\mathrm{V}}/E_{\mathrm{B-V}}$ or normalized total extinction with reciprocal of wavelength λ^{-1} is called interstellar extinction curve. Figure 3 shows a typical interstellar extinction curve for $R = 3.1$. Thus, the interstellar extinction curve separates out into four distinct parts - the infrared, the visible, the 2175 Å bump, and the far-UV rise. Extinction curves vary from region to region but they can (almost) all be parameterized by the total - to - selective extinction ratio, R , over the full wavelength range (0.1 to 2) μm. The value of R depends on the environment traversed by the line of sight. The diffuse ISM is characterized by $R = 3.1$, while dense molecular clouds have values in the range 4 to 6. In the Figure 3, 'toe' region is for far infrared and the linear region up to 'knee' is for the near infrared. Typically, the extinction rises through the IR with a power-law-like (higher order polynomial), rolls over slightly in the optical region ("knee"), shows a prominent feature (maximum extinction) at 2175 Å in the near-UV ("bump"), and has a sometimes steep rise in the far-UV ("fuv rise"). It is interesting that the interstellar extinction curve is found to be similar in all direction of the Milky Way. The microwave, sub-mm and radio waves are not affected by the presence of dust. Similarly gamma ray dissociates

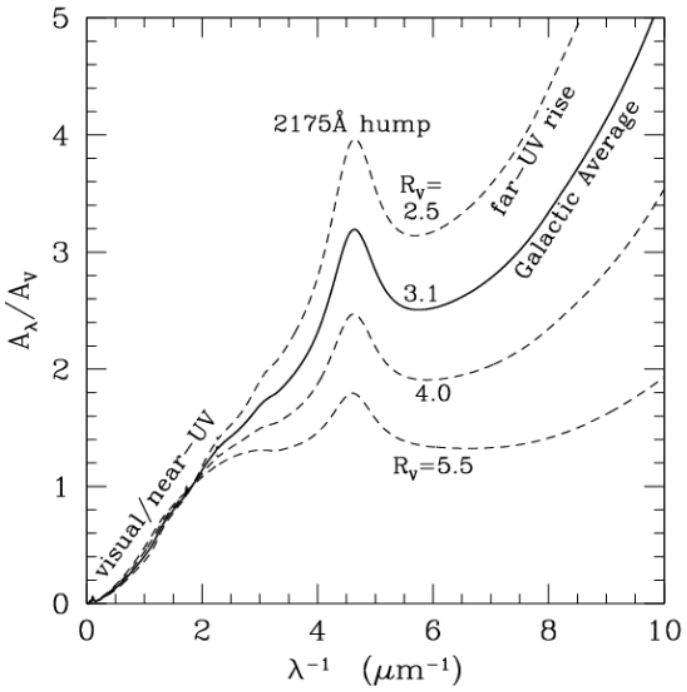

Figure 4: Interstellar extinction curves where observed extinction curves in different environments are compared with the *R*-parameterized curve (Cardelli et al., 1989).

the dust, loses energy but could not be absorbed or scattered by the dust. Structure in the extinction curve can provide important clues to the nature of the absorbing materials. The ultraviolet bump is the most prominent feature of the interstellar extinction curve. In Figure 4, four observed extinction curves are shown as a function of λ^{-1}. These curves show the range in wavelength behavior of the extinction laws in the interstellar medium. They found that extinction curves can be expressed approximately as a one-parameter family that varies linearly with R^{-1}. It means extinction decreases with increase in R. Here R varies from 2.5 to 5.5 where interstellar extinction in the near infrared band is almost similar for all possible R.

The work of Cardelli et al. (1989) provide a link between one measure of dust grain environment and the wavelength dependence of interstellar extinction. They found that the shape of UV extinction curves correlates with the parameter R. Figure 4 shows that extinction curves are very "flat", or "gray", in the UV roll over strongly in the optical and are characterized by large values of R. Steep UV curves remain steep in the optical and are characterized by small values of R.

By studying the peaks of the extinction curve, astrophysicists found that the interstellar dust contains water ice and silicates, and probably graphite as well. The sizes of the grains can be estimated from their scattering properties; usually they are smaller than one micrometre. The strongest scattering is due to grains of about 0.3 μm but smaller particles must also be present. Dust is mainly destroyed in the ISM by strong shock waves in the warm phases of the interstellar medium. Sputtering by impacting gas

Table 2: Properties of components of the interstellar medium. Values are approximate (Palen, 2001).

Type of nebula	Density (g cm^{-3})	Temperature (K)	Typical life time (yrs)	Typical size (pc)	Composition
HII region	10^{-25} - 10^{-17}	10,000	10 million	few - 100	Mostly hydrogen gas
Giant molecular cloud: cool clumps	10^{-20} - 10^{-18}	10	Billions	0.1	Hydrogen, molecular gas, dust
Giant molecular cloud: hot clumps	10^{-25} - 10^{-17}	30 - 100	Millions	0.1 - 3	Hydrogen, molecular gas
Reflection nebula	10^{-25} - 10^{-17}	< 1000	Millions-billions	< 1-10	Dusty gas
Emission nebula	10^{-25} - 10^{-17}	1000 - 10,000	Few thousand-100,000	0.01-a few	Atomic and molecular gas
Dark nebulae	10^{-25} - 10^{-17}	< 1000	Millions-billions	< 1 - 10	Dusty gas
Diffuse interstellar gas	10^{-27}	7,000-10,000	Not applicable	Not applicable	Hydrogen

species and vaporization by high velocity grain grain collisions return grain material to the gas phase. At the same time, shattering by grain grain collisions considerably modifies the grain size distribution (Tielens, 2005).

The Hubble relation can be derived theoretically, if it is assumed that the illumination of a dust cloud is inversely proportional to the square of the distance to the illuminating star, and that the dust clouds are uniformly distributed in space. The theoretical Hubble relation also gives an expression for the constant on the right-hand side, which involves the albedo and the phase function of the grains. The observations of reflection nebulae show that the albedo of interstellar grains must be quite high. It has not yet been possible to obtain its precise numerical value in this way, since the distances between the nebulae and their illuminating stars are not known well enough. One may also consider the surface brightness of dark nebulae that are not close enough to a star to be visible as reflection nebulae. These nebulae will still reflect the diffuse galactic light from all the stars in the Milky Way. Calculations show that if the dust grains have a large albedo, then the reflected diffuse light should be bright enough to be observable, and it has indeed been observed. Thus the dark nebulae are not totally dark. The diffuse galactic light constitutes about 20-30% of the total brightness of the Milky Way.

2.3 Use of IRAS Emission Maps to Estimate Dust Color Temperature and Visual Extinction

This section is basically concerned about the development of the methods for the calculation of dust color temperature and extinction. Dust color temperature is the equivalent

temperature of dust due to its color or wavelength and extinction is the sum of absorption and scattering.

Beichman, Neugebauer, et al. (1988) described about the IRAS mission established in 1975 and launched in 1983. The mission of the project was to conduct a sensitive and unbiased survey of the sky in four wavelength bands 12 μm, 25 μm, 60 μm and 100 μm. Langer et al. (1989) carried out a study of the infrared and carbon monoxide emission from the molecular cloud Barbard (B5) to investigate the correlations among dust column density, intensities of the CO isotope and visual extinction. They measured grain temperature using the ratio of 60 μm and 100 μm intensity by noting that for optically thin emission from grains at a single equilibrium temperature. The grain color temperature observed towards B5 at 12 μm and 25 μm data was (300 to 350) K but for 60 μm and 100 μm data, it was (25 to 28) K. The grain color temperature seen in B5 at 60 μm and 100 μm data are somewhat similar with those calculated for large graphite grains in equilibrium with the interstellar radiation field (ISRF) which is ~(20 to 28) K (Draine & Lee, 1984). The presence of emission at 12 μm and 25 μm from the cloud cannot be understood within the context of emission from conventional interstellar grains. A theory developed by Puget et al. (1985) predicts that the emission from the small, stochastically heated grains dominates at the shorter wavelengths and may enhance the 60 μm emission from the grains as well.

Dust color temperature and extinction can be calculated by using IRAS 60 μm and 100 μm flux densities as done previously by Wood et al. (1994). They investigated ~ 100 nearby molecular clouds using the extensive, all-sky database of IRAS. The clouds cover a wide range of physical properties including visual extinction, size, mass, degree of isolation, homogeneity and morphology. IRAS 100 μm and 60 μm co-added images were used to calculate the 100 μm optical depth of dust in the clouds. In the work, they calculated dust color temperature, $T_{\rm d}$ at each pixel in an image assuming that the observed ratio of 60 μm and 100 μm emission is due to blackbody radiation from dust grains at temperature $T_{\rm d}$, modified by power law emissivity spectral index. The calculation of temperature and extinction depend on three parameters where two constants that determine the spectral emissivity index and the conversion from 100 μm optical depth to visual extinction. Dust color temperature ($T_{\rm d}$) in each pixel of a FIR image can be obtained by assuming that the dust in a single beam is isothermal and that the observed ratio of 60 μm and 100 μm emission is due to black body radiation from dust grains at $T_{\rm d}$, so from modified power law of spectral emissivity index, the flux density of emission from dust grains at a wavelength λ_i, is given by

$$F_i = \frac{2hc}{\lambda_i^3}\left[\frac{1}{e^{hc/\lambda_i kT}-1}\right] N_{\rm d}\alpha\lambda_i^{-\beta}\Omega_i\,, \tag{2.17}$$

where $N_{\rm d}$ is column density of dust grains, α is a proportionality constant which relates the flux density and optical depth of the dust, β is spectral emissivity index and Ω_i is solid angle at λ_i by the detector.

Derivations of dust color temperature and column density from IRAS data is based on the assumption that the dust along each line of sight is in thermal equilibrium. Dust models of Desert et al. (1990) show that emission at 60 μm and 100 μm have contributions by big dust grains and very small dust grains. Very small dust grains are not in thermal equilibrium and emit mostly in the 60 μm band, while the big grain dusts are the primary contributors at 100 microns and longer. In the work of Wood et al. (1994), following assumptions and errors are assumed:

(i) At 60 μm and 100 μm, the dust is optically thin ($\tau_d \ll 1$). It can be verified from interstellar extinction curve which has mentioned by Draine & Lee (1984).

(ii) 60 μm and 100 μm beams subtend the same solid angle i.e., $\Omega_{60} \approx \Omega_{100}$. It is due to co-vibrational transition.

(iii) Dust emissivity is proportional to a power law [$\tau_{\rm d} \sim \lambda^{-\beta}$] with index $\beta = 1$. Hildebrand (1983) concluded that the dust emissivity power-law index is ~ 1 for 50 μm $\leq \lambda \leq$ 250 μm, and the index is ≥ 2 for $\lambda \sim$ 1000 μm. In addition, Wood et al. (1994) performed tests with $\beta = 2$ and found that the results are not significantly affected and conclude that this assumption is valid. It is obviously satisfied by Planck law of black body radiation.

(iv) The dust in the IRAS beam is at a single temperature. It means they are in thermal equilibrium locally.

(v) Zodiacal light can be removed by subtracting a linear gradient from the image.

To describe the observed inverse relationship between temperature and the emissivity spectral index (β), we use Dupac et al. (2003) equation

$$\beta = \frac{1}{\delta + \omega T_{\rm d}}, \tag{2.18}$$

where δ and ω are parameters. ω has dimension of inverse temperature. Since R is the ratio between flux densities at 60 μm and 100 μm, so we get

$$R = \left(\frac{60}{100}\right)^{-(\beta+3)} \left(\frac{e^{144/T_{\rm d}} - 1}{e^{240/T_{\rm d}} - 1}\right) \left(\frac{\Omega_{60}}{\Omega_{100}}\right) \tag{2.19}$$

Since emission is optically thin at 60 μm and 100 μm so $\Omega_{60} \approx \Omega_{100}$ thus above equation

reduces to

$$R = \left(\frac{60}{100}\right)^{-(\beta+3)} \left(\frac{e^{144/T_\mathrm{d}} - 1}{e^{240/T_\mathrm{d}} - 1}\right) \tag{2.20}$$

When β is known, T_d can be easily calculated but β depends on dust grain properties such as size, composition and compactness. For a perfect blackbody, $\beta = 0$, for amorphous layer lattice matter, $\beta \sim 1$ and for metals and crystalline dielectrics, $\beta \sim 2$ which is used in our calculation.

For smaller value of T_d, 1 can be neglected from both numerator and denominator of equation (2.20) so that the equation reduces to

$$R = (0.6)^{-(\beta+3)} \left(\frac{e^{144/T_\mathrm{d}}}{e^{240/T_\mathrm{d}}}\right)$$

$$\text{or} \quad R(0.6)^{(\beta+3)} = e^{-96/T_\mathrm{d}}$$

Taking natural logarithm on both sides, we get

$$\ln[R \times (0.6)^{(\beta+3)}] = \frac{-96}{T_\mathrm{d}} \tag{2.21}$$

$$\text{or} \quad T_\mathrm{d} = \frac{-96}{\ln[R \times (0.6)^{(\beta+3)}]} \tag{2.22}$$

This equation (2.22) is used to calculate dust color temperature or dust grain temperature. Similarly to calculate dust color temperature at 25 μm and 60 μm wave length region, equation (2.22) reduces to

$$T_\mathrm{d} = \frac{-623.7}{\ln[R \times (0.48)^{(\beta+3)}]}, \quad \text{where} \quad R = \frac{F(12\ \mu\mathrm{m})}{F(25\ \mu\mathrm{m})} \tag{2.23}$$

and

$$T_\mathrm{d} = \frac{-335.6}{\ln[R \times (0.42)^{(\beta+3)}]}, \quad \text{where} \quad R = \frac{F(25\ \mu\mathrm{m})}{F(60\ \mu\mathrm{m})} \tag{2.24}$$

respectively. After calculation of dust color temperature, dust optical depth at 100 μm can be calculated by using the formula

$$\tau_{100} = \frac{F_\lambda(100\ \mu\mathrm{m})}{B_\lambda(100\ \mu\mathrm{m}, T_\mathrm{d})}, \quad \text{where} \quad B(\lambda, T) = \frac{2hc}{\lambda^3}\left[\frac{1}{e^{hc/\lambda kT} - 1}\right] \tag{2.25}$$

is the Planck function and $F_\lambda(100\ \mu\mathrm{m})$ is the flux density at 100 μm. Now, optical depth at 100 μm can them be converted to V-band extinction,

$$A_v = X\tau_{100}, \tag{2.26}$$

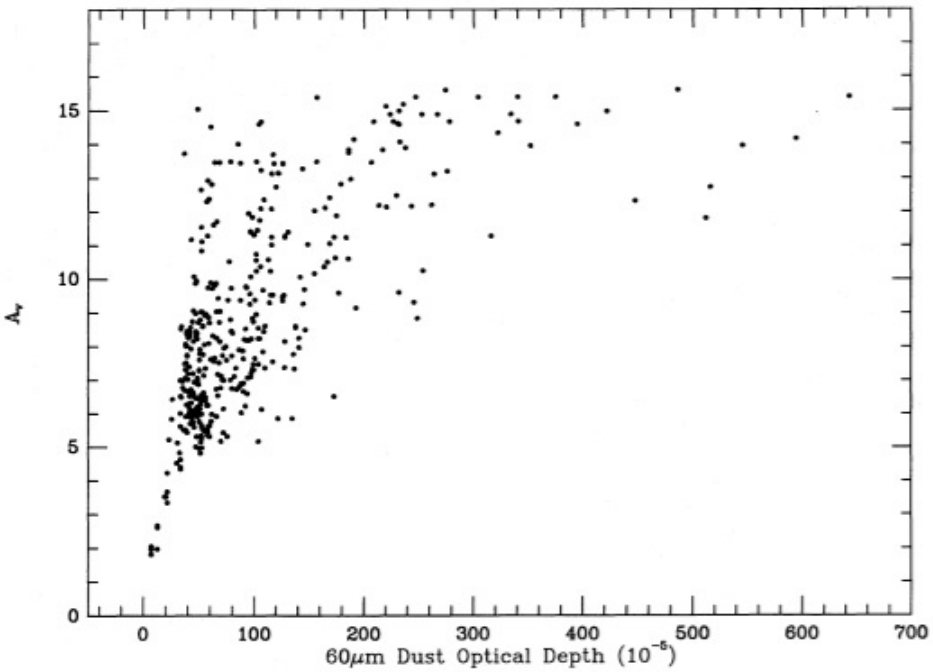

Figure 5: 60 μm optical depth verses visual extinction, determined from calibrated star counts at kron N-band.

where X is a parameter which converts the thermal emission properties of dust to its optical absorption qualities. τ_{100} can be converted to A_V by using method of Jarrett et al. (1989) where they have plotted a scattered graph between optical depth at 60 μm and visual extinction A_V. Assuming optically thin emission at 60 μm and 100 μm, Wood et al. (1994) multiplied the Jarrette et al. (1989) τ_{60} values by 100/60 to convert it into τ_{100}. Thus, the final empirical formula by Wood et al. (1994) for τ_{100} is

$$A_V(\text{mag}) = 15.078 \left[1 - e^{-\tau_{100}/641.3}\right] \tag{2.27}$$

Figure 5 is a graph of Jarrette et al. (1989) plotted between 60 μm optical depth verses visual extinction which showed a considerable scatter for $A_V > 10$ mag. In fact, using equation (2.27), maximum A_V possible is 15.078 mag (obtained from the graph) when clearly some clouds have much greater peak A_V-values.

An empirical method for determining the dust color temperature and the optical depth of dust using 60 and 100 micron bands from IRAS is presented in Nagata et al. (2002), but this method has been calibrated for galaxies and not for molecular cloud. Lagache et al. (1998) in their FIR study of interstellar cold dust in the galaxy found that there are at least two temperature components to the dust population They found that the warmer component, associated with diffuse dust, has a temperature around 17.5 K, while the colder component, associated with dense regions in the ISM, has a temperature around 15 K. Kramer et al. (2003) determined dust color temperature of cloud by using the ratio of flux densities per beam at 850 μm and 450 μm which are optically thin up to very

high column densities. In the derivation, dust color temperature distribution over the surface of the cloud, they assumed $\beta = 2$ as has generally been found for dust grains in molecular clouds (Ward-Thompson et al., 2002).

2.4 Estimation of Dust Mass Under IRAS Survey

Dust mass is another important dust property which is useful to analysis about cavity structure as a result so many informations about the star and its formation can be achieved. Since the longer wavelength measurements give us more precise dust masses due to the characteristics of the Planck curve, the far infrared emission which is used for the derivation of the dust mass is measured from the 100 μm IRAS images. The dust masses are estimated from the IR flux densities (Hildebrand, 1983). In order to estimate the dust masses from the infrared flux densities at 100 μm, following the calculation of Young et al. (1993), we need the background corrected value of flux density and convert it to the absolute flux density. The background correction is done by subtracting the average flux emitted by the external sources other than the object of interest.

Because of the relatively weak temperature dependence of emission from grains at frequencies such that $h\nu/kT \leq 1$, observations at sub millimeter wavelengths are particularly useful for estimating total masses of radiating dust clouds (Hildebrand et al., 1977). The determination of dust mass at a known distance is based on the flux density $F(\nu)$, dust temperature (T), grain emissivity $Q(\nu)$ and size of the grains (a). According to Hildebrand (1983), the flux density at frequency ν from an optically thin cloud at distance D containing N spherical dust grains each of radius a is given by

$$F_\nu = NB(\nu, T)Q(\nu)\frac{\sigma}{D^2} \tag{2.28}$$

where $\sigma = \pi a^2$ is the cross-section area of each dust grain, $Q(\nu)$ = grain emissivity and

$$B(\nu, T) = \frac{2h\nu^3}{c^2}\left[\frac{1}{e^{h\nu/kT} - 1}\right] \tag{2.29}$$

is Planck function. Here h is Planck constant, c is velocity of light, ν is frequency at which emission is observed and T is average temperature of the region.

$$F_\nu = NB(\nu, T)Q(\nu)\frac{\pi a^2}{D^2} \tag{2.30}$$

If v is volume of an individual grain, then total volume is written as

$$V = N \cdot v \tag{2.31}$$

Substituting the value of N from equation (2.30) to (2.31) equation, we get

$$V = \frac{F_\nu}{B(\nu,T)} \frac{D^2}{Q(\nu)} \frac{v}{\pi a^2} \tag{2.32}$$

If ρ is grain density then dust mass is written as

$$M_\mathrm{d} = V \cdot \rho = \frac{F_\nu}{B(\nu,T)} \frac{D^2}{Q(\nu)} \frac{v\rho}{\pi a^2} \tag{2.33}$$

$$\text{or} \quad M_\mathrm{d} = \frac{F_\nu}{B(\nu,T)} \frac{D^2}{3Q(\nu)} 4a\rho \tag{2.34}$$

[$\because$ $v = (4/3)\pi a^3$ is volume of a sphere]

$$M_\mathrm{d} = \frac{4a\rho}{3Q_(\nu)} \frac{F(\nu)D^2}{B(\nu,T)} \tag{2.35}$$

The greatest uncertainty lies in the quantity $\rho a/Q(\nu)$. For its calculation, different physicists have done sufficient work. Knacke & Thomson (1973) had calculated $Q(\nu)$ for silicate spheres using optical constants measured for lunar silicates. Aannestad (1975) had extended these calculations to include terrestrial silicates and to allow for the possibility that the silicate cores may have ice mantles. Both sets of calculations gave values of ρa/Q(ν) in the range (1 to 10) g cm^{-2} for $\lambda \approx 500$ μm. Calculations for graphite Werner & Salpeter (1969) gave a value of ρa/Q(ν) about 100 times larger. Hoyle & Wickramasinghe (1967) had suggested the possibility that $Q(\nu)$ may be greatly enhanced by impurities with resonances at sub millimeter wavelengths, but, as Purcell (1969) had shown, an upper limit may be placed on the far-infrared emissivity by applying the Kramers-Kronig relation. Aannestad (1975) had performed such a calculation for silicates under the assumption that the far-infrared emissivity is proportional to λ^{-1} between 40 and 1000. Since data indicates a steeper wavelength dependence for $Q(\nu)$, calculations were repeated by assuming that $Q(\nu)$ is proportional to λ^{-2} for $\lambda > 40$ μm. The resulting maximum value for Q gives a minimum value for $\rho a/Q(\nu)$ of 0.1 g cm^{-2}. For the following discussion, they had adopted the value 1 g cm^{-2} for $\rho a/Q(\nu)$ at 500 μm with $Q(\nu) \sim \lambda^{-2}$ (Hildebrand et al., 1977). According to Young et al. (1993), value of certain parameters for 100 μm emitter are as follows:

$$\begin{aligned}
\text{Weighed grain size } (a) &= 0.1 \ \mu\text{m} \\
\text{Grain density } (\rho) &= 3000 \text{ kg m}^{-3} \\
\text{Grain emissivity } [Q(\nu)] &= 0.0010 \text{ for } 100 \ \mu\text{m} \\
\text{Flux density } (S_\nu) &= f \times \text{MJy/sr} \times 5.288 \times 10^{-9}
\end{aligned}$$

Here, 1 MJy/Sr $= 1 \times 10^{-20}$ kg s^{-2} and f = relative flux density measured from the

IRAS image (Beichman, Neugebauer, et al., 1988).

Thus for 100 μm wavelength, equation (2.35) becomes

$$M_{\rm d} = 0.4 \left[\frac{F(\nu) D^2}{B(\nu, T)} \right] \tag{2.36}$$

which is the required expression for dust mass.

Hildebrand (1983) showed that for spherical dust grains

$$M_{\rm d} = \frac{4a\rho}{3Q_(\nu)} \frac{F(\nu) D^2}{B(\nu, T)} \frac{M_{\rm gas}}{M_{\rm dust}}, \tag{2.37}$$

where

$M_{\rm shell}$ = mass of the resolved portion of the dust shell,
$F(\nu)$ = flux density at 100 μm from the resolved region,
$B(\nu, T)$ = Planck's function at frequency ν and temperature T,
D = distance to the star,
a = radius of a dust grain,
ρ = density of the dust material, here assumed to be 3 g cm^{-3},
Q_ν = emissivity of the dust at frequency ν,
$M_{\rm gas}/M_{\rm dust}$ = gas to dust mass ratio, here assumed to be 100.

Wood et al. (1994) have measured dust mass and mass of gas so that gas to dust mass ratio also found ~ 1900 which is quite different than Hildebrand (1983). Other authors (Langer et al., 1989; Snell et al., 1989; Jarrett et al., 1989) have accepted the Hildebrand (1983) result that the gas-to-dust ratio is ~ 100. Wood et al. (1994) concluded that if only ~ 5% of the dust is detected in IRAS's 100 μm band, their result will be acceptable. It is remarkable that even though they saw only ~ 5% of the dust mass in a cloud.

2.5 Asymptotic Giant Branch (AGB) Star

2.5.1 Introduction

All low and intermediate mass stars of masses between ≈ 0.8 M$_\odot$ and 8 M$_\odot$ will end their life on the asymptotic giant branch stars. AGB stars are the final nuclear burning evolution stage of low and intermediate mass stars and is characterized by nuclear burning of hydrogen and helium in thin shells on top of electron-degenerate core of carbon and oxygen. This stage is characterized by low surface effective temperatures (~2000 K to

Table 3: Typical global properties of AGB stars (Habing & Olofsson, 2003).

Parameter	Value Range
Mass, M	$(0.8 - 8)$ $M_\odot$
Radius, R	$(200 - 600)$ $R_\odot$, $(1 - 3)$ AU
Temperature, $T_{\rm eff}$	$(2500 - 3500)$ K
Luminosity, $M_{\rm bol}$ (L)	$(-3.6$ to $-7.1)$ mag, $(10^3 - 10^4)$ $L_\odot$
Mass loss rate,$\dot{M}$	$(10^{-8} - 10^{-4})$ $M_\odot$ yr^{-1}
Variability period, P	$(30 - 2800)$ days
AGB time scale, $\tau_{\rm agb}$	$(10^5 - 5 \times 10^6)$ yr

3500 K), high luminosity (∼1000 $L_\odot$ to 10,000 $L_\odot$), intense mass loss (from 10^{-7} to 10^{-4} $M_\odot$ yr^{-1}) and a slow dust-driven wind (Habing, 1996). AGB stars are considered the primary source of dust in the interstellar medium (ISM) (Habing & Olofsson, 2003; Herwig, 2005).

Most AGB stars are identified as long-period variables (LPVs) with large amplitude pulsation. The strong pulsation produces shock waves which extend the outer layer of the AGB star for better condition of dust formation (Jones et al. (1981). The main site of dust formation is believed to be the cool envelopes around AGB stars and the envelopes are chemically fresh because of the strong binding force of CO molecules. The radiation pressure produced on newly formed dust grain may drive dusty stellar winds with high mass loss rates of (10^{-6} to 10^{-4}) $M_\odot$ yr^{-1} (Bowen, 1988b). Due to such dusty stellar winds and evolution of the central during AGB phase, cool and slowly expanding (10 km/s to 30 km/s) dust envelope are formed around the AGB stars. Furthermore, AGB stars are characterized by dynamical processes such as pulsation, shock wave, dust formation and mass loss rate. The spectral features are significantly different for stars with Oxygen - rich and Carbon -rich atmospheres.

During the evolution of AGB, the stars also evolve chemically, starting with oxygen-rich atmospheres and Helium burning forms ^{12}C, which is dredged up to the stellar surface by strong convection currents in the mantle so that carbon is injected into the stellar atmosphere. The stability of the CO molecule in the stellar atmosphere means that the carbon-to-oxygen ratio (C/O) which controls the chemistry around the star. Therefore AGB stars can either be oxygen-rich or carbon-rich depending on their ratio. For the O-rich AGB stars C/O can vary from approximately (C/O $\approx$ 0.4) to just less than unity, for C-rich stars, the ratio C/O is greater than unity. Other nuclear processes (e.g. the s-process) also occur in the He- and H-burning shells of AGB stars where other new elements are also dredged-up and enrich the dust formation region.

Certain known typical global properties of AGB stars are shown on Table 3.

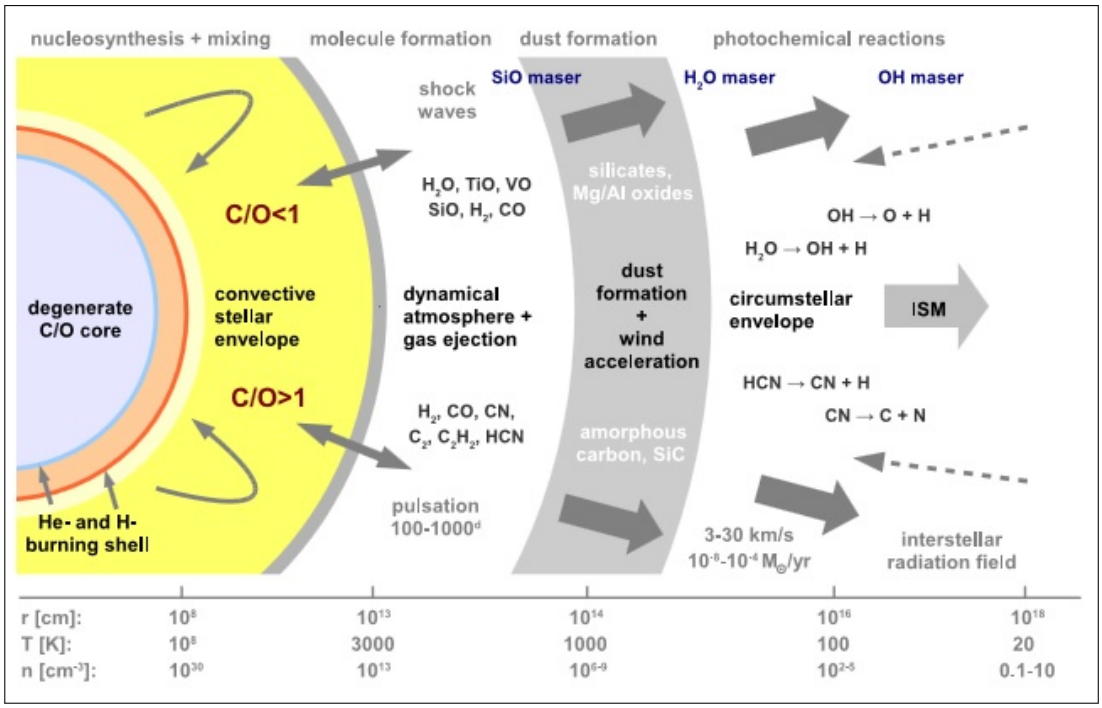

Figure 6: A schematic overview of an AGB star from the core, out to the circumstellar envelope. The top half represents an oxygen-rich chemistry and the bottom half represents a carbon-rich chemistry. (source: http://www.univie.ac.at/agb/).

2.5.2 AGB Star Structure

AGB stars are very complex objects characterized by different processes which take place at different locations within and outside of the star. Actually, there are mainly four parts which are recognized in the structure of an AGB star from its center to the outermost region. They are: degenerate dense core, convective stellar envelope, dynamical atmosphere or stellar atmosphere and circumstellar envelope.

Degenerate dense core is small and very hot with temperature up to $\sim 10^8$ K where heavy elements are produced by s-process nucleosynthesis. Convective stellar envelope is large, less dense, hot with temperature $\sim$ 3000 K, where nucleosynthesis products are brought to the surface. Dynamical atmosphere is tenuous and warm with temperature $\sim$ 1000 K where molecules and dust formation takes place and circumstellar envelope is large, extended and cool envelope where molecule destruction as well as formation takes place and the dust-driven stellar wind will move outwards at a typical speed of a few km/s. Outside the circumstellar envelope, there is ISM where ionization takes place and interstellar radiation field is acting inward.

Figure 6 is the schemetic structure of an AGB star. At the bottom of the figure, three different scales for distance, temperature and density are given with origin from the center of the AGB star. Certain known values such as radius of sun, length of an astronomical unit and the length of one parsec are listed in a box below the scale.

2.5.3 Classification of AGB Stars

According to Suh & Kwon (2009), AGB stars are classified into O-rich stars (M-type stars), C-rich stars (carbon stars), S stars and silicate carbon stars. They presented a catalog of AGB stars in our Galaxy from the IRAS PSC compiling the lists of previous works with verifying processes. There are 2 193 O-rich stars, 1 167 C-rich stars, 287 S stars and 36 silicate carbon stars found in the catalog. They will be oxygen-rich (M-type) or carbon-rich (C-type) or S-type depending on the chemistry of the outer envelope or the photosphere. It is believed that it is an evolutionary series where the M-type stars evolve into S and then C-type stars. The chemistry around AGB stars is controlled by the C/O ratio (Herwig, 2005).

During the AGB phase, mixing mechanisms dredge-up triple-α processed material from the He-burning shell which can cause the stellar atmosphere to evolve from being oxygen-rich (C/O < 1, M-type stars) through a stage where the relative amounts of oxygen and carbon are approximately equal (C/O $\sim$ 1, S-type stars) to being carbon-rich (C/O > 1, C-type stars). The spectral features are significantly different for O-rich and C-rich atmospheres of the stars. Initially, the abundance ratio of n(C) over n(O) is smaller than one (C/O < 1), they are classified as O-rich AGB stars of spectral type M. Chan & Kwok (1990) argued that a M-type star may become a carbon star when the star goes through C dredge-up processes and thus the abundance of Carbon is larger than that of Oxygen (Chan & Kwok, 1990). S stars are generally regarded as intermediate between M-type and C-type star in their properties. The chemistry of C and O AGB stars is a controversial topic in many areas of astronomy (Suh & Kwon, 2009). Figure 7 is a flow chart about classification of AGB stars which makes easy to understand it.

O-Rich AGB Stars

If the C/O ratio is less than unity, all the carbon will be bound into carbon monoxide (CO), which forms very easily and is very stable. For M-type AGB stars, the chemistry will be dominated by the remaining oxygen, leading to the formation of oxygen-rich molecules and particles, e.g. silicates and oxides. Due to the operation of hot bottom burning, intermediate-mass AGB stars (4 $M_\odot \leq M \leq 8\ M_\odot$) are O-rich stars (C/O < 1) which burns carbon at the base of the convective envelope, thus preventing the formation of a carbon star (Boothroyd & Sackmann, 1992). Infrared observations of AGB stars have revealed various types of dust grains in the envelopes around them. O-rich AGB stars (M-type Miras and OH/IR stars) typically show the 10 μm and 18 μm features in emission or absorption. Low mass-loss rate O-rich AGB (LMOA) stars with thin dust envelopes show the 10 μm and 18 μm emission features of amorphous silicate.

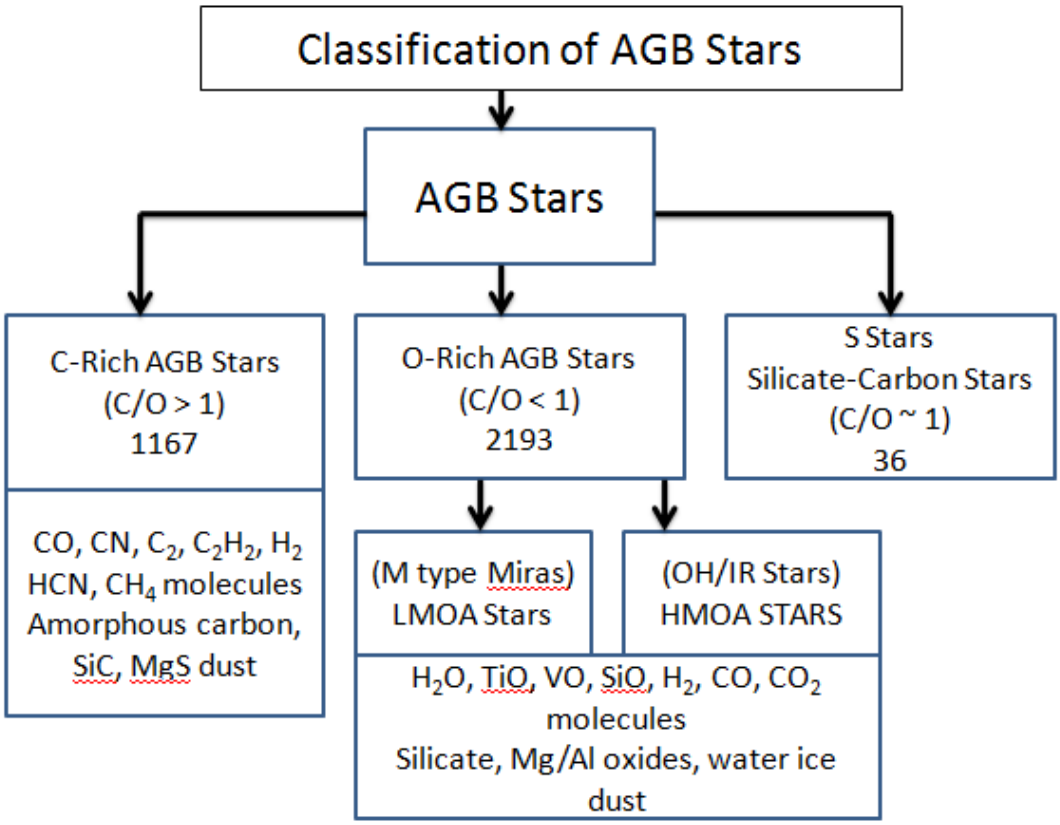

Figure 7: Classification of AGB stars on the basis of their chemistry and evolution of the central star. Masers OH, SiO, and H_2O have been found to be associated with O-rich AGB stars (Suh, 2014).

Where as high mass-loss rate O-rich AGB (HMOA) stars with thick dust envelopes show the absorbing features at the same wavelengths. Similarly LMOA stars show many molecular lines at NIR bands. The most conspicuous lines are the water vapor absorption at 1.9 μm and 2.9 μm, CO absorption at 2.3 μm produced in the expanded atmosphere of the central stars. Alumina (Al_2O_3) dust is believed to be one of the main dust species in O-rich AGB stars (Herwig, 2005).

C-Rich AGB Stars

The AGB stars having C/O ratio greater than one are termed as carbon - rich AGB stars which are formed after third dredge-up. It means due to dredge-up of carbon from the bottom of the convective envelope to the stellar surface, low-mass AGB stars ($M < 4\ M_\odot$) can turn in to C-rich (i.e. C/O > 1). One of the most dramatic effect of the third dredge-up is the transformation of AGB stars from M-type stars into C-type stars (Carbon stars). Before becoming a carbon star, all carbon atoms are assumed to be locked in the CO molecule and oxgen-rich molecules such as H_2O, TiO and SiO dominate the photo spheric spectra. But when the C/O ratio exceeds unity, all oxygen molecules are assumed to be locked within the CO molecule and the overabundant carbon atoms can

now form carbon-rich molecules like CH, C_2, CN and C_2H_2. The cosmic and solar abundance ratio between carbon and oxygen is C/O $\sim$ 0.4 to 0.5, but for carbon stars, the ratio C/O $>$ 1. Mostly ^{12}C isotope is produced from the He-burning shell that was dredged up during thermal pulses. Due to the number of carbon containing molecules such as CO and CN, the spectrum of Carbon stars differs dramatically from that of M-type stars.

Careful modelling of this process suggests that a minimum mass to form Carbon stars is 1.5 $M_\odot$. Mass of the stars below 1.5 $M_\odot$, they experience too few thermal pulses and the dredge up process is too weak to turn the star into a Carbon star. There is also a maximum mass to form carbon stars which comes from the concept of HBB. Since HBB can remove ^{12}C through the CNO-cycle, by turning it into ^{14}N. HBB tells us that the stars of masses $>$ 4 $M_\odot$ will block to form carbon stars. It means the maximum mass for Carbon stars is $\sim$ 4 $M_\odot$. Note that the HBB process switches off at the end of the AGB evolution. It is due to the reason that at the end of the AGB evolution, envelope mass is sufficiently low so HBB process becomes less efficient.

Infrared observations of carbon-rich asymptotic giant branch (AGB) stars have revealed certain types of carbon dust grains in the envelopes around them. They are amorphous carbon (AMC), silicon carbide (SiC) and magnesium sulphide (MgS) where AMC dust grains play a major role in producing the overall shape of the spectral energy distributions (SEDs) of carbon-rich AGB stars in the wavelength range (1 to 1000) μm. It is believed that featureless amorphous carbon (AMC) grains and SiC grains produce 11.3 μm emission band and 30 μm band that could be produced by small amount of MgS particles (Suh, 2000). Similarly HCN, H_2C_2 can produce absorption lines at 3.1 μm in the expanded atmosphere of the central stars (Suh, 2014). O-rich post AGB stars could not show polycyclic aromatic hydrocarbon (PAH) dust features but C-rich post-AGB stars typically show polycyclic aromatic hydrocarbon (PAH) dust features. It could be due to UV radiation from the hot central stars. Le Bertre et al. (2005) identified C-rich stars from the NIR data obtained from infrared telescope in space survey (IRTS).

S Stars and Silicate Carbon Stars

S stars have equal amounts of carbon and oxygen in their atmospheres (i.e. C/O $\sim$ 1). For the sample of S stars in the AGB phase are generally regarded as intermediate between M-type and carbon stars in their properties. Silicate carbon stars are the carbon stars with silicate dust features. For the sample of silicate carbon stars in the AGB phase, we use the same list as presented in Suh & Kwon (2009) except that one silicate carbon star (IRAS 04496 +6958) is excluded because it is not in our Galaxy (Suh & Kwon, 2009). Kwon & Suh (2014) revised and presented that sample of silicate carbon stars

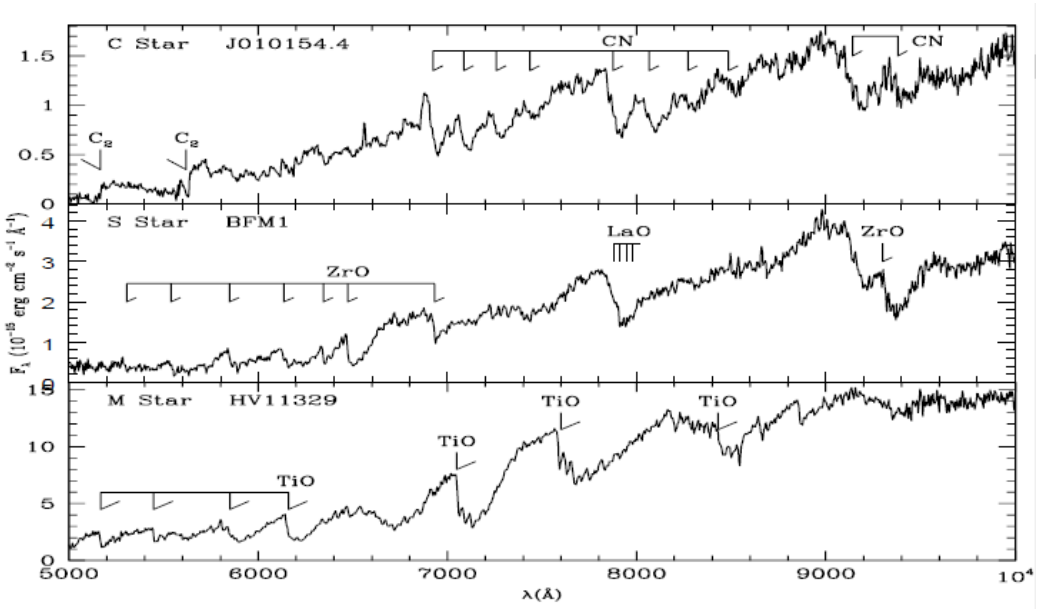

Figure 8: The spectra of an M star, an S star and a C star. The sequence M⟶S⟶C corresponds to a change from C/O < 1 to C/O ∼ 1 to C/O> 1 (Wood, 2010).

(29 confirmed and 27 unconfirmed). Hence according to the updated catalog, there are 3373 O-rich, 1168 C-rich, 362 S-type and 29 (+27) silicate carbon stars.

Classification of AGB stars can also be understood with the concept of spectra. The spectra of AGB stars fall into very characteristic groups: the spectra of oxygen-rich stars are dominated by oxygen-containing molecules such as TiO, the spectra of carbon-rich stars are dominated by molecules containing carbon (e.g. CN, C_2), and rarer stars in between with C/O ∼ 1 (S stars). Examples of these spectra are shown in Figure 8.

2.6 Asymptotic Giant Branch Evolution

2.6.1 History of AGB Evolution

The evolution of a star, once it reaches the main sequence, with nuclear reactions triggered in the central region, depends essentially on its mass. Figure 9 gives the tracks of the stars in the $L - T_s$ plane as they evolve. The diagonal branch running across (from top left to bottom right) gives the ZAMS. The following discussion highlights the key points and will walk through the stellar evolution (Padmanabhan, 2006).

To begin with, if $M < 0.08\ M_\odot$, nuclear reactions cannot be sustained in the contracting cloud for it to become a star. Such objects end up as planets or brown dwarfs, which are configurations in which the electron degeneracy pressure is significant and the material is fully convective. Similarly, systems with masses higher than about (60 to 100) $M_\odot$ are unstable and cannot last for significant period of time. Since radiation and thermal

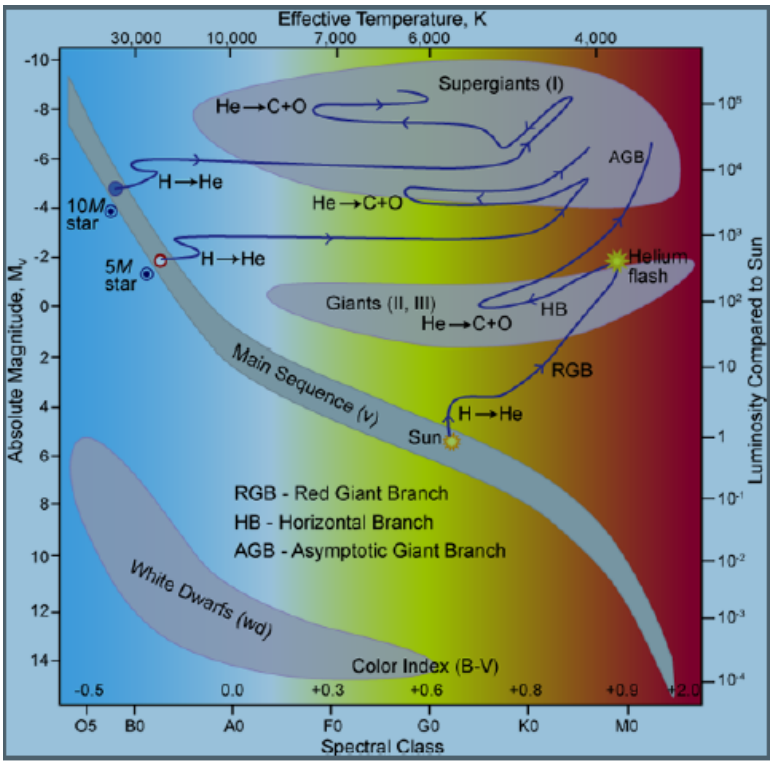

Figure 9: The Hertzsprung-Russell diagram in terms of luminosity and surface temperature (effective temperature). Three different evolutionary tracks are represented by the three blue lines, for stars of 1 $M_\odot$, 5 $M_\odot$ and 10 $M_\odot$. (Source:http://www.atnf.csiro.au/outreach/education/senior/astrophysics/stellarevolution_hrintro.html.)

energies in a star scale as $E_\gamma \propto T^4 R^3$, $E_{\rm th} \propto MT$, it follows that $E_\gamma / E_{\rm th} \propto T^3 R^3 / M \propto M^2$ (where we have used the result $T \propto M/R$). In a sufficiently high mass star, the radiation energy will dominate over thermal energy and blow it apart. This sets the upper and lower limits for variable stellar mass.

In the allowed mass range, stellar structure and evolution are characterized by some key values for the masses. Based on some features in the evolution which will be described below, we can divide the stars into low mass, intermediate mass and high mass stars. We recall that stars with $M \lesssim 1.3\ M_\odot$, have a radiative core while stars with $M \gtrsim 1.3\ M_\odot$, have a convective core. The first and the longest phase of stellar evolution occurs when stars act as gravitationally bound systems in which nuclear reactions fusing hydrogen into helium are taking place in the center. The process of combining four protons into a helium nuclei, releases about $0.03 m_{\rm p} c^2$ of energy, which is about a fraction 0.007 of the original energy $4 m_{\rm p} c^2$. Assuming that a fraction $\epsilon \approx 0.01$ of the total rest mass energy of the star can be made available for this nuclear reaction, the lifetime of the nuclear burning phase of the star will be about

$$t_{\rm ms} = \frac{\epsilon M}{L} \approx 3 \times 10^9\ {\rm yr} \left(\frac{\epsilon}{0.01} \right) \tag{2.38}$$

A more precise fitting formula for this time scale is given by

$$\frac{t_{\rm ms}}{10^6 \text{ yr}} = \frac{2550 + 669m^{2.5} + m^{4.5}}{0.0327m^{1.5} + 0.346m^{4.5}}, \quad m = \frac{M}{\mathrm{M}_\odot} \tag{2.39}$$

In fact $t_{\rm ms}$ represents the longest stretch of time in a star's life spent in steady state nuclear burning. Most of the scaling relations are applicable to such stars and they will form a band in the H-R diagram called the main sequence band. Since any given star spends maximum amount of time in the main sequence, it follows that a significant fraction of the stars that we observe will be found along the main sequence. Stars of different masses, of course, spend widely different amounts of time in the main sequence with the high mass stars spending less time (Padmanabhan, 2006).

When the star is in main sequence, it is essentially converting hydrogen into helium in its core and maintains balance between the energy produced and energy radiated out. Even in the main sequence, its radius and luminosity are varying slightly. For example, the 5 $\mathrm{M}_\odot$ star shown in Figure 9 will move from the ZAMS while burning hydrogen in the core. Eventually, at $t > t_{\rm ms}$, the hydrogen in the core runs out and the stellar evolution moves to the next stage. Since the electrostatic potential barrier between the helium nuclei is higher, further reactions which fuse the helium nuclei cannot take place immediately and the core begins to shrink under its own weight, in thermal time scale, and heats up. The hydrogen surrounding the core follows suit and will be compressed to high enough densities so that nuclear reactions are again ignited in the hydrogen shell. This is a somewhat peculiar situation in which the core is collapsing, taking the surrounding hydrogen shell along with it, leading to the energy production from the shell. The luminosity of the star increases and the increased pressure pushes the outer layers of the star further from the center making the star move into a red giant phase. (It is 'red' because the surface temperature $T_{\rm s} \propto (L/R^2)^{1/4}$ decreases with increasing R, making the black body peak shift to the redder side.) In massive stars ($M > \mathrm{M}_\odot$) there is a distinct evolutionary track. The time scale for this is very short and is well fitted by

$$\frac{t_{\rm HG}}{t_{\rm ms}} = \frac{0.543}{m^2 - 2.1m + 23.3}, \quad m = \frac{M}{\mathrm{M}_\odot} \tag{2.40}$$

The subscript HG stands for Hertzsprung Gap, as it is called. Since this time scale is very short, very few stars can be caught observationally in this phase thereby leading to a gap in the HR diagram in this region. Low mass stars do not go through this phase of the evolution does not have a distinct Hertzsprung gap. The next stage of evolution in moderate to high mass stars is usually called the giant phase branch. The luminosity of

the star at the base of the giant branch, $L_{\rm bgb}$, is essentially determined by its mass:

$$\frac{L_{\rm bgb}}{\rm L_\odot} = \frac{2.15m^2 + 0.22m^5}{1.0 + 1.4\times10^{-2}m^2 + 5.0\times10^{-6}m^4}, \quad \text{where} \quad m = \frac{M}{\rm M_\odot} \tag{2.41}$$

The radius and the luminosity of the star while on this track (giant branch) is reasonably well fitted by

$$\frac{R}{\rm R_\odot} = (0.25l^{0.4} + 0.8l^{0.67}), \quad \text{where} \quad m = \frac{M}{\rm M_\odot}; \quad l = \frac{L}{\rm L_\odot} \tag{2.42}$$

The collapse of the core to a sufficiently high density will trigger the next set of nuclear reactions producing carbon from helium. This ignition usually takes place when the luminosity is about $L = L_{\rm bgb} + 2000L_\odot$. When the helium ignition occurs, the core expands slightly and the envelope contracts (which is just the reverse of the original evolution) causing the star to move down ward horizontally. The star now settles to a new equilibrium configuration with a helium burning core and a hydrogen burning shell. During this period, the luminosity of the stars remain roughly constant (earning them the name horizontal branch stars) at

$$\frac{L_{\rm He}}{\rm L_\odot} = \left(0.763m^{0.46}\frac{L}{\rm L_\odot} + 50m^{0.1}\right), \quad \text{where} \quad m = \frac{M}{\rm M_\odot} \tag{2.43}$$

Its radius, however, decreases making the star evolve along the horizontal line . During its evolution in the horizontal branch, the stars convert the mass in the helium core (about 0.45 $\rm M_\odot$) into oxygen and carbon in almost equal proportion. These reactions typically release a fraction 7.2×10^{-4} of the rest mass energy. Taking the luminosity of a horizontal branch star to be about 50 $\rm L_\odot$, we find that the lifetime of a star in the horizontal branch is about $t_{\rm HB} \approx 7.2\times10^{-4}\times\left(\frac{0.45\ \rm M_\odot}{50\ \rm L_\odot}\right) = 0.1$ Gyr which is considerably shorter than the time spent in the main sequence. A more precise fitting function for the time scale for core helium burning is given by

$$\frac{t_{\rm He}}{t_{\rm ms}} = (0.0886 + 4.748\times10^{-4}m + 1.186\times10^{-6}m^2), \ (\text{if} \sim m \geq 10) \tag{2.44}$$

$$\frac{t_{\rm He}}{t_{\rm ms}} = (37.58 - 23.5m + 4.406m^2)^{-1}, \ (\text{if } m < 10) \tag{2.45}$$

Eventually, the helium in the core will get exhausted and a similar course of events take place again. The star will burn helium to carbon in an inner shell around the collapsing inert carbon core and, of course, hydrogen to helium in another outer shell. In a sufficiently high mass star, there could be onion-like structure with different nuclear reactions taking place at different shells. A high mass star ($M > 8\ \rm M_\odot$) can continue to burn hydrogen (for about 7×10^6 yr), helium (5×10^5 yr), carbon (600 yr), neon (1 yr), oxygen (0.5 yr) and silicon (1 day) leading to an iron core with the time scale spent in

each phase being progressively shorter as indicated in the bracket. The overall giant phase of evolution lasts for about $0.15t_{\rm ms}$. It is conventional to split this giant evolution into a red giant phase (before helium ignition) and a super giant phase (after core helium has been exhausted).

The outer regions of the star can expand to very large radii (of several AU) at this stage. The temperature in the star's envelope can get sufficiently low so that solid particles can condense out of vapour phase producing "dust". (This is exactly how you get soot particles up in the chimney.) The dust particles will be blown away from the star by radiation pressure thereby leading to a stellar wind which can result in a mass loss of up to several times 10^{-5} $\mathrm{M}_\odot$ yr^{-1}.

The evolution is different for low mass stars which do not get hot enough to ignite anything beyond helium. During the later part of evolution, the outer regions of the star undergo violent instabilities leading to an eventual ejection of significant fraction of material in the form of a planetary nebula. The core region will become a white dwarf supported by the degeneracy pressure of electrons.

2.6.2 Evolution from main-sequence

Once hydrogen burning begins in the core of a protostar, it becomes a main-sequence star. The main-sequence (hydrogen-burning) phase is by far the largest fraction of a star's lifetime, and therefore most stars observed in the sky are main-sequence stars. During this time, stars burn quietly, and change slowly. Stars on the ZAMS are in hydrostatic and thermal equilibrium with an almost homogeneous composition (mainly hydrogen). Once the star is born on the ZAMS, it undergoes quiescent hydrogen core burning for about $(80 - 90)\%$ of its life time on the main- sequence. During the main-sequence stage, stars burn hydrogen in their cores via nuclear fusion. They spent most of their lifetimes on the main-sequence. The duration of the MS depends on the stellar mass: the lower mass stars will consume all the fuel in the stellar core slower but higher mass stars consume quicker. The relationship between main-sequence lifetime, t, and mass, M, of a star can be expressed mathematically as

$$\frac{t}{\mathrm{t}_\odot} = \left(\frac{M}{\mathrm{M}_\odot}\right)^{-2.5} \tag{2.46}$$

where $\mathrm{t}_\odot$ is the main-sequence lifetime of the Sun and $\mathrm{M}_\odot$ is the mass of the Sun. The Sun's main-sequence lifetime is estimated to be 10 billion years. A star 10 times as massive as the Sun has a main-sequence lifetime of only 30 million years. A star 0.1 times as massive as the Sun has a main-sequence lifetime of 3 trillion years.

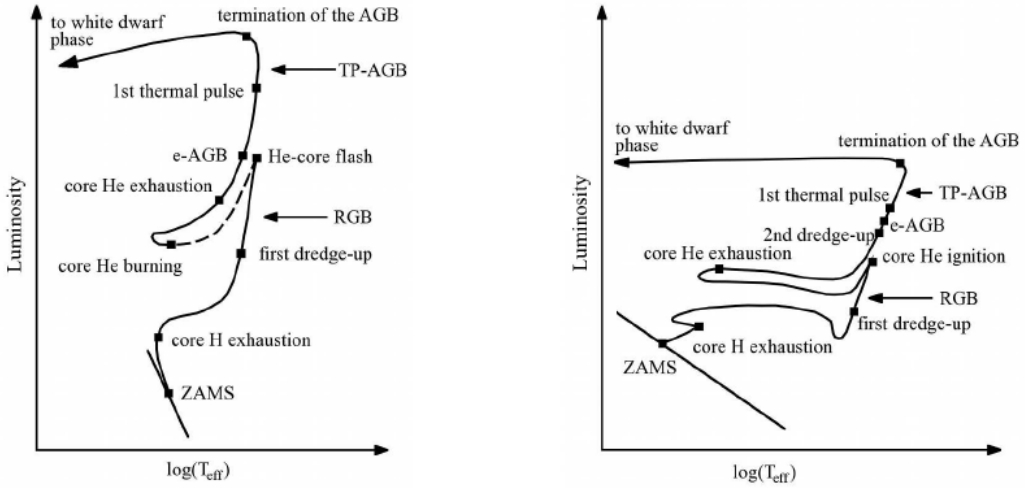

Figure 10: The evolution of a star in the HR diagram from the zero age main sequence (ZAMS) to the termination of the AGB for a 1 $M_\odot$ star (left) and a 5 $M_\odot$ star (right). The main stages of evolution mentioned in the text are marked (Maercker, 2009).

When the star is in main-sequence, it is essentially converting hydrogen into helium in its core and maintains balance between the energy produced and energy radiated out. Even in the main-sequence, its radius and luminosity are varying slightly. For example, the 5 $M_\odot$ star shown in Figure 10 will move from the ZAMS while burning hydrogen in the core. Eventually, at $t > t_{\rm ms}$, the hydrogen in the core runs out and the stellar evolution moves to the next stage. When stars leave the main-sequence, they begin burning hydrogen in an expanding thin shell around the core. Helium ash falls onto the core, increasing the mass and the density of this core. The hydrogen-burning shell grows in radius as the interior fuel is depleted. The outer layers of the star swell and cool, and so the star becomes a red giant, and occupies the giant branch on the H-R diagram.

MS stars with masses above 2 $M_\odot$ have a convective core surrounded by radiative envelope, stars with masses below 1 $M_\odot$ have a radiative core surrounded by a convective envelope and the MS stars with masses 1 $M_\odot \leq M \leq 2\ M_\odot$ have convective cores and convective outer envelopes with in between a radiative envelope. Hydrogen exhaustion in the core is followed by formation of a helium core where the star can not produce enough energy to stop contraction. As the central part of the star contracts, hydrogen burning starts in a shell surrounding the core via the CNO process. Energy production is concentrated in the regions of the highest hydrogen content and the highest temperature. This high temperature causes high pressure just outside of the core causing the hydrogen envelope to expand hence the star leaves the MS and evolves on to the red-giant branch (RGB) which occupies between 10^8 to 10^9 years for a one solar mass star. With increasing mass, the time on the RGB strongly decreases. In RGB, it is characterized by a convective envelope penetrating in to the deep layers. This penetration may be so deep that the convective envelope reaches material already processed by hydrogen

burning, enriched in helium (^{4}He), nitrogen (^{14}N) and carbon (^{13}C) while depleted in carbon (^{12}C) and oxygen. This brought to the surface in a process known as "dredge-up" or first "dredge-up" if it occurs on the RGB. In another way as the star ascends the HR diagram close to its Hayashi track, the outer convective envelope occupies about 70% of the total stellar mass. The convection zone reaches areas containing products of internal nucleosynthesis which are transported to the stellar surface. This phenomena is called the first dredge-up and it transports mainly products from the CNO cycle to the stellar surface (Padmanabhan, 2006).

The following rise in luminosity at almost constant temperature is known as RGB phase. Along the RGB, the star continues to expand due to the contracting core. The star has a hydrogen burning shell surrounding a helium core which heats as it contracts. This contraction lasts until the core becomes degenerate. It means the gravitational contraction will be balanced by degeneracy pressure which is independent of temperature and pressure. When the central temperature of the star has reached around 10^8 K, the central helium burning in the stellar core ignites which has not yet become electron-degenerate and heats up the core. As the energy production and temperature increases, degeneracy is lifted, temperature increases, pressure increases and core expands to find a new equilibrium configuration. At this stage, the hydrogen burning shell also has expanded and has lower temperature and density causing the shell to produce less energy than before. The star at this stage is called horizontal branch (HB) star which lasts for about 10% of the total stellar lifetime. On the horizontal branch, the star burns helium in the core, and hydrogen in a shell surrounding the core. The stars become hotter and smaller during this phase, and move across the H-R diagram. These stars stay at about the same luminosity.

For lower mass stars, the transition from the RGB towards the horizontal branch is more explosive. Central helium burning is ignited in the electron degenerate core. As pressure is no longer related to temperature, the material doesnot expand while temperature is strongly increasing due to helium burning. This creates an increasingly efficient helium burning as temperature still increases and increases the core luminosity significantly: the star undergoes a helium flash (Palen, 2001). It means if a star is about as massive as the Sun ($< 2\ M_\odot$), then it will undergo a helium flash while on the giant branch. During a helium flash, the star undergoes a series of changes deep within:

1. As helium ash from the hydrogen-burning shell falls onto the core, the helium core gains mass, and shrinks, increasing in density.

2. The electrons in the core become degenerate and the temperature increases without increasing the pressure, so the core can no longer expand.

3. The hydrogen-burning shell makes more ash; the helium core continues to grow.

4. The temperature in the degenerate core rises to 100 million K; the mass in the degenerate core accumulates to 0.6 $M_\odot$.

5. Helium fusion begins suddenly in the core.

6. Because the core is made of degenerate electrons, the pressure and temperature are not related. Even though the core gets hotter, the pressure stays the same, and the core does not expand.

7. However, the higher temperature increases the rate of helium burning, further increasing the temperature.

8. Temperature and burn rate increase until $T \approx 300$ million kelvin. For a few minutes, the energy production of the core of the star is about 100 times the entire energy production of the Milky Way Galaxy.

9. At 300 million kelvin, the electrons stop being degenerate, the interior expands, and the temperature and density drop.

10. This is all deep inside. Most of this energy is consumed in puffing up the core. The outside of the star contracts somewhat, raising the temperature, so that it becomes a yellow giant.

Stars with mass greater than 2 $M_\odot$ do not have helium flashes. The temperature rises too fast for the electrons to become degenerate. They do begin to burn helium in their cores, just not explosively. Once helium burning begins in any star, there are two sources of energy - the helium-burning core, which is turning helium into carbon and a little bit of carbon into oxygen, and the hydrogen-burning shell, which dumps more helium into the core as it burns outward through the star.

Eventually, the star runs out of helium in the core. It moves back across the horizontal branch as the surface temperature falls, and onto the asymptotic giant branch (AGB). A period of stellar evolution under taken by all low to intermediate mass stars (0.6 $M_\odot$ to 10 $M_\odot$) late in their life is called Asymptotic Giant Branch (AGB) phase. Figure 11 shows the internal structure of a star when it reaches the AGB. The structure is characterized by: (i) a small, very hot and dense core of carbon and oxygen; (ii) He- and H- alternately burning shells; (iii) a large, hot, and less dense stellar envelope; (vi) a warm atmosphere and a very large, diluted and cool circumstellar envelope. Although only short in duration, the AGB is very important due to the nucleosynthesis which occurs.

When a star exhausts the supply of hydrogen in its core, the core contracts and its temperature increases, causing the outer layers of the star to expand and cool. Stars at this stage of stellar evolution are known as AGB stars. While ascending the giant branch,

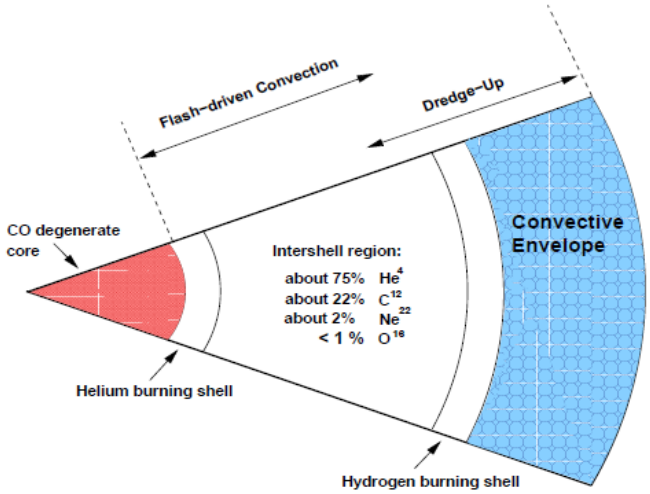

Figure 11: Schematic structure of an AGB star (not in scale), showing the degenerate CO core surrounded by a He-burning shell above the core and a H-burning shell below the deep convective envelope. Note a thin, inactive buffering layer of hydrogen in between the hydrogen burning shell and the convective envelope (Karakas et al., 2002).

the star is characterized by a contracting, inert core of helium, a hydrogen-burning shell, and an expanding envelope. The energy from the core and shell raises the luminosity by a factor of almost 10^3. The temperature in the core eventually reaches the point where helium can begin to fuse, forming (^{12}C). The star then moves to the left in the HR diagram, tracing the horizontal branch. After another 10^8 yr, helium burning exhausts itself in the core and shifts to an outer shell. The star, now containing two burning shells, ascends the asymptotic giant branch, so called because it approaches the original giant branch.

AGB stars are typically long period variables, and suffer large mass loss in the form of a stellar wind. A star may lose 50% to 70% of its mass during the AGB phase. The stellar winds from AGB stars are the main production sites of dust in the universe. The AGB stars emit the particles as a stellar wind with a velocity of $(5 - 75)$ km s^{-1}. The evolution that follows core helium burning depends strongly on the stellar mass. The mass determines how high the central temperature can become and the degree of degeneracy when heavier nuclear fuels are ignited. When the central helium supply is exhausted, helium will continue to burn in a shell, while the hydrogen burning shell is extinguished. In the HR diagram the star will move towards lower effective temperature and higher luminosity. This phase is quite similar to the red giant phase of low-mass stars, although the temperatures are slightly hotter. For this reason it is known as the asymptotic giant branch, AGB. After the early phase, when the helium shell catches up with the extinguished hydrogen shell, the AGB star enters what is known as the thermally pulsing phase, where hydrogen and helium shell burning alternate. A configuration with two burning shells is unstable, and in this phase the stellar material may become mixed or

matter may be ejected into space in a shell, like that of a planetary nebula. The thermally pulsing AGB continues until radiation pressure has led to the complete expulsion of the outer layers into a planetary nebula. Low and intermediate mass giants never become hot enough to ignite carbon burning in the core, which remains as a carbon oxygen white dwarf (Karttunen et al., 2007).

Depending on the temperature, density, and ionization state of a portion of the ISM, different heating and cooling mechanisms determine the temperature of the gas.The evolution on the AGB can be divided in two stages: the Early AGB (running almost parallel to the RGB in the HR-diagram), and the Thermal Pulse (TP-AGB) phase. These phases will be discussed in next topic.

2.6.3 Early AGB Phase

When the helium in the center has been converted in to carbon (and oxygen) i.e., trible alpha (3α) process has finished, the He-burning zone moves outward, and the core of C+O contracts until it has a very high density, approximately the same of a white dwarf. In such condition, size of the stellar envelope is about 10^6 m and temperature is about 10^8 K. The contraction of the core and the expansion of the envelope lead to a rapid increase in luminosity which is the start of the Early AGB phase: the stage at which He burns in a shell, producing most of the energy. While the abundance of He in the centre goes to zero, He-burning continues in a shell around a degenerate C-O core. The nuclear energy production is dominated by the He-shell that burns outward in mass. In the meantime, the H-layer around the He-shell expands and cools so efficiently that H-shell burning extinguishes so that convection of the envelope sets in and moves inwards. When helium in the core is used up, energy production shifts to helium burning in a shell and the outer layers of the star expands. The star evolves towards the early AGB phase and becomes a red giant for the second time following the track of RGB (Padmanabhan, 2006).

According to Iben (1983), the convective envelope of stars of $\gtrsim$ 4.6 $M_\odot$, reaches layers with processed material of the CNO-cycle after core He exhaustion. The elements (mainly He and N), are then dredged up to the surface (second DUP). The expansion of the outer layer extinguishes the hydrogen-burning shell in the intermediate mass stars, which causes the convective envelope to move inward for a second time. This second dredge up brings the hydrogen burning products, mainly helium and nitrogen to the surface but in case of low mass stars, hydrogen burning shell remains active, which avoids a deeper penetration of the convective envelope means hydrogen burning shell is not extinguished so that no second dredge up occurs.

In the HRD, the star of $\gtrsim$ 4.6 $M_\odot$, evolves almost parallel to the RGB, subsequent

shrinking of envelope leads to a decrease in luminosity and heats the inner region of the convective envelope. Consequently, the H-shell reignites, which marks the end of the early AGB phase. In the material that is dredged up hydrogen has been completely converted into helium, while in CNO cycle, (^{12}C) and (^{16}O) have been converted into (^{14}N). This material is mixed with the outer convective envelope and appears at the surface. The second dredge-up has a qualitatively similar but more dramatic effect than the first dredge-up phase which occurred on the Red Giant Phase. An additional important effect of a second dredge-up is the reduction of the mass of the H-exhausted core which limits the mass of the white dwarf. Thus the occurrence of second dredge-up increases the upper initial mass limit of stars that produce white dwarf (Herwig, 2005).

2.6.4 Thermally Pulsating AGB Phase

The thermally pulsating AGB phase is the stage of the AGB star's life where He and H are intermittently burning. At the end of the early AGB phase, the H-burning and He-burning shells are thin and close together which combined with the high temperature dependence of the He-burning reactions and makes the environment thermally unstable. After the helium exhaustion in the shell, the hydrogen-burning shell takes over until enough helium has been produced. The hydrogen burning in the shell produces freshly synthesized helium and consequently, a steady increase of the helium and consequently increase in the helium shell mass. If the helium shell is sufficiently massive, it will re-ignite and new helium-burning will control the evolution. In such condition, the helium burning shell is said to be thermally unstable and it undergoes thermal pulses recurrently. A thermal pulse or a He-shell flash is a cycle in which the energy source of the star alternates between the helium burning and the newly ignited hydrogen burning in two thin shells which are separated by helium rich intershell. The TP-AGB phase is characterized by two nuclear burning shells (H and He) surrounding an electron-degenerate carbon-oxygen core and a deep convective envelope. According to Schwarzschild & Härm (1967), thermal pulse may occur in both low and intermediate mass stars and huge amount of energy is released. Such sudden rise in energy production generates a convective layer between the H-and He-shell called the pulse-driven convective zone (PDCZ) which penetrates to the intershell region and mix carbon and oxygen enriched material to the surface (third dredge-up). Actually helium burning shell is thermally unstable and produces thermal pulses in every 10^4 years or so, depending on the core mass and composition of the star. In each thermal pulse, the He burning luminosity can reach up to $L_{\rm He} \sim 10^8$ L$_\odot$. Most of the luminosity goes into expanding the outer layers. This strong expansion drives the H-shell to cooler, less dense regions which has the effect of extinguishing the H-shell so that the inner edge of the deep convective envelope can then move inward (in mass) and mix to the surface the products of internal

nucleosynthesis. This mixing event, which can occur periodically (after each TP), is known as the third dredge-up (TDU) which is the mechanism for producing carbon stars (Karakas et al., 2002). It is important to note that mixing events occuring during these thermal pulses are responsible for the transport of carbon and s-process elements to the surface (Iben and Renzini 1983). After dredge-up, the star contracts, re-ignites the H-shell and enters a phase of quiescent H-burning, known as the interpulse phase. The thermally pulsing AGB is the phase after the first thermal pulse to the time when the star ejects its envelope, terminating the AGB phase.

Towards the end of the thermally pulsating-AGB phase, the stars undergo a heavy mass loss. Pulsations with increasing amplitudes, dust driven winds push the matter of the outer envelope to distances, where it loses its gravitational bound to the star and merges with the interstellar medium. During that time, the luminosity increases with decreasing mass of the H-shell. The duration of the TP-AGB phase is determined by the growing mass of the degenerate C-O core and the decreasing mass of the outer layers. As soon as the whole envelope is thrown out, the star ends this phase.

2.6.5 Thermal Pulses and Third Dredge-up

When the luminosity of the star is $\sim$ 3000 $L_{\odot}$, star becomes able to burn both He and H shells. Periodically, the He produced by H burning is accreted onto the He shell, and "helium shell flashes" occur as a result mass of the central core is increased by the "flashes" of the thin He-layer around the core into C, and a convective intershell develops. These short moments (timescales of $\sim$ several tens of years) are called "thermal pulses", and the object undergoes a luminosity modulation means luminosity increases sharply. During AGB evolution, the helium-burning shell is thermally unstable and causes energy bursts called thermal pulses or flashes repeating apparently every 10^4 years leading to the development of a convective zone in the shell (Karakas et al., 2002). As the star ascends the AGB, burning of hydrogen and helium will turn in to a process called thermal pulse cycle and the phase where hydrogen burning-shell dominates is known as the "inter-pulse phase" which is interrupted by the helium-shell instabilities. The thermal pulse drives the convective zone between the helium and hydrogen burning shells so that the fusion products of the helium-burning shell including (^{12}C) and some (^{16}O) are mixed throughout this region.

The creation of an intershell convection zone (ISCZ) allows the star to effectively mix up products from He-burning (mainly ^{12}C) into the intershell region and after the He-shell flash, the luminosity slowly increases to a maximum value just before the next shell flash. During this ‘quiet’ phase, the base of the convective envelope reaches into the intershell region enriched with new elements created in the ISCZ due to various processes, mainly

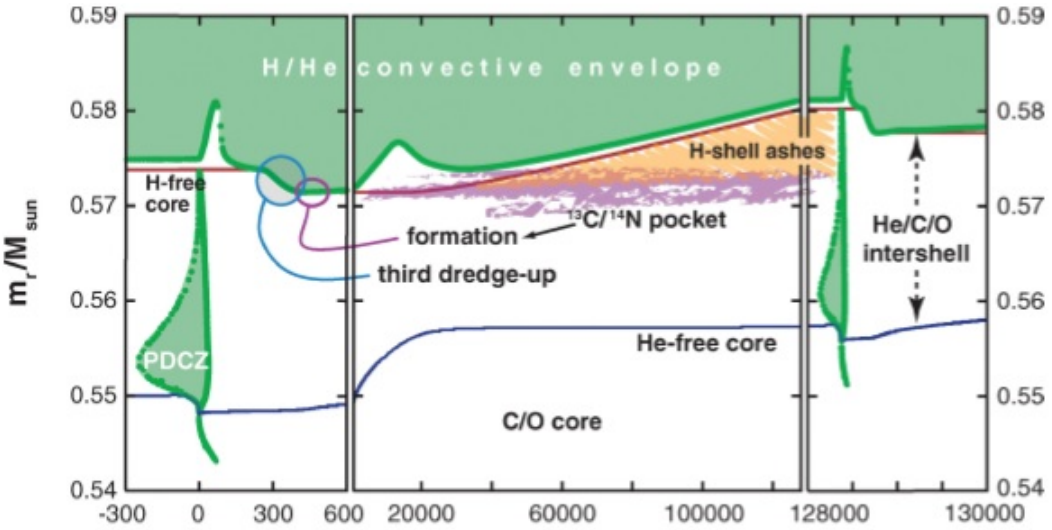

Figure 12: Schematic view of the process of the third dredge-up in a two solar mass AGB star after a thermal pulse. Red and blue line indicate the boundary of the H and He free core respectively. Green are the zones of convection (Herwig, 2005).

the s-process (will be discussed below), and mixes them up to the surface called third dredge-up (Figure 12). Actually Dredge-up is the convective mixing process which brings material processed by nucleosynthesis to the surface, where it can be observed and ejected into space through wind as mass loss. Mixing (Dredge-up) occurs when the envelope expands and cools as the core contracts after the end of a dominant nuclear burning event. The first dredge-up occurs to the deepening convective envelope after the end of H-core burning, the second dredge-up occurs to the descending convective instability after the end of He-core burning. After the end of the flash-burning in the He shell, each thermal pulse on the AGB provides similar favorable conditions for the convective dredge-up of material. This third dredge-up brings primary nucleosynthesis products from combined H-shell and He-shell burning to the surface which include in particular C, the s-process elements, as well as He (Herwig, 2005). An important process, fundamental for the creation of C-rich stars, happening during a thermal pulse is the dredge-up specially third dredge-up. It is possible when convection reaches the layers where nuclear processes occured and can bring material to the stellar surface. This matter is enriched by products of nuclear-burning, especially "new" carbon. The process is also called third dredge-up, if the process can last long enough, the abundance of C in the atmosphere will exceed the one of O. In the initial stage on the AGB, it has C/O ratio well below unity and in each third dredge-up mixes a certain amount of mass ($\sim 6 \times 10^{-3}$ $M_\odot$ for a core mass of 0.6 $M_\odot$, less for larger core masses) with the intershell-abundance distribution into the envelope (Herwig, 2005). The intershell contains 5 to 10 times more C than O and, as a result, the envelope C/O ratio increases with each dredge-up event until eventually the C/O ratio exceeds unity and a C star is formed. The process of the third dredge-up was discovered at the same time by Iben

(1975), Sugimoto & Nomoto (1975) and a schematic view of this process is shown in Figure 12. During early AGB phase, the He shell dominates nuclear production, burns outward in mass and reaches the H shell. At that point, nuclear energy release is dominated by the H shell and interrupted periodically by thermonuclear runway of He shell flash events that ignite a complex series of convective and other mixing events shown in Figure 12. According to Iben & Renzini (1981), four phases can be detected in a thermal-pulse cycle. An on-phase, when the He shell is burning brightly, produces luminosity up to $\sim 10^8$ $L_\odot$ and an energy that cannot be transported just by radiation alone, leading to the development of a convection zone in the He rich intershell, exactly above the He burning region called "intershell convective zone" driven by the thermal pulse. Composition of the intershell convective zone has shown in Figure 11.

There is a physical quantity λ which quantifies the efficiency of third dredge-up. It depends on physical parameters such as the core mass, metalicity as well as total mass of the star and is defined as the ratio of mass dredged-up by the convective envelope, $\Delta M_{\rm DUP}$, to the amount by which the core mass increased due to H-burning during the preceeding interpulse phase, $\Delta M_{\rm C}$;

$$\lambda = \frac{\Delta M_{\rm DUP}}{\Delta M_{\rm C}} \tag{2.47}$$

How λ depends on these factors is still unknown but λ increases with core and envelope mass and with decreasing metalicity (Karakas et al., 2002). The biggest difficulty encountered in estimating λ is due to the uncertainties in calculating the amount of convective overshoot occuring at the convective boundries. Karakas et al. (2002) have presented calculations with and without mass loss with the explicit aim of studying how dredge - up depends on mass and metalicity. These calculations show in agreement with many previous calculations. In the calculations, for intermediate mass stars,the parameter λ reaches very close to unity and it ($\lambda = 1$) implies that the core is not effectively growing.

2.6.6 Hot-Bottom Burning

This is the process of H-burning at the bottom of the convective envelope. This only occurs above a certain stellar mass > 4 $M_\odot$. The process stops when the envelope has lost too much mass. The evolution of thermal pulses on the AGB is not independent of stellar mass. For AGB stars with initial masses greater than 4 $M_\odot$, outer part of the H-shell is included in the convection of the envelope. Consequently, temperature at the bottom of the convective envelope rises and the dredged up C is efficiently converted into N. This process, called hot-bottom burning, causes massive AGB stars to remain O-rich. In another way for stars with $M \gtrsim 4$ $M_\odot$, the temperature at the base of the convective

envelope during the interpulse period becomes so high ($T_{\rm BCE} \gtrsim 3{\times}10^7$ K) that H-burning reactions take place. Thus the process when the CNO cycle operates on material in the convective envelope during interpulse period is called hot bottom burning (Herwig, 2005). It means for massive AGB stars ($M_{\rm star} > 4$ M$_\odot$), the convectively unstable envelope may penetrate into the top of the hydrogen shell where the temperature can reach as high as 10^8 K. Such penetration results in nuclear burning at the bottom of convective envelope. At this stage, the CN-cycle, processing (^{12}C) into (^{13}C) and (^{14}N),is activated. This process is known as hot-bottom burning and may destroy the newly-formed carbon and prevent the star from becoming a carbon star. Hot-bottom burning transfers dredged-up C efficiently into N, which initially prevents C-star formation (Boothroyd et al., 1993). The added production of nuclear energy leads to the break-down of the core mass-luminosity and core mass-interpulse period relations, resulting in higher luminosities and a sudden shortening of the interpulse period. However, at the end of the AGB evolution mass loss has reduced the envelope mass and hot-bottom burning becomes less efficient. According to Frost & Lattanzio (1996), the DUP of the carbon in intermediate mass stars with small envelope masses might become more efficient that HBB, which would lead to the most luminous C stars.

During HBB, the star may also experiance mass loss which is one of the major importance to the dredge-up process. Both hydrogen burning at the bottom of the envelope and mass loss from the stellar surface will reduce the mass of the envelope. AGB evolution ends to white dwarf stage, when the envelope mass becomes too small to support nuclear burning. Important consequences of HBB are the Production of (^{7}Li) (Cameron & Fowler, 1971) and (^{26}Al) by Mg-Al cycle (Mowlavi & Meynet, 2000).

2.6.7 S-Process Nucleosynthesis in AGB Stars

During the third dredge-up, the convective envelope does not only transport material from the He intershell region to the surface but also injects protons into the intershell which is the start of the slow neutron capture nucleosynthesis or s-process nucleosynthesis, (Gallino et al., 1998). The s-process creates heavy elements by neutron capture which is slow with respect to the competing β^- decay. AGB stars produce so-called s-process elements. The s-process is the process of slow neutron capture. Since binding energy per nucleon peaks is around Fe so neutron capture is the only way to make elements beyond the Fe peak. Approximately half of the known elements heavier than iron are produced by a process, called s-process (Arlandini et al., 1999) and the processing of material in the star (starting with H and He) causes the abundances of heavier elements in the star to change. AGB stars are particularly important for the production of s-process elements, and are known to be main site where about 50% of all elements heavier

than Fe are produced (Busso et al., 2004). It is also important for isotopic ratios and in some cases of lighter elements particularly at extremely low metalicity. Elements heavier than iron are formed through slow (if compared to the competing β-decay) neutron captures and during a neutron capture process, the mass number of an isotope increased by one, where as the following β-decay has no influence on the mass number. In this way, s-process produces heavier elements with mass number up to 204 (Herwig, 2005). For production of elements beyond iron, a neutron capture process is required. In AGB star, the helium rich intershell region provides a suitable environment for the production of s-process elements. The typical time scales for the slow and rapid neutron capture processes are thought to be 10^4 year and 10^4 second respectively. There are two possible sources of neutrons for the s-process in low and intermediate mass AGB stars (Herwig, 2005). The first neutron source is the ^{13}C(α,n)^{16}O reaction, which is found to be the dominant neutron source in low-mass AGB stars ((Smith et al., 1987) and (Gallino et al., 1998)). This reaction takes place at a temperature of 9.0×10^7 K in the He-rich intershell during interpulses. After a thermal pulse, the convective hydrogen envelope penetrates the upper layers of the intershell where it injects protons with decreasing number density with increasing depth. This mixing process is called partial mixing. It provides the necessary protons to transform the ^{12}C, which has been mixed throughout the intershell during the thermal pulse, into ^{13}C via the reaction ^{12}C(p,γ) ^{13}N(β^+)^{13}C creating a so-called ^{13}C-pocket. The second source is the ^{22}Ne(α,n)^{25}Mg reaction which is the dominant source in intermediate mass stars (Herwig, 2005). This reaction needs high temperatures of about 3.0×10^8 K which is obtained at the bottom of the convective thermal pulse. During He burning, ^{14}N is transformed into ^{22}Ne via ^{14}N$(\alpha, \gamma)^{18}$F$(\beta^+)^{18}$O$(\alpha, \gamma)^{22}$Ne. From these discussions, it is clear that neutrons are produced via mainly two reactions (equations (2.50) and (2.51) which are given below:

$$^{12}\mathrm{C} + \mathrm{p} \longrightarrow {}^{13}\mathrm{N} + \gamma \tag{2.48}$$

$$^{13}\mathrm{N} + {}^{+}\beta \longrightarrow {}^{13}\mathrm{C} + \nu \tag{2.49}$$

$$^{13}\mathrm{C} + \alpha \longrightarrow {}^{16}\mathrm{O} + \mathrm{n} \tag{2.50}$$

$$^{14}\mathrm{N} + \alpha \longrightarrow \gamma + {}^{18}\mathrm{F} \qquad {}^{18}\mathrm{F} + {}^{+}\beta \longrightarrow {}^{18}\mathrm{O} \tag{2.51}$$

$$^{18}\mathrm{O} + \alpha \longrightarrow \gamma + {}^{22}\mathrm{Ne} \qquad {}^{22}\mathrm{Ne} + \alpha \longrightarrow {}^{25}\mathrm{Mg} + \mathrm{n} \tag{2.52}$$

Similarly other possible neutron producing reactions involving ^{16}O, ^{17}O, ^{18}O, ^{21}Ne, ^{25}Mg or ^{26}Mg are

$$^{16}O + ^{16}O \longrightarrow ^{31}Si + n \tag{2.53}$$

$$^{17}O + \alpha \longrightarrow ^{20}Ne + n \tag{2.54}$$

$$^{18}O + \alpha \longrightarrow ^{21}Ne + n \tag{2.55}$$

$$^{21}Ne + \alpha \longrightarrow ^{24}Mg + n \tag{2.56}$$

$$^{25}Mg + \alpha \longrightarrow ^{28}Si + n \tag{2.57}$$

$$^{26}Mg + \alpha \longrightarrow ^{29}Si + n \tag{2.58}$$

The s-process does not produce elements beyond Pb and the counterpart of the s-process is the rapid neutron capture process (r-process), which produces heavy elements and requires very high temperature. Such high temperature is possible in objects like supernovae, novae and X - ray binaries.

2.6.8 Structural Evolution of AGB Star

Low mass stars are those stars which develop an electron - degenerate core immediately following the main sequence phase having lower limit of about (0.8 to 1.0) $M_\odot$ and upper limit of about (2.0 to 2.3) $M_\odot$ (Iben & Renzini, 1981). Intermediate mass stars are those which ignite helium "non-degenerately", but develop an electron-degenerate core of carbon-oxygen following the exhaustion of helium at the center with upper limit of about (8.0 to 9.0) $M_\odot$. When low mass stars behave quantitatively like intermediate mass stars during their subsequent evolution, low mass stars also develope an electron-degenerate core of carbon-oxygen after the exhaustion of central helium. This common phase of low and intermediate mass stars is referred as the asymptotic giant branch (AGB) phase and the stars are asymptotic giant branch stars. AGB stars are low and intermediate mass stars ranges $\sim 0.8\ M_\odot$ to $\sim 8.0\ M_\odot$ (Habing & Olofsson, 2003) driven by nuclear burning. It is final nuclear burning stage and this phase of evolution is characterized by nuclear burning of hydrogen and helium in thin shells on top of the electron degenerate core of carbon and oxygen or for most massive super AGB stars a core of oxygen, neon and magnesium. This part of the stellar evolution is characterized by luminous, very cool extended objects having high luminosity, low surface temperature(< 3500 K).

Low and intermediate mass stars proceed after completion of central hydrogen and helium burning through the AGB phase before they finally end their evolution as white dwarf (Weidemann & Koester, 1983). After the completion of central hydrogen burning on the main-sequence, hydrogen burns in a shell around the helium core and the envelope expands due to core contraction. Due to it, radius is increased and effective

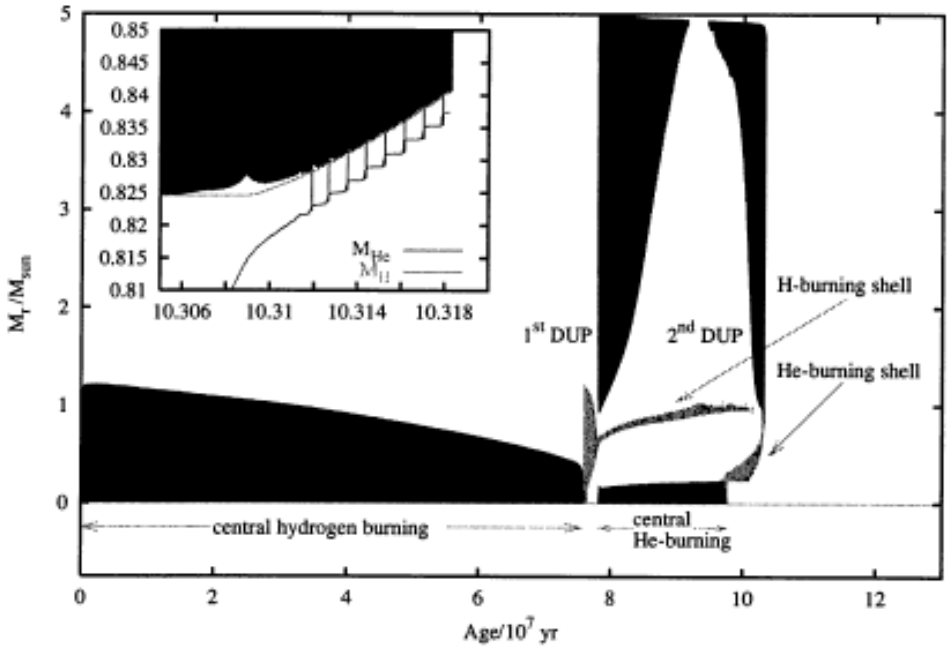

Figure 13: A graphical representation between mass-wise extension of convective regions and burning shell with time (age/10^7 yr). Light regions show burning shell and dark shaded regions show convectively unstable region. Inlet shows the evolution on the upper AGB. The spikes refer to the thermal pulses which will be discussed later (Bloecker, 1995).

temperature is decreased so that the star ascends the red giant branch (RGB). For stars of mass $M \lesssim 2$ $M_\odot$, the helium cores become electron-degenerate and ignite central helium burning at the tip of the RGB under degenerate conditions (helium core flash). But for intermediate mass stars, they do it non-degenerately. During the RGB evolution, the convective envelope moves downwards reaching layers which have previously experienced H-burning (first dredge-up) leading to the mixing of processed material to the surface (Figure 13). The star becomes a red giant for the first time, when first dredge-up takes place. Major results during first dredge-up are a doubling of the surface ^{14}N abundance, a reduction in surface ^{12}C abundance approximately 30%, the formation of a surface ^{12}C/^{13}C ratio of about 20 to 30, a reduction in surface Li and Be by several orders of magnitude and practically there is no change in the surface abundance of ^{16}O (Iben and Renzini 1983). In the dredge-up process, base of the convective envelope moves inward (in mass) through matter and is pushed out from the helium-burning shell. Due to it, opacity increases and temperature decreases in the expanding layers as a result there is an increase in the outward flux of energy produced by helium burning and the release of gravitational potential energy from the contracting core.

Second dredge-up phase accompanies the formation of an electron-degenerate core, following the exhaustion of central helium. For most massive intermediate mass stars, hydrogen has been completely converted into helium, both ^{12}C and ^{16}O have been completely converted into ^{14}N. During the second dredge-up phase, there is first increase in

temperature due to release of gravitational potential potential energy and then decrease in temperature due to energy loss via neutrinos in the rapidly contracting helium-exhausted core. It means for highly electron-degenerate core, temperature is not high enough for carbon to burn until the core mass approaches the Chandrasekhar mass (Iben & Renzini, 1983).

In order to understand AGB phases more clearly, they are further divided into two periods: early-AGB phase and thermally pulsating pulsating (TP-AGB) phase. First and the longest period is the early AGB phase. During this period, the hydrogen burning shell is extinct and the helium burning shell is narrow, provides most of the energy reaching the stellar surface. At the end of the early-AGB phase, hydrogen is re-ignited in a thin shell and the star begins to pulse thermally. It means the star has entered the thermally pulsating AGB (TP-AGB) phase.

Figure 12 shows the structural evolution of a thermally pulsing AGB star over time with the burning shells. During the TP-AGB, intervals of quiescent H-shell burning are interrupted by thermal pulses and the He-burning shell gradually moves further out in mass, reaching colder temperature layers and fades out. The H-burning shell moves outwards on top of the practically inactive He shell, increasing the mass of the He intershell with newly-synthesised He. Gravitational contraction by the core increases the temperature and densities of the He-burning shell. When the shell re-ignites, a thermal pulse is produced, causing a thermonuclear runway of He shell flash event. This interrupts the radiative state of the He intershell and makes it almost completely convective which transports away the excess of energy and thereby mix newly-synthesised carbon and oxygen within the He-rich intershell almost up to the H-burning shell. At the end of the thermal pulse, the intershell expands and radiates away the energy produced by the He burning so that the expansion ends the convective thermal pulse and lifts the H-burning shell to lower temperatures where it temporarily fades out. In such condition, the convective envelope penetrates the He-rich intershell to transport away the energy: such mixing process is called the third dredge-up. The efficiency of the third dredge-up is most important and will strongly effect the further chemical evolution of AGB stars.

2.6.9 Chemical Evolution of AGB Star

Figure 14 shows the chemical evolution of AGB stars so that their different stages can be understood. In main sequence, the chemical composition of the outer stellar envelope remains almost untouched by the nuclear fusion in the core. However, there is depletion of lithium (Li) in the chemical composition of main sequence stars, although the mechanism behind this depletion is not fully understood ((Pace et al., 2012), and

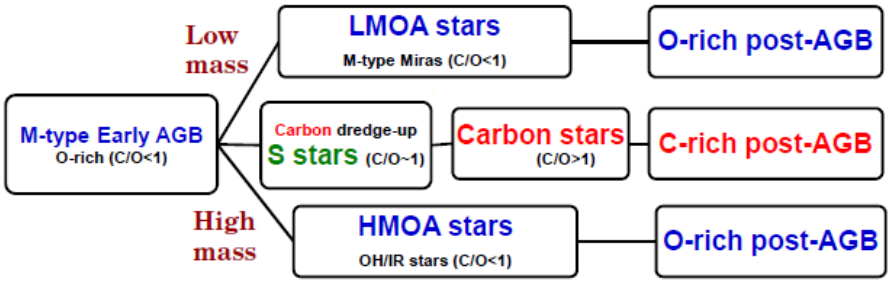

Figure 14: Possible evolutionary tracks for the classification of AGB stars. Low mass stars remain as M - type miras and high mass AGB stars remain as OH/IR stars but intermediate mass stars changes to carbon stars through S stars. (Suh, 2014).

references therein). Apart from Li, the chemical composition of the surface layer of main sequence stars resemble the initial composition of the star. The surface composition is altered by mixing events during which the large outer convective layers penetrate to the deep interior regions where products of internal nucleosynthesis takes place. These burning ashes are then transported by the convective envelope to the stellar surface where they alter the chemical composition of the surface. Such mixing events are called dredge-ups which can strongly change the surface composition.

The first dredge-up takes place during the ascend on the RGB (Iben, 1967) and its strength strongly depends on multiple factors like initial mass and metallicity. These factors determine how deep the first dredge-up will penetrate and how strong it alters the surface composition. During the first dredge-up, the outer convective zone penetrates into the layers with products of hydrogen burning via partial CNO processing during the main sequence. It means, the first dredge-up has main effect to change surface composition of light elements with depletion of ^{12}C abundance and an increase in ^{4}He, ^{13}C and especially ^{14}N (El Eid, 1994; Boothroyd & Sackmann, 1999).

The second dredge-up takes place during the E-AGB phase for stars with initial masses with $M > 4$ M$_{\odot}$. Like first dredge-up, the outer convective envelope penetrates into the inner regions with the end-products of H burning via the complete CNO cycle and hence it alters the surface abundances of the same isotopes as the first dredge-up: depletion of ^{12}C and an increase of the H-burning ashes ^{4}He, ^{13}C and ^{14}N, for which the strength of alteration is strongly dependent on initial mass (Becker & Iben, 1980; Becker, 1981).

During thermal pulses, He-burning shell becomes thermally unstable so that He-burning ashes at the bottom of the He intershell are mixed with higher intershell layers by the convective zone generated by the strong He-shell burning. In each thermal pulse, the envelope expands and the inner border of the envelope will first move away from the stellar core but when the star again contracts, the inner border of the convective envelope will penetrate the He intershell which lies below the inactive H-burning shell. This

mixing event is called the third dredge-up (TUP). It is believed that the efficiency of the TUP increases with increasing core mass and decreasing metallicity. It means each dredge-up mixes a certain amount of intershell material with the envelope. Actually, He-burning ashes consist of carbon and oxygen where carbon is five to ten times more abundant than oxygen so that ^{12}C is a direct product in the intershell of the triple-α reactions. On the other hand, oxygen is only significantly produced in the deeper radiative parts of the He shell as it requires higher temperatures to form than carbon.

Chemical evolution of AGB stars would be very different according to their initial mass and metalicity. Groenewegen et al. (1995) and Blöcker et al. (2000) presented certain scenarios by assuming solar metalicity for different initial masses. They are:

1. For masses, $M < 1.55$ M$_\odot$: Such stars lying in this mass range never become carbon stars beacuse they experience only a small number of thermal pulses until they terminate from their AGB evolution.

2. For masses, 1.55 M$_\odot$ $< M < 2$ M$_\odot$: Such stars lying in this mass range become carbon stars when they experience their last thermal pulse during the AGB phase. The stage to an S star is skipped.

3. For masses, 2 M$_\odot$ $< M < 4$ M$_\odot$: Such stars lying in this range experience sufficient number of thermal pulses , all the stars become carbon stars at some point. But after a few thermal pulses, they pass through the S star phase.

4. $M > 4$ M$_\odot$: Such stars lying in this range do not become carbon stars because they become hot enough during hot - button burning processing so that carbon is converted into ^{14}N by means of the CN cycle. But such stars always remain M type stars because their surface abundances changes significantly.

Carbon stars are generally believed to be the evolutionary successors of M-type Mira variables that have thin oxygen-rich dust envelopes. When AGB stars of intermediate mass range go through carbon 'dredge-up' processes, and thus the abundance of carbon is larger than that of oxygen, oxygen-rich dust grain formation ceases and the stars become visual carbon stars. After that phase, carbon-rich dust grains start forming and the stars evolve into infrared carbon stars with thick carbon-rich dust envelopes and very high mass loss rates (Iben, 1981; Chan & Kwok, 1990).

2.7 Post-AGB Star

When the mass of the H-rich envelope becomes very small i.e., in the range (10^{-2} – 10^{-3}) M$_\odot$ depending on the core mass, the envelope shrinks and the star leaves the AGB. Since the H-burning shell is fully active and the star follows the core mass-luminosity

relation so that the decrease in stellar radius occurs at almost constant luminosity. Thus the star follows a horizontal track in the H-R diagram towards higher effective temperatures and this phase of evolution is called the post-AGB phase of evolution. The typical timescale for this phase of evolution is $\sim 10^4$ yr. During this phase, the star remains in complete equilibrium :the evolution towards higher $T_{\rm eff}$ is caused by the decreasing mass of the envelope, which is eroded at the bottom by H-shell burning and at the top by continuing mass loss.

When the AGB star has exhausted its outer envelope, the AGB phase ends. At this stage the mass loss virtually stops, and the circumstellar gas and dust shell begins to drift away from the star. At the end of the TP-AGB phase, the envelope mass is strongly reduced down to 0.05 $M_\odot$ due to the strong mass loss and the star now evolves towards high temperatures at an almost constant luminosity. When the mass of the hydrogen - rich envelope drops to $\approx 10^{-3}$ $M_\odot$, it starts to contract at a constant luminosity which causes an increase in effective temperature. It leads to a radiatively driven wind which causes the circumstellar shell and may result in ionization of the circumstellar material. This is because the surface layer is gradually heating up due to the proximity of the stable burning thin H-shell which produces the luminosity. The star has now entered the post-asymptotic giant branch (post-AGB) phase. In other words, the star may become hot enough to ionize its circumstellar material so that in a few hundred years Oudmaijer (1996), it will be observed as planetary nebula. The star at this stage is known as post-AGB star. The short-lived post-AGB phase, as the star evolves toward to the PN phase, is also known as the proto - or pre - planetary nebula (PPN) phase. As the detached dust shell drifts away from the central star, the dust cools causing a PPN to have cool infrared colors. The star leaves the AGB with $T_{\rm eff} < 5000$ K but when $T_{\rm eff} > 30\,000$ K, it may ionize the remnant nebula. Typical post-AGB stars are expected to have luminosities around (10^3 to 10^4) $L_\odot$ (Bloecker, 1995) and masses are in the range 0.6 $M_\odot$ to 1 $M_\odot$.

2.8 Atmospheres of AGB Stars

AGB stars have huge atmosphere of low density and low temperature so that they do not exhibit well defined boundaries. They characterize different dynamical process such as pulsations, shock waves, molecules formation, dust formation and mass-loss. One of the most important character of AGB stars is the dynamic behavior of their atmosphere. Dynamic behavior means the pulsation leads to a periodic visual variability and time dependent molecule and dust formation. After thermal pulse, the AGB stars of initial mass below 4 $M_\odot$ can change the atmospheric chemical composition dramatically since processed elements, mostly notably ^{12}C, are dredge up to the surface by convective mixing. All the phenomena which are distributed over a large distance scale with

mutual complex influences are responsible to the extended atmospheric and circumstellar structure. In the dynamical atmosphere, molecule and dust formation takes place where as in the circumsteller structure molecules destruction and formation takes place. In this section, we describe some important aspects on the pulsation, the molecule formation and the dust production process.

2.8.1 Variability and Pulsations

Variability is a very common property of AGB stars which causes pulsation. It means the pulsations lead to a variation in the luminosity of the stars, making them variable stars. On the basis of evolutionary stage, low-mass giants exhibit various degrees of variability. AGB stars belong to the class of long period variables (LPV). Depending on the periodicity and amplitude of the light curve, LPV or Giant branch variable stars are classified in to Mira variables, semi-regular variables (SRV) and irregular variables (Lb). The variability classification is determined by the variability of the star in the V-band. Mira variables have large visual amplitudes > 2.5 magnitude in the V-band and regular variations in their light curves, semi-regular variables have smaller visual amplitudes < 2.5 magnitude with certain definite periodicity and irregular variables show no or very little periodicity. AGB stars exhibit an important fourth class, known as OH/IR stars which are generally believed to be the last evolutionary phase of an O-rich AGB star emitting OH masers at 1 ,612 MHz. OH/IR stars are Mira type long period variable stars having large amplitude pulsations with high mass-loss rates and their stellar wind is driven by radiation pressure on dust grains and momentum transfer to the gas molecules via collisions (Suh, 2014).

Typical periods for the Miras are of the order of hundreds of days, and essentially all stars on the thermal pulsating AGB are variable stars (> 90%), covering the entire mass range 0.8 $M_\odot \leq M \leq 8\ M_\odot$ (Wood et al., 1999). In case of early AGB phase, the atmosphere of AGB stars remain pulsationally unstable with pulsation period dependent on radius and mass. A relation between period, mass and radius given by Fox & Wood (1982) is

$$P \propto R^{\alpha} M^{-\beta}, \tag{2.59}$$

where $\alpha \approx 1.5$ to 2.5 and $\beta \approx 0.5$ to 1.0.

2.8.2 Molecule Formation

AGB stars are cool stars having low temperature in their atmosphere which is the favorable condition for the formation of molecules and this has important consequences

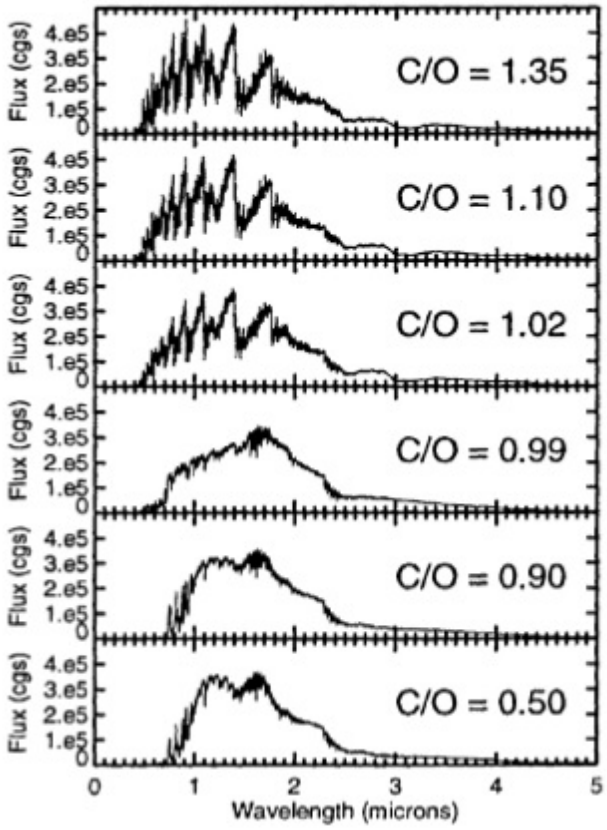

Figure 15: Model spectra for stars of 1 solar mass, $T_{eff} = 3000$ K, $\log g = 0$ and different C/O ratio (Gustafsson et al., 2003). Here g is surface gravity.

for the atmospheric structure and the photometric and spectral appearance of AGB stars (Tsuji, 1966). In the cool and extended atmosphere of AGB stars, with effective temperatures between 2500 K and 3500 K, a variety of dfferent molecule species can develop. Due to the distinct absorption and emission features of molecules above the continuum forming photosphere, it leads to a complicated spectrum. Depending on the underlying chemistry, completely dfferent chemical reactions are favored. The chemical composition of the medium determines which molecules are likely to form in the atmosphere. Due to the high binding energy of CO, it plays key role so that only excess atoms of C or O can form new compounds in carbon-rich or oxygen-rich stars, respectively. It means the chemistry in the stellar atmosphere is dominated by the high dissociation energy of the CO molecule.

Table 4 lists the most abundant atoms and molecules in both C-rich and O-rich AGB stars, obtained for a local thermal equilibrium (LTE) calculation by Markwick et al. (2000). The less abundant species out of carbon and oxygen is almost completely locked up in CO molecules but the remaining atoms of the more abundant element form other molecules. It is the reason due to which the ratio of C/O has great importance in the context of AGB stars. In case of a carbon-rich environment (C/O > 1), the most abundant species are CN, CH, C_2, C_3, HCN, C_2H_2 and in case of an oxygen-rich regime (C/O

Table 4: Most abundant atoms and molecules found in the local thermodynamic equilibrium atmosphere of an O-rich (C/O = 0.75 and $T_{\rm eff}$ = 2215 K) and a C-rich (C/O= 1.54 and $T_{\rm eff}$ = 2300 K) star. The fractional abundance is given with respect to H_2 with $x(y) = x \times 10^b$ (Markwick et al., 2000).

O-rich		C-rich	
Species	Abundance	Species	Abundance
H_2	1	H_2	1
H	2.1(-1)	H	3.5(-1)
CO	1.3(-3)	CO	1.6(-3)
H_2O	2.9(-4)	C_2H_2	2.2(-4)
N_2	1.2(-4)	C_2H	1.1(-4)
SiO	6.9(-5)	N_2	9.5(-5)
S	2.6(-5)	HCN	8.5(-5)
OH	9.0(-6)	Si	3.6(-5)
SH	7.7(-6)	CS	2.3(-5)
O	1.3(-6)	SiS	9.8(-6)
H_2S	7.2(-7)	C_3H	9.5(-6)

< 1), the abundant molecules are H_2, TiO, SiO, OH or VO where CO is present in both cases. Figure 15 shows synthetic spectra for 1 solar mass AGB stars with different C/O ratios. It is remarkable how the spectra change while going from the oxygen-rich case to the carbon-rich case. The chemistry of the atmosphere is determined by the ratio C/O and tight bond of the CO molecule, radiative dissociation through the UV field of the chromosphere or the dissociation by shocks may release enough carbon to produce carbon molecules and even carbon dust in M-type AGB stars (Cherchneff, 2006).

2.8.3 Dust Formation

From the study of dust condensation around classical novae, Gehrz (1988) suggested that grains condense on time scales of several weeks, much shorter than the pulsation periods for AGB stars. There are several evidences for the existence of dust around the AGB stars. From the extinction curve, it is clear that dust particles absorb ultraviolet radiation coming from starlight and re-emits longer wavelength infrared radiation. Warm dust emits infrared radiation, causing excess emission in the infrared part of the spectral energy distribution. Spectral features are the direct evidences of dust around AGB stars. Dust is dominated by amorphous carbon in C-rich stars but O-rich stars contain dust composed mainly of silicates.

When the temperature of the gas is sufficiently low (< 2000 K), molecules start to stick together to form molecular cluster. In the beginning, it happens randomly and eventually due to more favourable conditions, molecules and atoms add so that clusters start to grow. When the clusters act as solid materials, they are called dust grains. Dust formation depends on the temperature and density of the gas. The high densities and low

temperatures in the medium behind a shock wave allow for the formation of dust grains and the dust species formed depend on the number chemical routes. In case of C-rich AGB stars, all the available oxygen is tied up in molecular CO so that the dust grains formed to be amorphous carbon (Tielens, 1990), polyaromatic hydrocarbons (PAHs) (Feigelson & Frenklach, 1989), and to some extent silicon carbide (SiC), magnesium sulphide (MgS) or iron (Fe). Similarly, in case of O-rich AGB stars, all carbons are bound in CO, and the grains formed are silicates such as Mg_2SiO_4 or $MgSiO_3$ (Dorschner & Henning, 1995). If the adsorption rate of new atoms and molecules is higher than the evaporation rate, dust grains will grow. It is possible when the time scale for grain growth is smaller than the time scale for the change in temperature and density. The dust grains interact with the radiation field from the star and are accelerated, dragging along the gas through dynamic coupling. The outward increasing expansion velocity of the circumstellar envelope causes a decrease in density so that formation of dust grains stop.

Both theoretical and empirical considerations agree that the grain formation time scale is much shorter than the pulsation periods of AGB stars so that it is expected that the dust size distribution is likely to be a Gaussian distribution rather than a power law which is more relevant to interstellar dust (Suh, 2014). Generally estimated dust-gas ratio is 0.005 to 0.02 but Draine et al. (2007) calculated the average dust-gas ratio in the Milky way to be 0.01 and suggested that higher the metallicity, increase the ratio.

2.9 Mass-Loss and Termination of the AGB Phase

When a star enters the TP-AGB phase, it can experience a large number of thermal pulses. There are two limitations for the number of thermal pulses and the duration of the TP-AGB phase. The limitations are (i) the decreasing mass of the H-rich envelope and (ii) the growing mass of the degenerate C/O core. If the C/O core mass reaches the Chandrasekhar mass limit, $M_{\rm Ch} \approx 1.4\ {\rm M}_{\odot}$, carbon will be ignited in the centre which is so-called 'carbon flash' which has power to disrupt the whole star. But observations of white dwarfs tell us that this probably never happens in real AGB stars, even when the total mass is $8\ {\rm M}_{\odot}$, much larger than $M_{\rm Ch}$. It is due to the reason that mass loss on AGB becomes so strong that the entire H-rich envelope can be removed before the core has grown significantly. From the mass-loss rate, the life time of the TP-AGB phase is (1 to 2) $\times 10^6$ yr.

2.10 Mass-Loss on AGB Stars

Mass loss in the form of molecular gas and dust is one of the key characteristics of AGB stars. Huge convection currents inside AGB stars carry the material produced in the thin helium-burning shell up to the surface of the star. These heavier nuclei can be detected in the star's spectrum, which provides insight into the undergoing processes deep within the star. The outer layer of an AGB star loses a mass of about 10^{-4} $M_{\odot}$ per year due to increase in pulsation (this is about 100 times more than in the case of RGB stars). Mass loss is an important mechanism that enriches the interstellar medium with matter processed in the interior of AGB stars. This is responsible for the chemical evolution of galaxies and the Universe as a whole. The production of stardust is the starting point of the formation of all solid bodies ranging from planetesimals to asteroids and planets. The ejected material is comprised of mixtures of carbon, oxygen, and other elements. The carbon rich molecules from the stardust tend to shroud the star in the form of clouds. As the dust clouds expand, they absorb ultraviolet, visual, and near-infra-red radiation very efficiently and re-emit them at longer wavelengths (mainly in the range of 5 μm to 100 μm). Thus, AGB stars are more luminous in the infra-red than at visible wavelengths. The expanding cloud can also be observed at radio wavebands.

2.10.1 A Qualitative Description

A star can loss mass only when it overcomes the gravitational pull acting on it and is accelerated to a velocity greater than escape velocity. To happen this, the accelerated wind has to turn from subsonic to supersonic. The mass-loss on the AGB star is a key parameter for the evolution of the stars because it affects their lifetime and luminosity. It is generated by a physical process acting on a smaller time scale than the thermal pulses discussed above. The formation of a cold circumstellar shell during the AGB phase is a consequences of the large radial pulsation that bring envelop material high above the atmosphere. When the recreation of this material starts, the new pulsation wave is already happening and prevents infall of the material. The density in this circumstellar shell increases to such levels that the molecules can form solid particles (dust). The radiation pressure on the dust causes an outward movements of the dust shell with a certain expansion velocity. At the end of the AGB, the mass loss rate has risen to such high value, virtually the entire hydrogen rich envelope is expelled from the central star (Padmanabhan, 2006). At the onset of the AGB, mass-loss rate is low i.e., about 10^{-8} $M_{\odot}$ yr^{-1} but as the star evolves up the AGB, the mass-loss rate increases to an intense wind with a rate up to 10^{-4} $M_{\odot}$ yr^{-1}. Due to mass-loss, a thick circumstellar envelop of dust and gas around the star is formed which is rich in nucleosynthesized material. The rate of ejection of matter is higher than the growth rate of the core so that

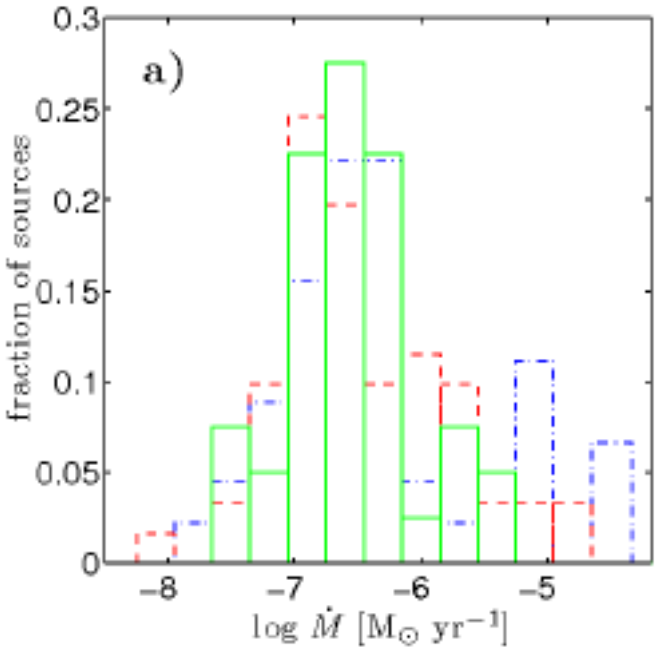

Figure 16: Distribution of mass-loss rate for C-type stars (dashed red line), S-type stars (solid green line) and M-type stars (dashed-dotted blue line) (Ramstedt et al., 2009).

all the matter around the core is dispersed in to space which is the end point of the AGB evolution and beginning of the post-AGB evolution. In practice, it is possible when the stellar envelope mass becomes less than about 0.01 $M_\odot$.

The mass-loss rate of AGB star depends on its luminosity and varies with pulsations as well as with the thermal pulse cycle. The efficient dust formation in the dynamical envelope plays an important role to drive the wind by radiation pressure on the dust grains (Kwok, 1975) which is able to induce very large mass-loss rates (10^{-8} to 10^{-4}) $M_\odot$ yr^{-1} in full consistent with theoretical and observational interpretation.

When the star is in the AGB phase, mass-loss is driven by large-amplitude radial pulsations and mass increases with increasing luminosity. While the envelope mass decreases because of the mass-loss, the core mass is growing as a result of hydrogen and helium burning in the shell. If the stellar luminosity is provided essentially by H-burning, then the rate of growth of core mass is proportional to luminosity and inversely proportional to the efficiency of energy production (Padmanabham, 2001). The mass-loss rate distributions are very similar for C-, S- and M-type of stars (Ramstedt et al., 2009) which is shown in the Figure 16.

2.10.2 A Quantitative Description

Low and intermediate mass stars in the range (0.8 to 8) $M_\odot$ during the late stages of their evolution reach to the Asymptotic Giant Branch phase. This phase of stellar evolution

is characterized by strong mass loss so that the dust and gas are expelled at rates up to 10^{-4} $M_\odot$ yr^{-1}. The heavy mass-loss of AGB stars is one of the most important contribution for mass return from stars to the interstellar medium (ISM). Maeder (1992) has proposed that mass loss from these stars contributes about half of the gas by recycling so that mass loss is very important for the chemical evolution of our Galaxy. Mass loss from AGB stars seems to occur through two distinct mechanisms:

(i) Shocks due to pulsations produce gas over densities which can trigger the formation of dust.

(ii) The radiation pressure on dust makes this dust to overcome the gravity of the star so that it can be accelerated with a velocity greater than escape velocity.

Hydrodynamic models suggest that large amplitude pulsations are necessary for accelerating the mass outflow from the surface of AGB stars until the gas becomes cool enough so that the dense elements can condense into dust grains. These dust grains absorb and scatter the radiation from the stellar radiation field to the gas as a result the flow velocity may exceed the escape velocity (Gilman, 1972). When the star has completed the AGB phase, it somehow develops a less massive (10^{-7} $M_\odot$ yr^{-1}) but faster wind up to 10^3 km s^{-1}. Such wind sweeps up the circumstellar material, possibly creating shocks and high-density shells. At high stellar temperature, ultraviolet photons are produced which can heat the dust, excite, ionize, and dissociate gas molecules (when $T_{\rm eff}$ > (20 to 30) $\times 10^3$ K) (Cerrigone et al., 2012). Mass-loss grows with time until super-wind regime sets in, which quickly turns into a planetary nebula by throwing all the envelope away and leaving a bare core which evolves to high temperatures. Vassiliadis & Wood (1993) represented the above situation with suitable analytical fits in which mass loss rate ($\dot{M}$) grows exponentially with the luminosity up to the formation of the planetary nebula.

In many calculations of AGB evolution, a simple dimensional formula for the early mass loss rate without any physical interpretation given by Reimers (1975) is

$$\dot{M} = 4 \times 10^{-13} \frac{\eta L R}{M}, \tag{2.60}$$

where $\dot{M}$ is mass loss rate in $M_\odot$ yr^{-1} and L is stellar luminosity, R is stellar radius and M is stellar mass in solar unit. η is a fitting parameter whose value is calibrated in such a way that it recovers the observed morphology of horizontal branch stars in Galactic Globular clusters. Renzini & Fusi Pecci (1988) suggested that for this normalization, $\eta \sim 0.5$.

Different scientists such as Lamers (1981), de Jager et al. (1988), and Nieuwenhuijzen & de Jager (1988) have given other empirical mass-loss formulae , but they do not dis-

tinguish between the strong and well-described dust-driven winds (Schröder & Cuntz, 2005) and are physically very different for non dust-driven winds. Recently, Schröder & Cuntz (2005) assumed that wind is the result from the spillover the extended chromosphere which is possibly due to the action of waves. They obtained a relation modified to the original Reimers law by including two new factors i.e., how the height of the chromosphere depends on surface gravity and how the mechanical energy flux depends, mainly, on the effective temperature. It means a modified version of the (Reimers, 1975) law where additional dependencies on the effective temperature and surface gravity follow from a physically motivated consideration of the mechanical energy flux responsible for the wind. The modification has taken into account to estimate the rate of magneto-accoustic heating of the chromosphere where the stellar wind starts from the top of the chromosphere rather than from the photosphere. Their formula which is close to the Reimers law is

$$\dot{M} = 8 \times 10^{-14} \frac{\eta' LR}{M} \left(\frac{T_{\rm eff}}{4000K} \right)^{3.5} \left(1 + \frac{\rm g_\odot}{4300g} \right), \tag{2.61}$$

where g and $\rm g_\odot$ are stellar and solar surface gravity in solar unit respectively and according to (Schröder & Cuntz, 2005), the constant η' is equal to unity. The mass loss rate given by the Schroder-Cuntz formula and Reimers formula agree to within a factor of 2 ($\eta \sim 0.5$ and $\eta' \sim 1.0$) (Figure 17). In case of Schroder-Cuntz formula, there is an additional gravity dependent term so that mass loss is more concentrated to the higher luminosities. After the application of both formulae, it is found that for ordinary giants, the two new factors do not make much difference, which explains the long-lasting success of the Reimers relation.

2.11 Dust Driven Winds

Winds of asymptotic giant branch (AGB) stars are thought to be driven by the combination of pulsation - induced shock waves and radiation pressure on dust. Atmospheric shock waves, which are triggered by stellar pulsations and large-scale convective motions, play a critical role in the mass-loss mechanism of asymptotic giant branch (AGB) stars. The strong radiating shocks propagate outwards through the stellar atmosphere, intermittently lifting gas to distances where temperatures are low enough to allow for the formation and growth of dust grains. These particles absorb and scatter stellar photons, resulting in an outwards-directed acceleration of the dust. Through dust-gas collisions, momentum is transferred to the gas, triggering a stellar wind. Dust grains has important role in mass-loss of AGB stars and its absence, the opacity in outer layers of the stars is very small. But opacity can be increased by a thousand times if 1% mass is condensed

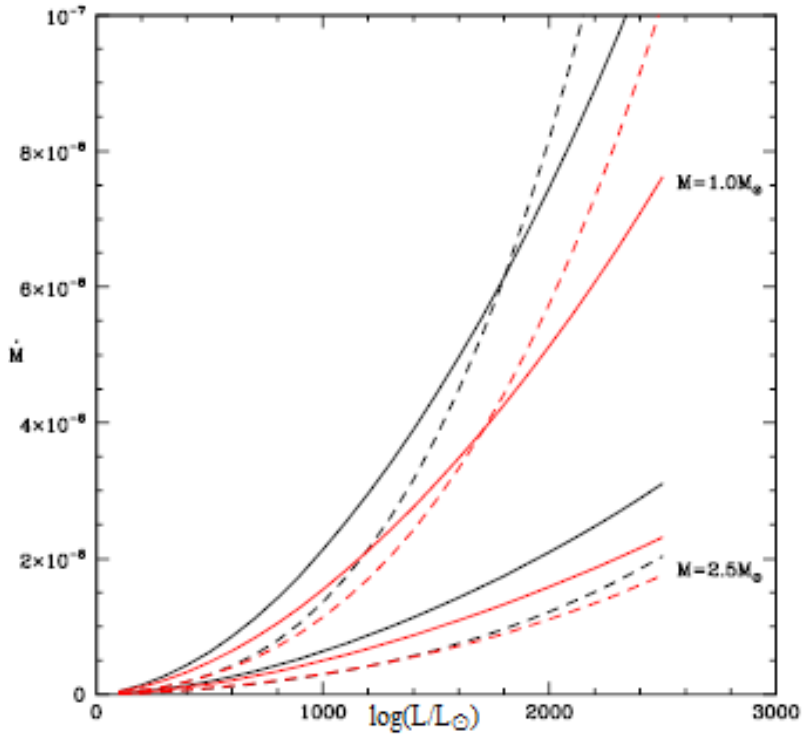

Figure 17: The mass loss rate $\dot{M}$ in $M_\odot$ yr^{-1} plotted against $\log(L/L_\odot)$ for red giant stars of mass 1 and 2.5 $M_\odot$, and abundances $Z = 0.02$ (thick lines) and $Z = 0.004$ (thin lines). Solid lines show mass loss rates from Reimers formula where as dashed lines show mass loss rates from Schroder-Cuntz formula are shown as dashed lines (Wood, 2010).

into dust grains. Due to this reason AGB stars can lose mass by radiation pressure (Jones et al., 1981).

Thus in case of spherical dust shell, the outward radiation force per unit mass is

$$F_{\rm rad} = \frac{K_{\rm pr}(r)}{c}\frac{L}{4\pi r^2} \tag{2.62}$$

where

L = luminosity of the central star,

c = speed of light,

r = the distance from the stellar center and

$K_{\rm pr}$ = the radiation pressure opacity (cm^{-1})

$K_{\rm pr}$ is given by

$$K_{\rm pr} = \pi a^2 N_{\rm g} \langle Q_{\rm pr} \rangle \tag{2.63}$$

Here, $N_{\rm g}$ is the dust grain number density, $\langle Q_{pr} \rangle$ is the Planck mean value of the radiation

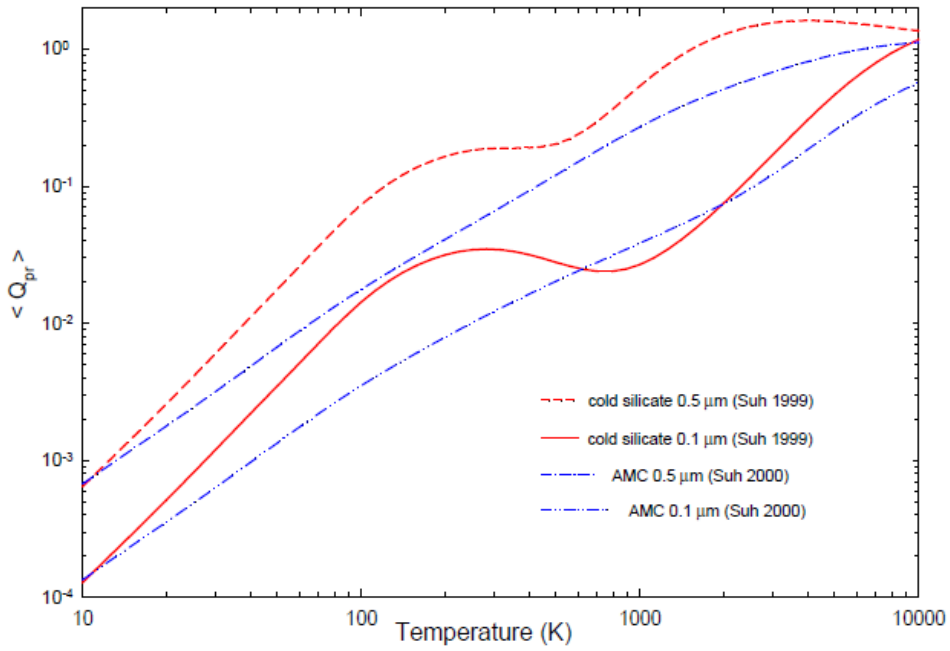

Figure 18: Graph between Planck mean values of the radiation pressure efficiency factors and temperature for amorphous carbon and silicate for different spherical grain radii (Suh, 2014).

efficiency factor (Q_{pr}) and is given by

$$Q_{\rm pr} = Q_{\rm ext} - \langle cos\theta \rangle Q_{\rm sca}\,, \tag{2.64}$$

where $Q_{\rm ext}$ is the extinction efficiency factor, $Q_{\rm sca}$ is the scattering efficiency factor and θ is the angle between incident wave and the scattered wave. Thus the Planck mean value of the efficiency factor $Q(\lambda)$ which is a function of temperature is given by

$$Q = 15\left(\frac{hc}{\pi kT}\right)^4 \int_0^\infty Q(\lambda)\lambda^{-5}\left[e^{hc/(\lambda kT)} - 1\right]^{-1} d\lambda \tag{2.65}$$

To estimate dust temperature, the Planck mean values of the absorption factors ($Q_{\rm abs}$) are useful and to estimate the dynamical effects of dust grains, the Planck mean values of the radiation pressure efficiency factors ($Q_{\rm pr}$) are useful which is important in studying stellar winds and mass-loss from AGB stars (Kozasa et al., 1984). The dynamics of the inner, dust-free region of the atmosphere are not sensitive to change in the luminosity. Gas opacities are too low to produce significant radiative acceleration. Planck mean values of the radiation pressure efficiency factors for amorphous carbon and silicate for different spherical grain radii are shown in Figure 18. For amorphous carbon grains, there is nearly linear relation between them and bigger grain size has their values high but for silicate grains, they show linear relation up to certain value and then rise and fall. Once when dust grains are formed in the envelopes around AGB stars, they can be efficiently accelerated faster than the escape velocity (Bowen, 1988a) by the

radiation force equation (2.62) which is the mechanism for mass- loss of AGB stars. The mechanisms driving such strong mass loss are not fully understood, but it is likely that both dynamical pulsations and radiation pressure on dust particles play a role.

2.12 Infrared Astronomical Satellite (IRAS) Survey

To study stellar objects, there are various types of space observatories. Major IR space observatories developed in the last 25 years are IRAS (1983), COBE (1990), ISO (1995), SPITZER (2003) and HERSCHEL (2008). First all sky survey at far IR wavelengths carried out in 1983 by the Infrared Astronomical Satellite (IRAS) which opened a new era in modern infrared astronomy. Thousands of galaxies were detected to emit infrared light. After IRAS, a long series of observations were started to explore the IR universe. Actually in 1980s, the first generation infrared space telescope and infrared astronomical satellite (IRAS; Neugebauer et al. (1984) were launched which worked in two mid-infrared bands (12 μm and 25 μm) and two far infrared bands (60 μm and 100 μm). They discovered many mass losing AGB stars, post AGB stars, planetary nebulae, white dwarfs, etc in the milky way and the magellanic clouds. Infrared Space Observatory (ISO) (Kessler et al., 1996) with the Short Wave Spectrometer (SWS) works in the range of 2.4 μm to 45 μm. They were used spectroscopically to observe several AGB stars and obtained infrared spectra provide most valuable information about dusty environment around the AGB star. The Galactic Plane Survey of the Spitzer Space Telescope (Werner et al., 2004) in the galactic plane at the 3.6 μm, 4.5 μm, 5.8 μm, 8 μm , 24 μm and 70 μm bands provides high resolution and sensitive infrared images but without filters between 8 μm and 24 μm, AGB stars can't be separated in mid infrared color-color diagrams. The Wide field Infrared Survey Explorer (WISE) launched on 2009 December 14. The Two Micron All Sky Survey (2MASS) (Skrutskie et al., 2006) is used in three near infrared, J (1.25 μm), H (1.65 μm) and K (2.17 μm) bands which are most informative to complete the infrared spectral energy distribution (SED) of AGB stars.

Our work is under infrared astronomical satellite (IRAS) survey. Actually, IRAS survey is an unbiased all-sky survey which contains cryogenically cooled telescope orbiting above the Earth's atmosphere and works at 12 μm, 25 μm, 60 μm and 100 μm wave length bands. The objectives, instrumentation and limitation of the IRAS survey are briefly described.

Infrared observations are important to understand solar system objects and regions of star formation. It helps to reveal astronomical sources obscured by interstellar dust, to identify galaxies with large bursts of newly formed stars and in describing the emission mechanism present in active galactic nuclei. Unbiased and sensitive all-sky surveys at

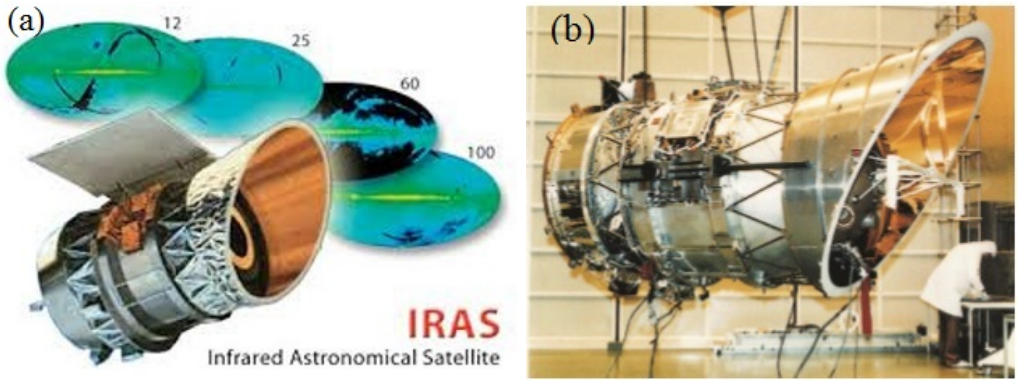

Figure 19: (a) The Infrared Astronomical Satellite (IRAS) and (b) Infrared Astronomical Satellite (IRAS) during the magnetic moment test conducted in the Netherlands. The satellite was slowly spun and the variations to the magnetic field were measured. (Source: https://www.jpl.nasa.gov/missions/infrared-astronomical-satellite-iras/)

infrared wavelenghts are difficult because of the obscurtion of the Earth's atmosphere and because of the thermal emission from warm telescopes and the atmosphere. The Infrared Astronomical Satellite (IRAS) mission was designed to overcome these difficulties by conducting all-sky survey from a space satellite with a cooled telescope. The Infrared Astronomical Satellite (IRAS), shown in Figure 19(a,b), scanned more than 96% of the sky at wavelengths from 10 to 100 μm with a sensitivity as close as practical to the limitation set by the fluctuations in the thermal emission from zodiacal background. The point source catalog produced from this survey is intended to be highly reliable (>99.8%) (Neugebauer et al., 1984).

IRAS was a joint project of the US, UK and the Netherlands which performed an unbiased, sensitive all sky survey at 12, 25, 60 and 100 μm. The satellite design and survey strategy were optimized for maximally reliable detection of point sources. Additional Observations or AOs known as pointed observations interspersed with the survey observations. This path-breaking infrared satellite doubled the number of known astronomical sources and made numerous important scientific advances. Archival research with IRAS data continues nearly 20 years after this historic mission. The Infrared Astronomical Satellite (IRAS) surveyed 96% of the sky from January 1983 through November 1983. It was conducted in four wavelength bands centered at 12 μm, 25 μm, 60 μm and 100 μm and spent approximately two-thirds of its 300 day mission performing an unbiased survey of the sky. The mission led to the 1984 release of the IRAS Point Source Catalog (PSC), which contains some 250,000 sources. IRAS scanned the sky repeatedly by multiple detectors, and over half of the sky was covered by more than twelve individual detector scans per wavelength band. In the 1970s, astronomers around the world began to consider the possibility of placing an infrared telescope on a satellite in orbit around the Earth. This telescope would be above the Earth's atmosphere and could view the sky at the mid and far infrared wavelengths which could not be detected on Earth. It

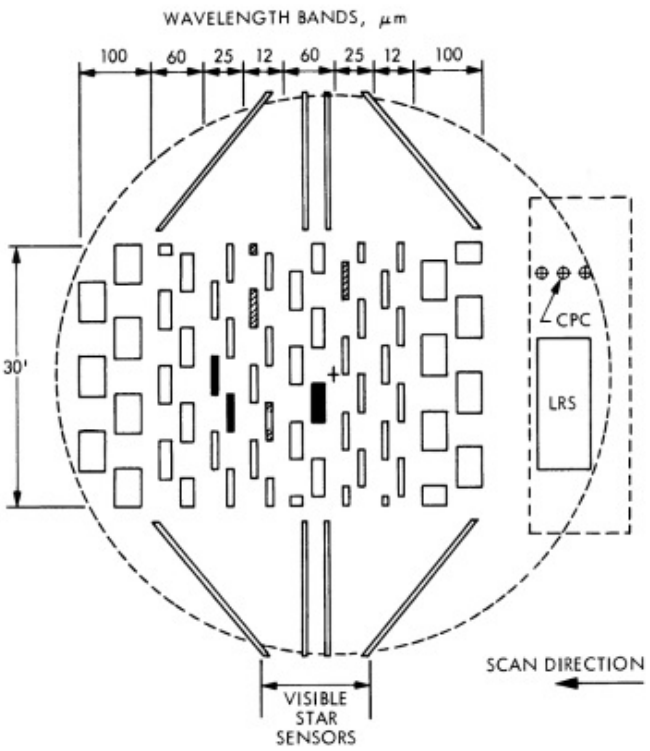

Figure 20: Schematic drawing of the IRAS focal plane. The rectangles in the central portion each represent a detector,filter,and field lens combination of the survey array. The image of the source comes up the focal plane in the direction indicated. The shaded detectors are in operative or essentially so; these anomalies were known before launch (Neugebauer et al., 1984).

could view a large area of the sky and observe regions for a longer period of time. By 1977, an international collaboration was formed by the Netherlands, United States and Great Britain to develop IRAS. The American team built the telescope, detectors and cooling system. The British built the satellite ground station and control center and the Dutch team built the space craft which included the on board computer sand pointing system. The entire telescope was cooled to a temperature of just a few degrees above absolute zero because otherwise the telescope itself would emit infrared radiation which would interfere with the observations. A space infrared telescope must be cooler than the objects in space that it will observe. IRAS discoveries included a disk of dust grains around the star Vega, six new comets, and very strong infrared emission from interacting galaxies as well as wisps of warm dust called infrared cirrus which could be found in almost every direction of space. IRAS also revealed for the first time the core of our galaxy, the MilkyWay (Neugebauer et al., 1984).

IRAS satellite consists of a space craft and a liquid helium cryostat containing a cooled telescope which is $f/9.6$ Ritchey-Chretien design with a 5.5 m focal length and 0.57 m aperture and beryllium mirrors cooled to less than 10 K. A system of internal cold baffles reduces the system's response to off-axis radiation. External baffles and the sunshade (at 100 K) reduce the heat load on the cold optical system from the sun and

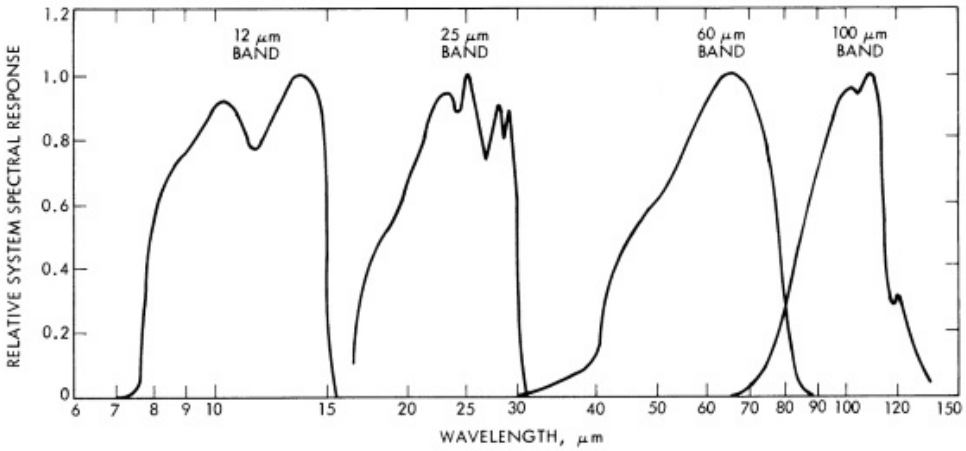

Figure 21: The spectral response of the IRAS detector, field lens, and filter combination of the survey band. Quoted flux densities have been calculated at wavelengths of 12 μm, 25 μm, 60 μm, and 100 μm assuming the energy distribution of the source is flat in flux per logarithmic frequency interval (Neugebauer et al., 1984).

earth. The combined flux at the focal plane from all bright sources of off-axis emission during normal survey is less than a few percent of the thermal emission of the zodiacal dust particles over the range of observing angles used (Pouw, 1983). The focal plane assembly, located at the Cassegrain focus of the telescope, and cooled to less than 3 K, is shown schematically in Figure 20. Sixty-two infrared detectors in the survey array are arranged so that every source crossing the field of view can be seen by at least two detectors in each of four wavelength bands. Each detector is preceded by a field lens and spectral filters. The spectral characteristics of the filters are shown in Figure 21. The electronics are direct coupled, permitting a measurement of the total flux entering the telescope. Silicon detectors are used to detect stars at visible wavelengths for position control and reconstruction.

The low-resolution spectrometer (LRS) is a slit less spectrometer with a wavelength range from 7.5 μm to 23 μm. On the basis of timing derived from the survey array, spectra with a resolution of approximately 20 are extracted from the data stream for all sufficiently bright point sources that cross the LRS aperture. The chopped photometric channel (CPC) operates during selected pointed observations, mapping infrared sources simultaneously at 50 μm and 100 μm with higher spatial resolution than normally provided by the survey array. The CPC has an internal cooled chopper and thus avoids the need for signal modulation by scanning and provides an absolute flux reference (Wildeman et al., 1983).

The satellite was launched into a 900 km altitude near-polar orbit on 1983 January 26 GMT. The cryogenic helium supply was exhausted on 1983 November 22 GMT. The orbit has an inclination of 99° with respect to the Earth's equator and precesses so that it remains close to the plane of the terminator. The telescope could point away from the

local vertical by up to 30° by rotating the entire satellite. Scans of the sky were performed by rotating about the vector from the satellite to the Sun at fixed solar elongation angles between 60° and 120°. In survey scans, the bore sight swept across the sky at a rate of 3.85° per minute.

2.13 A Catalog of AGB Stars in IRAS PSC

Generally asymptotic giant branch (AGB) stars are classified in to oxygen- rich(M-type) and carbon-rich (C-type). But in the catalog provided by Suh & Kwon (2009), (AGB) stars are classified into four types: O-rich stars (M-type Miras and OH=IR stars), C-rich stars (C-type stars or carbon stars), S stars, and silicate carbon stars. They presented the catalog of 2193 O-rich stars, 1167 C-rich stars, 287 S stars and 36 silicate carbon stars.The catalog of Galactic AGB stars based on reports of different IRAS resolution spectrographs. Data of Low Resolution Spectrograph (LRS: λ = 8 μm to 22 μm) are very useful to identify important features of O-rich and C-rich dust grains in AGB stars (Kwok et al., 1997). Infrared Space Observatory (ISO) has Short Wave Length Spectrometer (SWS: λ = 2.4 μm to 45.2 μm) and Long Wave Length Spectrometer(LWS: λ = 43 μm to 197 μm) which are useful to identify more detailed dust features (Suh, 2002). Near Infrared Spectrometer (NIRS; 1.4 μm to 4.0 μm; (Murakami et al., 1994) data are useful for identifying the molecular feature of AGB stars. The radio OH and SiO survey (Lewis et al., 1990) for IRAS color-selected objects have been very useful to identify AGB stars. The infrared astronomical satellite (IRAS) works at 12 μm, 25 μm, 60 μm and 100 μm wavelength band which lie in the infrared and far from infrared region. It is suitable to observe dust particles which absorbs ultraviolet radiation and emits infrared radiation. The Mid-course Space Experiment (MSX) Egan et al. (2003) provided useful photometric data at 8.28 μm, 12.13 μm, 14.65 μm, 21.34 μm wavelength bands and the 2MASS data project Skrutskie et al. (2006) provide the PSC that contains fluxes at J, H, and K bands. Suh & Kwon (2011) updated the catalog with SiO maser sources for O-rich AGB stars and additional sources for C-rich AGB stars. The updated catalog contains 3 003 O-rich and 1 168 C-rich AGB stars with their IRAS colors and has the largest confirmed AGB collection so far. So this catalog is most useful entry for the future study of AGB stars.

First all sky survey at far IR wavelengths carried out in 1983 by the Infrared Astronomical Satellite (IRAS) which opened a new era in modern infrared astronomy. Thousands of galaxies were detected to emit infrared light. After IRAS, a long series of observations were started to explore the IR universe. Actually in 1980s, the first generation infrared space telescope and infrared astronomical satellite (IRAS; Neugebauer et al. (1984) were launched which worked in two mid-infrared bands (12 μm and 25 μm) and two

far infrared bands (60 μm and 100 μm). They discovered many mass losing AGB stars, post AGB stars, planetary nebulae, white dwarfs, etc in the milky way and the magellanic clouds. Infrared Space Observatory (ISO; (Kessler et al., 1996) with the Short Wave Spectrometer (SWS) works in the range of 2.4 μm to 45 μm. They were used spectroscopically to observe several AGB stars and obtained infrared spectra provide most valuable information about dusty environment around the AGB star. The Galactic Plane Survey of the Spitzer Space Telescope (Werner et al., 2004) in the galactic plane at the 3.6 μm, 4.5 μm, 5.8 μm, 8 μm ,24 μm and 70 μm bands provides high resolution and sensitive infrared images but without filters between 8 μm and 24 μm, AGB stars can't be separated in mid infrared color-color diagrams. The Wide field Infrared Survey Explorer(WISE) launched on 2009 December 14. The Two Micron All Sky Survey (2MASS) (Skrutskie et al., 2006) is used in three near infrared, J (1.25 μm), H (1.65 μm) and K (2.17 μm) bands which are most informative to complete the infrared spectral energy distribution (SED) of AGB stars. Further detail about the catalog and the classification of AGB stars has described in the subsection 2.7.3.

2.14 An Evolutionary Catalogue of Galactic Post-AGB and related Objects

A preliminary compilation was presented by Szczerba & Górny (2001) including about 220 stars. Szczerba et al. (2007) further studied all the literature available on the NASA Astrophysics Data System (ADS) up to 2006 and the revised catalog is named as " the Torun catalog of Galactic post-AGB and related objects". This catalogue of Galactic post-AGB and related objects was developed to facilitate the research on the late evolution of intermediate mass stars. It also helps to identify new post-AGB objects among AKARI sources. The catalog contains 326 very likely, 107 possible and 64 disqualified post-AGB stars. They further revised the catalog which contains 391 very likely, 83 possible and 66 unlikely post-AGB stars.

Post-AGB stars are being strongly obscured by their circumstellar dusty envelopes so that they are difficult and often impossible to detect in optical wavelengths. In the past, for discovery of post-AGB stars mostly sky surveys such as the 2 μm Sky Survey (Neugebauer & Leighton, 1969), the Air Force Infrared Sky Survey (Kleinmann et al., 1981) and especially the InfraRed Astronomical Satellite (IRAS) survey (Beichman, Neugebauer, et al., 1988) were in use. Thus by organizing knowledge of post-AGB stars in our Galaxy Szczerba et al. (2007), developed an evolutionary on-line catalog available at http://www.ncac.torun.pl/postagb. Post-AGB objects collected during their database include the following classes:

- IRAS selected sources named IRASsel in the catalog: These are the sources considered to be post-AGB on the basis of their IRAS colors, found to be in

between of AGB stars and of planetary nebulae (Kwok et al., 1987; Suárez et al., 2006). Most of the selected objects are optically faint because the selection criteria focus on the circumstellar material properties. This group contains 115 objects in the catalog.

- High Galactic latitude supergiants named hglsg in the catalog: Bidelman (1951) was the first man to point out the existence of such supergiants (e.g. 89Her). According to him, massive supergiants are generally not expected to be found at high Galactic latitudes. It is therefore possible that high-latitude supergiants are in fact low-mass stars in their final stages of evolution. In the catalog, there are 63 objects from this class of stars.

- High Galactic latitude B-type supergiants named hglB in the catalog and hot post-AGB objects named as hotpAGB: Hot, B-type supergiants are similar to main sequence B-type stars (effective temperature, gravity), were discovered in studies of the B-star population in the Galactic halo (Moehler & Heber, 1998). Szczerba et al. (2007) classified that hglB are very likely post-AGB objects which have B spectral type, located at high Galactic latitudes ($|b| > 15°$) and early-type (A and B) supergiants, located at lower latitudes ($|b| < 15°$). Such sources were included in their catalogue as hotpAGB. There are 9 and 18 post-AGB objects in the catalog from hglb and hotpAGB group of stars respectively.

- Bright stars with infrared (IR) excess named IRexc in the catalog: The IR excess criterion was proposed by Parthasarathy & Pottasch (1986), Pottasch & Parthasarathy (1988) and others, together to estimate dust mass. It is one of the criteria that have been used to select candidate post-AGB sources. In the catalog, there are 34 objects from this source.

- UV Her-type stars named UV Her in the catalog: There is a small group of variable stars among Population II supergiants, called UU Her after the best studied member of group 3 (Sasselov, 1984). From this group also Szczerba et al. (2007) found 13 number of objects.

- RV Tau stars named as RV Tau in the catalog: The RV Tau stars are highly luminous variable stars. They show alternating deep and shallow minima, periods between 30 and 150 days, and spectral types F, G and K (Preston et al., 1963). Most of them show IR excess, as evidence of a recent mass loss typical of the AGB phase of evolution (Jura, 1986). 99 objects are found from this group of RV Tau stars in the catalog.

- R CrB stars named as R CrB; extremely helium stars named eHe and Late thermal Pulse objects named as LTP in the catalog: The R CrB stars are rare H-deficient

Table 5: Distribution of the very likely post-AGB objects into various classes (Szczerba et al., 2007).

Class	Number of objects
IRASsel	115
hglsgl	63
hglb	9
hotpAGB	18
Irexc	34
UV Her	13
RV Tau	99
R CrB	36
eHe	16
LTP	2
21 micron	12
refneb	4

and C-rich supergiants. They undergo irregular declines of up to 8 mag when dust forms in clumps along the line of sight (Clayton, 1996). There are two major models which explain their origin i.e., a merger scenario (Webbink, 1984) and a final helium-shell flash scenario (Fujimoto, 1977). In the catalog, there are 36 very likely post-AGB objects from R CrB stars, 16 from eHe stars and 2 from LTP stars.

- 21 micron emission sources named as 21 micron in the catalog: There is a group of 12 sources. They show a spectacular emission band at 21 microns (Kwok et al., 1989) confirmed by the Infrared Space Observatory. All these sources are C-rich and show s-process element enhancement (Van Winckel & Reyniers, 2000) and 12 objects are included in the catalog from 21 micron sources.
- Reflection nebulosity named as refneb in the catalog: There are a few famous objects (Red Rectangle, Minkowski Footprint, Egg Nebula, AFGL618) which have indicated the characteristic and allowed these sources to be discovered prior to IRAS. There are 4 objects included in the catalog from this source.

The distribution of the very likely post-AGB objects found from various classes is shown in Table 5. The number of objects mentioned in the table in various classes are not only very likely post-AGB objects. For example, there are 99 stars classified as RV Tau in the SIMBAD database. Out of these, 80 are in the list of very likely post-AGB objects, two are possible, 12 are disqualified and 5 are not considered in the catalog because they are LMC sources.

2.15 Motivation

Due to following reasons, we are motivated to do this research work:

- The AGB star and its surroundings are the natural laboratory in which we can study its effect in the interstellar medium. A catalog of AGB stars in IRAS PSC was developed by Suh & Kwon (2009). They classified AGB stars and provided their coordinates which is the preliminary stage of our research work.
- Current status of modeling and nucleosynthesis of AGB stars are reviewed by Herwig (2005). In recent years, the principles of AGB evolution have been investigated leading to improve and redefine models, for example hot-bottom burning or the third dredge-up. The post processing s-process model reproduces many observations.
- The Infrared Astronomical Satellite (IRAS) mission launched on January 25, 1983. It was the first-ever space-based observatory to perform a survey of the entire sky at infrared wavelengths. According to Neugebauer et al. (1984), the IRAS contains a cryogenically cooled telescope orbiting above the Earth's atmosphere to make an unbiased all sky survey at 12 μm, 25 μm, 60 μm and 100 μm. It was a joint project of United States , the Netherlands and the United Kingdom .
- Using the extensive all sky database of IRAS, Wood et al. (1994) studied the IRAS images of nearby 100 dark molecular clouds. The IRAS 60 μm and 100 μm co-added images were used to calculate dust color temperature, 100 μm optical depth and visual extinction of dust in the clouds.
- AKARI infrared sky survey was used by Szczerba et al. (2007) to complete an evolutionary catalogue of galactic post-AGB and their related objects. They completed the catalogue dividing it in to three categories: very likely, possible and disqualified post-AGB objects. They measured different parameters. Derived distances of the stars from the observation region are used to calculate dust mass.
- There are 462 far infrared loops identified by Kiss et al. (2004) and Könyves et al. (2007) using 60 μm and 100 μm processed IRAS data where they calculated distances of the 73 far infrared loops which are used to calculate dust mass around the desired region. We intend to investigate new FIR loop or cavity candidates similar to 462 far infrared loops (Kiss et al., 2004; Könyves et al., 2007).
- Jha et al. (2017) presented dust color temperature, dust mass and inclination angle of four far infrared loops namely G007+18, G143+07, G214-01 and G323-02 which are located within 1° from nearby pulsars PSR J1720-1633, PSR J0406+6138, PSR J0652-0142 and PSR J1535-5848, respectively. They found

the dust color temperature of the core region which lie in the range (19.4 ± 1.2) K to (25.3 ± 1.7) K, whereas the range increased to (33 ± 2) K to (47 ± 3) K for the outer region. They measured average dust mass of each pixel of the four loops which lie in the range 2.96×10^{26} kg to 1822.2×10^{26} kg. The dust color temperature and dust mass distribution maps show that the low temperature region has greater density as expected. We have used similar method for calculation of dust color temperature and dust mass.

CHAPTER 3

3. MATERIALS AND METHODS

3.1 Region of Interest: Catalog

One of the most important part to start research is the region of interest and it strongly belongs to the catalogue of the related fields. To enter into the region of interest, asymptotic giant branch (AGB) stars are selected. For AGB stars, two widely used important catalogue are available. One catalog is based on types of AGB stars (Suh & Kwon, 2009) and another catalog is about post AGB stars (Szczerba et al., 2007). Candidates of these two catalogue are further analyzed with third catalog provided by Könyves et al. (2007) which is about far infrared cavity.

3.1.1 AGB Based Systematic Search on Infrared Astronomical Satellite (IRAS)

A catalog of AGB stars in IRAS point source catalogue (PSC) was provided by Suh & Kwon (2009). The catalog of AGB stars of our Galaxy from the sources listed in the IRAS PSC was developed by compiling the lists of their previous works. In the catalog, AGB stars are divided into four groups: O-rich stars, C-rich stars, S-stars, and SiC-stars. Here O-type AGB stars have oxygen-rich atmospheres in which C/O < 1, C-type stars have carbon rich atmospheres where C/O > 1 and S types stars are some what transitional between the two having C/O ~ 1 and SiC stars are carbon stars with silicate dust features. They will be oxygen-rich (M-type) or carbon-rich (C-type) or S- type depending on the chemistry of the outer envelope or the photosphere. For large scale sample of AGB stars, they presented infrared two-color diagrams from the observations at near infrared bands. O-rich AGB stars typically show 10 μm and 18 μm features in emission and absorption band respectively. Two thousand one hundred ninety three O-rich AGB stars are listed there. C-rich AGB stars are believed to be formed by amorphous carbon grains and SiC grains producing the 11.3 μm emission feature. One thousand one hundred sixty seven C-rich AGB stars are identified and verified there. Similarly there are two hundred eighty seven S-stars and thirty six SiC-stars are identified but not verified. The catalog

presented by Suh & Kwon (2009) is further revised by the same author in 2011. They added and produced a list of 3 003 O-rich, 1 168 C-rich, 362 S-type and 35 SiC-stars in our Milky way galaxy.

In addition of the catalog, there is another on-line catalogue about galactic post-AGB stars referred as 'Torun catalogue' developed by Szczerba et al. (2007). The catalogue contains 326 very likely post-AGB stars and 107 possible post-AGB star candidates. For very likely post-AGB stars, the catalog provides optical and infrared photometry, infrared spectroscopy and spectral types, etc. Later, the catalogue has been revised by the same author in 2010. In the newly revised catalogue, there are 391 very likely and 83 possible post-AGB stars. So basically these two types of catalogue are used in this work. Systematic search has been carried out on IRAS in both AGB and post-AGB using SkyView Virtual Observatory (http://skyview.gsfc.nasa.gov/current/cgi/query.pl) during the period January to April, 1915. We intend to search an isolated cavity like structure in all available IRAS bands (12 μm, 25 μm , 60 μm and 100 μm). SkyView isn't exactly a telescope but the collection of large number of data base of astronomical surveys that simulate the images taken by telescopes or satellites. The systematic steps which were carried out using SkyView Virtual Observatory are described below:

Step-I: Input Parameters

We have used as input parameters in the SkyView Virtual Observatory (http://skyview .gsfc.nasa.gov/current/cgi/query.pl)as follows:

- Coordinate: Galactic coordinate system
- Projection: Gnomonic (A non conformal map projection obtained by projecting points of three dimensional celestial objects on the surface of sphere)
- Image Size (pixel) : 500×500
- Image Size (degrees) : $1.0° \times 1.0°$, $2.5° \times 2.5°$
- Brightness Scaling: Histogram Equilization (by making uniform bins for the distribution of flux)
- Color Table: Stern Special (Dark black shows minimum flux density and white shows its maximum value)
- Provenance : NASA IJAC/Jet Propulsion Laboratory
- Copyright : Public Domain

Step-II: Preliminary Images Downloaded

There are 132 all sky surveys available in the Sky View Observatory. We have used 12 μm, 25 μm, 60 μm and 100 μm IRAS bands to find cavity like structure around AGB

Stars. For the proper study of the isolated cavity structure, emission at 60 and 100 μm bands is essential. Also it should not have any connection with larger molecular cloud present nearby.

There are altogether 1 168 carbon rich AGB stars with their coordinates provided by Suh & Kwon (2011). The coordinates of AGB stars were entered as hour, minute, second for longitude and for latitude degree, minute, second such. All the coordinates are listed in the appendix A. The AGB coordinates were entered in four different bands and and images were down loaded. In the first stage ,we have down loaded J2000 JPEG images. Figure 22 shows a few cavity-like structures around AGB stars at 100 μm IRAS maps.

Step-III: Cross - View in the literature:
SIMBAD (http://simbad.u-strasbg.fr/simbad/sim-fid) was used to cross check whether the cavity candidates are already studied and published or not. It was done for all possible candidates. Finally, unpublished cavity-like structures are selected for the further study. As an example, objects found within 10 arcmin around the AGB star AGB0415+5441 is listed on Table 6.

Table 6: Objects found within 10 arcmin around the star AGB0415+5441 where the first column lists the name of the objects given in SIMBAD as identifier, second column lists the distance from the star, third column shows type of the object given (mostly normal star). Positions, V-magnitude and references are listed in last four columns. (Source: https://adsabs.harvard.edu.)

Identifier	Dist. (asec)	Type	R.A.(J2000) [hh mm ss.s]	Dec.(J2000) [dd mm ss.s]	Mag (v)	References 1850-2018
TYC 3723-485-1	241.6	*	04 14 48.2	54 44 24.5	12.4	0
RRF 1558	342.7	Rad	04 15 47.7	54 46 16.0	-	1^a
TYC 3723-421-1	345.9	*	04 15 41.9	54 39 46.9	12.0	0
TYC 3723-608-1	346.7	*	04 15 01.5	54 46 46.4	11.3	0
GB6 B 0410+5438	350.1	Rad	01 14 38.0	54 45 35.0	-	1^b
TYC 3723-603-1	355.3	*	04 15 41.7	54 42 56.9	10.2	0
TYC 3723-236-1	407.3	*	04 15 47.2	54 43 47.2	10.9	0
TYC 3723-361-1	442.0	*	04 14 36.7	54 47 18.5	11.5	0

In addition, the probable candidates were cross-viewed in the literature using ADS abstract service (https://adsabs.harvard.edu). General opinion through our co-supervisor and collaborators was taken into consideration. These images were further cross-viewed by the M.Sc. (Dissertation) students. Thirty cavity-like structures at 100 μm IRAS maps are shown in Figure 22. Similarly same cavity like structures around the same AGB stars at 60 μm IRAS maps are shown in Figure 23. On third column of Table 6, '$*$': represents star and 'Rad': represents radio source. The references 'a'and 'b'given in the last column are the Catalog provided by Reich et al. (1997) and Vollmer et al. (2010) respectively. No authors have been studied these point sources and their ISM surroundings. It is therefore we intend to study this image in order to understand the region behind its formation and evolution.

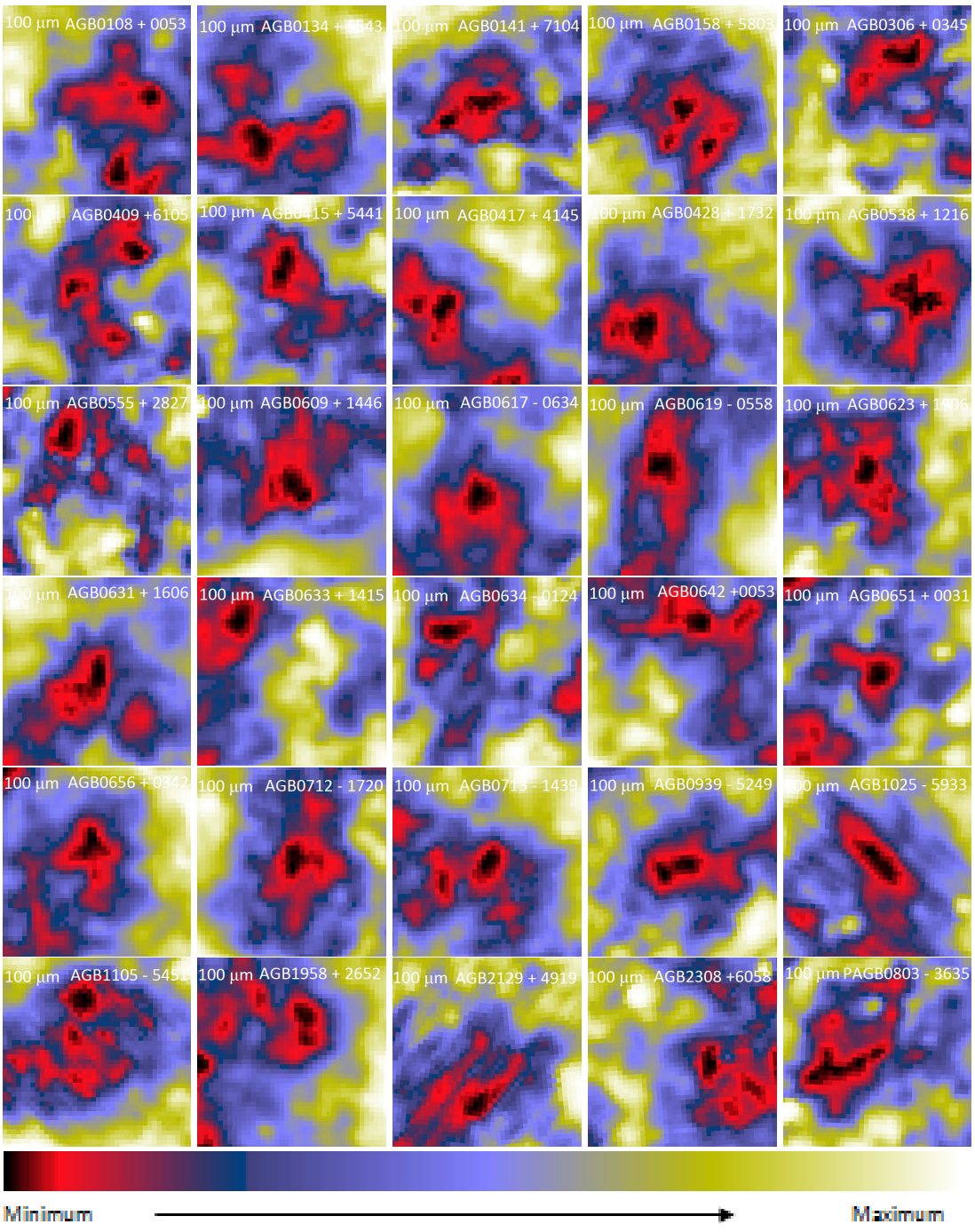

Figure 22: 1.0° × 1.0° IRAS images of cavity-like structures around AGB stars at 100 μm IRAS band. Color bar is shown at the buttom, which represents the way of variation of relative flux density. This range is different for different images. As an example, the minimum and maximum flux density for AGB0108+0053 and AGB0134+5543 are found to be 21.63 MJy/sr, 26.30 MJy/sr and 12.46 MJy/sr, 13.70 MJy/sr, respectively. The name of AGB stars are given.

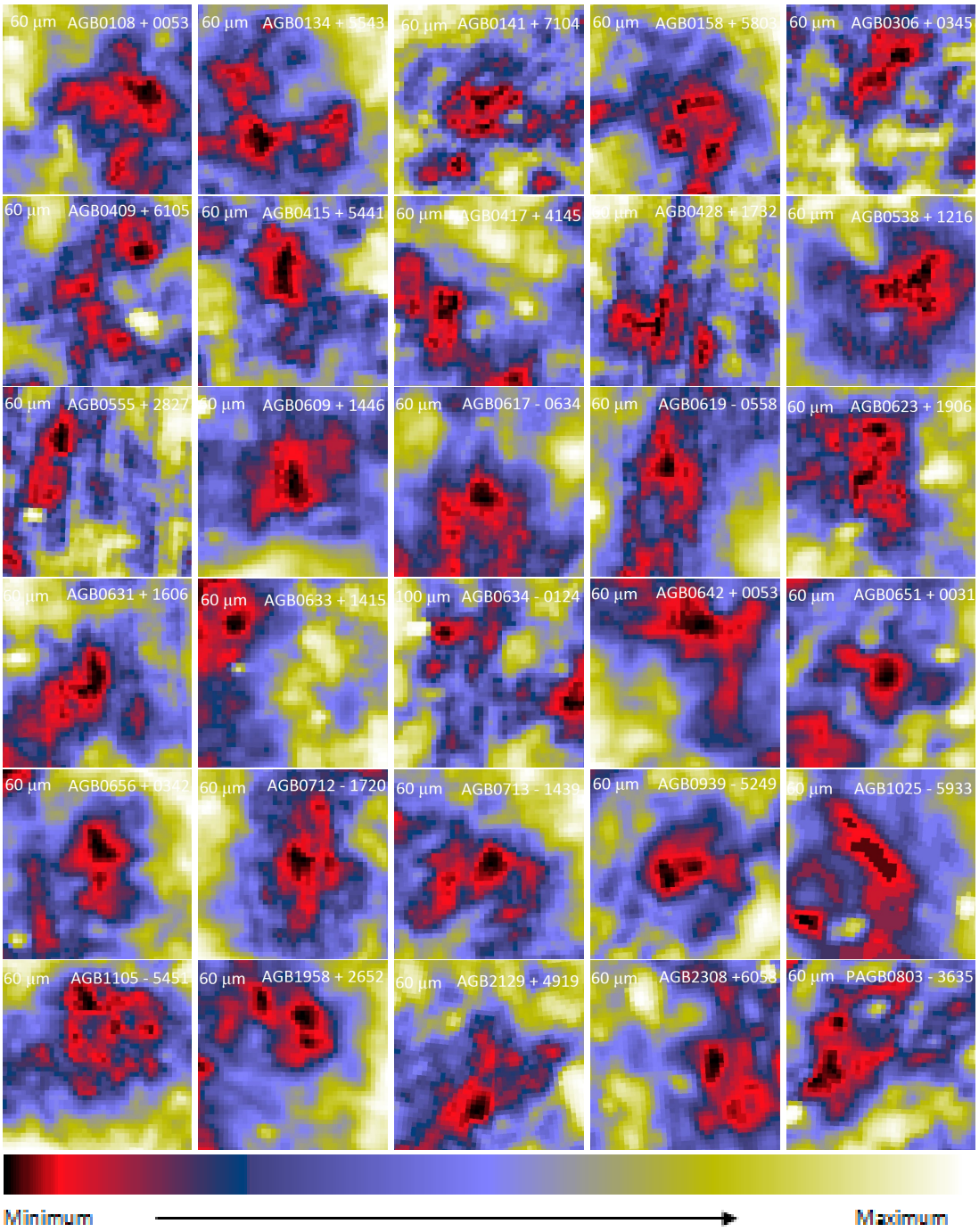

Figure 23: Few images of 1.0° × 1.0° field in IRAS 60 μm maps keeping AGB stars at the center of the images. Color bar is shown, which represents the way of variation of relative flux density which is different for different images. As an example, the minimum and maximum flux density for AGB0108+0053 and AGB0134+5543 are found to be 3.98 MJy/sr, 4.93 MJy/sr and 1.05 MJy/sr, 1.49 MJy/sr, respectively. The name of AGB stars are given. Here, cavity-like structures in 60 and 100 μm maps are found to be different. The difference in flux density is important for the calculation of dust color temperature and the dust mass.

Step-IV: Focusing/entering the possible candidates

Extended emission around the region of interest can be checked by performing search at larger view. For this, $2.5^\circ \times 2.5^\circ$ field has been considered 100 μm IRAS survey. Strong cavity within the extended emission is difficult to observe and is relatively difficult to understand because of several processes occured in the past. Images at larger view are shown in Figure 24.

Step-V: Image processing at Aladin2.5 software

We have downloaded FITS images of selected cavity at 60 μm and 100 μm IRAS maps using Skyview (http://skyview.gsfc.nasa.gov/current/cgi/query.pl). These images are processed in the software Aladin2.5 to make contour maps. Finally, flux density at 60 μm and 100 μm were measured and dust color temperature, Planck function, dust mass, etc. were calculated and studied by using ORIGIN5.0 and 8.0

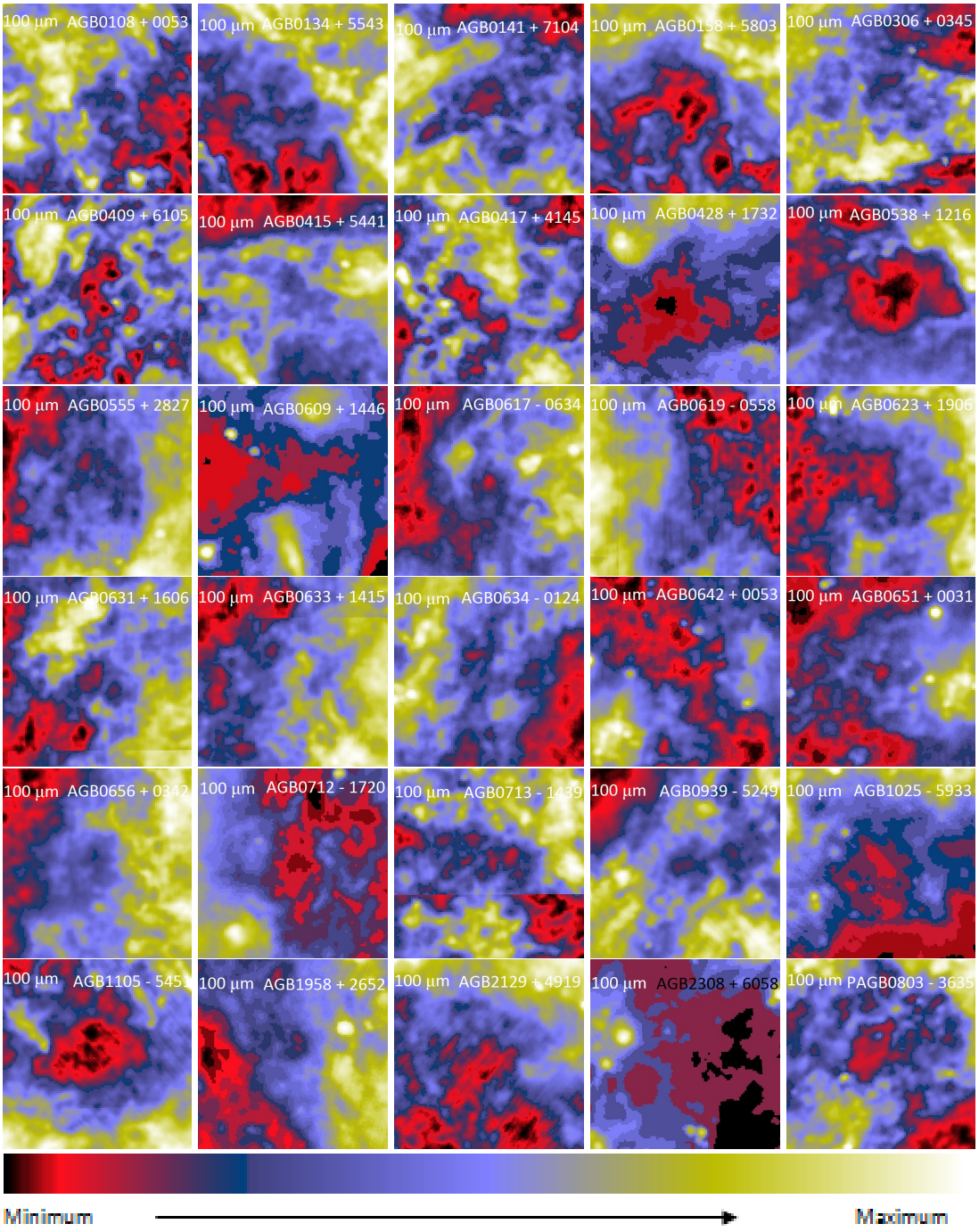

Figure 24: Corresponding images at larger view ($2.5^\circ \times 2.5^\circ$) at 100 μm IRAS survey. Color bar is shown at the bottom, which represents the variation of relative flux density. Extended dust emission (white) can be seen. These regions are not included in the study because of high extinction at far infrared wavelength.

3.1.2 Candidate Selection (Suh & Kwon, 2009)

There are four types of AGB star. Out of them, C-rich AGB stars are most important for biological life. It contains carbon compounds such as aromatic hydrocarbons, benzene, methane, etc. which are important for biological life. Such compounds are found to form in C-rich AGB stars. There are 1 168 C-rich AGB stars. When a systematic search was carried out on those stars using IRAS survey at 60 and 100 μm bands in pixels, different kinds of structures were observed. To select appropriate candidates, following selection criteria were made:

- There should be at least three-fold minimum flux density in the cavity.
- The structure should be isolated and its size is more than 0.5 degree in diameter.
- There should be a flux minima and the features can be seen in all 4 bands of IRAS survey.
- The structure should be prominent in 60 and 100 μm that enables us to study the fluxes emitted from the dust and grain.
- The most important thing is that the selected structure should not yet studied or published.

Figure 25 shows a cavity like structure around C-rich AGB star AGB0609+1446 at all four bands: 12 μm, 25 μm, 60 μm, and 100 μm . At 60 μm and 100 μm IRAS maps, the elongated (north-south) cavity can be seen. In 12 μm, cavity-like structure is noticed, but it is hardly identified at 25 μm. Therefore, the cavity-like structure is found to prominent at larger wavelengths. Therefore we intend to study dust color temperature distribution using 60 μm and 100 μm IRAS images.

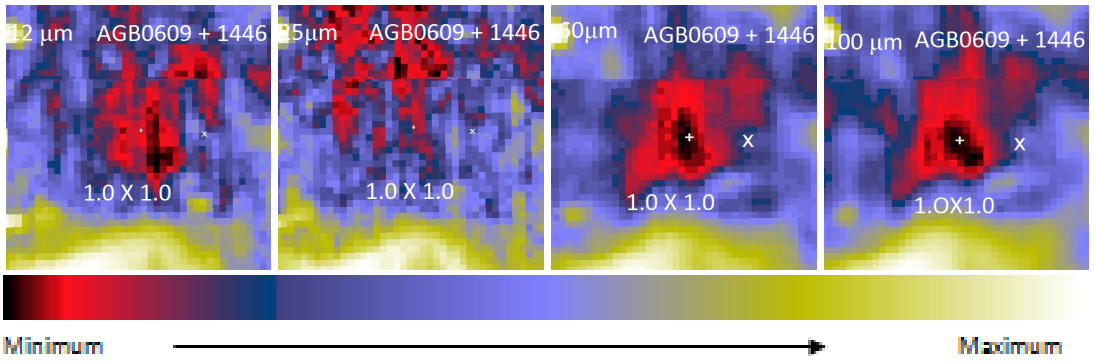

Figure 25: The cavity like structure around the AGB star AGB0609+1446 centered at R.A. (J2000) = 06^h 09^m 55.87^s and Dec. (J2000) = +14° 46' 10.4". In all four IRAS bands (12 μm, 25 μm, 60 μm and 100 μm), the emission is found to be strong. The range of flux density in 12 μm, 25 μm, 60 μm and 100 μm were 2.68 MJy/sr to 4.35 MJy/sr, 6.48 MJy/sr to 8.1 MJy/sr, 4.45 MJy/sr to 10.29 MJy/sr and 27.12 MJy/sr to 50.13 MJy/sr, respectively. Color bar is shown at the bottom which represents the way of variation of relative flux density. The field of the image is 1.0° × 1.0°. The position of the AGB star AGB0609+1446 is shown in 60 μm and 100 μm images.

Figure 26 shows cavity-like structure around C-rich AGB stars namely AGB0415+5441, AGB0609+1446, AGB0631+1606 and AGB0642+0053. The emission can be seen at 60 μm and 100 μm IRAS maps. In each case, position of the AGB star is found to be off located from the cavity center. This clearly indicates that the proper motion of the AGB star and the cavity might not be same.

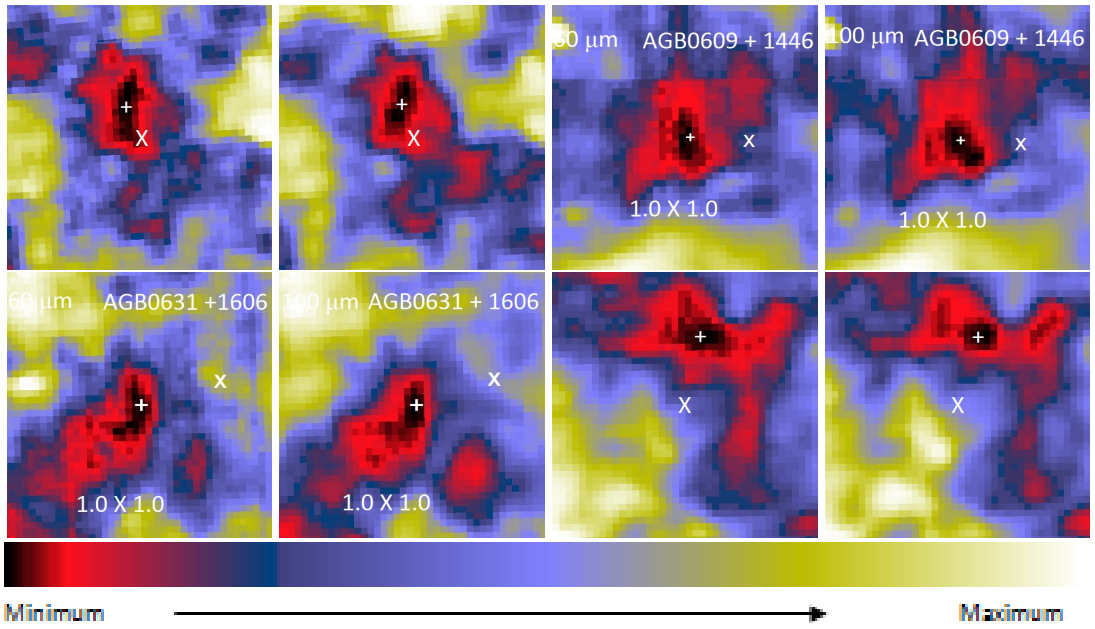

Figure 26: Cavity like structures around the C-rich AGB stars AGB 0415+5441, AGB 0609+1446, AGB 0631+1606 and AGB 0642+0053 at 60 μm (left) and 100 μm (right) IRAS maps, respectively. Color bar is shown at the buttom which represents the variation of relative flux density from minimum to maximum. The field of the image is 1.0° × 1.0°. The position of the central coordinate of the cavity is represented by '+' and position of the AGB star is denoted by 'X'. IRAS band and name of the AGB star are given in the image.

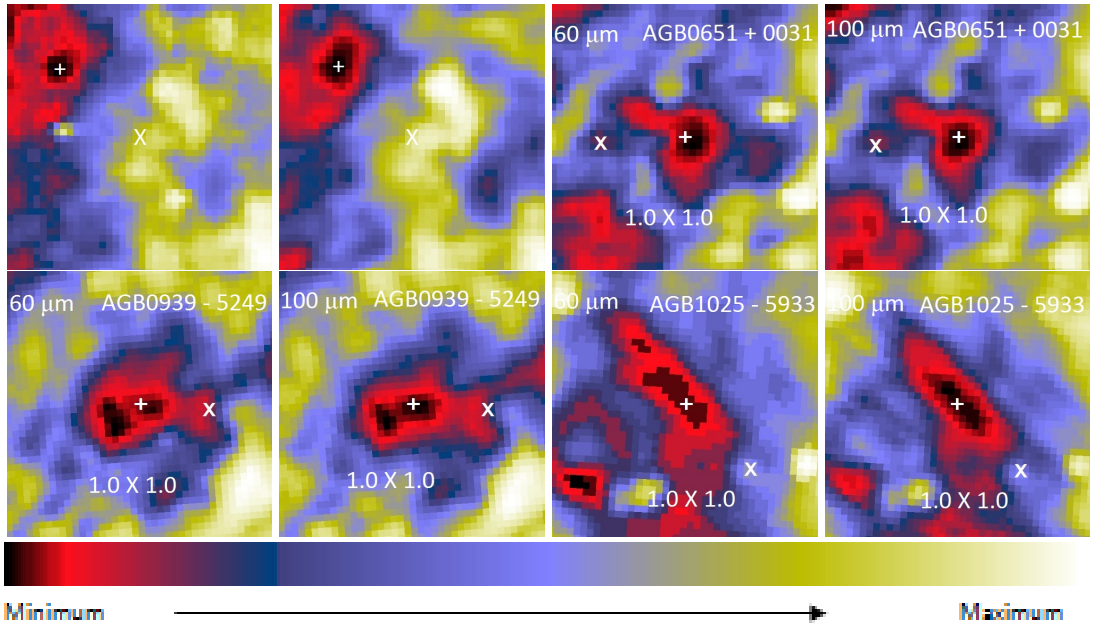

Figure 27: Dust cavities around the selected AGB stars namely AGB0633+1415, AGB0651+0031, AGB0939-5249, and AGB1025-5933 are at 60 μm (left) and 100 μm (right) IRAS maps respectively. Color bar is shown at the buttom which represents the variation of relative flux density from minimum to maximum. The field of the image is 1.0° × 1.0°. The position of the central coordinate of the cavity is represented by '+' and position of the AGB star is denoted by 'X'. IRAS band and name of the AGB star are given in the image.

Table 7: A list of selected cavity- like structure around AGB stars. CCRAS1 to CCRAS8 are named for the cavity-like structures where C stands for cavity, CR stands for C-rich, A stands for asymptotic giant branch and S the star. The third and fourth columns represent the name of the nearby AGB star and distance from the cavity center. The last two column show the positions of the center of the cavity.

S.N.	Name	Nearby AGB Star	Distance (deg)	R.A.(J2000) [hh mm ss.s]	Dec.(J2000) [dd mm ss.s]
1	CCRAS1	AGB0415+5441	0.14	04 15 03.0	54 41 00.0
2	CCRAS2	AGB0609+1446	0.22	06 09 55.9	14 46 10.4
3	CCRAS3	AGB0631+1606	0.36	06 32 38.1	15 59 47.9
4	CCRAS4	AGB0633+1415	0.41	06 33 01.0	14 15 00.0
5	CCRAS5	AGB0642+0053	0.29	06 41 43.0	01 09 22.8
6	CCRAS6	AGB0651+0031	0.33	06 49 47.1	00 31 32.4
7	CCRAS7	AGB0939-5249	0.42	09 40 50.6	−52 48 32.0
8	CCRAS8	AGB1025-5933	0.56	10 26 54.7	−59 18 22.5

Figure 27 shows cavity-like structure around C-rich AGB stars namely AGB0633+1415, AGB0651+0031, AGB0939-5249 and AGB1025-5933. The emission can be seen at 60 μm and 100 μm IRAS maps. In each case, position of the AGB star is found to be off located from the cavity center. This clearly indicates that the proper motion of the AGB star and the cavity might not be same.

Finally, we have selected eight cavity-like structure for the further study. The name (coined by us), nearby AGB star, distance to the nearby AGB star and the position co-ordinate of the cavities are listed on the Table 7.

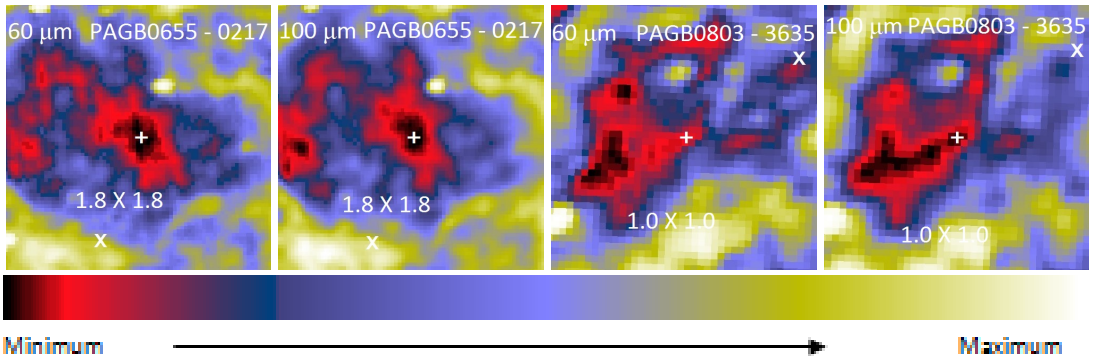

Figure 28: Two selected far infrared cavity images around post-AGB star at 60 μm (left) and 100 μm (right). Cavities are strong and emission feature can be seen clearly. The position of the central coordinate of the cavity is represented by '+' and position of the AGB star is denoted by 'X'. Pixel size, IRAS band and name of the AGB star are given in the image.

Table 8: A list of selected cavity like structure around post AGB stars (third column) under 60 μm and 100 μm IRAS maps. CCRPAS1 and CCRPAS2 are selected cavity like structure where C stands for cavity, C stands for carbon rich, PA for post asymptotic giant branch and S for star. The third and fourth columns show the name of the nearby PAGB star from the center of cavity and their distance respectively. The last two column show the positions of the center of the cavity.

S.N.	Name of the cavity	Nearby AGB star	Distance (deg)	R.A.(J2000) hh mm ss.s	Dec.(J2000) dd mm ss.s
1	CCRPAS1	PAGB0653-0216	0.72	06 51 54.0	−01 35 43.0
2	CCRPAS2	PAGB0801-3651	0.82	08 04 07.2	−37 11 43.0

3.1.3 Candidates Selection (Szczerba et al., 2007)

A preliminary compilation was presented by Szczerba & Górny (2001) including about 220 stars. Szczerba et al. (2007) further studied all the literature available on the NASA Astrophysics Data System (ADS) up to 2006 and the revised catalog is named as " the Torun catalog of Galactic post-AGB and related objects". The catalog contains 326 very likely, 107 possible and 64 disqualified post-AGB stars. They further revised the catalog which contains 391 very likely, 83 possible and 66 unlikely post-AGB stars. During the systematic search on the post-AGB stars, only 23 very likely post-AGB stars lie in C-rich AGB stars. It means only 23 stars are post-AGB stars which lie within 1 168 C-rich AGB stars. Remaining all possible post-AGB stars did not lie within 1 168 C-rich AGB stars. Out of 23 candidates only two candidates fulfilled above mentioned selection criteria. Two selected cavity-like structures around post-AGB stars have selected for the further study which are shown in Figure 28. The name of the cavities, nearby AGB star, distance between the cavities and the nearby post-AGB star and the position co-ordinate of the cavities in the Table 8.

3.2 Far Infrared Cavity Based Systematic Search on IRAS

Catalogue of far infrared loops in the galaxy was compiled by Könyves et al. (2007). In the catalog, they used 60 μm and 100 μm ISSA plates (IRAS Sky Survey Atlas) to explore the distribution of dust emission. By using the “geom" and “mosaic" procedures of the IPAC Sky view package, they created composite images of the $12.5^\circ \times 12.5^\circ$ sized individual ISSA plates. They searched for loop or arc like features in these images in the $1^\circ \leq D \leq 40^\circ$ diameter range. In the catalog, there are 462 far infrared loops. Out of them, 317 loops are in first, third and forth galactic quadrants where as 145 loops lie in second galactic quadrant. It means the catalog contains the basic properties of 462 loops and based on indicator objects (massive stars, dark clouds, supernova remnants, etc.), distances are estimated for 73 loops.

3.2.1 Candidates Selection (Könyves et al., 2007)

There are 462 far infrared loops in our galaxy. In the catalog, authors have derived distances for 137 loops and measured additional physical quantities. To calculate dust mass, derived distance from the star is needed. We tried to find out the AGB stars which lie within the loops (KK-loops) to estimate. For this, we measured distance between center of AGB stars and KK-loops. From this, we found the closest KK-loop from the AGB star. Again major diameter and minor diameter of the KK-loop are given. Here, we compared measured distance with both diameters. If the measured distance is less than both diameters, then we can say that the AGB star lies within the KK-loop. Detail calculations are given in the appendix. The selected candidates (cavities) which lie within KK-loops are AGB0141+7104, AGB0409+6105, AGB0538+1216, AGB0555+2827, AGB0617-0634, AGB0619-0558, AGB0712-1720 and AGB1105-5451. The name of AGB stars, nearby KK-Loop, distance between AGB star and KK-Loop, major and minor diameter of KK-Loop and the position of the cavities in the Table 9. Finally, eight cavities around the AGB star lying within the KK-Loop have selected. In Table 10, we mentioned name of the cavities, nearby AGB stars, distance between AGB star and the cavity and center position of the cavities.

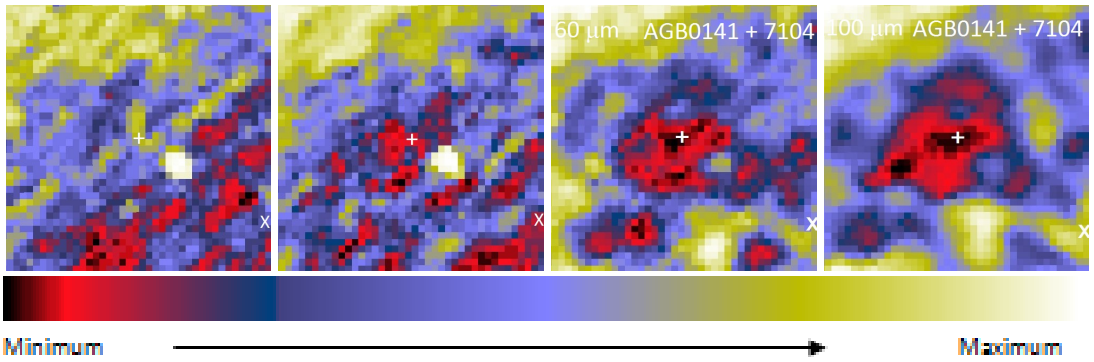

Figure 29: Far infrared cavity within the KK-loop G128-03 centered at R.A. (J2000) = 01^h 46^m 57.2^s and Dec. (J2000) = +71° 24' 57.1". In all four IRAS bands - 12 μm, 25 μm, 60 μm and 100 μm, emission is found strong. The range of flux density in 12 μm, 25 μm, 60 μm and 100 μm were 1.07MJy/sr to 1.42 MJy/sr, 4.00 MJy/sr to 4.29 MJy/sr, 1.52 MJy/sr to 2.09 MJy/sr and 14.97 MJy/sr to 17.14 MJy/sr respectively. Color bar is shown at the bottom which represents the way of variation of relative flux density. The field of the image is 1.0° × 1.0°. The position of the central coordinate of the cavity is represented by '+' and position of the AGB star is denoted by 'X'. JPEG images of the selected candidates in 60 μm and 100 μm bands are shown in Figure 30 and 31.

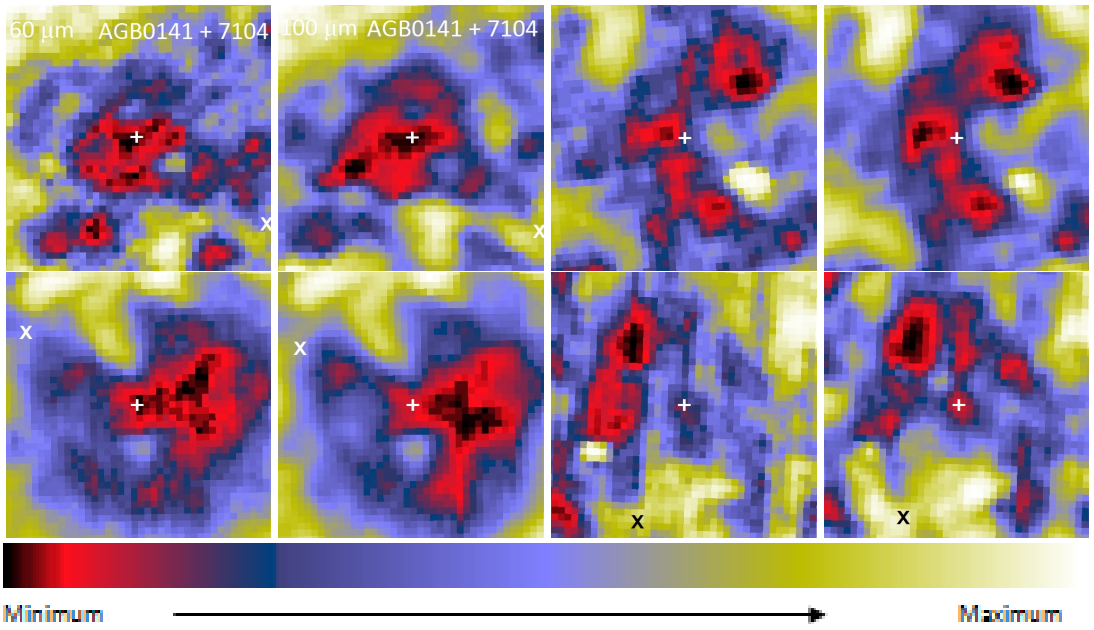

Figure 30: Images of the far infrared cavities around the selected AGB stars namely AGB0141+7104, AGB0409+6105, AGB0538+1216 and AGB0555+2827 are at 60 μm (left) and 100 μm (right), respectively. Color bar is shown at the bottom which represents the variation of relative flux density. The field of the image is 1.0° × 1.0°. The position of the central coordinate of the cavity is represented by '+' and position of the AGB star is denoted by 'X'. Pixel size, IRAS band and name of the AGB star are given in the image.

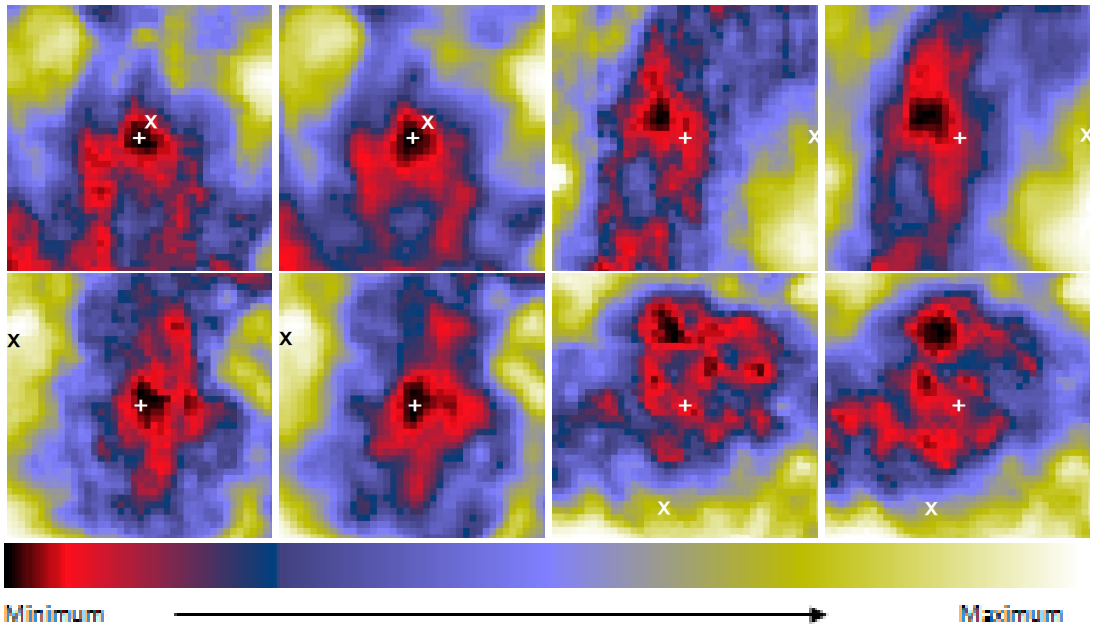

Figure 31: Far infrared images of the selected cavities around the AGB stars namely AGB0617-0634, AGB0619-0558, AGB0712-1720 and AGB1105-5451 are at 60 μm (left) and 100 μm (right), respectively. Color bar is shown at the bottom which represents the variation of relative flux density. The field of the image is $1.0^\circ \times 1.0^\circ$. The position of the central coordinate of the cavity is represented by '+' and position of the AGB star is denoted by 'X'. Pixel size, IRAS band and name of the AGB star are given in the image.

Table 9: A list of selected C-rich AGB stars are in first column where as name of nearby KK-loops are in second column. Here KK stands for (Kiss et al., 2004) and (Könyves et al., 2007). Third column represents the closest distance between the AGB star and the KK-loop, forth column shows major and minor diameter of the nearby KK-loops and positions of the AGB stars are shown in last two column.

S.N.	AGB Star	Nearby KK-Loop	Distance (deg.)	Major/Minor diameter (deg.)	R.A. (J2000) hh mm ss	Dec.(J2000) dd mm ss
1	AGB0141+7104	G125+09	3.02	6.1/5.4	01 41 01	71 04 00
2	AGB0409+6105	G143+07	1.00	4.5/3.0	04 09 00	61 05 00
3	AGB0538+1216	G195-11	3.01	4.3/3.4	05 38 03	12 16 00
4	AGB0555+2827	G182+00	1.54	4.7/4.1	05 55 00	28 27 00
5	AGB0617-0634	G212-11	2.90	8.4/7.1	06 17 08	−06 34 00
6	AGB0619-0558	G212-11	2.79	8.4/7.1	06 19 06	−05 58 00
7	AGB0712-1720	G229-03	1.53	3.7/3.6	07 12 04	−17 20 00
8	AGB1105-5451	G287+04	0.72	2.2/1.7	11 05 01	−54 51 00

Table 10: A list of selected far infrared cavity-like structure found around the C-rich AGB stars. CASKK1 to CASKK8, where C stands for cavity, A stands for asymptotic giant branch, S is for star and KK is taken as (Kiss et al., 2004) and (Könyves et al., 2007). Third column represents the name of the nearby AGB star, fourth column represents the distances between center of the cavities and the near by stars. Positions of the center of the cavities are shown in the Last two column.

S.N.	Name of the Cavity	Nearby AGB Star	Distance (deg.)	R.A.(J2000) hh mm ss.s	Dec.(J2000) dd mm ss.s
1	CASKK1	AGB0141+7104	1.50	01 46 57.2	71 24 57.1
2	CASKK2	AGB0409+6105	0.00	04 09 00.0	61 05 00.0
3	CASKK3	AGB0538+1216	0.48	05 36 17.2	12 03 33.6
4	CASKK4	AGB0555+2827	0.49	05 54 04.5	28 52 38.3
5	CASKK5	AGB0617-0634	0.10	06 17 18.4	−06 38 08.4
6	CASKK6	AGB0619-0558	0.70	06 21 04.5	−05 58 31.6
7	CASKK7	AGB0712-1720	1.32	07 06 51.3	−17 34 36.5
8	CASKK8	AGB1105-5451	0.41	11 04 17.6	−54 29 05.5

3.3 Method (Image Processing): Aladin Software

Aladin is an interactive sky atlas developed and maintained in 1999 by the Center de Donne's astronomiques de Strasbourg (CDS). It is used for the identification of astronomical sources through visual analysis of reference sky images (Bonnarel et al., 2000). Aladin v2.5 is a service providing simultaneous access to digitized images of the sky, astronomical catalogues, databases, interactively access related data and information from the SIMBAD database, NED (NASA Extragalactic Database), VizieR and other achieves for all known sources in the field. The driving motivation is to facilitate direct, visual comparison of observational data at all wavelength with images of the optical sky and with reference catalogue (http://aladin.u-strasbg.fr).

Aladin v2.5 is one of the handy and extensively used software in the data reduction processes covering all wave length regions. It is particularly useful for multi-spectral cross identifications of astronomical sources, observation preparation and quality control of new data sets (by comparison with standard catalogues covering the same region of sky). It is used to analyze each pixels of the FITS image lying in the region of interest. We can get information about, energy spectrum, the relative flux density, different types of contour maps with coordinates of each pixel including longitude and latitude of the desired structure.

Aladin defines an astronomical image, an astronomical catalogue, a graphical overlay and a view. In Aladin sky atlas, there are 4 components to the data visualization window shown in Figure 32:

- The Stack: The stack represents all the data loaded in memory and which can be displayed in a view. The stack is structured as a set of "planes" stacked one above another. The user - symbolized by the eye - observes the stack from the top. It

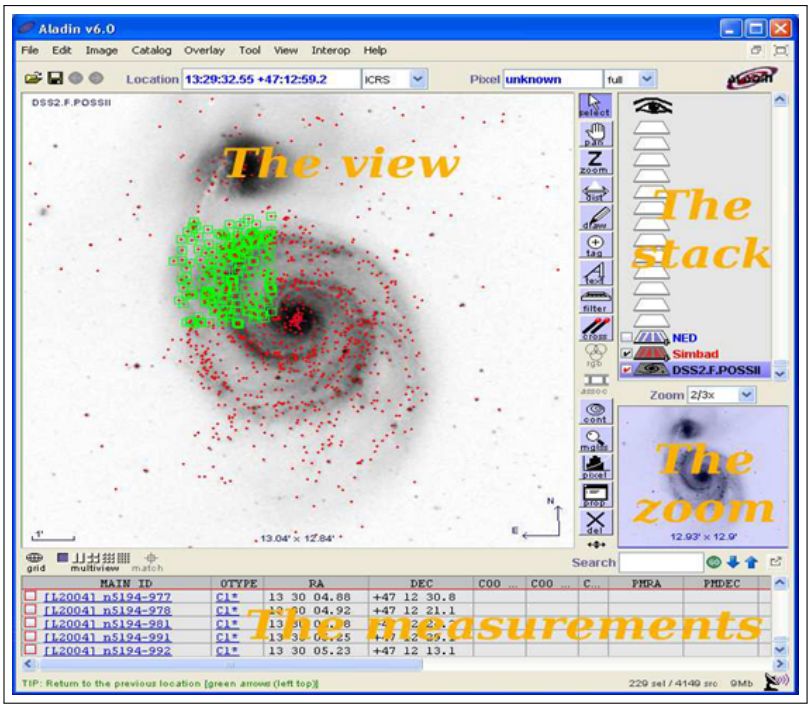

Figure 32: Overview of data visualization. (source : http://aladin.u-strasbg.fr/java/Aladin.exe) in Aladin software.

shows all the downloaded data as a stack of "planes". The user eye is on the top of this stack and sees all activated planes by transparency.

- The Zoom: It is located on the bottom right of the main window. It displays an illustration of the total image on which is superimposed a translucent blue rectangle. It shows the image area currently visible according to the factor and the centre of the zoom.
- The View: The viewing panel is the main component of the Aladin interface. The view shows a display of the data activated in the stack. Most of the time, it is an image onto which graphical symbols are overdrawn to represent the sources from catalogues. It displays the image area currently visible according to the activated stack planes, zoom factor and the overlaid graphics and table planes.
- The Measurements: It is located at the bottom of the Aladin main window. It is used to visualize measures associated to the sources. It is a really powerful tool that enables you to select, sort and filter tables. It shows the measurements associated to the objects selected in the view via the mouse.

Tool bar is located vertically in between the stack and the view which enables a quick access to the most used tools:

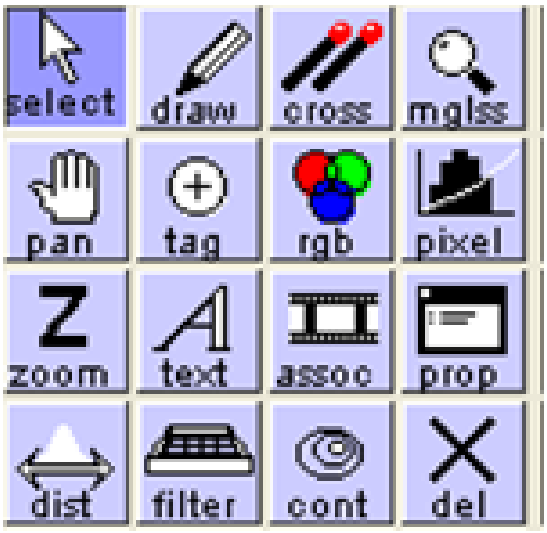

Figure 33: Tool bars of Aladin v8. (source:http://aladin.ustrasbg.fr/java/Aladin.exe).

Select Mode:	select objects in the view
Pan Mode:	moving the view
Zoom Mode:	adjusting the zoom factor for the view
dist:	Graphical addition for measuring distances
draw:	Graphical addition for hand-drawings
tag:	Graphical addition to tag a location
text:	Graphical addition to write text
filter:	Generate filters for catalogues
cross:	catalogues cross-match tool
rgb:	Colour images generator
assoc:	Generate images associations (mosaics or animated sequences)
cont:	Contour generator
mglss:	Activate/deactivate the magnification glass
pixel:	Opens the window that controls the pixel dynamics
prop:	Open the properties window
del:	Deletes the current element

All these mentioned tool bars are used in Aladin v6 and Aladin v8 but in Aladin v2.5 “pad" and “hist" are included dut “assoc" and “pixels" toolbar are not included. The tool bar of Aladin v8 is shown in Figure 33.

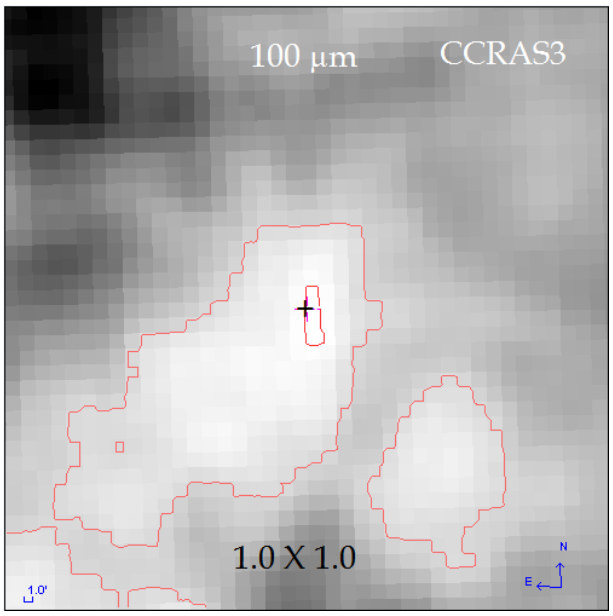

Figure 34: Contour map in the CCRAS3 around AGB0631+1606 region (Table 7) at 100 μm IRAS map with contour level 1 and 38, corresponds to 16.25 MJy/sr and 18.49 MJy/sr respectively. The symbol '+' represents the center of the field of view. Size, name of cavity and IRAS band is shown in the figure.

3.3.1 Contour Map

Aladin v2.5 is used to draw contour map in certain contour level of FITS images of the region of interest. There are two types of images obtained from sky view virtual observatory. They are JPEG and FITS images. JPEG images of the selected candidates has shown in the article 3.1.2, 3.1.3 and 3.2.1. We intend to study the cavity structure at 60 μm and 100 μm. We adopted the method of drawing contours at different levels so that we can separate the region of maximum and minimum flux density. The contour level in 100 μm and 60 μm FITS images are chosen independently to make the best contour level. Contour levels represent the value of flux density in MJy/sr. The 'Jy'is the abbreviation for jansky which is a unit of electromagnetic flux density. (1 Jy = 1 $\times$ 10^{-26} kg s^{-2} = 1 x 10^{-26} W s^{-2} Hz^{-1}). We are interested in these minima to study the flux density within the region because we concern our focus on temperature profile and the mass distribution of the dust driven region within the cavity structure including AGB star. We are intend to study the temperature and mass profile of isolated symmetric spherical cavity structure . By using FITS images in Aladin 2.5 software, different contour map with varying contour level can be drawn. Taking strong cavity, high flux difference with minimum flux lying within the contour and closed bigger contour map of the selected candidates has drawn. Contour map of the cavity CCRAS3 (Table 5) region is shown in Figure 34.

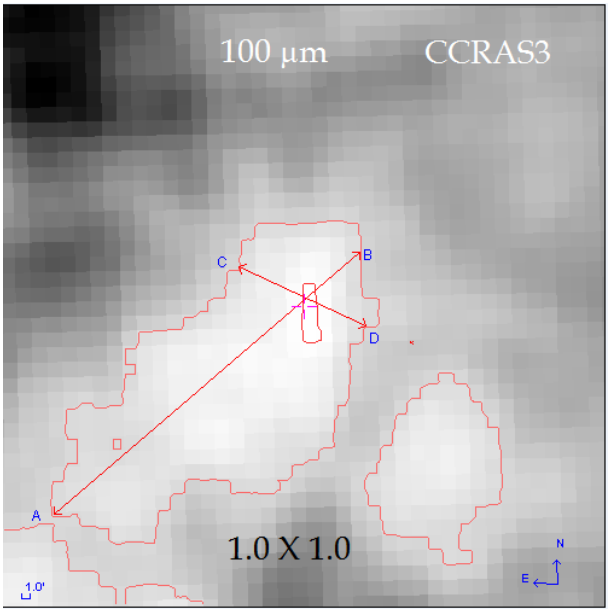

Figure 35: Contour map in the cavity CAGBS3 around AGB0631+1606 region (Table 7) at 100 μm IRAS map. The line AB and CD represents the major and minor diameters passing through minimum flux region. Size, name of cavity and IRAS band is shown in the figure.

3.3.2 Size of the core region

To measure size of the core region, we need contour map. In the contour map, major and minor diameters are drawn. Major diameter is the largest diameter passing through minimum flux region and minor diameter is the smallest diameter passing through minimum flux region. To measure the major and minor diameter for each FITS image, we used a simple expression, $l = R \times \theta$, where R is the distance of the structure from us and θ is the pixel size (in radian). After calculation the major and minor diameter of the cavity region, size of the core region can be calculated. So size of the cavity is equal to the product of major and minor diameters. In the Figure 35, AB and CD represents major and minor diameters. To study the variation of flux density other lines can be drawn.

3.3.3 Flux Density Variation

By tagging in the pixel within contour level, flux density of that pixel cab be obtained. We studied the flux density of all pixel lying inside outermost contour of the 100 μm interested region and find the flux density of the corresponding pixels in 60 μm using the software Aladin v2.5, which was used to calculate the dust color temperature, Planck function and mass of each pixel due to the contribution of dust. Here we found the region of the maximum and minimum flux density and studied about their variation in each image.

3.3.4 Background Correction

There are various sources of energy around our region of interest which can increase the flux of the region of interest. These sources should be identified and their fluxes at the desired wavelengths should be removed from the region of interest. The flux emitted by other sources lying nearby the region of interest but not the from the region of interest is called background flux. Actually the flux emitted by the background sources is called the background flux. The flux density obtained from Aladinv 2.5 is total flux density (background flux + flux due to dust). The flux density obtained is corrected by subtracting it with the background flux density. The minimum flux density which doesn't lie within the contour map is supposed as background. The background emission is subtracted from the field using the method adopted in Aryal et al. (2010). For this, the average value of the background flux is obtained by noting and summing up of the minimum flux densities around the region of interest and dividing the sum by total number of pixels with these minimum flux densities. When this background flux is subtracted from the obtained flux density of each pixel in the region of interest, it is said to be background corrected flux density. If there is no background flux outside the region of interest by taking minimum flux inside the isocontour, we have to take a difference between second minimum say (a) and minimum flux say (b) and divided by 2 which is the background flux density. Mathematically, background flux= $\frac{a-b}{2}$. When it is subtracted from the obtained flux density. we get corrected flux density.

3.3.5 Background Corrected Flux Density

When the background flux density is subtracted from the total flux density from each pixel of the region of interest, we get corrected flux density which is final corrected data for the analysis. Microsoft Office Excel (2007) is used for the calculation of dust color temperature, Planck function, dust mass, visual extinction, etc. For calculation of dust color temperature, flux densities are needed. For Planck function, wavelength at 100 μm and dust color temperature is required. For dust mass, we need flux density at 100 μm, distance of the cavity and Planck function.

3.3.6 Dust Color Temperature

Dust color temperature is one of the most important parameter to study far infrared cavity. For its calculation, we adopted the method proposed by Dupac et al. (2003) and

Schnee et al. (2005). According to them, dust color temperature is given by

$$T_{\rm d} = \frac{-96}{\ln\left(R \times 0.6^{3+\beta}\right)} \tag{3.1}$$

Where $R = \frac{F(60\ \mu m)}{F(100\ \mu m)}$ and β is spectral emissivity index. Here $F(60)$ and $F(100)$ are flux densities at 60 μm and 100 μm respectively. β depends on dust grain properties such as composition, size, and compactness. For reference, a pure blackbody would have $\beta = 0$, the amorphous layer-lattice matter has $\beta \sim 1$, and the metals and crystalline dielectrics have $\beta \sim 2$. In our calculation, β is taken as 2. Detail derivation and description of equation (3.1) has given in literature review (chapter 2.3). Average dust color temperature can be measured after finding the slope $F(60)/F(100)$ from the graph plotted between $F(60)$ and $F(100)$.

3.3.7 Planck Function

The Planck function $B(\nu, T)$ is the function of temperature and wavelength. It is used to calculate dust mass and is given by the expression:

$$B(\nu, T) = \frac{2hc}{\lambda^3}\left[\frac{1}{e^{hc/(\lambda kT)} - 1}\right] \tag{3.2}$$

where, h = Planck constant, c = velocity of light, ν = frequency at which the emission is observed, and T = temperature of each pixel. When λ and T is known, Planck function can be calculated. Detail description about equation ((3.2)) has given in literature review (chapter 2.3).

3.3.8 Dust Mass

For calculation of dust mass, we used the expression given by Hildebrand (1983),

$$M_{\rm dust} = \frac{4a\rho}{3Q_\nu}\frac{S_\nu D^2}{B(\nu, T)} \tag{3.3}$$

According to Young et al. (1993), weighted grain size (a) = 0.1 μm, grain density (ρ) = 3000 kgm^{-3}, grain emissivity (Q_ν) = 0.0010 (for 100 μm) so that equation (3.3) becomes

$$M_{\rm dust} = 0.4\frac{S_\nu D^2}{B(\nu, T)} \tag{3.4}$$

Where S_ν = flux density at 100 μm, D = known distance of the loop and $B(\nu, T)$ = Planck function. Detail description of equation (3.3) and (3.4) has given in the literature review

section (chapter 2.4).

3.3.9 Visual Extinction

Extinction is the sum of scattering and absorption which takes place in the dusty environment. The visual extinction ($A_{\rm V}$) is very important parameter that relates distance and magnitude by the relation

$$m - M = 5 \log r - 5 + A_{\rm V} \tag{3.5}$$

Where m and M represent the apparent and absolute magnitudes respectively. Actually magnitude is the measurement of brightness of a star. If the brightness is measured at unknown distance r, then it is called apparent magnitude and when it is measured at 10 pc, then it is called absolute magnitude. Here, we have calculated the values of ($A_{\rm V}$) using the expression (2.27) in chapter two given by Wood et al. (1994). The relation is

$$A_{\rm V}({\rm mag}) = 15.078[1 - \exp{(-\tau_{100}/641.3)}] \tag{3.6}$$

where,

$$\tau_{100} = \frac{F_\lambda(100\ \mu{\rm m})}{B_\lambda(100\ \mu{\rm m}, T_{\rm d})} \tag{3.7}$$

is optical depth and $F_\lambda(100\ \mu{\rm m})$ is the flux at 100 μm.

$$B(\lambda, T) = \frac{2hc}{\lambda^3}\left[\frac{1}{e^{hc/\lambda kT} - 1}\right] \tag{3.8}$$

is the Planck function.

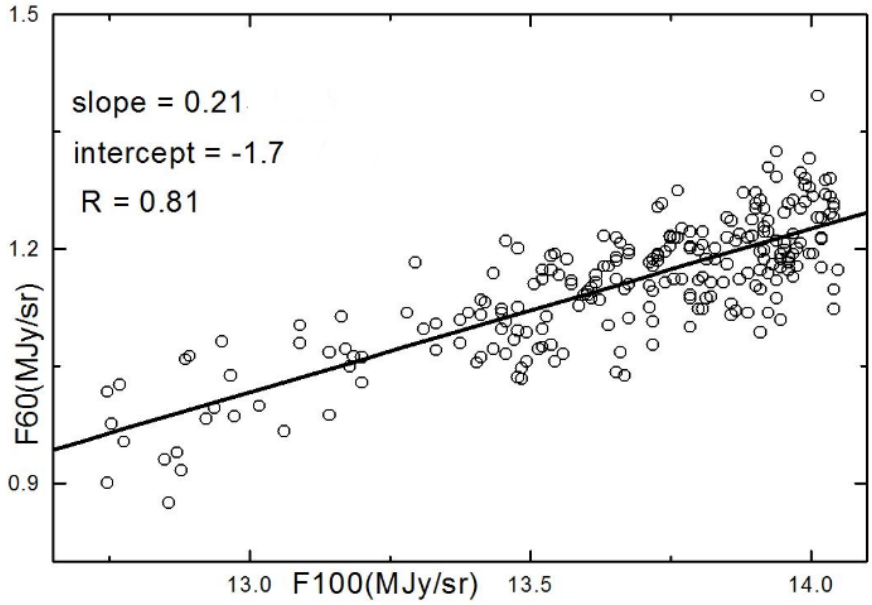

Figure 36: Scatter and best fit plot between flux densities 100 μm and 60 μm in the cavity CASKK6 around the AGB 0619-0558. Here, the slope, intercept and the correlation coefficient (R) are given. The slope of the best fitted line has been used to estimate average dust color temperature.

3.4 Plots: Linear, Gaussian and Contour maps

There are different methods and different softwares to make plots so that calculated values can be studied and analyzed. In this work, ORIGIN5.0 and 8.0 softwares are used to obtain linear, Gaussian, polynomial and contour maps. For three-dimensional contour map, ORIGIN8.0 is used. Generally we plot a linear fit of scattered graph between flux density at 100 μm and 60 μm as shown in Figure 36. From the slope of the linear fit, we calculate average dust color temperature which is used to estimate the maximum permissible error. Best fit of scattered plot between visual extinction and dust color temperature of the cavity CASKK6 is also shown in Figure 37. Here, we also have plotted best fit of the scattering plot between Planck function and diameter shown in Figure 38.

In the interstellar medium, different dynamical processes took place which can trigger anisotropy (or polytropy) and inhomogeniety in the region. Gaussian distribution is important to represent real valued random variables whose distributions are not known. If the number of events are very large, then the Gaussian distribution function may be used to describe physical events. Such features can be understood by studying the deviation in the Gaussian disturbance. We use Gaussian fit to check the deviation from the random process, e.g., in the dust color temperature and dust mass distribution. For the same cavity, Gaussian fit of dust color temperature and dust mass are shown in Figures 39 and 40 respectively. In the interstellar medium, gases are mostly neutral or partially ionized. Maxwellian distribution is used to describe speed of gaseous particles. They move freely

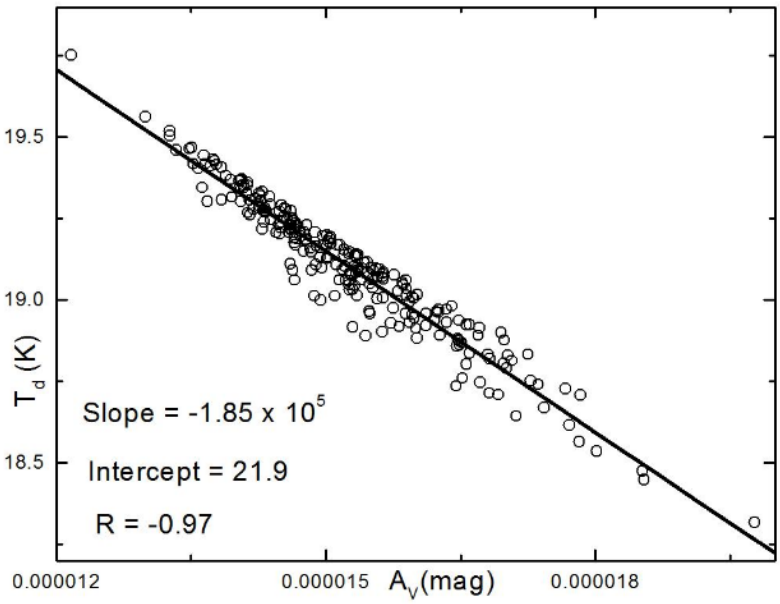

Figure 37: Scatter and best fit plot between visual extinction and dust color temperature of the cavity CASKK6 around the AGB 0619-0558. Here, the slope, intercept and the correlation coefficient (R) are given. The slope and intercept of the best fitted line has been used to find a mathematical relation between them.

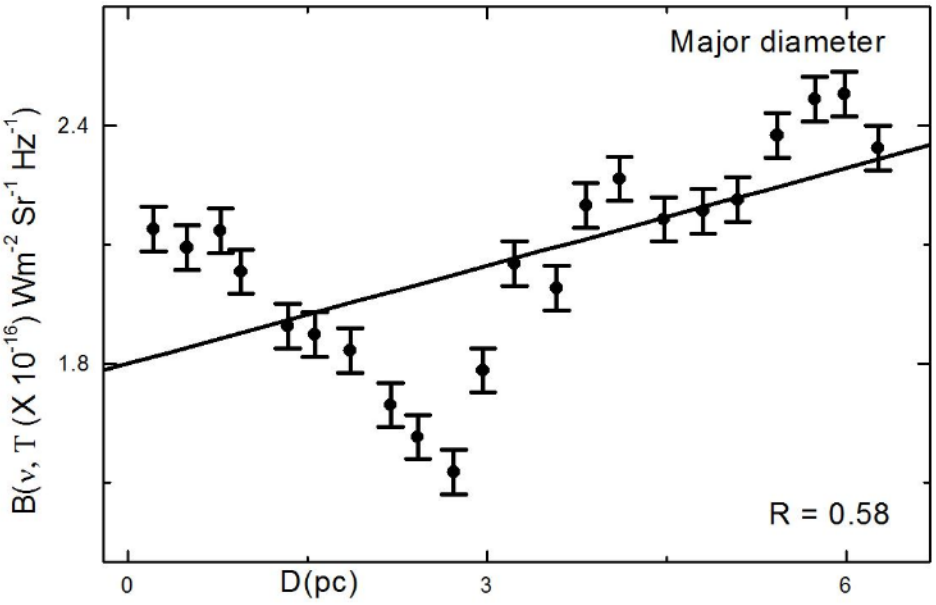

Figure 38: Scatter and best fit plot between Planck function and extension of the cavity CASKK6 around the AGB 0619-0558. The correlation coefficient (R) is given.

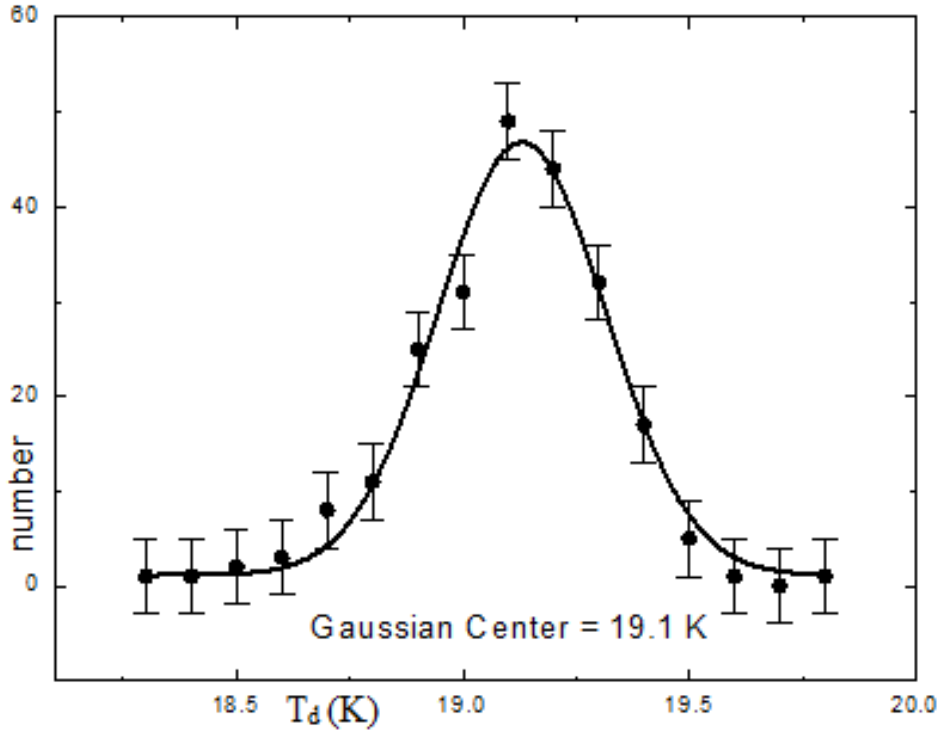

Figure 39: Gaussian fit of dust color temperature distribution in the region of interest CASKK6 around the AGB0939-5249. The solid curve represents the Gaussian fit and $\pm\frac{\sigma}{\sqrt{n}}$ are the error bars. The Gaussian center and offset value are shown in the figure. There is good agreement between observed and fitted curve. It means, the dust color temperature distribution in the CCRAS7 around the AGB0619-0558 is in the local thermodynamic equilibrium.

inside a stationary container without interacting with one another, except for a very brief collisions in which they exchange energy and momentum with each other or with their thermal environment. These gases obey either Maxwellian velocity distribution or Saha distribution. If these distributions co-exist, local thermodynamical equilibrium can be expected. In such condition, temperature of dust grain remains constant within the mean free path and wavelength of the radiation should be of the order of mean free path of the dust or grain. It means Gaussian distribution is expected, if the gases and radiation are in thermal equilibrium (Karttunen et al., 2007). Any deviation in the Gaussian distribution is a measure of anisotropic (or polytropic) processes.

From the Gaussian distribution of dust mass, hydrodynamic equilibrium can be studied and to study the thermal equilibrium in the region of interest. We plot dust color temperature and check the Gaussian nature with the help of Gaussian fit. In the Gaussian fit, the parameters are area, offset value, width and height which are used to compare between the various region of interest. The error bars $\pm\frac{\sigma}{\sqrt{n}}$ are given in the histogram of Gaussian distribution.

To plot contour map, we use ORIGIN8.0. For the interpretation, we plot contour map of flux density at 100 μm, contour map of dust color temperature, contour map of dust

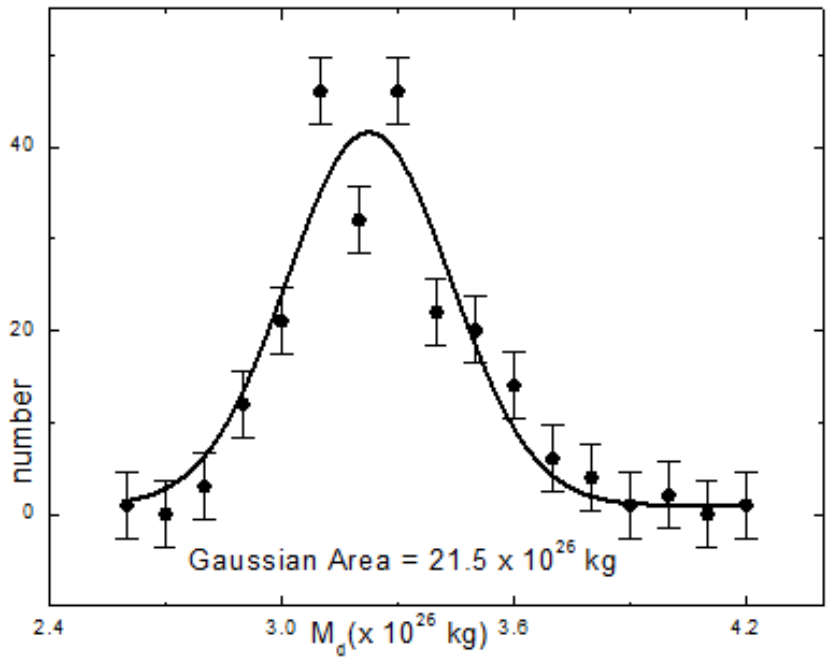

Figure 40: Gaussian fit of dust mass with error bars in the region of interest CASKK6 around the AGB0619-0558. The solid curve represents the Gaussian fit and $\pm\frac{\sigma}{\sqrt{n}}$ are the error bars which are represented by solid circle. Here, n stands to represent number of data in that bin. Gaussian area is shown in the figure which shows that there is good agreement between observed and fitted curve. From the Gaussian fit of dust color temperature and dust mass, it is found that distribution of dust color temperature is not similar with the distribution of dust mass.

mass and contour map of visual extinction of the same far infrared cavity CASKK6 as an example and they are shown in Figure 41, 42, 43 and 44 respectively. In the contour map of flux density, we study different range of flux in the region of interest. In the contour map of dust color temperature, we study the variation of dust color temperatures which show the range of temperature. In the contour map of dust mass, we study the distribution of dust mass within the region of interest. Similarly in the contour map of visual extinction, we study how it varies in the pixels and can be compared with dust color temperature and dust mass. From these four contour map, we can generalize an idea that how the four parameters (flux density, dust color temperature, dust mass and visual extinction) vary in the region of interest.

Summary of method is shown in the form of flow chart in the Figures 45, 46 and 47 in detail.

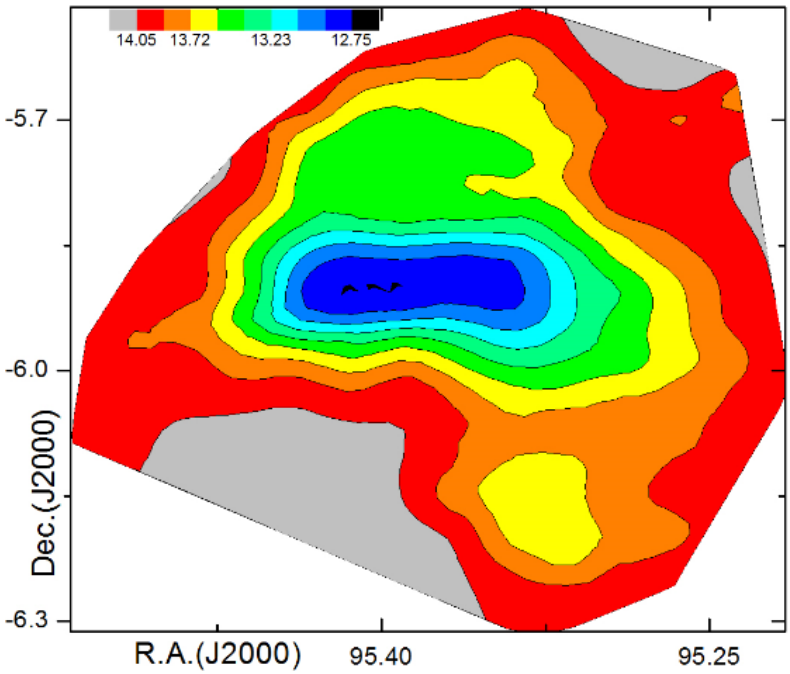

Figure 41: Contour map of flux density at 100 μm in the region of interest CASKK6 around the AGB0619-0558. The color bars with the values of flux density (in MJy/sr) are shown. One strong minima region can be seen in the map which is elongated along east-west direction

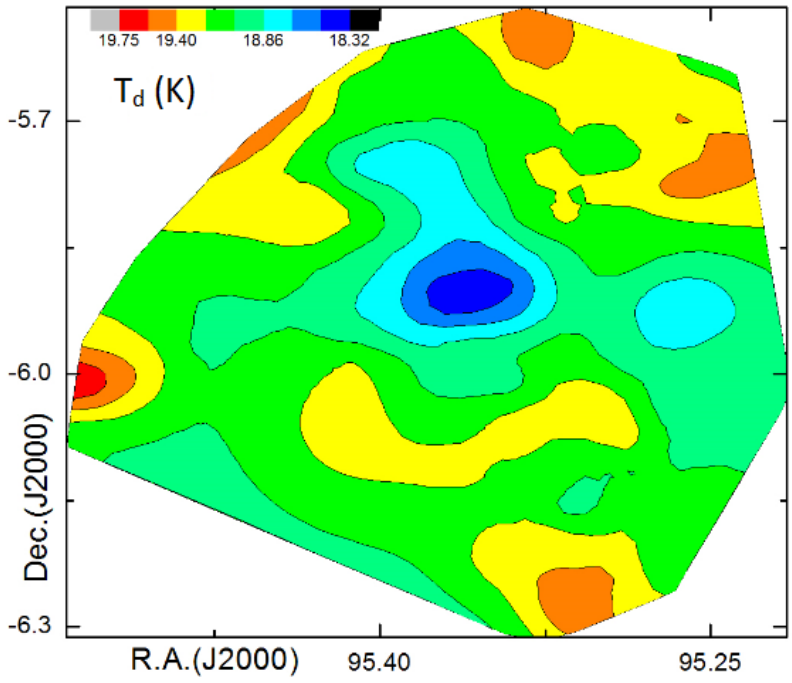

Figure 42: Contour map of dust color temperature in the region of interest CASKK6 around the AGB0619-0558 where shown contour level is in Kelvin. Minimum dust color temperature was found at R.A.(J2000) = 06^h 21^m 28.1^s & Dec.(J2000) = $-05°$ 54' 41.2". Similarly maximum dust color temperature was found at R.A.(J2000) = 06^h 22^m 08.7^s & Dec.(J2000) = $-06°$ 00' 48.2". We discuss the situation in the section result and discussion.

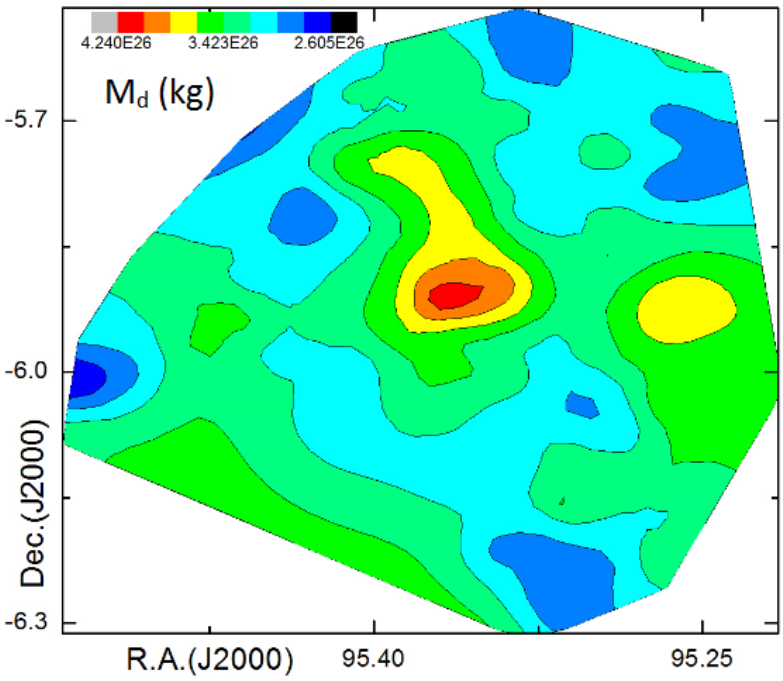

Figure 43: Contour map of dust mass distribution in the region of interest CASKK6 around the AGB0619-0558. Contour map of dust color temperature and dust mass showed that mass density is maximum in the region of minimum temperature. It shows general trend (the lower the temperature, higher the masses). We discuss the situation in the result and discussion section.

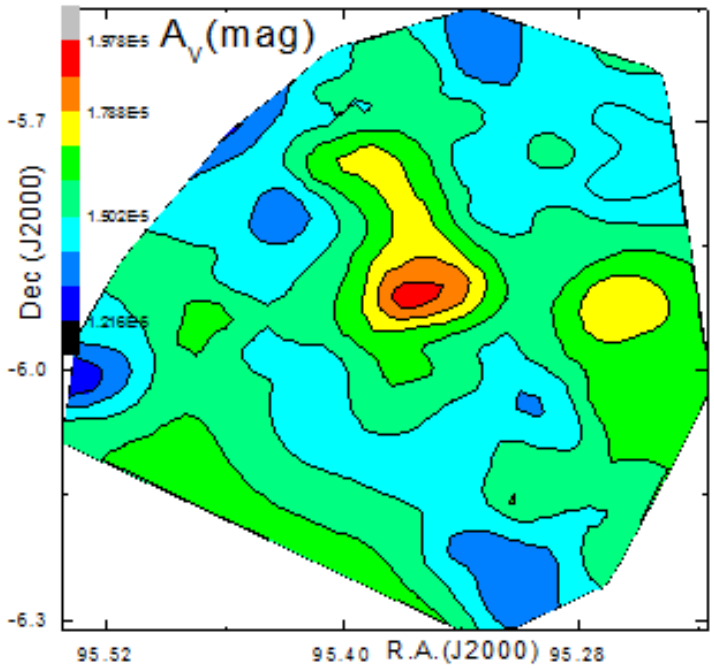

Figure 44: Contour map of visual extinction distribution in the region of interest CASKK6 around the AGB0619-0558. Contour map of dust color temperature and visual extinction showed that higher the dust color temperature lower the visual extinction and vice-versa. We discuss the situation in the result and discussion section.

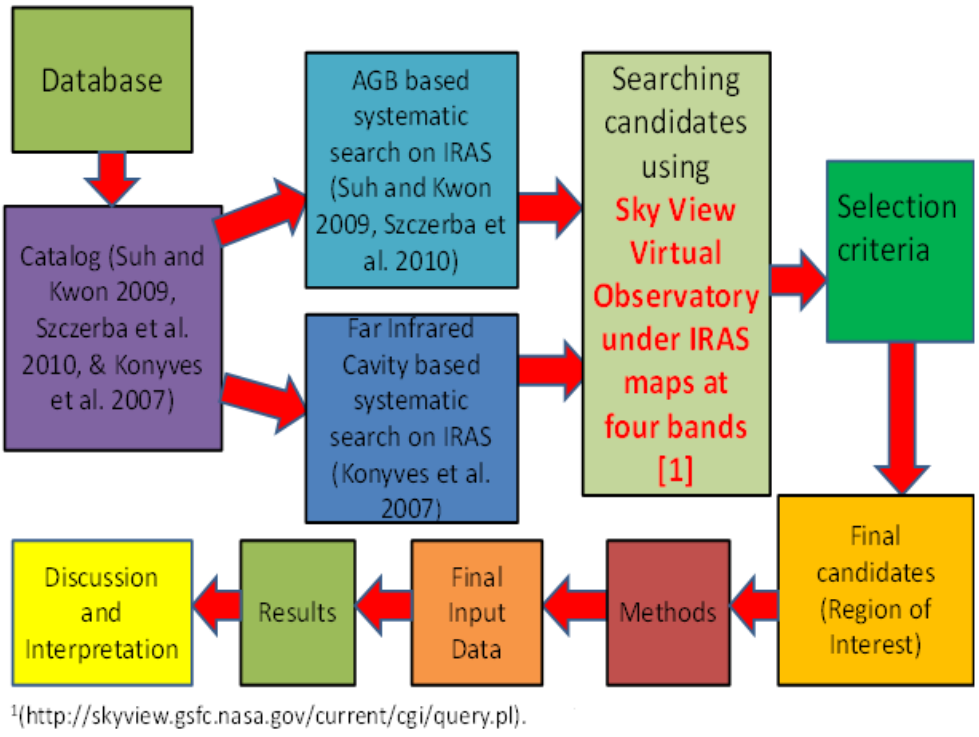

Figure 45: Summary of methods in flow chart. The primary data has been converted to secondary.

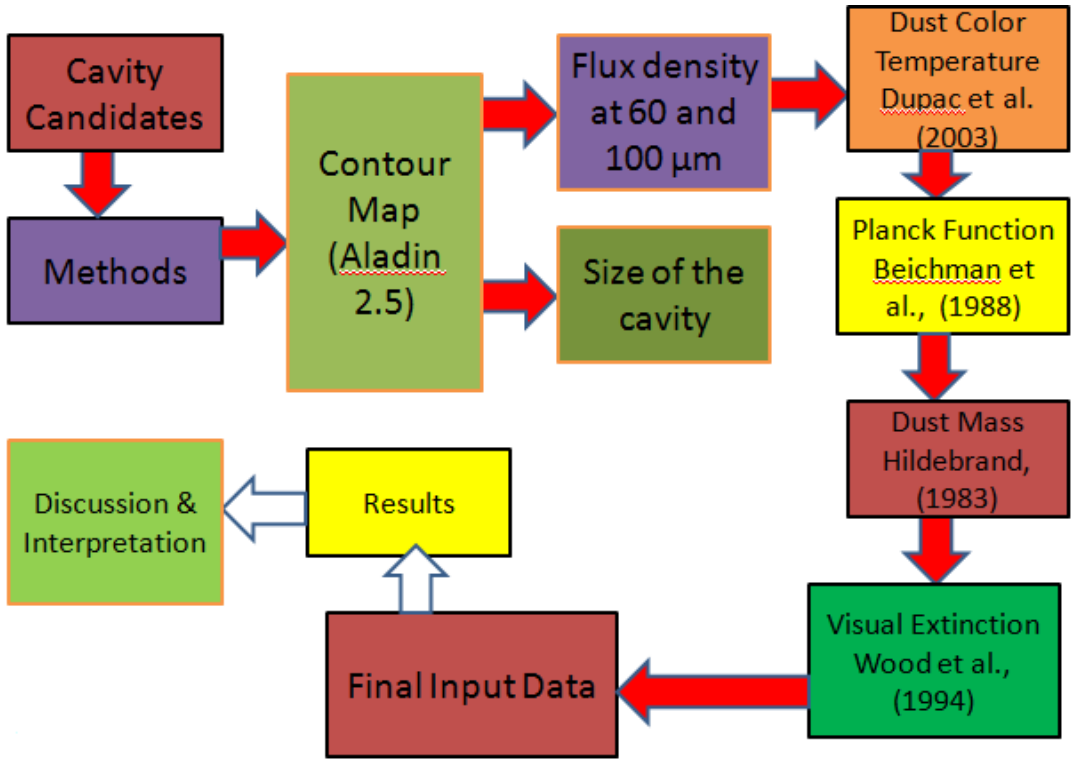

Figure 46: Summary of methods in flow chart. The secondary data has been used to calculate dust color temperature, dust mass, Planck function and visual extinction (Dupac et al., 2003; Beichman, Wilson, et al., 1988; Hildebrand, 1983; Wood et al., 1994).

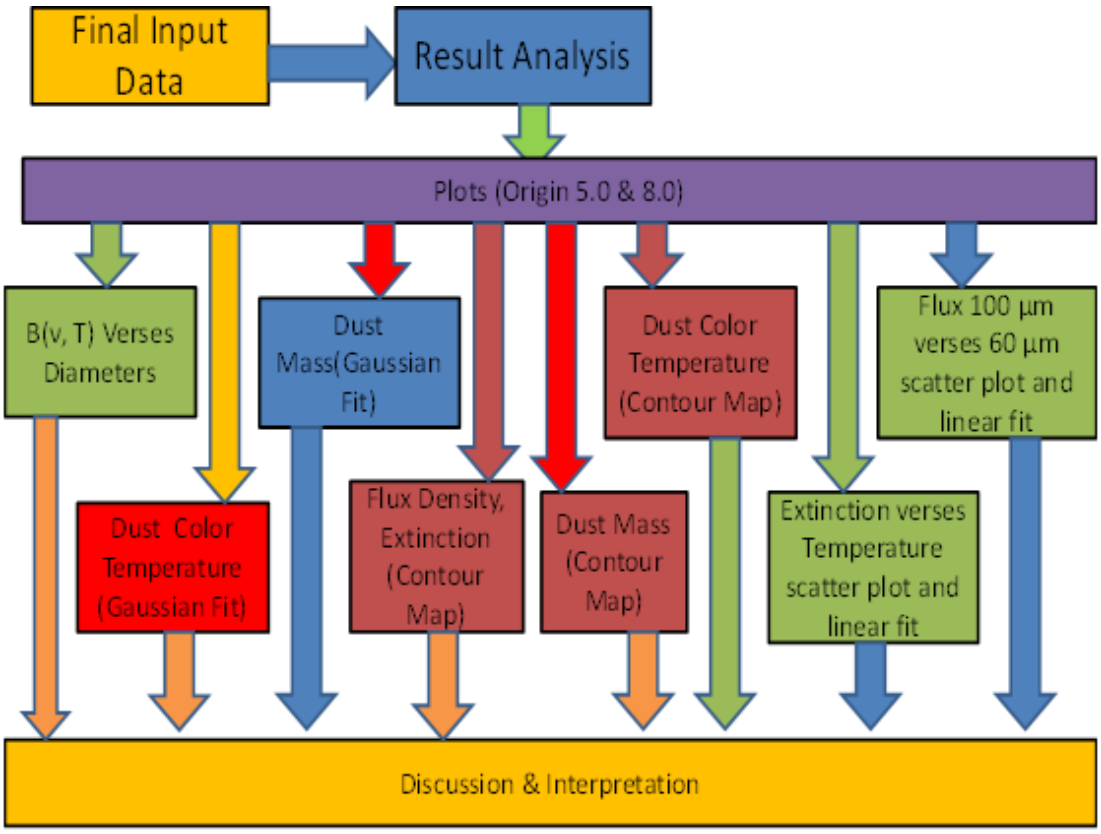

Figure 47: Summary of the plottings, interpretations and discussion in flow chart.

CHAPTER 4

4. RESULTS AND DISCUSSION

4.1 Eight New Far Infrared Cavity Candidates Around Asymptotic Giant Branch (AGB) Stars

In this section, we describe the physical properties of eight isolated far infrared cavities around AGB stars which are not yet studied. These cavities are found around the AGB stars listed in the catalog provided by Suh & Kwon (2009). The selection criteria for the cavities are as follows: (a) the major diameter should be greater than 0.50°, (b) the maximum to minimum flux density difference should be at least 3.0, (c) the AGB star should be located nearby (within 1° from the center of the cavity), (d) cavity should be isolated (no similar flux minima around 2° radius of the cavity, and (e) should not be studied at far infrared wavelengths. These cavities are at unknown distances so dust color temperature and Planck function are calculated and their distributions are described. In addition, the distribution of Planck function and dust color temperature along the extension and the compression of the cavity are studied and discussed. The 'extension'corresponds to major diameter of the cavity passing through minimum flux at longer wavelengths (100 μm) and compression represents the minor diameter of the cavity passing through the minimum flux region at 100 μm wavelength.

Figure 48 shows 100 μm IRAS images of the eight cavities around the AGB stars namely AGB0415+5441, AGB0609+1446, AGB0631+1606, AGB0633+1415, AGB0642+0053, AGB0651+0031, AGB0939-5249 and AGB1025-5933 towards left (a,c,e,g) and corresponding contour map of their flux density towards right (b,d,f,h). In the color bar of the image, black color represents the minimum flux density region and the red color represents the maximum flux density region. These two region have two possibilities that is either they absorb the long wavelength due to the presence of dust or do not have materials that emits longer wavelength. But white color indicates the region of high flux density where intense emission from the dust is taking place. It means, white pixels represent that the emission is maximum at 100 μm wavelength but dark pixels show the minimum flux region.

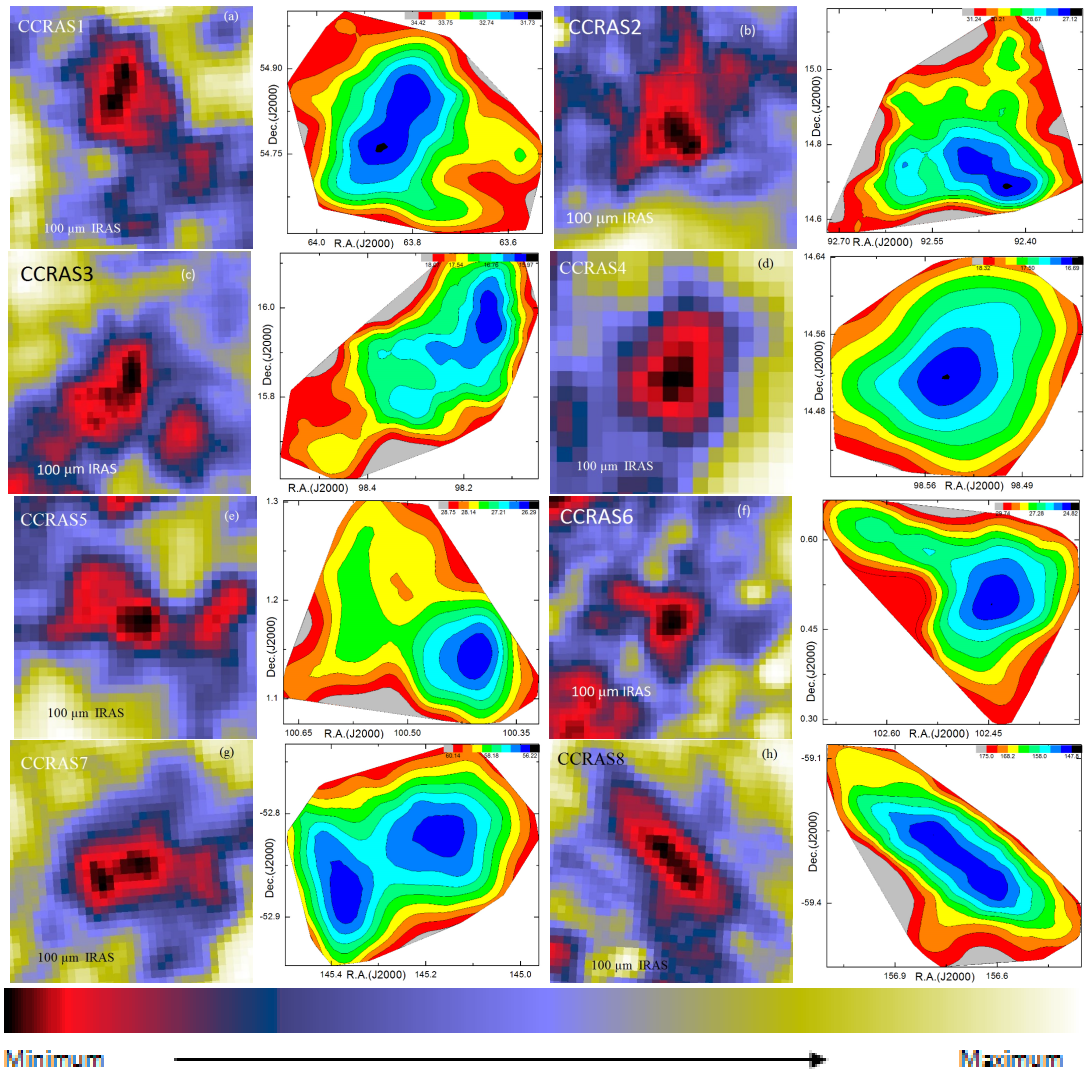

Figure 48: Images of the cavities and corresponding contour map at 100 μm IRAS maps located nearby AGB star AGB0415+5441 (CCRAS1) (a), AGB0609+1446 (CCRAS2) (b), AGB0631+1606 (CCRAS3) (c), AGB0633+1415 (CCRAS4) (d), AGB0642+0053 (CCRAS5) (e), AGB0651+0031 (CCRAS6) (f), AGB0939-5249 (CCRAS7) (g) and AGB1025-5933 (CCRAS8) (h). Color bar is shown at the buttom, which represents the range of relative flux density It is different for different cavities: 31.73 MJy/sr to 34.41 MJy/sr for CCRAS1, 27.12 MJy/sr to 31.24 MJy/sr for CCRAS2, 15.97 MJy/sr to 18.06 MJy/sr for CCRAS3, 16.69 MJy/sr to 18.32 MJy/sr for CCRAS4, 26.29 MJy/sr to 28.74 MJy/sr for CCRAS5, 24.82 MJy/sr to 29.73 MJy/sr for CCRAS6, 56.22 MJy/sr to 60.13 MJy/sr for CCRAS7 and 147.88 MJy/sr to 174.93 MJy/sr for CCRAS8 at 100 micron .

The cavity CCRAS1 is one of the deepest cavity where maximum to minimum flux density ratio is found to be 1.1 which is located at R.A.(J2000) = 04^h 15^m 03.0^s, Dec.(J2000) = 54° 41' 00.0" (l = 149.6° and b = 2.7°). Size of the cavity is defined as its major and minor diameters passing through minimum flux region. Therefore diameters are drawn through minimum flux region at 100 μm wavelength. Here size of the cavity is found about 0.5° × 0.2°. The shape of the cavity is like 'head'of housefly and is elongated along north-south direction. Since it is located at 2.7° Galactic latitude with position angle 316.3°. Therefore it is in the Galactic plane inclined by ∼ 44.0°. It means, the cavity is very close to the galactic plane so that it is located in the strong radiation field emitted from the disk of the Milky Way. Extension of the cavity is located along north-south direction and compression is along east-west direction.

The cavity CCRAS2 is located at R.A.(J2000) = 06^h 09^m 55.9^s, Dec.(J2000) = 14° 46' 10.4" (l = 195.1° and b = −2.2°). Here size of the cavity is about 0.6° × 0.2°. For the calculation of its size, major and minor diameters are drawn at 100 μm wavelength by considering minimum flux region as a reference. The cavity is extended along north-south direction and is compressed along east-west direction. Since it is located at −2.2° Galactic latitude with position angle 298.8°, so it is close to the Galactic plane, similar to the cavity CCRAS1.

The shape of the cavity CCRAS3 is elongated along east-west direction and is compressed along north-south direction. It is located at R.A.(J2000) = 06^h 32^m 38.1^s, Dec.(J2000) = 15° 59' 47.9" (l = 196.58° and b = 3.2°). Since it is located at 3.2° Galactic latitude with position angle 297.3°. Here size of the cavity is about 0.7° × 0.2°.

The cavity CCRAS4 is found at R.A.(J2000) = 06^h 33^m 01^s, Dec.(J2000) = 14° 15' 00.0" (l = 198.2° and b = 2.5°). It is extended along east-west and compressed along north-south direction. The size of the cavity is about 0.3° × 0.2°. It is also near to the Galactic plane because it is located at Galactic latitude 2.5° with position angle 297.4°.

The cavity CCRAS5 has the shape of 'octopus'elongated along east-west direction and is compressed along north-south direction which is located at R.A.(J2000) = 06^h 41^m 43.0^s, Dec.(J2000) = 01° 09' 22.8" (l = 210.8° and b = −1.6°). Here size of the cavity is about 0.3° × 0.1° and position angle is 297.2°. This cavity is the smallest in size.

The cavity CCRAS6 is located at R.A.(J2000) = 06^h 49^m 47.1^s, Dec.(J2000) = 00° 32' 32.4" (l = 212.3° and b = −0.1°). It is elongateded along north-south and is compressed along east-west. Here size of the cavity is about 0.4° × 0.2° and position angle is 297.1°.

Cavity CCRAS7 is like the shape of 'a fish'extended along east-west and compressed along north-south. It is located at R.A.(J2000) = 09^h 40^m 50.6^s, Dec.(J2000) = −52° 48' 3" (l = 276.4° and b = −0.1°). Here size of the cavity is about 0.3° × 0.2° and position

angle is 318.9°.

The cavity CCRAS8 is located at R.A.(J2000) = 10^h 26^m 54.7^s, Dec.(J2000) = −59° 18' 22.5" (l = 285.4° and b = −1.4°). Here size of the cavity is about 0.6° × 0.2° and position angle is 328.3°. The cavity has wider range along north-south and narrower range is along east-west direction.

4.1.1 Flux Density at 60 μm and 100 μm

Flux density at 60 μm and 100 μm IRAS images are measured in all eight cavities nearby to the AGB stars. For this, we used the FITS images that we receive from the IRAS survey, and the ALADIN software. They are plotted in a graph and are discussed separately. The graph is scattered plot with linear fit. Figure 49(a) belongs to the cavity CCRAS1 where flux density extends along east-west and is compressed along north-south direction. In the scatter plot, a good correlation is noticed which is found to be broader with increasing 100 μm flux density. The best fit line has correlation coefficient 0.81, slope 0.21 with standard error 0.01 and the dust color temperature obtained from the linear fit is 23.1 K. It means there is a good correlation between the two flux densities.

Figure 49(b) is the scatter plot and best fit between flux densities $F(60)$ and $F(100)$ of the cavity CCRAS2 where both flux densities are equally spread along east-west part and compressed along north-south part. Correlation coefficient obtained from the linear fit is 0.72, which is fairly a good value. The cavity shows a strong east-west elongation, indicating the external cause rather than the effect of radiation field of the Galactic plane. Slope of the linear fit is 0.29 with standard error 0.02. From the linear fit, dust color temperature is found 25.3 K. The absolute value of flux density per pixel in both CCRAS1 and CCRAS2 are similar to each other in both 60 and 100 μm wavelengths.

Figure 49(c) is for the cavity CCRAS3. From the figure, it can be seen that there is good correlation between the flux densities at 60 and 100 microns at their higher flux values but less correlation in the lower values. Distribution of flux density at higher and middle part is wider along compressive region than the lower flux density region. Using the value of the slope of best fit line, the dust color temperature is found to be 22.5 K which is less than CCRAS1 and CCRAS2.

Similarly, scattered plot and best fit of flux densities in the cavity CCRAS4 is shown in Figure 49(d). From the figure, it is found that there is a poor correlation between the two IRAS flux densities which suggests that the cavity might not be isolated and stable. Here the value of correlation coefficient is 0.75. From the best fit, dust color temperature is found to be 23.9 K. A relatively low temperature suggests that dust particles are possibly more interacting because of small mean free path.

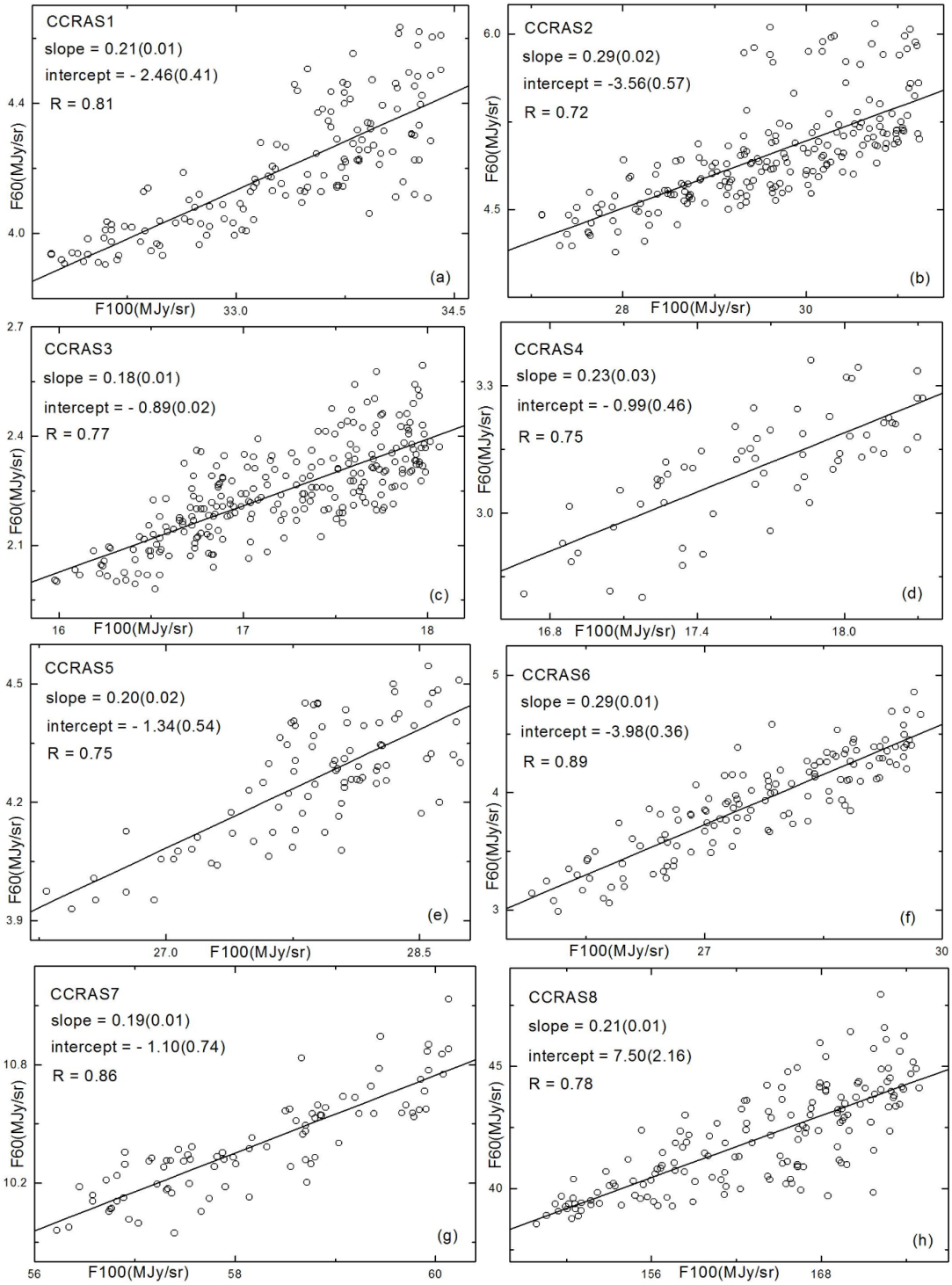

Figure 49: Scattered plot between flux densities at 60 μm ($F60$) and 100 μm ($F100$) of the cavities located nearby AGB stars namely AGB0415+5441 (CCRAS1) (a), AGB0609+1446 (CCRAS2) (b), AGB0631+1606 (CCRAS3) (c), AGB0633+1415 (CCRAS4) (d), AGB0642+0053 (CCRAS5) (e), AGB0651+0031 (CCRAS6) (f), AGB0939-5249 (CCRAS7) (g) and AGB1025-5933 (CCRAS8) (h). The best fit line (solid line) with their slopes, correlation coefficient (R) and intercepts are shown. The figures in the parenthesis represent standard errors in the respected statistical parameters in the linear fit.

Figure 49(e) shows a widely spread scatter plot in the higher flux density region and it goes narrow in the lower flux region. So there is a poor correlation between $F(60)$ and $F(100)$ in case of the cavity CCRAS5. Dust color temperature obtained from the linear fit is 23.1 K. In the next section, we discuss the distribution of dust color temperature as well as maps.

In the case of cavity CCRAS6, the scattered plot shows that there is a good correlation between the two flux densities through out the region. From the linear fit, correlation coefficient, slope and standard error are found to be 0.88, 0.28 and 0.01 respectively. Using the value of slope, dust color temperature is found as 25.2 K. Figure 49(f) shows that the cavity extends widely along east-west and contracts along north-south region. There is a little difference in dust color temperature, as noticed from linear fit and calculated value, which will be confirmed and discussed in the next section.

The cavity CCRAS7 is slightly different than the previously mentioned cavities. Scatter plot of Figure 49(g) shows that the cavity extends along east-west direction and contracts along north-south direction. But in the contracting region, there is wide spread of low flux density than in the high flux density region. The absolute value of flux density per pixel of the cavity CCRAS7 is quite large than that of the previously described cavities at both 60 and 100 μm wavelengths. The longer values of flux densities might come from the radiation. Since the location of the cavity is ($l = 276.5^\circ$ and $b = -0.1^\circ$) suggests that the excessive radiation field originates from the bulge of the Milky way. Dust color temperature found from the best fit is 22.8 K.

The cavity CCRAS8 is quite different than the previously mentioned far infrared cavities. This cavity CCRAS8 shows a very high flux density than the others. Similar to the cavity CCRAS7, the location of this cavity ($l = 285.4^\circ$ and $b = -1.4^\circ$) favors the higher value of flux density because of nearby bulge The cavity extends along east-west and contracts along north-south. Figure 49(h) shows that the contracting region is less broadening at low flux density region and sufficient broadening at high flux density region. But in general, there is good a correlation between the two flux densities in the cavity. Using the slope of the best fit line, we get 23.3 K dust color temperature. The cavity is surrounded by strong emission of 100 μm, suggesting an isolated and stable cavity.

To sum up, we can say that cavity CCRAS6, CCRAS7 and CCRAS8 showed strong correlation but other five cavities showed a good correlation between flux densities at IRAS long wavelengths.

4.1.2 Distribution of Dust Color Temperature

In this section, we have calculated dust color temperature of each pixels of the above mentioned eight cavities by using expression (2.22), given in chapter 2. Here we discuss dust color temperature through contour map and Gaussian fit. After calculation of dust color temperature, Planck function $B(\nu, T)$ has also been calculated and analyzed. In the next section, we discuss the variation of Planck function and temperature with the extension (major diameter) and compression (minor diameter) passing through minimum flux (minima) at 100 μm of the cavity.

Figure 50 shows the contour map or the dust color map of all eight cavities. Values of the dust color temperature are shown in the color bars. Position of minimum temperature and maximum temperature region are clearly shown in the figure. In Figure 50(a), minimum flux region does not lie in the minimum temperature region. Minimum dust color temperature lies at the boarder of the cavity in the north-west part where as maximum dust color temperature region lies near the boarder of the cavity at the south-east part. It means density of the dust material might be higher in the north-west part and is lower in the south-east part of the cavity CCRAS1.

For cavity CCRAS2, as shown in Figure 50(b), the minimum temperature region does not lie in the minimum flux density region, but the minimum temperature region lies near the centre extended along north-south direction. Maximum temperature region lies at the north-east corner of the cavity. Most of the contours are extended along north-south direction. Central part of the cavity is free from maximum temperature which suggests that the central part contains less amount of dusty materials responsible for far infrared emission (Gautam & Aryal, 2017).

Like cavity CCRAS2, minimum temperature region of the cavity CCRAS3 does not lie in the minimum flux density region. But maximum temperature region lies at the boundry towards east-ward side of the cavity, shown in Figure 50(c). In this case, less number of contours are surrounded suggesting that the distribution of Planck function might be uniform. Uniform distribution of Planck function means the cavity is thermodynamically stable.

In case of cavity CCRAS4, minimum flux density and minimum temperature region are different which is unusual behavior but the minimum temperature contour is surrounded by many other contours suggesting that the distribution of Planck function might not be uniform. Maximum temperature contour lies towards south-east direction which has less dense materials. This cavity is quite different than cavities CCRAS1, CCRAS2 and CCRAS3, as shown in Figure 50(d).

Figure 50(e) describes dust color temperature map of CCRAS5 where most of the

contours are elongated along north-south direction. It means the cavity might not be affected by the radiation field of the Galactic plane. Minimum temperature contour lies towards southern part where as maximum temperature contour lies at the northern part of the cavity. This distribution is just opposite of CCRAS1.

In cavity CCRAS6, maximum temperature contour lies at the boundary of the northern part where as minimum temperature contour lies fully inside the cavity as shown in Figure 50(f). This region is completely surrounded by other contour like in the case of CCRAS4. It makes non-uniform distribution of Planck's function which will be justified in the next section.

Figure 50(g) is about CCRAS7 where maximum temperature contour lies towards southern part of the cavity but minimum temperature region lies at the south-east part of the cavity. This cavity is quite different than others.

In case of cavity CCRAS8, minimum temperature region lies at the northern part where as the maximum temperature region lies at the southern part of the cavity. Figure 50(h) shows that the most of the contours are extended along north-south direction at all levels.

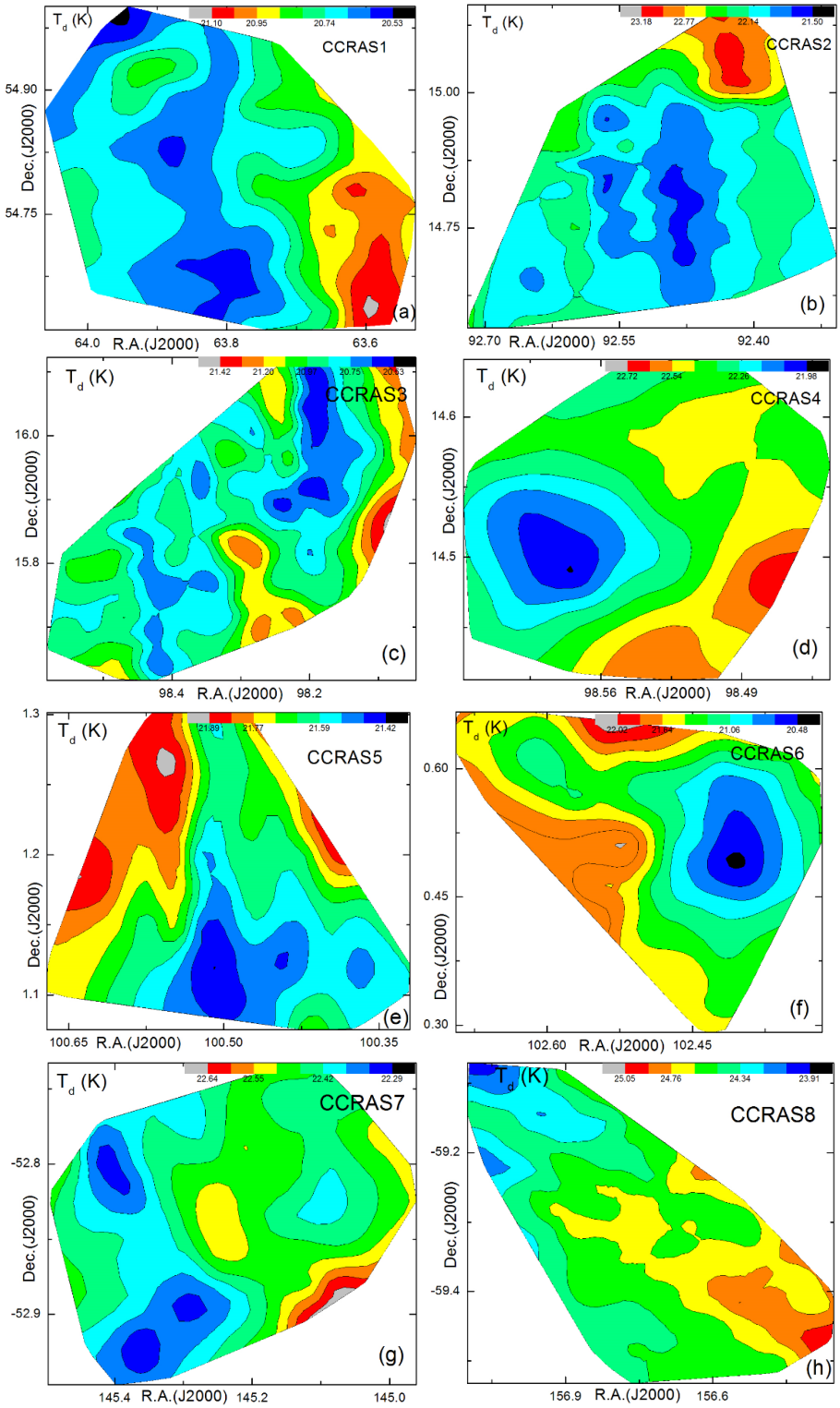

Figure 50: Contour map of dust color temperature (T_d) of the cavity CCRAS1 (a), CCRAS2 (b), CCRAS3 (c), CCRAS4 (d), CCRAS5 (e), CCRAS6 (f), CCRAS7 (g) and CCRAS8 (h) located near to the AGB stars namely AGB0415+5441, AGB0609+1446, AGB0631+1606, AGB0633+1415, AGB0642+0053, AGB0651+0031, AGB0939-5249 and AGB1025-5933. Color bars with temperature (in K) are shown in the contour level.

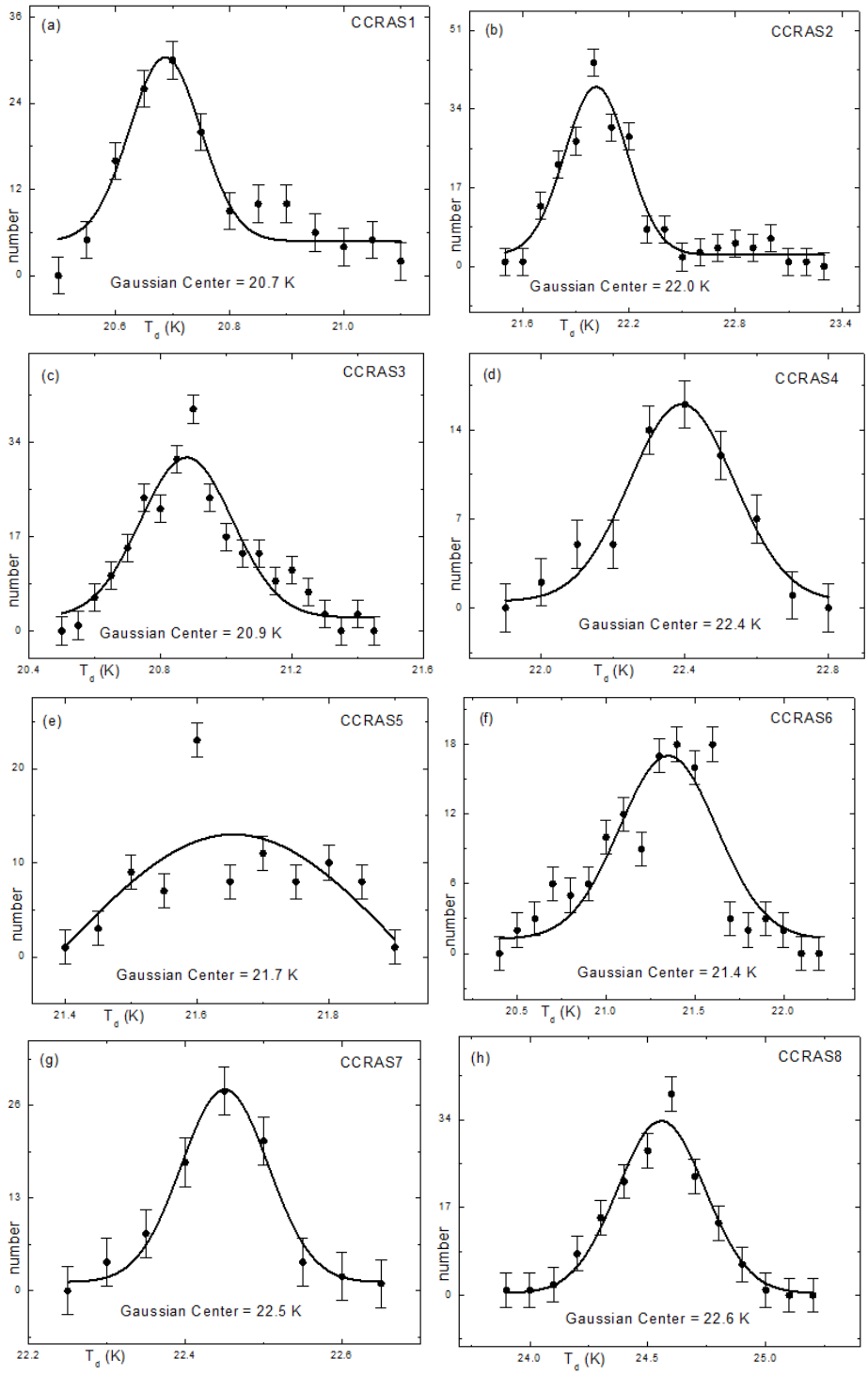

Figure 51: Distribution of dust color temperature of the cavity CCRAS1 (a), CCRAS2 (b), CCRAS3 (c), CCRAS4 (d), CCRAS5 (e), CCRAS6 (f), CCRAS7 (g) and CCRAS8 (h). The name of the cavity are given. The solid line represents the Gaussian curve. The Gaussian centers are given. The error bars represent the standard error of the deviation.

Figure 51 shows distribution of dust color temperature of the selected eight cavities. Solid curves represent the Gaussian fit and vertical line shows the error bar, representing standard error of the distribution.

Figure 51(a) is for the cavity CCRAS1 where minimum and maximum dust color temperature are found to be (20.5 ± 0.61) K and (21.1 ± 0.50) K respectively. The errors are calculated using the values of dust color temperature obtained from $F(60)$ verses $F(100)$ plots. Value of Gaussian center is seen at 20.7 K. Here the Gaussian curve is found to be sufficient sharp and shows good agreement with the temperature distribution in the range up to 20.8 K and after 20.8 K temperature, it shows positive skewness means large number of data lie towards right curve. It is therefore, a deviation from Gaussian distribution at the higher temperature is seen. The full width half maxima (FWHM) of the Gaussian fit is distinct and broaden suggesting the cavity is well defined and isolated.

The distribution of dust color temperature of the cavity CCRAS2 is given in Figure 51(b) where the Gaussian curve is sharp and broaden like the cavity CCRAS2, showing good Gaussian fit in the dust color temperature distribution. Perfect Gaussian distribution is seen up to temperature 22.3 K and after it, positive skewness is found. Due to sharp and broaden Gaussian curve, it suggests that the cavity is isolated. Minimum and maximum dust color temperature are found to be (21.5 ± 0.95) K and (23.2 ± 0.51) K. Gaussian center is at 22.0 K, shown in the figure. Dust particles of the cavity CCRAS2 is at higher temperature than CCRAS1. It further suggests that higher temperature region violets the Gaussian distribution.

Gaussian fitted with observed distribution of dust color temperature curve of the cavity CCRAS3 is shown in Figure 51(c). Here, the distribution is perfect Gaussian in all temperature range and is slightly different than that of the cavities CCRAS1 and CCRAS2 showing slight positive skewness. The minimum and maximum dust color temperature are found to be (20.5 ± 0.50) K and (21.4 ± 0.28) K respectively. The Gaussian center is seen at 20.9 K. The full width half maxima of the Gaussian fit is not very sharp but is wider than the previous cavities. Offset value of dust color temperature is only 0.9 K so it suggests that the matter (dust) within the cavity is probably in the thermal equilibrium.

A perfect Gaussian fit is seen in the dust color temperature distribution of the cavity CCRAS4 which is shown in Figure 51(d). The full width half maxima of the Gaussian fit is sharp enough and broader than the cavities CCRAS1, CCRAS2 and CCRAS3. Since the Gaussian fit is sharp, broad and shows a good agreement with the dust color temperature distribution, it suggests that the flux minima of the cavity is extended and well connected with its environment. Here minimum and maximum dust color temperature are found to be (22.0 ± 0.48) K and (22.7 ± 0.30) K respectively. Since the distribution is perfect Gaussian so the left curve is the mirror reflection of right curve

and vice-versa.

Figure 51(e) shows the distribution of dust color temperature of the cavity CCRAS5 which is completely non Gaussian. The minimum and maximum dust color temperature is found to be (21.4 ± 0.43) K and (21.9 ± 0.31) K with offset of 0.5 K temperature suggesting the better condition of thermal equilibrium. This will be verified in the section when we discuss the distribution of Planck function. An offset of < 2 K suggests that the core of the loop is stable. In the figure, a deviation from the Gaussian fit suggests that the cavity is not symmetrical, probably affected by external factors. In the next section, we will discuss about the distribution of Planck function along the extension and compression of the cavity.

A good Gaussian fit is seen in the dust color temperature distribution of the cavity CCRAS6 but at higher temperature, it shows non Gaussian nature with negative skewness which is shown in Figure 51(f). Here minimum and maximum values of dust color temperature are (20.5 ± 1.17) K and (22.0 ± 0.80) K respectively. The full width half maxima is similar to that of the cavity CCRAS3.

Figure 51(g) shows the dust color temperature distribution of the cavity CCRAS7. We noticed a perfect Gaussian fit of the dust color temperature. It means mean, mode and median of the data lie towards the mean value where left curve is mirror reflection of right curve and vice-versa. In this case, there is minimum offset value i.e., 0.3 K in comparison with other cavities. Here, minimum and maximum value of dust color temperature are found as (22.3 ± 0.40) K and (22.6 ± 0.20) K respectively (Gautam & Aryal, 2018a). The nature of temperature distribution in Gaussian fit of the cavity CCRAS7 is similar with the distribution in CCRAS4.

Distribution of dust color temperature of the cavity CCRAS8 is shown in Figure 51(h). Figure shows a good agreement between Gaussian fit and dust color temperature distribution with slight negative skewness. In this case, the Gaussian curve is less sharp than CCRAS7 which suggests that the flux minima of the cavity is less extended and well connected with its environment. Minimum and maximum dust color temperature are found as (23.9 ± 0.21) K and (25.0 ± 0.45) K respectively (Gautam & Aryal, 2018b).

At the end, it is found that cavities CCRAS1 and CCRAS2 showed sharp peak with Gaussian agreement, cavities CCRAS4, CCRAS6, CCRAS7 and CCRAS8 showed broad width with Gaussian agreement and cavity CCRAS4 showed completely non-Gaussian nature which is possibly due to external factors.

4.1.3 Distribution of Planck Function Along the Extension and the Compression of the Cavities

Extension corresponds to the major diameter means, the longest diameter of the cavity passing through the minimum flux at 100 μm IRAS maps. Figure 52 shows the variation of Planck function $B(\nu, T)$ along extension of the cavity. Flux density along major diameter are measured by using ALADIN2.5 software with the left-end taking as reference point in the diameter. The reference position is either towards the north-west direction or south-west direction. For the calculation of Planck function, we need dust color temperature and to calculate dust color temperature, flux density at 60 μm and 100 μm IRAS map is needed. Using equation (2.22) and (2.29) of chapter 2, dust color temperature and Planck function along both diameters are calculated.

The main concept is that, if the Planck function is independent with distance (major or minor or both), it can be concluded that the materials (dusts, grains, etc.) will be in local thermodynamic equilibrium through out the cavity. In other words, these materials behave as a perfect black body along the major or minor diameter. In such case, the mean free path of the particles or materials on the way is of the order of the reciprocal of absorption coefficient and the dust color temperature remains uniform within the mean free path.

When we analyze Figure 52, we get different nature of their distribution. Only in cavity CCRAS8 Figure 52(h), there is a strong correlation between Planck function and major diameter. Here, Planck function decreases with distance and the diameter extends from north-west to south-east direction. Due to strong correlation, we can say that the materials (dust, grain, etc.) behave as a black body. It further suggests that the neutral gases that obey Maxwellian velocity distribution co-exist with Planck theory of black body radiation along the major diameter of this cavity. This makes the cavity isolated and stable.

For cavities CCRAS1, CCRAS3, CCRAS4 and CCRAS7, there is a poor correlation so that Planck function fluctuates with distance (major diameter). Here the best fit line has negative slope which signifies that Planck function decreases with distance and diameters extend from north-west to south-east direction. Thus the materials of such cavities along major diameters do not behave as a black body, i.e., their velocity distribution do not co-exist with Planck theory. Such cavities are relatively unstable.

Similarly, for cavities CCRAS2, CCRAS5 and CCRAS6, they also have poor correlation between Planck function and major diameter. But in these cavities, the best fit line shows positive slope means Planck function increases with major diameter. The major diameters extend from south-west to north-east.

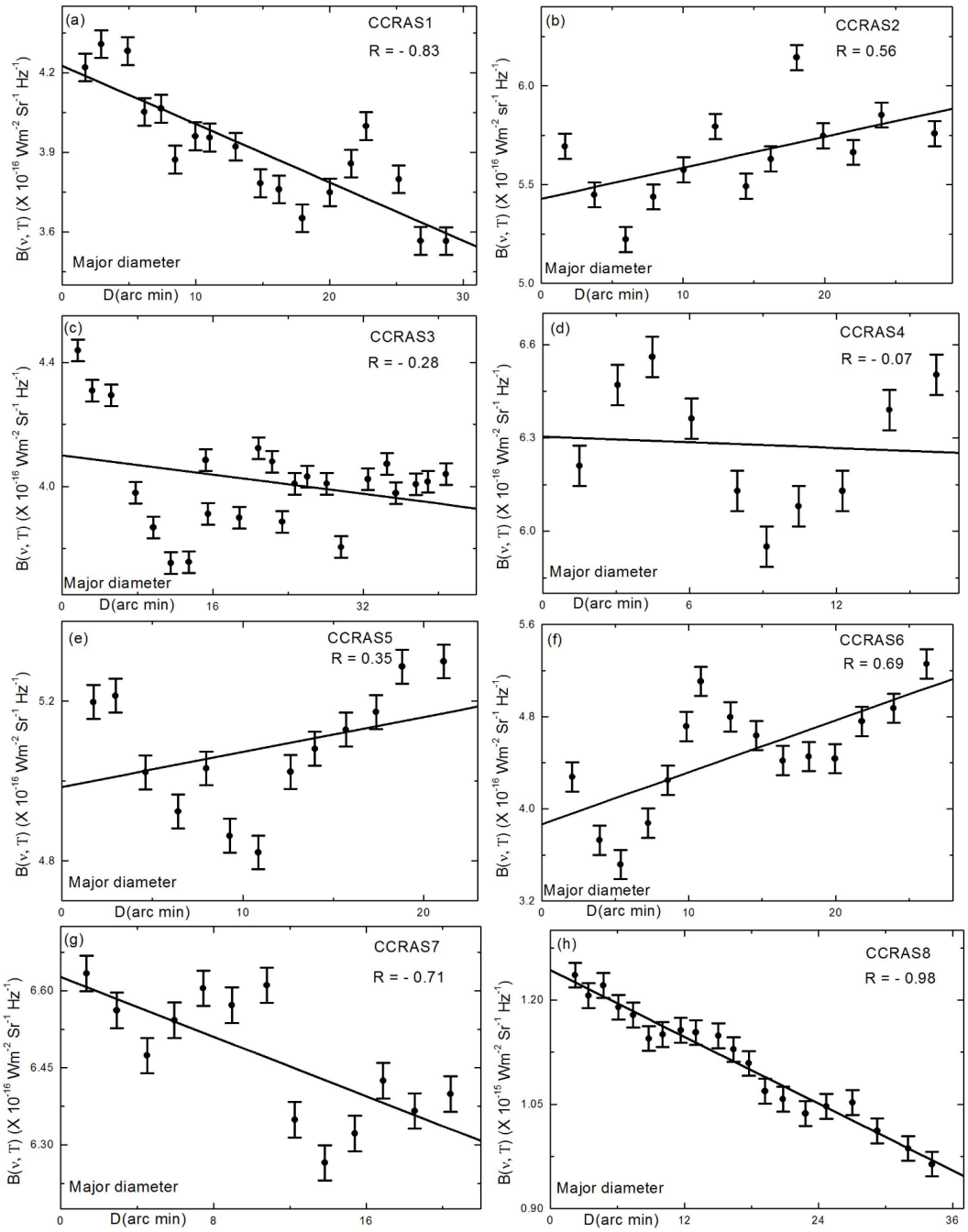

Figure 52: Variation of Planck function $B(\nu, T)$ of the inner cavity CCRAS1 (a), CCRAS2 (b), CCRAS3 (c), CCRAS4 (d), CCRAS5 (d), CCRAS6 (e), CCRAS6 (f), CCRAS7 (g) and CCRAS8 (h) with the distance along major diameter. The south-west point of the major diameter is assumed as a reference point i.e., left-end represents reference point taken at zero arc-minute. In the best fit, correlation coefficient is shown. The error bars represent the standard error (±se) of the deviation. The negative value of correlation coefficient signifies the negative slope.

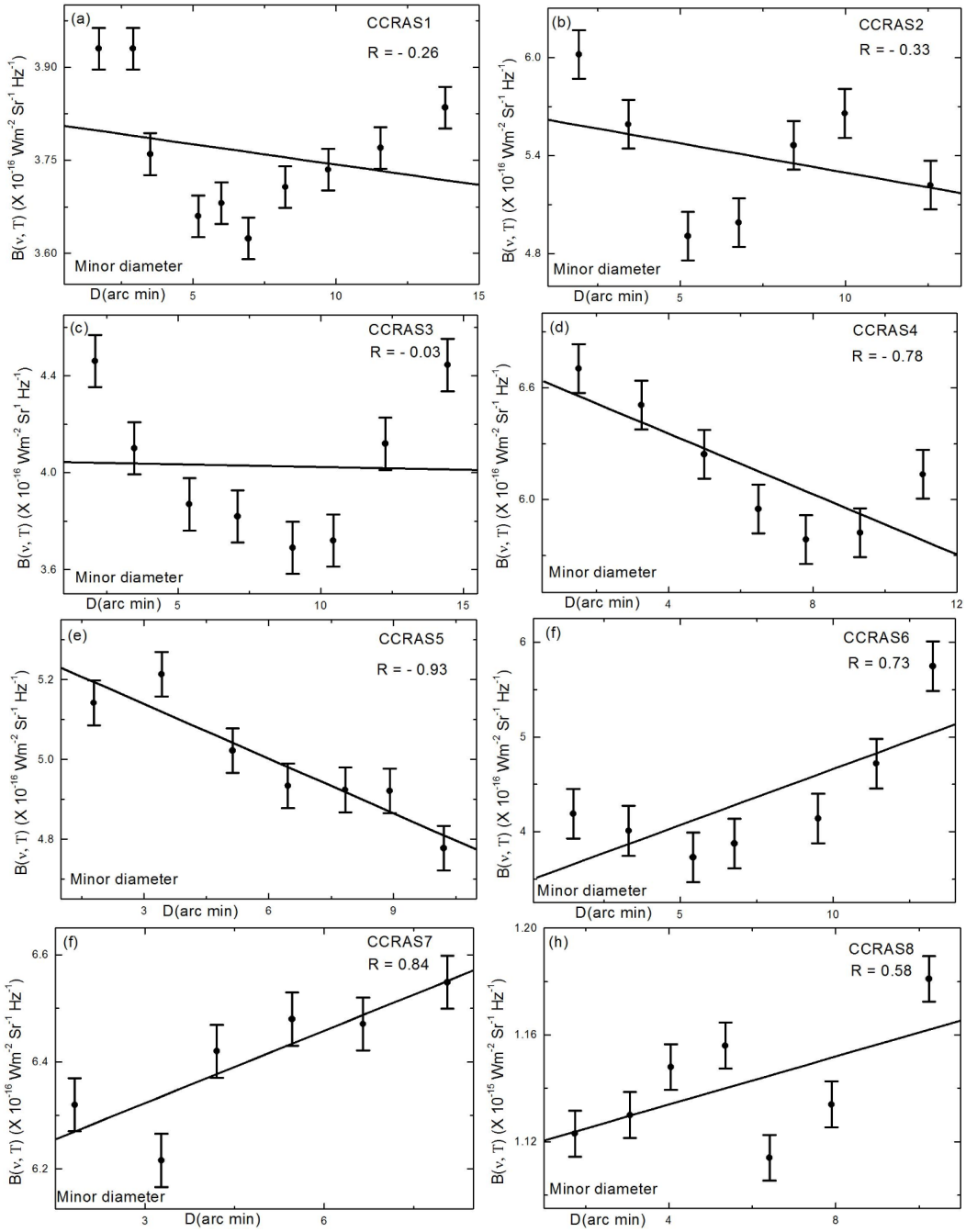

Figure 53: Variation of Planck function $B(\nu, T)$ of the cavity CCRAS1 (a), CCRAS2 (b), CCRAS3 (c), CCRAS4 (d), CCRAS5 (d), CCRAS6 (e), CCRAS6 (f), CCRAS7 (g) and CCRAS8 (h) with the distance along minor diameter. The south-west point of the major diameter is assumed as a reference point i.e., left-end represents the reference point taken as zero arc-minute. The correlation coefficient of the line is shown. The error bars represent the standard error (±se) of the deviation. The negative value of correlation coefficient signifies the negative slope.

Compression corresponds to the minor diameter, means the smallest diameter of the cavity passing through the minimum flux at 100 μm IRAS maps. Figure 53 shows the variation of Planck function $B(\nu, T)$ along compression of the cavity. Flux density along minor diameter are measured by using ALADIN2.5 software with the left-end point taking as reference point in the diameter. The reference position is either in the north-west direction or south-west direction.

When we analyze the Figure 53, different nature of their distribution is found. Cavities CCRAS1, CCRAS2, CCRAS3, CCRAS4 and CCRAS5 show poor correlation between Planck function and minor diameter with negative slope in their best fit lines. It means Planck function decreases with distance and the diameters extend from north-west to south-east direction. There is random distribution of Planck function in the cavities CCRAS2, CCRAS3 and CCRAS5. It means the dusts and the radiation field are not in the thermal equilibrium. For cavities CCRAS6, CCRAS7 and CCRAS8, there is also a poor correlation between Planck function and minor diameter and the slope of the best fit is positive. It means Planck function increases with minor diameter. Here, the minor diameters extend from south-west to north-east.

4.1.4 Distribution of Visual Extinction with Dust Color Temperature

The visual extinction (A_V) is very important parameter that relates distance and magnitude by the relation

$$m - M = 5 \log r - 5 + A_{\mathrm{V}} \tag{4.1}$$

Where m and M represent the apparent and absolute magnitudes respectively. The distance is represented by the symbol r. Here, we have calculated the values of A_V using the expression (2.27) in chapter two given by Wood et al. (1994). The relation is

$$A_{\mathrm{V}}(\mathrm{mag}) = 15.078\,(1 - \exp\,(-\tau_{100}/641.3)) \tag{4.2}$$

where,

$$\tau_{100} = \frac{F_\lambda(100\ \mu m)}{B_\lambda(100\ \mu m, T_{\mathrm{d}})} \tag{4.3}$$

is optical depth and $F_\lambda(100\ \mu\mathrm{m})$ is the flux at 100 μm.

$$B(\lambda, T) = \frac{2hc}{\lambda^3}\left[\frac{1}{e^{hc/\lambda kT} - 1}\right] \tag{4.4}$$

is the Planck function. After the calculation of visual extinction, they are plotted with dust color temperature of each pixels.

Interestingly, the visual extinction is found to be maximum for low temperature region and it is systematically decreased with the increase of temperature. Though the range of decrease is very small (slope is negative $\times 10^{-6}$).

Figure 54 describes how visual extinction varies with dust color temperature. All eight cavities show mostly systematic order i.e., extinction is maximum at low temperature and decreases with rise in temperature having slope negative in all cases. Correlation coefficient is also negative and ranges from -0.64 to -0.92 which shows that there is good correlation between the plotted data. The cavity CCRAS2 has the highest correlation coefficient and the cavity CCRAS7 has the least. Cavities CCRAS1, CCRAS2 and CCRAS3 show one type of behavior where scattering of the data are extended in lower temperature region, cavities CCRAS4, CCRAS5, CCRAS6 and CCRAS7 show another type of behavior where the data are extended in the middle temperature region and there is extension along higher temperature region in case of cavity CCRAS8. For cavity CCRAS7, there is good correlation, for CCRAS1, CCRAS3, CCRAS4, CCRAS5 and CCRAS7, there is better correlation and for the cavities CCRAS2 and CCRAS6, there is best correlation.

The best fit lines between the A_V and T_d for eight far infrared cavities CCRAS1, CCRAS2, CCRAS3, CCRAS4, CCRAS5, CCRAS6, CCRAS7 and CCRAS8 are found to be

$$T_d = -1.4 \times 10^5 A_V + 23.6 \tag{4.5}$$

$$T_d = -3.0 \times 10^5 A_V + 25.8 \tag{4.6}$$

$$T_d = -2.7 \times 10^5 A_V + 23.6 \tag{4.7}$$

$$T_d = -4.5 \times 10^5 A_V + 25.3 \tag{4.8}$$

$$T_d = -2.1 \times 10^5 A_V + 24.4 \tag{4.9}$$

$$T_d = -2.6 \times 10^5 A_V + 25.0 \tag{4.10}$$

$$T_d = -0.8 \times 10^5 A_V + 24.2 \tag{4.11}$$

$$T_d = -0.6 \times 10^5 A_V + 26.6 \tag{4.12}$$

respectively. Taking log and solving, we found

$$T_{\rm d} \times A_{\rm V} = 1.7 \times 10^{-4} \tag{4.13}$$
$$T_{\rm d} \times A_{\rm V} = 0.9 \times 10^{-4} \tag{4.14}$$
$$T_{\rm d} \times A_{\rm V} = 0.9 \times 10^{-4} \tag{4.15}$$
$$T_{\rm d} \times A_{\rm V} = 0.6 \times 10^{-4} \tag{4.16}$$
$$T_{\rm d} \times A_{\rm V} = 1.3 \times 10^{-4} \tag{4.17}$$
$$T_{\rm d} \times A_{\rm V} = 1.0 \times 10^{-4} \tag{4.18}$$
$$T_{\rm d} \times A_{\rm V} = 3.0 \times 10^{-4} \tag{4.19}$$
$$T_{\rm d} \times A_{\rm V} = 4.0 \times 10^{-4} \tag{4.20}$$

respectively. From these results between visual extinction and dust color temperature, we got an important relation which relates them. The relation is

$$A_{\rm V} \times T_{\rm d} = \zeta \tag{4.21}$$

Here, ζ is a constant and ranges from 0.6×10^{-4} to 4.0×10^{-4}. This result is very close to the calculated value.

Finally, it is concluded that higher the temperature, lower the visual extinction and vice-versa in case of a particular cavity.

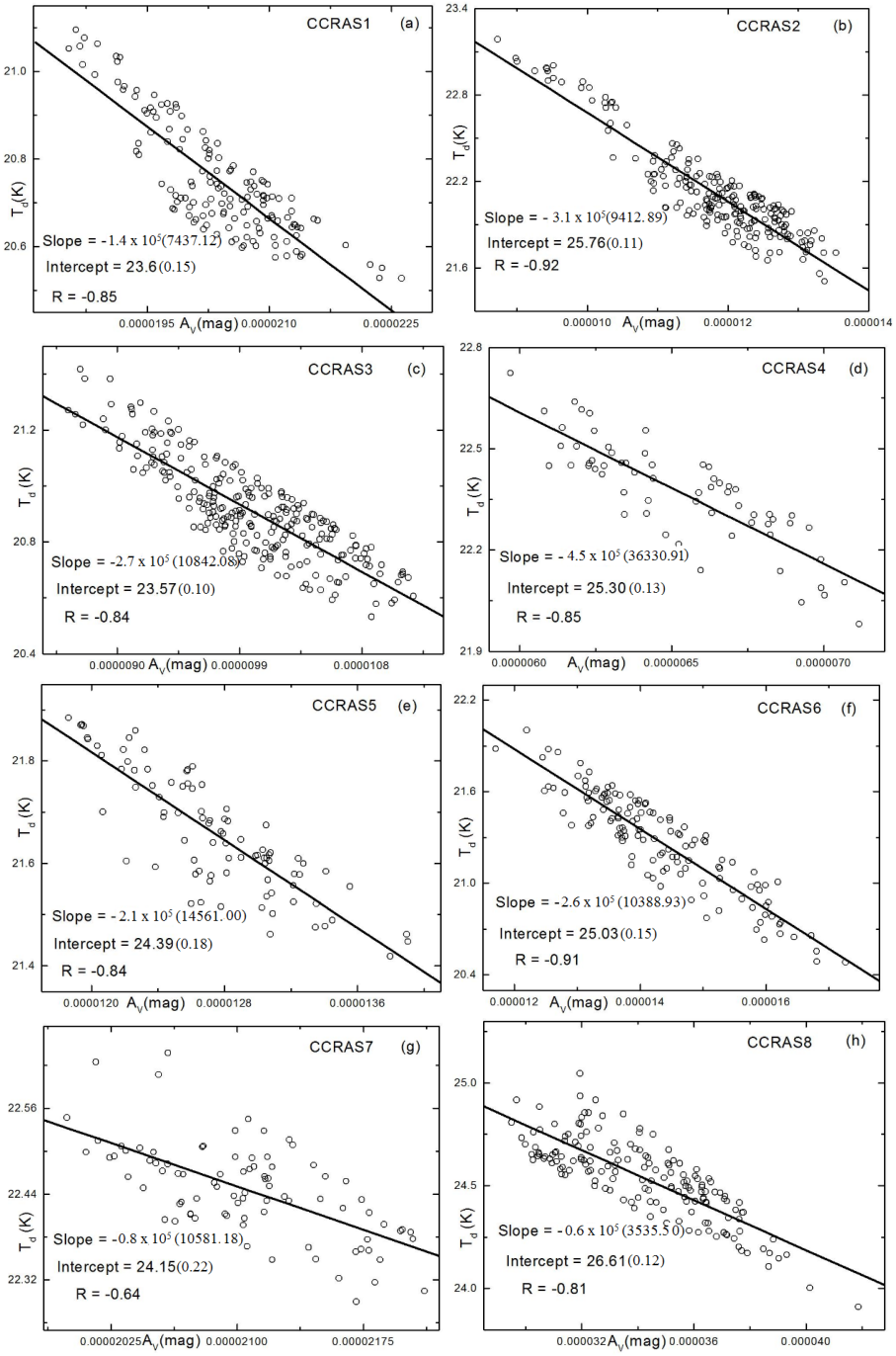

Figure 54: Plot between visual extinction (A_V) and dust color temperature (T_d) of the cavities located nearby AGB stars namely AGB0415+5441 (CCRAS1) (a), AGB0609+1446 (CCRAS2) (b), AGB0631+1606 (CCRAS3) (c), AGB0633+1415 (CCRAS4) (d), AGB0642+0053 (CCRAS5) (e), AGB0651+0031 (CCRAS6) (f), AGB0939-5249 (CCRAS7) (g) and AGB1025-5933 (CCRAS8) (h). The best fit line (solid line) with their slopes, correlation coefficient (R) and intercept are shown. The figures in the parenthesis represent standard errors in the respected statistical parameters in the linear fit. The dust color temperature is found to decrease with the increase of visual extinction.

To study the variation of visual extinction of the eight cavities, their contour maps are plotted which are shown in Figure 55. When the contour maps of the cavities are compared with their contour maps of dust color temperature Figure 50, different behavior could be seen and clear picture about their relation could be obtained. Mostly minimum temperature region has maximum visual extinction and vice-versa. If we look the particular cavity, all pixels of the cavities CCRAS1, CCRAS3, CCRAS4, CCRAS5 and CCRAS6 strongly show higher the visual extinction, lower the temperature and vice-versa but in case of cavities CCRAS2, CCRAS7 and CCRAS8, certain pixels show above mentioned nature and remaining pixels show different nature. Hence, in general, it is concluded that $A_{\mathrm{V}} \times T_{\mathrm{d}}$ is constant and is very very less than one.

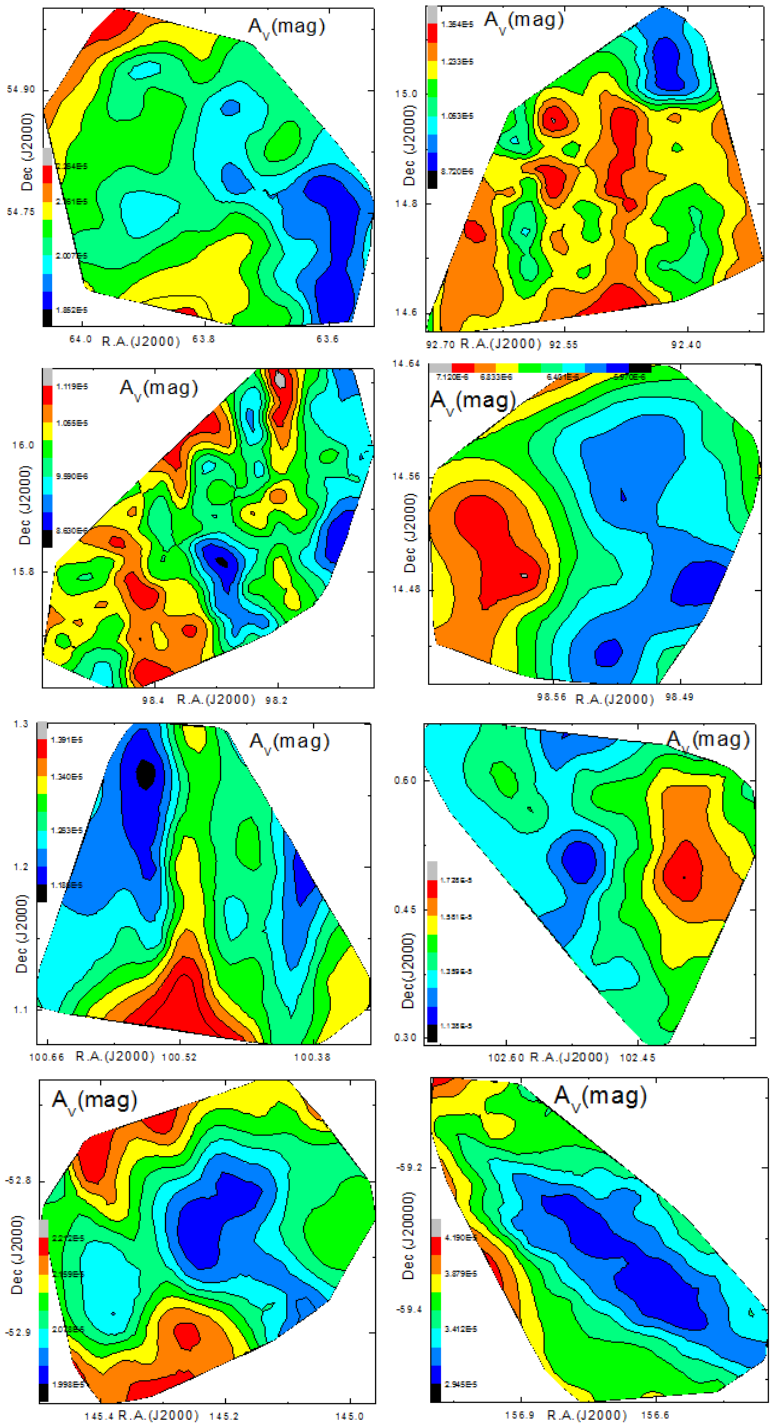

Figure 55: Contour map of visual extinction (A_V) of the cavities located nearby AGB stars namely AGB0415+5441 (CCRAS1) (a), AGB0609+1446 (CCRAS2) (b), AGB0631+1606 (CCRAS3) (c), AGB0633+1415 (CCRAS4) (d), AGB0642+0053 (CCRAS5) (e), AGB0651+0031 (CCRAS6) (f), AGB0939-5249 (CCRAS7) (g) and AGB1025-5933 (CCRAS8) (h). Colour index shows the variation of visual extinction with in the cavity.

4.1.5 Conclusion

We have studied physical properties such as flux densities, dust color temperature, Planck function, etc. of 8 far infrared cavities around AGB stars namely AGB0415+5441, AGB0609+1446, AGB0631+1606, AGB0633+1415, AGB0642+0053, AGB0651+0031, AGB0939-5249 and AGB1025-5933 located within $-1.6°$ to $3.2°$ in the Galactic plane. These cavities are studied how their dust color temperature, Planck function, extinction distribute in concerning the pixels within the cavity specially along their extension and compression region. The conclusions are as follows:

- All eight far infrared cavities have different shape but cavity CCRAS5 has shape like an octopus and cavity CCRAS7 has shape like a fish which are extending along east-west direction. Remaining other six cavities are mostly extending along north-south direction. Size of the cavities are shown on the Table 8 where CCRAS3 is the biggest cavity and CCRAS5 is the smallest cavity. Cavity CCRAS8 has the highest flux (174.93 MJy/sr) and CCRAS3 has the lowest flux (18.06 MJy/sr) at 100 μm which has shown on the appendix B.

- Minimum dust color temperature of all eight cavities are (20.5 ± 0.61) K, (21.5 ± 0.95) K, (20.5 ± 0.50) K, (22.0 ± 0.48) K, (21.4 ± 0.43) K, (20.5 ± 1.17) K, (22.3 ± 0.21) K and (23.9 ± 0.15) K respectively. Similarly their respective maximum dust color temperature are (21.1 ± 0.50) K, (23.2 ± 0.51) K, (21.4 ± 0.0.28) K, (22.7 ± 0.30) K, (21.9 ± 0.30) K, (22.0 ± 0.81) K, (22.6 ± 0.12) K and (25.0 ± 0.45) K. It means cavity CCRAS8 is at higher temperature and cavity CCRAS1 is at lower temperature. Detail is shown on Table 11. The offset value in dust color temperature of all eight cavities is less than 2 K which suggests that the core of all the cavities are stable.

- Cavity CCRAS5 is completely non-Gaussian where as cavities CCRAS1, CCRAS2, CCRAS3 and CCRAS6 show more or less Gaussian nature with skewness but cavities CCRAS4, CCRAS7 and CCRAS8 show perfect Gaussian nature.

- The cavities CCRAS1, CCRAS3,CCRAS4, CCRAS7 show non-uniform distribution of Planck function along major diameters passing through minimum flux where their slope is negative. Similarly the cavities CCRAS1, CCRAS2, CCRAS3, CCRAS4 and CCRAS5 show similar behavior along minor diameters. It means dust particles are oscillating in order to get dynamical equilibrium. Such cavities are unstable and is found that they are disturbed by external factors. The materials in the cavity do not strictly obey Maxwellian velocity distribution. It

possibly indicates that such behavior is due to presence of wind emitted from the nearby AGB star. For the cavities CCRAS2, CCRAS5 and CCRAS6, there is poor correlation between Planck function and major diameters with positive slope but cavities CCRAS6, CCRAS7 and CCRAS8 show similar nature along minor diameters. So these cavities are also unstable and do not obey Maxwellian velocity distribution. For the cavity CCRAS8, there is good correlation between Planck function and major diameter so it should be stable, behaves as black body and obeys Maxellian velocity distribution.

- In the best fit of scattering plot between visual extinction and dust color temperature, there is a systematic trend found with negative slope and correlation coefficient. Correlation coefficient ranges from -0.64 to -0.92 which justifies that there is good correlation between them. When the calculated average value of visual extinction are analyzed, it is found that higher the flux density, higher the visual extinction and vice-versa. Here cavity CCRAS4 has the lowest visual extinction and cavity CCRAS8 has the highest visual extinction which are shown in Table 11. For the particular cavity, higher the temperature, lower the visual extinction and vice-versa. This result is agreed by the cavities CCRAS1, CCRAS2, CCRAS4 and CCRAS5 but cavities CCRAS2, CCRAS6, CCRAS7 and CCRAS8 showed anti result which may possibly due to oscillation of dust particles in different directions. Here, the product of visual extinction and dust color temperature is found to be consistent and ranges from 0.6×10^{-4} to 4.0×10^{-4}.

- From the distribution of visual extinction in the contour map of all eight far infrared cavities, it is found that higher temperature region has low visual extinction and vice-versa which also has proved by linear fit between visual extinction and dust color temperature.

4.2 General Discussion

In this section, we discuss physical properties of all eight cavities which are obtained from calculations and graphs. Table 9 shows the location of the cavities in the equatorial coordinate system (R.A. and Dec.), size of the cavities, values of maximum and minimum dust color temperatures, average values of visual extinction (in mag). From the Table 11, it is clear that the biggest cavity is CCRAS3 and the smallest cavity is CCRAS5. Maximum dust color temperature of the cavity CCRAS1 has lowest value among the eight and maximum dust color temperature of cavity CCRAS8 has the highest value among them.

Scattering plots of all the cavities between $F(60)$ and $F(100)$ show systematic behavior

having positive slope, intercept and correlation coefficient where correlation coefficient ranges from 0.72 to 0.89 which justifies there is good correlation between them. Similar systematic behavior is strongly seen in the scattering plot between visual extinction and dust color temperature. But in this case, slope and correlation coefficient both are negative. Here correlation coefficient ranges from -0.64 to -0.92 which signifies that there is also good correlation between them. If we analyze the scattering plot between distance (along major and minor diameters) with Planck function, systematic trend is not found. Higher the dust color temperature, lower the visual extinction is found from contour map of dust color temperature and visual extinction. But from Table 11, cavities CCRAS1, CCRAS2, CCRAS4 and CCRAS5 showed inverse relation between dust color temperature and visual extinction but cavities CCRAS2, CCRAS6, CCRAS7 and CCRAS8 showed direct relation means anti correlation between dust color temperature and visual extinction. But if we see the product of dust color temperature and visual extinction, their product is found consistent and is less than 1. The cavities which showed anti-correlation is possibly due to oscillation of dust particles in different directions in order to get dynamical equilibrium. It also has published in JoAA (Gautam & Aryal, 2019). According to them, such oscillation, specially sinusoidal oscillation of dust particles in the deep sky in frozen state is happening.

Figure 56 is for the study of far infrared spectral distributions of the eight far infrared cavities. In Figure 56(a), four cavities are compared to each other and with nebula MBM 20 “cirus cloud" by Weiland et al. (1986) and in Figure 56(b), other four cavities are compared to each other and with skeleton nebula by Aryal & Weinberger (2006). In all four cavities in figure (a), there is increase in flux density with increase in wave length from 12 μm to 25 μm, decrease in flux density with increase in wave length from 60 μm to 100 μm and then sharp increase in flux density with increase in wave length. Variation of flux density from 12 μm to 25 μm and 60 μm to 100 μm of all four cavities are more or less similar but their variation from 25 μm to 60 μm is quite different. When we compare these variation with nebula MBM 20, no similarities are found and they are quite different which differentiates between nebula and far infrared cavities. Similarly, if we analyze the figure (b), cavities CCRAS5 and CCRAS6 show similar nature with less steeper with the cavities CCRAS1, CCRAS2, CCRAS3 and CCRAS4 but two cavities CCRAS7 and CCRAS8 show increase in wave length with increase in flux density in all four bands. Variation of flux density with wave length from 25 μm to 60 μm and 60 μm to 100 μm is similar in Skeleton nebula and CCRAS8 which is due to radiation pressure and effect of near by bulge in CCRAS8. Figure (b) also justified that in case of far infrared cavities, there is either steeper or less steeper decrease in flux density from 25 μm to 60 μm.

Table 11: Calculated values of 8 far infrared cavities where first column represents name of the cavities, next two columns represent positions of the cavities in equatorial coordinate system fourth for size, fifth and sixth for maximum and minimum dust color temperature and last column represents the average visual extinction.

Cavities	R.A. hh mm ss	Dec. dd mm ss	Size (deg × deg)	T_{max} (K)	T_{min} (K)	A_V ($\times 10^{-5}$mag)
CCRAS1	04 15 11.8	54 51 08.4	0.5×0.2	21.1 ± 0.50	20.5 ± 0.61	2.1
CCRAS2	06 09 45.9	14 41 26.6	0.6×0.2	23.2 ± 0.51	21.5 ± 0.95	1.2
CCRAS3	06 32 40.6	15 59 47.9	0.7×0.2	21.4 ± 0.28	20.5 ± 0.50	1
CCRAS4	06 34 12.2	14 30 53.4	0.3×0.2	22.7 ± 0.30	22.0 ± 0.48	0.7
CCRAS5	06 41 34.8	01 08 46.8	0.3×0.1	21.9 ± 0.30	21.4 ± 0.43	1.3
CCRAS6	06 49 46.6	00 29 12.6	0.4×0.2	22.0 ± 0.80	20.5 ± 1.17	1.4
CCRAS7	09 41 28.4	−52 53 41.2	0.3×0.2	22.6 ± 0.10	22.3 ± 0.21	2.1
CCRAS8	10 27 08.4	−59 15 33.3	0.6×0.2	25.0 ± 0.45	23.9 ± 0.15	3.4

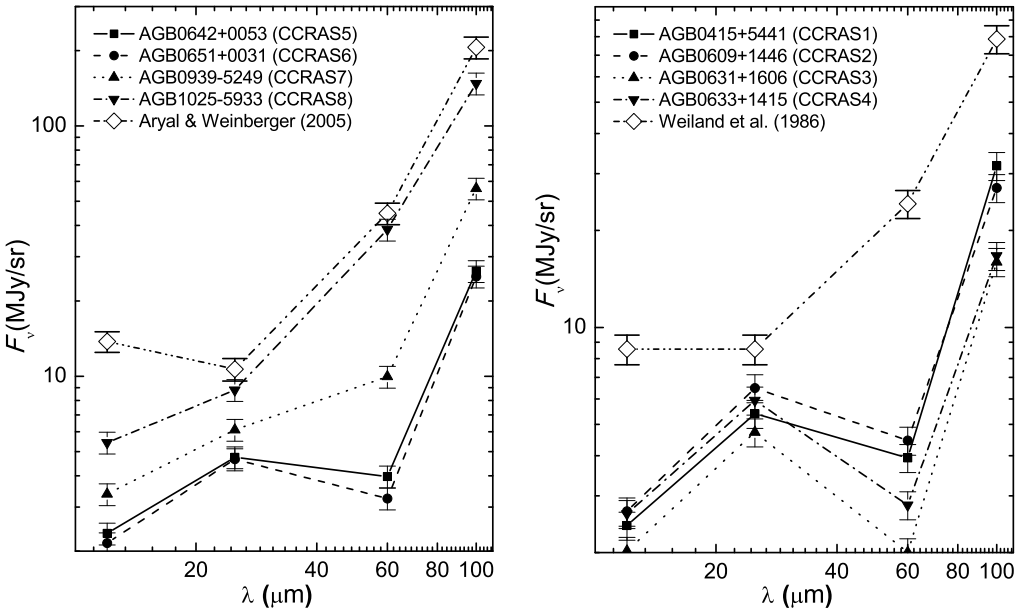

Figure 56: (a) Far infrared spectral distributions of the cavities located at nearby AGB star AGB0415+5441 (CCRAS1), AGB0609+1446 (CCRAS2), AGB0631+1606 (CCRAS3), AGB0633+1415 (CCRAS4) and (b) AGB0642+0053 (CCRAS5), AGB0651+0031 (CCRAS6), AGB0939-5249 (CCRAS7) and AGB1025-5933 (CCRAS8). The top most graph in figure (a) is of skeleton nebula by Aryal & Weinberger (2006) and the top most graph in figure (b) is of nebula MBM 20 " cirus cloud" by Weiland et al. (1986) for comparative study respectively.

4.3 Two New Far Infrared Cavities Around Post-Asymptotic Giant Branch Stars

In this section, we describe the physical properties of two cavities namely CCRPAS1 and CCRPAS2 around the post-AGB stars PAGB0655-0217 and PAGB0803-3635 listed in the catalog (Szczerba et al., 2007). These two cavities were investigated by using sky view virtual observatory (http://skyview.gsfc.nasa.gov/current/cgi/query.pl) while searching on IRAS maps at 60 μm and 100 μm wavelengths. Here, we describe the dust color temperature, Planck function, dust mass and visual extinction distribution. Additionally the distribution of Planck function and dust color temperature along extension and compression of the cavities are also described. Here, extension and compression are major and minor diameter at 100 μm wavelength passing through minimum flux. The distance of these two cavities are found to be available in the catalog so that it is possible to calculate dust mass within the cavity as well as their distributions. In the interpretation section, we study FIR spectral distributions and compared it with the cavities discussed in the chapter 4.2.

The flux density obtained from ALADIN2.5 is total flux density (sum of the background flux and flux due to dust). The flux density obtained is corrected by subtracting it with the background flux density. The minimum flux density which doesn't lie within the

contour map is supposed as background. The background emission is subtracted from the field using the method adopted in Aryal et al. (2010). For it, The average value of the background flux is obtained by noting and summing up of the minimum flux densities around the region of interest and dividing the sum by total number of pixels with these minimum flux densities. When this background flux is subtracted from the obtained flux density of each pixel in the region of interest, it is said to be background corrected flux density.

For calculation of dust color temperature, we adopted the method proposed by Dupac et al. (2003) and Schnee et al. (2005). According to them, dust color temperature is given by

$$T_{\mathrm{d}} = \frac{-96}{\ln\left(R \times 0.6^{3+\beta}\right)} \tag{4.22}$$

where, $R = \frac{F(60\ \mu m)}{F(100\ \mu m)}$ and β is spectral emissivity index.

Here $F(60)$ and $F(100)$ are flux densities at 60 μm and 100 μm respectively. The derivation and detail description of equation (4.22) is given in the literature review section (chapter 2.3). When a graph is plotted between $F(60\ \mu\mathrm{m})$ and $F(100\ \mu\mathrm{m})$, dust color temperature and Planck function can be calculated by using their slope ($F(60)/F(100)$).

For the calculation of dust mass, we used the expression given by Hildebrand (1983),

$$M_{\mathrm{dust}} = \frac{4a\rho}{3Q_\nu}\frac{S_\nu D^2}{B(\nu, T)} \tag{4.23}$$

According to Young et al. (1993), weighted grain size (a) = 0.1 μm, grain density (ρ) = 3000 kg m^{-3}, grain emissivity (Q_ν) = 0.0010 (for 100 μm) so that equation (4.23) becomes

$$M_{\mathrm{dust}} = 0.4\frac{S_\nu D^2}{B(\nu, T)} \tag{4.24}$$

where S_ν = flux density at 100 μm, D = known distance of the loop and $B(\nu, T)$ = Planck function.

Detail description of equation (4.23) and (4.24) has described in the literature review section (chapter 2.4).

Here, the values of visual extinction A_{V} are calculated by using the expression (2.27) in chapter 2 given by Wood et al. (1994). The relation is

$$A_{\mathrm{V}}(\mathrm{mag}) = 15.078\left(1 - \exp\left(-\tau_{100}/641.3\right)\right) \tag{4.25}$$

where,

$$\tau_{100} = \frac{F_\lambda(100\ \mu m)}{B_\lambda(100\ \mu m, T_\mathrm{d})} \tag{4.26}$$

is optical depth and $F_\lambda(100\ \mu\mathrm{m})$ is the flux at 100 μm.

$$B(\lambda, T) = \frac{2hc}{\lambda^3}\left[\frac{1}{e^{hc/\lambda kT} - 1}\right] \tag{4.27}$$

is the Planck function. After the calculation of visual extinction, their distributions are studied with dust color temperature of each pixels.

Here, we describe the physical properties of two new loop candidates around the post-AGB stars.

4.3.1 Cavity CCRPAS1 Nearby PAGB0655-0217

The cavity CCRPAS1 is found to be located nearby the post-AGB star named PAGB0655-0217. Their positions are R.A.(J2000) = $06^h\ 53^m\ 01^s$ (Galactic longitude, l = 215.4°) and Dec.(J2000) = −02° 16' 00" (Galactic latitude, b = −0.1°) and R.A.(J2000) = $06^h\ 51^m\ 54.0^s$ and Dec.(J2000) = −01° 35' 43" respectively. Figure 57(a) is the image of the cavity at 100 μm IRAS map of size 1.8° × 1.8° and, Figure 57(b) is its contour map. The contour map shows how flux density is distributed within the cavity. The minimum value of flux density at the minima is found to be 16.749 MJy sr^{-1} (= 1.67×10^{-19} kg s^{-2}). The size of the cavity is found to be 1.0° × 0.3° which is extended along north-west to south-east with minima at the central region.

For calculating of dust color temperature using equation (4.22), we need flux density at 60 μm and 100 μm wavelengths. There are 439 pixels in the field of view within the contour level 1-38 in the FITS (Flexible Image Transport System) image. ALADIN2.5 software has been usedto get raw data of relative flux density. The values of dust color temperature of each pixel is calculated and listed in the Appendix A. From the table, calculated minimum and maximum dust color temperature are found to be (16.7 ± 0.5) K and (19.5 ± 0.3) K respectively with offset value 2.8 K. Such low offset in dust color temperature suggests that the core region or say the cavity is in thermal equilibrium. Figure 57(b) shows that most of the inner contours are surrounded by their outer contours taking center as minima.

Figure 57(c) is scatter plot between $F(60)$ and $F(100)$ where spreading can be seen at all flux levels, which suggests that there might be various types of interstellar dust and grain. The chemical composition of the materials in the interstellar medium can be known by using spectroscopic data which is not available till date. The average value of dust color temperature calculated from the slope of the linear fit is 24.4 K. Figure 57(d) describes

the distribution of dust color temperature where minimum temperature region lies at the minimum flux region near the center of the cavity but maximum temperature region lies towards north-east at the maximum flux region. The solid curve of Figure 57(e) represents the Gaussian fit. The Gaussian center is seen at 19.4 K where $\pm\sigma/\sqrt{n}$ is error bar or standard error. A very good Gaussian fit is seen where the full width maxima of the Gaussian fit is sharp and wider suggesting the cavity is well defined and isolated.

Distribution of dust color temperature and dust mass are shown in Figure 57(d,f) with color bars. Generally, minimum temperature region of the ISM is at higher density and higher density leads to have larger mass. When we carefully study Figure 57(d,f), same situation is noticed. It means that the minimum temperature and the massive region are the same. Similarly maximum temperature and minimum mass region are the same, which is usual behavior, suggesting that the distribution of materials within the cavity follow cosmological principle. However, the minimum temperature and massive region is found to be extended north-south as shown in Figure 57(d,f).

Figure 57(e,g) suggest that the Gaussian distribution is found to be in good agreement in both dust color temperature and dust mass distributions. But different in width and skewness are noticed in the Gaussian fit which is due to external factors possibly from the nearby PAGB0655-0217 star.

Figure 57(h) is the scatter plot between visual extinction and dust color temperature which shows a systematic distribution with high correlation correlation coefficient i.e., -0.97 is found. From the best fit, we found

$$T_{\rm d} = -1.8 \times 10^5 A_{\rm V} + 22.7 \tag{4.28}$$

Taking log and solving, we found a very important relation between visual extinction and dust color temperature. The relation is

$$T_{\rm d} \times A_{\rm V} = 1.3 \times 10^{-4} \tag{4.29}$$

which is very close to the calculated value. Finally, it is concluded that higher the temperature, lower the visual extinction and vice-versa which is verified by contour map of dust color temperature and visual extinction shown in Figure 57(d) and Figure 57(i) respectively.

Figure 58(a,b) show the distribution of Planck function with extension (major diameter) and compression (minor diameter) passing through flux minima. In both Figure 58(a,b), distribution of Planck function with distance is similar i.e., first decreases, becomes minimum and then increases. It repeats again. It means they are strongly dependent.

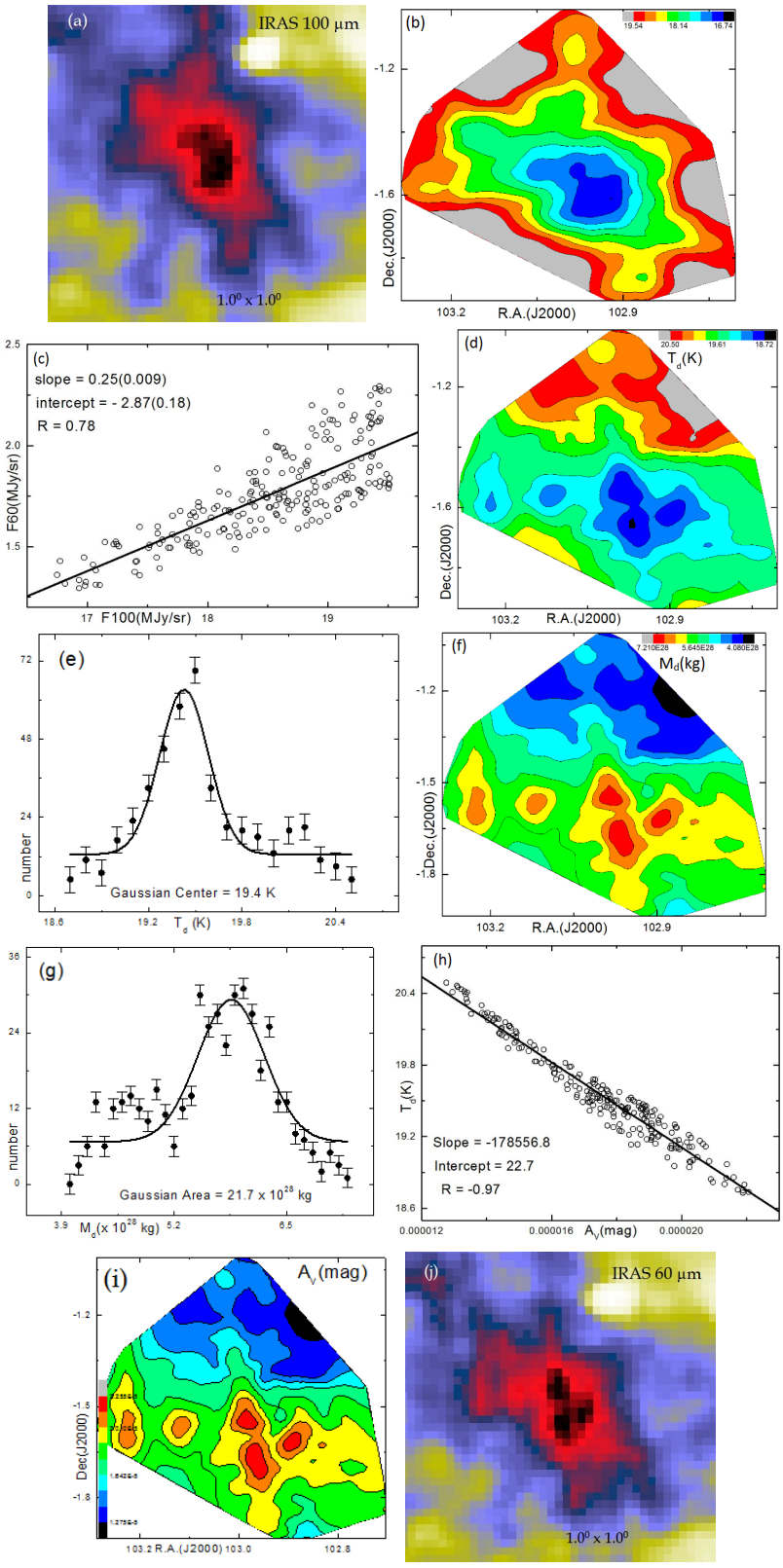

Figure 57: (a) Image of the cavity CCRPAS1 nearby PAGB0655-0217 centered at R.A.(J2000) = 06^h 51^m 54.02^s and Dec.(J2000) = −01° 35' 43". (b) Contour map of flux density at 100 μm wavelength. (c) Flux at 100 μm verses 60 μm plot. (d), (f) and (i) are the contour map of dust color temperature, dust mass and visual extinction respectively. Solid curves of (e) and (g) represents the Gaussian fit of the respective dust color temperature and the dust mass, (h) Visual extinction verses dust color temperature at 100 μm, (i) contour map of visual extinction and (j) 60 μm IRAS image, for comparison. The values given in the bracket is the standard error.

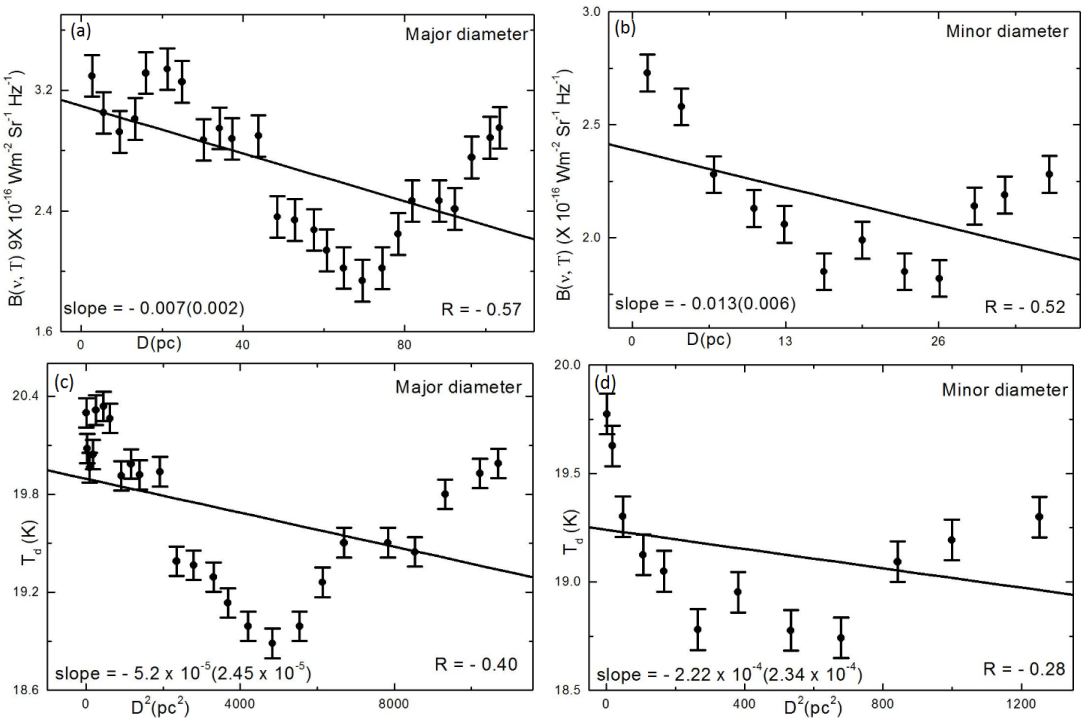

Figure 58: Variation of Planck function $B(\nu, T)$ in the cavity CCRPAS1 with the distance along both diameters: (a) and (b) along major diameter, (c) and (d) along minor diameter. The south-west point or north-west point of the diameter is assumed as a reference point i.e., the leftist point is the reference point. In the best fit, correlation coefficient and the slope of the line are shown. The error bars represent the standard error (±se) of the deviation.

From equation (4.24), expression of dust mass at 100 μm wavelength is written as

$$M_{\rm dust} = 0.4\frac{S_\nu D^2}{B(\nu, T)} \tag{4.30}$$

At a particular wavelength and at a constant temperature $B(\nu, T)$ becomes constant so that the expression reduces to

$$M_{\rm dust} \propto S_\nu D^2 \tag{4.31}$$

For uniform flux density at 100 μm wavelength, the expression again becomes

$$M_{\rm dust} \propto D^2 \tag{4.32}$$

The non-relativistic dust particle obeys Maxwellian velocity distribution, then mass is proportional to temperature so the expression (4.32) can be written as

$$T_{\rm d} \propto D^2 \tag{4.33}$$

Figure 58(c,d) show the variation of dust color temperature with D^2 along major and minor diameters of the cavity respectively. The nature of variation of dust color tem-

perature with D^2 in Figure 58(c,d) is exactly similar to that of the variation of Planck function with D as in Figure 58(a,b). Thus it clearly signifies that the dusts and grains within the cavity neither be in thermal equilibrium with the far infrared radiation nor strictly obey the Maxwellian velocity distribution. It is caused due to external effects which has a significant role in the formation of structure in the cavity.

4.3.2 Cavity CCRPAS2 Nearby PAGB0803-3635

The cavity CCRPAS2 found nearby post-AGB star named PAGB0803-3635 which is located at R.A.(J2000) = 08^h 03^m 01.7^s (Galactic longitude, $l = 253.0°$) and Dec.(J2000) = $-37°$ 35' 47.9" (Galactic latitude, $b = -03.0°$) is centered at R.A.(J2000) = 08^h 04^m 7.2^s and Dec.(J2000) = $-37°$ 11' 48". Figure 59(a) is the image of the cavity at 100 μm IRAS survey of field $1.0° \times 1.0°$. Figure 59(b) is its contour map which shows how flux density is distributed within the cavity. The minimum value of flux density at the minima is found to be 28.537 MJy sr^{-1} (= 2.85×10^{-19} kg s^{-2}). The size of the cavity is found to be 0.9×0.4 which is extended along south-west to north-east.

There are 494 pixels in the field of view within the contour level $1 - 50$ in the FITS (Flexible Image Transport System) image in ALADIN2.5 software to get raw data of relative flux density. The calculated minimum and maximum dust color temperature are found to be (21.6 ± 0.09) K and (22.5 ± 0.05) K respectively with offset value 0.9 K. Such low offset temperature suggests that the core region or say the cavity is in thermal equilibrium.

Figure 59(c) is scatter plot between $F(60)$ and $F(100)$ where concentrated data is obtained at low flux levels. The average value of dust color temperature calculated from slope of the linear fit is 23.6 K. Figure 59(d) describes the distribution of dust color temperature where minimum temperature region does not lie at the minimum flux region. The solid curve of Figure 59(e) represents the Gaussian fit. The Gaussian center is seen at 21.8 K where $\pm\sigma/\sqrt{n}$ is error bar (or standard error). A very good Gaussian fit is seen where the full width maxima of the Gaussian fit is sharp and wide suggesting the cavity is well defined and isolated.

Distribution of dust color temperature and dust mass are shown in Figure 59(d,f) with color bars. Generally, minimum temperature region of the ISM is at higher density and higher density leads to have larger mass in the region of interest. When we analyze Figure 59(d,f), same condition is found. It means we can clearly say that the minimum temperature and maximum mass region are the same. Similarly, maximum temperature and minimum mass region are also similar, which is a usual behavior. For dust mass, Gaussian area is 49.8×10^{27} kg. However, the minimum temperature and the massive

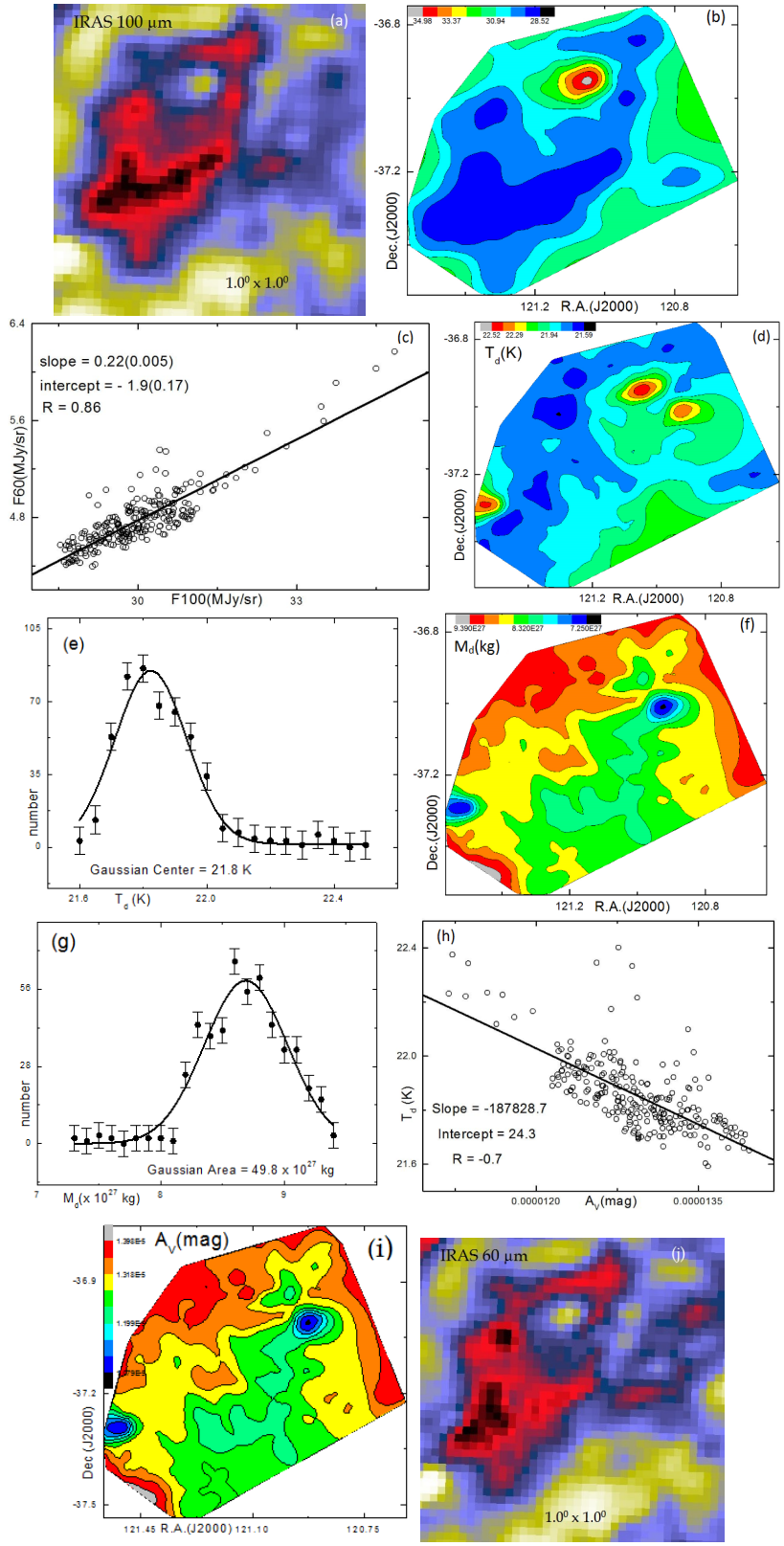

Figure 59: (a) Image of the cavity CCRPAS1 nearby PAGB0655-0217 centered at R.A.(J2000) = 08^h 04^m 7.21^s and Dec.(J2000) = −37° 11' 48.0". (b) Contour map of flux density at 100 μm wavelength. (c) Flux at 100 μm verses 60 μm plot. (d), (f) and (i) are the contour map of dust color temperature, dust mass and visual extinction respectively. Solid curves of (e) and (g) represents the Gaussian fit of the respective dust color temperature and the dust mass. (h) Visual extinction verses dust color temperature at 100 μm. (i) Contour map of visual extinction. (j) 60 μm IRAS image, for comparison. The values given in the bracket is the standard error.

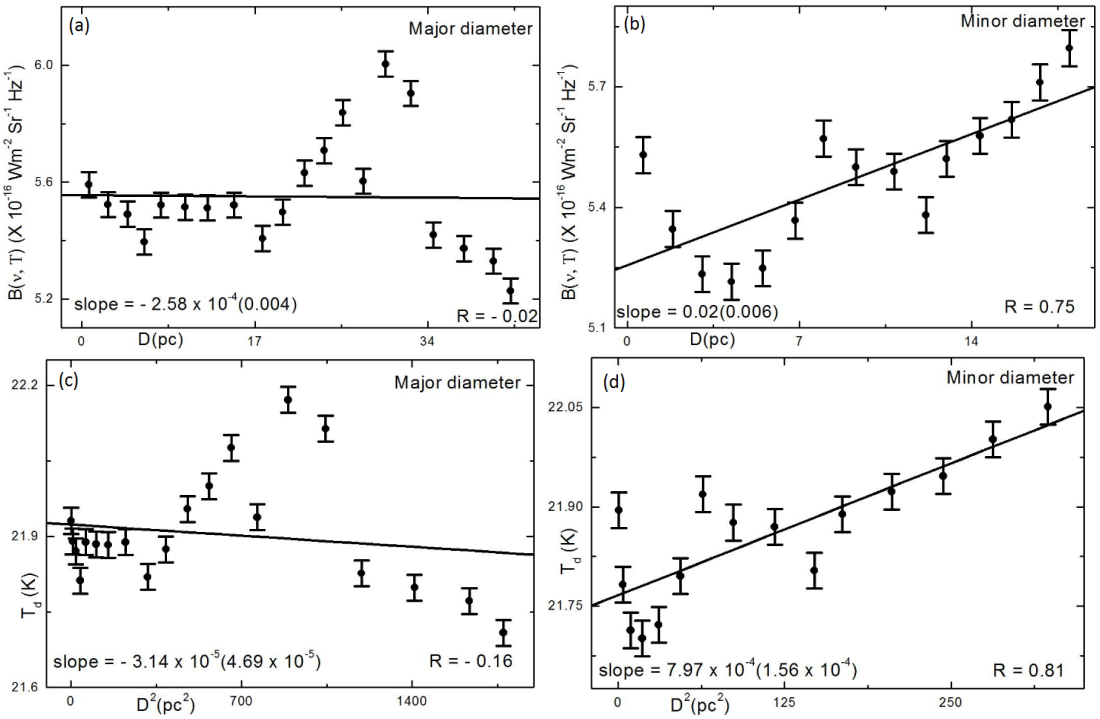

Figure 60: Variation of Planck function $B(\nu, T)$ in the cavity CCRPAS2 with the distance along both diameters: (a) and (b) along major diameter, (c) and (d) along minor diameter. The south-west point or north-west point of the diameter is assumed as a reference point i.e., the leftist point is the reference point. In the best fit, correlation coefficient and slope of the line are shown. The error bars represent the standard error (±se) of the deviation.

region is found to be extended south-west to north-east shown in Figure 59(d,f). Figure 59(e,g) suggest that the Gaussian distribution is found to be in good agreement in both dust color temperature and dust mass distributions. But different in width and skewness are found in the Gaussian fit which is due to external factors possibly from the nearby post-AGB stars.

Figure 59(h) is the best fit between visual extinction and dust color temperature where slope and correlation coefficient are negative and shows best correlation. From the best fit, we found

$$T_{\rm d} = -1.9 \times 10^5 A_{\rm V} + 24.3 \tag{4.34}$$

Taking log and solving, we found a relation between visual extinction and dust color temperature. The relation is

$$T_{\rm d} \times A_{\rm V} = 1.3 \times 10^{-4} \tag{4.35}$$

which is very close to the calculated value. Finally, it is concluded that higher the temperature, lower the visual extinction and vice-versa. This conclusion is strongly supported and verified by contour map of dust color temperature and visual extinction

shown in Figure 59(d) and Figure 59(i) respectively.

Figure 60(a,b) show the distribution of Planck function with extension (major diameter) and compression (minor diameter) passing through minima. In both Figure 60(a,b), distribution of Planck function with diameter is similar i.e., it first decreases, becomes minimum and then increases. It repeats again. In the case of major diameter, they are slightly independent and in the case of minor diameter, they are dependent.

Figure 60(c,d) show the variation of dust color temperature with D^2 along major and minor diameters of the cavity respectively. The nature of variation of dust color temperature with D^2 in Figure 60(c,d) is exactly similar to that of the variation of Planck function with D as in Figure 60(a,b). Thus, it clearly signifies that the dusts and grains within the cavity neither be in exactly thermal equilibrium with the far infrared radiation nor strictly obey the Maxwellian velocity distribution. It might be caused due to external effects which has a significant role in the formation of structure in the cavity.

4.3.3 Conclusion

A systematic search was done in far infrared region under IRAS survey and found two cavity like structures located nearby post-AGB stars. We studied a few physical properties such as dust color temperature, Planck function, dust mass, visual extinction, etc. of the cavities. Following are the conclusions:

- The size of the cavity CCRPAS1 is found to be $\sim 1.0^\circ \times 0.3^\circ$ centered at R.A.= (J2000) $06^h\ 51^m\ 54.02^s$ and Dec.(J2000) = -01° 35' 43". Similarly the size of the cavity CCRPAS2 is found to be $\sim 0.9^\circ \times 0.4^\circ$ centered at R.A.(J2000) = $08^h\ 04^m\ 7.21^s$ and Dec.(J2000) = -37° 11' 48.0".
- The dust color temperature of the cavities CCRPAS1 and CCRPAS2 is found to be in the range (18.7 ± 0.5) K to (20.5 ± 0.3) K and (21.6 ± 0.09) K to (22.5 ± 0.05) K with an offset value of about 1.8 K and 0.9 K respectively. Such low offset value of temperature suggests that the dusts in the cavities are almost in thermal equilibrium.
- Both the cavities show excellent Gaussian fit of dust color temperature with sharp peak and positive skewness but distribution of dust mass show Gaussian-like nature with sharp peak and negative skewness.
- From the contour map of both the cavities, it is found that the lower temperature region is massive and showed high visual extinction and vice-versa. A very interesting result is that the contour map of dust mass and visual extinction are exactly the same which also verifies that the distribution of particles in both cavities support cosmological principle.

Table 12: Calculated values of two far infrared cavities where first column represents name of the cavities, next two columns represent positions of the cavities in equatorial coordinate system, fourth for size, fifth and sixth for minimum and maximum dust color temperature, last two column represent the average visual extinction and total dust mass of the cavities.

Cavities	R.A. hh mm ss	Dec. dd mm ss	Size (deg×deg)	T_{min} (K)	T_{max} (K)	A_V (mag)	M_d (kg)
CCRPAS1	06 51 54	−01 35 43	1.0×0.3	18.7±0.5	20.5±0.3	1.8×10^{-5}	2.5×10^{31}
CCRPAS2	08 04 07	−37 11 48	0.9×0.4	21.6±0.1	22.5 ± 0.1	1.3×10^{-5}	0.4×10^{31}

- Dust mass of each pixel of the cavities CCRPAS1 and CCRPAS2 are found to be 5.6×10^{28} kg and 8.7×10^{27} kg, respectively. It means cavity CCRPAS1 is heavier than CCRPAS2.
- From the plot between visual extinction and dust color temperature, it is concluded that the product $T_d \times A_V$ is constant and is equal to 3.0×10^{-4}. It means that, higher the temperature, lower the visual extinction and vive-versa. It is also verified by contour map of dust color temperature and visual extinction.

4.4 General Discussion

In this section, we discuss physical properties of two cavities which are obtained from calculations and graphs. Table 12 shows the location of the cavities in the equatorial coordinate system (R.A. and Dec.), size of the cavities, values of maximum and minimum dust color temperatures, average values of visual extinction (in mag) and dust mass of the cavities. From the Table 12, it is clear that the cavity CCRPAS2 is larger than CCRPAS1. Cavity CCRPAS2 is at higher temperature than CCRPAS1.

Scattering plots between $F(60)$ and $F(100)$ show systematic behavior having positive slope and correlation coefficient where correlation coefficients are 0.78 and 0.86 respectively which justify that there is better correlation between them. Similar systematic behavior is strongly seen in the scattering plot between visual extinction and dust color temperature where slope and correlation coefficient both are negative. Here correlation coefficients are −0.97 and −0.70 respectively which signifies that there is also excellent correlation between them. From the best fit, it is found that the product of dust color temperature and visual extinction is constant which is also verified by contour map of dust color temperature and visual extinction. If we analyze the scattering plot between dust color temperature and Planck function with distance (along major and minor diameters passing through minima), systematic trend is not found where dust particles are oscillating in order to get dynamical equilibrium.

We also studied FIR spectral distribution and compared it with the cavities CCRAS1

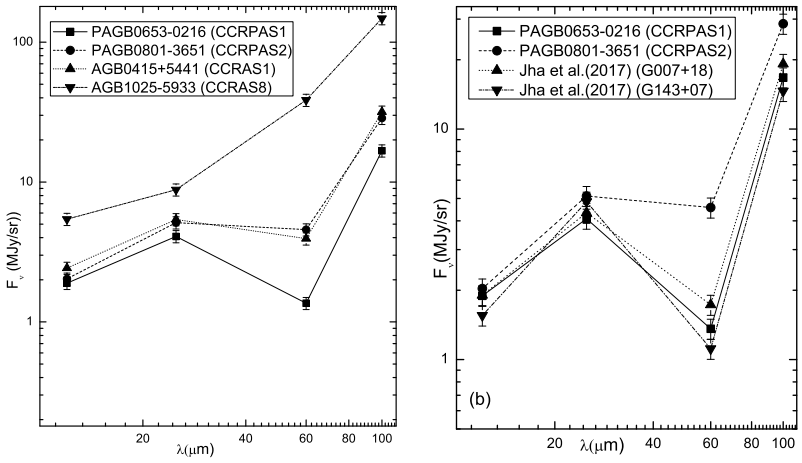

Figure 61: (a) Far infrared spectral distributions of the cavities located nearby PAGB star PAGB0653-0216 (CCRPAS1) and PAGB0801-3651 (CCRPAS2) where the top most two graphs are of the cavities CCRAS1 and CCRAS8, for comparison. (b) Comparison of FIR distribution of the cavities with Jha et al. (2017).

and CCRAS8; chapter 4.1) and Jha et al. (2017). Before comparing FIR spectral distribution, it is important to note physical process of wind blow. Actually, the AGB stars emit the particles as a stellar wind with a velocity of (5 to 75) km s^{-1} Kartunnen et al., (2007). Due to such wind blow, FIR cavities are pumped by AGB stars. But in case of pulsars, physical situation is quite different that the pulsars emit beam of electromagnetic radiation instead of matter. Figure 61 (a) shows the study of far infrared spectral distributions of the two far infrared cavities (CCRPAS1 and CCRPAS2) with other two cavities (CCRAS1 and CCRAS8) which are studied in the chapter 4.1. In case of the cavities CCRPAS1 and CCRPAS2, there is increase in flux density with increase in wave length from 12 μm to 25 μm, decrease in flux density with increase in wave length from 25 μm to 60 μm and then sharp increase in flux density with increase in wave length from 60 μm to 100 μm. Variation of flux density from 12 μm to 25 μm and 60 μm to 100 μm of two cavities are more or less similar but their variation from 25 μm to 60 μm is quite different. When we compare these variation with cavity CCRAS1, similar nature is found. Similarly, if we analyze them with CCRAS8, their variation is found to be different showing continuous increase in flux density with increase in wavelength in all four bands. Such a variation of flux density of CCRAS8 might be due to radiation pressure and effect of near by bulge of the galaxy. Figure 61 (b) is the comparative study of FIR spectral distributions of the two cavities with Jha et al. (2017) where similar nature is found. Hence, with certain exception, it also justified that far infrared cavities show negative slope in transition from 25 μm to 60 μm.

4.5 Eight New Far Infrared Cavities Around C-Rich AGB Stars Located Within The Far Infrared loops (K.K. Loops)

In this chapter, we describe some physical properties of eight new far infrared cavities

named CASKK1, CASKK2, CASKK3, CASKK4, CASKK5, CASKK6, CASKK7 and CASKK8 where C stands for cavity, A stands for asymptotic giant branch, S is for star and KK is taken in comparison with Kiss et al. (2004) and Könyves et al. (2007) listed in the catalog provided by Suh & Kwon (2009) around carbon-rich AGB stars located within the far infrared (FIR) loop based catalog which was reported by Kiss et al. (2004) and Könyves et al. (2007), called Galactic Infrared Loop (GIRL) catalog. There are 462 FIR loops where 137 loops have derived distances which are used to measure dust mass. These eight cavities were selected while searching on IRAS maps at 60 μm and 100 μm wavelengths.

Here, we measure the dust color temperature, Planck function, dust mass and visual extinction of the cavities separately. Expression (2.35) of dust mass mentioned in chapter 2 showed that lower the values of Planck function, higher its masses. Since frequency or wavelength are fixed so that the parameter which affects the Planck function is only dust color temperature. Here, first we report the nature of distribution of dust color temperature and dust mass in all pixels of the cavities which are located nearby AGB stars and later their maps and graphs will be discussed. Additionally, we study the distribution of Planck function and dust color temperature along extension and compression of the cavity. Here extension means major or the longest diameter at longer wavelength (100 μm) passing through minimum flux region. Similarly compression corresponds the minor or the shortest diameter at the same longer wavelengths passing through the same minima region.

4.5.1 FIR Cavity CASKK1 Nearby the AGB0141+7104 Located Within G125+09

The cavity CASKK1 is found to be located nearby the AGB star named AGB0141+7104 at R.A.(J2000) = 01^h 41^m 01^s (Galactic longitude, l = 127.0°) and Dec.(J2000) = 71° 04' 00" (Galactic latitude, b = 8.6°) which is centered at R.A.(J2000) = 01^h 46^m 57.2^s and Dec.(J2000) = 71° 24' 57.1". Figure 62(a) is the image of the cavity at 100 μm IRAS maps in size 1.0° × 1.0° and Figure 62(b) is its contour map which shows how flux density is distributed within the cavity. The minimum value of flux density at the minima is found to be 14.973 MJy sr^{-1} (= 1.49 × 10^{-19} kg s^{-2}). The size of the cavity is found to be 0.7° × 0.2° which is extended along east-west direction. Similarly size of the KK-loop G125+09 given in the catalog Könyves et al. (2007) is 6.1° × 5.4° and the distance between AGB0141+7104 and G125+09 is 3.1° which shows that the AGB star is within the KK-loop G125+09. The cavity is located at 8.6° galactic latitude with position angle 348.7° so that it is in the galactic plane inclined by ~ 11.0°.

Figure 62(c) is scatter plot between $F(60)$ and $F(100)$ where concentrated data is obtained

at middle flux levels. The value of correlation coefficient (R) is 0.68, suggesting a very good correlation between them. The average value of dust color temperature calculated from slope of the linear fit is 22.2 K. Figure 62(d) describes the distribution of dust color temperature where minimum temperature region does not lie at the minimum flux region. The solid curve of Figure 62(e,g) represents the Gaussian fit of dust color temperature and dust mass. The cavity is 220 pc far from us Könyves et al. (2007). The Gaussian fit of dust mass showed that the mass distribution is inhomogeneous. The larger value of FWHM, indicates that the cavity contains several equal mass region. Total mass of the cavity is found to be 1.86×10^{28} kg, larger than the Gaussian value. The Gaussian center of dust color temperature is found as 20.2 K and Gaussian area of dust mass is found to be 0.34×10^{27} kg. The statistical $\pm\sigma/\sqrt{n}$ is error bar shown in the fitted graph. A very good Gaussian fit is seen in both dust color temperature and dust mass where the full width half maxima of the Gaussian fit is sharp and wide suggesting the cavity is well defined and isolated. Very good Gaussian nature further suggests that the cavity follows isotropic nature.

The values of dust color temperature and dust mass are calculated by using expressions (4.22) and (4.24) which are listed in Appendix A. The calculated minimum and maximum dust color temperature are found to be (19.7 ± 0.62) K and (21.1 ± 0.28) K respectively with offset value 1.4 K. Such low offset temperature suggests that the core region or say cavity is in thermal equilibrium. Similarly calculated average dust mass of the cavity is found to be 4.93×10^{25} kg.

Gaussian distribution of dust mass is shown in Figure 62(g). Like to dust color temperature map, we discuss the mass aggregation in the cavity. In normal condition, the lower temperature region shows the larger mass aggregation which is obtained in cavity CASKK1. It means the cavity CASKK1 supports the cosmological principle (homogeneous and isotropy). But if this principle is violated, the polytropic rather than isotropic behavior can be suspected.

Figure 62(h) is the linear fit of the scattered plot between visual extinction and dust color temperature which shows best correlation coefficient i.e., -0.92. From the best fit, we found

$$T_{\mathrm{d}} = -2.2 \times 10^{5} A_{\mathrm{V}} + 22.2 \tag{4.36}$$

Taking log and solving, we found a very important relation between visual extinction and dust color temperature. The relation is

$$T_{\mathrm{d}} \times A_{\mathrm{V}} = 1.0 \times 10^{-4} \tag{4.37}$$

which is very close to the calculated value. Finally , it is concluded that higher the temperature, lower the visual extinction and vice-versa. This conclusion is strongly supported and verified by contour map of dust color temperature and visual extinction shown in Figure 62(d) and Figure 62(i) respectively.

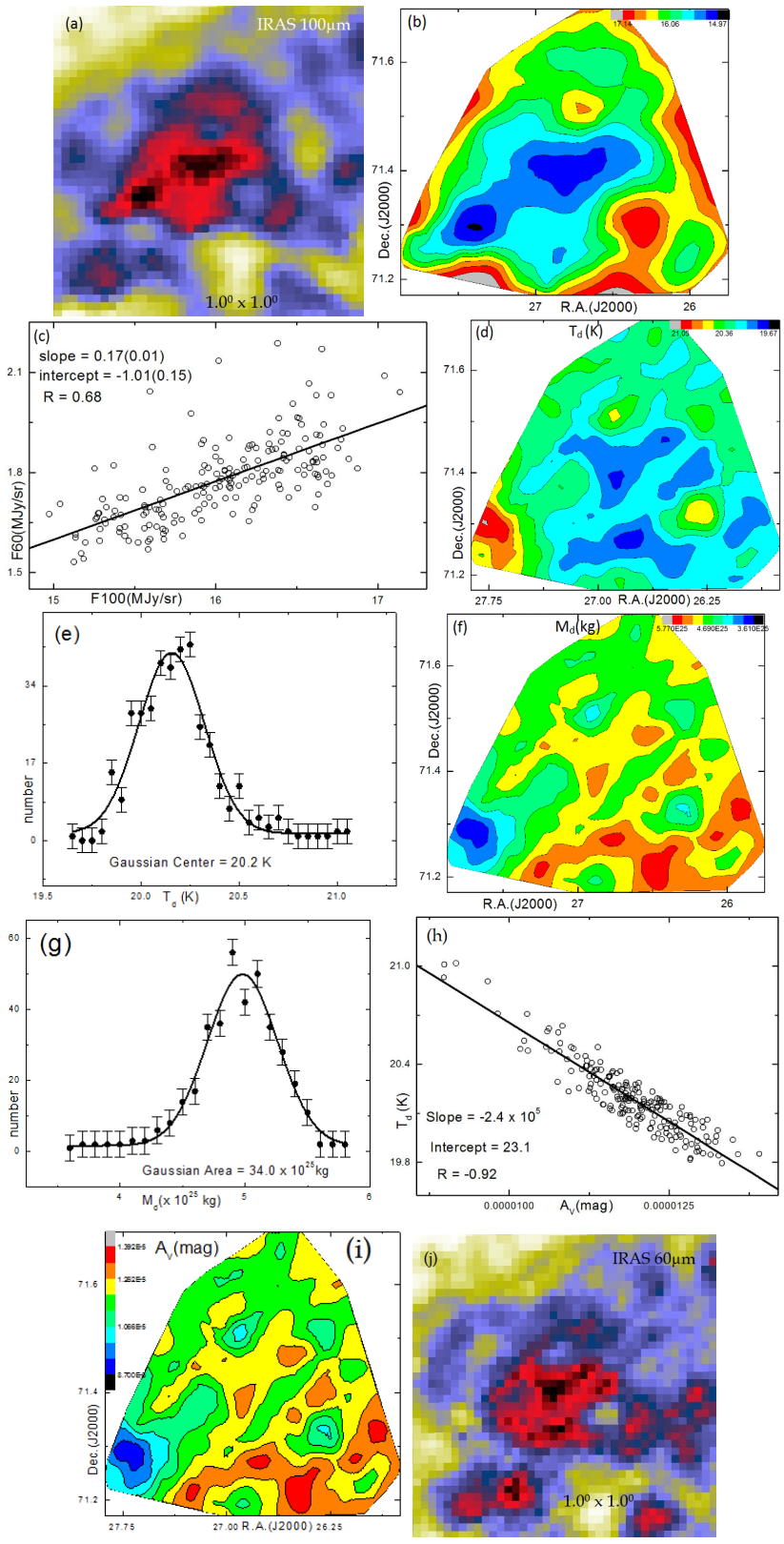

Figure 62: (a) Image of the cavity CASKK1 nearby AGB0141+7104 centered at R.A.(J2000) = 01^h 46^m 57.22^s and Dec.(J2000) = 71° 24' 57.1". (b) Contour map of flux density at 100 μm wavelength. (c) Flux at 100 μm verses 60 μm plot. (d), (f) and (i) are contour map of dust color temperature, dust mass and visual extinction respectively. Solid curves of (e) and (g) represents the Gaussian fit of the respective dust color temperature and the dust mass. (i) 60 μm IRAS image, for comparison. The values given in the bracket is the standard error.

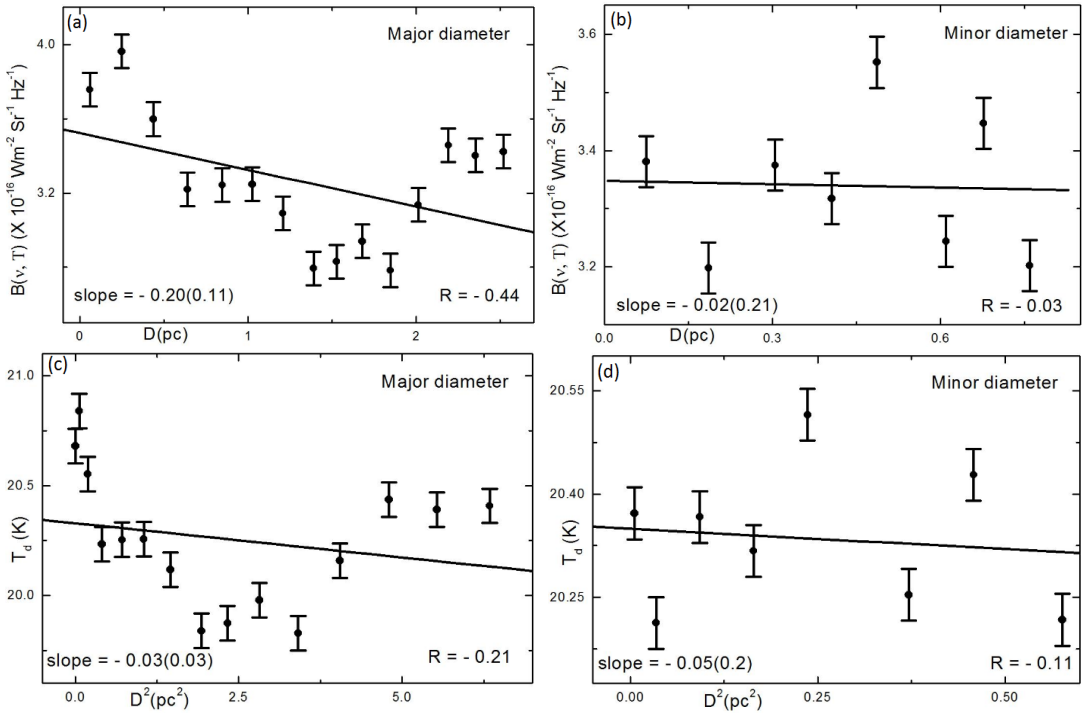

Figure 63: Variation of Planck function $B(\nu, T)$ in the cavity CASKK1 with the distance along both diameters (a) and (b) along major diameter, (c) and (d) along minor diameter. The south-west point or north-west point of the diameter is assumed as a reference point i.e.,the left-end point represents the reference point. The correlation coefficient and the slope of the best fit are shown. The error bars represent the standard error (±se) of the deviation.

Figure 63(a,b) show the distribution of Planck function along extension (major diameter and compression (minor diameter) passing through minima. In both Figure 63(a,b), distribution of Planck function with distance is similar i.e., first decreases, becomes minimum and then increases. It repeats again. In case of both diameters, slope and correlation coefficient (R) are negative. Since the correlation coefficient is small and negative so that there is very poor correlation between the data. It means the materials that are along major and minor diameters do not behave like a black body, i.e., their velocity distribution do not co-exist with Planck theory. Therefore the cavity is relatively unstable.

Figure 63(c,d) show the variation of dust color temperature with D^2 along major and minor diameters of the cavity respectively. The nature of variation of dust color temperature with D^2 in Figure 63(c,d) is exactly similar to that of the variation of Planck function with D as in Figure 63(a,b). Thus it clearly signifies that the dusts and grains within the cavity neither be in exactly thermal equilibrium with the far infrared radiation nor strictly obey the Maxwellian velocity distribution. It is possibly due to nearby AGB wind or any other similar point sources.

4.5.2 FIR Cavity CASKK2 Nearby the AGB0409+6105 Located Within G143+07

The cavity CASKK2 nearby to the AGB star named AGB0409+6105 is found to be located at R.A.(J2000) = 04^h 09^m 00^s (Galactic longitude, l = 144.6°) and Dec.(J2000) = 61° 05' 00" (Galactic latitude, b = 6.8°). Figure 64(a) is the image of the cavity at 100 μm IRAS maps of field 1.0° × 1.0°. Figure 64(b) is its contour map which shows how flux density is distributed within the cavity. The minimum value of flux density at the minima is found to be 18.831 MJy sr^{-1} (= 1.883×10^{-19} kg s^{-2}). The size of the cavity is found to be 0.6° × 0.2° which is extended along north-south direction. Similarly size of the KK-loop G143+07 given in the catalog Könyves et al. (2007) is 4.5° × 3.0° and the distance between AGB0409+6105 and G143+07 is 1.0°. It means the AGB star is within the KK-loop G143+07. The cavity is located at 6.8° galactic latitude with position angle 317.1° so that it is in the galactic plane inclined by ∼ 43.0°.

A broad scatter is seen in the higher flux density region and narrow scatter in low flux density region obtained in the scatter plot in Figure 64(c) between $F(60)$ and $F(100)$. From the linear fit, slope and correlation coefficient (R) are found to be 0.21 and 0.72 respectively. Correlation coefficient shows that there is good correlation between the flux densities. From the linear fit, the dust color temperature is found to be 23.2 K. The calculated minimum and maximum dust color temperature are found to be (19.0±0.93) K and (20.4±0.65) K respectively. The cavity is surrounded by strong emission of 100 μm, suggesting a stable and an isolated cavity.

Contour map of dust color temperature and dust mass are shown in Figure 64(d,f) with color bars. From the figure, it is found that minimum temperature region is massive and vice-versa. It means the distribution primarily follow the cosmological principle so that it is homogeneous and isotropic. The solid curve of Figure 64(e,g) represents the Gaussian fit of dust color temperature and dust mass. Both Gaussian fit are found to be very sharp and in well agreement with temperature and mass. It suggests that the flux minima of the cavity extended and well connected with its environment. The cavity is 900 pc far from us (Könyves et al., 2007). The Gaussian fit of dust mass showed that the mass distribution is homogeneous. The larger value of FWHM, indicates that the cavity contains several equal mass region. Total mass of the cavity is found to be 3.58×10^{29} kg, larger than the Gaussian value. The Gaussian center of dust color temperature is found as 20.1 K and Gaussian area of dust mass is found to be 0.63×10^{28} kg. The statistical $\pm\sigma/\sqrt{n}$ error bar is shown.

Figure 64(h) is the best fit between visual extinction and dust color temperature which shows a systematic trend with best correlation coefficient i.e., −0.95. From the best fit,

we found

$$T_{\mathrm{d}} = -1.9 \times 10^{5} A_{\mathrm{V}} + 23.0 \tag{4.38}$$

Taking log and solving, we found a very important relation between visual extinction and dust color temperature. The relation is

$$T_{\mathrm{d}} \times A_{\mathrm{V}} = 1.3 \times 10^{-4} \tag{4.39}$$

which is very close to the calculated value. Finally , it is concluded that higher the temperature, lower the visual extinction and vice-versa. It is strongly supported and verified by contour map of dust color temperature and visual extinction shown in Figure 64(d) and Figure 64(i) respectively.

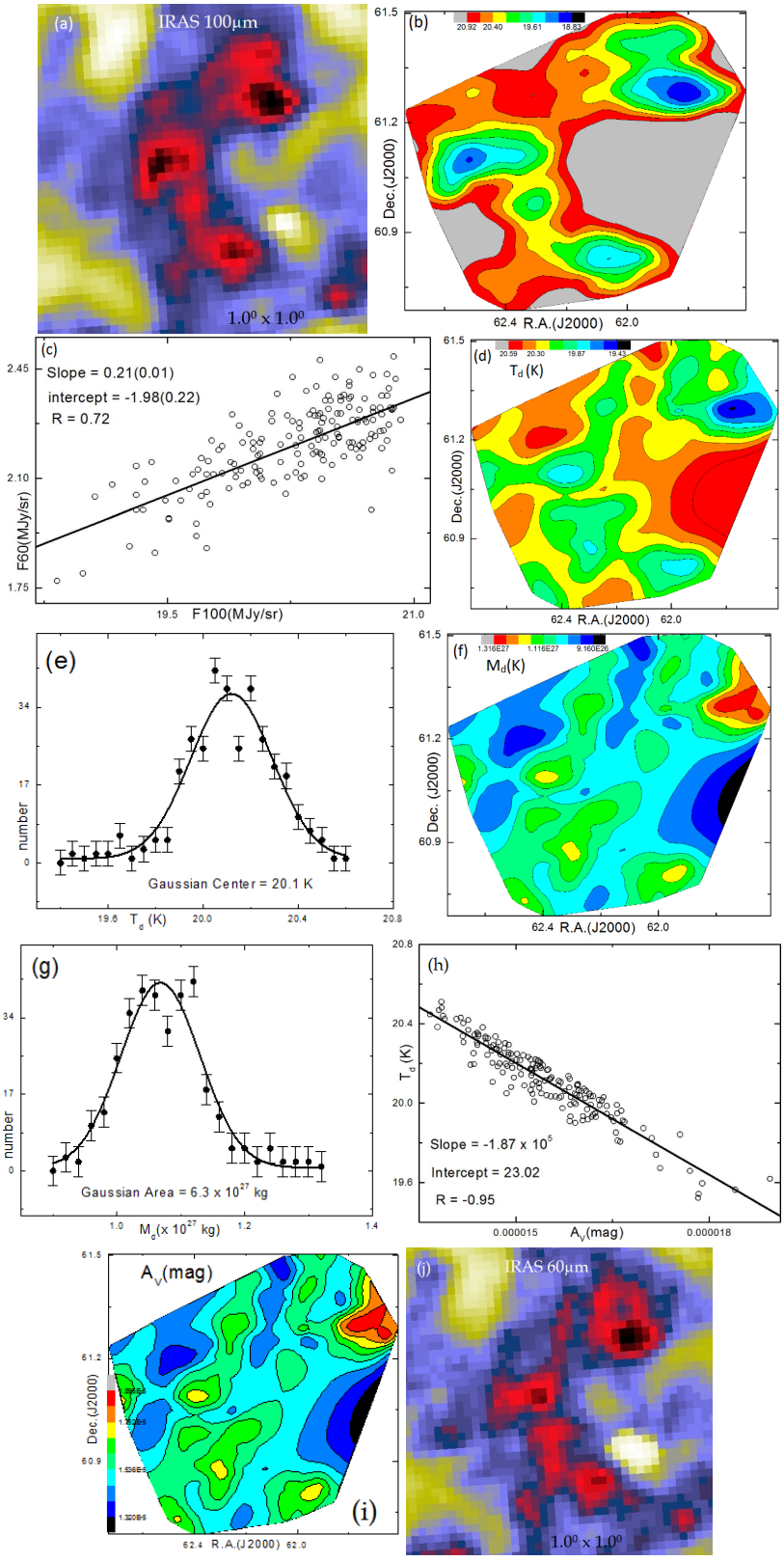

Figure 64: (a) Image of the cavity CASKK2 nearby to the AGB0409+6105 centered at R.A.(J2000) = 04^h 09^m 00^s and Dec.(J2000) = 61° 05' 00". (b) Contour map of flux density at 100 μm wavelength. (c) Flux at 100 μm verses 60 μm plot. (d), (f) and (i) are contour map of dust color temperature, dust mass and visual extinction respectively. Solid curves of (e) and (g) represents the Gaussian fit of the respective dust color temperature and the dust mass. (h) Best fit between visual extinction and dust color temperature at 100 μm and (j) 60 μm IRAS image, for comparison. The values given in the bracket is the standard error.

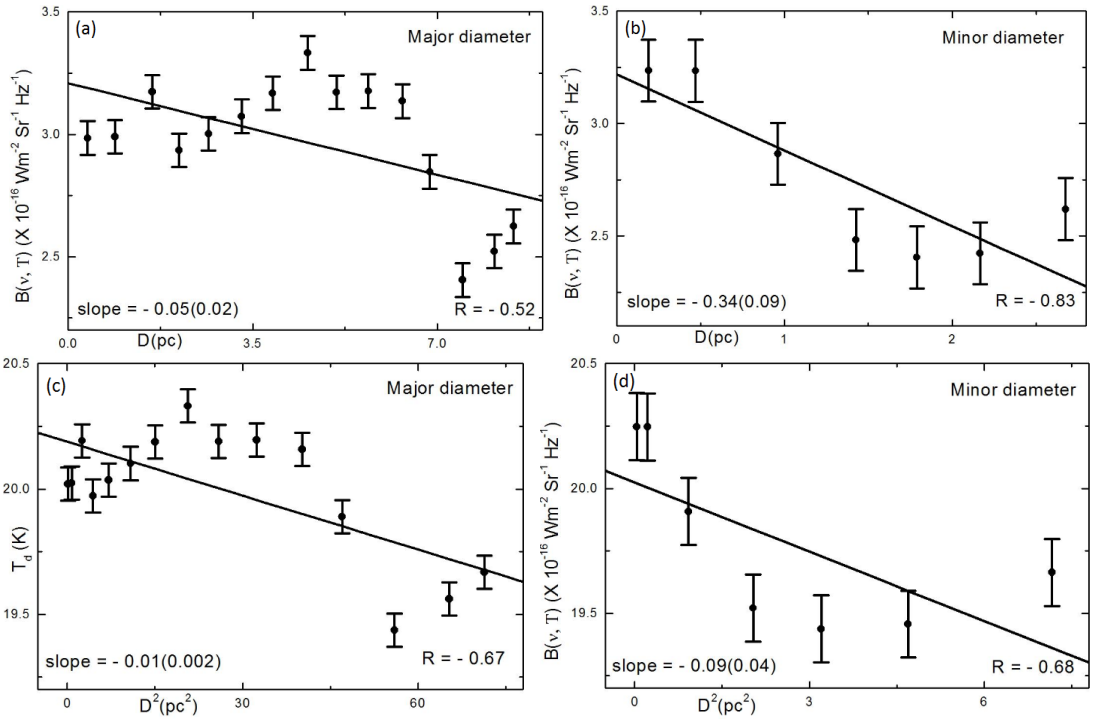

Figure 65: Variation of Planck function $B(\nu, T)$ in the cavity CASKK2 with the distance along both diameters (a) and (b) along major diameter, (c) and (d) along minor diameter. The south-west point or north-west point of the diameter is assumed as a reference point i.e.,the left-end point represents the reference point. The correlation coefficient and the slope of the line are shown. The error bars represent the standard error (±se) of the deviation.

Figure 65(a,b) show the distribution of Planck function with extension (major diameter) and compression (minor diameter) passing through minima. In both Figure 65(a,b), distribution of Planck function with distance is similar i.e., first decreases, becomes minimum and then increases. It repeats again. In case of both diameters, slope and correlation coefficient (R) are negative.

Figure 65(c,d) show the variation of dust color temperature with D^2 along major and minor diameters of the cavity respectively. The nature of variation of dust color temperature with D^2 in Figure 65(c,d) is exactly similar to that of the variation of Planck function with D as in Figure 65(a,b). Thus it clearly signifies that the dusts and grains within the cavity neither be in exactly thermal equilibrium with the far infrared radiation nor strictly obey the Maxwellian velocity distribution. It is due to the external effect caused by AGB star or any other similar point sources.

4.5.3 FIR Cavity CASKK3 Nearby the AGB0538+1216 Located Within G195-11

The cavity is found to be is located at R.A.(J2000) = 05^h 38^m 03^s, Dec.(J2000) = 12° 16' 00" (l = 193.4° and b = −10.2°) centered at R.A.(J2000) = 05^h 36^m 17.23^s, Dec.(J2000) = 12° 03' 33.6". The maximum to minimum flux density ratio of the cavity CASKK3

at 100 μm is found to be 1.1. Figure 66(a) is the image of the cavity at 100 μm IRAS maps at pixel size $1.0^\circ \times 1.0^\circ$ and Figure 66(b) is its contour map which shows how flux density is distributed within the cavity. The minimum value of flux density at the minima is found to be 21.63 MJy sr^{-1} (= 2.16×10^{-19} kg s^{-2}). Size of the cavity is defined as its major and minor diameters passing through minimum flux region. Therefore diameters are drawn through minimum flux region at 100 μm wavelength. Here size of the cavity is found about $0.7^\circ \times 0.4^\circ$. Like wise, the size of KK-loop G195-11 given in the catalog Könyves et al. (2007) is $4.3^\circ \times 43.4^\circ$ where distance between AGB0538+1216 and G195-11 is 3.0°. Therefore, the AGB star is located within the KK-loop. The shape of the cavity is shown in Figure 61(a,b) which is elongated along north-east to south-west direction. It is located at -10.2° galactic latitude with position angle 300.9° so it is in the galactic plane inclined by $\sim 59.0^\circ$. It means the cavity is very close to the galactic plane so that it is located in the strong radiation field emitted from the disk of the Milky Way.

Figure 66(c) is a scatter plot between the $F(60)$ and $F(100)$ data where a broader scatter is seen through out the region of interest. Here, the correlation coefficient (R) is 0.72 which shows that there is good correlation between the data. The cavity shows strong east-west elongation, indicating the external cause rather than the effect of radiation field of the Galactic plane. From the linear fit, the dust color temperature is found to be 23.3 K. The calculated minimum and maximum dust color temperature are found to be (22.3 ± 0.25) K and (23.1 ± 0.05) K respectively.

Contour map of dust color temperature and dust mass are shown in Figure 66(d,f) with color bars. From the figure, it is found that minimum temperature region is massive. It means the distribution is homogeneous and isotropic. The solid curve of Figure 66(e,g) represents the Gaussian fit of dust color temperature and dust mass. The cavity is 400 pc far from us (Könyves et al., 2007). The larger value of FWHM, indicates that the cavity contains several equal mass region. Total mass of the cavity is found to be 3.9×10^{28} kg, larger than the Gaussian value. The Gaussian center of dust color temperature is found as 22.6 K and Gaussian area of dust mass is 0.4×10^{27} kg. The $\pm\frac{\sigma}{\sqrt{n}}$ is the standard error of tha data shown in the graph. Dust mass distribution is found to be in agreement with Gaussian distribution which supports homogeneous distribution. The height of Gaussian fit suggests the on-going mass loading process in the cavity and it is possible due to strong external effect. The nearby AGB star provides such effects.

Best fit of the scattering plot between visual extinction and dust color temperature shown in Figure 66 shows a systematic trend with better correlation coefficient i.e., -0.84. From the best fit, we found

$$T_{\rm d} = -3.6 \times 10^5 A_{\rm V} + 25.5 \tag{4.40}$$

Taking log and solving, we found a very important relation between visual extinction and dust color temperature. The relation is

$$T_{\mathrm{d}} \times A_{\mathrm{V}} = 0.8 \times 10^{-4} \tag{4.41}$$

which is very close to the calculated value. Finally , it is concluded that higher the temperature, lower the visual extinction and vice-versa which is strongly supported and verified by contour map of dust color temperature and visual extinction shown in Figure 66(d) and Figure 66(i) respectively.

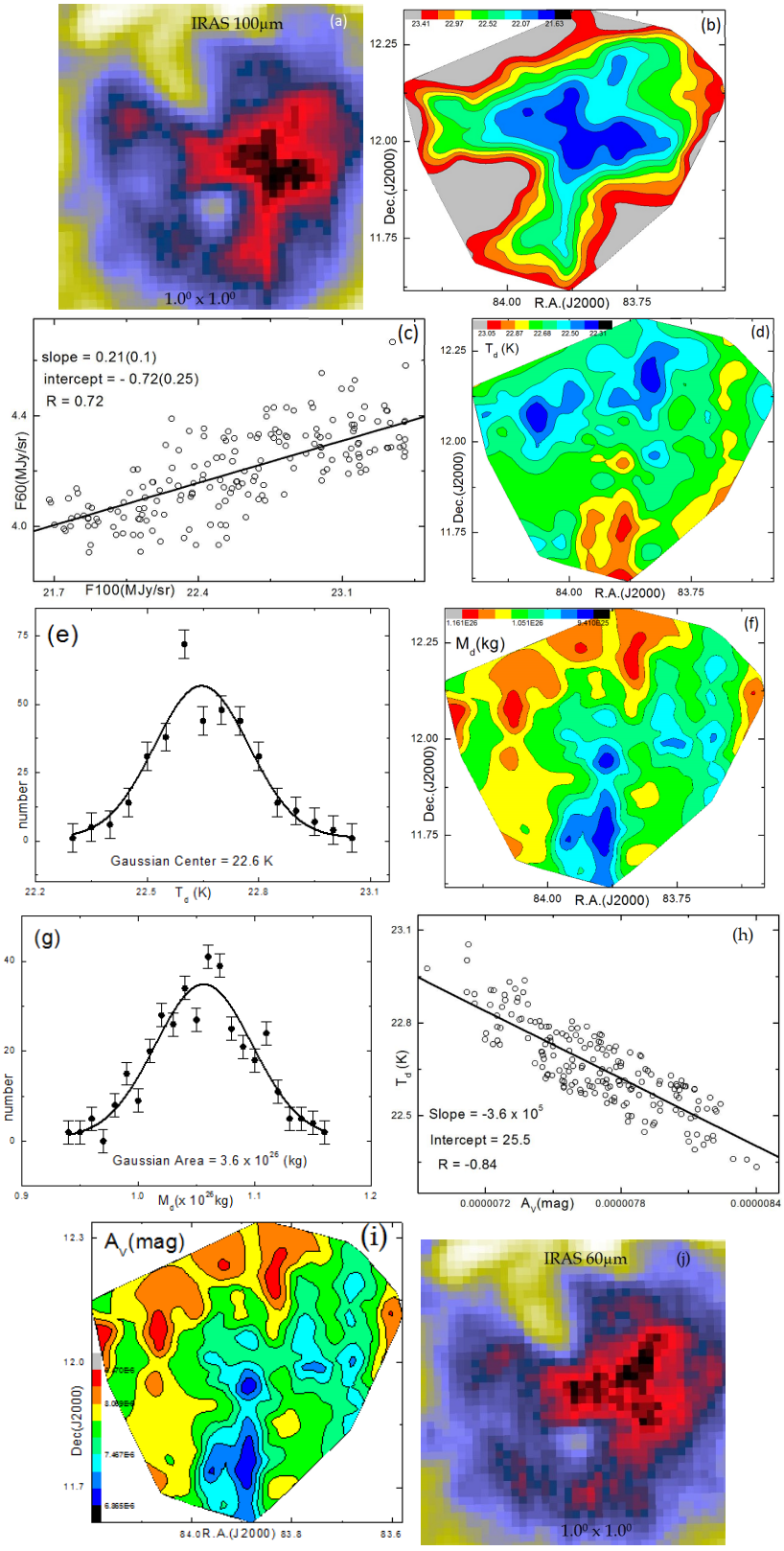

Figure 66: (a) Image of the cavity CASKK3 nearby to the AGB0409+6105 centered at R.A.(J2000) = 05^h 36^m 17.23^s and Dec.(J2000) = 12° 03' 33.6". (b) Contour map of flux density at 100 μm wavelength. (c) Flux at 100 μm verses 60 μm plot. (d), (f) and (i) are contour map of dust color temperature, dust mass and visual extinction respectively. Solid curves of (e) and (g) represents the Gaussian fit of the respective dust color temperature and the dust mass. (h) Best fit between visual extinction and dust color temperature at 100 μm and (j) 60 μm IRAS image, for comparison. The values given in the bracket is the standard error.

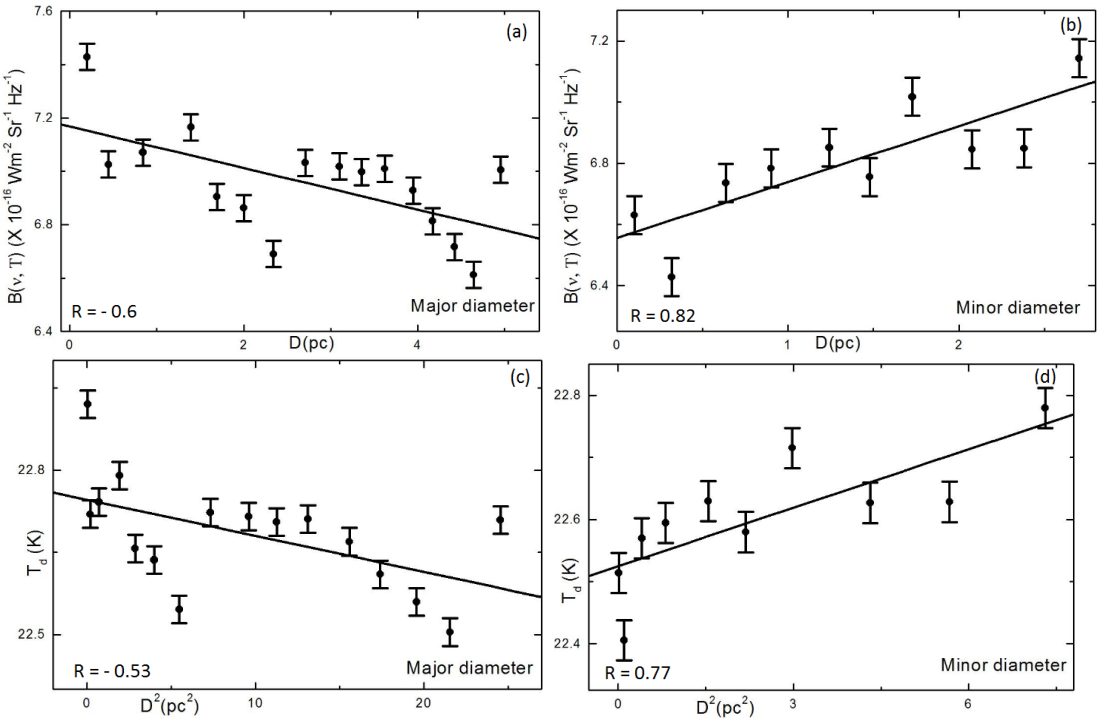

Figure 67: Variation of Planck function $B(\nu, T)$ in the cavity CASKK3 with the distance along both diameters (a) and (b) along major diameter, (c) and (d) along minor diameter. The south-west point or north-west point of the diameter is assumed as a reference point i.e.,the left-end point represents the reference point. The correlation coefficient and the slope of the line are shown. The error bars represent the standard error (±se) of the deviation.

Figure 67(a,b) show the distribution of Planck function with extension (major diameter) and compression (minor diameter) passing through minima. In both Figure 67(a,b), distribution of Planck function with distance is similar i.e., first decreases, becomes minimum and then increases. It repeats again. In case of both diameters, slope and correlation coefficient (R) are negative in case of major diameter but they are positive in minor diameter. Since the regression coefficient is not small so that there is moderate correlation between the data.

Figure 67(c,d) show the variation of dust color temperature with D^2 along major and minor diameters of the cavity respectively. The nature of variation of dust color temperature with D^2 in Figure 67(c,d) is exactly similar to that of the variation of Planck function with D as in Figure 67(a,b). Thus, it clearly signifies that the dusts and grains within the cavity neither be in exactly thermal equilibrium with the far infrared radiation nor strictly obey the Maxwellian velocity distribution. It is due to the external effect caused by AGB star or any other similar point sources.

4.5.4 FIR Cavity CASKK4 Nearby the AGB0555+2827 Located Within G182+00

The cavity is found to be located at R.A.(J2000) = 05^h 55^m 00^s, Dec.(J2000) = 28° 27' 00" (l = 181.5° and b = 1.5°) centered at R.A.(J2000) = 05^h 54^m 04.5^s, Dec.(J2000) = 28° 52' 38.3". The maximum to minimum flux density ratio of the cavity CASKK4 at 100 μm is found to be 1.1. Figure 68(a) is the image of the cavity at 100 μm IRAS maps at pixel size 1.0° × 1.0° and Figure 68(b) is its contour map which shows how flux density is distributed within the cavity. The minimum value of flux density at the minima is found to be 21.451 MJy sr^{-1} (= 2.145×10^{-19} kg s^{-2}). Size of the cavity is defined as its major and minor diameters passing through minimum flux region. Therefore diameters are drawn through minimum flux region at 100 μm wavelength. Here size of the cavity is found about 0.7° × 0.4°. Like wise, the size of KK-loop G182+00 given in the catalog Könyves et al. (2007) is 4.7° × 4.1° where distance between AGB0555+2827 and G182+00 is 1.54° hence the AGB star is located within the KK-loop. The shape of the cavity is shown in Figure 68(a,b) which is elongated along north-east to south-west direction. Since it is located at 1.5° galactic latitude with position angle 300.3° so it is in the galactic plane inclined by ∼ 60°. It means the cavity is very close to the galactic plane so that it is located in the strong radiation field emitted from the disk of the Milky Way.

There are 381 pixels in the field of view within the contour level 1-102 in the FITS (Flexible Image Transport System) image in ALADIN2.5 software to get raw data of relative flux density. Figure 68(c) is scatter plot between $F(60)$ and $F(100)$ where there is high gathering and spreading at the middle flux levels. The average value of dust color temperature calculated from slope of the linear fit is 23.3 K.The calculated minimum and maximum dust color temperature in the vicinity of the cavity are found to be (18.6 ± 1.16) K and (19.8 ± 0.86) K respectively.

Contour map of dust color temperature and dust mass are shown in Figure 68(d,f) with color bars. From the figure, it is found that minimum mass region is found to be at the high temperature region, supporting the cosmological principle. Therefore the distribution is homogeneous and isotropic. The solid curve of Figure 68(e,g) represents the Gaussian fit of dust color temperature and dust mass. The cavity is 3800 pc far from us (Könyves et al., 2007). Total mass of the cavity is found to be 1.1×10^{31} kg, larger than the Gaussian value. The Gaussian center of dust color temperature is found as 19.3 K and Gaussian area of dust mass is found to be 0.9×10^{29} kg. Dust mass distribution is found to be in agreement with Gaussian distribution which supports homogeneous distribution. The height of Gaussian fit suggests the on-going mass loading process in the cavity and it is possible due to strong external effect. The nearby AGB star provides such effects.

Linear fit of the plot between visual extinction and dust color temperature shown in Figure 68 shows a systematic trend with best correlation coefficient i.e., −0.98. From the best fit, we found

$$T_{\mathrm{d}} = -1.1 \times 10^{5} A_{\mathrm{V}} + 21.9 \tag{4.42}$$

Taking log and solving it, we found a relation between them. The relation is

$$T_{\mathrm{d}} \times A_{\mathrm{V}} = 2.0 \times 10^{-4} \tag{4.43}$$

which is very close to the calculated value. It means similar trend is found as found in the previous cavities. This result is strongly supported and verified by contour map of dust color temperature and visual extinction shown in Figure 68(d) and Figure 68(i) respectively.

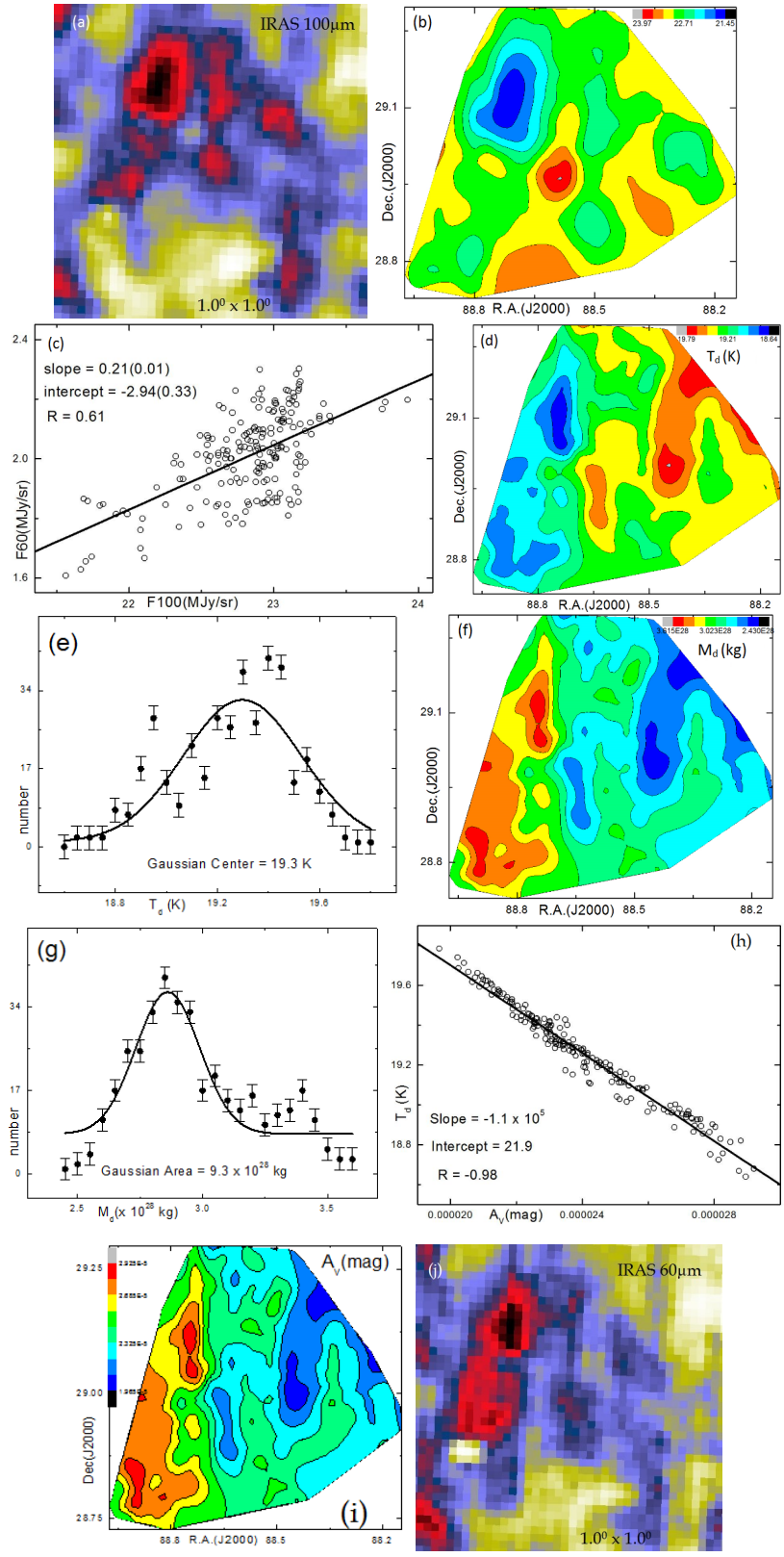

Figure 68: (a) Image of the cavity CASKK4 nearby to the AGB0555+2827 centered at R.A.(J2000) = 05^h 54^m 04.5^s and Dec.(J2000) = 28° 52' 38.3". (b) Contour map of flux density at 100 μm wavelength. (c) Flux at 100 μm verses 60 μm plot. (d), (f) and (i) are the contour map of dust color temperature, dust mass and visual extinction respectively. Solid curves of (e) and (g) represents the Gaussian fit of the respective dust color temperature and the dust mass. (h) Best fit between visual extinction and dust color temperature at 100 μm and (j) 60 μm IRAS image, for comparison. The values given in the bracket is the standard error.

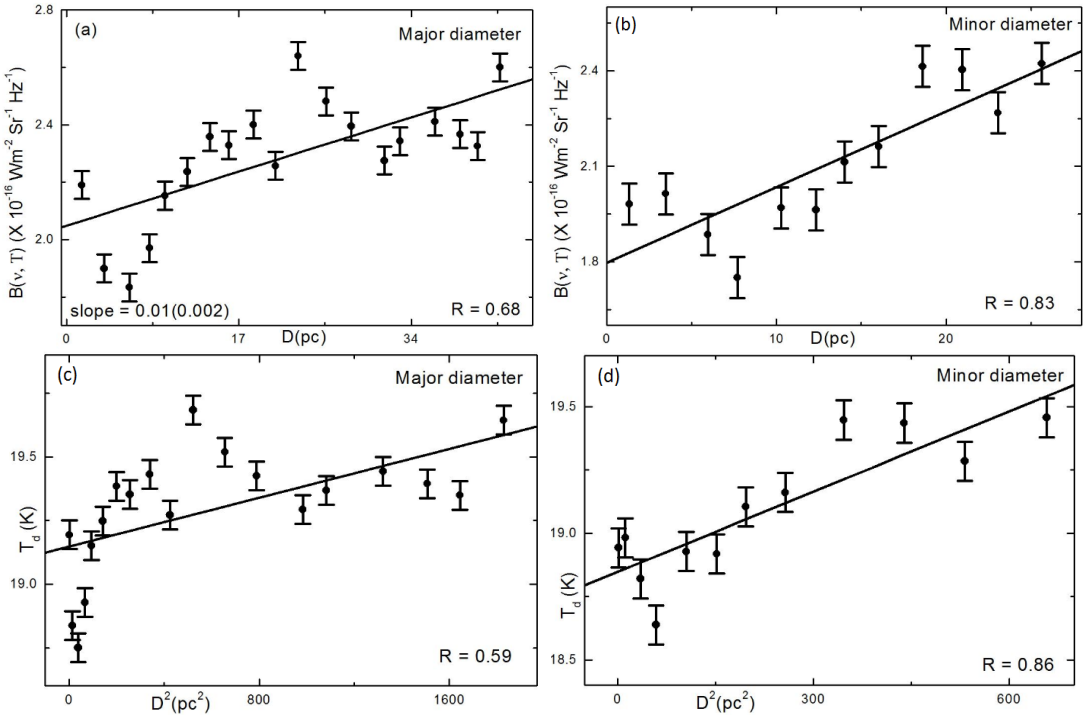

Figure 69: Variation of Planck function $B(\nu, T)$ in the cavity CASKK4 with the distance along both diameters (a) and (b) along major diameter, (c) and (d) along minor diameter. The south-west point or north-west point of the diameter is assumed as a reference point i.e.,the left-end point represents the reference point. The correlation coefficient and the slope of the line are shown. The error bars represent the standard error (±se) of the deviation.

Figure 69(a,b) show the distribution of Planck function with extension and compression passing through minima. In both Figure 69(a,b), distribution of Planck function with distance is similar i.e., first decreases, becomes minimum and then increases. It repeats again. But some how it looks like a random distribution. In case of both diameters, slope and correlation coefficient (R) are positive . Correlation coefficient is high in case of minor diameter than major diameter so there is good correlation between the data in minor diameter.

Figure 69(c,d) show the variation of dust color temperature with D^2 along major and minor diameters of the cavity respectively. The nature of variation of dust color temperature with D^2 in Figure 69(c,d) is exactly similar to that of the variation of Planck function with D as in Figure 69(a,b). Thus, it clearly signifies that the dusts and grains within the cavity neither be in exactly thermal equilibrium with the far infrared radiation nor strictly obey the Maxwellian velocity distribution. It is due to the external effect caused by AGB star or any other similar point sources.

4.5.5 FIR Cavity CASKK5 Nearby the AGB0617-0634 Located Within G212-11

The cavity is found to be located at R.A.(J2000) = 06^h 17^m 08^s, Dec.(J2000) = −06° 34' 00" (l = 214.9° and b = −10.6°) centered at R.A.(J2000) = 06^h 17^m 18.4^s, Dec.(J2000) = −06° 38' 08.4". The maximum to minimum flux density ratio of the cavity CASKK5 at 100 μm is found to be 1.1. Figure 70(a) is the image of the cavity at 100 μm IRAS maps at pixel size 1.0° × 1.0° and Figure 70(b) is its contour map which shows how flux density is distributed within the cavity. The minimum value of flux density at the minima is found to be 14.283 MJy sr^{-1} (= 1.428×10^{-19} kg s^{-2}). Size of the cavity is defined as its major and minor diameters passing through minimum flux region. Therefore diameters are drawn through minimum flux region at 100 μm wavelength. Here size of the cavity is found about 0.6° × 0.3°. Like wise, the size of KK-loop G212-11 given in the catalog Könyves et al. (2007) is 8.4° × 7.1° where distance between AGB0617-0634 and G212-11 is 2.91° hence the AGB star is located within the KK-loop. The shape of the cavity is shown in Figure 70(a,b) which is elongated along north south direction. Since it is located at −10.6° galactic latitude with position angle 296.5° so it is in the galactic plane inclined by ∼ 64.0°.

In Figure 70(c), flux densities 60 μm are plotted against 100 μm and fitted linearly to find the slope. This slope has been used to calculate average value of dust color temperature. From the figure, it is found that at higher values of flux densities, large number of observations are found than that of the smaller, indicating the presence of different chemical species at the core and surrounding region. A spectroscopic information is needed to track out relative abundance of materials in the dust and grain of the cavity but no spectroscopic data are available till date. From the linear fit, correlation coefficient (R) is found to be 0.83 which shows that there is good correlation between the plotted data. The average value of dust color temperature calculated from the slope of the linear fit is 21.6 K.The calculated minimum and maximum dust color temperature in the vicinity of the cavity are found to be (19.2 ± 0.47) K and (19.7 ± 0.27) K respectively.

Contour map of dust color temperature and dust mass are shown in Figure 70(d,f) with color bars. From the figure, it is found that minimum mass region is found to be at the high temperature region and vice-versa, supporting the cosmological principle. Therefore the distribution is homogeneous and isotropic. The solid curve of Figure 70(e,g) represents the Gaussian fit of dust color temperature and dust mass. The cavity is 500 pc far from us (Könyves et al., 2007). Total mass of the cavity is found to be 8.1×10^{28} kg, larger than the Gaussian value. The Gaussian center of dust color temperature is found as 19.6 K and Gaussian area of dust mass is found to be 1.0×10^{27} kg.

Best fit between visual extinction and dust color temperature shown in Figure 70 shows a systematic trend with excellent correlation coefficient i.e., −0.84. From the best fit, we

found

$$T_{\rm d} = -1.8 \times 10^5 A_{\rm V} + 22.2 \tag{4.44}$$

Taking log and solving, we found

$$T_{\rm d} \times A_{\rm V} = 1.3 \times 10^{-4} \tag{4.45}$$

which is very close to the calculated value. Thus, it is concluded that higher the dust color temperature, lower the visual extinction and vice-versa. This conclusion is strongly supported and verified by contour map of dust color temperature and visual extinction shown in Figure 70(d) and Figure 70(i) respectively.

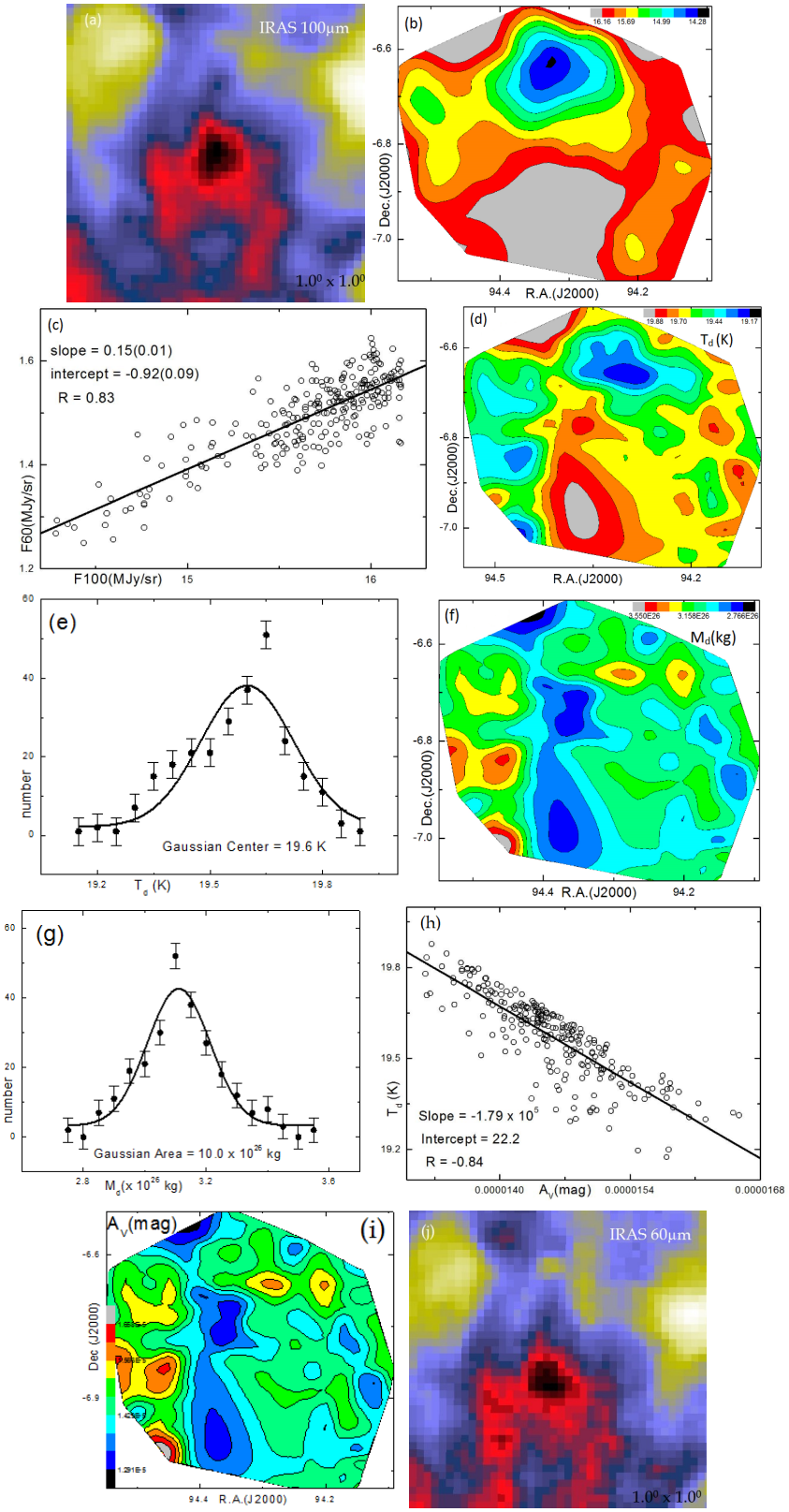

Figure 70: (a) Image of the cavity CASKK5 nearby to the AGB0617-0634 centered at R.A.(J2000) = 06^h 17^m 18.39^s and Dec.(J2000) = −06° 38' 08.4". (b) Contour map of flux density at 100 μm wavelength. (c) Flux at 100 μm verses 60 μm plot. (d), (f) and (i) are the contour map of dust color temperature, dust mass and visual extinction respectively. Solid curves of (e) and (g) represents the Gaussian fit of the respective dust color temperature and the dust mass. (h) Best fit between visual extinction and dust color temperature at 100 μm and (j) 60 μm IRAS image, for comparison. The values given in the bracket is the standard error.

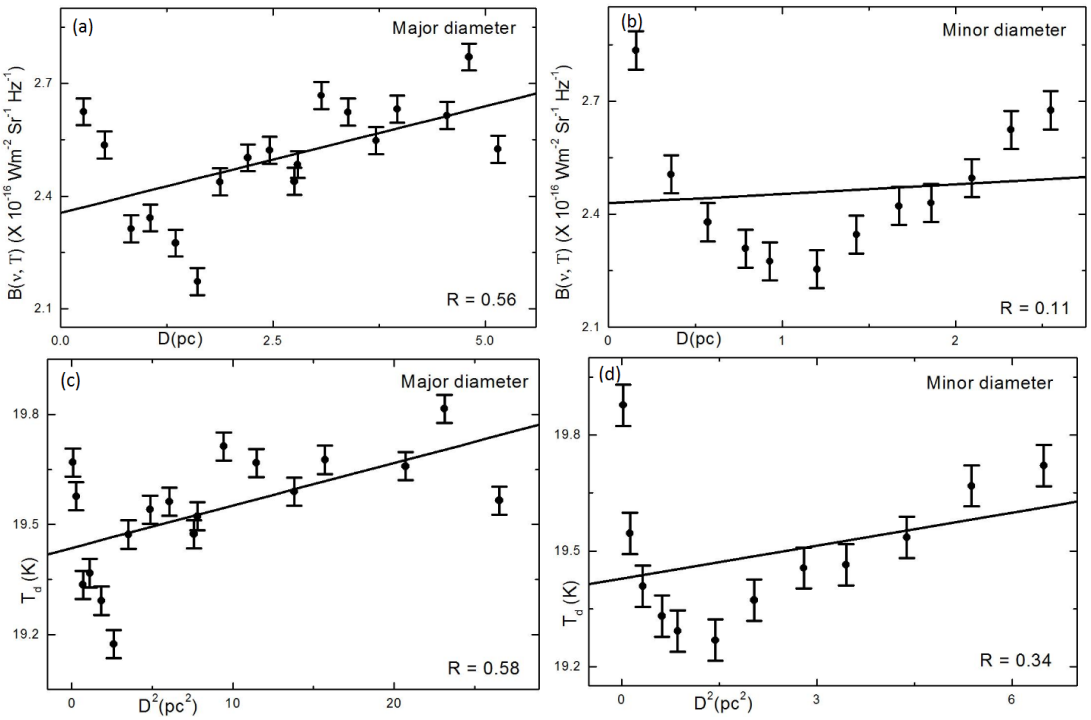

Figure 71: Variation of Planck function $B(\nu, T)$ in the cavity CASKK with the distance along both diameters (a) and (b) along major diameter, (c) and (d) along minor diameter. The south-west point or north-west point of the diameter is assumed as a reference point i.e.,the left-end point represents the reference point. The correlation coefficient and the slope of the line are shown. The error bars represent the standard error (±se) of the deviation.

Figure 71(a,b) show the distribution of Planck function with extension (major diameter) and compression (minor diameter) passing through minima. In both Figure 71(a,b), distribution of Planck function with distance is similar i.e., first decreases, becomes minimum and then increases. It repeats again in case of major diameter. But some how it looks like a random distribution. In case of both diameters, slope and correlation coefficient (R) are positive . Correlation coefficient is small so there is poor correlation between the data.

Figure 71(c,d) show the variation of dust color temperature with D^2 along major and minor diameters of the cavity respectively. The nature of variation of dust color temperature with D^2 in Figure 71(c,d) is exactly similar to that of the variation of Planck function with D as in Figure 71(a,b). Thus, it clearly signifies that the dusts and grains within the cavity neither be in exactly thermal equilibrium with the far infrared radiation nor strictly obey the Maxwellian velocity distribution.

4.5.6 FIR Cavity CASKK6 Nearby the AGB0619-0558 Located Within G212-11

The cavity is found to be located at R.A.(J2000) = 06^h 19^m 06^s, Dec.(J2000) = −05° 58' 00" (l = 214.6° and b = −9.9°) centered at R.A.(J2000) = 06^h 21^m 04.5^s, Dec.(J2000)

= −05° 58' 31.6". The maximum to minimum flux density ratio of the cavity CASKK6 at 100 μm is found to be 1.1. Figure 72(a) is the image of the cavity at 100 μm IRAS maps at pixel size $1.0^\circ \times 1.0^\circ$ and Figure 72(b) is its contour map which shows how flux density is distributed within the cavity. The minimum value of flux density at the minima is found to be 12.747 MJy sr^{-1} (= 1.27×10^{-19} kg s^{-2}). Size of the cavity is defined as its major and minor diameters passing through minimum flux region. Therefore diameters are drawn through minimum flux region at 100 μm wavelength. Here size of the cavity is found about $0.7^\circ \times 0.3^\circ$. Like wise, the size of KK-loop G212-11 given in the catalog Könyves et al. (2007) is $8.4^\circ \times 7.1^\circ$ where distance between AGB0617-0634 and G212-11 is 2.79° hence the AGB star is located within the KK-loop. The shape of the cavity is shown in Figure 72(a,b) which is elongated along north south direction where the centered minimum flux density is completely surrounded by other higher flux density region. It means the matter with in the cavity are in certain order and follow cosmological principle. It is located at −9.9° galactic latitude with position angle 296.6° so it is in the galactic plane inclined by $\sim 63.0^\circ$.

Figure 72(c) is a scatter plot between 60 μm flux densities are 100 μm flux densities and is fitted to find the slope. This slope has been used to calculate average value of dust color temperature. From the figure, it is found that at higher values of flux densities, large number of observations are found than that of the smaller, indicating the presence of different chemical species at the core and surrounding region. From the linear fit, correlation coefficient (R) is found to be 0.81 which shows that there is good correlation between the plotted data. The average value of dust color temperature calculated from the slope of the linear fit is 23.1 K.The calculated minimum and maximum dust color temperature in the vicinity of the cavity are found to be (18.3 ± 1.2) K and (19.8 ± 0.83) K respectively.

Figure 72(d,f) show contour map of dust color temperature and dust mass with color bars. From the figure, it is found that minimum mass region is found to be at the high temperature region and vice-versa, supporting the cosmological principle. Therefore the distribution is homogeneous and isotropic. The solid curve of Figure 72(e,g) represents the Gaussian fit of dust color temperature and dust mass where Gaussian fit agreed the Gaussian distribution. The height of the Gaussian fit of dust mass suggests the on-going mass loading process in the cavity. The cavity is 500 pc far from us (Könyves et al., 2007). Total mass of the cavity is found to be 7.55×10^{28} kg, larger than the Gaussian value. The Gaussian center of dust color temperature is found as 19.1 K and Gaussian area of dust mass is found to be 2.2×10^{27} kg.

Figure 72 is the best fit between visual extinction and dust color temperature which shows a systematic trend with best correlation coefficient i.e., −0.97. From the best fit,

we found

$$T_{\mathrm{d}} = -1.3 \times 10^{5} A_{\mathrm{V}} + 25.5 \tag{4.46}$$

Taking log and solving, we found a very important relation between visual extinction and dust color temperature. The relation is

$$T_{\mathrm{d}} \times A_{\mathrm{V}} = 0.8 \times 10^{-4} \tag{4.47}$$

which is very close to the calculated value. Finally , it is concluded that higher the temperature, lower the visual extinction and vice-versa which is strongly supported and verified by contour map of dust color temperature and visual extinction shown in Figure 72(d) and Figure 72(i) respectively.

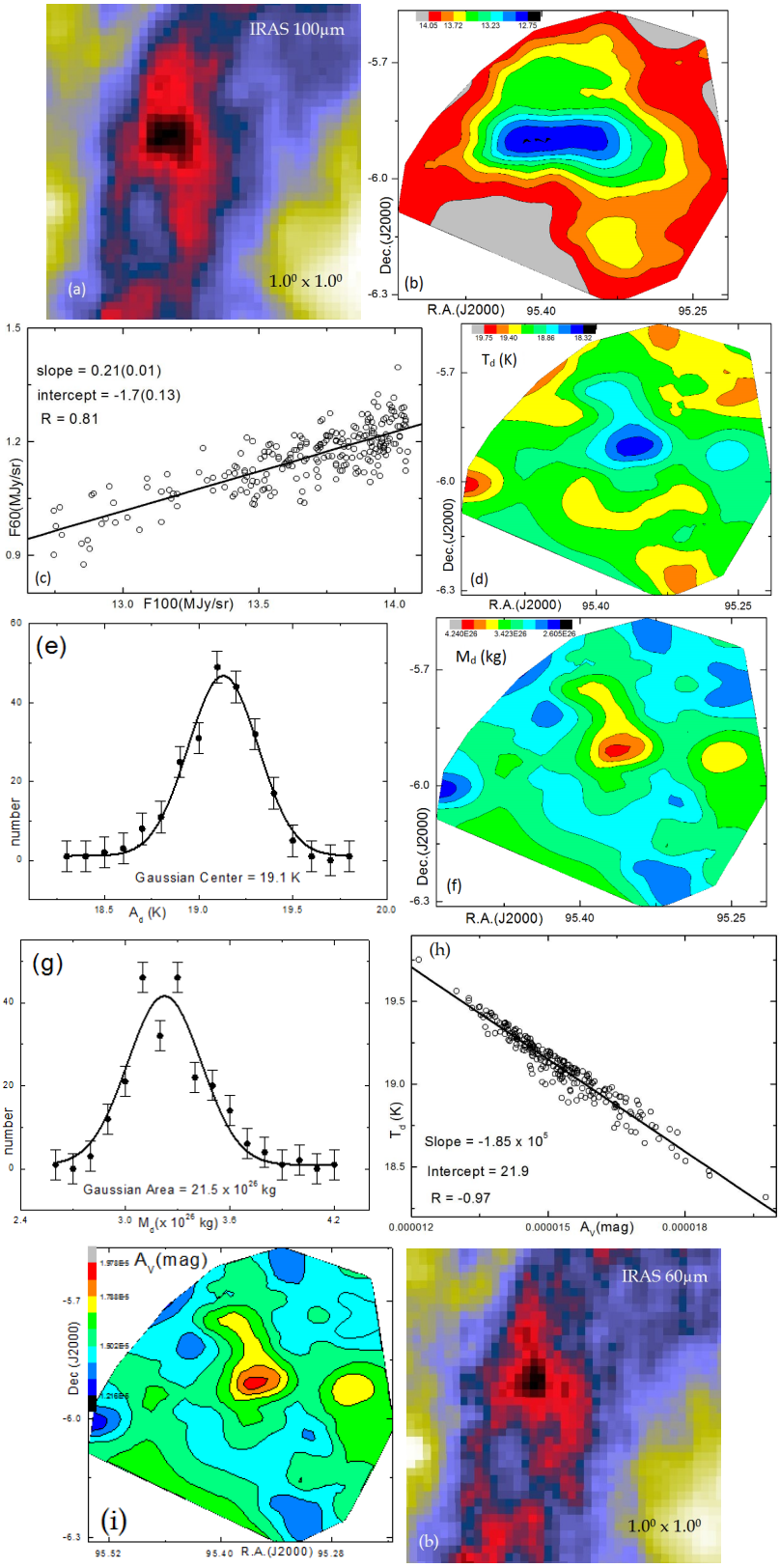

Figure 72: (a) Image of the cavity CASKK6 nearby to the AGB0619-0558 centered at R.A.(J2000) = 06^h 21^m 04.48^s and Dec.(J2000) = -05° 58' 31.6". (b) Contour map of flux density at 100 μm wavelength. (c) Flux at 100 μm verses 60 μm plot. (d), (f) and (i) are the contour map of dust color temperature, dust mass and visual extinction respectively. Solid curves of (e) and (g) represents the Gaussian fit of the respective dust color temperature and the dust mass. (h) Best fit between visual extinction and dust color temperature at 100 μm and (j) 60 μm IRAS image, for comparison. The values given in the bracket is the standard error.

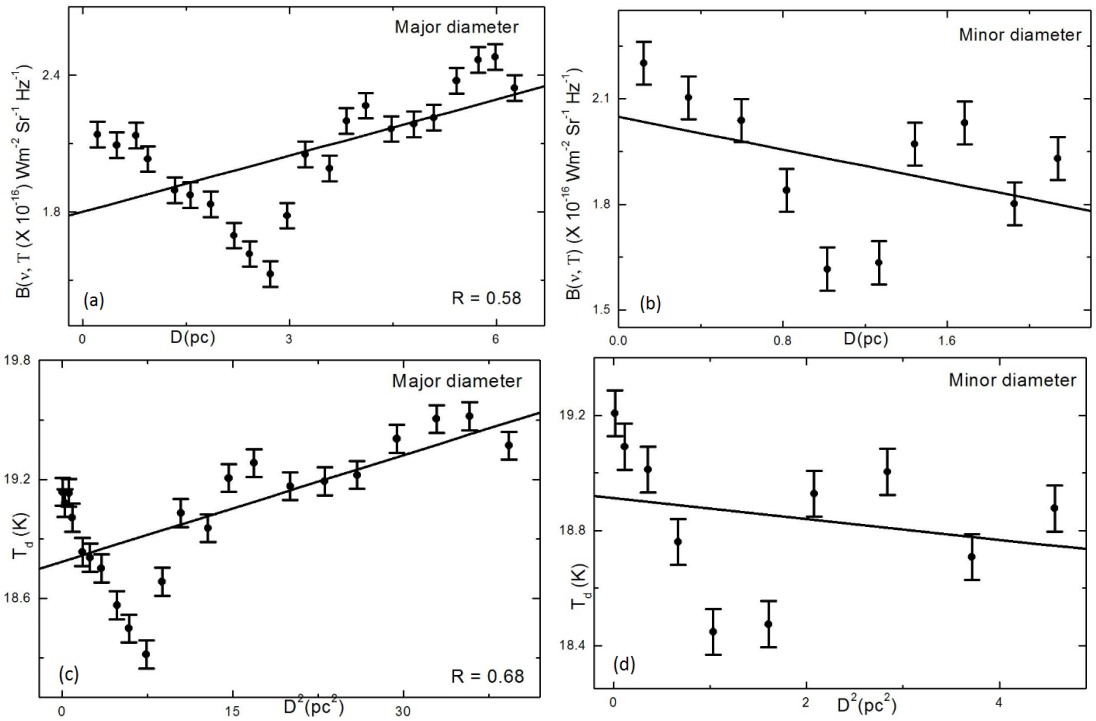

Figure 73: Variation of Planck function $B(\nu, T)$ in the cavity CASKK6 with the distance along both diameters (a) and (b) along major diameter, (c) and (d) along minor diameter. The south-west point or north-west point of the diameter is assumed as a reference point i.e., the left-end point represents the reference point. The correlation coefficient and the slope of the line are shown. The error bars represent the standard error (±se) of the deviation.

Figure 73(a,b) show the distribution of Planck function with extension and compression passing through minimum flux density. In both Figure 73(a,b), distribution of Planck function with distance is similar i.e., first decreases, becomes minimum and then increases. It repeats again. But some how it looks like a random distribution. In case of extension, slope and correlation coefficient (R) are large and positive where as they are small and negative in case of compression.

Figure 73(c,d) show the variation of dust color temperature with D^2 along extension and compression of the cavity respectively. The nature of variation of dust color temperature with D^2 in Figure 73(c,d) is similar to that of the variation of Planck function with D as in Figure 73(a,b). Thus, it clearly signifies that the dusts and grains within the cavity neither be in exactly thermal equilibrium with the far infrared radiation nor strictly obey the Maxwellian velocity distribution.

4.5.7 FIR Cavity CASKK7 Nearby the AGB0712-1720 Located Within G229-03

The cavity is found to be located at R.A.(J2000) = 07^h 12^m 04^s, Dec.(J2000) = −17° 20' 00" (l = 230.7° and b = −3.4°) centered at R.A.(J2000) = 07^h 06^m 51.34^s, Dec.(J2000) = −17° 34' 36.5". The maximum to minimum flux density ratio of the cavity CASKK7 at

100 μm is found to be 1.1. Figure 74(a) is the JPG image of the cavity at 100 μm IRAS maps at pixel size $1.0^\circ \times 1.0^\circ$ and Figure 74(b) is its contour map. The minimum value of flux density at the minima is found to be 11.639 MJy sr^{-1} (= 1.164×10^{-19} kg s^{-2}). Here size of the cavity is found about $0.8^\circ \times 0.3^\circ$ and the size of KK-loop G229-03 given in the catalog Könyves et al. (2007) is $3.7^\circ \times 3.6^\circ$ where distance between AGB0712-1720 and G229-03 is 1.5°. It means, the AGB star is located within the KK-loop. The shape of the cavity is shown in Figure 74(a,b) which is elongated along north-south direction. Since it is located at -3.41° galactic latitude with position angle 297.4° so it is in the galactic plane inclined by $\sim 63.0^\circ$.

There are 297 pixels in the field of view within the contour level 1-35 in the FITS image in ALADIN2.5 software to get raw data of relative flux density. Figure 74(c) is the scatter plot between $F(60)$ and $F(100)$ where a best line is fitted to calculate average value of dust color temperature from its slope. There is good correlation between the data. The average value of dust color temperature calculated from slope of the linear fit is found to be 23.3 K. The calculated minimum and maximum dust color temperature in the vicinity of the cavity are found to be (17.7 ± 1.4) K and (19.5 ± 0.95) K respectively.

Contour map of dust color temperature and dust mass with color bars are shown in Figure 74(d,f). From the figure, it is found that minimum mass region is found to be at the high temperature region and vice-versa, supporting the cosmological principle. Therefore the distribution is homogeneous and isotropic. The solid curve of Figure 74(e,g) represents the Gaussian fit of dust color temperature and dust mass where Gaussian fit agreed the Gaussian distribution. The height of the Gaussian fit of dust mass suggests the on-going mass loading process in the cavity. It is possible only if there is strong external effect. The cavity is 1300 pc far from us (Könyves et al., 2007). Total mass of the cavity is found to be 7.5×10^{29} kg, larger than the Gaussian value. The Gaussian center of dust color temperature is found as 18.6 K and Gaussian area of dust mass is found to be 2.85×10^{28} kg.

Best fit of the scattering plot between visual extinction and dust color temperature shown in Figure 74 shows a systematic trend with best correlation coefficient i.e., -0.98. From the best fit, we found

$$T_\mathrm{d} = -1.5 \times 10^5 A_\mathrm{V} + 21.2 \tag{4.48}$$

Taking log and solving, we found a very important relation between them. The relation is

$$T_\mathrm{d} \times A_\mathrm{V} = 1.6 \times 10^{-4} \tag{4.49}$$

which is very close to the calculated value and showed similar trend as before. This conclusion is strongly supported and verified by contour map of dust color temperature and visual extinction shown in Figure 74(d) and Figure 74(i) respectively.

Distribution of Planck function with extension and compression passing through minimum flux density are shown in Figure 75(a,b). Similarly the variation of dust color temperature with D^2 along extension and compression of the cavity respectively are shown in Figure 75(c,d). There looks like a random distribution. In case of extension, slope and correlation coefficient (R) are small and negative where as they are small and positive in case of compression. Such distribution suggests that dust particles are not in local thermodynamic equilibrium and are not following the Maxwellian velocity distribution.

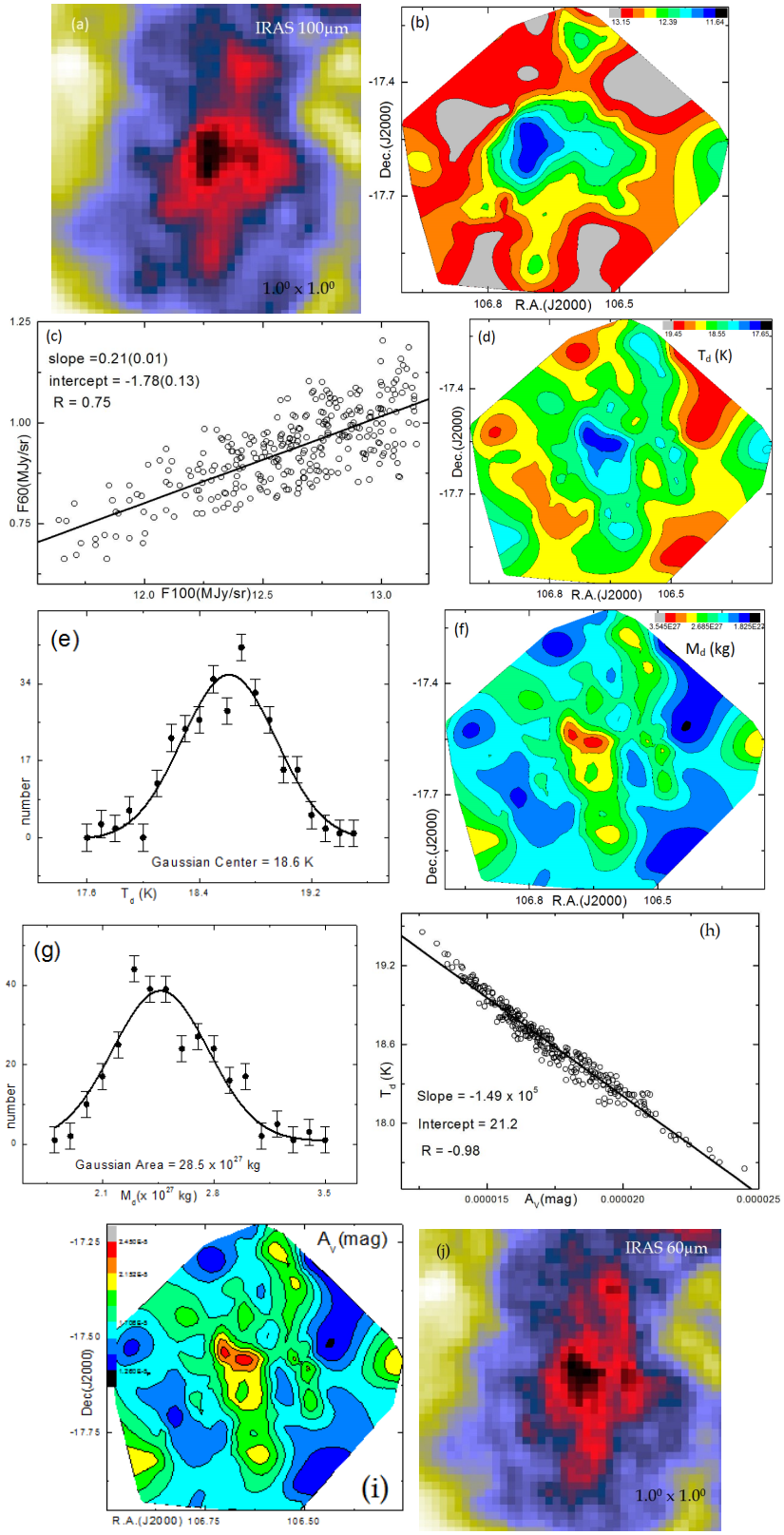

Figure 74: (a) Image of the cavity CASKK7 nearby to the AGB0712-1720 centered at R.A.(J2000) = 07^h 06^m 51.34^s and Dec.(J2000) = $-17°$ 34' 36.5". (b) Contour map of flux density at 100 μm wavelength. (c) Flux at 100 μm verses 60 μm plot. (d), (f) and (i) are the contour map of dust color temperature, dust mass and visual extinction respectively. Solid curves of (e) and (g) represents the Gaussian fit of the respective dust color temperature and the dust mass. (h) Best fit between visual extinction and dust color temperature at 100 μm and (j) 60 μm IRAS image, for comparison. The values given in the bracket is the standard error.

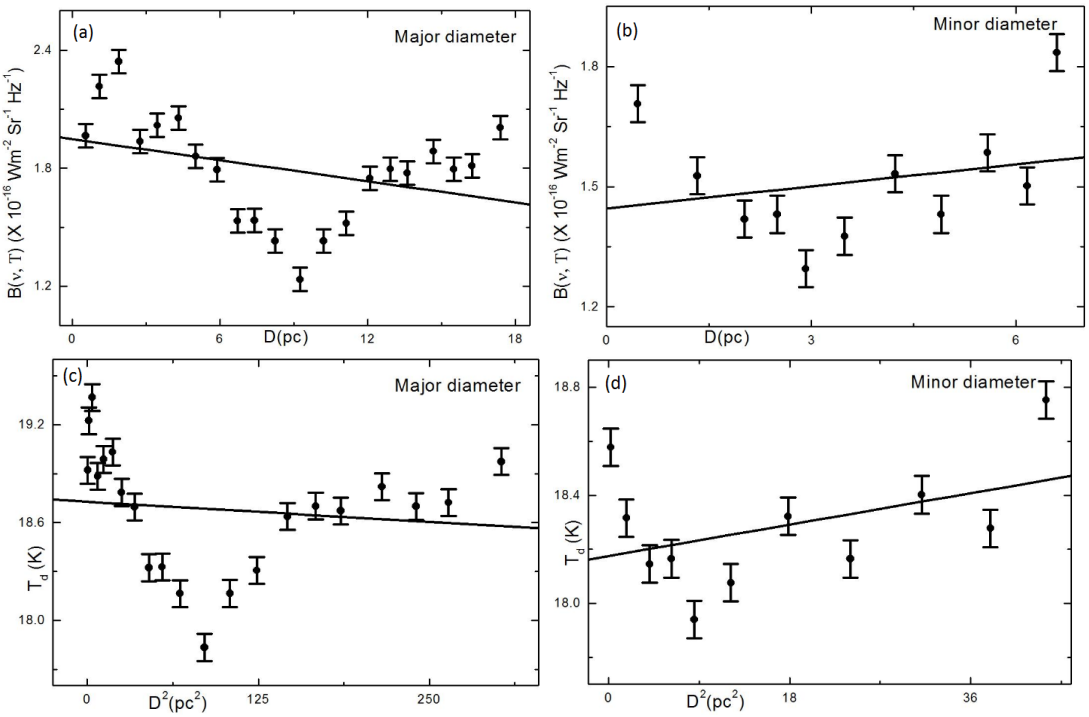

Figure 75: Variation of Planck function $B(\nu, T)$ in the cavity CASKK7 with the distance along both diameters (a) and (b) along major diameter, (c) and (d) along minor diameter. The south-west point or north-west point of the diameter is assumed as a reference point i.e.,the left-end point represents the reference point. The correlation coefficient is shown. The error bars represent the standard error (±se) of the deviation.

4.5.8 FIR Cavity CASKK8 Nearby the AGB1105-5451 Located Within G287+04

The cavity CASKK8 is found to be located nearby the AGB star at R.A.(J2000) = 11^h 05^m 01^s, Dec.(J2000) = −54° 51' 00" (l = 287.9° and b = 4.9°) centered at R.A.(J2000) = 11^h 04^m 17.6^s, Dec.(J2000) = −54° 29' 05.5". Figure 76(a,b) are the JPG image and contour map of the cavity at 100 μm IRAS survey. The cavity is at 1.5° × 1.5° pixel size. The maximum to minimum flux density ratio of the cavity CASKK11 at 100 μm is found to be 1.2. The minimum value of flux density at the minima is found to be 17.2 MJy sr^{-1} (= 1.72×10^{-19} kg s^{-2}). Here size of the cavity is found about 1.0° × 0.5° and the size of KK-loop G287+04 given in the catalog Könyves et al. (2007) is 2.2° × 1.7° where distance between AGB1105-5451 and G287+04 is 0.7° hence the AGB star is located within the KK-loop. Since the cavity is located at 4.9° galactic latitude with position angle 336.4° so it is in the galactic plane inclined by ∼ 24.0°.

There are 782 pixels in the field of view within the contour level 1-51 in the FITS image in ALADIN2.5 software. Scatter plot between $F(60)$ and $F(100)$ is shown in Figure 76(c) where a best line is fitted to calculate average value of dust color temperature. There is high scattering and extension in the higher and the middle flux region. Since correlation coefficient is not small so that there is normal correlation is seen between the data. The average value of dust color temperature calculated from slope of the linear fit

is found to be 23.5 K. The calculated minimum and maximum dust color temperature in the vicinity of the cavity are found to be (21.4 ± 0.51) K and (22.6 ± 0.23) K respectively.

From the contour map of dust color temperature and dust mass Figure 76(d,f) showed that the minimum mass region is found to be at the high temperature region and vice-versa, supporting the cosmological principle. Therefore the distribution is homogeneous and isotropic. The solid curve of Figure 76(e,g) represents the Gaussian fit of dust color temperature and dust mass where Gaussian fit agreed the Gaussian distribution. The height of the Gaussian fit of dust mass suggests the on-going mass loading process in the cavity. It is possible only if there is strong external effect. The cavity is 2600 pc far from us (Könyves et al., 2007). 3.6×10^{30} kg is the calculated total mass of the cavity which is larger than the Gaussian value. The Gaussian center of dust color temperature is found as 22.0 K and Gaussian area of dust mass is found to be 0.3×10^{29} kg.

Figure 76 is the best fit between visual extinction and dust color temperature which shows a systematic trend with excellent correlation coefficient i.e., -0.92. From the best fit, we found

$$T_{\mathrm{d}} = -3.9 \times 10^{5} A_{\mathrm{V}} + 25.0 \tag{4.50}$$

Taking log and solving it, we got a relation between visual extinction and dust color temperature. The relation is

$$T_{\mathrm{d}} \times A_{\mathrm{V}} = 0.6 \times 10^{-4} \tag{4.51}$$

which is very close to the calculated value. Finally , it is concluded that higher the temperature, lower the visual extinction and vice-versa. This conclusion is strongly supported and verified by contour map of dust color temperature and visual extinction shown in Figure 76(d) and Figure 76(i) respectively.

Distribution of Planck function along extension and compression passing through minimum flux density are shown in Figure 77(a,b). Similarly the variation of dust color temperature with D^2 along extension and compression of the cavity respectively are shown in Figure 77(c,d). It looks like a random distribution. In both cases, slope and correlation coefficient (R) are small and negative. It means, there is very poor correlation between the data and dust particles did not show local thermodynamic equilibrium.

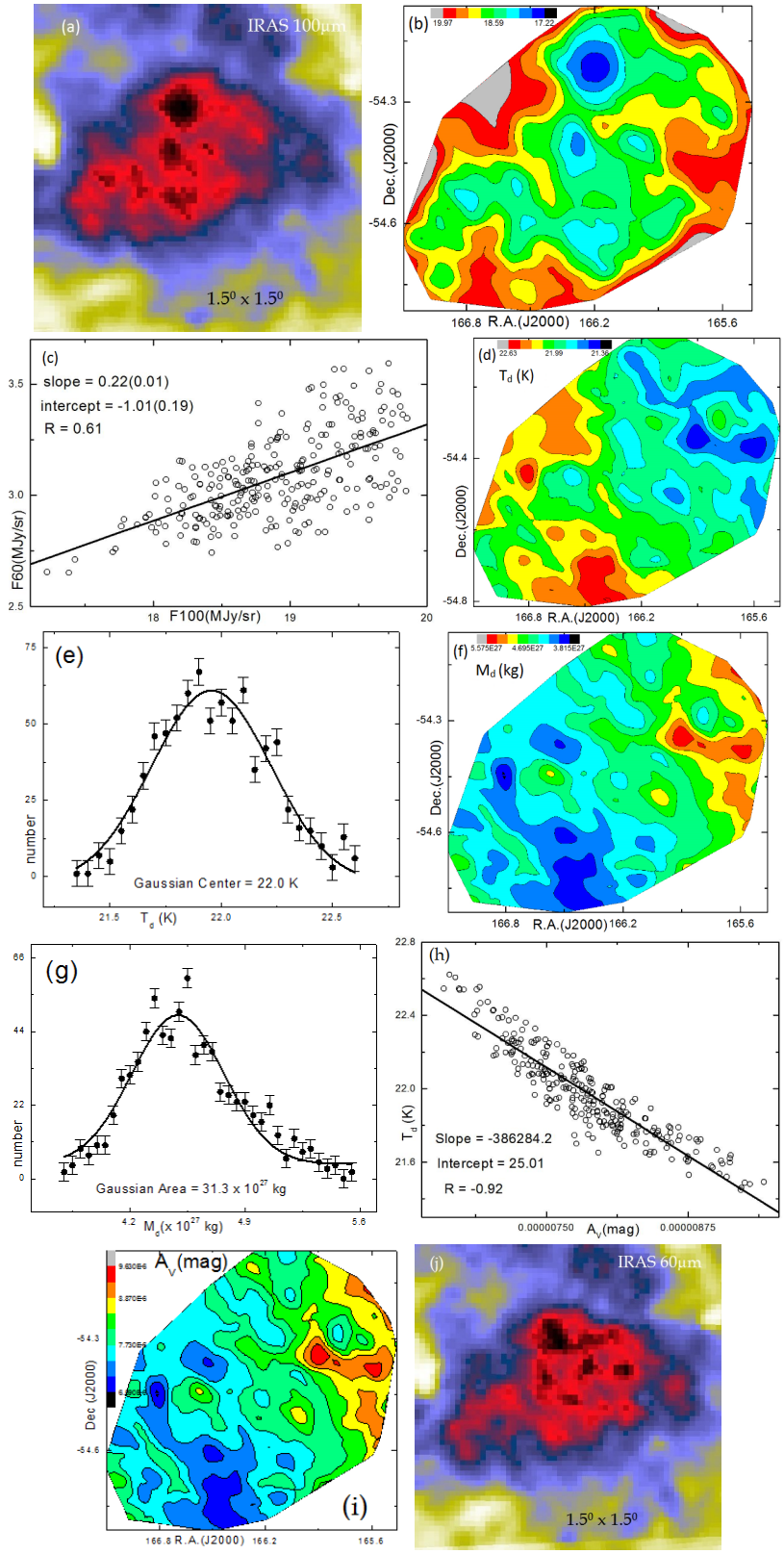

Figure 76: (a) Image of the cavity CASKK8 nearby to the AGB1105-5441 centered at R.A.(J2000) = 11^h 04^m 17.62^s and Dec.(J2000) = $-54°$ 29' 05.5". (b) Contour map of flux density at 100 μm wavelength. (c) Flux at 100 μm verses 60 μm plot. (d), (f) and (i) are the contour map of dust color temperature, dust mass and visual extinction respectively. Solid curves of (e) and (g) represents the Gaussian fit of the respective dust color temperature and the dust mass. (h) Best fit between visual extinction and dust color temperature at 100 μm and (j) 60 μm IRAS image, for comparison. The values given in the bracket is the standard error.

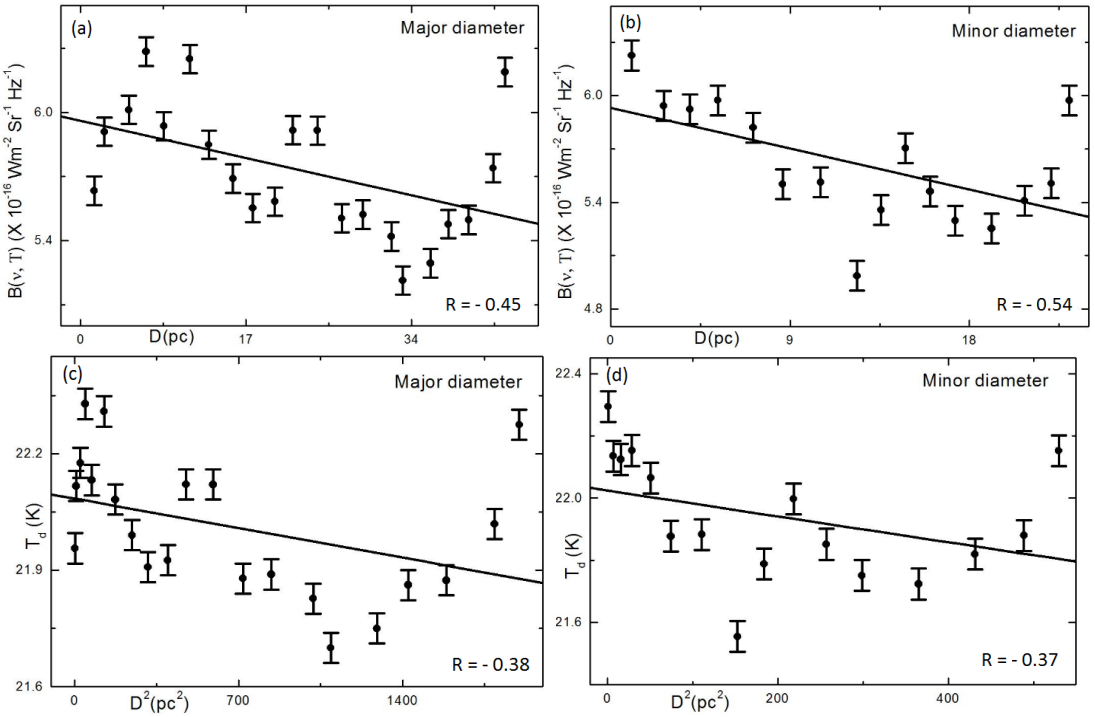

Figure 77: Variation of Planck function $B(\nu, T)$ in the cavity CASKK8 with the distance along both diameters (a) and (b) along major diameter, (c) and (d) along minor diameter. The south-west point or north-west point of the diameter is assumed as a reference point i.e.,the left-end point represents the reference point. The correlation coefficient is shown. The error bars represent the standard error (±se) of the deviation.

4.5.9 Conclusion

In this section, a systematic search was done under IRAS survey in far infrared (60 μm and 100 μm) region of eight far infrared cavities around C-rich AGB stars. We studied physical properties such as dust color temperature, Planck function, dust mass and visual extinction of the core region of the cavities. Following are the conclusions:

- The size of the respective cavities are found to be $0.7^\circ \times 0.2^\circ$, $0.6^\circ \times 0.2^\circ$, $0.7^\circ \times 0.4^\circ$, $0.6^\circ \times 0.4^\circ$, $0.6^\circ \times 0.3^\circ$, $0.7^\circ \times 0.3^\circ$, $0.8^\circ \times 0.3^\circ$, and $1.0^\circ \times 0.5^\circ$ respectively. Here cavity CASKK2 is the smallest and CASKK8 is the biggest among the eight cavities.

- The dust color temperature of the cavities CASKK1 to CASKK8 from the slope of best fit are found to be 22.2 K, 23.2 K, 23.3 K, 23.3 K, 21.6 K, 23.1 K, 23.3 K and 23.5 K respectively. Cavity CASKK8 has the highest average dust color temperature and the cavity CASKK5 has the lowest value.

- Calculated minimum and maximum dust color temperature of the cavities are found to be (19.7±0.62) K and (21.1±0.28) K, (19.4±0.93) K and (20.6±0.65) K,

(22.3 ± 0.25) K and (23.1 ± 0.05) K, (18.6 ± 1.16) K and (19.8 ± 0.86) K, (19.2 ± 0.47) K and (19.7 ± 0.27) K, (18.3 ± 1.20) K and (19.8 ± 0.83) K, (17.7±1.40) K and (19.5±0.95) K, (21.4±0.51) K and (22.6±0.23) K respectively. Here offset value of dust color temperature of all the cavities is less than 2 K, suggests that the dusts in the cavities are almost in thermal equilibrium. Cavity CASKK7 is the coldest and cavity CASKK3 is the hottest.

- Cavity CASKK4 has very poor Gaussian fit of both dust color temperature and dust mass. Cavity CASKK6 showed excellent Gaussian fit of dust color temperature but poor of dust mass. Likewise, cavities CASKK2, CASKK5 and CASKK8 showed poor Gaussian fit of both quantities and cavity CASKK1, CASKK3 and CASKK7 showed good Gaussian fit.

- Total dust mass of the respective cavities are found as 1.86×10^{28} kg, 3.58×10^{29} kg, 3.9×10^{28} kg, 1.1×10^{31} kg, 8.1×10^{28} kg, 7.55×10^{28} kg, 7.48×10^{29} kg, and 3.56×10^{30} kg. If we consider average dust mass of the eight cavities, the cavity CASKK4 is the heaviest (2.97×10^{28} kg) and the cavity CASKK1 is the lightest (4.93×10^{25} kg).

- From the contour map of dust color temperature and dust mass, it is found that most of the cavities more or less follow cosmological principle so that the particles are homogeneous and isotropy.

- From Gaussian fit of dust color temperature, it is found that cavities CASKK3, CASKK7 and CASKK8 mostly show symmetric behavior. But cavity CASKK1 shows positive skewed nature where as cavities CASKK2, CASKK4, CASKK5 and CASKK6 show negative skewed nature.

- Similarly, from Gaussian fit of dust mass, it is found that cavities CASKK1 and CASKK3 show negative skewed behavior but remaining six cavities show positive skewed nature.

- Distribution of Planck function along extension and compression for all the eight cavities show that they are oscillating in order to get dynamical equilibrium so that they are not in thermal equilibrium and same situation is obtained in case of distribution of dust color temperature along D^2.

- Visual extinction of the respective cavities are found to be 1.2×10^{-5} mag, 1.5×10^{-5} mag, 0.8×10^{-5} mag, 2.4×10^{-5} mag, 1.5×10^{-5} mag, 1.5×10^{-5} mag, 1.7×10^{-5} mag and 0.8×10^{-5} mag. From above results, it is found that $A_V \times T_d$ is consistent and ranges from 0.77×10^{-4} to 2.40×10^{-4}. It means, higher the visual extinction, lower the dust color temperature and vice versa. Here, all cavities except CASKK2 and CASKK4 showed this relation. The anti correlation

of two cavities is possibly due to oscillation of dust particles in different direction. This conclusion is strongly supported and verified by contour map of dust color temperature and visual extinction also.

4.6 General Discussion

In this section, we discuss the results obtained from calculations, graphs and maps about physical properties of all eight cavities. Table 13 shows the location of the cavities in the equatorial coordinate system (R.A and Dec.), size of the cavities, values of maximum and minimum dust color temperatures (in K), average values of visual extinction (in mag) and total dust mass (in kg) of the cavities. From the Table 13, the biggest cavity is CASKK8 and the smallest cavity is CASKK4. Maximum dust color temperature of the cavity CASKK7 has its lowest value among the eight and maximum dust color temperature of cavity CASKK3 has the highest its value among them.

Scattering plots of all the cavities between $F(60)$ and $F(100)$ show systematic behavior having positive slope, intercept and correlation coefficient where correlation coefficient ranges from 0.6 to 0.9 which justifies there is good correlation between them. Similar systematic behavior is strongly seen in the scattering plot between visual extinction and dust color temperature. But in this case, slope and correlation coefficient both are negative. Here correlation coefficient ranges from -0.84 to -0.98 which signifies that there is the best correlation between them. Cavity CASKK4 has the highest dust mass and cavity CASKK1 has the lowest dust mass. But mass of the two cavities obtained from the calculation are excess means are more than a solar mass which is unexpected result. All these masses have been re calculated but found same results. The reason behind the excessive mass is because of distance that we have taken from the literature (Könyves et al., 2007). This distance calculation has been made considering associated object found in the cavity. This object might be in the background. For the verification, parallax angle of other nearby objects should be known. It is not available now. In this situation, we adopted Odenwald & Rickard (1987), assumed 200 pc distance and re calculated mass of the two cavities. Their mass found in the order of 10^{28} kg which is now much lower and consistent with the mass of cavities. From the best fit of scattered plot between Planck function and distance (major and minor diameters), systematic trend could not be found.

From the best fit between visual extinction and dust color temperature of all eight cavities, we found $A_V \times T_d$ = consistent. Here, all cavities except CASKK2 and CASKK4 showed this result. The anti correlation showed by the two cavities is possibly due to oscillation of dust-grain in different directions. It is also verified by contour map of dust color

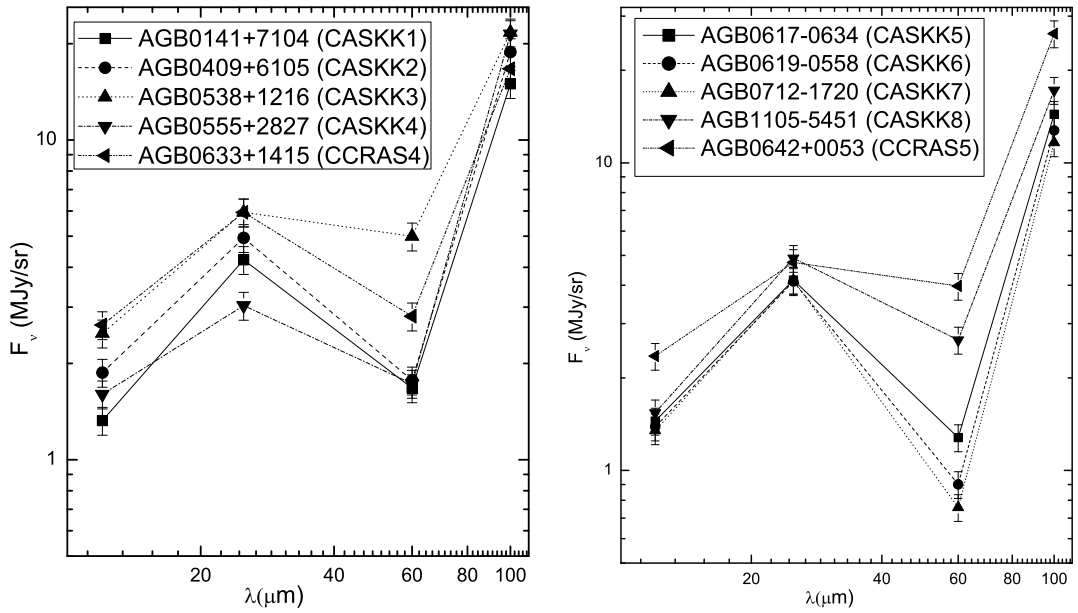

Figure 78: (a) Far infrared spectral distributions of the cavities located at nearby AGB star AGB0141+7104 (CASKK1), AGB0409+6105 (CASKK2), AGB0538+1216 (CASKK3), AGB0555+2827 (CASKK4) and (b) AGB0617-0634 (CASKK5), AGB0619-0558 (CASKK6), AGB0712-1720 (CASKK7) and AGB1105-5451 (CASKK8). The top most graph in figure (a) is of the cavity CCRAS4 and the top most graph in figure (b) is of the cavity CCRAS5 for comparative study respectively.

temperature and visual extinction of all eight cavities. Figure 78 is for the study of far infrared spectral distributions of the eight far infrared cavities. In Figure 78(a), FIR spectral distributions of four cavities CASKK1, CASKK2, CASKK3 and CASKK4 are compared to each other and with the cavity CCRAS4 explained in first chapter of result and discussion and in Figure 78(b), other four cavities CASKK5, CASKK6,CASKK6 and CASKK8 are compared to each other and with the cavity CCRAS5 explained in first chapter of our result and discussion. In all four cavities in Figure 78(a), there is increase in flux density with increase in wave length from 12 μm to 25 μm and from 60 μm to 100 μm but there is decrease in flux density with increase in wave length from 25 μm to 60 μm. Variation of flux density from 12 μm to 25 μm and 60 μm to 100 μm of all four cavities are more or less similar but their variation from 25 μm to 60 μm is quite different with varying slope. When we compare these variation with the cavity CCRAS4, no more differences except slopes are found. Such variation of flux density with wave length is found one of the fundamental character of far infrared cavities. Similarly, if we analyze the Figure 78(b), all four cavities CASKK5, CASKK6, CASKK7 and CASKK8 show similar nature with more or less steeper with each other in all four bands. In this case, flux density at 60 μm are found distinct but in other three bands, they are overlapped to each other. Variation of flux density with wave length from 12 μm to 25 μm and 60 μm to 100 μm is with positive slope but from 25 μm to 60 μm is with negative slope. When we compare these cavities with the cavity CCRAS5, similar nature with varying slope is found. From this discussion, it is conformed that there is positive slope from 12 μm

to 25 μm and 60 μm to 100 μm but there is negative slope from 25 μm to 60 μm in case of far infrared cavities.

Table 13: Calculated values of eight far infrared cavities where first column represents name of the cavities, next two columns represent positions of the cavities in equatorial coordinate system, fourth column for size of the cavities, fifth and sixth columns for maximum and minimum dust color temperature and last two columns represent the average visual extinction and total dust mass of the cavities.

Cavities	R.A. hh mm ss	Dec. dd mm ss	Size (deg×deg)	T_{max} (K)	T_{min} (K)	A_V (mag)	M_d ($\times 10^{29}$kg)
CASKK1	01 49 36.6	71 17 51.7	0.7×0.2	21.1±0.28	19.7±0.62	1.2×10^{-5}	0.2
CASKK2	94 07 16.6	61 16 53.9	0.6×0.2	20.6±0.65	19.4±0.93	1.5×10^{-5}	3.6
CASKK3	05 35 08.3	12 02 10.3	0.7×0.4	23.1±0.05	22.3±0.25	0.8×10^{-5}	0.4
CASKK4	04 54 50.1	29 07 12.6	0.6×0.4	19.8±0.86	18.6±1.16	2.4×10^{-5}	113.4
CASKK5	06 17 17.2	−63 81 2.3	0.6×0.3	19.7±0.27	19.2±0.47	1.5×10^{-5}	0.8
CASKK6	06 21 40.2	−55 44 4.7	0.7×0.3	19.8±0.83	18.3±1.20	1.5×10^{-5}	0.8
CASKK7	07 06 50.8	−17 36 06.5	0.8×0.3	19.5±0.95	17.7±1.40	1.7×10^{-5}	7.5
CASKK8	11 04 42.2	−54 12 37.2	1.0×0.5	22.6±0.23	21.4±0.51	0.8×10^{-5}	35.6

4.7 Comparison with Published Previous Works

Here, we discuss our results with the previously published similar works.

Wood et al. (1994) investigated nearly 100 nearby molecular clouds using the extensive all sky database of IRAS. The clouds covered a wide range of physical properties including visual extinction, size, mass, temperature, degree of ionization, morphology and homogeneity. They used 60 μm and 100 μm IRAS images to calculate the mentioned physical properties and their calculated dust temperature in the center of the cloud cores was in the range (20 to 25) K which is consistent with their conclusion that the dust on the exteriors of the clouds is heated by the interstellar radiation field. In our calculation, the dust color temperature of all the cavities are found in the range (17 to 26) K which is nearly similar with the result of Wood et al. (1994).

Jha et al. (2017) presented dust color temperature, dust mass and inclination angle of four far infrared loops namely G007+18, G143+07, G214-01 and G323-02 which are located within 1° from nearby pulsars PSR J1720-1633, PSR J0406+6138, PSR J0652-0142 and PSR J1535-5848, respectively. They found the dust color temperature of the core region which lie in the range (19.4 ± 1.2) K to (25.3 ± 1.7) K, whereas the range increased to (33 ± 2) K to (47 ± 3) K for the outer region. They measured average dust mass of each pixel of the four loops which lie in the range 2.96×10^{26} kg to 1822.2×10^{26} kg. The dust color temperature and dust mass distribution maps show that the low temperature region has greater density as expected. We have used similar method for calculation of dust color temperature and dust mass. Dust color temperature of our cavities lie in the range (17 to 26) K, where as average dust mass range is 4.9×10^{25} kg to 5.6×10^{28} kg.

Jha & Aryal (2018) measured dust color temperature of two far infrared cavities lying nearly at the galactic plane (−3°) using IRIS and AKARI maps where IRIS is used at 60 μm and 100 μm where as AKARI is used at 90 μm and 140 μm. From IRIS, the measured dust color temperature of the two cavities are found to lie in the range (23.4 ± 1.3) K to (24.1 ± 1.4) K with an offset of only 0.7 K and (22.2 ± 1.2) K to (24.6 ± 1.3) K, with an offset of about 2.4 K respectively. Similarly from AKARI, the measured dust color temperature of the cavities lie in the range (26.0 ± 1.5)K to (28.1 ± 1.6) K, with an offset of 2.1 K and (25.4 ± 1.4) K to (29.7 ± 1.7) K,with a larger offset of 4.3 K respectively. The difference between the value of average dust color temperatures at IRIS and AKARI is found to be (3.2 ± 0.9) K and (4.1 ± 1.2) K in the respective cavities. At longer wavelengths (AKARI) dust color temperature is found larger than in the shorter wavelength (IRIS) region. We used similar method for

calculation of dust color temperature but used 60 μm and 100 μm IRAS map and found the results matching nearly to IRIS survey but little bit far from the AKARI survey which is usual behavior.

Aryal & Weinberger (2006) have determined the dust colour temperature of the skeleton nebula using (Henning et al., 1990). The average dust colour temperature in the nebular region was found to be (27 ± 4) K which is quite near to our calculated values. They also measured the dust color temperature throughout the nebular region by using the 60 μm and 100 μm IRAS map and compared the resulting I(100 μm)/I(60 μm) values at each map location with the values given for dust grain models by Dwek (1986). They further estimated the total mass of the skeleton nebula using the relation given by Hildebrand (1983). Based on fluxes of 3.2×10^4 MJy/sr at 100 μm , and assuming a gas-to-dust mass ratio (g:d) of 150, $D = 0.2$ kpc, and $T_{\rm d} = (27 \pm 4)$ K, the total mass is (3.5 ± 2.3) $M_\odot$ which is also more or less close to our calculated dust mass of the cavities. Far infrared spectral distribution of skeleton nebula and MBM 20 nebula are comparable with our results which help to make an idea about the far infrared cavities.

Weinberger & Aryal (2004) studied dust structures around two planetary nebula (PNe) NGC 6826 and NGC 2899 under 60 μm and 100 μm IRAS maps. They found different structures. These structures apparently started to form the Asymptotic Giant Branch (AGB) phase, which are not spherically symmetric, and can shape the halos of PNe because of interaction. Later they (Aryal& Weinberger,2009) extended their study and noticed that NGC 6826 is a giant($\sim 2^\circ$) bipolar dust emission, whose axis is along the proper motion of the central star. They found that the NGC 2899 is located at the center of a 14×11 pc quadrupolar cavity, whose directions of axes coincide with the directions of the main axes of the optical PN. In both cases,the formation of these structures appears to have commenced in the asymptotic giant branch (AGB) phase. Therefore, the effect of wind emitted from AGB star has an important role in the process of shaping structure. In our case, we noticed several such cavity like structures located nearby the AGB stars, having similar size, positions and dust properties.

Aryal et al. (2010) found a dust structure around the planetary nebula NGC 1514 at 60 μm and 100 μm IRAS maps. They found the 60 μm and 100 μm flux densities of this region and calculated dust colour temperature which is around (29 ± 3) K. We have used same method for calculation of dust color temperature and found around (17 to 26) K in our far infrared cavities. Therefore the dust color temperature of nebula is at the upper limit than that of the far infrared cavities.

Ueta et al. (2006) presented the first results of the MIRIAD (MIPS Infra Red Imaging of AGB Dust shells) project using the Spitzer Space Telescope. They successfully detected a faint (< 5MJy/sr), extended (400") far-infrared nebula around the asymptotic giant

branch (AGB) star R Hya. They suggested that the detected far-IR nebula is due to a bow shock at the interface of the interstellar medium and the AGB wind of this moving star. In our case, we found several possible AGB wind region in the 100 μm contour maps of the cavities where the dust color temperature and dust mass distribution show Gaussian nature.

Aryal et al. (2010) presented about a giant dusty bipolar structure around the planetary nebula NGC 1514 using IRAS maps at 12 μm, 25 μm, 60 μm and 100 μm wavelength band. According to them, the transition from spherically symmetric asymptotic giant branch mass loss to aspherical planetary nebulae is an intriguing problem of stellar astrophysics. They detected a huge (2.6 pc) dust emission region around the evolved planetary nebula NGC 1514 at 12 μm. Additionally, they found two giant (2.1 pc and 0.9 pc) bipolar dust emission structures centred on NGC 1514 at 100 μm and 60 μm IRAS maps, so that they suspected that each of these regions is physically connected to the planetary nebula. Such concept of dust emission structure provided us to work on the far infrared cavities around the AGB stars under IRAS maps.They measured dust color temperature as (29 ± 3) K using 60 μm and 100 μm IRAS maps and (30 ± 3) K using 12 μm and 25 μm maps. We used similar method and found dust color temperature in the range (17 to 26) K. Total mass of all structures is (2.2 ± 1.4) $M_{\odot}$ but in our case, it lies in the range (0.01 to 1.81) $M_{\odot}$.

CHAPTER 5

5. CONCLUSIONS AND RECOMMENDATIONS

5.1 Conclusion

The physical properties of eighteen far infrared cavities at far infrared (60 μm and 100 μm) IRAS maps are studied. These cavities are found to be located around AGB stars near the Galactic plane. These cavities are further studied at mid infrared (12 μm and 25 μm) maps. We studied dust color temperature, dust mass, Planck function, visual extinction, variation of Planck function along major and minor diameter passing through minimum flux density region and variation of visual extinction with dust color temperature of the core region of the cavities. For the calculation of dust mass, distance is needed. For this, we used the database given by Szczerba et al. (2007), Kiss et al. (2004) and Könyves et al. (2007). We conclude our results as follows:

1. We studied a catalog of AGB stars (IRAS point source catalog) provided by Suh & Kwon (2009) and tried to find out lying within the far infrared loops (Kiss et al. 2004 and Koenyves et al. 2007). Distance between the selected AGB stars and the KK-loops are found in the range (0.72 to 3.02) arc deg. As expected, a large number of AGB stars have been found which are located within the far infrared loops in the interstellar medium. The selected AGB stars lie within the KK-loops in the range (2.2 to 8.4) arc deg along major diameter. After the selection of AGB stars from different catalogs as mentioned in the chapter methods and materials (chapter 3), strong far infrared cavities around the AGB stars are selected and studied.

2. Size of the core region of the cavities CCRAS1, CCRAS2, CCRAS3, CCRAS4, CCRAS5, CCRAS6, CCRAS7, CCRAS8, CCRPAS1 and CCRPAS2 are found to be 0.5°× 0.2°, 0.6°× 0.2°, 0.7°× 0.2°, 0.3°× 0.2°, 0.3°× 0.14°, 0.4°× 0.2°, 0.3°× 0.2°, 0.6°× 0.2°, 1.0°× 0.3° and 0.9°× 0.4° respectively. Similarly size of the remaining cavities CASKK1, CASKK2, CASKK3, CASKK4, CASKK5, CASKK6, CASKK7 and CASKK8 are 0.7°× 0.2°, 0.6°× 0.2°, 0.7°× 0.4°, 0.6°× 0.4°, 0.6°× 0.3°, 0.7°× 0.3°, 0.8°× 0.3°, 1.0°× 0.5° respectively.

3. Minimum and maximum dust color temperature of all eighteen far infrared cavities using 60 μm and 100 μm IRAS maps are measured. Cavity CASKK7 has the lowest dust color temperature i.e., (17.7 ± 1.40) K and the cavity CCRAS8 has the highest dust color temperature i.e., (25.0 ± 0.45) K. From the calculated dust color temperature, it is found that higher the flux density, higher the dust color temperature and vice versa. But in lower wave length region, dust color temperature are found higher which is obtained by measuring it in 12 μm, 25 μm and 60 μm IRAS maps.

4. In all eighteen cavities, we have plotted Gaussian fit for dust color temperature. Cavities CASKK4, CCRAPS2 and CCRAS6 showed a very poor Gaussian fit but cavities CASKK6, CCRAS7 and CCRAS8 showed a very good agreement with Gaussian fit.

5. We measured and analyzed dust mass of ten far infrared cavities. Cavity CASKK1 has the lowest average mass of each pixel and total mass of the cavity among the ten. Average dust mass of the cavity is 4.93×10^{25} kg and total mass is 1.86×10^{28} kg. Similarly cavity CCRPAS1 has the highest average dust mass and total dust mass among the ten. Average dust mass of the cavity is 5.60×10^{28} kg and total dust mass is 2.47×10^{31} kg.

6. From the contour map of dust color temperature and dust mass of the ten cavities, it is found that most of the cavities except CASKK1 and CCRPAS2 follow cosmological principle so that distribution of the particles are homogeneous and isotropy at large scale. Two cavities which are not following the cosmological principle possibly due to many unknown nearby sources.

7. Distribution of Planck function along extension and compression are nearly random means the particles along extension and compression passing through minima are not in thermal equilibrium and are not obeying Maxwellian velocity distribution which is possibly due to external factors.

8. We measured visual extinction of all the eighteen cavities and they are fitted linearly in the scattered plot with their dust color temperature. Mostly all the cavities show excellent correlation between the data with highest correlation coefficient −0.98. From this result, we found a new relation i.e. $A_V \times T_d$ = constant.

9. We worked in four bands (12 μm, 25 μm, 60 μm and 100 μm) under IRAS maps specially on two cavities CCRAS7 and CCRAS8. We measured dust color temperature at the boundary of 12 μm and 25 μm, 25 μm and 60 μm and 60 μm and 100 μm wavelength region where dust color temperature is found higher in low wave length region. From the Gaussian fit of all three temperature, it is

found that low temperature region perfectly follows Gaussian distribution but as the temperature increases, it violets the Gaussian distribution.

10. We measured flux density of all eighteen far infrared cavities in four IRAS bands and their spectral distributions are studied. Most of the cavities except CCRAS7 and CCRAS8 showed similar nature i.e., there is positive slope in the transition from 12 μm to 25 μm and 60 μm to 100 μm but there is negative slope from 25 μm to 60 μm which is one of the most important property of the far infrared cavities found in this work.

5.2 Recommendation

We strongly recommend following works to be carried out in the future.

1. It is found that the product of dust color temperature and visual extinction of all eighteen cavities give a consistent value in certain range. This study can be extended for KK-loops (Jha et al., 2017) using AKARI survey (90 μm and 140 μm) also.
2. The superposition and suitable interaction of these loops with the AGB stars or other sources can be studied and additionally the amount of expelled mass from the central region can be calculated in order to estimate the energy required for the structure formation.
3. Our work can be extended for near infrared wavelength using SPITZER data and 12 μm and 25 μm IRAS data. These surveys can be used to study the upper limit for the dust color temperature, to estimate the size of the dust and grain.
4. This work can be further extended to study interaction between far infrared cavities and the AGB stars or planetary nebula or white dwarf under IRAS survey in all four bands.

5.3 Limitations of the Study

Following facts are the limitations of this study:

1. The precession of our calculations depend on the resolution of IRAS telescope. The error bars is the statistical one. This do not include instrumental error.
2. Since the spectroscopy of data is not known, the nature of dust species is unidentified. This is possible only when we will have telescopes with better resolution (up to arc seconds) with far infrared spectroscopy.

CHAPTER 6

6. SUMMARY

In this thesis, we searched far infrared cavities nearby the AGB stars and have studied their physical properties (dust color temperature, dust mass, visual extinction, size of the cavities, variation of Planck function along extension and compression, variation of flux density with wave length in four different bands specially at 12 μm, 25 μm, 60 μm and 100 μm, distribution of dust color temperature and visual extinction, etc.) of the far infrared (FIR) cavities around the AGB stars in the ISM. The FIR cavities are located close to the galactic plane. Our aim is to understand the formation and evolution process of such cavities. In this work, we selected 18 FIR cavities around the AGB stars. For the selection of the cavities, three catalogs were extensively used. One catalog is AGB based IRAS point source catalog provided by Suh & Kwon (2009), second catalog is about post-AGB stars named "the Torun catalog of Galactic post-AGB and related objects" provided by Szczerba et al. (2007) and third one is Far Infrared Loop based, provided by Kiss et al. (2004) and Könyves et al. (2007) in the IRAS maps also called Galactic Infrared Loop (GIRL) catalog. We have used Infrared Astronomical Satellite (IRAS) survey for the database. We have searched cavity like structures systematically in far infrared (60 μm and 100 μm) IRAS maps. For the selection of FIR cavities, following selection criteria were imposed: (a) There should be strong cavity in closed region with minimum flux density. The structure should be isolated and its size is more than 0.5 degree in diameter. (b) There should be a minima and the features can be seen in all four bands of IRAS survey. (c) The structure should be prominent in 60 μm and 100 μm that enables us to study the fluxes emitted from the dust and grain. (d) The most important thing is that the selected structure should not yet studied or less studied.

From the catalog about AGB based IRAS point source provided by Suh & Kwon (2009), eight FIR cavities around the AGB stars without derived distance were selected. From the catalog about post-AGB stars provided by Szczerba et al. (2007), two FIR cavities around the post-AGB stars with derived distance were selected. Besides these, other eight FIR cavities around the AGB stars provided by Suh & Kwon (2009) lying with in the far infrared loops (Kiss et al., 2004) and (Könyves et al., 2007) in the IRAS maps

with known distances were selected. We have used the method developed by Dupac et al. (2003) and Schnee et al. (2005), to calculate dust color temperature and the method developed by Hildebrand (1983) to calculate dust mass in the region of interest. For the calculation of optical depth and visual extinction of all the cavities, we used the method developed by Wood et al. (1994). We have calculated size, dust color temperature, Planck function, dust mass, optical depth and visual extinction. Calculated results of all the eighteen FIR cavities have been plotted and discussed. The slope of the best fit of scattered plot between flux at 60 μm (F60) versus flux at 100 μm (F100) is used to calculate the average temperature in the core region of each cavity. From the best fit between visual extinction and dust color temperature, a relation between them is found. In the paragraphs below we present summary of our results:

In the first section of result and discussion, we have studied all sky distribution of the selected eight far infrared cavities around the AGB stars discovered by Suh & Kwon (2009) in all four bands of IRAS maps using sky view virtual observatory. We have studied 60 μm and 100 μm far infrared images of core region of the cavities which are found to be located within 0.6° from AGB stars AGB0415+5441, AGB0609+1446, AGB0631+1606, AGB0633+1415, AGB0642+0053, AGB0651+0031, AGB0939-5249 and AGB1025-5933 respectively. The average value of dust color temperature are calculated by using the slope of the scattered plot between F(60) and F(100) which are used to calculate error in the dust color temperature. The dust color temperature, dust mass and visual extinction maps have been studied. The distribution of dust color temperature, dust mass, visual extinction of all eight cavities have been studied by Gaussian fit. The variation of flux density in four bands with wave lengths and distribution of dust color temperature and Planck function along diameters (major and minor passing through minima) were studied and compared. From this chapter we made out the following conclusions:

CCRAS3 is the biggest cavity and CCRAS5 is the smallest among the eight cavities. CCRAS1 has showed the lowest dust color temperature and the cavity CCRAS8 has the highest dust color temperature. Scattering plots of all the cavities between $F(60)$ and $F(100)$ show systematic behavior having positive slope, intercept and correlation coefficient where correlation coefficient ranges from 0.72 to 0.89 which justifies there is good correlation between them. Similar systematic behavior is strongly seen in the scattering plot between visual extinction and dust color temperature. But in this case, slope and correlation coefficient both are negative. Here correlation coefficient ranges from -0.64 to -0.92 which signifies a good agreement. From the best fit, it is found that the product of visual extinction and dust color temperature is consistent and is very very less than one. It means higher the visual extinction, lower the dust color temperature and vice-versa which is also approved by contour map of visual extinction and dust color

temperature. This result is disagreed by certain cavities due to oscillation of dust-grain in different directions. Similarly the scattering plot between distance (along major and minor diameters) with Planck function, did not show systematic trend. The offset value of dust color temperature of all the eight cavities is less than 2 K which suggests that the core of all the cavities are stable but there is random variation along both diameters suggesting external factors possibly due to near by AGB wind. From the Gaussian fit of dust color temperature at 100 μm wave length, cavity CCRAS5 showed completely non-Gaussian nature, cavities CCRAS4, CCRAS7 and CCRAS8 showed perfect Gaussian nature but as the wave length is decreased, increased dust color temperature violates the Gaussian fit. FIR spectral distributions of all the cavities except CCRAS7 and CCRAS8 showed different behavior possibly due to nearby bulge of the Galaxy.

Two new far infrared cavities around post-AGB stars based in the catalog provided by Szczerba et al. (2007) were searched in 60 and 100 μm IRAS maps and found they are centered at R.A.(J2000) = 06^h 51^m 54.0^s, Dec.(J2000) = -01° 35' 43" and R.A.(J2000) = 08^h 04^m 7.2^s, Dec.(J2000) = -37° 11' 48" respectively. In IRAS maps, their dust color temperatures, dust mass and visual extinction were calculated and studied by using different statistical methods. The distribution of dust color temperature and Planck function along extension and compression of both the cavities were also studied. The result of this chapter can be summarized as follows:

It is found that cavity CCRPAS1 is at lower temperature and CCRPAS2 is at higher temperature with an offset value of about 1.8 K and 0.9 K respectively. Such low offset value of temperature suggests that the dusts in the cavities are almost isolated, stable and in thermal equilibrium. Both the cavities show excellent Gaussian fit of dust color temperature with sharp peak and positive skewness but distribution of dust mass show moderate Gaussian fit with sharp peak and negative skewness. From the contour map of three plots of both the cavities, it is found that less temperature region is massive as well as high visual extinction and vice-versa. A very interesting result is that contour map of dust mass and visual extinction are exactly same which also verifies that dust particles of both the cavities strongly support cosmological principle. Average dust mass of each pixel of the cavities CCRPAS1 and CCRPAS2 are respectively calculated as 5.6×10^{28} kg and 8.7×10^{27} kg. From the plot between visual extinction and dust color temperature, it is concluded that $(T_\mathrm{d} \times A_\mathrm{V})$ is constant and is equal to 1.3×10^{-4}. It means higher the temperature, lower the visual extinction and vive-versa. It is also verified by contour map of dust color temperature and visual extinction. FIR distributions of both the cavities showed similar nature i.e., negative slope in transition from 25 μm to 60 μm and positive slope from 12 μm to 25 μm and 60 μm to 100 μm.

In the next chapter eight far infrared cavities CASKK1, CASKK2, CASKK3, CASKK4, CASKK5, CASKK6, CASKK7 and CASKK8 around the AGB stars AGB0141+7104,

AGB0409+6105, AGB0538+1216, AGB0555+2827, AGB0617-0634, AGB0619-0558, AGB0712-1720 and AGB1105-5451 lying with in the KK-loops named G125+09, G143+07, G195-11, G182+00, G212-11, G212-11, G229-03 and G287+04 respectively were selected. Flux density at 60 μm and 100 μm, dust color temperature, Planck function, dust mass and visual extinction are calculated and analyzed. The distribution of flux density, dust color temperature, dust mass and visual extinction were studied by using contour map, Gaussian fit and linear fit of the data. Variation of flux density in four bands with wave lengths were studied. Distribution of Planck function and dust color temperature along the extension and compression of the cavities were also studied. The results of this chapter can be summarized as follows:

From the calculated value, it is concluded that the cavity CASKK2 is the smallest and CASKK8 is the biggest among the eight cavities. Calculated minimum and maximum dust color temperature showed that cavity CASKK7 is the coldest and cavity CASKK3 is the hottest. Here offset value of dust color temperature of all the cavities is less than 2 K, suggests that the dusts in the cavities are almost in thermal equilibrium. From the three different contour maps of dust color temperature, dust mass, and visual extinction, it is found that most of the cavities more or less follow cosmological principle so that the particles are homogeneous and isotropy. Cavities CASKK3, CASKK4, CASKK7 and CASKK8 has very poor Gaussian fit of both dust color temperature and dust mass. Cavity CASKK6 showed excellent Gaussian fit of dust color temperature but poor of dust mass. Likewise cavities CASKK1, CASKK2 and CASKK5 showed poor Gaussian fit of both quantities. Poor Gaussian fit suggests that the particles are not following the natural process means they are effected by external causes possibly due to near by AGB wind. If we consider average dust mass per pixel of the eight cavities, the material of the cavity CASKK4 is found to be the heaviest (2.97×10^{28} kg) and the cavity CASKK1 is the lightest (4.93×10^{25} kg). The massive dust represents the polyaromatic hydrocarbons and the lightest dust represents the carbon or silicon compounds. From the best fit between visual extinction and dust color temperature, it is found that $A_V \times T_d$ = consistent and ranges from 0.6×10^{-4} to 2.0×10^{-4}. It means, higher the visual extinction, lower the dust color temperature and vice versa. This conclusion is strongly supported and verified by contour map of dust color temperature and visual extinction also. One important thing is that contour map of dust mass and visual extinction are exactly same in all the cavities. Distribution of Planck function along extension and compression is non-uniform means the particles along extension and compression passing through minima are oscillating in order to get dynamical equilibrium. Hence they are not in thermal equilibrium and are not obeying Maxwellian velocity distribution which is possibly due to external factors. FIR distributions of all eight cavities showed similar nature with the previously mentioned cavities CCRPAS1 and CCRPAS2.

REFERENCES

Aannestad, P. A. (1975, August). Absorptive properties of silicate core-mantle grains. *Astrophysical Journal*, *200*, 30-41. doi: 10.1086/153757

Arlandini, C., Käppeler, F., Wisshak, K., Gallino, R., Lugaro, M., Busso, M., & Straniero, O. (1999, November). Neutron Capture in Low-Mass Asymptotic Giant Branch Stars: Cross Sections and Abundance Signatures. *Astrophysical Journal*, *525*, 886-900. doi: 10.1086/307938

Aryal, B., Rajbahak, C., & Weinberger, R. (2010, February). A giant dusty bipolar structure around the planetary nebula ngc 1514. *Monthly Notices of the Royal Astronomical Society*, *402*, 1307-1312. Retrieved from http://adsabs.harvard.edu/abs/2010MNRAS.402.1307A doi: 10.1111/j.1365-2966.2009.15966.x

Aryal, B., & Weinberger, R. (2006, March). A new large high latitude cone-like far-ir nebula. *Astronomy and Astrophysics*, *448*, 213-219. Retrieved from http://adsabs.harvard.edu/abs/2006A%26A...448..213A doi: 10.1051/0004-6361:20042440

Becker, S. A. (1981, August). The thick helium-burning shell phase and the second blue loop. *Astrophysical Journal*, *248*, 298-310. doi: 10.1086/159154

Becker, S. A., & Iben, I., Jr. (1980, April). The asymptotic giant branch evolution of intermediate-mass stars as a function of mass and composition. II - Through the first major thermal pulse and the consequences of convective dredge-up. *Astrophysical Journal*, *237*, 111-129. doi: 10.1086/157850

Beichman, C. A., Neugebauer, G., Habing, H. J., Clegg, P. E., & Chester, T. J. (Eds.). (1988). *Infrared astronomical satellite (IRAS) catalogs and atlases. Volume 1: Explanatory supplement* (Vol. 1).

Beichman, C. A., Wilson, R. W., Langer, W. D., & Goldsmith, P. F. (1988, September). Infrared limb brightening in the Barnard 5 cloud. *The Astrophysical Journal Letters*, *332*, L81-L85. doi: 10.1086/185271

Bidelman, W. P. (1951, March). Spectral Classification of Stars Listed in Miss Payne's Catalogue of C Stars. *Astrophysical Journal*, *113*, 304. doi: 10.1086/145399

Blöcker, T., Herwig, F., Schönberner, D., & El Eid, M. (2000). How to Make Carbon Stars: A New Approach to Model Boundaries of Convective Regions. In R. F. Wing (Ed.), *The carbon star phenomenon* (Vol. 177, p. 524).

Bloecker, T. (1995, July). Stellar evolution of low- and intermediate-mass stars. II. Post-AGB evolution. *Astronomy and Astrophysics*, *299*, 755.

Bonnarel, F., Fernique, P., & Bienaymé, O. (2000, April). The ALADIN interactive sky atlas. A reference tool for identification of astronomical sources. *Astronomy and Astrophysics, Supplement*, *143*, 33-40. doi: 10.1051/aas:2000331

Boothroyd, A. I., & Sackmann, I.-J. (1992, July). Breakdown of the core mass-luminosity relation at high luminosities on the asymptotic giant branch. *The Astrophysical Journal Letters*, *393*, L21-L24. doi: 10.1086/186441

Boothroyd, A. I., & Sackmann, I.-J. (1999, January). The CNO Isotopes: Deep Circulation in Red Giants and First and Second Dredge-up. *Astrophysical Journal*, *510*, 232-250. doi: 10.1086/306546

Boothroyd, A. I., Sackmann, I.-J., & Ahern, S. C. (1993, October). Prevention of High-Luminosity Carbon Stars by Hot Bottom Burning. *Astrophysical Journal*, *416*, 762. doi: 10.1086/173275

Bowen, G. H. (1988a, June). Dynamical modeling of long-period variable star atmospheres. *Astrophysical Journal*, *329*, 299-317. doi: 10.1086/166378

Bowen, G. H. (1988b). The Mechanism of Mass Loss from Pulsating Cool Stars. In R. Stalio & L. A. Willson (Eds.), *Pulsation and mass loss in stars* (Vol. 148, p. 3). doi: 10.1007/978-94-009-3029-2_1

Brand, P. W. J. L., & Zealey, W. J. (1975, February). Cloud structure in the galactic plane - A cosmic bubble bath. *Astronomy and Astrophysics*, *38*, 363-371.

Busso, M., Straniero, O., Gallino, R., & Abia, C. (2004). s-Processing in AGB Stars and the Composition of Carbon Stars. *Origin and Evolution of the Elements*, 67.

Cameron, A. G. W., & Fowler, W. A. (1971, February). Lithium and the s-PROCESS in Red-Giant Stars. *Astrophysical Journal*, *164*, 111. doi: 10.1086/150821

Cardelli, J. A., Clayton, G. C., & Mathis, J. S. (1989, October). The relationship between infrared, optical, and ultraviolet extinction. *Astrophysical Journal*, *345*, 245-256. doi: 10.1086/167900

Cerrigone, L., Menten, K. M., & Kamiński, T. (2012, June). CO observations of water-maser post-asymptotic giant branch stars and detection of a high-velocity

outflow in IRAS 15452-5459. *Astronomy and Astrophysics*, *542*, A15. doi: 10.1051/0004-6361/201118683

Chan, S. J., & Kwok, S. (1990, October). Evolution of infrared carbon stars. *Astronomy and Astrophysics*, *237*, 354-368.

Cherchneff, I. (2006, September). A chemical study of the inner winds of asymptotic giant branch stars. *Astronomy and Astrophysics*, *456*, 1001-1012. doi: 10.1051/0004-6361:20064827

Clayton, G. C. (1996, March). The R Coronae Borealis Stars. *Publications of the Astronomical Society of the Pacific*, *108*, 225. doi: 10.1086/133715

Cox, D. P. (2005, September). The Three-Phase Interstellar Medium Revisited. *Annual Review of Astron and Astrophys*, *43*, 337-385. doi: 10.1146/annurev.astro.43.072103.150615

de Jager, C., Nieuwenhuijden, H., & van der Hucht, K. A. (1988, December). Mass Loss Rates in the Hertzprung-Russell Diagram. *Bulletin d'Information du Centre de Donnees Stellaires*, *35*, 141.

Desert, F.-X., Boulanger, F., & Puget, J. L. (1990, October). Interstellar dust models for extinction and emission. *Astronomy and Astrophysics*, *237*, 215-236.

Dorschner, J., & Henning, T. (1995). Dust metamorphosis in the galaxy. *Astronomy and Astrophysics Reviews*, *6*, 271-333. doi: 10.1007/BF00873686

Draine, B. T., Dale, D. A., Bendo, G., Gordon, K. D., Smith, J. D. T., Armus, L., ... Teplitz, H. I. (2007, July). Dust Masses, PAH Abundances, and Starlight Intensities in the SINGS Galaxy Sample. *Astrophysical Journal*, *663*, 866-894. doi: 10.1086/518306

Draine, B. T., & Lee, H. M. (1984, October). Optical properties of interstellar graphite and silicate grains. *Astrophysical Journal*, *285*, 89-108. doi: 10.1086/162480

Dupac, X., Bernard, J.-P., & Boudet, N. (2003, June). Inverse temperature dependence of the dust submillimeter spectral index. *Astronomy and Astrophysics*, *404*, L11-L15. doi: 10.1051/0004-6361:20030575

Dwek, E. (1986, March). Temperature fluctuations and infrared emission from dust particles in a hot gas. *Astrophysical Journal*, *302*, 363-370. doi: 10.1086/163995

Egan, M. P., Price, S. D., & Kraemer, K. E. (2003, December). The Midcourse Space Experiment Point Source Catalog Version 2.3. In *American astronomical society meeting abstracts* (Vol. 35, p. 1301).

El Eid, M. F. (1994, May). CNO isotopes in red giants: theory versus observations. *Astronomy and Astrophysics*, *285*, 915-928.

Feigelson, E. D., & Frenklach, M. (1989, December). PAH formation in carbon-rich circumstellar envelopes. In L. J. Allamandola & A. G. G. M. Tielens (Eds.), *Interstellar dust* (Vol. 135, p. 479-483).

Fox, M. W., & Wood, P. R. (1982, August). Theoretical growth rates, periods, and pulsation constants for long-period variables. *Astrophysical Journal*, *259*, 198-212. doi: 10.1086/160160

Frost, C. A., & Lattanzio, J. C. (1996, December). On the Numerical Treatment and Dependence of the Third Dredge-up Phenomenon. *Astrophysical Journal*, *473*, 383. doi: 10.1086/178152

Fujimoto, M. Y. (1977). On the Origin of R-Type Carbon Stars: Possibility of Hydrogen Mixing during Helium Flicker. *Publications of the Astronomical Society of Japan*, *29*, 331-350.

Gallino, R., Arlandini, C., & Busso, M. (1998, April). Evolution and Nucleosynthesis in Low-Mass Asymptotic Giant Branch Stars. II. Neutron Capture and the S-Process. *Astrophysical Journal*, *497*, 388-403. doi: 10.1086/305437

Gautam, A. K., & Aryal, B. (2017). Study of dusty environment around a carbon-rich agb star in far infrared maps at latitude 15°. *ISST Journal of Applied Physics*, *8*(1), 92-96.

Gautam, A. K., & Aryal, B. (2018a). A study of dusty environment at far infrared iras map around the mass-losing carbon-rich agb star at latitude −53°. *ISST Journal of Applied Physics*, *9*(1), 24-28.

Gautam, A. K., & Aryal, B. (2018b). A study of dusty environment at far infrared iras map around the mass -losing carbon-rich agb star at latitude −59.6°. *International Journal of Multidisciplinary Research Review*, *1*(35), 45-50.

Gautam, A. K., & Aryal, B. (2019, April). A study of four low-latitude ($|l| < 10°$) far-infrared cavities. *Journal of Astrophysics and Astronomy*, *40*, 16. doi: 10.1007/s12036-019-9578-1

Gehrz, R. D. (1988). The infrared temporal development of classical novae. *Annual Review of Astron and Astrophys*, *26*, 377-412. doi: 10.1146/annurev.aa.26.090188.002113

Gilman, R. C. (1972, December). On the Coupling of Grains to the Gas in Circumstellar Envelopes. *Astrophysical Journal*, *178*, 423-426. doi: 10.1086/151800

Groenewegen, M. A. T., van den Hoek, L. B., & de Jong, T. (1995, January). The evolution of galactic carbon stars. *Astronomy and Astrophysics*, *293*, 381-395.

Gustafsson, B., Edvardsson, B., Eriksson, K., Mizuno-Wiedner, M., Jørgensen, U. G., & Plez, B. (2003, January). A Grid of Model Atmospheres for Cool Stars. In I. Hubeny, D. Mihalas, & K. Werner (Eds.), *Stellar atmosphere modeling* (Vol. 288, p. 331).

Habing, H. J. (1996). Circumstellar envelopes and Asymptotic Giant Branch stars. *Astronomy and Astrophysics Reviews*, *7*, 97-207. doi: 10.1007/PL00013287

Habing, H. J., & Olofsson, H. (Eds.). (2003). *Asymptotic giant branch stars.*

Henning, T., Pfau, W., & Altenhoff, W. J. (1990, January). Infrared and radio emission from very young and massive stellar objects. *Astronomy and Astrophysics*, *227*, 542-552.

Herwig, F. (2005, September). Evolution of Asymptotic Giant Branch Stars. *Annual Review of Astron and Astrophys*, *43*, 435-479. doi: 10.1146/annurev.astro.43 .072103.150600

Hildebrand, R. H. (1983, September). The Determination of Cloud Masses and Dust Characteristics from Submillimetre Thermal Emission. *Quarterly Journal of the Royal Astronomical Society*, *24*, 267.

Hildebrand, R. H., Whitcomb, S. E., Winston, R., Stiening, R. F., Harper, D. A., & Moseley, S. H. (1977, September). Submillimeter photometry of extragalactic objects. *Astrophysical Journal*, *216*, 698-705. doi: 10.1086/155512

Hoyle, F., & Wickramasinghe, N. C. (1967, June). Impurities in Interstellar Grains. *Nature*, *214*, 969-971. doi: 10.1038/214969a0

Iben, I., & Renzini, A. (Eds.). (1981). *Physical processes in red giants*. Springer Netherlands. doi: 10.1007/978-94-009-8492-9

Iben, I., Jr. (1967, February). Stellar Evolution.VI. Evolution from the Main Sequence to the Red-Giant Branch for Stars of Mass 1 M_{sun}, 1.25 M_{sun}, and 1.5 M_{sun}. *Astrophysical Journal*, *147*, 624. doi: 10.1086/149040

Iben, I., Jr. (1975, March). Thermal pulses; p-capture, alpha-capture, s-process nucleosynthesis; and convective mixing in a star of intermediate mass. *Astrophysical Journal*, *196*, 525-547. doi: 10.1086/153433

Iben, I., Jr. (1981, May). The carbon star mystery - Why do the low mass ones become such, and where have all the high mass ones gone. *Astrophysical Journal*, *246*, 278-291. doi: 10.1086/158921

Iben, I., Jr., & Renzini, A. (1983). Asymptotic giant branch evolution and beyond. *Annual Review of Astron and Astrophys*, *21*, 271-342. doi: 10.1146/annurev.aa .21.090183.001415

Jarrett, T. H., Dickman, R. L., & Herbst, W. (1989, October). Far-infrared emission in the Rho Ophiuchi region - A comparison with molecular gas emission and visual extinction. *Astrophysical Journal*, *345*, 881-893. doi: 10.1086/167958

Jha, A., Aryal, B., & Weinberger, R. (2017). A study of dust color temperature and dust mass distributions of four far infrared loops. *Revista Mexicana de Astronomía y Astrofísica*, *53*(2), 467–476.

Jha, A. K., & Aryal, B. (2018, April). Dust color temperature distribution of two fir cavities at iris and akari maps. *Journal of Astrophysics and Astronomy*, *39*, 24. doi: 10.1007/s12036-018-9517-6

Jones, T. W., Ney, E. P., & Stein, W. A. (1981, November). Pulsations Grain Condensation and Mass Loss in Long-Period Variable Stars. *Astrophysical Journal*, *250*, 324. doi: 10.1086/159378

Jura, M. (1986, October). RV Tauri stars as post-asymptotic giant branch objects. *Astrophysical Journal*, *309*, 732-736. doi: 10.1086/164642

Karakas, A. I., Lattanzio, J. C., & Pols, O. R. (2002). Parameterising the Third Dredge-up in Asymptotic Giant Branch Stars. *Publications of the Astronomical Society of Australia*, *19*, 515-526. doi: 10.1071/AS02013

Karttunen, H., Krüger, P., Oja, H., Poutanen, M., & Donner, K. J. (Eds.). (2007). *Fundamental Astronomy*.

Kessler, M. F., Steinz, J. A., Anderegg, M. E., Clavel, J., Drechsel, G., Estaria, P., ... Ximénez de Ferrán, S. (1996, November). The Infrared Space Observatory (ISO) mission. *Astronomy and Astrophysics*, *315*, L27-L31.

Kiss, C., Moor, A., & Toth, L. V. (2004, January). VizieR Online Data Catalog: Far-infrared loops in the 2nd Galactic Quadrant (Kiss+, 2004). *VizieR Online Data Catalog*, *1000*.

Kleinmann, S. G., Gillett, F. C., & Joyce, R. R. (1981). Preliminary results of the Air Force infrared sky survey. *Annual Review of Astron and Astrophys*, *19*, 411-456. doi: 10.1146/annurev.aa.19.090181.002211

Knacke, R. F., & Thomson, R. K. (1973, June). Infrared Extinction Cross Sections of Silicate Grains. *Publications of the Astronomical Society of the Pacific*, *85*, 341. doi: 10.1086/129467

Könyves, V., Kiss, C., Moór, A., Kiss, Z. T., & Tóth, L. V. (2007, March). Catalogue of far-infrared loops in the Galaxy. *Astronomy and Astrophysics*, *463*, 1227-1234. doi: 10.1051/0004-6361:20065438

Kozasa, T., Hasegawa, H., & Seki, J. (1984, January). Grain formation in the expanding gas flow around cool luminous stars. *Astrophysics and Space Science*, *98*, 61-79. doi: 10.1007/BF00651951

Kramer, C., Richer, J., Mookerjea, B., Alves, J., & Lada, C. (2003, March). Dust properties of the dark cloud IC 5146. Submillimeter and NIR imaging. *Astronomy and Astrophysics*, *399*, 1073-1082. doi: 10.1051/0004-6361:20021823

Kwok, S. (1975, June). Radiation pressure on grains as a mechanism for mass loss in red giants. *Astrophysical Journal*, *198*, 583-591. doi: 10.1086/153637

Kwok, S., Hrivnak, B. J., & Boreiko, R. T. (1987, January). Ground-based observations of IRAS candidates for late asymptotic giant branch stars. *Astrophysical Journal*, *312*, 303-313. doi: 10.1086/164874

Kwok, S., Volk, K., & Bidelman, W. P. (1997, October). Classification and Identification of IRAS Sources with Low-Resolution Spectra. *The Astrophysical Journal Supplement*, *112*, 557-584. doi: 10.1086/313038

Kwok, S., Volk, K. M., & Hrivnak, B. J. (1989, October). A 21 micron emission feature in four proto-planetary nebulae. *The Astrophysical Journal Letters*, *345*, L51-L54. doi: 10.1086/185550

Kwon, Y.-J., & Suh, K.-W. (2014, August). A New Catalog of Silicate Carbon Stars. *Journal of Korean Astronomical Society*, *47*, 123-135. doi: 10.5303/JKAS.2014.47.4.123

Lagache, G., Abergel, A., Boulanger, F., & Puget, J.-L. (1998, May). The interstellar cold dust observed by COBE. *Astronomy and Astrophysics*, *333*, 709-720.

Lamers, H. J. G. L. M. (1981, April). Mass loss from O and B stars. *Astrophysical Journal*, *245*, 593-608. doi: 10.1086/158835

Langer, W. D., Wilson, R. W., Goldsmith, P. F., & Beichman, C. A. (1989, February). Dust and gas emission in Barnard 5. *Astrophysical Journal*, *337*, 355-381. doi: 10.1086/167108

Le Bertre, T., Tanaka, M., Yamamura, I., Murakami, H., & MacConnell, D. J. (2005, February). Carbon Stars in the Infrared Telescope in Space Survey. *Publications of the Astronomical Society of the Pacific*, *117*, 199-206. doi: 10.1086/427986

Lewis, B. M., Eder, J., & Terzian, Y. (1990, October). New OH/IR stars from color-selected IRAS sources. II - an unbiased 1612 MHz survey. *Astrophysical Journal*, *362*, 634-651. doi: 10.1086/169302

Maeder, A. (1992, October). Stellar yields as a function of initial metallicity and mass limit for black hole formation. *Astronomy and Astrophysics*, *264*, 105-120.

Maercker, M. (2009). *Asymptotic Giant Branch stars viewed up-close and far-off : The physics, chemistry, and evolution of their circumstellar envelopes* (Unpublished doctoral dissertation). University of Stockholm.

Markwick, A. J., Millar, T. J., & Charnley, S. B. (2000, May). On the Abundance Gradients of Organic Molecules along the TMC-1 Ridge. *Astrophysical Journal*, *535*, 256-265. doi: 10.1086/308814

Moehler, S., & Heber, U. (1998, July). PG 1323-086 and PG 1704+222 - two post-AGB stars at high galactic latitudes. *Astronomy and Astrophysics*, *335*, 985-990.

Mowlavi, N., & Meynet, G. (2000, September). Aluminum 26 production in asymptotic giant branch stars. *Astronomy and Astrophysics*, *361*, 959-976.

Murakami, H., Bock, J., Freund, M. M., & Guo, H. (1994, June). The Infrared Telescope in Space (IRTS). *Astrophysical Journal*, *428*, 354-362. doi: 10.1086/174246

Nagata, H., Shibai, H., Takeuchi, T. T., & Onaka, T. (2002, October). A New Empirical Method for Estimating the Far-Infrared Flux of Galaxies. *Publications of the Astronomical Society of Japan*, *54*, 695-705. doi: 10.1093/pasj/54.5.695

Neugebauer, G., Habing, H. J., van Duinen, R., Aumann, H. H., Baud, B., Beichman, C. A., . . . Young, E. (1984, March). The Infrared Astronomical Satellite (IRAS) mission. *The Astrophysical Journal Letters*, *278*, L1-L6. doi: 10.1086/184209

Neugebauer, G., & Leighton, R. B. (1969). *Two-micron sky survey. A preliminary catalogue*.

Nieuwenhuijzen, H., & de Jager, C. (1988, September). The relation between rotational velocity and mass-loss for massive stars. *Astronomy and Astrophysics*, *203*, 355-360.

Odenwald, S. F., & Rickard, L. J. (1987, July). Hydrodynamical processes in the Draco molecular cloud. *Astrophysical Journal*, *318*, 702-711. doi: 10.1086/165404

Oudmaijer, R. D. (1996, February). A search for hot post-AGB stars in the IRAS Point Source Catalog. *Astronomy and Astrophysics*, *306*, 823.

Pace, G., Castro, M., Meléndez, J., Théado, S., & do Nascimento, J.-D., Jr. (2012, May). Lithium in M 67: From the main sequence to the red giant branch. *Astronomy and Astrophysics*, *541*, A150. doi: 10.1051/0004-6361/201117704

Padmanabhan, T. (2006). *An Invitation To Astrophysics* (Vol. 8). doi: 10.1142/6010

Palen, S. E. (2001). *Schaum's outline of astronomy*. New York, United States of America: McGraw Hill Professional.

Parthasarathy, M., & Pottasch, S. R. (1986, January). The far-infrared (IRAS) excess in HD 161796 and related stars. *Astronomy and Astrophysics*, *154*, L16-L19.

Pottasch, S. R., & Parthasarathy, M. (1988, March). The far-infrared (IRAS) excess in luminous F-G stars. *Astronomy and Astrophysics*, *192*, 182-186.

Pouw, A. (1983, January). The IRAS spacecraft. *Journal of the British Interplanetary Society*, *36*, 17-20.

Preston, G. W., Krzeminski, W., Smak, J., & Williams, J. A. (1963, February). A Spectroscopic and Photoelectric Survey of the RV Tauri Stars. *Astrophysical Journal*, *137*, 401. doi: 10.1086/147520

Puget, J. L., Leger, A., & Boulanger, F. (1985, January). Contribution of large polycyclic aromatic molecules to the infrared emission of the interstellar medium. *Astronomy and Astrophysics*, *142*, L19-L22.

Purcell, E. M. (1969, November). On the Absorption and Emission of Light by Interstellar Grains. *Astrophysical Journal*, *158*, 433. doi: 10.1086/150207

Ramstedt, S., Schöier, F. L., & Olofsson, H. (2009, May). Circumstellar molecular line emission from S-type AGB stars: mass-loss rates and SiO abundances. *Astronomy and Astrophysics*, *499*, 515-527. doi: 10.1051/0004-6361/200911730

Reich, P., Reich, W., & Furst, E. (1997, December). The Effelsberg 21 CM radio continuum survey of the Galactic plane between L = 95.5 deg and L = 240 deg. *Astronomy and Astrophysics, Supplement*, *126*, 413-435. doi: 10.1051/aas:1997274

Reimers, D. (1975). Circumstellar envelopes and mass loss of red giant stars. In B. Baschek, W. H. Kegel, & G. Traving (Eds.), *Problems in stellar atmospheres and envelopes.* (p. 229-256).

Renzini, A., & Fusi Pecci, F. (1988). Tests of evolutionary sequences using color-magnitude diagrams of globular clusters. *Annual Review of Astron and Astrophys*, *26*, 199-244. doi: 10.1146/annurev.aa.26.090188.001215

Sasselov, D. D. (1984, July). The UU Her-type stars - Possible tracers of recent star formation at high galactic latitudes. *Astrophysics and Space Science*, *102*, 161-178. doi: 10.1007/BF00651069

Schnee, S. L., Ridge, N. A., Goodman, A. A., & Li, J. G. (2005, November). A COMPLETE Look at the Use of IRAS Emission Maps to Estimate Extinction and Dust Temperature. *Astrophysical Journal*, *634*, 442-450. doi: 10.1086/491729

Schröder, K.-P., & Cuntz, M. (2005, September). A New Version of Reimers' Law of Mass Loss Based on a Physical Approach. *The Astrophysical Journal Letters*, *630*, L73-L76. doi: 10.1086/491579

Schwarzschild, M., & Härm, R. (1967, December). Hydrogen mixing by helium-shell flashes. *Astrophysical Journal*, *150*, 961. doi: 10.1086/149396

Skrutskie, M. F., Cutri, R. M., Stiening, R., Weinberg, M. D., Schneider, S., Carpenter, J. M., ... Wheelock, S. (2006, February). The Two Micron All Sky Survey (2MASS). *Astronomical Journal*, *131*, 1163-1183. doi: 10.1086/498708

Smith, V. V., Lambert, D. L., & McWilliam, A. (1987, September). Neutron-exposure variations in MS and S stars, and the implications for s-process nucleosynthesis. *Astrophysical Journal*, *320*, 862-865. doi: 10.1086/165601

Snell, R. L., Schloerb, F. P., & Heyer, M. H. (1989, February). Comparison of the far-infrared and carbon monoxide emission in Heiles' Cloud 2 and B18. *Astrophysical Journal*, *337*, 739-753. doi: 10.1086/167145

Suárez, O., García-Lario, P., Manchado, A., Manteiga, M., Ulla, A., & Pottasch, S. R. (2006, October). A spectroscopic atlas of post-AGB stars and planetary nebulae selected from the IRAS point source catalogue. *Astronomy and Astrophysics*, *458*, 173-180. doi: 10.1051/0004-6361:20054108

Sugimoto, D., & Nomoto, K. (1975). Thermal instability of helium-burning shell in stars evolving toward carbon-detonation supernovae. *Publications of the Astronomical Society of Japan*, *27*, 197-213.

Suh, K.-W. (2000, July). Optical properties of the carbon dust grains in the envelopes around asymptotic giant branch stars. *Monthly Notices of the Royal Astronomical Society*, *315*, 740-750. doi: 10.1046/j.1365-8711.2000.03482.x

Suh, K.-W. (2002, May). Crystalline silicates in the envelopes and discs around oxygen-rich asymptotic giant branch stars. *Monthly Notices of the Royal Astronomical Society*, *332*, 513-528. doi: 10.1046/j.1365-8711.2002.05303.x

Suh, K.-W. (2014, December). Astrophysics of Dusty Stellar Winds from AGB Stars. *Journal of Korean Astronomical Society*, *47*, 219-233. doi: 10.5303/JKAS.2014 .47.6.219

Suh, K.-W., & Kwon, Y.-J. (2009, August). A Catalog of AGB Stars in IRAS PSC. *Journal of Korean Astronomical Society*, *42*, 81-91. doi: 10.5303/JKAS.2009 .42.4.081

Suh, K.-W., & Kwon, Y.-J. (2011, November). Infrared two-colour diagrams for AGB stars using AKARI, MSX, IRAS and near-infrared data. *Monthly Notices of the Royal Astronomical Society*, *417*, 3047-3060. doi: 10.1111/j.1365-2966.2011 .19462.x

Szczerba, R., & Górny, S. K. (Eds.). (2001, August). *Post-AGB Objects as a Phase of Stellar Evolution* (Vol. 265). doi: 10.1007/978-94-015-9688-6

Szczerba, R., Siodmiak, N., Stasinska, G., & Borkowski, J. (2007, November). An Evolving Catalogue of Post-AGB and Related Objects. In F. Kerschbaum, C. Charbonnel, & R. F. Wing (Eds.), *Why galaxies care about agb stars: Their importance as actors and probes* (Vol. 378, p. 465).

Tielens, A. G. G. M. (1990, April). Fhe size distribution of interstellar dust. In *Topical seminar on astrophysics and particle physics, p. 13 - 17* (p. 13-17).

Tielens, A. G. G. M. (2005). *The Physics and Chemistry of the Interstellar Medium*.

Trumpler, R. J. (1930a). Preliminary results on the distances, dimensions and space distribution of open star clusters. *Lick Observatory Bulletin*, *14*, 154-188. doi: 10.5479/ADS/bib/1930LicOB.14.154T

Trumpler, R. J. (1930b, October). Spectrophotometric Measures of Interstellar Light Absorption. *Publications of the Astronomical Society of the Pacific*, *42*, 267. doi: 10.1086/124051

Tsuji, T. (1966). The Atmospheric Structure of Late-Type Stars, I. Physical Properties of Cool Gaseous Mixtures and the Effect of Molecular Line Absorption on Stellar Opacities. *Publications of the Astronomical Society of Japan*, *18*, 127.

Ueta, T., Speck, A. K., & Stencel, R. E. (2006, September). Detection of a Far-Infrared Bow Shock Nebula around R Hya: The First MIRIAD Results. *The Astrophysical Journal Letters*, *648*, L39-L42. doi: 10.1086/507627

Van Winckel, H., & Reyniers, M. (2000, February). A homogeneous study of the s-process in the 21 mu m carbon-rich post-AGB objects. *Astronomy and Astrophysics*, *354*, 135-149.

Vassiliadis, E., & Wood, P. R. (1993, August). Evolution of low- and intermediate-mass stars to the end of the asymptotic giant branch with mass loss. *Astrophysical Journal*, *413*, 641-657. doi: 10.1086/173033

Vollmer, B., Gassmann, B., & Derrière, S. (2010, February). The SPECFIND V2.0 catalogue of radio cross-identifications and spectra. SPECFIND meets the Virtual Observatory. *Astronomy and Astrophysics*, *511*, A53. doi: 10.1051/0004-6361/200913460

Ward-Thompson, D., André, P., & Kirk, J. M. (2002, January). The initial conditions of isolated star formation - V. ISOPHOT imaging and the temperature and energy balance of pre-stellar cores. *Monthly Notices of the Royal Astronomical Society*, *329*, 257-276. doi: 10.1046/j.1365-8711.2002.04969.x

Webbink, R. F. (1984, February). Double white dwarfs as progenitors of R Coronae Borealis stars and Type I supernovae. *Astrophysical Journal*, *277*, 355-360. doi: 10.1086/161701

Weidemann, V., & Koester, D. (1983, May). The upper mass limit for white dwarf progenitors and the initial-final mass relation for low and intermediate mass stars. *Astronomy and Astrophysics*, *121*, 77-84.

Weiland, J. L., Blitz, L., Dwek, E., Hauser, M. G., Magnani, L., & Rickard, L. J. (1986, July). Infrared cirrus and high-latitude molecular clouds. *The Astrophysical Journal Letters*, *306*, L101-L104. doi: 10.1086/184714

Weinberger, R., & Aryal, B. (2004, July). Huge dust structures and cavities around pne: Ngc 6826 and ngc 2899. In M. Meixner, J. H. Kastner, B. Balick, & N. Soker (Eds.), *Asymmetrical planetary nebulae iii: Winds, structure and the thunderbird* (Vol. 313, p. 112). Retrieved from http://adsabs.harvard.edu/abs/2004ASPC..313..112W

Werner, M. W., Roellig, T. L., Low, F. J., Rieke, G. H., Rieke, M., Hoffmann, W. F., ... Cruikshank, D. P. (2004, September). The Spitzer Space Telescope Mission. *The Astrophysical Journal Supplement*, *154*, 1-9. doi: 10.1086/422992

Werner, M. W., & Salpeter, W. E. (1969). Grain temperatures in interstellar dust clouds. *Monthly Notices of the Royal Astronomical Society*, *145*, 249. doi: 10.1093/mnras/145.3.249

Wildeman, K. J., Beintema, D. A., & Wesselius, P. R. (1983, January). The Dutch Scientific Instrument on board IRAS. *Journal of the British Interplanetary Society*, *36*, 21-26.

Wood, D. O. S., Myers, P. C., & Daugherty, D. A. (1994, December). IRAS images of nearby dark clouds. *The Astrophysical Journal Supplement*, *95*, 457-501. doi: 10.1086/192107

Wood, P. R. (2010). Evolutionary and pulsation properties of AGB stars . *Memorie della Societa Astronomica Italiana*, *81*, 883.

Wood, P. R., Alcock, C., Allsman, R. A., Alves, D., Axelrod, T. S., Becker, A. C., ... Welch, D. L. (1999). MACHO observations of LMC red giants: Mira and semi-regular pulsators, and contact and semi-detached binaries. In T. Le Bertre, A. Lebre, & C. Waelkens (Eds.), *Asymptotic giant branch stars* (Vol. 191, p. 151).

Young, K., Phillips, T. G., & Knapp, G. R. (1993, June). Circumstellar shells resolved in IRAS survey data. II - Analysis. *Astrophysical Journal*, *409*, 725-738. doi: 10.1086/172702

Appendix A

Database of Cavities

Table 14: The Database of far infrared cavity CCRAS1 nearby AGB star AGB0415+5441. The first two columns represent position of the pixels with in the cavity. The next two columns give values of relative flux density at 60 μm and 100 μm that have obtained after processing the FITS image using ALADIN 2.5 software. The calculated values of dust color temperature (in K), Planck function for 100 μm and visual extinction (in mag) of the corresponding pixels,respectively.

R.A.(J2000) hh mm ss	Dec.(J2000) dd mm ss	$F(60)$ (MJy)	$F(100)$ (MJy)	$T_{\rm d}$ (K)	$B(\nu, T)$ ($\times 10^{-16}$) Js^{-2}	A_V ($\times 10^{-5}$) mag
04 15 46.1	55 00 04.3	4.11	34.32	20.53	3.57	2.26
04 15 55.3	54 58 26.9	4.12	34.23	20.55	3.60	2.24
04 15 46.1	54 58 30.7	4.06	33.92	20.53	3.57	2.24
04 15 35.2	54 58 34.5	4.23	34.26	20.66	3.73	2.16
04 15 45.6	54 57 00.7	4.23	34.23	20.66	3.74	2.15
04 15 34.8	54 57 08.1	4.25	34.00	20.71	3.80	2.10
04 15 23.9	54 57 04.7	4.23	33.84	20.71	3.80	2.09
04 15 15.1	54 57 12.0	4.15	33.71	20.65	3.72	2.13
04 15 04.3	54 57 15.6	4.23	33.75	20.73	3.82	2.08
04 14 53.8	54 57 22.8	4.40	34.27	20.83	3.96	2.04
04 15 43.51	54 55 38.0	4.38	34.11	20.84	3.97	2.02
04 15 34.7	54 55 41.7	4.35	33.64	20.87	4.00	1.98
04 15 23.1	54 55 45.5	4.20	33.27	20.76	3.86	2.03
04 15 12.2	54 55 49.2	4.03	32.98	20.62	3.68	2.11
04 15 03.0	54 55 56.4	4.18	33.22	20.74	3.84	2.04
04 14 52.1	54 55 56.4	4.34	33.91	20.83	3.94	2.02
04 15 53.9	54 54 00.5	4.25	34.08	20.71	3.79	2.11
04 15 43.5	54 54 08.0	4.32	33.84	20.81	3.93	2.03
04 15 33.5	54 54 08.2	4.15	33.31	20.71	3.79	2.07
04 15 22.6	54 54 11.9	4.03	32.59	20.67	3.75	2.04
04 15 12.6	54 54 15.6	3.97	32.35	20.64	3.71	2.05
04 15 03.4	54 54 15.6	4.10	32.68	20.74	3.83	2.01
04 14 50.5	54 54 26.4	4.34	33.93	20.82	3.94	2.03
04 16 14.8	54 52 29.9	4.16	34.15	20.60	3.66	2.19
04 16 03.9	54 52 26.6	4.21	33.99	20.68	3.76	2.13
04 15 55.1	54 52 30.5	4.23	33.85	20.72	3.80	2.09
04 15 44.3	54 52 38.0	4.21	33.25	20.77	3.87	2.02
04 15 31.8	54 52 31.0	4.03	32.76	20.65	3.72	2.07
04 15 20.9	54 52 41.9	3.90	32.10	20.60	3.65	2.07
04 15 12.6	54 52 45.6	3.94	31.87	20.67	3.74	2.00
04 15 02.6	54 52 49.2	4.14	32.40	20.82	3.93	1.94
04 14 52.2	54 52 52.8	4.26	33.34	20.82	3.94	1.99
04 14 40.1	54 52 52.7	4.42	34.28	20.86	3.99	2.02
04 16 03.9	54 51 03.8	4.17	33.76	20.67	3.74	2.12
04 15 53.9	54 51 00.5	4.18	33.61	20.69	3.78	2.09
04 15 42.6	54 51 15.2	4.08	33.05	20.66	3.73	2.08
04 15 31.4	54 51 15.4	3.97	32.46	20.62	3.68	2.07
04 15 21.4	54 51 19.1	3.91	32.05	20.61	3.67	2.05
04 15 11.8	54 51 08.4	3.94	31.73	20.68	3.76	1.98
04 15 01.75	54 51 15.6	4.01	32.14	20.71	3.80	1.99
04 14 49.7	54 51 19.2	4.12	32.75	20.75	3.84	2.00
04 14 39.7	54 51 22.7	4.26	33.85	20.75	03.8	2.07
04 16 02.2	54 49 37.5	4.22	33.85	20.71	3.79	2.10
04 15 51.8	54 49 41.4	4.12	33.34	20.66	3.74	2.10
04 15 41.3	54 49 45.2	4.04	32.92	20.64	3.71	2.09
04 15 32.6	54 49 49.0	3.93	32.50	20.57	3.62	2.11
04 15 22.2	54 49 49.1	3.91	31.95	20.63	3.69	2.04
04 15 10.9	54 50 00.0	3.98	31.98	20.70	3.78	1.99
04 15 02.2	54 49 49.2	4.03	32.14	20.73	3.82	1.98
04 14 51.8	54 49 49.2	4.08	32.82	20.70	3.78	2.04
04 14 39.3	54 49 49.1	4.22	33.76	20.72	3.81	2.09
04 14 30.1	54 49 56.1	4.39	34.01	20.87	4.00	2.00
04 14 20.9	54 50 03.1	4.50	34.41	20.92	4.08	1.99
04 16 00.5	54 48 07.6	4.30	34.23	20.74	3.84	2.10
04 15 50.9	54 48 00.6	4.13	33.25	20.69	3.77	2.07
04 15 40.9	54 48 04.4	4.04	32.65	20.68	3.75	2.04
04 15 30.9	54 48 08.2	3.92	32.18	20.60	3.66	2.07
04 15 20.5	54 48 01.1	3.94	31.98	20.65	3.72	2.02
04 15 10.9	54 48 08.4	4.01	32.10	20.72	3.80	1.99
04 15 00.1	54 48 01.2	4.13	32.37	20.81	3.92	1.94
04 14 50.9	54 48 08.4	4.17	33.13	20.75	3.84	2.03

continued on next page

Table 14 – continued from previous page

R.A.(J2000) hh mm ss	Dec.(J2000) dd mm ss	$F(60)$ (MJy)	$F(100)$ (MJy)	T_d (K)	$B(\nu,T)$ $(\times10^{-16})$ Js^{-2}	A_V $(\times10^{-5})$ mag
04 14 37.6	54 48 04.6	4.33	33.66	20.84	3.97	1.99
04 14 29.3	54 48 22.5	4.37	33.66	20.89	4.03	1.96
04 14 18.9	54 48 33.1	4.46	34.10	20.92	4.07	1.97
04 16 02.1	54 46 30.3	4.31	34.21	20.75	3.85	2.09
04 15 50.9	54 46 34.2	4.16	33.14	20.73	3.82	2.04
04 15 40.0	54 46 23.7	3.99	32.09	20.69	3.77	2.00
04 15 30.9	54 46 23.8	3.92	31.80	20.65	3.72	2.01
04 15 19.2	54 46 27.5	3.91	31.82	20.64	3.71	2.02
04 15 10.1	54 46 42.0	4.02	32.29	20.70	3.78	2.01
04 15 00.9	54 46 31.2	4.19	32.64	20.83	3.96	1.94
04 14 49.3	54 46 45.6	4.28	33.17	20.86	3.99	1.95
04 14 39.3	54 46 45.4	4.38	33.60	20.91	4.06	1.95
04 14 28.9	54 46 56.1	4.51	33.49	21.05	4.25	1.85
04 14 18.1	54 47 13.9	4.46	33.74	20.98	4.14	1.91
04 14 08.9	54 47 02.8	4.48	34.25	20.93	4.08	1.97
04 16 00.4	54 44 56.7	4.27	33.95	20.75	3.84	2.08
04 15 50.4	54 44 49.8	4.13	33.10	20.71	3.79	2.05
04 15 39.2	54 45 11.7	4.04	32.11	20.74	3.84	1.97
04 15 29.6	54 45 01.0	3.94	31.73	20.69	3.77	1.98
04 15 20.9	54 45 01.1	3.94	31.91	20.66	3.73	2.01
04 15 08.8	54 45 15.6	4.04	32.48	20.70	3.78	2.02
04 14 59.7	54 45 22.8	4.14	33.12	20.72	3.81	2.04
04 14 48.9	54 45 22.7	4.27	33.28	20.84	3.96	1.98
04 14 38.5	54 45 29.8	4.37	33.56	20.90	4.05	1.95
04 14 28.1	54 45 22.5	4.44	33.66	20.96	4.12	1.92
04 14 16.4	54 45 40.3	4.44	33.42	20.99	4.17	1.89
04 14 06.9	54 45 40.0	4.47	33.94	20.96	4.12	1.94
04 16 00.8	54 43 23.1	4.29	33.87	20.78	3.88	2.05
04 15 50.4	54 43 37.8	4.09	32.91	20.69	3.77	2.05
04 15 40.0	54 43 34.4	4.02	32.23	20.71	3.80	2.00
04 15 28.8	54 43 41.8	3.97	32.14	20.67	3.74	2.02
04 15 20.9	54 43 41.9	3.93	32.19	20.62	3.68	2.06
04 15 09.2	54 43 42.0	4.04	32.69	20.66	3.74	2.06
04 14 58.8	54 43 42.0	4.13	33.44	20.67	3.74	2.10
04 14 48.9	54 43 45.5	4.28	33.81	20.77	3.87	2.05
04 14 38.5	54 43 49.0	4.46	33.77	20.97	4.13	1.92
04 14 27.7	54 43 59.7	4.43	33.75	20.94	4.10	1.94
04 14 18.1	54 44 03.1	4.46	33.40	21.02	4.20	1.87
04 14 09.0	54 44 06.4	4.41	33.79	20.92	4.07	1.95
04 15 59.9	54 41 56.8	4.25	33.55	20.77	3.88	2.04
04 15 50.4	54 41 57.0	4.08	32.72	20.71	3.79	2.03
04 15 39.6	54 42 08.1	4.01	32.38	20.68	3.75	2.03
04 15 28.8	54 41 57.4	3.95	32.42	20.60	3.66	2.08
04 15 20.0	54 42 08.3	3.96	32.48	20.61	3.67	2.08
04 15 08.0	54 42 08.4	4.01	33.07	20.58	3.63	2.14
04 14 58.0	54 42 19.2	4.14	33.70	20.64	3.71	2.13
04 14 46.8	54 42 26.3	4.32	34.02	20.78	3.89	2.06
04 14 37.7	54 42 19	04.5	34.34	20.92	4.07	1.99
04 14 28.5	54 42 22.5	4.49	34.19	20.95	4.10	1.96
04 14 19.0	54 42 33.1	4.55	33.81	21.06	4.26	1.87
04 14 08.2	54 42 40.0	4.45	34.23	20.90	4.04	1.99
04 15 58.2	54 40 34.0	4.20	33.73	20.71	3.79	2.09
04 15 49.1	54 40 30.6	4.09	33.03	20.68	3.75	2.07
04 15 39.1	54 40 30.9	4.02	32.82	20.63	3.69	2.09
04 15 31.2	54 40 45.4	3.99	32.80	20.60	3.66	2.11
04 15 19.2	54 40 52.7	3.97	32.75	20.58	3.63	2.12
04 15 06.32	54 41 03.6	3.99	32.99	20.58	3.63	2.14
04 14 58.0	54 41 07.2	4.14	33.49	20.67	3.74	2.10
04 14 48.1	54 41 07.1	4.29	33.70	20.80	3.91	2.03
04 14 37.3	54 41 07.0	4.45	34.11	20.91	4.05	1.98
04 14 25.6	54 41 06.8	4.58	34.25	21.02	4.21	1.91
04 14 16.1	54 41 10.2	4.60	34.35	21.03	4.22	1.91
04 15 58.6	54 39 18.4	4.28	34.34	20.71	3.79	2.13
04 15 49.5	54 39 15.0	4.26	33.91	20.74	3.83	2.08
04 15 39.5	54 39 11.7	4.15	33.70	20.65	3.72	2.13
04 15 27.9	54 39 22.6	4.14	33.74	20.64	3.71	2.14
04 15 18.8	54 39 22.7	4.09	33.45	20.62	3.69	2.13
04 15 08.0	54 39 12.0	4.01	33.04	20.59	3.64	2.13
04 14 56.8	54 39 19.2	4.04	33.12	20.61	3.67	2.12
04 14 48.5	54 39 26.3	4.17	33.24	20.74	3.83	2.04
04 14 36.9	54 39 26.2	4.40	33.75	20.91	4.05	1.96
04 14 25.2	54 39 33.2	4.61	34.12	21.08	4.28	1.87
04 15 17.1	54 37 52.7	4.11	34.10	20.56	3.60	2.22
04 15 07.2	54 37 52.8	4.13	33.59	20.64	3.71	2.13
04 14 57.2	54 37 49.2	4.13	33.47	20.66	3.73	2.11
04 14 46.4	54 38 03.5	4.18	33.49	20.71	3.80	2.07
04 14 36.1	54 37 56.2	4.32	33.93	20.80	3.91	2.04

continued on next page

Table 14 – continued from previous page

R.A.(J2000) hh mm ss	Dec.(J2000) dd mm ss	$F(60)$ (MJy)	$F(100)$ (MJy)	T_d (K)	$B(\nu,T)$ $(\times10^{-16})$ Js^{-2}	A_V $(\times10^{-5})$ mag
04 14 25.3	54 38 03.2	4.63	34.13	21.09	4.31	1.86
04 14 58.0	54 36 37.2	4.30	34.21	20.75	3.84	2.09
04 14 46.0	54 36 37.1	4.33	34.26	20.77	3.87	2.08
04 14 26.1	54 36 51.3	4.62	34.26	21.06	4.26	1.89
04 14 14.9	54 37 1.8	04.6	34.41	21.03	4.22	1.92

Table 15: The Database of far infrared cavity CCRAS2 nearby AGB star AGB0609+1446. The first two columns represent position of the pixels with in the cavity. The next two columns give values of relative flux density at 60 μm and 100 μm that have obtained after processing the FITS image using ALADIN 2.5 software. The calculated values of dust color temperature (in K), Planck function for 100 μm and visual extinction (in mag) of the corresponding pixels,respectively.

R.A.(J2000) hh mm ss	Dec.(J2000) dd mm ss	$F(60)$ (MJy)	$F(100)$ (MJy)	T_d (K)	$B(\nu,T)$ $(\times10^{-16})$ Js^{-2}	A_V $(\times10^{-5})$ mag
06 09 43.19	15 09 27.2	6.0892	30.751	23.00	7.60	0.95
06 09 42.94	15 08 4.4	5.9846	30.309	22.99	7.56	0.94
06 09 43.69	15 06 34.4	5.9705	30.275	22.98	7.55	0.94
06 09 37.23	15 06 41.5	5.9147	30.717	22.85	7.28	0.99
06 09 43.69	15 05 0.8	6.0578	29.608	23.18	7.98	0.87
06 09 36.48	15 04 57.1	5.852	30.175	22.89	7.36	0.96
06 09 49.41	15 03 38	5.7647	30.434	22.76	7.11	1.01
06 09 43.44	15 03 38	5.8834	29.433	23.05	7.70	0.90
06 09 36.98	15 03 37.9	5.852	30.025	22.92	7.42	0.95
06 09 49.91	15 02 15.2	5.5834	30.434	22.59	6.77	1.06
06 09 43.69	15 02 15.2	5.8381	29.324	23.03	7.66	0.90
06 09 37.23	15 02 15.1	5.9357	30.183	22.96	7.52	0.94
06 09 32.01	15 02 7.9	5.824	30.842	22.74	7.07	1.03
06 10 2.58	15 00 30.8	5.1195	30.734	22.09	5.86	1.23
06 09 55.87	15 00 30.8	5.3322	30.559	22.33	6.28	1.14
06 09 50.65	15 00 34.4	5.4927	29.866	22.60	6.80	1.03
06 09 44.69	15 00 34.4	5.7578	29.641	22.90	7.38	0.94
06 09 37.73	15 00 34.4	5.824	29.608	22.97	7.52	0.93
06 09 31.27	15 00 37.9	5.7403	30.592	22.71	7.01	1.03
06 10 8.04	14 59 36.8	5.3637	30.534	22.36	6.34	1.13
06 10 2.33	14 59 36.8	5.0043	29.975	22.10	5.88	1.20
06 09 55.87	14 59 36.8	5.1649	29.349	22.37	6.36	1.08
06 09 50.4	14 59 29.6	5.3288	29.233	22.55	6.71	1.02
06 09 43.45	14 59 40.4	5.5416	28.757	22.85	7.29	0.93
06 09 37.98	14 59 40.4	5.6323	29.108	22.88	7.34	0.93
06 09 31.52	14 59 40.3	5.6182	30.133	22.67	6.94	1.02
06 10 23.2	14 58 17.5	5.3176	30.251	22.36	6.35	1.12
06 10 16.74	14 58 10.3	4.8029	30.515	21.80	5.38	1.33
06 10 9.78	14 58 17.6	4.9052	30.268	21.95	5.62	1.27
06 10 5.06	14 58 17.6	5.0226	29.969	22.12	5.91	1.19
06 09 57.36	14 58 10.4	4.827	30.075	21.90	5.54	1.28
06 09 52.14	14 58 10.4	4.821	30.4	21.84	5.44	1.31
06 09 45.44	14 58 10.4	5.0166	30.092	22.09	5.87	1.21
06 09 39.97	14 58 10.4	4.9474	30.172	22.01	5.72	1.24
06 09 33.51	14 58 10.3	5.2754	30.805	22.23	6.11	1.19
06 10 28.16	14 56 33.1	5.4018	30.805	22.35	6.33	1.14
06 10 22.95	14 56 33.1	5.2363	29.714	22.38	6.38	1.10
06 10 17.23	14 56 40.3	4.6374	30.057	21.70	5.22	1.35
06 10 11.02	14 56 40.4	4.7969	29.996	21.88	5.51	1.28
06 10 4.81	14 56 40.4	4.9083	29.486	22.08	5.85	1.18
06 09 58.35	14 56 40.4	4.6795	29.635	21.82	5.41	1.29
06 09 52.14	14 56 36.8	4.7096	30.022	21.79	5.35	1.32
06 09 46.18	14 56 47.6	4.8962	29.679	22.04	5.77	1.21
06 09 39.72	14 56 44	4.9022	29.794	22.02	5.75	1.22
06 09 33.02	14 56 47.5	5.2032	30.585	22.19	6.05	1.19
06 10 27.91	14 55 3.1	5.3477	30.875	22.29	6.21	1.17
06 10 22.45	14 55 6.7	4.9985	29.354	22.20	6.06	1.14
06 10 16.73	14 55 6.7	4.6856	29.758	21.80	5.38	1.30
06 10 11.27	14 55 6.8	4.9775	29.758	22.11	5.89	1.19
06 10 5.06	14 55 10.4	4.9083	29.574	22.07	5.83	1.19
06 09 58.35	14 55 17.6	4.7216	29.714	21.85	5.46	1.28
06 09 52.64	14 55 17.6	4.6765	29.811	21.79	5.35	1.31
06 09 46.43	14 55 17.6	4.7337	29.354	21.92	5.58	1.24
06 09 39.73	14 55 10.4	4.9353	29.468	22.11	5.91	1.17
06 09 33.76	14 55 13.9	5.1279	30.409	22.15	5.97	1.20
06 09 27.06	14 55 28.3	5.146	30.884	22.09	5.86	1.24
06 10 28.9	14 53 40.3	5.4379	30.69	22.41	6.43	1.12
06 10 23.19	14 53 36.7	5.1279	29.319	22.34	6.30	1.09
06 10 16.73	14 53 29.5	4.845	29.618	22.00	5.70	1.22

continued on next page

Table 15 – continued from previous page

R.A.(J2000) hh mm ss	Dec.(J2000) dd mm ss	$F(60)$ (MJy)	$F(100)$ (MJy)	T_d (K)	$B(\nu,T)$ $(\times10^{-16})$ Js^{-2}	A_V $(\times10^{-5})$ mag
06 10 10.03	14 53 36.8	4.9685	29.328	22.17	6.01	1.15
06 10 4.31	14 53 33.2	4.6915	29.389	21.87	5.50	1.26
06 09 58.85	14 53 44	4.7126	29.609	21.86	5.47	1.27
06 09 52.64	14 53 40.4	4.6976	29.67	21.83	5.43	1.29
06 09 45.69	14 53 47.6	4.7548	29.187	21.97	5.67	1.21
06 09 39.73	14 53 54.8	4.9022	29.407	22.09	5.86	1.18
06 09 33.52	14 53 51.1	5.158	30.339	22.19	6.04	1.18
06 09 27.31	14 53 54.7	5.2092	30.805	22.16	5.99	1.21
06 10 22.94	14 51 59.5	5.1761	29.741	22.31	6.26	1.12
06 10 15.98	14 52 3.1	4.6404	29.635	21.78	5.34	1.31
06 10 10.27	14 52 10.4	4.6404	29.284	21.84	5.43	1.27
06 10 4.56	14 52 6.8	4.6885	29.152	21.91	5.56	1.23
06 09 58.85	14 52 3.2	4.502	29.152	21.71	5.23	1.31
06 09 51.65	14 52 10.4	4.5621	29.345	21.74	5.28	1.31
06 09 46.19	14 52 14	4.7337	29.169	21.96	5.63	1.22
06 09 39.98	14 52 14	4.824	29.512	21.99	5.69	1.22
06 09 33.27	14 52 13.9	5.152	30.515	22.16	5.98	1.20
06 10 22.68	14 50 36.7	5.2122	29.811	22.34	6.30	1.11
06 10 16.48	14 50 47.5	4.5772	29.67	21.70	5.22	1.34
06 10 10.27	14 50 44	4.6163	29.354	21.80	5.37	1.28
06 10 4.31	14 50 40.4	4.7186	28.712	22.02	5.74	1.18
06 09 58.6	14 50 44	4.3695	28.598	21.66	5.14	1.31
06 09 52.64	14 50 44	4.5501	28.703	21.84	5.44	1.24
06 09 45.94	14 50 47.6	4.6253	29.134	21.85	5.45	1.26
06 09 40.23	14 50 47.6	4.848	29.644	21.99	5.70	1.22
06 09 34.02	14 50 54.7	5.2423	30.602	22.23	6.11	1.18
06 10 28.89	14 49 3.1	5.122	30.224	22.17	6.01	1.18
06 10 22.93	14 48 59.5	4.8902	29.134	22.13	5.93	1.16
06 10 16.72	14 49 6.7	4.5321	29.284	21.72	5.25	1.31
06 10 9.77	14 49 14	4.7397	29.116	21.97	5.66	1.21
06 10 3.81	14 49 14	4.4809	28.176	21.85	5.46	1.21
06 09 58.35	14 49 14	4.2281	28.237	21.56	4.99	1.33
06 09 51.9	14 49 10.4	4.3665	28.29	21.71	5.22	1.27
06 09 45.94	14 49 10.4	4.6284	28.562	21.95	5.62	1.19
06 09 39.73	14 49 10.4	4.8902	29.398	22.08	5.85	1.18
06 09 33.53	14 49 10.3	5.2092	30.119	22.28	6.20	1.14
06 10 28.64	14 47 36.7	5.0828	29.67	22.23	6.11	1.14
06 10 23.18	14 47 36.7	5.0617	28.826	22.36	6.34	1.07
06 10 16.72	14 47 36.7	4.6043	28.73	21.89	5.53	1.22
06 10 10.76	14 47 40.4	4.6644	28.457	22.01	5.72	1.17
06 10 3.81	14 47 33.2	4.5441	27.771	22.00	5.70	1.14
06 09 57.86	14 47 44	4.3846	27.657	21.84	5.44	1.20
06 09 51.9	14 47 36.8	4.1348	27.921	21.51	4.91	1.34
06 09 45.69	14 47 44	4.5531	28.193	21.93	5.59	1.19
06 09 39.74	14 47 44	4.8992	28.888	22.18	6.02	1.13
06 09 33.78	14 47 51.1	5.155	29.591	22.32	6.27	1.11
06 09 27.32	14 47 47.5	5.2333	30.532	22.23	6.11	1.17
06 10 28.63	14 46 10.3	5.0708	29.626	22.23	6.10	1.14
06 10 22.68	14 46 13.9	4.9113	28.58	22.25	6.14	1.09
06 10 16.47	14 46 13.9	4.6524	28.677	21.95	5.63	1.20
06 10 10.02	14 46 6.8	4.7307	28.387	22.09	5.86	1.14
06 10 4.56	14 46 14	4.4719	27.745	21.92	5.58	1.17
06 09 58.1	14 46 17.6	4.189	27.446	21.65	5.14	1.26
06 09 52.4	14 46 21.2	4.3093	27.622	21.76	5.31	1.22
06 09 45.94	14 46 21.2	4.514	27.718	21.97	5.66	1.15
06 09 40.23	14 46 21.2	4.6644	28.492	22.00	5.71	1.17
06 09 34.03	14 46 21.1	5.0437	29.152	22.28	6.20	1.11
06 09 26.83	14 46 24.7	5.155	30.066	22.23	6.12	1.16
06 09 21.12	14 46 17.4	5.155	30.84	22.10	5.89	1.23
06 10 28.38	14 44 40.3	5.0136	29.319	22.22	6.09	1.13
06 10 22.42	14 44 40.3	4.9233	28.009	22.36	6.35	1.04
06 10 16.72	14 44 47.5	4.5742	28.668	21.87	5.49	1.23
06 10 10.26	14 44 47.6	4.6284	28.738	21.92	5.57	1.21
06 10 4.31	14 44 47.6	4.6163	27.912	22.05	5.80	1.13
06 09 58.35	14 44 51.2	4.192	27.314	21.68	5.18	1.24
06 09 52.15	14 44 51.2	4.2883	27.393	21.78	5.34	1.21
06 09 45.94	14 44 51.2	4.4027	27.894	21.82	5.40	1.21
06 09 40.23	14 44 51.2	4.6524	28.281	22.02	5.75	1.16
06 09 33.29	14 44 47.5	4.9443	28.835	22.24	6.12	1.11
06 09 27.83	14 44 58.3	5.0678	29.881	22.18	6.02	1.17
06 09 20.38	14 44 58.2	5.0437	30.778	22.00	5.72	1.27
06 10 34.58	14 42 59.4	4.8781	30.224	21.93	5.59	1.27
06 10 28.87	14 43 6.7	4.824	29.029	22.07	5.84	1.17
06 10 22.92	14 43 6.7	4.7999	28.36	22.17	6.00	1.11
06 10 16.71	14 43 10.3	4.6163	28.721	21.91	5.55	1.22
06 10 10.51	14 43 6.8	4.5892	28.756	21.87	5.49	1.23
06 10 3.56	14 43 6.8	4.502	28.14	21.88	5.51	1.20

continued on next page

Table 15 – continued from previous page

R.A.(J2000) hh mm ss	Dec.(J2000) dd mm ss	$F(60)$ (MJy)	$F(100)$ (MJy)	T_d (K)	$B(\nu,T)$ $(\times10^{-16})$ Js^{-2}	A_V $(\times10^{-5})$ mag
06 09 57.61	14 43 14	4.2973	27.63	21.74	5.28	1.23
06 09 52.15	14 43 17.6	4.2792	27.648	21.72	5.25	1.24
06 09 46.69	14 43 14	4.4027	27.481	21.89	5.52	1.17
06 09 39.74	14 43 17.6	4.52	27.885	21.95	5.62	1.17
06 09 33.54	14 43 17.5	4.7668	28.07	22.19	6.03	1.09
06 09 27.58	14 43 21.1	4.9624	29.284	22.17	6.01	1.15
06 09 20.63	14 43 21	5.0527	30.752	22.02	5.74	1.26
06 10 40.28	14 41 36.5	5.0497	30.62	22.04	5.77	1.25
06 10 34.58	14 41 43.8	4.821	29.829	21.93	5.60	1.25
06 10 28.37	14 41 43.9	4.8059	28.976	22.07	5.82	1.17
06 10 22.42	14 41 43.9	4.8781	28.378	22.25	6.14	1.09
06 10 16.71	14 41 36.7	4.6284	28.527	21.95	5.63	1.19
06 10 9.76	14 41 47.6	4.7036	29.064	21.94	5.61	1.22
06 10 3.56	14 41 47.6	4.6314	28.378	21.98	5.68	1.17
06 09 58.1	14 41 44	4.3665	28.29	21.71	5.22	1.27
06 09 50.91	14 41 47.6	4.3093	27.947	21.70	5.22	1.26
06 09 45.7	14 41 47.6	4.4538	27.499	21.95	5.62	1.15
06 09 40.49	14 41 54.8	4.4568	27.12	22.02	5.74	1.11
06 09 33.29	14 41 54.7	4.6464	27.639	22.13	5.94	1.09
06 09 26.59	14 41 58.3	4.8692	28.976	22.13	5.94	1.15
06 09 20.89	14 41 54.6	4.9956	30.347	22.03	5.75	1.24
06 10 40.53	14 40 2.9	4.9685	30.585	21.96	5.64	1.27
06 10 34.32	14 40 13.8	4.833	30.005	21.92	5.57	1.27
06 10 28.12	14 40 21.1	4.8059	29.143	22.04	5.77	1.19
06 10 22.42	14 40 17.5	4.9233	28.633	22.25	6.14	1.10
06 10 16.46	14 40 13.9	4.7066	28.668	22.01	5.73	1.18
06 10 10.51	14 40 17.6	4.7638	28.853	22.04	5.78	1.17
06 10 3.31	14 40 14	4.7517	28.844	22.03	5.76	1.18
06 09 57.61	14 40 21.2	4.5561	28.897	21.81	5.39	1.26
06 09 51.4	14 40 24.8	4.4628	28.281	21.82	5.40	1.23
06 09 45.95	14 40 24.8	4.4538	27.411	21.96	5.64	1.14
06 09 39.99	14 40 24.8	4.517	27.499	22.02	5.74	1.13
06 09 33.29	14 40 28.3	4.7819	28.088	22.20	6.05	1.09
06 09 26.35	14 40 35.5	4.9443	29.776	22.07	5.83	1.20
06 10 40.77	14 38 43.7	5.0226	30.866	21.97	5.66	1.28
06 10 34.82	14 38 43.8	4.8421	30.189	21.90	5.53	1.28
06 10 27.62	14 38 43.9	4.8631	29.565	22.02	5.75	1.21
06 10 22.16	14 38 51.1	4.8992	29.011	22.16	5.98	1.14
06 10 16.46	14 38 51.1	4.7487	29.424	21.93	5.59	1.24
06 10 9.76	14 38 47.6	4.9624	30.189	22.02	5.74	1.24
06 10 3.81	14 38 51.2	5.0497	30.233	22.10	5.88	1.21
06 09 58.1	14 38 51.2	4.7788	30.136	21.84	5.44	1.30
06 09 51.65	14 38 51.2	4.6103	29.24	21.81	5.39	1.27
06 09 45.95	14 38 51.2	4.6343	28.492	21.97	5.65	1.19
06 09 38.75	14 38 54.8	4.7216	28.642	22.03	5.77	1.17
06 09 32.8	14 38 54.7	5.1309	29.67	22.28	6.20	1.13
06 10 41.01	14 37 13.7	5.0648	30.875	22.01	5.72	1.27
06 10 34.32	14 37 24.6	4.9504	30.391	21.97	5.66	1.26
06 10 27.12	14 37 13.9	4.9835	30.022	22.07	5.83	1.21
06 10 22.66	14 37 17.5	5.0798	30.136	22.15	5.96	1.19
06 09 51.65	14 37 24.8	4.8962	30.77	21.86	5.47	1.32
06 09 44.96	14 37 21.2	4.9835	30.409	22.00	5.72	1.25
06 09 39	14 37 24.8	5.2243	30.356	22.25	6.15	1.16
06 10 40.26	14 35 36.5	5.1069	30.673	22.08	5.85	1.23
06 10 40.75	14 34 17.3	5.1912	30.69	22.17	5.99	1.20

Table 16: The Database of far infrared cavity CCRAS nearby AGB star AGB0631+1606. The first two columns represent position of the pixels with in the cavity. The next two columns give values of relative flux density at 60 μm and 100 μm that have obtained after processing the FITS image using ALADIN 2.5 software. The calculated values of dust color temperature (in K), Planck function for 100 μm and visual extinction (in mag) of the corresponding pixels,respectively.

R.A.(J2000) hh mm ss	Dec.(J2000) dd mm ss	$F(60)$ (MJy)	$F(100)$ (MJy)	T_d (K)	$B(\nu,T)$ $(\times10^{-16})$ Js^{-2}	A_V $(\times10^{-5})$ mag
06 32 55.86	16 7 17.9	2.37	17.83	20.99	4.17	1.01
06 32 50.36	16 7 14.3	2.21	17.81	20.69	3.77	1.11
06 32 43.37	16 7 17.9	2.26	17.82	20.79	3.90	1.08
06 32 37.37	16 7 10.7	2.32	17.70	20.92	4.07	1.02
06 32 30.38	16 7 21.5	2.35	17.57	21.02	4.20	0.98
06 32 25.88	16 7 14.3	2.49	17.67	21.27	4.56	0.91
06 32 18.88	16 7 17.8	2.59	17.97	21.38	4.72	0.89
06 33 0.85	16 5 40.6	2.44	17.91	21.11	4.32	0.97
06 32 53.86	16 5 40.7	2.28	17.32	20.96	4.12	0.99

continued on next page

Table 16 – continued from previous page

R.A.(J2000) hh mm ss	Dec.(J2000) dd mm ss	$F(60)$ (MJy)	$F(100)$ (MJy)	T_d (K)	$B(\nu,T)$ $(\times10^{-16})$ Js^{-2}	A_V $(\times10^{-5})$ mag
06 32 49.61	16 5 47.9	2.12	17.42	20.61	3.66	1.12
06 32 43.37	16 5 40.7	2.08	17.13	20.59	3.65	1.10
06 32 36.87	16 5 33.5	2.19	16.96	20.86	4.00	1.00
06 32 30.63	16 5 47.9	2.21	16.89	20.92	4.07	0.98
06 32 24.88	16 5 44.3	2.35	17.16	21.13	4.36	0.93
06 32 18.64	16 5 37	2.50	17.71	21.28	4.58	0.91
06 33 1.85	16 4 14.2	2.43	17.72	21.14	4.37	0.95
06 32 54.35	16 4 7.1	2.29	17.12	21.02	4.20	0.96
06 32 48.61	16 4 17.9	2.11	17.04	20.68	3.75	1.07
06 32 42.37	16 4 3.5	2.04	16.84	20.58	3.63	1.09
06 32 36.87	16 4 7.1	2.13	16.51	20.86	3.99	0.97
06 32 30.63	16 4 3.5	2.18	16.55	20.95	4.12	0.95
06 32 24.88	16 4 10.7	2.32	17.02	21.10	4.32	0.93
06 32 17.14	16 4 10.6	2.46	17.75	21.19	4.44	0.94
06 33 6.84	16 2 33.4	2.33	17.94	20.90	4.04	1.04
06 33 0.6	16 2 37	2.41	17.41	21.19	4.45	0.92
06 32 54.85	16 2 44.3	2.24	16.99	20.96	4.13	0.97
06 32 49.86	16 2 40.7	2.06	17.03	20.58	3.63	1.10
06 32 43.11	16 2 37.1	2.02	16.55	20.61	3.67	1.06
06 32 36.37	16 2 47.9	2.09	16.28	20.84	3.97	0.97
06 32 30.38	16 2 33.5	2.15	16.49	20.92	4.07	0.95
06 32 24.14	16 2 40.7	2.31	17.06	21.08	4.29	0.93
06 32 18.14	16 2 40.6	2.46	17.76	21.19	4.45	0.94
06 33 6.84	16 1 21.4	2.25	17.63	20.81	3.92	1.06
06 33 0.84	16 1 17.8	2.31	17.17	21.05	4.24	0.95
06 32 54.6	16 0 59.9	2.27	16.86	21.05	4.24	0.93
06 32 48.61	16 0 59.9	2.07	16.84	20.65	3.72	1.06
06 32 41.87	16 1 3.5	2.00	16.36	20.63	3.69	1.04
06 32 36.12	16 0 56.3	2.03	16.09	20.77	3.87	0.98
06 32 30.88	16 1 14.3	2.10	16.27	20.85	3.98	0.96
06 32 23.64	16 1 3.5	2.28	16.89	21.08	4.28	0.93
06 32 17.4	16 1 17.8	2.46	17.85	21.16	4.40	0.95
06 33 13.07	15 59 36.9	2.32	17.72	20.92	4.08	1.02
06 33 6.58	15 59 55	2.17	17.29	20.73	3.83	1.06
06 33 1.34	15 59 37	2.26	17.06	20.97	4.14	0.97
06 32 55.85	15 59 40.7	2.21	16.95	20.90	4.05	0.98
06 32 50.1	15 59 55.1	2.09	16.74	20.72	3.80	1.03
06 32 40.62	15 59 40.7	2.03	16.36	20.68	3.75	1.02
06 32 36.62	15 59 47.9	2.00	15.98	20.73	3.83	0.98
06 32 31.38	15 59 51.5	2.06	16.25	20.78	3.88	0.98
06 32 24.64	15 59 37.1	2.22	17.04	20.90	4.04	0.99
06 32 16.9	15 59 40.6	2.44	17.60	21.19	4.44	0.93
06 32 10.91	15 59 40.6	2.53	17.95	21.27	4.55	0.93
06 33 25.05	15 58 3.2	2.28	17.96	20.78	3.89	1.09
06 33 19.56	15 58 21.3	2.36	17.61	21.04	4.23	0.98
06 33 13.07	15 58 21.3	2.33	17.29	21.06	4.26	0.95
06 33 7.08	15 58 10.6	2.23	17.10	20.91	4.06	0.99
06 33 0.59	15 58 10.6	2.18	16.93	20.86	3.99	1.00
06 32 54.35	15 58 3.5	2.27	16.87	21.05	4.25	0.93
06 32 49.85	15 58 3.5	2.07	16.71	20.68	3.76	1.05
06 32 42.11	15 57 56.3	2.02	16.22	20.71	3.79	1.01
06 32 35.62	15 58 17.9	2.00	15.99	20.72	3.81	0.99
06 32 29.63	15 58 17.9	2.04	16.24	20.75	3.84	0.99
06 32 22.64	15 58 21.5	2.22	16.93	20.94	4.10	0.97
06 32 16.9	15 58 17.8	2.44	17.56	21.20	4.46	0.93
06 32 11.91	15 58 28.6	2.51	17.96	21.23	4.50	0.94
06 33 43.26	15 56 25.7	2.35	17.81	20.97	4.14	1.01
06 33 38.02	15 56 33	2.26	17.64	20.83	3.95	1.05
06 33 31.78	15 56 40.3	2.24	17.32	20.88	4.01	1.02
06 33 25.79	15 56 26	2.12	17.22	20.65	3.72	1.09
06 33 19.55	15 56 51.3	2.24	17.01	20.96	4.12	0.97
06 33 12.57	15 56 40.5	2.18	16.91	20.85	3.98	1.00
06 33 6.33	15 56 47.8	2.18	16.81	20.89	4.03	0.98
06 33 1.33	15 56 37	2.15	16.81	20.82	3.94	1.00
06 32 55.34	15 56 33.5	2.20	16.79	20.93	4.09	0.97
06 32 48.35	15 56 44.3	2.09	16.56	20.76	3.86	1.01
06 32 42.11	15 56 44.3	2.02	16.26	20.68	3.76	1.02
06 32 36.12	15 56 58.7	2.02	16.11	20.73	3.82	0.99
06 32 29.63	15 56 55.1	2.08	16.19	20.85	3.98	0.96
06 32 24.14	15 56 47.9	2.23	16.88	20.98	4.15	0.96
06 32 17.15	15 56 58.6	2.41	17.71	21.10	4.32	0.96
06 33 49.49	15 54 37.6	2.39	18.02	20.98	4.15	1.02
06 33 45	15 54 59.3	2.26	17.47	20.86	3.99	1.03
06 33 39.01	15 54 41.4	2.21	17.19	20.85	3.98	1.02
06 33 32.28	15 54 59.5	2.19	16.85	20.89	4.03	0.98
06 33 25.29	15 54 52.4	2.07	16.83	20.66	3.73	1.06
06 33 19.8	15 55 6.9	2.17	16.66	20.90	4.05	0.97

continued on next page

Table 16 – continued from previous page

R.A.(J2000) hh mm ss	Dec.(J2000) dd mm ss	$F(60)$ (MJy)	$F(100)$ (MJy)	T_d (K)	$B(\nu,T)$ $(\times10^{-16})$ Js^{-2}	A_V $(\times10^{-5})$ mag
6 33 12.56	15 54 56.1	2.11	16.74	20.75	3.84	1.02
06 33 8.57	15 54 56.2	2.10	16.53	20.80	3.91	1.00
06 33 0.58	15 55 10.6	2.09	16.41	20.80	3.91	0.99
06 32 55.09	15 54 56.3	2.07	16.50	20.74	3.83	1.01
06 32 49.1	15 55 17.9	1.98	16.52	20.53	3.57	1.09
06 32 42.36	15 55 3.5	2.00	16.31	20.63	3.70	1.04
06 32 36.87	15 55 7.1	2.05	16.23	20.76	3.86	0.99
06 32 29.88	15 55 21.5	2.12	16.44	20.87	4.00	0.97
06 32 21.9	15 55 21.5	2.33	17.15	21.10	4.32	0.93
06 33 43.5	15 53 47.3	2.20	17.46	20.75	3.85	1.07
06 33 36.76	15 53 40.2	2.27	17.13	20.98	4.14	0.97
06 33 30.27	15 53 36.7	2.15	16.72	20.86	3.98	0.99
06 33 24.03	15 53 29.6	2.13	16.77	20.80	3.91	1.01
06 33 19.04	15 53 33.3	2.18	16.72	20.91	4.05	0.97
06 33 12.56	15 53 33.3	2.20	16.71	20.96	4.12	0.95
06 33 6.32	15 53 40.6	2.12	16.55	20.83	3.95	0.99
06 32 59.83	15 53 37	1.99	16.41	20.59	3.65	1.06
06 32 54.84	15 53 40.7	2.02	16.48	20.63	3.69	1.05
06 32 49.35	15 53 40.7	2.06	16.41	20.74	3.83	1.01
06 32 41.61	15 53 29.9	2.02	16.43	20.65	3.72	1.04
06 32 34.13	15 53 51.5	2.08	16.55	20.75	3.84	1.01
06 32 28.89	15 53 55.1	2.23	16.76	21.00	4.17	0.94
06 32 21.65	15 53 51.5	2.48	17.48	21.29	4.59	0.90
06 33 50.23	15 52 10	2.32	17.94	20.88	4.01	1.05
06 33 42.99	15 51 55.7	2.24	17.37	20.85	3.98	1.03
06 33 37.5	15 51 52.2	2.22	17.08	20.90	4.05	0.99
06 33 31.76	15 51 59.5	2.22	16.83	20.96	4.12	0.96
06 33 27.27	15 51 59.6	2.14	16.86	20.79	3.89	1.02
06 33 19.79	15 52 3.3	2.13	16.81	20.78	3.89	1.02
06 33 13.05	15 51 59.7	2.21	16.86	20.93	4.08	0.97
06 33 6.56	15 52 10.6	2.17	16.73	20.88	4.02	0.98
06 33 0.58	15 52 14.2	2.08	16.49	20.77	3.87	1.00
06 32 53.59	15 52 7.1	2.07	16.60	20.71	3.80	1.03
06 32 47.6	15 52 7.1	2.12	16.46	20.84	3.97	0.98
06 32 41.61	15 52 7.1	2.08	16.50	20.77	3.87	1.00
06 32 35.38	15 52 25.1	2.14	16.62	20.86	3.99	0.98
06 32 29.39	15 52 21.5	2.32	16.86	21.16	4.39	0.90
06 32 23.15	15 52 14.3	2.54	17.61	21.38	4.72	0.88
06 33 50.72	15 50 43.5	2.20	17.72	20.68	3.76	1.11
06 33 43.73	15 50 29.3	2.20	17.44	20.75	3.85	1.07
06 33 38.49	15 50 36.6	2.19	17.22	20.79	3.89	1.04
06 33 31.76	15 50 36.7	2.19	16.85	20.89	4.03	0.98
06 33 25.77	15 50 33.2	2.18	16.84	20.87	4.01	0.99
06 33 19.53	15 50 36.9	2.29	16.83	21.11	4.32	0.91
06 33 14.29	15 50 36.9	2.35	16.90	21.20	4.46	0.89
06 33 6.06	15 50 37	2.28	16.94	21.05	4.24	0.94
06 33 0.82	15 50 47.8	2.17	16.67	20.89	4.03	0.97
06 32 54.59	15 50 47.9	2.18	16.66	20.92	4.07	0.96
06 32 47.85	15 50 40.7	2.14	16.68	20.83	3.95	0.99
06 32 41.11	15 50 47.9	2.14	16.59	20.85	3.98	0.98
06 32 35.63	15 50 47.9	2.20	16.75	20.94	4.10	0.96
06 32 30.14	15 50 58.7	2.35	17.01	21.18	4.42	0.90
06 32 22.15	15 50 51.5	2.58	17.72	21.42	4.78	0.87
06 34 14.4	15 48 51.4	2.37	17.99	20.95	4.11	1.03
06 34 8.17	15 49 9.5	2.34	17.88	20.92	4.07	1.03
06 34 1.93	15 48 58.9	2.37	17.96	20.96	4.12	1.03
06 33 55.45	15 49 2.6	2.38	17.87	21.01	4.19	1.00
06 33 49.46	15 49 2.8	2.28	17.58	20.88	4.01	1.03
06 33 44.22	15 49 6.5	2.19	17.52	20.72	3.80	1.08
06 33 38.49	15 49 10.2	2.24	17.33	20.87	4.01	1.02
06 33 31.25	15 49 3.1	2.21	16.99	20.89	4.03	0.99
06 33 25.51	15 49 10.4	2.12	16.82	20.76	3.86	1.02
06 33 18.53	15 49 14.1	2.26	16.72	21.06	4.27	0.92
06 33 12.54	15 48 59.7	2.36	16.75	21.27	4.56	0.86
06 33 6.31	15 49 10.6	2.36	16.77	21.26	4.54	0.87
06 33 0.32	15 49 3.4	2.23	16.73	21.02	4.20	0.94
06 32 53.34	15 49 21.5	2.16	16.67	20.88	4.01	0.98
06 32 48.1	15 49 7.1	2.12	16.89	20.73	3.82	1.04
06 32 40.86	15 49 14.3	2.20	16.77	20.94	4.09	0.96
06 32 35.38	15 49 14.3	2.26	16.86	21.03	4.22	0.94
06 32 28.64	15 49 14.3	2.39	17.08	21.24	4.51	0.89
06 34 13.14	15 47 21.4	2.38	17.98	20.97	4.14	1.02
06 34 7.66	15 47 36	2.41	17.90	21.05	4.24	0.99
06 34 1.67	15 47 25.3	2.43	17.97	21.08	4.28	0.99
06 33 55.19	15 47 29.1	2.38	17.91	20.99	4.16	1.01
06 33 50.2	15 47 32.8	2.26	17.81	20.79	3.89	1.08
06 33 43.72	15 47 32.9	2.21	17.71	20.72	3.80	1.09

continued on next page

Table 16 – continued from previous page

R.A.(J2000) hh mm ss	Dec.(J2000) dd mm ss	$F(60)$ (MJy)	$F(100)$ (MJy)	T_d (K)	$B(\nu, T)$ $(\times 10^{-16})$ Js^{-2}	A_V $(\times 10^{-5})$ mag
06 33 37.23	15 47 22.2	2.22	17.32	20.84	3.96	1.03
06 33 32.24	15 47 29.5	2.19	17.05	20.83	3.95	1.01
06 33 25.01	15 47 33.2	2.12	16.75	20.77	3.88	1.02
06 33 19.02	15 47 36.9	2.15	16.58	20.89	4.02	0.97
06 33 11.79	15 47 29.7	2.22	16.51	21.06	4.26	0.91
06 33 5.81	15 47 40.6	2.33	16.68	21.22	4.48	0.87
06 32 59.57	15 47 26.2	2.21	16.93	20.92	4.07	0.98
06 32 53.09	15 47 47.9	2.22	17.03	20.91	4.06	0.99
06 32 46.85	15 47 33.5	2.20	17.33	20.79	3.89	1.05
06 32 41.11	15 47 40.7	2.24	17.21	20.90	4.04	1.00
06 32 34.63	15 47 33.5	2.29	17.23	21.00	4.17	0.97
06 32 28.64	15 47 55.1	2.41	17.50	21.15	4.39	0.94
06 34 7.65	15 45 55.2	2.36	17.92	20.96	4.13	1.02
06 34 1.66	15 45 55.3	2.35	17.94	20.93	4.08	1.03
06 33 55.43	15 46 9.9	2.37	18.07	20.94	4.09	1.04
06 33 49.69	15 46 10	2.33	17.96	20.89	4.02	1.05
06 33 42.71	15 45 59.3	2.20	17.76	20.68	3.76	1.11
06 33 35.73	15 45 59.4	2.16	17.54	20.66	3.73	1.11
06 33 31.74	15 45 59.5	2.17	17.21	20.76	3.85	1.05
06 33 24.76	15 46 17.6	2.08	16.81	20.67	3.74	1.06
06 33 18.52	15 45 59.7	2.12	16.76	20.78	3.89	1.01
06 33 12.29	15 46 21.3	2.23	16.58	21.05	4.24	0.92
06 33 5.55	15 46 10.6	2.29	16.73	21.13	4.36	0.90
06 32 59.57	15 46 21.4	2.24	17.21	20.90	4.04	1.00
06 32 53.08	15 46 17.9	2.27	17.29	20.93	4.09	0.99
06 32 46.35	15 46 25.1	2.30	17.60	20.92	4.06	1.02
06 32 41.11	15 46 21.5	2.30	17.64	20.90	4.05	1.02
06 32 35.63	15 46 21.5	2.34	17.61	20.99	4.16	0.99
06 32 29.14	15 46 35.9	2.46	17.89	21.16	4.40	0.96
06 34 7.89	15 44 39.6	2.31	17.74	20.90	4.04	1.03
06 34 2.4	15 44 36.1	2.31	17.86	20.87	4.00	1.05
06 33 54.67	15 44 43.5	2.30	17.91	20.85	3.97	1.06
06 33 49.93	15 44 43.6	2.30	17.77	20.88	4.02	1.04
06 33 42.95	15 44 43.7	2.22	17.66	20.74	3.83	1.08
06 33 37.96	15 44 29.4	2.19	17.54	20.71	3.80	1.09
06 33 30.98	15 44 33.1	2.20	17.28	20.79	3.90	1.04
06 33 24.5	15 44 44	2.20	17.16	20.82	3.94	1.02
06 33 17.52	15 44 51.3	2.17	17.04	20.81	3.92	1.02
06 33 12.53	15 44 33.3	2.29	16.89	21.08	4.29	0.93
06 33 5.3	15 44 37	2.34	17.06	21.15	4.39	0.91
06 32 59.32	15 44 40.6	2.35	17.26	21.11	4.33	0.94
06 32 52.58	15 44 44.3	2.34	17.49	21.03	4.21	0.98
06 32 47.6	15 44 33.5	2.34	17.71	20.96	4.13	1.01
06 32 41.86	15 44 51.5	2.33	17.82	20.92	4.07	1.03
06 32 34.63	15 44 47.9	2.41	17.98	21.03	4.21	1.00
06 34 12.86	15 43 5.8	2.30	17.86	20.85	3.97	1.06
06 34 6.13	15 42 58.8	2.27	17.76	20.83	3.94	1.06
06 34 0.89	15 42 58.9	2.27	17.66	20.85	3.98	1.04
06 33 54.66	15 42 55.5	2.33	17.57	20.98	4.15	1.00
06 33 49.92	15 42 59.2	2.31	17.51	20.96	4.13	1.00
06 33 43.94	15 43 10.1	2.23	17.65	20.77	3.87	1.07
06 33 36.46	15 42 59.4	2.23	17.50	20.81	3.92	1.05
06 33 29.98	15 43 6.7	2.21	17.60	20.74	3.83	1.08
06 33 24.24	15 43 6.8	2.26	17.87	20.78	3.88	1.08
06 33 18.51	15 42 59.7	2.24	17.75	20.76	3.86	1.08
06 33 12.03	15 43 10.5	2.31	17.51	20.96	4.12	1.00
06 33 5.79	15 42 59.8	2.43	17.53	21.19	4.45	0.93
06 32 59.56	15 43 10.6	2.41	17.45	21.18	4.43	0.93
06 32 53.08	15 43 25.1	2.47	17.59	21.26	4.54	0.91
06 32 47.1	15 43 10.7	2.43	17.86	21.10	4.31	0.97
06 34 18.58	15 41 35.7	2.32	17.97	20.86	3.99	1.06
06 34 12.1	15 41 35.9	2.35	17.70	20.99	4.17	1.00
06 34 7.61	15 41 28.8	2.28	17.60	20.87	4.01	1.03
06 34 1.63	15 41 28.9	2.26	17.43	20.88	4.02	1.02
06 33 53.4	15 41 29.1	2.26	17.37	20.90	4.04	1.01
06 33 48.92	15 41 36.4	2.22	17.36	20.82	3.94	1.04
06 33 42.69	15 41 36.5	2.17	17.51	20.69	3.76	1.09
06 33 36.7	15 41 33	2.25	17.60	20.81	3.92	1.05
06 33 30.97	15 41 43.9	2.32	17.96	20.87	4.00	1.05
06 33 5.04	15 41 58.6	2.54	17.93	21.30	4.60	0.92
06 32 58.56	15 41 47.9	2.42	17.89	21.08	4.29	0.98
06 32 53.08	15 41 58.7	2.49	17.92	21.20	4.46	0.95
06 34 19.56	15 39 54.9	2.33	17.93	20.90	4.04	1.04
06 34 12.84	15 40 5.8	2.30	17.76	20.88	4.02	1.04
06 34 8.35	15 39 55.2	2.31	17.71	20.91	4.06	1.02
06 34 1.62	15 39 55.3	2.33	17.42	21.02	4.21	0.97
06 33 53.89	15 40 2.7	2.32	17.37	21.01	4.19	0.97

continued on next page

Table 16 – continued from previous page

R.A.(J2000) hh mm ss	Dec.(J2000) dd mm ss	$F(60)$ (MJy)	$F(100)$ (MJy)	T_d (K)	$B(\nu,T)$ $(\times10^{-16})$ Js^{-2}	A_V $(\times10^{-5})$ mag
06 33 48.16	15 40 2.8	2.29	17.36	20.96	4.13	0.99
06 33 41.68	15 40 6.5	2.20	17.54	20.74	3.83	1.08
06 33 35.95	15 40 13.8	2.30	17.91	20.84	3.97	1.06
06 34 7.59	15 38 36	2.42	17.90	21.07	4.27	0.99
06 34 1.11	15 38 25.3	2.38	17.58	21.08	4.28	0.96
06 33 54.88	15 38 43.5	2.36	17.37	21.10	4.31	0.95
06 33 48.15	15 38 29.2	2.26	17.40	20.89	4.03	1.01
06 33 42.67	15 38 32.9	2.20	17.76	20.67	3.75	1.11
06 33 54.62	15 37 6.3	2.42	17.65	21.15	4.38	0.95
06 33 48.39	15 37 17.2	2.37	17.75	21.02	4.20	0.99
06 33 41.91	15 36 59.3	2.30	17.99	20.82	3.94	1.07

Table 17: The Database of far infrared cavity CCRAS4 nearby AGB star AGB0633+1415. The first two columns represent position of the pixels with in the cavity. The next two columns give values of relative flux density at 60 μm and 100 μm that have obtained after processing the FITS image using ALADIN 2.5 software. The calculated values of dust color temperature (in K), Planck function for 100 μm and visual extinction (in mag) of the corresponding pixels,respectively.

R.A.(J2000) hh mm ss	Dec.(J2000) dd mm ss	$F(60)$ (MJy)	$F(100)$ (MJy)	T_d (K)	$B(\nu,T)$ $(\times10^{-16})$ Js^{-2}	A_V $(\times10^{-5})$ mag
06 34 12.19	14 38 8.9	3.15	18.26	22.27	6.17	0.70
06 34 5.99	14 38 27	3.13	18.07	22.29	6.22	0.68
06 33 58.55	14 38 19.9	3.21	18.16	22.40	6.41	0.67
06 34 18.38	14 36 46	3.15	18.12	22.31	6.24	0.68
06 34 11.19	14 36 42.5	3.09	17.67	22.34	6.31	0.66
06 34 5.98	14 36 42.6	3.13	17.56	22.43	6.47	0.64
06 33 59.53	14 36 42.7	3.15	17.62	22.46	6.52	0.64
06 33 54.08	14 36 46.4	3.19	17.83	22.45	6.51	0.64
06 34 24.57	14 35 12.3	3.21	18.20	22.39	6.40	0.67
06 34 18.62	14 35 19.6	3.14	17.83	22.37	6.36	0.66
06 34 11.43	14 35 16.1	3.11	17.38	22.45	6.51	0.63
06 34 5.97	14 35 16.2	3.09	17.28	22.46	6.52	0.62
06 33 59.28	14 35 16.3	3.12	17.27	22.51	6.62	0.61
06 33 54.32	14 35 12.8	3.13	17.64	22.41	6.44	0.64
06 33 47.87	14 35 16.5	3.22	18.18	22.41	6.44	0.66
06 34 30.02	14 33 52.9	3.18	18.09	22.37	6.36	0.67
06 34 24.56	14 34 0.3	3.14	17.98	22.33	6.29	0.67
06 34 18.36	14 33 53.2	3.07	17.64	22.31	6.25	0.66
06 34 11.92	14 33 49.7	3.02	17.17	22.37	6.36	0.63
06 34 6.21	14 33 57	3.05	17.09	22.45	6.51	0.62
06 33 59.02	14 33 53.5	3.08	17.25	22.44	6.49	0.62
06 33 53.07	14 33 53.6	3.15	17.58	22.46	6.52	0.63
06 33 47.12	14 33 53.7	3.21	18.21	22.38	6.38	0.67
06 34 30.75	14 32 26.5	3.10	17.95	22.28	6.19	0.68
06 34 24.31	14 32 23.1	2.96	17.70	22.10	5.89	0.71
06 34 18.36	14 32 16	2.92	17.34	22.14	5.95	0.69
06 34 12.16	14 32 26.9	2.91	16.91	22.24	6.14	0.65
06 34 6.21	14 32 34.2	3.02	16.88	22.45	6.51	0.61
06 34 0.5	14 32 23.5	3.07	17.24	22.42	6.46	0.63
06 33 53.81	14 32 16.4	3.18	17.64	22.49	6.58	0.63
06 33 48.11	14 32 20.1	3.27	18.30	22.45	6.51	0.66
06 34 30.25	14 30 42.1	3.06	17.81	22.24	6.14	0.68
06 34 23.8	14 30 49.5	2.88	17.34	22.07	5.82	0.70
06 34 18.1	14 30 42.4	2.82	17.05	22.04	5.79	0.69
06 34 12.4	14 30 46.1	2.81	16.69	22.14	5.95	0.66
06 34 5.7	14 30 46.2	2.93	16.85	22.30	6.24	0.63
06 34 0	14 30 39.1	3.08	17.24	22.45	6.51	0.62
06 33 54.05	14 30 39.2	3.25	17.81	22.55	6.70	0.62
06 34 29.99	14 29 22.9	3.09	17.84	22.28	6.20	0.68
06 34 23.3	14 29 26.7	2.90	17.42	22.09	5.86	0.70
06 34 17.35	14 29 16	2.80	17.18	21.98	5.67	0.71
06 34 12.39	14 29 12.5	2.89	16.89	22.22	6.09	0.65
06 34 6.19	14 29 12.6	2.97	17.06	22.31	6.25	0.64
06 33 59.75	14 29 23.5	3.15	17.42	22.51	6.62	0.62
06 33 53.55	14 29 12.8	3.36	17.86	22.72	7.03	0.60
06 34 28.74	14 28 0.2	3.12	17.98	22.30	6.24	0.68
06 34 23.78	14 27 56.7	3.02	17.86	22.17	6.01	0.70
06 34 18.58	14 27 46	3.00	17.47	22.24	6.13	0.67
06 34 12.63	14 27 46.1	3.02	17.27	22.35	6.32	0.64
06 34 6.43	14 27 46.2	3.11	17.35	22.46	6.54	0.62
06 33 59.74	14 27 39.1	3.20	17.56	22.56	6.72	0.61
06 33 54.04	14 27 53.6	3.34	18.06	22.64	6.87	0.62
06 34 29.97	14 26 33.8	3.18	18.30	22.30	6.24	0.69

continued on next page

Table 17 – continued from previous page

R.A.(J2000) hh mm ss	Dec.(J2000) dd mm ss	$F(60)$ (MJy)	$F(100)$ (MJy)	T_d (K)	$B(\nu,T)$ $(\times10^{-16})$ Js^{-2}	A_V $(\times10^{-5})$ mag
06 34 24.27	14 26 33.9	3.14	18.16	22.28	6.20	0.69
06 34 18.07	14 26 19.6	3.18	18.02	22.39	6.39	0.66
06 34 12.87	14 26 19.7	3.20	17.70	22.50	6.61	0.63
06 34 6.18	14 26 9	3.25	17.63	22.61	6.82	0.61
06 33 59.98	14 26 12.7	3.23	17.94	22.49	6.58	0.64
06 34 17.82	14 25 4	3.27	18.32	22.45	6.50	0.66
06 34 11.37	14 24 53.3	3.32	18.03	22.60	6.80	0.62
06 34 5.92	14 24 46.2	3.32	18.01	22.62	6.82	0.62
06 34 0.47	14 24 49.9	3.34	18.30	22.55	6.71	0.64

Table 18: The Database of far infrared cavity CCRAS5 nearby AGB star AGB0642+0053. The first two columns represent position of the pixels with in the cavity. The next two columns give values of relative flux density at 60 μm and 100 μm that have obtained after processing the FITS image using ALADIN 2.5 software. The calculated values of dust color temperature (in K), Planck function for 100 μm and visual extinction (in mag) of the corresponding pixels,respectively.

R.A.(J2000) hh mm ss	Dec.(J2000) dd mm ss	$F(60)$ (MJy)	$F(100)$ (MJy)	T_d (K)	$B(\nu,T)$ $(\times10^{-16})$ Js^{-2}	A_V $(\times10^{-5})$ mag
06 42 17.12	1 18 4.8	4.5002	28.345	21.85	5.45	1.22
06 42 11.36	1 18 4.8	4.4346	28.064	21.82	5.41	1.22
06 42 5.36	1 17 54	4.2931	28.304	21.62	5.09	1.31
06 41 59.36	1 17 50.4	4.3234	28.569	21.61	5.07	1.32
06 41 53.6	1 17 50.4	4.5103	28.734	21.79	5.36	1.26
06 42 22.64	1 16 31.2	4.48	28.354	21.82	5.41	1.23
06 42 17.12	1 16 20.4	4.4472	27.874	21.87	5.49	1.19
06 42 10.64	1 16 13.2	4.4522	27.824	21.88	5.51	1.19
06 42 5.12	1 16 24	4.2855	28.014	21.66	5.15	1.28
06 41 58.88	1 16 20.4	4.2552	28.147	21.60	5.06	1.31
06 41 53.6	1 16 27.6	4.3436	28.279	21.68	5.19	1.28
06 42 23.6	1 14 54	4.4017	28.072	21.78	5.35	1.23
06 42 16.88	1 14 54	4.4017	27.742	21.84	5.45	1.20
06 42 10.88	1 15 8.4	4.4497	27.899	21.87	5.49	1.20
06 42 4.88	1 15 4.8	4.3057	27.998	21.69	5.20	1.27
06 41 59.12	1 14 57.6	4.2375	28.056	21.60	5.06	1.30
06 41 53.12	1 14 50.4	4.2956	27.99	21.68	5.18	1.27
06 41 47.36	1 15 4.8	4.3941	28.469	21.71	5.22	1.28
06 42 23.84	1 13 45.6	4.3688	27.874	21.78	5.35	1.23
06 42 16.88	1 13 27.6	4.3638	27.675	21.81	5.39	1.21
06 42 11.6	1 13 34.8	4.4522	27.899	21.87	5.49	1.19
06 42 5.12	1 13 31.2	4.2627	28.163	21.61	5.07	1.31
06 41 58.88	1 13 20.4	4.2501	28.056	21.61	5.08	1.30
06 41 53.36	1 13 24	4.3107	28.056	21.68	5.19	1.27
06 41 48.08	1 13 24	4.2905	28.254	21.63	5.10	1.30
06 41 41.36	1 13 24	4.4775	28.577	21.78	5.34	1.26
06 42 23.36	1 11 54	4.3916	27.924	21.80	5.37	1.22
06 42 16.88	1 11 57.6	4.2981	27.609	21.75	5.29	1.23
06 42 11.36	1 11 54	4.3941	27.766	21.83	5.42	1.20
06 42 5.6	1 11 54	4.1642	28.023	21.52	4.93	1.34
06 41 58.88	1 11 54	4.2577	28.13	21.61	5.07	1.30
06 41 53.12	1 11 50.4	4.2451	27.882	21.64	5.12	1.28
06 41 47.12	1 11 57.6	4.2147	27.841	21.61	5.07	1.29
06 41 41.36	1 11 54	4.2223	27.725	21.64	5.12	1.27
06 41 34.87	1 11 57.6	4.4067	27.758	21.85	5.45	1.20
06 42 28.41	1 10 34.8	4.5457	28.552	21.86	5.47	1.23
06 42 22.88	1 10 34.8	4.3411	27.866	21.75	5.30	1.24
06 42 16.88	1 10 38.4	4.2501	27.576	21.70	5.21	1.24
06 42 11.36	1 10 31.2	4.3461	27.717	21.78	5.35	1.22
06 42 4.88	1 10 34.8	4.1718	27.808	21.57	5.01	1.31
06 41 59.12	1 10 20.4	4.1289	27.766	21.53	4.94	1.32
06 41 53.36	1 10 24	4.1743	27.386	21.64	5.13	1.26
06 41 46.64	1 10 31.2	4.0809	27.154	21.58	5.02	1.27
06 41 41.6	1 10 16.8	4.0556	26.972	21.58	5.02	1.26
06 41 34.87	1 10 27.6	4.1263	26.766	21.70	5.21	1.21
06 41 28.63	1 10 34.8	4.2299	27.493	21.69	5.20	1.24
06 42 34.89	1 8 54	4.4851	28.61	21.78	5.35	1.26
06 42 28.65	1 8 50.4	4.4017	28.263	21.75	5.29	1.25
06 42 22.88	1 8 50.4	4.2779	27.758	21.70	5.21	1.25
06 42 17.12	1 8 57.6	4.187	27.667	21.61	5.07	1.28
06 42 10.88	1 8 54	4.3057	27.766	21.73	5.26	1.24
06 42 5.6	1 8 57.6	4.1238	27.94	21.49	4.88	1.34
06 41 59.84	1 8 46.8	4.0632	27.609	21.48	4.86	1.33
06 41 53.36	1 8 50.4	4.0758	27.072	21.58	5.03	1.26
06 41 45.68	1 8 46.8	3.9722	26.766	21.52	4.92	1.28

continued on next page

Table 18 – continued from previous page

R.A.(J2000) hh mm ss	Dec.(J2000) dd mm ss	$F(60)$ (MJy)	$F(100)$ (MJy)	T_d (K)	$B(\nu,T)$ $(\times10^{-16})$ Js^{-2}	A_V $(\times10^{-5})$ mag
06 41 41.6	1 8 39.6	3.9293	26.443	21.52	4.93	1.26
06 41 35.11	1 8 50.4	3.9747	26.294	21.60	5.06	1.22
06 41 29.59	1 8 57.6	4.0556	27.047	21.57	5.00	1.27
06 41 23.35	1 8 57.6	4.2804	28.246	21.62	5.08	1.31
06 42 40.65	1 7 34.8	4.4244	28.378	21.76	5.30	1.26
06 42 34.89	1 7 27.6	4.3941	28.172	21.76	5.31	1.25
06 42 27.68	1 7 27.6	4.331	28.089	21.70	5.22	1.27
06 42 22.4	1 7 31.2	4.2905	28.139	21.65	5.13	1.29
06 42 18.56	1 7 31.2	4.2577	28.097	21.62	5.08	1.30
06 42 11.6	1 7 27.6	4.2476	28.246	21.58	5.02	1.32
06 42 5.84	1 7 24	4.1718	28.511	21.45	4.82	1.39
06 42 0.32	1 7 20.4	4.0783	28.039	21.42	4.78	1.38
06 41 54.8	1 7 13.2	4.0455	27.27	21.51	4.92	1.30
06 41 46.4	1 7 24	3.952	26.931	21.46	4.84	1.31
06 41 41.36	1 7 16.8	3.952	26.584	21.52	4.94	1.27
06 41 35.36	1 7 31.2	4.0076	26.575	21.59	5.04	1.24
06 41 28.87	1 7 20.4	4.0404	27.303	21.50	4.90	1.31
06 41 23.59	1 7 31.2	4.1971	28.039	21.56	4.99	1.32
06 41 16.87	1 7 20.4	4.3107	28.544	21.60	5.06	1.33
06 42 41.13	1 6 8.4	4.4497	28.552	21.75	5.30	1.27
06 42 35.85	1 5 54	4.4118	28.354	21.75	5.29	1.26
06 42 29.12	1 6 8.4	4.4042	28.718	21.67	5.17	1.31
06 41 59.84	1 6 1.2	4.1996	28.618	21.46	4.84	1.39
06 41 54.32	1 6 4.8	4.0859	27.75	21.48	4.87	1.34
06 41 47.6	1 5 57.6	4.1011	27.518	21.54	4.96	1.31
06 41 41.6	1 5 57.6	4.1213	27.394	21.58	5.03	1.28
06 41 35.84	1 5 46.8	4.1112	27.187	21.61	5.07	1.26
06 41 28.39	1 5 54	4.1238	27.634	21.54	4.97	1.31
06 41 22.87	1 6 1.2	4.2552	28.304	21.58	5.02	1.33
06 41 17.11	1 6 4.8	4.3208	28.701	21.58	5.03	1.34
06 41 46.64	1 4 38.4	4.3006	28.742	21.55	4.99	1.36
06 41 41.12	1 4 31.2	4.3461	28.271	21.69	5.19	1.28
06 41 36.08	1 4 31.2	4.2804	28.006	21.66	5.15	1.28
06 41 29.11	1 4 34.8	4.2552	28.304	21.58	5.02	1.33

Table 19: The Database of far infrared cavity CCRAS6 nearby AGB star AGB0651+0031. The first two columns represent position of the pixels with in the cavity. The next two columns give values of relative flux density at 60 μm and 100 μm that have obtained after processing the FITS image using ALADIN 2.5 software. The calculated values of dust color temperature (in K), Planck function for 100 μm and visual extinction (in mag) of the corresponding pixels,respectively.

R.A.(J2000) hh mm ss	Dec.(J2000) dd mm ss	$F(60)$ (MJy)	$F(100)$ (MJy)	T_d (K)	$B(\nu,T)$ $(\times10^{-16})$ Js^{-2}	A_V $(\times10^{-5})$ mag
06 50 46.36	0 40 0	4.58	29.51	21.73	5.17	1.34
06 50 40.36	0 39 52.8	4.33	28.62	21.60	4.98	1.35
06 50 34.84	0 39 45.6	4.27	28.30	21.59	4.96	1.34
06 50 28.84	0 40 0	4.27	28.84	21.50	4.82	1.41
06 50 23.08	0 39 49.2	4.38	29.52	21.52	4.85	1.43
06 50 46.6	0 38 19.2	4.39	29.14	21.59	4.95	1.38
06 50 41.32	0 38 26.4	4.10	27.81	21.48	4.79	1.36
06 50 35.08	0 38 15.6	3.97	27.39	21.41	4.68	1.38
06 50 28.36	0 38 26.4	3.87	27.36	21.28	4.50	1.43
06 50 22.12	0 38 26.4	4.00	27.88	21.35	4.60	1.42
06 50 17.08	0 38 19.2	4.31	28.66	21.58	4.93	1.37
06 50 10.6	0 38 33.6	4.86	29.64	22.00	5.62	1.24
06 49 46.84	0 38 15.6	4.39	29.21	21.58	4.94	1.39
06 49 40.6	0 38 30	4.39	29.41	21.54	4.88	1.42
06 50 46.36	0 37 3.6	4.45	29.28	21.63	5.02	1.37
06 50 41.08	0 36 56.4	4.19	27.96	21.56	4.91	1.34
06 50 34.6	0 37 0	3.90	27.27	21.34	4.59	1.40
06 50 29.08	0 36 49.2	3.74	27.03	21.19	4.36	1.46
06 50 23.08	0 36 45.6	3.78	27.20	21.20	4.38	1.46
06 50 16.84	0 36 45.6	3.94	27.41	21.36	4.62	1.40
06 50 10.84	0 36 49.2	4.15	27.49	21.59	4.96	1.30
06 50 3.88	0 36 45.6	4.17	28.32	21.48	4.79	1.39
06 49 58.6	0 36 45.6	4.23	28.39	21.53	4.87	1.37
06 49 52.84	0 36 42	4.13	28.40	21.42	4.70	1.42
06 49 46.36	0 36 45.6	3.93	27.77	21.29	4.51	1.45
06 49 40.6	0 36 45.6	3.82	28.06	21.11	4.25	1.55
06 49 34.84	0 36 45.6	4.01	28.57	21.25	4.45	1.51
06 49 28.84	0 36 52.8	4.11	28.83	21.33	4.56	1.49
06 49 23.08	0 36 56.4	4.20	29.55	21.31	4.54	1.53
06 50 39.88	0 35 8.4	4.45	28.88	21.70	5.13	1.32

continued on next page

Table 19 – continued from previous page

R.A.(J2000) hh mm ss	Dec.(J2000) dd mm ss	$F(60)$ (MJy)	$F(100)$ (MJy)	T_d (K)	$B(\nu, T)$ $(\times 10^{-16})$ Js^{-2}	A_V $(\times 10^{-5})$ mag
06 50 33.64	0 35 19.2	4.05	27.81	21.43	4.71	1.39
06 50 28.84	0 35 22.8	3.90	27.44	21.31	4.54	1.42
06 50 23.32	0 35 22.8	3.79	27.41	21.17	4.34	1.48
06 50 17.08	0 35 19.2	3.85	27.01	21.32	4.56	1.39
06 50 10.84	0 35 4.8	3.85	26.64	21.39	4.66	1.34
06 50 4.84	0 35 15.6	3.81	26.83	21.30	4.52	1.40
06 49 58.6	0 35 12	3.72	27.12	21.14	4.30	1.48
06 49 52.84	0 35 8.4	3.67	27.01	21.10	4.24	1.50
06 49 45.88	0 35 22.8	3.55	26.65	21.00	4.11	1.53
06 49 41.32	0 35 19.2	3.42	26.62	20.84	3.90	1.61
06 49 34.6	0 35 15.6	3.49	27.08	20.85	3.91	1.63
06 49 29.56	0 35 30	3.75	28.30	20.99	4.09	1.63
06 49 22.84	0 35 30	3.97	28.30	21.24	4.44	1.50
06 49 16.6	0 35 22.8	4.35	29.31	21.52	4.85	1.42
06 50 39.4	0 33 49.2	4.66	29.73	21.79	5.26	1.33
06 50 34.12	0 33 56.4	4.43	28.88	21.67	5.08	1.34
06 50 28.12	0 33 49.2	4.26	28.54	21.54	4.88	1.37
06 50 21.64	0 33 45.6	4.08	28.10	21.41	4.68	1.41
06 50 16.12	0 33 52.8	3.85	27.58	21.22	4.41	1.47
06 50 11.32	0 33 49.2	3.95	27.06	21.43	4.72	1.35
06 50 5.08	0 33 49.2	3.82	26.82	21.31	4.54	1.39
06 49 57.4	0 33 42	3.64	26.50	21.15	4.31	1.45
06 49 52.36	0 33 45.6	3.54	26.19	21.08	4.21	1.46
06 49 45.16	0 33 42	3.39	25.96	20.92	4.00	1.53
06 49 40.84	0 33 56.4	3.26	25.97	20.74	3.77	1.62
06 49 34.84	0 33 56.4	3.30	26.35	20.73	3.76	1.65
06 49 28.12	0 33 52.8	3.49	26.83	20.90	3.97	1.59
06 49 23.56	0 34 3.6	3.78	27.54	21.15	4.31	1.50
06 49 16.84	0 34 0	4.10	28.80	21.32	4.55	1.49
06 50 15.88	0 32 26.4	4.50	29.52	21.64	5.03	1.38
06 50 9.64	0 32 26.4	4.34	28.54	21.63	5.02	1.34
06 50 4.84	0 32 15.6	4.14	27.25	21.63	5.02	1.28
06 49 58.12	0 32 15.6	3.81	26.44	21.38	4.64	1.34
06 49 51.4	0 32 8.4	3.50	25.62	21.12	4.27	1.41
06 49 45.88	0 32 19.2	3.30	25.39	20.89	3.96	1.51
06 49 40.84	0 32 30	3.17	25.46	20.70	3.71	1.61
06 49 35.32	0 32 19.2	3.20	25.99	20.65	3.65	1.67
06 49 29.08	0 32 22.8	3.37	26.53	20.79	3.83	1.63
06 49 22.84	0 32 19.2	3.67	27.41	21.03	4.15	1.55
06 49 15.88	0 32 33.6	4.10	28.97	21.28	4.50	1.51
06 50 4.12	0 30 52.8	4.58	27.85	22.02	5.65	1.16
06 49 57.4	0 30 49.2	3.86	26.30	21.46	4.76	1.30
06 49 52.12	0 30 52.8	3.43	25.53	21.05	4.18	1.44
06 49 45.88	0 31 3.6	3.24	25.00	20.89	3.96	1.49
06 49 40.84	0 31 3.6	3.08	25.10	20.63	3.63	1.63
06 49 35.32	0 30 56.4	3.10	25.72	20.55	3.54	1.71
06 49 29.08	0 30 52.8	3.33	26.48	20.74	3.77	1.65
06 49 22.6	0 30 42	3.68	27.80	20.98	4.08	1.60
06 49 15.88	0 30 52.8	4.13	29.21	21.28	4.50	1.53
06 50 9.64	0 29 22.8	4.70	29.55	21.86	5.38	1.29
06 50 4.12	0 29 26.4	4.38	27.42	21.88	5.41	1.19
06 49 57.4	0 29 4.8	3.74	25.92	21.38	4.64	1.31
06 49 52.36	0 29 26.4	3.35	25.29	20.98	4.08	1.46
06 49 46.6	0 29 12	3.14	24.82	20.77	3.81	1.53
06 49 40.36	0 29 30	2.98	25.15	20.49	3.46	1.71
06 49 34.36	0 29 19.2	3.06	25.80	20.48	3.45	1.76
06 49 28.36	0 29 22.8	3.37	26.61	20.78	3.82	1.64
06 49 22.36	0 29 26.4	3.73	28.11	20.99	4.09	1.61
06 50 10.12	0 27 49.2	4.36	28.78	21.62	5.00	1.35
06 50 3.88	0 27 52.8	4.07	26.89	21.61	4.98	1.27
06 49 57.4	0 27 52.8	3.60	26.09	21.17	4.35	1.41
06 49 52.12	0 27 56.4	3.42	25.52	21.03	4.15	1.45
06 49 46.12	0 27 52.8	3.27	25.55	20.82	3.87	1.55
06 49 39.64	0 27 56.4	3.19	25.82	20.67	3.68	1.65
06 49 34.36	0 27 49.2	3.27	26.52	20.66	3.66	1.70
06 49 27.88	0 27 49.2	3.54	27.35	20.88	3.94	1.63
06 49 22.36	0 27 52.8	3.84	28.84	21.01	4.12	1.65
06 50 9.88	0 26 22.8	4.53	28.68	21.82	5.32	1.27
06 50 4.36	0 26 26.4	4.15	27.35	21.62	5.01	1.28
06 49 57.88	0 26 26.4	3.77	26.67	21.28	4.49	1.40
06 49 52.36	0 26 22.8	3.59	26.45	21.10	4.24	1.47
06 49 46.6	0 26 19.2	3.58	26.53	21.06	4.19	1.49
06 49 40.36	0 26 30	3.57	27.11	20.96	4.05	1.57
06 49 34.36	0 26 19.2	3.66	27.82	20.95	4.05	1.62
06 49 27.88	0 26 19.2	3.89	28.78	21.07	4.21	1.61
06 50 8.92	0 25 3.6	4.69	29.36	21.88	5.41	1.28
06 50 4.12	0 24 52.8	4.14	27.79	21.54	4.88	1.34

continued on next page

Table 19 – continued from previous page

R.A.(J2000) hh mm ss	Dec.(J2000) dd mm ss	$F(60)$ (MJy)	$F(100)$ (MJy)	T_d (K)	$B(\nu,T)$ $(\times10^{-16})$ Js^{-2}	A_V $(\times10^{-5})$ mag
06 49 57.88	0 24 45.6	3.92	27.30	21.36	4.61	1.39
06 49 52.12	0 24 49.2	3.84	27.02	21.31	4.54	1.40
06 49 46.12	0 24 52.8	3.77	27.27	21.17	4.34	1.48
06 49 39.88	0 24 56.4	3.80	28.00	21.10	4.24	1.55
06 49 34.36	0 24 56.4	3.94	28.73	21.14	4.29	1.57
06 50 4.6	0 23 19.2	4.33	28.77	21.58	4.95	1.37
06 49 57.88	0 23 30	4.07	27.90	21.44	4.72	1.39
06 49 51.64	0 23 22.8	4.02	27.59	21.42	4.70	1.38
06 49 46.36	0 23 26.4	3.99	27.83	21.35	4.60	1.42
06 49 40.36	0 23 26.4	3.93	28.58	21.15	4.32	1.56
06 49 34.12	0 23 30	4.11	29.17	21.27	4.48	1.53
06 49 59.32	0 22 0	4.36	28.92	21.59	4.96	1.37
06 49 52.36	0 21 49.2	4.26	28.45	21.56	4.91	1.36
06 49 45.4	0 21 52.8	4.16	28.39	21.46	4.75	1.40
06 49 40.84	0 21 56.4	4.11	28.72	21.34	4.58	1.47
06 49 34.36	0 22 3.6	4.24	29.42	21.37	4.62	1.50
06 49 51.88	0 20 22.8	4.29	29.21	21.47	4.77	1.44
06 49 46.12	0 20 26.4	4.24	28.88	21.46	4.76	1.43
06 49 40.12	0 20 12	4.23	29.08	21.42	4.69	1.46
06 49 34.6	0 20 19.2	4.30	29.51	21.43	4.71	1.47
06 49 51.16	0 19 0	4.40	29.61	21.53	4.86	1.43
06 49 45.16	0 18 52.8	4.29	29.25	21.46	4.76	1.45
06 49 39.16	0 18 45.6	4.26	29.34	21.41	4.69	1.47
06 49 45.64	0 17 30	4.41	29.55	21.54	4.88	1.42
06 49 40.12	0 17 33.6	4.45	29.59	21.58	4.94	1.41

Table 20: The Database of far infrared cavity CCRAS7 nearby AGB star AGB0939-5249. The first two columns represent position of the pixels with in the cavity. The next two columns give values of relative flux density at 60 μm and 100 μm that have obtained after processing the FITS image using ALADIN 2.5 software. The calculated values of dust color temperature (in K), Planck function for 100 μm and visual extinction (in mag) of the corresponding pixels,respectively.

R.A.(J2000) hh mm ss	Dec.(J2000) dd mm ss	$F(60)$ (MJy)	$F(100)$ (MJy)	T_d (K)	$B(\nu,T)$ $(\times10^{-16})$ Js^{-2}	A_V $(\times10^{-5})$ mag
09 40 33.98	-52 43 58.3	10.772	59.931	22.48	6.57	2.15
09 40 24.47	-52 43 58.2	10.725	59.851	22.46	6.54	2.15
09 41 41.41	-52 46 18.1	10.576	59.905	22.39	6.39	2.20
09 41 31.89	-52 46 18.4	10.556	59.664	22.40	6.41	2.19
09 41 21.57	-52 46 4.1	10.552	59.384	22.42	6.46	2.16
09 41 12.45	-52 45 57.1	10.556	59.771	22.39	6.40	2.20
09 41 2.13	-52 45 50	10.552	59.237	22.43	6.48	2.15
09 40 53.8	-52 45 42.8	10.583	58.903	22.48	6.56	2.11
09 40 43.89	-52 45 39.2	10.543	58.863	22.46	6.53	2.12
09 40 32.39	-52 45 39.1	10.463	58.703	22.44	6.48	2.13
09 40 22.87	-52 45 24.6	10.546	58.85	22.46	6.54	2.12
09 40 12.96	-52 45 17.2	10.666	59.891	22.43	6.48	2.17
09 41 50.57	-52 47 51.5	10.43	58.169	22.47	6.54	2.09
09 41 40.64	-52 47 40.9	10.204	58.717	22.30	6.24	2.21
09 41 32.7	-52 47 44.7	10.284	58.556	22.36	6.34	2.17
09 41 21.59	-52 47 37.7	10.493	58.703	22.45	6.51	2.12
09 41 11.27	-52 47 27.1	10.374	58.143	22.44	6.50	2.10
09 41 2.14	-52 47 20	10.33	57.982	22.43	6.48	2.10
09 40 52.22	-52 47 16.4	10.327	57.168	22.51	6.62	2.03
09 40 41.5	-52 47 20	10.314	57.315	22.49	6.58	2.05
09 40 31.58	-52 47 1.9	10.31	57.489	22.47	6.55	2.07
09 40 22.85	-52 46 54.6	10.354	57.875	22.46	6.52	2.09
09 40 10.95	-52 46 43.6	10.596	58.823	22.49	6.59	2.10
09 40 3.81	-52 46 36.2	10.781	59.437	22.53	6.66	2.10
09 41 59.34	-52 49 14	10.692	59.357	22.49	6.59	2.12
09 41 49.8	-52 49 14.3	10.297	58.009	22.41	6.45	2.12
09 41 41.07	-52 49 14.5	10.015	56.941	22.37	6.36	2.11
09 41 30.74	-52 49 4	10.055	57.662	22.32	6.28	2.16
09 41 20.02	-52 49 4.2	10.32	57.889	22.44	6.49	2.10
09 41 11.68	-52 48 57.1	10.343	57.529	22.48	6.57	2.06
09 41 0.56	-52 48 50	10.294	56.901	22.51	6.63	2.02
09 40 51.42	-52 48 39.2	10.214	56.714	22.49	6.59	2.02
09 40 40.7	-52 48 39.2	10.181	56.447	22.50	6.60	2.01
09 40 30.78	-52 48 24.7	10.138	56.581	22.46	6.54	2.04
09 40 21.65	-52 48 17.4	10.171	57.328	22.41	6.44	2.09
09 40 12.52	-52 48 13.6	10.333	57.822	22.45	6.51	2.09
09 40 1.8	-52 48 2.6	10.639	59.077	22.49	6.59	2.11
09 39 52.28	-52 48 5.9	10.904	59.931	22.54	6.69	2.11
09 41 49.05	-52 50 47.9	10.284	57.795	22.43	6.47	2.10

continued on next page

Table 20 – continued from previous page

R.A.(J2000) hh mm ss	Dec.(J2000) dd mm ss	$F(60)$ (MJy)	$F(100)$ (MJy)	T_d (K)	$B(\nu,T)$ $(\times10^{-16})$ Js^{-2}	A_V $(\times10^{-5})$ mag
09 41 39.11	-52 50 51.8	10.108	56.821	22.43	6.47	2.07
09 41 29.97	-52 50 41.2	10.072	56.768	22.41	6.44	2.07
09 41 20.43	-52 50 34.2	10.148	57.368	22.40	6.41	2.10
09 41 10.5	-52 50 30.7	10.281	57.288	22.47	6.55	2.06
09 41 0.17	-52 50 20	10.357	56.901	22.55	6.69	2.00
09 40 50.23	-52 50 16.4	10.237	56.821	22.49	6.59	2.03
09 40 40.3	-52 50 9.2	10.108	56.581	22.45	6.51	2.04
09 40 29.97	-52 50 5.5	10.068	56.754	22.41	6.44	2.07
09 40 22.03	-52 49 54.6	10.164	57.315	22.41	6.44	2.09
09 40 11.7	-52 49 50.8	10.383	58.316	22.43	6.47	2.12
09 40 0.98	-52 49 36.2	10.635	59.197	22.48	6.56	2.12
09 39 50.66	-52 49 28.7	10.881	60.131	22.52	6.63	2.13
09 41 49.48	-52 52 28.7	10.516	58.61	22.47	6.55	2.10
09 41 38.34	-52 52 11	10.125	56.888	22.43	6.47	2.07
09 41 29.19	-52 52 4	9.9758	56.341	22.40	6.42	2.06
09 41 19.65	-52 52 4.2	10.055	56.741	22.41	6.43	2.08
09 41 8.92	-52 51 57.1	10.197	57.542	22.41	6.43	2.10
09 41 1.36	-52 51 53.6	10.383	57.569	22.50	6.60	2.05
09 40 50.23	-52 51 50	10.37	57.435	22.50	6.61	2.04
09 40 41.09	-52 51 35.6	10.314	57.355	22.48	6.57	2.05
09 40 30.36	-52 51 35.5	10.31	57.141	22.50	6.61	2.03
09 40 20.82	-52 51 21	10.32	57.555	22.47	6.54	2.07
09 40 10.49	-52 51 13.6	10.552	58.77	22.47	6.56	2.11
09 40 0.16	-52 51 6.1	10.868	59.918	22.53	6.66	2.12
09 41 48.32	-52 53 47.9	10.529	58.797	22.46	6.53	2.12
09 41 38.37	-52 53 41	10.194	57.221	22.43	6.48	2.08
09 41 28.42	-52 53 41.2	9.9592	56.22	22.40	6.43	2.06
09 41 19.67	-52 53 41.4	9.9956	57.035	22.35	6.32	2.12
09 41 8.93	-52 53 30.7	10.128	58.143	22.32	6.27	2.18
09 40 58.19	-52 53 23.6	10.317	58.703	22.36	6.35	2.17
09 40 47.85	-52 53 12.8	10.447	58.677	22.43	6.47	2.13
09 40 36.31	-52 53 12.7	10.576	58.543	22.51	6.62	2.08
09 40 27.17	-52 52 54.7	10.566	58.503	22.51	6.61	2.08
09 40 20.01	-52 52 51	10.835	58.663	22.62	6.84	2.02
09 40 8.48	-52 52 43.5	10.944	59.451	22.61	6.81	2.05
09 41 45.96	-52 55 21.6	10.572	59.838	22.39	6.40	2.20
09 41 37.2	-52 55 14.6	10.181	57.902	22.37	6.35	2.14
09 41 27.25	-52 55 11.2	9.9458	57.395	22.29	6.22	2.17
09 41 18.09	-52 55 0.6	10.121	57.742	22.35	6.32	2.15
09 41 8.54	-52 55 0.7	10.33	58.797	22.36	6.35	2.18
09 40 57.4	-52 54 53.6	10.596	59.704	22.41	6.44	2.18
09 40 47.45	-52 54 46.4	10.752	60.078	22.46	6.52	2.16
09 40 38.69	-52 54 35.6	10.854	60.065	22.51	6.62	2.13
09 40 29.54	-52 54 17.5	11.133	60.131	22.64	6.87	2.06
09 41 35.64	-52 56 48.3	10.403	59.037	22.38	6.37	2.18
09 41 26.08	-52 56 41.3	10.297	58.757	22.35	6.32	2.19
09 41 16.12	-52 56 30.6	10.536	59.784	22.38	6.38	2.20

Table 21: The Database of far infrared cavity CCRAS8 nearby AGB star AGB1025-5933. The first two columns represent position of the pixels with in the cavity. The next two columns give values of relative flux density at 60 μm and 100 μm that have obtained after processing the FITS image using ALADIN 2.5 software. The calculated values of dust color temperature (in K), Planck function for 100 μm and visual extinction (in mag) of the corresponding pixels,respectively.

R.A.(J2000) hh mm ss	Dec.(J2000) dd mm ss	$F(60)$ (MJy)	$F(100)$ (MJy)	T_d (K)	$B(\nu,T)$ $(\times10^{-16})$ Js^{-2}	A_V $(\times10^{-5})$ mag
10 28 22.98	-59 4 14.6	39.835	171.68	23.91	9.64	4.19
10 28 12.25	-59 4 29.5	39.699	168.47	24.00	9.87	4.01
10 28 0.58	-59 4 33.5	41.158	169.28	24.19	10.34	3.85
10 27 47.04	-59 4 41	42.35	172.85	24.24	10.46	3.88
10 27 37.23	-59 4 48.5	44.92	172.76	24.61	11.44	3.55
10 28 23.05	-59 5 48.2	40.982	169.81	24.15	10.23	3.90
10 28 10.91	-59 5 59.5	39.932	166.56	24.11	10.13	3.87
10 28 1.1	-59 6 10.6	40.216	165.94	24.17	10.29	3.79
10 27 49.41	-59 6 11	41.101	165.62	24.32	10.67	3.65
10 27 36.8	-59 6 22.1	42.366	167.81	24.42	10.95	3.60
10 27 25.58	-59 6 25.9	43.723	170.47	24.52	11.21	3.58
10 28 24.05	-59 7 25.4	42.701	171.51	24.34	10.72	3.76
10 28 11.44	-59 7 40.3	40.97	166.32	24.27	10.55	3.71
10 27 59.74	-59 7 40.7	40.908	166.32	24.26	10.52	3.72
10 27 48.98	-59 7 30.2	40.879	166.75	24.24	10.47	3.74
10 27 38.7	-59 7 52	40.891	166.34	24.26	10.52	3.72
10 27 27.01	-59 7 55.9	41.998	166.37	24.42	10.94	3.57

continued on next page

Table 21 – continued from previous page

R.A.(J2000) hh mm ss	Dec.(J2000) dd mm ss	$F(60)$ (MJy)	$F(100)$ (MJy)	T_d (K)	$B(\nu,T)$ $(\times10^{-16})$ Js^{-2}	A_V $(\times10^{-5})$ mag
10 27 14.38	-59 8 6.8	43.064	169.15	24.48	11.09	3.59
10 28 23.65	-59 8 55.4	43.326	172.78	24.38	10.84	3.75
10 28 11.96	-59 9 3.1	42.27	166.88	24.44	11.00	3.57
10 28 1.66	-59 9 10.6	41.333	165.11	24.37	10.81	3.59
10 27 51.37	-59 9 21.7	40.386	165.83	24.20	10.37	3.76
10 27 37.79	-59 9 18.5	40.363	164.37	24.25	10.50	3.68
10 27 26.56	-59 9 29.5	40.5	164.22	24.28	10.57	3.65
10 27 16.26	-59 9 29.6	41.021	165.26	24.32	10.67	3.64
10 27 4.09	-59 9 44.1	44.035	172.23	24.50	11.16	3.63
10 28 14.82	-59 10 33	41.708	169.15	24.28	10.56	3.76
10 28 2.65	-59 10 44.2	40.658	161.18	24.42	10.93	3.47
10 27 49.54	-59 10 48.2	40.459	160.31	24.42	10.94	3.45
10 27 38.76	-59 10 48.4	39.762	161.16	24.28	10.57	3.58
10 27 26.58	-59 10 52.3	40.085	161.29	24.33	10.69	3.55
10 27 17.22	-59 10 59.6	40.357	160.93	24.38	10.84	3.49
10 27 7.38	-59 11 6.9	41.288	161.92	24.49	11.11	3.43
10 26 53.32	-59 11 6.9	43.734	169.4	24.56	11.32	3.52
10 28 14.88	-59 12 3	41.05	169.4	24.17	10.29	3.87
10 28 3.17	-59 12 14.2	39.983	162.29	24.27	10.55	3.62
10 27 50.51	-59 12 14.6	39.637	157.1	24.42	10.94	3.38
10 27 39.26	-59 12 14.8	39.716	154.85	24.52	11.21	3.25
10 27 27.08	-59 12 33	39.654	155.72	24.48	11.09	3.30
10 27 17.7	-59 12 33.2	39.291	156.46	24.39	10.86	3.39
10 27 5.51	-59 12 33.3	39.279	157.48	24.35	10.75	3.44
10 26 53.79	-59 12 47.7	40.681	158.33	24.53	11.24	3.31
10 26 42.07	-59 12 44.1	43.519	167.39	24.61	11.44	3.44
10 28 15.4	-59 13 18.5	41.555	171.72	24.16	10.27	3.93
10 28 3.68	-59 13 33.4	40.187	165.52	24.18	10.32	3.77
10 27 51.02	-59 13 37.3	39.45	158.95	24.32	10.67	3.50
10 27 40.7	-59 13 44.8	39.58	155.23	24.49	11.11	3.28
10 27 26.63	-59 13 59.5	39.506	151.71	24.62	11.47	3.11
10 27 18.19	-59 14 6.8	38.871	150.83	24.55	11.29	3.14
10 27 7.87	-59 13 59.7	38.774	150.37	24.56	11.30	3.13
10 26 54.73	-59 14 6.9	39.466	156.17	24.43	10.96	3.35
10 26 43	-59 14 10.5	41.884	158.48	24.71	11.73	3.18
10 26 30.8	-59 14 21.2	44.131	165.22	24.78	11.92	3.26
10 26 20.47	-59 14 35.4	46.226	173.87	24.75	11.83	3.45
10 28 4.2	-59 15 3.3	42.361	169.98	24.34	10.73	3.72
10 27 52	-59 15 7.3	41.305	162.2	24.48	11.09	3.44
10 27 41.68	-59 15 14.8	40.278	159.08	24.44	10.99	3.40
10 27 28.06	-59 15 25.8	39.393	152.34	24.57	11.35	3.16
10 27 18.21	-59 15 29.6	38.899	148.58	24.65	11.56	3.02
10 27 6.94	-59 15 29.7	38.553	147.88	24.62	11.49	3.03
10 26 56.14	-59 15 47.7	39.364	150.6	24.64	11.53	3.07
10 26 43.93	-59 15 44.1	40.602	156.27	24.60	11.43	3.21
10 26 31.25	-59 15 47.6	41.333	160.01	24.57	11.33	3.32
10 26 19.51	-59 16 5.4	42.894	164.47	24.63	11.49	3.36
10 26 9.18	-59 16 1.6	45.607	173.57	24.67	11.62	3.51
10 27 52.98	-59 16 40.9	43.626	171.49	24.47	11.07	3.64
10 27 41.71	-59 16 48.4	42.14	160.12	24.68	11.65	3.23
10 27 30.44	-59 16 59.4	40.335	155.98	24.57	11.35	3.23
10 27 18.69	-59 17 6.8	39.319	153.89	24.50	11.14	3.25
10 27 6.95	-59 17 3.3	39.069	149.41	24.64	11.54	3.04
10 26 55.67	-59 17 14.1	39.262	149.94	24.65	11.56	3.05
10 26 44.39	-59 17 14.1	39.336	151.73	24.59	11.39	3.13
10 26 33.11	-59 17 24.8	40.307	154.72	24.62	11.48	3.17
10 26 21.36	-59 17 21	40.743	157.68	24.57	11.34	3.27
10 26 9.14	-59 17 31.6	43.274	167.28	24.58	11.36	3.46
10 27 42.69	-59 18 18.3	43.978	172.95	24.47	11.07	3.67
10 27 30.93	-59 18 18.6	42.662	160.65	24.74	11.81	3.20
10 27 19.18	-59 18 26	41.47	156.78	24.72	11.74	3.14
10 27 8.37	-59 18 36.9	40.119	153.02	24.66	11.59	3.11
10 26 54.73	-59 18 33.3	39.37	150.16	24.66	11.59	3.05
10 26 46.27	-59 18 44.1	39.16	150.05	24.63	11.51	3.07
10 26 33.57	-59 18 51.2	39.416	151.05	24.63	11.50	3.09
10 26 21.81	-59 18 47.4	40.159	155.42	24.57	11.34	3.22
10 26 9.11	-59 19 8.8	41.447	159.76	24.59	11.40	3.29
10 25 57.82	-59 19 4.9	44.018	168.32	24.64	11.54	3.43
10 27 32.37	-59 19 55.8	44.512	172.87	24.55	11.28	3.60
10 27 21.08	-59 19 59.5	42.179	164.43	24.52	11.21	3.45
10 27 9.79	-59 20 6.8	41.05	157.61	24.62	11.47	3.23
10 26 58.02	-59 19 59.7	40.102	153.43	24.64	11.53	3.13
10 26 45.32	-59 20 10.5	39.098	151.03	24.58	11.37	3.12
10 26 34.02	-59 20 17.6	39.171	150.62	24.61	11.45	3.09
10 26 21.79	-59 20 13.8	39.608	150.47	24.69	11.66	3.04
10 26 10.02	-59 20 24.4	40.942	156.74	24.64	11.52	3.20
10 25 59.66	-59 20 38.6	42.673	162.73	24.66	11.59	3.30

continued on next page

Table 21 – continued from previous page

R.A.(J2000) hh mm ss	Dec.(J2000) dd mm ss	$F(60)$ (MJy)	$F(100)$ (MJy)	$T_{\rm d}$ (K)	$B(\nu,T)$ $(\times10^{-16})$ Js^{-2}	A_V $(\times10^{-5})$ mag
10 25 46.01	-59 20 38.2	45.391	168.34	24.84	12.09	3.27
10 27 21.57	-59 21 36.7	44.29	170.57	24.60	11.42	3.51
10 27 9.33	-59 21 40.4	42.406	162.69	24.62	11.49	3.33
10 26 57.08	-59 21 36.9	40.823	156.66	24.62	11.48	3.21
10 26 46.72	-59 21 44.1	39.835	152.19	24.65	11.56	3.10
10 26 35.42	-59 21 51.2	39.37	149.2	24.70	11.70	3.00
10 26 23.17	-59 22 5.5	39.676	149.64	24.73	11.78	2.99
10 26 11.86	-59 22 12.5	40.692	152.79	24.76	11.86	3.03
10 25 58.67	-59 22 22.9	42.35	158.04	24.80	11.97	3.10
10 25 46.9	-59 22 11.8	43.643	165.24	24.71	11.72	3.32
10 25 36.06	-59 22 18.6	45.715	171.72	24.76	11.86	3.41
10 27 9.34	-59 23 10.4	43.223	169.19	24.50	11.14	3.57
10 26 58.5	-59 23 21.3	41.861	161.22	24.60	11.42	3.32
10 26 45.78	-59 23 14.1	40.8	156.42	24.63	11.50	3.20
10 26 34.46	-59 23 28.4	40.216	153.32	24.66	11.59	3.11
10 26 23.15	-59 23 35.5	40.38	150.5	24.81	12.00	2.95
10 26 12.3	-59 23 38.9	41.186	154.36	24.77	11.90	3.05
10 25 58.64	-59 23 34.9	42.185	158.65	24.75	11.83	3.15
10 25 47.31	-59 23 52.6	43.246	162.37	24.76	11.86	3.22
10 25 36.47	-59 23 45	44.245	168.41	24.67	11.62	3.41
10 25 25.62	-59 23 55.4	46.572	172.48	24.85	12.11	3.35
10 27 21.61	-59 24 40.3	44.687	174.35	24.52	11.20	3.66
10 27 11.24	-59 24 40.4	43.246	169.47	24.49	11.12	3.58
10 26 59.45	-59 24 44.1	42.44	166.41	24.49	11.11	3.52
10 26 47.66	-59 24 40.5	41.873	163.12	24.53	11.22	3.42
10 26 34.92	-59 24 58.4	41.68	158.21	24.69	11.67	3.19
10 26 21.71	-59 25 5.4	41.861	157.7	24.74	11.80	3.14
10 26 11.81	-59 24 58.1	42.378	155.3	24.92	12.31	2.97
10 26 0.48	-59 25 5	42.997	158.38	24.88	12.21	3.05
10 25 49.63	-59 25 15.5	43.592	162.58	24.80	11.98	3.19
10 25 37.36	-59 25 11.5	44.148	167.9	24.68	11.64	3.39
10 25 24.63	-59 25 11	46.089	172.61	24.78	11.91	3.41
10 27 22.57	-59 25 55.9	44.058	173.82	24.45	11.01	3.71
10 27 11.25	-59 26 6.8	42.906	169.64	24.43	10.98	3.63
10 26 59.92	-59 26 3.3	42.469	166.94	24.47	11.07	3.54
10 26 48.59	-59 26 6.9	42.571	166.71	24.49	11.14	3.52
10 26 36.79	-59 26 17.6	43.008	167.24	24.54	11.25	3.49
10 26 24.99	-59 26 21.1	43.002	165.88	24.59	11.39	3.42
10 26 12.72	-59 26 28.1	43.144	164.3	24.67	11.61	3.33
10 25 59.97	-59 26 35	43.598	162.73	24.80	11.97	3.20
10 25 50.53	-59 26 38.3	44.216	164.18	24.83	12.06	3.20
10 25 38.25	-59 26 41.5	44.767	165.64	24.85	12.13	3.21
10 25 25.5	-59 26 51.8	46.413	170.08	24.92	12.31	3.25
10 27 23.07	-59 27 22.3	43.802	173.16	24.44	10.98	3.71
10 27 10.32	-59 27 36.8	42.77	169.51	24.42	10.94	3.64
10 26 59.93	-59 27 40.5	42.69	169.34	24.41	10.92	3.65
10 26 48.12	-59 27 40.5	43.433	170.76	24.47	11.07	3.63
10 26 37.25	-59 27 44	43.853	171.78	24.49	11.13	3.63
10 26 23.55	-59 27 51.1	44.103	171.12	24.55	11.29	3.56
10 26 12.69	-59 28 1.7	43.961	168.34	24.64	11.52	3.44
10 25 58.99	-59 27 57.8	44.307	167.92	24.70	11.70	3.37
10 25 49.54	-59 28 1.1	44.943	166.3	24.85	12.13	3.22
10 25 37.72	-59 28 7.9	45.953	167.92	24.94	12.36	3.19
10 25 25.91	-59 28 14.6	47.934	172.21	25.05	12.68	3.19
10 27 23.56	-59 29 3.1	43.439	173.55	24.37	10.81	3.78
10 27 11.75	-59 29 6.8	43.008	169.89	24.44	10.99	3.63
10 27 1.82	-59 28 56.1	43.473	169.68	24.52	11.19	3.56
10 26 49.06	-59 29 3.3	44.154	173.72	24.47	11.06	3.69
10 26 14.55	-59 29 17.3	44.364	172.68	24.53	11.24	3.61
10 26 1.78	-59 29 35	44.37	170.66	24.61	11.44	3.51
10 25 49.49	-59 29 31.1	44.886	172.25	24.62	11.48	3.53
10 27 14.6	-59 30 33.2	43.365	173.29	24.37	10.80	3.77
10 27 1.35	-59 30 33.3	43.706	173.1	24.42	10.95	3.72
10 26 49.53	-59 30 33.3	44.897	174.72	24.53	11.24	3.65
10 25 52.28	-59 31 1.2	45.164	174.5	24.58	11.36	3.61
10 27 3.72	-59 31 56.1	44.12	174.93	24.42	10.93	3.76

Table 22: The Database of far infrared cavity CCRPAS1 nearby post-AGB star PAGB0655-0217. The first two columns represent position of the pixels with in the cavity. The next two columns give values of relative flux density at 60 μm and 100 μm that have obtained after processing the FITS image using ALADIN 2.5 software. The calculated values of dust color temperature (in K), Planck function and dust mass for 100 μm and visual extinction (in mag) of the corresponding pixels,respectively.

R.A.(J2000) hh mm ss	Dec.(J2000) dd mm ss	$F(60)$ (MJy)	$F(100)$ (MJy)	$T_{\rm d}$ (K)	$B(\nu,T)$ $(\times10^{-16})$ Js^{-2}	$M_{\rm d}$ $(\times10^{28})$ kg	$A_{\rm V}$ $(\times10^{-5})$ mag
6 52 1.8	-1 0 43.6	2.21	19.42	20.30	3.30	4.43	1.39
6 51 56.61	-1 0 37.1	2.24	19.42	20.37	3.38	4.32	1.35
6 52 2.23	-1 2 1.3	2.09	19.35	20.08	3.05	4.77	1.49
6 51 56.61	-1 1 54.8	2.10	19.07	20.17	3.15	4.56	1.42
6 51 49.7	-1 2 1.3	2.15	19.22	20.23	3.22	4.49	1.40
6 52 2.66	-1 3 38.5	2.03	19.03	20.04	3.01	4.76	1.49
6 51 56.18	-1 3 19.1	2.05	18.90	20.10	3.07	4.62	1.45
6 51 48.84	-1 3 38.5	2.12	19.02	20.21	3.19	4.48	1.40
6 52 8.28	-1 5 9.2	2.01	19.36	19.93	2.89	5.04	1.58
6 52 1.8	-1 4 56.2	2.00	19.03	19.96	2.92	4.89	1.53
6 51 56.61	-1 5 2.7	2.08	18.87	20.18	3.16	4.49	1.41
6 51 48.84	-1 5 9.2	2.09	19.11	20.13	3.11	4.62	1.45
6 52 13.9	-1 6 39.9	2.14	19.34	20.19	3.18	4.58	1.43
6 52 7.85	-1 6 39.9	2.04	19.28	20.01	2.97	4.88	1.52
6 52 1.8	-1 6 39.9	2.03	18.97	20.04	3.01	4.74	1.48
6 51 56.18	-1 6 33.4	2.06	18.71	20.17	3.14	4.47	1.40
6 51 49.7	-1 6 39.9	2.06	18.99	20.11	3.09	4.63	1.45
6 51 42.79	-1 6 39.9	2.20	19.34	20.30	3.30	4.41	1.38
6 52 7.41	-1 8 10.6	2.11	19.36	20.12	3.10	4.70	1.47
6 52 2.66	-1 8 17.1	2.07	18.92	20.14	3.12	4.57	1.43
6 51 56.18	-1 8 23.6	2.06	18.49	20.23	3.21	4.33	1.35
6 51 50.13	-1 8 10.6	2.09	18.99	20.17	3.15	4.54	1.42
6 51 42.79	-1 8 10.6	2.13	19.21	20.19	3.17	4.56	1.42
6 52 7.41	-1 9 54.3	2.14	19.52	20.14	3.12	4.70	1.47
6 52 1.8	-1 9 47.8	2.13	19.02	20.23	3.22	4.44	1.39
6 51 56.61	-1 9 54.3	2.11	18.53	20.32	3.32	4.20	1.31
6 51 50.13	-1 9 54.3	2.11	18.96	20.20	3.19	4.48	1.40
6 51 44.51	-1 9 47.8	2.16	19.25	20.24	3.23	4.49	1.40
6 51 38.47	-1 9 28.4	2.29	19.43	20.46	3.49	4.19	1.31
6 52 2.23	-1 11 25	2.14	19.08	20.25	3.24	4.43	1.38
6 51 56.18	-1 11 18.5	2.20	18.87	20.41	3.43	4.14	1.30
6 51 49.7	-1 11 12.1	2.19	19.13	20.33	3.34	4.31	1.35
6 51 43.65	-1 11 18.5	2.28	19.40	20.45	3.47	4.20	1.31
6 52 7.85	-1 12 42.8	2.21	19.47	20.29	3.28	4.46	1.39
6 52 2.23	-1 12 36.3	2.11	19.08	20.17	3.15	4.55	1.42
6 51 55.32	-1 12 49.3	2.17	18.96	20.34	3.34	4.27	1.33
6 51 48.4	-1 12 42.8	2.25	19.36	20.39	3.41	4.27	1.34
6 51 44.08	-1 12 36.3	2.30	19.50	20.46	3.48	4.21	1.32
6 52 12.6	-1 14 20	2.16	19.37	20.23	3.21	4.53	1.42
6 52 7.85	-1 14 0.5	2.09	19.20	20.12	3.10	4.66	1.46
6 52 2.23	-1 14 13.5	2.03	19.02	20.03	3.00	4.77	1.49
6 51 55.32	-1 14 26.5	2.11	18.75	20.26	3.26	4.33	1.35
6 51 49.7	-1 14 13.5	2.20	19.12	20.35	3.36	4.28	1.34
6 51 45.38	-1 13 54.1	2.27	19.51	20.41	3.43	4.28	1.34
6 52 18.22	-1 15 31.2	2.12	19.43	20.13	3.10	4.71	1.47
6 52 13.46	-1 15 44.2	2.01	19.08	19.99	2.95	4.86	1.52
6 52 7.41	-1 15 31.3	1.91	18.82	19.82	2.78	5.09	1.59
6 52 2.23	-1 15 31.3	1.91	18.72	19.84	2.80	5.02	1.57
6 51 57.04	-1 15 37.7	1.99	18.57	20.06	3.03	4.61	1.44
6 51 50.13	-1 15 44.2	2.09	18.81	20.20	3.19	4.44	1.39
6 51 44.08	-1 15 31.3	2.12	19.41	20.13	3.10	4.71	1.47
6 52 20.38	-1 17 8.4	2.07	19.17	20.08	3.05	4.73	1.48
6 52 13.03	-1 17 14.9	1.94	18.71	19.92	2.88	4.89	1.53
6 52 7.85	-1 17 14.9	1.87	18.50	19.82	2.77	5.02	1.57
6 52 1.37	-1 17 2	1.87	18.49	19.81	2.77	5.02	1.57
6 51 55.75	-1 17 2	1.90	18.34	19.91	2.87	4.80	1.50
6 51 49.27	-1 17 14.9	1.99	18.63	20.03	3.00	4.67	1.46
6 51 43.65	-1 17 21.4	2.10	19.02	20.17	3.15	4.55	1.42
6 51 37.6	-1 17 8.4	2.27	19.50	20.41	3.42	4.29	1.34
6 52 55.38	-1 18 32.6	1.83	19.50	19.51	2.47	5.94	1.86
6 52 49.33	-1 18 26.2	1.90	19.20	19.72	2.68	5.40	1.69
6 52 42.85	-1 18 39.1	1.96	19.11	19.86	2.82	5.10	1.59
6 52 37.23	-1 18 52.1	2.03	19.27	19.99	2.95	4.91	1.53
6 52 31.18	-1 18 45.6	2.10	19.35	20.10	3.07	4.74	1.48
6 52 24.7	-1 18 45.6	2.07	19.27	20.07	3.04	4.77	1.49
6 52 19.08	-1 18 32.7	2.04	18.97	20.07	3.04	4.70	1.47
6 52 13.9	-1 18 32.7	1.99	18.59	20.05	3.02	4.63	1.45
6 52 7.85	-1 18 39.2	1.85	18.37	19.80	2.75	5.02	1.57
6 52 0.93	-1 18 52.1	1.77	18.36	19.62	2.58	5.35	1.67
6 51 55.75	-1 18 45.6	1.87	18.37	19.85	2.80	4.93	1.54

continued on next page

Table 22 – continued from previous page

R.A.(J2000) hh mm ss	Dec.(J2000) dd mm ss	$F(60)$ (MJy)	$F(100)$ (MJy)	$T_{\rm d}$ (K)	$B(\nu,T)$ $(\times10^{-16})$ Js^{-2}	$M_{\rm d}$ $(\times10^{28})$ kg	$A_{\rm V}$ $(\times10^{-5})$ mag
6 51 50.56	-1 18 45.6	1.97	18.64	19.99	2.95	4.75	1.49
6 51 43.65	-1 18 45.6	2.07	19.14	20.10	3.07	4.68	1.46
6 51 38.46	-1 18 39.2	2.14	19.44	20.16	3.14	4.66	1.46
6 52 54.52	-1 20 9.8	1.83	19.52	19.50	2.47	5.95	1.86
6 52 48.47	-1 20 22.8	1.86	18.96	19.69	2.65	5.38	1.68
6 52 41.98	-1 20 9.9	1.89	18.77	19.79	2.74	5.15	1.61
6 52 36.8	-1 20 9.9	1.88	18.78	19.76	2.72	5.20	1.62
6 52 31.61	-1 20 9.9	1.92	18.76	19.86	2.82	5.00	1.56
6 52 26.43	-1 20 16.4	1.92	18.83	19.85	2.81	5.04	1.58
6 52 20.38	-1 20 3.4	1.94	18.84	19.89	2.85	4.97	1.55
6 52 13.03	-1 20 16.4	1.93	18.51	19.94	2.90	4.80	1.50
6 52 6.55	-1 20 29.3	1.81	18.45	19.69	2.65	5.24	1.64
6 52 0.93	-1 20 22.8	1.73	18.29	19.55	2.51	5.49	1.72
6 51 55.75	-1 20 22.8	1.89	18.35	19.88	2.84	4.86	1.52
6 51 48.83	-1 20 16.4	2.00	18.57	20.07	3.04	4.60	1.44
6 51 44.08	-1 20 16.4	2.09	19.06	20.15	3.13	4.58	1.43
6 51 38.03	-1 20 3.4	2.14	19.36	20.18	3.17	4.60	1.44
6 53 1.43	-1 22 0	1.93	19.50	19.73	2.69	5.45	1.70
6 52 55.38	-1 22 6.5	1.77	19.28	19.43	2.40	6.05	1.89
6 52 48.9	-1 21 47	1.79	18.79	19.58	2.54	5.56	1.74
6 52 42.42	-1 21 40.6	1.76	18.35	19.60	2.56	5.39	1.69
6 52 35.94	-1 21 53.5	1.72	18.17	19.54	2.50	5.47	1.71
6 52 30.32	-1 21 47.1	1.81	18.40	19.70	2.65	5.21	1.63
6 52 24.7	-1 21 40.6	1.91	18.66	19.85	2.81	5.00	1.56
6 52 19.08	-1 21 47.1	1.88	18.70	19.79	2.74	5.12	1.60
6 52 11.3	-1 21 47.1	1.92	18.42	19.94	2.90	4.77	1.49
6 52 5.69	-1 21 53.6	1.80	18.45	19.66	2.62	5.31	1.66
6 52 0.07	-1 21 53.6	1.71	18.30	19.50	2.47	5.58	1.75
6 51 54.45	-1 21 53.6	1.82	18.38	19.73	2.69	5.14	1.61
6 51 49.27	-1 21 47.1	1.96	18.84	19.92	2.88	4.92	1.54
6 51 42.78	-1 21 53.6	2.13	19.04	20.22	3.21	4.46	1.39
6 51 37.17	-1 21 34.1	2.21	19.25	20.34	3.35	4.32	1.35
6 51 30.69	-1 21 47.1	2.27	19.45	20.42	3.43	4.26	1.33
6 51 25.07	-1 21 34.1	2.30	19.36	20.49	3.53	4.13	1.29
6 51 20.75	-1 21 40.6	2.28	19.43	20.43	3.45	4.23	1.32
6 52 54.95	-1 23 17.8	1.77	19.25	19.42	2.39	6.05	1.89
6 52 49.33	-1 23 11.3	1.74	18.59	19.50	2.47	5.67	1.77
6 52 43.71	-1 22 58.3	1.71	18.10	19.54	2.50	5.44	1.70
6 52 37.23	-1 23 17.8	1.68	17.97	19.49	2.46	5.50	1.72
6 52 29.89	-1 23 24.3	1.79	18.06	19.73	2.69	5.06	1.58
6 52 24.27	-1 23 24.3	1.86	18.35	19.83	2.78	4.95	1.55
6 52 19.08	-1 23 24.3	1.87	18.41	19.82	2.78	4.99	1.56
6 52 12.17	-1 23 4.8	1.87	18.40	19.83	2.78	4.97	1.55
6 52 5.26	-1 23 24.3	1.81	18.24	19.75	2.70	5.08	1.59
6 51 58.34	-1 23 11.3	1.76	18.45	19.58	2.54	5.47	1.71
6 51 54.45	-1 23 17.8	1.76	18.45	19.58	2.54	5.47	1.71
6 51 49.27	-1 23 17.8	1.95	18.65	19.95	2.91	4.83	1.51
6 51 42.78	-1 23 17.8	2.10	18.72	20.24	3.23	4.36	1.36
6 51 37.6	-1 23 4.8	2.17	18.97	20.32	3.33	4.29	1.34
6 51 31.55	-1 23 11.3	2.23	19.19	20.41	3.42	4.22	1.32
6 51 25.5	-1 23 17.8	2.27	19.11	20.49	3.52	4.08	1.28
6 51 20.75	-1 23 11.3	2.17	19.02	20.31	3.31	4.32	1.35
6 51 12.97	-1 23 11.3	2.11	19.36	20.11	3.09	4.72	1.48
6 52 54.95	-1 25 1.4	1.75	19.30	19.38	2.35	6.17	1.93
6 52 48.47	-1 24 42	1.73	18.67	19.45	2.42	5.80	1.81
6 52 41.55	-1 25 1.5	1.71	18.04	19.55	2.51	5.41	1.69
6 52 36.8	-1 24 55	1.67	17.88	19.49	2.45	5.48	1.71
6 52 30.75	-1 24 55	1.70	17.91	19.57	2.53	5.33	1.67
6 52 23.84	-1 24 48.5	1.76	18.17	19.63	2.59	5.27	1.65
6 52 18.65	-1 24 48.5	1.80	18.08	19.74	2.70	5.04	1.58
6 52 11.74	-1 24 42	1.77	18.10	19.68	2.64	5.16	1.61
6 52 4.82	-1 24 42	1.67	17.97	19.48	2.44	5.54	1.73
6 51 59.21	-1 24 35.6	1.67	18.19	19.43	2.40	5.71	1.78
6 51 54.02	-1 24 48.5	1.72	18.26	19.52	2.48	5.53	1.73
6 51 48.4	-1 24 42	1.89	18.08	19.94	2.90	4.69	1.47
6 51 42.78	-1 24 35.6	1.88	18.32	19.87	2.82	4.88	1.53
6 51 36.3	-1 24 48.5	1.99	18.59	20.05	3.02	4.63	1.45
6 51 32.41	-1 24 48.5	1.98	18.78	19.99	2.95	4.79	1.50
6 51 26.36	-1 25 1.5	1.99	18.83	20.00	2.97	4.78	1.49
6 51 19.45	-1 25 14.4	2.00	18.84	20.02	2.98	4.75	1.49
6 51 12.97	-1 24 48.5	1.99	19.08	19.93	2.89	4.96	1.55
6 51 4.76	-1 24 48.5	2.00	19.38	19.90	2.86	5.09	1.59
6 52 55.81	-1 26 25.7	1.76	19.31	19.41	2.38	6.11	1.91
6 52 48.9	-1 26 19.2	1.70	18.67	19.40	2.37	5.92	1.85
6 52 42.42	-1 26 32.2	1.70	18.08	19.52	2.48	5.48	1.71
6 52 35.5	-1 26 12.7	1.66	17.93	19.46	2.43	5.55	1.73
6 52 29.45	-1 26 19.2	1.66	17.86	19.46	2.43	5.53	1.73

continued on next page

Table 22 – continued from previous page

R.A.(J2000) hh mm ss	Dec.(J2000) dd mm ss	$F(60)$ (MJy)	$F(100)$ (MJy)	$T_{\rm d}$ (K)	$B(\nu,T)$ $(\times10^{-16})$ Js^{-2}	$M_{\rm d}$ $(\times10^{28})$ kg	$A_{\rm V}$ $(\times10^{-5})$ mag
6 52 24.7	-1 26 19.2	1.68	18.02	19.47	2.44	5.55	1.74
6 52 19.08	-1 26 19.2	1.70	17.92	19.55	2.51	5.37	1.68
6 52 12.6	-1 26 25.7	1.67	17.82	19.50	2.47	5.43	1.70
6 52 6.12	-1 26 19.2	1.68	17.78	19.53	2.49	5.37	1.68
6 52 0.5	-1 26 6.3	1.59	17.92	19.30	2.29	5.89	1.84
6 51 53.59	-1 26 25.7	1.62	17.85	19.37	2.34	5.73	1.79
6 51 48.83	-1 26 19.2	1.73	17.91	19.64	2.59	5.19	1.62
6 51 43.65	-1 26 12.8	1.72	17.92	19.60	2.56	5.27	1.65
6 51 38.03	-1 26 19.2	1.77	18.30	19.62	2.58	5.33	1.67
6 51 31.12	-1 26 19.2	1.82	18.40	19.73	2.69	5.15	1.61
6 51 26.8	-1 26 25.7	1.83	18.75	19.67	2.62	5.37	1.68
6 51 19.88	-1 26 19.2	1.85	18.76	19.70	2.65	5.31	1.66
6 51 11.67	-1 26 12.7	1.89	19.07	19.74	2.69	5.33	1.67
6 51 5.62	-1 26 19.2	1.94	19.28	19.78	2.74	5.29	1.66
6 50 58.71	-1 25 59.8	1.98	19.54	19.83	2.79	5.27	1.65
6 53 2.3	-1 27 56.4	1.81	19.40	19.49	2.46	5.93	1.86
6 52 54.95	-1 28 9.3	1.69	19.21	19.26	2.25	6.43	2.01
6 52 50.63	-1 27 56.4	1.71	18.70	19.40	2.37	5.93	1.85
6 52 42.85	-1 27 37	1.74	18.40	19.55	2.51	5.51	1.72
6 52 36.37	-1 27 56.4	1.68	18.15	19.45	2.42	5.64	1.76
6 52 31.18	-1 28 9.4	1.67	18.06	19.45	2.42	5.62	1.76
6 52 24.7	-1 27 43.5	1.69	18.06	19.50	2.46	5.52	1.73
6 52 19.52	-1 27 56.4	1.68	17.96	19.49	2.45	5.50	1.72
6 52 12.17	-1 27 43.5	1.65	17.71	19.49	2.45	5.43	1.70
6 52 6.12	-1 28 2.9	1.63	17.68	19.45	2.41	5.51	1.72
6 52 1.8	-1 27 56.4	1.51	17.52	19.18	2.18	6.06	1.89
6 51 54.45	-1 27 37	1.51	17.52	19.18	2.18	6.04	1.89
6 51 48.83	-1 27 56.4	1.60	17.59	19.39	2.36	5.60	1.75
6 51 44.08	-1 27 50	1.62	17.46	19.47	2.44	5.39	1.68
6 51 37.6	-1 27 50	1.65	17.90	19.44	2.40	5.60	1.75
6 51 32.85	-1 27 43.5	1.71	18.12	19.52	2.49	5.48	1.71
6 51 25.07	-1 27 56.4	1.74	18.49	19.53	2.49	5.57	1.74
6 51 20.31	-1 27 37	1.81	18.69	19.64	2.59	5.42	1.70
6 51 13.4	-1 27 37	1.83	19.06	19.60	2.56	5.61	1.75
6 51 6.92	-1 27 37	1.86	19.17	19.65	2.61	5.53	1.73
6 50 59.57	-1 27 17.5	1.96	19.37	19.82	2.77	5.25	1.64
6 53 7.48	-1 29 20.6	1.89	19.36	19.66	2.62	5.56	1.74
6 53 1.43	-1 29 20.6	1.74	19.28	19.37	2.34	6.19	1.94
6 52 54.95	-1 29 14.1	1.70	19.12	19.31	2.29	6.28	1.96
6 52 50.2	-1 29 33.6	1.72	18.94	19.38	2.36	6.04	1.89
6 52 42.85	-1 29 20.6	1.78	18.70	19.56	2.52	5.58	1.74
6 52 37.67	-1 29 14.2	1.72	18.35	19.50	2.47	5.60	1.75
6 52 31.18	-1 29 20.7	1.66	18.22	19.40	2.37	5.79	1.81
6 52 25.57	-1 29 20.7	1.64	18.03	19.39	2.37	5.73	1.79
6 52 19.52	-1 29 27.2	1.63	17.78	19.41	2.38	5.61	1.75
6 52 13.03	-1 29 20.7	1.60	17.44	19.42	2.39	5.49	1.72
6 52 7.85	-1 29 20.7	1.59	17.37	19.41	2.38	5.49	1.72
6 52 0.93	-1 29 14.2	1.43	17.40	18.99	2.02	6.49	2.03
6 51 55.32	-1 29 14.2	1.36	17.16	18.88	1.93	6.68	2.09
6 51 49.7	-1 29 14.2	1.51	17.25	19.24	2.23	5.81	1.82
6 51 42.78	-1 29 20.7	1.56	17.31	19.35	2.33	5.59	1.75
6 51 38.03	-1 29 27.2	1.56	17.59	19.30	2.28	5.79	1.81
6 51 31.98	-1 29 33.6	1.59	18.03	19.27	2.26	6.00	1.88
6 51 26.36	-1 29 14.2	1.68	18.18	19.45	2.41	5.66	1.77
6 51 19.02	-1 29 14.2	1.75	18.52	19.53	2.49	5.59	1.75
6 51 13.83	-1 29 27.1	1.80	19.01	19.56	2.52	5.68	1.77
6 51 7.35	-1 29 7.7	1.85	19.45	19.56	2.52	5.81	1.82
6 53 7.48	-1 30 57.8	1.87	19.35	19.63	2.59	5.62	1.76
6 53 1	-1 30 44.9	1.73	19.08	19.38	2.35	6.10	1.91
6 52 54.95	-1 30 57.8	1.65	19.00	19.22	2.21	6.47	2.02
6 52 48.9	-1 30 44.9	1.71	18.94	19.36	2.33	6.11	1.91
6 52 42.85	-1 30 51.4	1.76	18.76	19.51	2.48	5.70	1.78
6 52 38.1	-1 30 44.9	1.68	18.35	19.42	2.39	5.77	1.81
6 52 31.18	-1 30 51.4	1.59	18.13	19.25	2.23	6.10	1.91
6 52 25.57	-1 30 57.9	1.56	17.87	19.23	2.22	6.05	1.89
6 52 19.08	-1 30 51.4	1.56	17.71	19.26	2.25	5.92	1.85
6 52 13.47	-1 31 4.4	1.53	17.28	19.29	2.28	5.71	1.78
6 52 7.42	-1 30 44.9	1.51	17.22	19.25	2.24	5.79	1.81
6 52 0.93	-1 30 51.4	1.40	17.19	18.96	2.00	6.48	2.03
6 51 55.32	-1 30 51.4	1.32	16.99	18.80	1.87	6.82	2.13
6 51 50.13	-1 31 4.4	1.43	17.15	19.04	2.06	6.25	1.95
6 51 43.22	-1 31 4.4	1.52	17.24	19.28	2.26	5.73	1.79
6 51 38.46	-1 30 57.9	1.57	17.41	19.37	2.34	5.59	1.75
6 51 31.98	-1 30 57.9	1.53	17.75	19.19	2.19	6.10	1.91
6 51 25.93	-1 30 38.4	1.63	18.19	19.33	2.31	5.92	1.85
6 51 19.45	-1 30 38.4	1.73	18.38	19.52	2.48	5.57	1.74
6 51 13.83	-1 30 38.4	1.80	19.13	19.52	2.48	5.79	1.81

continued on next page

Table 22 – continued from previous page

R.A.(J2000) hh mm ss	Dec.(J2000) dd mm ss	$F(60)$ (MJy)	$F(100)$ (MJy)	$T_{\rm d}$ (K)	$B(\nu,T)$ $(\times10^{-16})$ Js^{-2}	$M_{\rm d}$ $(\times10^{28})$ kg	$A_{\rm V}$ $(\times10^{-5})$ mag
6 53 7.49	-1 32 28.5	1.78	19.26	19.46	2.42	5.98	1.87
6 53 0.57	-1 32 22.1	1.74	18.97	19.43	2.40	5.95	1.86
6 52 53.66	-1 32 22.1	1.63	18.93	19.16	2.16	6.58	2.06
6 52 49.77	-1 32 28.6	1.66	18.99	19.23	2.22	6.43	2.01
6 52 44.15	-1 32 15.6	1.75	18.64	19.51	2.47	5.68	1.77
6 52 37.24	-1 32 9.1	1.68	18.35	19.40	2.38	5.81	1.82
6 52 31.19	-1 32 22.1	1.55	18.18	19.14	2.14	6.39	2.00
6 52 25.14	-1 32 22.1	1.49	17.89	19.06	2.08	6.48	2.03
6 52 19.52	-1 32 22.1	1.53	17.63	19.22	2.21	6.00	1.88
6 52 13.47	-1 32 22.1	1.53	17.25	19.28	2.27	5.73	1.79
6 52 7.42	-1 32 9.2	1.50	17.26	19.21	2.21	5.88	1.84
6 52 0.93	-1 32 22.1	1.35	17.18	18.84	1.90	6.80	2.13
6 51 54.45	-1 32 28.6	1.31	17.07	18.75	1.83	7.00	2.19
6 51 49.7	-1 32 22.1	1.38	17.12	18.93	1.97	6.54	2.04
6 51 43.65	-1 32 9.2	1.52	17.15	19.29	2.28	5.67	1.77
6 51 38.03	-1 32 15.6	1.53	17.04	19.35	2.33	5.51	1.72
6 51 30.68	-1 32 9.2	1.49	17.68	19.10	2.11	6.29	1.97
6 51 25.07	-1 32 9.1	1.62	18.17	19.30	2.29	5.98	1.87
6 51 18.58	-1 32 9.1	1.74	18.50	19.52	2.49	5.59	1.75
6 51 12.97	-1 32 2.7	1.80	19.40	19.47	2.44	5.99	1.87
6 53 8.78	-1 33 59.2	1.83	19.16	19.58	2.54	5.67	1.77
6 53 1.87	-1 33 59.3	1.75	18.89	19.47	2.43	5.83	1.82
6 52 54.95	-1 33 46.3	1.60	18.83	19.14	2.14	6.61	2.07
6 52 49.77	-1 33 59.3	1.67	18.83	19.30	2.28	6.22	1.94
6 52 42.42	-1 33 52.8	1.70	18.57	19.42	2.39	5.84	1.83
6 52 38.53	-1 33 46.3	1.64	18.33	19.32	2.30	6.00	1.87
6 52 31.62	-1 33 52.8	1.55	18.26	19.11	2.12	6.47	2.02
6 52 25.57	-1 33 52.8	1.51	18.15	19.04	2.06	6.61	2.07
6 52 19.09	-1 33 52.8	1.58	17.92	19.27	2.25	5.99	1.87
6 52 13.47	-1 33 52.8	1.55	17.62	19.27	2.26	5.87	1.84
6 52 6.55	-1 33 46.4	1.51	17.60	19.17	2.17	6.10	1.91
6 52 1.8	-1 33 59.3	1.37	17.26	18.87	1.92	6.75	2.11
6 51 54.88	-1 33 59.3	1.31	17.11	18.74	1.82	7.06	2.21
6 51 48.83	-1 33 59.3	1.34	16.94	18.85	1.91	6.68	2.09
6 51 43.65	-1 33 59.3	1.45	16.97	19.13	2.14	5.97	1.87
6 51 38.03	-1 33 46.4	1.45	16.94	19.16	2.16	5.91	1.85
6 51 32.84	-1 33 46.4	1.45	17.58	19.00	2.03	6.51	2.04
6 51 25.5	-1 33 33.4	1.55	18.21	19.14	2.15	6.38	2.00
6 51 19.88	-1 33 33.4	1.68	18.68	19.35	2.33	6.03	1.89
6 51 13.4	-1 33 13.9	1.82	19.40	19.51	2.47	5.90	1.84
6 53 7.49	-1 35 23.5	1.86	19.14	19.64	2.60	5.54	1.73
6 53 1.87	-1 35 17	1.70	18.85	19.35	2.33	6.09	1.90
6 52 54.52	-1 35 17	1.59	18.75	19.12	2.12	6.64	2.08
6 52 48.47	-1 35 4.1	1.67	18.83	19.28	2.27	6.24	1.95
6 52 43.29	-1 35 10.6	1.69	18.51	19.41	2.38	5.85	1.83
6 52 38.53	-1 35 23.5	1.68	18.45	19.38	2.36	5.89	1.84
6 52 32.05	-1 35 17.1	1.58	18.49	19.15	2.15	6.45	2.02
6 52 25.57	-1 35 17.1	1.57	18.34	19.15	2.16	6.40	2.00
6 52 19.52	-1 35 23.6	1.65	18.26	19.36	2.34	5.87	1.83
6 52 13.04	-1 35 10.6	1.60	17.99	19.31	2.29	5.91	1.85
6 52 8.28	-1 35 17.1	1.54	17.83	19.20	2.19	6.11	1.91
6 52 0.93	-1 35 17.1	1.46	17.48	19.07	2.09	6.30	1.97
6 51 55.32	-1 35 17.1	1.38	17.07	18.94	1.98	6.47	2.02
6 51 49.27	-1 35 17.1	1.38	16.91	18.97	2.01	6.34	1.98
6 51 43.65	-1 35 23.6	1.43	16.77	19.13	2.14	5.90	1.84
6 51 38.03	-1 35 30	1.38	16.97	18.97	2.00	6.38	1.99
6 51 31.98	-1 35 17.1	1.38	17.39	18.85	1.91	6.84	2.14
6 51 26.36	-1 35 10.6	1.49	17.98	19.04	2.06	6.56	2.05
6 51 19.45	-1 34 51.1	1.66	18.57	19.33	2.31	6.05	1.89
6 53 7.06	-1 36 54.2	1.86	19.33	19.62	2.57	5.65	1.77
6 53 1.44	-1 36 54.2	1.75	19.12	19.41	2.38	6.05	1.89
6 52 55.39	-1 36 54.2	1.64	19.07	19.16	2.16	6.64	2.08
6 52 48.91	-1 36 47.8	1.69	19.09	19.28	2.26	6.34	1.98
6 52 43.29	-1 36 54.2	1.78	18.91	19.52	2.48	5.72	1.79
6 52 38.53	-1 36 47.8	1.80	18.90	19.56	2.52	5.63	1.76
6 52 32.05	-1 36 47.8	1.68	18.93	19.28	2.27	6.28	1.96
6 52 25.57	-1 36 41.3	1.67	18.82	19.29	2.27	6.23	1.95
6 52 19.52	-1 36 47.8	1.74	18.68	19.48	2.44	5.74	1.80
6 52 12.17	-1 36 47.8	1.66	18.30	19.39	2.36	5.83	1.82
6 52 7.42	-1 36 34.8	1.55	17.88	19.20	2.19	6.13	1.92
6 52 0.93	-1 36 28.4	1.49	17.51	19.14	2.14	6.14	1.92
6 51 54.88	-1 36 34.8	1.40	16.98	19.00	2.03	6.30	1.97
6 51 50.13	-1 36 28.4	1.33	16.93	18.84	1.90	6.69	2.09
6 51 44.08	-1 36 47.8	1.38	16.79	18.99	2.02	6.24	1.95
6 51 38.03	-1 36 21.9	1.32	16.82	18.82	1.89	6.71	2.10
6 51 33.71	-1 36 34.8	1.34	17.50	18.74	1.83	7.20	2.25
6 51 26.79	-1 36 41.3	1.50	17.85	19.09	2.10	6.38	1.99

continued on next page

Table 22 – continued from previous page

R.A.(J2000) hh mm ss	Dec.(J2000) dd mm ss	$F(60)$ (MJy)	$F(100)$ (MJy)	$T_{\rm d}$ (K)	$B(\nu,T)$ $(\times10^{-16})$ Js^{-2}	$M_{\rm d}$ $(\times10^{28})$ kg	$A_{\rm V}$ $(\times10^{-5})$ mag
6 51 19.45	-1 36 21.9	1.59	18.44	19.19	2.19	6.33	1.98
6 51 13.4	-1 36 21.9	1.71	19.21	19.30	2.28	6.33	1.98
6 52 37.45	-1 38 8.8	1.93	19.48	19.73	2.68	5.46	1.71
6 52 31.84	-1 38 15.3	1.81	19.34	19.51	2.47	5.88	1.84
6 52 25.35	-1 38 5.5	1.76	19.09	19.43	2.40	5.98	1.87
6 52 18.44	-1 38 12	1.77	18.89	19.50	2.47	5.76	1.80
6 52 13.47	-1 37 59.1	1.68	18.46	19.39	2.36	5.87	1.84
6 52 6.99	-1 37 55.8	1.51	17.91	19.11	2.12	6.37	1.99
6 52 1.15	-1 37 55.8	1.46	17.45	19.07	2.08	6.30	1.97
6 51 54.24	-1 37 46.1	1.29	16.93	18.73	1.82	7.00	2.19
6 51 49.27	-1 37 59.1	1.31	16.84	18.80	1.87	6.77	2.12
6 51 43.86	-1 38 2.3	1.36	16.75	18.95	1.99	6.33	1.98
6 51 38.25	-1 37 59.1	1.31	16.95	18.78	1.85	6.88	2.15
6 51 31.98	-1 38 2.3	1.39	17.60	18.86	1.92	6.91	2.16
6 51 25.93	-1 37 59.1	1.52	17.91	19.12	2.13	6.33	1.98
6 51 20.09	-1 38 8.8	1.55	18.35	19.11	2.12	6.50	2.03
6 51 14.26	-1 38 5.5	1.69	18.99	19.29	2.28	6.27	1.96
6 51 8.64	-1 38 18.5	1.79	19.50	19.42	2.39	6.13	1.92
6 52 24.7	-1 39 58.9	1.86	19.35	19.60	2.56	5.68	1.78
6 52 19.95	-1 39 42.7	1.82	18.88	19.63	2.59	5.49	1.72
6 52 13.68	-1 39 39.5	1.64	18.44	19.30	2.28	6.07	1.90
6 52 8.28	-1 39 36.3	1.52	17.85	19.12	2.13	6.30	1.97
6 52 1.37	-1 39 29.8	1.44	17.33	19.05	2.07	6.30	1.97
6 51 55.32	-1 39 33	1.31	16.98	18.75	1.84	6.95	2.17
6 51 50.56	-1 39 33	1.29	16.98	18.72	1.81	7.05	2.21
6 51 43	-1 39 26.6	1.41	17.05	19.02	2.05	6.26	1.96
6 51 37.81	-1 39 29.8	1.39	17.30	18.90	1.95	6.68	2.09
6 51 31.33	-1 39 36.3	1.49	17.69	19.10	2.11	6.30	1.97
6 51 26.14	-1 39 26.5	1.57	18.12	19.20	2.20	6.20	1.94
6 51 19.66	-1 39 39.5	1.64	18.45	19.29	2.27	6.11	1.91
6 51 13.83	-1 39 39.5	1.67	18.81	19.30	2.28	6.19	1.94
6 51 7.78	-1 39 29.8	1.76	19.17	19.43	2.40	6.02	1.88
6 52 24.49	-1 41 19.9	1.95	19.50	19.78	2.73	5.37	1.68
6 52 19.09	-1 41 16.7	1.84	19.11	19.62	2.58	5.58	1.74
6 52 13.68	-1 41 10.2	1.68	18.69	19.34	2.32	6.07	1.90
6 52 7.63	-1 41 13.5	1.57	18.10	19.21	2.20	6.18	1.93
6 52 2.02	-1 41 10.2	1.52	17.68	19.17	2.17	6.12	1.91
6 51 55.53	-1 41 7	1.36	17.44	18.80	1.87	7.02	2.19
6 51 49.7	-1 41 10.2	1.34	17.29	18.78	1.86	7.00	2.19
6 51 42.78	-1 41 7	1.43	17.41	18.99	2.02	6.48	2.03
6 51 37.6	-1 41 3.8	1.46	17.43	19.07	2.09	6.28	1.96
6 51 32.19	-1 41 3.8	1.51	17.83	19.10	2.11	6.35	1.98
6 51 25.06	-1 41 7	1.60	18.11	19.29	2.27	6.00	1.88
6 51 19.88	-1 41 7	1.63	18.35	19.29	2.27	6.07	1.90
6 51 13.83	-1 41 7	1.66	18.53	19.33	2.31	6.03	1.89
6 51 7.99	-1 40 57.2	1.71	18.90	19.37	2.34	6.06	1.90
6 51 2.16	-1 40 57.2	1.77	19.32	19.42	2.39	6.08	1.90
6 52 19.95	-1 42 47.4	1.89	19.36	19.68	2.63	5.53	1.73
6 52 13.9	-1 42 37.7	1.80	19.02	19.55	2.51	5.70	1.78
6 52 7.85	-1 42 41	1.69	18.52	19.41	2.38	5.85	1.83
6 52 1.58	-1 42 41	1.65	18.13	19.40	2.37	5.76	1.80
6 51 55.32	-1 42 31.2	1.47	17.93	18.99	2.02	6.67	2.09
6 51 49.05	-1 42 34.5	1.39	17.76	18.82	1.89	7.07	2.21
6 51 42.35	-1 42 41	1.48	17.88	19.03	2.05	6.56	2.05
6 51 37.38	-1 42 37.7	1.51	17.88	19.09	2.10	6.39	2.00
6 51 31.55	-1 42 37.7	1.56	18.00	19.20	2.20	6.17	1.93
6 51 25.06	-1 42 44.2	1.58	18.21	19.20	2.19	6.24	1.95
6 51 19.44	-1 42 44.2	1.57	18.25	19.17	2.17	6.33	1.98
6 51 13.39	-1 42 37.7	1.61	18.44	19.24	2.23	6.23	1.95
6 51 7.78	-1 42 31.2	1.72	18.66	19.43	2.40	5.85	1.83
6 51 1.94	-1 42 28	1.78	19.17	19.47	2.44	5.91	1.85
6 52 13.04	-1 44 8.4	1.90	19.43	19.68	2.63	5.55	1.73
6 52 6.99	-1 44 5.2	1.78	19.15	19.48	2.44	5.89	1.84
6 52 1.58	-1 44 5.2	1.71	18.82	19.38	2.35	6.01	1.88
6 51 55.96	-1 44 2	1.58	18.49	19.15	2.15	6.47	2.02
6 51 48.19	-1 44 8.4	1.49	18.23	18.97	2.00	6.84	2.14
6 51 43.43	-1 44 8.4	1.58	18.38	19.17	2.17	6.37	1.99
6 51 37.6	-1 44 2	1.60	18.23	19.26	2.25	6.10	1.91
6 51 31.98	-1 43 58.7	1.60	18.16	19.27	2.26	6.05	1.89
6 51 24.85	-1 44 11.7	1.58	18.14	19.23	2.22	6.14	1.92
6 51 19.66	-1 44 1.9	1.56	18.23	19.15	2.15	6.37	1.99
6 51 12.96	-1 44 1.9	1.58	18.40	19.17	2.17	6.37	1.99
6 51 8.42	-1 44 8.4	1.64	18.56	19.28	2.26	6.17	1.93
6 51 1.94	-1 43 55.4	1.70	18.98	19.34	2.31	6.17	1.93
6 50 55.89	-1 44 8.4	1.74	19.20	19.37	2.35	6.15	1.92
6 52 6.99	-1 45 35.9	1.82	19.44	19.51	2.47	5.92	1.85
6 52 2.02	-1 45 35.9	1.73	19.20	19.34	2.32	6.22	1.95

continued on next page

Table 22 – continued from previous page

R.A.(J2000) hh mm ss	Dec.(J2000) dd mm ss	$F(60)$ (MJy)	$F(100)$ (MJy)	T_d (K)	$B(\nu,T)$ $(\times10^{-16})$ Js^{-2}	M_d $(\times10^{28})$ kg	A_V $(\times10^{-5})$ mag
6 51 55.53	-1 45 29.4	1.63	18.87	19.19	2.19	6.49	2.03
6 51 49.27	-1 45 35.9	1.58	18.69	19.11	2.12	6.64	2.08
6 51 43.21	-1 45 39.2	1.63	18.63	19.23	2.22	6.30	1.97
6 51 36.52	-1 45 39.2	1.68	18.55	19.37	2.35	5.94	1.86
6 51 31.55	-1 45 32.7	1.70	18.40	19.45	2.41	5.73	1.79
6 51 24.85	-1 45 35.9	1.63	18.41	19.28	2.26	6.12	1.91
6 51 20.96	-1 45 35.9	1.66	18.58	19.31	2.29	6.10	1.91
6 51 14.47	-1 45 35.9	1.70	18.57	19.41	2.38	5.87	1.83
6 51 7.34	-1 45 39.1	1.73	18.74	19.44	2.41	5.86	1.83
6 51 1.29	-1 45 42.4	1.72	19.02	19.36	2.33	6.13	1.92
6 50 56.32	-1 45 32.6	1.69	19.08	19.27	2.26	6.35	1.99
6 50 49.62	-1 45 32.6	1.77	19.38	19.41	2.38	6.13	1.92
6 51 54.88	-1 47 6.6	1.80	19.43	19.45	2.42	6.04	1.89
6 51 49.05	-1 47 16.4	1.70	19.21	19.27	2.26	6.40	2.00
6 51 43.65	-1 47 9.9	1.68	18.83	19.31	2.29	6.17	1.93
6 51 36.52	-1 47 3.4	1.76	18.83	19.50	2.47	5.74	1.79
6 51 31.33	-1 47 6.6	1.73	18.59	19.49	2.45	5.71	1.78
6 51 24.2	-1 47 13.1	1.73	18.74	19.44	2.41	5.85	1.83
6 51 19.66	-1 47 3.4	1.76	18.83	19.50	2.47	5.74	1.79
6 51 13.61	-1 46 53.6	1.77	19.10	19.47	2.43	5.91	1.85
6 51 8.21	-1 47 6.6	1.84	19.21	19.59	2.55	5.66	1.77
6 51 3.02	-1 47 3.4	1.78	19.18	19.48	2.44	5.91	1.85
6 50 56.32	-1 46 56.9	1.78	19.26	19.44	2.41	6.01	1.88
6 50 50.05	-1 47 0.1	1.81	19.41	19.48	2.44	5.97	1.87
6 51 43.43	-1 48 50.3	1.76	19.15	19.43	2.40	6.00	1.87
6 51 38.24	-1 48 43.8	1.77	18.94	19.50	2.47	5.77	1.80
6 51 30.9	-1 48 34.1	1.78	18.61	19.58	2.54	5.51	1.72
6 51 24.63	-1 48 34.1	1.77	18.78	19.53	2.49	5.66	1.77
6 51 19.88	-1 48 27.6	1.80	18.98	19.55	2.51	5.70	1.78
6 51 14.26	-1 48 27.6	1.79	19.34	19.47	2.43	5.98	1.87
6 51 3.24	-1 48 27.6	1.86	19.49	19.57	2.53	5.78	1.81
6 50 56.1	-1 48 24.3	1.81	19.35	19.50	2.47	5.90	1.84
6 50 50.05	-1 48 34	1.81	19.47	19.48	2.45	5.98	1.87
6 51 43.43	-1 50 11.3	1.73	19.22	19.35	2.33	6.21	1.94
6 51 36.73	-1 50 4.8	1.74	18.83	19.44	2.41	5.87	1.84
6 51 30.46	-1 50 1.6	1.74	18.63	19.49	2.45	5.71	1.78
6 51 25.28	-1 49 58.3	1.77	18.64	19.56	2.52	5.57	1.74
6 51 19.44	-1 50 4.8	1.78	19.07	19.49	2.46	5.83	1.82
6 51 15.34	-1 49 51.8	1.84	19.51	19.52	2.49	5.90	1.84
6 50 53.94	-1 49 48.6	1.82	19.54	19.48	2.45	6.01	1.88
6 50 48.97	-1 50 1.5	1.81	19.51	19.46	2.43	6.05	1.89
6 51 43	-1 51 38.8	1.69	19.04	19.28	2.27	6.31	1.97
6 51 36.51	-1 51 35.5	1.72	18.67	19.45	2.41	5.81	1.82
6 51 31.33	-1 51 38.8	1.73	18.48	19.51	2.47	5.62	1.76
6 51 24.84	-1 51 38.8	1.76	18.49	19.57	2.53	5.50	1.72
6 51 20.09	-1 51 38.8	1.81	19.12	19.55	2.51	5.73	1.79
6 50 49.62	-1 51 22.5	1.81	19.50	19.47	2.44	6.02	1.88
6 51 43	-1 52 56.5	1.69	19.05	19.30	2.28	6.28	1.96
6 51 37.38	-1 53 6.3	1.76	18.56	19.56	2.52	5.53	1.73
6 51 31.33	-1 53 6.3	1.83	18.65	19.69	2.65	5.29	1.65
6 51 25.06	-1 53 6.3	1.86	18.62	19.77	2.72	5.14	1.61
6 51 18.15	-1 53 6.2	1.85	19.23	19.62	2.57	5.62	1.76
6 51 44.08	-1 54 37	1.73	19.08	19.37	2.35	6.11	1.91
6 51 36.73	-1 54 37	1.77	18.88	19.50	2.46	5.76	1.80
6 51 30.68	-1 54 33.7	1.90	18.83	19.80	2.76	5.14	1.61
6 51 25.71	-1 54 40.2	1.92	18.92	19.83	2.79	5.10	1.59
6 51 19.66	-1 54 30.5	1.95	19.36	19.79	2.74	5.31	1.66
6 51 42.78	-1 56 7.7	1.85	19.35	19.59	2.55	5.72	1.79
6 51 37.38	-1 56 7.7	1.86	19.16	19.65	2.61	5.53	1.73
6 51 31.11	-1 55 54.7	2.00	19.20	19.93	2.89	5.00	1.56
6 51 24.63	-1 55 58	2.02	19.23	19.96	2.92	4.95	1.55

Table 23: The Database of far infrared cavity CCRPAS2 nearby post-AGB star PAGB0803-3635. The first two columns represent position of the pixels with in the cavity. The next two columns give values of relative flux density at 60 μm and 100 μm that have obtained after processing the FITS image using ALADIN 2.5 software. The calculated values of dust color temperature (in K), Planck function and dust mass for 100 μm and visual extinction (in mag) of the corresponding pixels,respectively.

R.A.(J2000) hh mm ss	Dec.(J2000) dd mm ss	$F(60)$ (MJy)	$F(100)$ (MJy)	T_d (K)	$B(\nu,T)$ $(\times10^{-16})$ Js^{-2}	M_d $(\times10^{27})$ kg	A_V $(\times10^{-5})$ mag
8 3 30.37	-36 44 54.9	4.78	30.98	21.71	5.23	9.36	1.39
8 3 39.05	-36 46 14.2	4.79	30.64	21.77	5.33	9.08	1.35
8 3 31.26	-36 46 17.7	4.70	30.14	21.75	5.30	8.99	1.34

continued on next page

Table 23 – continued from previous page

R.A.(J2000) hh mm ss	Dec.(J2000) dd mm ss	$F(60)$ (MJy)	$F(100)$ (MJy)	$T_{\rm d}$ (K)	$B(\nu,T)$ $(\times10^{-16})$ Js^{-2}	$M_{\rm d}$ $(\times10^{27})$ kg	$A_{\rm V}$ $(\times10^{-5})$ mag
8 3 23.77	-36 46 21.1	4.77	30.78	21.73	5.26	9.23	1.37
8 3 47.43	-36 47 40.7	4.77	30.61	21.76	5.30	9.11	1.36
8 3 38.44	-36 47 51.4	4.65	29.86	21.75	5.30	8.89	1.32
8 3 31.54	-36 47 51.3	4.62	29.66	21.75	5.30	8.84	1.32
8 3 23.75	-36 47 54.7	4.67	29.85	21.77	5.33	8.84	1.32
8 3 16.86	-36 47 47.4	4.81	30.90	21.75	5.29	9.22	1.37
8 4 16.5	-36 49 10.8	4.86	30.92	21.80	5.37	9.09	1.35
8 4 8.11	-36 49 18	4.82	30.33	21.85	5.46	8.77	1.31
8 4 1.21	-36 49 7.2	4.71	30.16	21.76	5.31	8.96	1.33
8 3 54.02	-36 49 14.4	4.64	30.08	21.70	5.21	9.11	1.36
8 3 46.82	-36 49 17.9	4.55	29.53	21.70	5.22	8.94	1.33
8 3 39.03	-36 49 32.2	4.60	29.38	21.77	5.33	8.70	1.30
8 3 30.93	-36 49 28.5	4.58	29.41	21.75	5.29	8.78	1.31
8 3 24.34	-36 49 24.7	4.61	29.71	21.73	5.26	8.92	1.33
8 3 15.94	-36 49 35.3	4.71	30.53	21.71	5.23	9.22	1.37
8 4 39.3	-36 50 26.1	4.86	30.87	21.80	5.37	9.07	1.35
8 4 31.8	-36 50 26.3	4.73	30.19	21.78	5.34	8.93	1.33
8 4 24	-36 50 33.5	4.66	29.88	21.76	5.30	8.90	1.32
8 4 16.51	-36 50 33.6	4.62	29.73	21.74	5.27	8.90	1.33
8 4 9.31	-36 50 40.8	4.59	29.40	21.76	5.31	8.75	1.30
8 4 1.51	-36 50 44.4	4.58	29.39	21.75	5.30	8.76	1.30
8 3 54.31	-36 50 44.4	4.57	29.54	21.72	5.24	8.90	1.33
8 3 46.52	-36 50 47.9	4.59	29.41	21.76	5.31	8.74	1.30
8 3 39.62	-36 50 47.8	4.59	29.22	21.79	5.36	8.60	1.28
8 3 31.52	-36 50 51.3	4.60	29.33	21.79	5.36	8.65	1.29
8 3 24.62	-36 50 51.1	4.66	29.78	21.77	5.33	8.83	1.31
8 3 16.83	-36 50 54.6	4.76	30.43	21.78	5.34	9.01	1.34
8 5 17.7	-36 51 33.5	4.74	30.75	21.70	5.22	9.31	1.39
8 5 9.9	-36 51 41	4.74	30.78	21.70	5.21	9.33	1.39
8 5 1.8	-36 51 44.8	4.86	31.00	21.78	5.34	9.17	1.36
8 4 46.81	-36 51 48.8	4.83	30.61	21.81	5.40	8.96	1.33
8 4 39.31	-36 51 52.5	4.73	30.42	21.74	5.28	9.10	1.35
8 4 31.51	-36 51 56.3	4.65	30.09	21.72	5.24	9.07	1.35
8 4 24.61	-36 51 56.3	4.68	30.04	21.75	5.29	8.96	1.33
8 4 16.51	-36 51 56.4	4.67	29.91	21.76	5.31	8.90	1.33
8 4 9.31	-36 52 0	4.67	29.69	21.80	5.37	8.74	1.30
8 4 1.51	-36 52 10.8	4.72	29.67	21.86	5.47	8.56	1.27
8 3 54.91	-36 52 14.4	4.71	29.67	21.85	5.45	8.60	1.28
8 3 47.41	-36 52 14.3	4.70	29.74	21.83	5.42	8.67	1.29
8 3 40.81	-36 52 10.6	4.66	29.50	21.82	5.41	8.60	1.28
8 3 30.91	-36 52 24.9	4.70	29.74	21.82	5.41	8.67	1.29
8 3 25.51	-36 52 21.2	4.74	30.27	21.78	5.34	8.96	1.33
8 3 17.71	-36 52 24.6	4.84	30.79	21.80	5.37	9.06	1.35
8 5 16.22	-36 53 7.2	4.78	30.95	21.71	5.24	9.34	1.39
8 5 9.02	-36 53 11	4.77	30.67	21.74	5.28	9.17	1.37
8 5 1.22	-36 53 22	4.71	30.69	21.68	5.19	9.34	1.39
8 4 54.32	-36 53 15	4.77	30.70	21.74	5.27	9.19	1.37
8 4 47.42	-36 53 29.6	4.73	30.42	21.74	5.28	9.10	1.35
8 4 39.32	-36 53 26.1	4.71	30.47	21.72	5.24	9.18	1.37
8 4 31.82	-36 53 26.3	4.76	30.72	21.72	5.25	9.24	1.38
8 4 24.61	-36 53 26.3	4.89	30.77	21.85	5.46	8.91	1.33
8 4 16.81	-36 53 22.8	5.01	31.18	21.90	5.55	8.88	1.32
8 4 10.21	-36 53 26.4	4.99	31.19	21.88	5.51	8.94	1.33
8 4 2.71	-36 53 22.8	5.02	30.74	21.98	5.68	8.54	1.27
8 3 55.21	-36 53 37.2	4.89	30.15	21.95	5.62	8.47	1.26
8 3 47.7	-36 53 40.7	4.77	30.09	21.84	5.45	8.72	1.30
8 3 39.6	-36 53 40.6	4.74	29.82	21.85	5.46	8.63	1.28
8 3 32.7	-36 53 47.7	4.72	30.18	21.78	5.34	8.93	1.33
8 5 10.84	-36 54 40.9	4.74	30.67	21.71	5.23	9.26	1.38
8 5 2.14	-36 54 44.8	4.66	30.51	21.65	5.13	9.39	1.40
8 4 54.34	-36 54 48.6	4.69	30.58	21.67	5.17	9.35	1.39
8 4 48.03	-36 54 48.8	4.77	30.55	21.77	5.32	9.07	1.35
8 4 40.53	-36 54 48.9	4.83	30.81	21.79	5.35	9.09	1.35
8 4 32.42	-36 54 45.4	5.06	31.65	21.88	5.51	9.08	1.35
8 4 25.22	-36 55 3.5	5.14	32.05	21.90	5.53	9.14	1.36
8 4 17.12	-36 54 56.4	5.38	32.80	22.01	5.73	9.04	1.35
8 4 10.21	-36 54 56.4	5.61	33.49	22.11	5.90	8.96	1.33
8 4 2.11	-36 55 0	5.50	32.44	22.17	6.01	8.53	1.27
8 3 54.9	-36 55 7.2	5.16	30.79	22.11	5.90	8.23	1.23
8 3 48	-36 55 14.3	4.85	30.11	21.92	5.57	8.53	1.27
8 3 40.79	-36 55 17.8	4.71	30.08	21.78	5.34	8.90	1.33
8 3 33.59	-36 55 21.3	4.83	30.44	21.85	5.45	8.82	1.31
8 5 9.66	-36 56 3.8	4.74	30.65	21.71	5.23	9.25	1.38
8 5 3.36	-36 56 18.4	4.72	30.59	21.70	5.22	9.26	1.38
8 4 55.55	-36 56 25.8	4.76	30.81	21.72	5.24	9.29	1.38
8 4 47.45	-36 56 18.8	4.87	31.12	21.78	5.34	9.20	1.37
8 4 39.34	-36 56 26.1	5.02	31.54	21.86	5.47	9.11	1.36

continued on next page

Table 23 – continued from previous page

R.A.(J2000)	Dec.(J2000)	$F(60)$	$F(100)$	$T_{\rm d}$	$B(\nu, T)$	$M_{\rm d}$	A_V
hh mm ss	dd mm ss	(MJy)	(MJy)	(K)	$(\times 10^{-16})$ Js^{-2}	$(\times 10^{27})$ kg	$(\times 10^{-5})$ mag
8 4 33.33	-36 56 26.2	5.19	32.22	21.92	5.57	9.13	1.36
8 4 25.53	-36 56 37.1	5.54	33.68	22.02	5.75	9.25	1.38
8 4 18.02	-36 56 30	6.03	34.50	22.33	6.29	8.66	1.29
8 4 9.91	-36 56 30	6.33	34.98	22.52	6.64	8.32	1.24
8 4 2.71	-36 56 37.2	5.91	33.74	22.34	6.32	8.44	1.26
8 3 56.4	-36 56 40.8	5.34	31.32	22.20	6.06	8.16	1.21
8 3 49.79	-36 56 33.5	4.79	29.93	21.89	5.52	8.56	1.27
8 3 41.08	-36 56 44.2	4.68	29.86	21.78	5.34	8.83	1.32
8 3 31.77	-36 56 51.3	4.84	30.51	21.84	5.45	8.84	1.32
8 5 18.69	-36 57 29.9	4.77	30.58	21.76	5.30	9.11	1.36
8 5 9.68	-36 57 33.8	4.70	30.25	21.74	5.27	9.06	1.35
8 5 3.08	-36 57 37.6	4.70	30.46	21.71	5.23	9.20	1.37
8 4 55.57	-36 57 41.4	4.84	31.04	21.76	5.31	9.23	1.37
8 4 48.36	-36 57 38	5.05	31.51	21.89	5.53	9.00	1.34
8 4 40.55	-36 57 45.3	5.13	31.86	21.91	5.56	9.05	1.35
8 4 33.04	-36 57 45.4	5.29	32.43	21.98	5.67	9.03	1.35
8 4 25.83	-36 57 52.7	5.72	33.46	22.21	6.08	8.69	1.29
8 4 18.02	-36 57 56.4	6.09	34.66	22.36	6.34	8.63	1.28
8 4 10.21	-36 58 3.6	6.17	34.85	22.40	6.42	8.57	1.28
8 4 3.31	-36 58 3.6	5.59	33.02	22.17	6.01	8.68	1.29
8 3 55.5	-36 57 52.8	5.08	31.16	21.98	5.67	8.68	1.29
8 3 48.89	-36 58 7.1	4.70	29.60	21.85	5.46	8.56	1.28
8 3 42.28	-36 58 17.8	4.80	29.58	21.96	5.64	8.29	1.23
8 3 33.26	-36 58 21.3	4.90	30.19	21.96	5.63	8.46	1.26
8 5 34.04	-36 59 2.8	4.81	30.84	21.76	5.31	9.17	1.36
8 5 26.23	-36 59 6.8	4.64	30.28	21.67	5.16	9.26	1.38
8 5 18.42	-36 59 10.7	4.56	29.72	21.67	5.17	9.08	1.35
8 5 11.2	-36 58 56.5	4.54	29.81	21.64	5.12	9.19	1.37
8 5 2.19	-36 59 14.8	4.61	30.18	21.66	5.15	9.26	1.38
8 4 56.79	-36 59 11.4	4.81	30.75	21.77	5.33	9.11	1.36
8 4 49.27	-36 59 15.1	5.02	31.41	21.88	5.50	9.02	1.34
8 4 41.16	-36 59 22.5	5.10	31.78	21.90	5.54	9.06	1.35
8 4 33.95	-36 59 29.8	5.21	32.02	21.97	5.66	8.93	1.33
8 4 26.74	-36 59 29.9	5.35	32.81	21.98	5.68	9.13	1.36
8 4 18.63	-36 59 26.4	5.59	33.51	22.10	5.88	9.01	1.34
8 4 12.32	-36 59 22.8	5.36	32.57	22.03	5.76	8.93	1.33
8 4 3.9	-36 59 30	5.07	31.47	21.92	5.57	8.92	1.33
8 3 55.19	-36 59 40.8	4.80	30.03	21.88	5.51	8.61	1.28
8 3 49.48	-36 59 40.7	4.90	29.25	22.12	5.91	7.81	1.16
8 3 40.47	-36 59 44.2	5.11	29.19	22.34	6.31	7.30	1.09
8 3 32.35	-36 59 33.3	5.15	30.04	22.23	6.12	7.76	1.15
8 5 41.28	-37 0 32.5	4.78	30.56	21.77	5.33	9.06	1.35
8 5 33.47	-37 0 36.5	4.63	29.85	21.73	5.26	8.95	1.33
8 5 25.95	-37 0 36.8	4.52	29.63	21.65	5.13	9.13	1.36
8 5 18.44	-37 0 37.1	4.41	29.20	21.60	5.06	9.11	1.36
8 5 10.63	-37 0 37.3	4.41	29.20	21.60	5.05	9.12	1.36
8 5 3.11	-37 0 37.6	4.55	29.77	21.66	5.15	9.13	1.36
8 4 56.8	-37 0 41.4	4.71	30.25	21.75	5.29	9.04	1.35
8 4 49.29	-37 0 41.5	4.86	30.84	21.81	5.39	9.04	1.35
8 4 41.77	-37 0 38.1	5.00	31.19	21.89	5.53	8.91	1.33
8 4 34.26	-37 0 56.2	5.03	31.43	21.88	5.51	9.01	1.34
8 4 26.15	-37 0 56.3	5.06	31.48	21.91	5.56	8.95	1.33
8 4 18.93	-37 1 3.6	5.15	31.68	21.97	5.65	8.85	1.32
8 4 11.72	-37 1 3.6	5.09	31.22	21.98	5.67	8.70	1.29
8 4 4.5	-37 1 3.6	4.90	30.32	21.94	5.60	8.54	1.27
8 3 56.69	-37 1 0	4.83	29.79	21.95	5.63	8.36	1.25
8 3 49.48	-37 1 7.1	5.03	29.40	22.22	6.09	7.62	1.13
8 3 42.56	-37 1 17.8	5.19	29.37	22.39	6.39	7.25	1.08
8 3 33.84	-37 1 21.3	5.19	30.34	22.23	6.10	7.85	1.17
8 5 49.42	-37 1 44.1	4.69	30.37	21.70	5.22	9.19	1.37
8 5 41.91	-37 1 51.7	4.67	30.09	21.74	5.27	9.01	1.34
8 5 33.49	-37 2 2.8	4.57	29.61	21.70	5.22	8.96	1.33
8 5 26.88	-37 2 10.3	4.51	29.25	21.70	5.22	8.85	1.32
8 5 18.76	-37 1 59.9	4.42	29.07	21.63	5.10	9.00	1.34
8 5 11.55	-37 2 7.3	4.39	29.15	21.59	5.04	9.13	1.36
8 5 4.03	-37 2 7.6	4.52	29.53	21.67	5.16	9.03	1.34
8 4 57.12	-37 2 11.3	4.68	30.14	21.74	5.28	9.02	1.34
8 4 49	-37 2 11.5	4.82	30.40	21.84	5.45	8.81	1.31
8 4 41.79	-37 2 11.7	4.98	30.70	21.96	5.63	8.61	1.28
8 4 33.97	-37 2 15.4	4.94	30.68	21.91	5.56	8.71	1.30
8 4 26.75	-37 2 29.9	4.93	30.56	21.92	5.57	8.66	1.29
8 4 20.14	-37 2 26.4	4.93	30.38	21.96	5.64	8.51	1.27
8 4 11.72	-37 2 26.4	4.98	30.39	22.00	5.71	8.40	1.25
8 4 5.41	-37 2 26.4	4.96	30.23	22.01	5.72	8.34	1.24
8 3 56.39	-37 2 37.2	4.95	29.99	22.04	5.78	8.19	1.22
8 3 49.77	-37 2 40.7	4.96	29.70	22.10	5.88	7.98	1.19
8 3 42.25	-37 2 47.8	5.03	29.88	22.14	5.95	7.92	1.18

continued on next page

Table 23 – continued from previous page

R.A.(J2000)	Dec.(J2000)	$F(60)$	$F(100)$	$T_{\rm d}$	$B(\nu, T)$	$M_{\rm d}$	$A_{\rm V}$
hh mm ss	dd mm ss	(MJy)	(MJy)	(K)	$(\times 10^{-16})$ Js^{-2}	$(\times 10^{27})$ kg	$(\times 10^{-5})$ mag
8 5 56.67	-37 3 13.7	4.76	30.56	21.76	5.30	9.10	1.36
8 5 49.46	-37 3 21.3	4.62	29.93	21.71	5.23	9.04	1.35
8 5 42.24	-37 3 25.2	4.60	29.73	21.72	5.25	8.95	1.33
8 5 34.13	-37 3 36.4	4.58	29.49	21.73	5.26	8.85	1.32
8 5 26.91	-37 3 36.7	4.57	29.25	21.77	5.32	8.68	1.29
8 5 19.09	-37 3 40.6	4.51	29.19	21.72	5.24	8.80	1.31
8 5 11.27	-37 3 44.5	4.49	29.29	21.68	5.18	8.93	1.33
8 5 4.05	-37 3 44.8	4.60	29.63	21.73	5.27	8.89	1.32
8 4 56.54	-37 3 52.2	4.70	30.15	21.76	5.31	8.97	1.34
8 4 49.62	-37 3 41.5	4.82	30.37	21.84	5.44	8.81	1.31
8 4 41.8	-37 3 52.5	4.88	30.32	21.91	5.56	8.61	1.28
8 4 34.88	-37 3 59.8	4.93	30.32	21.97	5.66	8.46	1.26
8 4 27.06	-37 3 56.3	4.86	30.01	21.94	5.61	8.45	1.26
8 4 19.54	-37 3 56.4	4.85	29.86	21.96	5.63	8.37	1.25
8 4 11.72	-37 4 7.2	4.89	29.95	21.99	5.68	8.32	1.24
8 4 4.2	-37 4 7.2	4.96	30.13	22.02	5.75	8.28	1.23
8 3 57.28	-37 4 14.4	4.95	29.98	22.04	5.78	8.19	1.22
8 3 49.76	-37 4 10.7	4.90	29.80	22.02	5.74	8.20	1.22
8 3 41.94	-37 4 14.2	4.80	30.04	21.88	5.51	8.62	1.28
8 5 57.61	-37 4 47.2	4.75	30.75	21.71	5.23	9.28	1.38
8 5 48.89	-37 4 51.3	4.63	29.89	21.73	5.26	8.98	1.34
8 5 41.68	-37 5 6.1	4.60	29.76	21.71	5.23	8.99	1.34
8 5 35.06	-37 5 2.8	4.60	29.69	21.72	5.25	8.93	1.33
8 5 27.54	-37 5 6.7	4.60	29.31	21.79	5.36	8.63	1.29
8 5 18.81	-37 5 14.3	4.63	29.46	21.80	5.37	8.66	1.29
8 5 12.8	-37 5 14.5	4.68	29.67	21.81	5.39	8.69	1.29
8 5 4.37	-37 5 7.5	4.67	29.68	21.80	5.38	8.71	1.30
8 4 57.15	-37 5 18.5	4.73	30.03	21.81	5.39	8.79	1.31
8 4 50.23	-37 5 18.7	4.77	30.29	21.80	5.38	8.90	1.32
8 4 43.01	-37 5 18.9	4.80	30.11	21.87	5.49	8.67	1.29
8 4 34.89	-37 5 26.2	4.85	30.07	21.92	5.58	8.51	1.27
8 4 26.77	-37 5 22.7	4.86	29.82	21.97	5.66	8.32	1.24
8 4 19.55	-37 5 22.8	4.85	29.80	21.97	5.65	8.33	1.24
8 4 11.42	-37 5 26.4	4.89	29.84	22.00	5.71	8.26	1.23
8 4 5.1	-37 5 37.2	4.93	29.99	22.02	5.74	8.25	1.23
8 3 57.28	-37 5 44.4	4.85	29.85	21.96	5.64	8.36	1.24
8 3 50.36	-37 5 47.9	4.77	29.74	21.90	5.53	8.49	1.26
8 3 41.63	-37 5 51.4	4.84	30.24	21.88	5.51	8.67	1.29
8 5 56.44	-37 6 13.7	4.88	30.96	21.81	5.38	9.08	1.35
8 5 50.73	-37 6 21.2	4.74	30.00	21.83	5.42	8.74	1.30
8 5 42.31	-37 6 36	4.65	29.88	21.74	5.28	8.93	1.33
8 5 35.08	-37 6 25.6	4.66	29.83	21.77	5.32	8.85	1.32
8 5 26.66	-37 6 33.1	4.68	29.60	21.82	5.41	8.63	1.29
8 5 19.14	-37 6 33.4	4.70	29.59	21.85	5.45	8.57	1.28
8 5 12.21	-37 6 33.7	4.71	29.77	21.82	5.41	8.68	1.29
8 5 4.69	-37 6 44.7	4.67	29.81	21.78	5.35	8.80	1.31
8 4 57.47	-37 6 41.3	4.70	29.85	21.80	5.38	8.76	1.30
8 4 49.94	-37 6 37.9	4.74	30.11	21.80	5.38	8.85	1.32
8 4 41.82	-37 6 48.9	4.78	30.23	21.83	5.42	8.80	1.31
8 4 34.9	-37 6 56.2	4.84	30.09	21.91	5.56	8.54	1.27
8 4 27.68	-37 6 52.7	4.87	30.07	21.94	5.61	8.46	1.26
8 4 19.55	-37 6 56.4	4.86	29.97	21.95	5.63	8.41	1.25
8 4 12.03	-37 6 56.4	4.86	29.97	21.95	5.62	8.42	1.25
8 4 5.1	-37 7 0	4.88	29.84	22.00	5.70	8.26	1.23
8 3 58.48	-37 7 7.2	4.82	29.67	21.96	5.64	8.31	1.24
8 3 49.75	-37 7 7.1	4.74	29.62	21.89	5.52	8.47	1.26
8 3 41.93	-37 7 14.2	4.95	30.28	21.99	5.69	8.40	1.25
8 5 50.16	-37 7 51.2	4.79	30.49	21.80	5.37	8.97	1.34
8 5 43.24	-37 7 48	4.71	29.94	21.80	5.37	8.80	1.31
8 5 35.11	-37 7 55.6	4.68	29.72	21.81	5.39	8.71	1.30
8 5 27.59	-37 7 52.3	4.63	29.53	21.78	5.35	8.72	1.30
8 5 20.36	-37 7 56.2	4.67	29.46	21.83	5.43	8.57	1.28
8 5 12.53	-37 7 52.9	4.67	29.73	21.79	5.36	8.77	1.31
8 5 4.71	-37 7 56.7	4.64	29.84	21.75	5.29	8.91	1.33
8 4 57.49	-37 8 18.5	4.67	29.73	21.79	5.36	8.76	1.30
8 4 49.96	-37 8 4.3	4.71	30.00	21.79	5.35	8.85	1.32
8 4 42.43	-37 8 15.3	4.75	30.19	21.80	5.37	8.88	1.32
8 4 36.11	-37 8 15.4	4.81	30.18	21.87	5.48	8.69	1.29
8 4 27.38	-37 8 26.3	4.90	29.99	21.99	5.69	8.33	1.24
8 4 19.25	-37 8 26.4	4.84	29.97	21.93	5.59	8.47	1.26
8 4 10.82	-37 8 40.8	4.84	29.76	21.97	5.66	8.31	1.24
8 4 4.2	-37 8 30	4.78	29.61	21.93	5.59	8.36	1.24
8 3 57.27	-37 8 33.6	4.73	29.24	21.94	5.61	8.23	1.23
8 3 49.45	-37 8 29.9	4.72	29.41	21.90	5.55	8.37	1.25
8 3 43.42	-37 8 37.1	4.92	29.95	22.01	5.73	8.25	1.23
8 5 50.5	-37 9 28.4	4.82	30.63	21.80	5.37	9.00	1.34
8 5 43.28	-37 9 36	4.68	29.86	21.78	5.34	8.83	1.31

continued on next page

Table 23 – continued from previous page

R.A.(J2000)	Dec.(J2000)	$F(60)$	$F(100)$	$T_{\rm d}$	$B(\nu, T)$	$M_{\rm d}$	A_V
hh mm ss	dd mm ss	(MJy)	(MJy)	(K)	$(\times 10^{-16})$ Js^{-2}	$(\times 10^{27})$ kg	$(\times 10^{-5})$ mag
8 5 34.24	-37 9 36.4	4.61	29.30	21.80	5.38	8.61	1.28
8 5 29.12	-37 9 40.2	4.59	29.19	21.80	5.37	8.59	1.28
8 5 20.39	-37 9 40.6	4.57	29.18	21.77	5.33	8.64	1.29
8 5 11.96	-37 9 37.3	4.60	29.49	21.76	5.31	8.77	1.31
8 5 5.33	-37 9 33.9	4.60	29.83	21.70	5.22	9.02	1.34
8 4 57.5	-37 9 37.7	4.62	29.98	21.70	5.21	9.09	1.35
8 4 50.28	-37 9 45.1	4.69	29.98	21.77	5.32	8.89	1.32
8 4 41.84	-37 9 52.5	4.70	30.07	21.76	5.32	8.93	1.33
8 4 34.92	-37 9 59.8	4.71	30.02	21.79	5.35	8.86	1.32
8 4 27.99	-37 9 56.3	4.76	29.79	21.87	5.50	8.56	1.27
8 4 21.06	-37 9 56.3	4.80	29.53	21.96	5.64	8.26	1.23
8 4 12.63	-37 10 0	4.76	29.35	21.95	5.62	8.25	1.23
8 4 4.8	-37 10 3.6	4.68	29.01	21.93	5.59	8.19	1.22
8 3 56.97	-37 10 0	4.63	29.00	21.87	5.50	8.33	1.24
8 3 50.04	-37 10 17.9	4.64	29.09	21.87	5.49	8.37	1.25
8 3 44.02	-37 10 10.7	4.76	29.90	21.86	5.47	8.64	1.29
8 3 36.19	-37 10 17.7	4.91	30.59	21.90	5.54	8.72	1.30
8 3 29.26	-37 10 24.8	5.02	30.98	21.94	5.61	8.72	1.30
8 3 12.69	-37 10 31.6	4.89	30.43	21.90	5.55	8.67	1.29
8 3 4.86	-37 10 27.8	4.85	30.48	21.86	5.47	8.80	1.31
8 2 57.63	-37 10 38.3	4.87	30.68	21.85	5.45	8.89	1.32
8 2 50.4	-37 10 34.5	4.85	30.91	21.79	5.36	9.11	1.36
8 5 51.13	-37 10 40.4	4.84	30.66	21.82	5.41	8.96	1.33
8 5 42.4	-37 10 55.2	4.66	29.79	21.77	5.33	8.82	1.31
8 5 36.08	-37 10 59.1	4.52	29.02	21.76	5.30	8.64	1.29
8 5 28.85	-37 11 3	4.48	28.83	21.74	5.27	8.64	1.29
8 5 20.71	-37 11 3.4	4.48	29.02	21.71	5.23	8.77	1.31
8 5 12.88	-37 11 14.5	4.58	29.22	21.78	5.35	8.62	1.28
8 5 5.35	-37 11 11.1	4.65	29.72	21.77	5.33	8.80	1.31
8 4 58.42	-37 11 11.3	4.67	29.92	21.76	5.31	8.91	1.33
8 4 51.5	-37 11 18.7	4.66	29.79	21.77	5.33	8.82	1.31
8 4 43.66	-37 11 22.5	4.65	29.65	21.79	5.35	8.75	1.30
8 4 36.43	-37 11 22.6	4.62	29.45	21.79	5.35	8.69	1.29
8 4 28.3	-37 11 22.7	4.61	29.32	21.80	5.38	8.61	1.28
8 4 20.77	-37 11 26.4	4.62	29.08	21.84	5.45	8.43	1.26
8 4 12.03	-37 11 37.2	4.60	28.78	21.88	5.51	8.25	1.23
8 4 6.31	-37 11 40.8	4.56	28.70	21.85	5.46	8.30	1.24
8 3 58.17	-37 11 37.2	4.58	28.75	21.86	5.48	8.29	1.23
8 3 51.24	-37 11 44.3	4.63	29.33	21.81	5.40	8.58	1.28
8 3 45.22	-37 11 40.7	4.83	30.14	21.89	5.53	8.61	1.28
8 3 36.18	-37 11 40.5	4.91	30.65	21.89	5.53	8.75	1.30
8 3 27.44	-37 11 54.8	4.90	30.71	21.87	5.50	8.83	1.31
8 3 20.21	-37 11 51	4.85	30.57	21.84	5.44	8.88	1.32
8 3 12.37	-37 11 54.4	4.75	30.06	21.83	5.42	8.76	1.30
8 3 5.14	-37 11 57.8	4.70	29.90	21.80	5.37	8.79	1.31
8 2 57.91	-37 12 1.1	4.69	29.93	21.78	5.35	8.83	1.32
8 2 51.28	-37 12 4.5	4.68	30.39	21.70	5.21	9.22	1.37
8 2 42.84	-37 12 4.1	4.75	30.77	21.70	5.22	9.31	1.39
8 2 36.21	-37 12 3.8	4.81	31.02	21.73	5.27	9.30	1.38
8 5 51.47	-37 12 17.5	4.86	30.28	21.89	5.53	8.65	1.29
8 5 43.33	-37 12 21.6	4.64	29.62	21.78	5.35	8.75	1.30
8 5 36.41	-37 12 29.1	4.48	29.02	21.71	5.23	8.75	1.30
8 5 27.97	-37 12 29.5	4.43	28.71	21.70	5.22	8.69	1.29
8 5 21.04	-37 12 29.8	4.46	28.88	21.70	5.22	8.74	1.30
8 5 13.5	-37 12 30	4.61	29.22	21.81	5.39	8.56	1.27
8 5 5.97	-37 12 37.5	4.71	29.55	21.86	5.48	8.52	1.27
8 4 58.74	-37 12 41.3	4.70	29.71	21.82	5.42	8.66	1.29
8 4 50.91	-37 12 41.5	4.65	29.51	21.80	5.38	8.66	1.29
8 4 43.67	-37 12 45.3	4.64	29.21	21.85	5.46	8.45	1.26
8 4 36.14	-37 12 49	4.56	29.02	21.80	5.37	8.54	1.27
8 4 28	-37 12 56.3	4.56	28.87	21.82	5.41	8.43	1.26
8 4 20.77	-37 12 56.4	4.54	28.86	21.81	5.38	8.46	1.26
8 4 13.54	-37 12 56.4	4.54	28.72	21.82	5.42	8.38	1.25
8 4 6.61	-37 13 0	4.58	28.78	21.86	5.47	8.31	1.24
8 3 59.98	-37 13 0	4.68	29.39	21.86	5.48	8.47	1.26
8 3 51.84	-37 13 14.3	4.89	30.02	21.97	5.67	8.37	1.25
8 3 44	-37 13 14.3	4.94	30.51	21.94	5.61	8.60	1.28
8 3 36.17	-37 13 3.3	4.96	30.78	21.92	5.57	8.72	1.30
8 3 28.93	-37 13 14	4.85	30.59	21.84	5.44	8.89	1.32
8 3 19.89	-37 13 24.6	4.76	30.09	21.82	5.41	8.78	1.31
8 3 13.56	-37 13 17.2	4.71	30.00	21.79	5.36	8.84	1.32
8 3 5.73	-37 13 17	4.66	29.80	21.77	5.32	8.84	1.32
8 2 58.79	-37 13 24	4.71	29.93	21.81	5.39	8.78	1.31
8 2 50.65	-37 13 34.5	4.76	30.53	21.76	5.31	9.08	1.35
8 2 42.52	-37 13 23.3	4.81	30.86	21.76	5.31	9.19	1.37
8 2 28.65	-37 13 26.2	4.90	30.99	21.83	5.42	9.04	1.35
8 5 51.5	-37 13 47.5	4.79	30.14	21.85	5.46	8.71	1.30

continued on next page

Table 23 – continued from previous page

R.A.(J2000)	Dec.(J2000)	$F(60)$	$F(100)$	$T_{\rm d}$	$B(\nu, T)$	$M_{\rm d}$	A_V
hh mm ss	dd mm ss	(MJy)	(MJy)	(K)	$(\times 10^{-16})$ Js^{-2}	$(\times 10^{27})$ kg	$(\times 10^{-5})$ mag
8 5 44.27	-37 13 40.7	4.58	29.51	21.73	5.27	8.85	1.32
8 5 35.53	-37 13 55.6	4.50	29.01	21.73	5.27	8.70	1.29
8 5 29.2	-37 13 59.4	4.42	28.76	21.69	5.19	8.75	1.30
8 5 20.76	-37 14 7	4.46	28.82	21.72	5.25	8.67	1.29
8 5 14.13	-37 13 56.4	4.57	29.10	21.79	5.37	8.56	1.27
8 5 5.99	-37 14 11.1	4.73	29.37	21.92	5.57	8.32	1.24
8 4 59.96	-37 14 11.3	4.69	29.34	21.88	5.50	8.42	1.25
8 4 52.13	-37 14 11.5	4.57	29.09	21.79	5.36	8.57	1.28
8 4 43.38	-37 14 15.3	4.54	28.79	21.81	5.40	8.42	1.25
8 4 36.15	-37 14 19	4.57	28.65	21.87	5.48	8.25	1.23
8 4 29.22	-37 14 11.9	4.55	28.73	21.83	5.43	8.36	1.24
8 4 21.68	-37 14 33.5	4.55	28.97	21.79	5.36	8.54	1.27
8 4 13.84	-37 14 33.6	4.62	28.94	21.87	5.49	8.32	1.24
8 4 6	-37 14 33.6	4.79	29.47	21.97	5.65	8.23	1.23
8 3 57.86	-37 14 33.6	4.97	30.03	22.06	5.80	8.17	1.22
8 3 51.53	-37 14 44.3	5.07	30.91	22.01	5.73	8.52	1.27
8 3 43.09	-37 14 44.2	5.08	30.96	22.02	5.73	8.53	1.27
8 3 35.55	-37 14 51.3	5.02	30.79	21.97	5.67	8.58	1.28
8 3 28.02	-37 14 51.2	4.86	30.49	21.86	5.48	8.79	1.31
8 3 21.38	-37 14 51	4.79	30.24	21.84	5.44	8.78	1.31
8 3 13.84	-37 15 1.7	4.78	30.34	21.81	5.39	8.88	1.32
8 3 6.31	-37 14 57.8	4.80	30.32	21.84	5.44	8.81	1.31
8 2 58.47	-37 14 54	4.88	30.61	21.87	5.49	8.81	1.31
8 2 51.53	-37 15 0.9	4.92	30.89	21.86	5.48	8.91	1.33
8 5 59.68	-37 15 17.1	4.91	30.45	21.93	5.58	8.61	1.28
8 5 51.84	-37 15 13.9	4.72	29.78	21.84	5.44	8.65	1.29
8 5 44.3	-37 15 21.5	4.52	29.18	21.73	5.26	8.77	1.31
8 5 36.16	-37 15 21.9	4.44	28.85	21.69	5.20	8.76	1.30
8 5 28.02	-37 15 18.7	4.40	28.61	21.68	5.19	8.71	1.30
8 5 21.39	-37 15 26.2	4.43	28.77	21.70	5.21	8.72	1.30
8 5 14.15	-37 15 40.8	4.52	28.93	21.77	5.33	8.58	1.28
8 5 6.31	-37 15 30.3	4.67	28.95	21.92	5.58	8.20	1.22
8 4 59.98	-37 15 41.3	4.66	28.97	21.91	5.55	8.24	1.23
8 4 50.03	-37 15 37.9	4.59	28.76	21.87	5.49	8.27	1.23
8 4 44	-37 15 48.8	4.51	28.68	21.80	5.38	8.42	1.25
8 4 37.67	-37 15 56.2	4.57	28.54	21.89	5.52	8.16	1.22
8 4 29.22	-37 15 52.7	4.58	28.78	21.86	5.48	8.30	1.24
8 4 21.69	-37 16 3.5	4.66	29.19	21.87	5.50	8.38	1.25
8 4 14.15	-37 16 3.6	4.78	29.57	21.94	5.61	8.33	1.24
8 4 6.91	-37 16 10.8	4.92	29.91	22.02	5.75	8.22	1.22
8 3 59.67	-37 16 7.2	5.12	30.77	22.08	5.84	8.31	1.24
8 3 51.83	-37 15 59.9	5.16	31.18	22.05	5.80	8.49	1.26
8 3 43.08	-37 15 56.2	5.12	31.24	22.01	5.72	8.62	1.28
8 3 36.45	-37 16 10.6	5.03	30.85	21.98	5.67	8.59	1.28
8 3 28.61	-37 16 21.2	4.96	30.64	21.94	5.61	8.62	1.28
8 3 21.67	-37 16 24.7	4.92	30.68	21.90	5.53	8.75	1.30
8 3 13.53	-37 16 20.8	4.92	30.71	21.89	5.53	8.78	1.31
8 6 7.25	-37 16 35.8	5.36	30.42	22.37	6.37	7.54	1.12
8 5 59.41	-37 16 43.5	5.16	29.66	22.31	6.25	7.50	1.12
8 5 51.57	-37 16 43.9	4.65	29.22	21.86	5.47	8.44	1.26
8 5 44.63	-37 16 47.9	4.51	28.91	21.76	5.31	8.60	1.28
8 5 36.79	-37 16 48.3	4.44	28.74	21.71	5.24	8.67	1.29
8 5 29.86	-37 17 6.6	4.42	28.63	21.71	5.22	8.65	1.29
8 5 22.32	-37 16 59.7	4.41	28.64	21.69	5.20	8.70	1.29
8 5 14.48	-37 17 0	4.46	28.64	21.75	5.29	8.55	1.27
8 5 6.03	-37 16 56.7	4.53	28.63	21.83	5.42	8.34	1.24
8 5 0.6	-37 17 4.1	4.63	28.73	21.92	5.57	8.14	1.21
8 4 51.55	-37 17 4.3	4.60	28.69	21.89	5.53	8.20	1.22
8 4 43.71	-37 17 8	4.55	28.76	21.83	5.42	8.38	1.25
8 4 36.17	-37 17 15.4	4.60	28.79	21.87	5.49	8.28	1.23
8 4 29.23	-37 17 11.9	4.66	28.91	21.92	5.58	8.18	1.22
8 4 21.69	-37 17 15.5	4.74	29.25	21.95	5.62	8.22	1.22
8 4 15.35	-37 17 22.8	4.90	29.89	22.00	5.71	8.26	1.23
8 4 7.51	-37 17 26.4	5.02	30.37	22.05	5.80	8.28	1.23
8 4 0.27	-37 17 33.6	5.18	30.98	22.10	5.89	8.31	1.24
8 6 15.74	-37 18 5.3	5.34	30.53	22.34	6.31	7.64	1.14
8 6 7.29	-37 18 13	5.26	29.77	22.39	6.39	7.36	1.10
8 5 59.15	-37 18 13.5	4.98	29.08	22.23	6.11	7.52	1.12
8 5 52.21	-37 18 24.7	4.55	28.78	21.83	5.42	8.39	1.25
8 5 44.06	-37 18 21.5	4.42	28.69	21.70	5.21	8.70	1.29
8 5 37.13	-37 18 25.5	4.47	28.70	21.75	5.29	8.57	1.28
8 5 29.88	-37 18 18.6	4.45	28.72	21.73	5.26	8.62	1.28
8 5 22.04	-37 18 18.9	4.44	28.75	21.70	5.22	8.70	1.29
8 5 14.5	-37 18 26.4	4.43	28.61	21.72	5.25	8.61	1.28
8 5 6.65	-37 18 26.7	4.52	28.69	21.81	5.39	8.41	1.25
8 4 59.71	-37 18 34.1	4.63	28.78	21.92	5.57	8.16	1.22
8 4 50.66	-37 18 37.9	4.67	28.91	21.93	5.59	8.17	1.22

continued on next page

Table 23 – continued from previous page

R.A.(J2000) hh mm ss	Dec.(J2000) dd mm ss	$F(60)$ (MJy)	$F(100)$ (MJy)	$T_{\rm d}$ (K)	$B(\nu,T)$ $(\times10^{-16})$ Js^{-2}	$M_{\rm d}$ $(\times10^{27})$ kg	$A_{\rm V}$ $(\times10^{-5})$ mag
8 4 43.42	-37 18 41.7	4.63	28.93	21.88	5.51	8.29	1.23
8 4 36.78	-37 18 49	4.63	28.98	21.88	5.50	8.32	1.24
8 4 29.84	-37 18 49.1	4.73	29.21	21.94	5.61	8.22	1.22
8 4 21.69	-37 18 49.1	4.79	29.48	21.97	5.65	8.24	1.23
8 4 14.75	-37 19 0	4.87	29.88	21.98	5.67	8.32	1.24
8 4 7.81	-37 18 52.8	5.08	30.65	22.06	5.81	8.33	1.24
8 6 14.88	-37 19 35.3	5.16	30.52	22.17	5.99	8.04	1.20
8 6 7.33	-37 19 43	4.84	29.62	21.98	5.68	8.24	1.23
8 5 59.79	-37 19 43.5	4.54	28.88	21.80	5.37	8.49	1.26
8 5 52.54	-37 19 43.9	4.37	28.66	21.65	5.14	8.81	1.31
8 5 44.7	-37 19 37.1	4.41	28.64	21.69	5.20	8.70	1.29
8 5 38.06	-37 19 41	4.44	28.75	21.71	5.23	8.68	1.29
8 5 30.21	-37 19 52.2	4.51	28.81	21.78	5.34	8.51	1.27
8 5 22.37	-37 19 59.7	4.50	28.89	21.76	5.30	8.60	1.28
8 5 15.12	-37 20 0	4.50	28.83	21.77	5.32	8.56	1.27
8 5 8.48	-37 19 56.6	4.57	28.87	21.83	5.43	8.41	1.25
8 4 59.73	-37 19 56.9	4.66	28.99	21.91	5.56	8.24	1.23
8 4 51.58	-37 20 7.9	4.72	29.20	21.93	5.60	8.24	1.23
8 4 44.34	-37 20 11.6	4.72	29.24	21.93	5.59	8.26	1.23
8 4 37.7	-37 20 15.4	4.71	29.27	21.91	5.56	8.31	1.24
8 4 29.55	-37 20 11.9	4.74	29.39	21.93	5.59	8.31	1.24
8 4 22.61	-37 20 26.3	4.81	29.68	21.95	5.62	8.35	1.24
8 4 15.36	-37 20 19.2	4.86	30.07	21.94	5.60	8.48	1.26
8 4 7.21	-37 20 22.8	5.07	30.53	22.07	5.83	8.27	1.23
8 6 14.32	-37 21 12.5	4.91	30.96	21.84	5.44	8.98	1.34
8 6 7.97	-37 21 5.8	4.66	29.54	21.81	5.39	8.66	1.29
8 6 0.43	-37 21 13.4	4.42	28.91	21.66	5.16	8.85	1.32
8 5 52.58	-37 21 10.3	4.42	28.79	21.68	5.18	8.79	1.31
8 5 45.33	-37 21 14.3	4.44	28.78	21.71	5.23	8.70	1.29
8 5 36.88	-37 21 18.3	4.46	28.82	21.72	5.25	8.67	1.29
8 5 29.94	-37 21 29.4	4.50	28.92	21.74	5.29	8.64	1.29
8 5 23	-37 21 33.3	4.59	29.00	21.83	5.42	8.45	1.26
8 5 14.54	-37 21 37.2	4.62	29.11	21.84	5.45	8.44	1.26
8 5 7.6	-37 21 33.8	4.64	29.13	21.86	5.47	8.40	1.25
8 5 0.65	-37 21 34	4.67	29.34	21.86	5.47	8.46	1.26
8 4 53.11	-37 21 41.4	4.73	29.35	21.92	5.57	8.32	1.24
8 4 45.26	-37 21 38	4.77	29.51	21.93	5.60	8.32	1.24
8 4 37.1	-37 21 49	4.79	29.65	21.94	5.60	8.36	1.24
8 4 29.56	-37 21 49.1	4.84	29.82	21.95	5.62	8.37	1.25
8 4 22.91	-37 21 49.1	4.84	29.99	21.93	5.59	8.48	1.26
8 4 14.76	-37 21 45.6	4.98	30.42	22.00	5.71	8.42	1.25
8 6 14.96	-37 22 38.9	4.81	30.98	21.74	5.27	9.28	1.38
8 6 7.71	-37 22 39.4	4.64	29.76	21.76	5.30	8.86	1.32
8 6 0.47	-37 22 43.4	4.52	29.36	21.70	5.21	8.90	1.33
8 5 52.31	-37 22 43.9	4.50	29.16	21.70	5.22	8.83	1.31
8 5 44.76	-37 22 33.5	4.52	29.17	21.73	5.26	8.76	1.30
8 5 38.12	-37 22 41	4.53	29.11	21.75	5.30	8.68	1.29
8 5 30.87	-37 22 52.2	4.51	29.12	21.73	5.25	8.75	1.30
8 5 23.93	-37 22 56	4.59	29.28	21.78	5.34	8.65	1.29
8 5 15.17	-37 22 52.8	4.69	29.27	21.90	5.53	8.36	1.24
8 5 7.92	-37 23 3.8	4.68	29.39	21.86	5.48	8.47	1.26
8 4 59.77	-37 23 4.1	4.67	29.52	21.83	5.42	8.60	1.28
8 4 52.82	-37 23 4.3	4.75	29.64	21.89	5.52	8.48	1.26
8 4 45.57	-37 23 8	4.83	29.99	21.91	5.56	8.51	1.27
8 4 38.62	-37 23 15.3	4.93	30.27	21.97	5.66	8.44	1.26
8 4 30.17	-37 23 22.7	4.95	30.39	21.98	5.67	8.46	1.26
8 4 21.71	-37 23 19.1	5.03	30.75	21.99	5.70	8.52	1.27
8 6 14.4	-37 24 5.3	4.81	30.96	21.74	5.28	9.27	1.38
8 6 8.66	-37 24 16.5	4.66	30.48	21.66	5.15	9.35	1.39
8 6 0.51	-37 24 20.6	4.66	29.79	21.77	5.33	8.83	1.31
8 5 53.56	-37 24 24.6	4.63	29.69	21.76	5.31	8.84	1.32
8 5 45.1	-37 24 25.1	4.63	29.76	21.74	5.28	8.90	1.32
8 5 38.76	-37 24 21.8	4.63	29.45	21.80	5.38	8.65	1.29
8 5 31.81	-37 24 25.7	4.62	29.48	21.78	5.34	8.71	1.30
8 5 24.56	-37 24 29.6	4.70	29.47	21.86	5.48	8.49	1.26
8 5 15.8	-37 24 30	4.74	29.53	21.90	5.54	8.41	1.25
8 5 8.24	-37 24 37.4	4.76	29.43	21.94	5.60	8.30	1.24
8 5 0.99	-37 24 34	4.69	29.64	21.83	5.42	8.63	1.28
8 4 52.84	-37 24 45	4.79	29.96	21.88	5.52	8.58	1.28
8 4 45.28	-37 24 41.6	4.87	30.34	21.90	5.55	8.64	1.29
8 4 36.82	-37 24 45.4	5.03	30.71	22.01	5.72	8.48	1.26
8 4 30.48	-37 24 38.3	5.13	30.99	22.06	5.80	8.43	1.26
8 5 53.29	-37 25 43.8	4.80	30.88	21.74	5.28	9.24	1.37
8 5 46.64	-37 25 37	4.83	30.65	21.81	5.38	8.99	1.34
8 5 37.58	-37 25 55.4	4.79	30.60	21.78	5.34	9.06	1.35
8 5 31.53	-37 25 52.1	4.76	30.13	21.82	5.41	8.80	1.31
8 5 23.37	-37 25 56.1	4.69	29.71	21.82	5.41	8.68	1.29

continued on next page

Table 23 – continued from previous page

R.A.(J2000) hh mm ss	Dec.(J2000) dd mm ss	$F(60)$ (MJy)	$F(100)$ (MJy)	T_d (K)	$B(\nu,T)$ $(\times10^{-16})$ Js^{-2}	M_d $(\times10^{27})$ kg	A_V $(\times10^{-5})$ mag
8 5 16.42	-37 26 3.5	4.74	29.55	21.90	5.54	8.43	1.25
8 5 9.47	-37 26 7.4	4.75	29.61	21.90	5.54	8.44	1.26
8 4 59.8	-37 26 7.7	4.77	29.75	21.89	5.53	8.49	1.26
8 4 53.76	-37 26 15	4.82	30.12	21.89	5.52	8.62	1.28
8 4 45.29	-37 26 18.8	4.99	30.68	21.96	5.65	8.58	1.28
8 4 38.34	-37 26 8.1	5.09	31.01	22.01	5.73	8.55	1.27
8 5 31.56	-37 27 32.9	4.80	30.68	21.77	5.33	9.10	1.35
8 5 24	-37 27 18.8	4.70	29.90	21.80	5.37	8.79	1.31
8 5 15.24	-37 27 26.4	4.65	29.48	21.82	5.40	8.61	1.28
8 5 8.89	-37 27 37.4	4.72	29.64	21.86	5.47	8.55	1.27
8 5 1.94	-37 27 44.8	4.79	30.00	21.87	5.49	8.63	1.28
8 4 54.68	-37 27 34.2	4.90	30.42	21.92	5.57	8.62	1.28
8 4 46.52	-37 27 41.6	5.01	30.84	21.96	5.64	8.64	1.29
8 5 31.29	-37 28 52.1	4.80	30.93	21.73	5.27	9.27	1.38
8 5 24.33	-37 28 52.4	4.72	29.97	21.81	5.39	8.79	1.31
8 5 16.77	-37 28 49.1	4.67	29.47	21.83	5.43	8.57	1.28
8 5 8.91	-37 29 0.2	4.75	29.63	21.89	5.52	8.47	1.26
8 5 1.65	-37 28 56.8	4.85	30.14	21.91	5.56	8.56	1.27
8 4 54.39	-37 28 57	4.99	30.56	21.98	5.68	8.49	1.26
8 5 32.52	-37 30 11.3	4.85	31.01	21.77	5.32	9.20	1.37
8 5 24.96	-37 30 11.6	4.77	30.34	21.80	5.37	8.92	1.33
8 5 16.49	-37 30 22.7	4.74	29.62	21.88	5.51	8.49	1.26
8 5 9.53	-37 30 30.2	4.75	29.67	21.89	5.52	8.49	1.26
8 5 1.67	-37 30 23.2	4.94	30.22	21.99	5.69	8.39	1.25
8 4 54.1	-37 30 23.4	5.02	30.77	21.98	5.67	8.57	1.28
8 5 24.99	-37 31 59.6	4.82	30.65	21.80	5.38	9.01	1.34
8 5 18.03	-37 31 49.1	4.84	30.16	21.90	5.53	8.61	1.28
8 5 8.95	-37 32 11	4.91	30.41	21.93	5.59	8.59	1.28
8 5 1.99	-37 31 56.8	4.95	30.57	21.95	5.62	8.59	1.28

Table 24: The Database of far infrared cavity CASKK1 nearby to the AGB star AGB0141+7104 located with in G125+09. The first two columns represent position of the pixels with in the cavity. The next two columns give values of relative flux density at 60 μm and 100 μm that have obtained after processing the FITS image using ALADIN 2.5 software. The calculated values of dust color temperature (in K), Planck function and dust mass for 100 μm and visual extinction (in mag) of the corresponding pixels,respectively.

R.A.(J2000) hh mm ss	Dec.(J2000) dd mm ss	$F(60)$ (MJy)	$F(100)$ (MJy)	T_d (K)	$B(\nu,T)$ $(\times10^{-16})$ Js^{-2}	M_d $(\times10^{27})$ kg	A_V $(\times10^{-5})$ mag
1 46 48.81	71 41 52.3	1.88	16.66	20.28	3.21	5.05	1.22
1 46 26.65	71 41 44.9	1.88	16.69	20.27	3.21	5.08	1.22
1 46 6.02	71 41 48.3	1.90	16.55	20.35	3.29	4.90	1.18
1 45 51.49	71 41 51.6	1.89	16.75	20.27	3.21	5.10	1.23
1 47 28.51	71 40 7.7	1.81	16.51	20.14	3.06	5.25	1.27
1 47 7.14	71 40 18.7	1.83	16.51	20.19	3.12	5.16	1.24
1 46 48.82	71 40 18.7	1.85	16.42	20.27	3.21	4.99	1.20
1 46 25.93	71 40 18.5	1.91	16.26	20.43	3.40	4.67	1.13
1 46 10.66	71 40 18.3	1.87	16.37	20.32	3.27	4.88	1.18
1 45 50.82	71 40 18	1.84	16.58	20.19	3.12	5.18	1.25
1 45 33.27	71 40 17.5	1.87	16.75	20.23	3.16	5.16	1.25
1 48 4.29	71 38 40.8	1.86	16.50	20.26	3.20	5.03	1.21
1 47 42.95	71 38 52	1.84	16.42	20.25	3.18	5.03	1.21
1 47 25.42	71 38 48.6	1.80	16.18	20.21	3.14	5.03	1.21
1 47 6.37	71 38 48.7	1.84	16.26	20.27	3.21	4.94	1.19
1 46 46.55	71 38 48.7	1.84	16.23	20.29	3.22	4.91	1.18
1 46 24.45	71 38 48.5	1.88	16.21	20.39	3.34	4.73	1.14
1 46 12.25	71 38 41.2	1.83	16.24	20.26	3.19	4.96	1.20
1 45 51.67	71 38 44.4	1.79	16.35	20.14	3.07	5.20	1.25
1 45 29.57	71 38 47.4	1.83	16.51	20.20	3.13	5.14	1.24
1 48 36.93	71 37 13.5	1.91	16.62	20.36	3.31	4.90	1.18
1 48 21.7	71 37 6.7	1.90	16.40	20.39	3.35	4.78	1.15
1 48 4.97	71 37 17.9	1.87	16.35	20.33	3.27	4.87	1.18
1 47 45.93	71 37 11.1	1.86	16.06	20.39	3.34	4.69	1.13
1 47 25.38	71 37 11.4	1.83	16.03	20.33	3.27	4.78	1.15
1 47 4.83	71 37 18.7	1.79	16.01	20.23	3.16	4.94	1.19
1 46 46.56	71 37 22.3	1.78	16.09	20.19	3.12	5.02	1.21
1 46 29.05	71 37 22.2	1.80	16.03	20.25	3.19	4.91	1.18
1 46 9.27	71 37 14.7	1.75	16.00	20.14	3.07	5.08	1.23
1 45 48.71	71 37 21.5	1.75	16.08	20.11	3.03	5.18	1.25
1 45 31.96	71 37 24.7	1.79	16.22	20.17	3.10	5.11	1.23
1 45 11.4	71 37 24.1	1.85	16.53	20.25	3.18	5.07	1.22
1 49 16.37	71 35 3.5	1.94	16.67	20.41	3.37	4.82	1.16
1 48 59.62	71 35 49.9	1.91	16.49	20.38	3.33	4.82	1.16
1 48 42.89	71 35 50.5	1.89	16.40	20.36	3.31	4.83	1.16

continued on next page

Table 24 – continued from previous page

R.A.(J2000) hh mm ss	Dec.(J2000) dd mm ss	$F(60)$ (MJy)	$F(100)$ (MJy)	$T_{\rm d}$ (K)	$B(\nu,T)$ $(\times10^{-16})$ Js^{-2}	$M_{\rm d}$ $(\times10^{27})$ kg	$A_{\rm V}$ $(\times10^{-5})$ mag
1 48 23.88	71 35 43.9	1.87	16.26	20.35	3.30	4.81	1.16
1 48 4.87	71 35 40.8	1.87	16.20	20.37	3.32	4.76	1.15
1 47 45.87	71 35 44.7	1.81	16.10	20.26	3.20	4.90	1.18
1 47 26.86	71 35 37.8	1.77	16.02	20.19	3.12	5.01	1.21
1 47 6.34	71 35 45.1	1.79	16.03	20.22	3.15	4.96	1.20
1 46 46.58	71 35 41.5	1.76	15.95	20.19	3.11	4.99	1.20
1 46 29.09	71 35 45	1.73	15.87	20.13	3.06	5.06	1.22
1 46 9.33	71 35 44.7	1.75	15.81	20.19	3.12	4.95	1.19
1 45 52.6	71 35 55.2	1.75	15.90	20.17	3.10	5.00	1.21
1 45 35.88	71 35 47.6	1.80	16.06	20.25	3.19	4.91	1.18
1 45 13.06	71 35 57.7	1.80	16.44	20.14	3.06	5.24	1.26
1 44 54.07	71 35 46.2	1.79	16.55	20.10	3.02	5.34	1.29
1 44 34.33	71 35 34.6	1.83	16.64	20.15	3.08	5.27	1.27
1 49 19.19	71 34 15.4	1.91	16.64	20.34	3.29	4.93	1.19
1 49 3.23	71 34 5.3	1.89	16.51	20.33	3.28	4.92	1.19
1 48 42.74	71 34 9.7	1.85	16.42	20.27	3.21	4.99	1.20
1 48 22.25	71 34 13.9	1.85	16.34	20.28	3.22	4.95	1.19
1 48 4.02	71 34 10.8	1.80	16.31	20.19	3.11	5.11	1.23
1 47 42.76	71 34 4	1.75	16.23	20.09	3.00	5.27	1.27
1 47 25.31	71 34 11.4	1.79	16.11	20.21	3.14	5.01	1.21
1 47 7.85	71 34 4.3	1.80	16.15	20.21	3.14	5.01	1.21
1 46 44.31	71 34 22.3	1.78	16.04	20.20	3.13	4.99	1.20
1 46 29.89	71 34 7.8	1.79	15.91	20.26	3.19	4.86	1.17
1 46 8.63	71 34 18.3	1.76	15.88	20.19	3.12	4.97	1.20
1 45 49.65	71 34 18	1.80	15.94	20.28	3.22	4.83	1.16
1 45 30.66	71 34 24.7	1.78	16.30	20.14	3.06	5.20	1.25
1 45 13.97	71 34 13.4	1.79	16.14	20.19	3.11	5.05	1.22
1 44 54.22	71 34 19.8	1.79	16.29	20.16	3.09	5.14	1.24
1 44 35.24	71 34 19	1.88	16.53	20.31	3.25	4.96	1.20
1 48 56.26	71 32 46.4	1.87	16.51	20.29	3.23	4.99	1.20
1 48 39.57	71 32 43.4	1.86	16.27	20.32	3.26	4.86	1.17
1 48 22.89	71 32 43.9	1.77	16.27	20.12	3.04	5.22	1.26
1 48 3.18	71 32 48	1.77	16.24	20.12	3.04	5.21	1.26
1 47 44.23	71 32 48.3	1.76	16.14	20.12	3.05	5.17	1.25
1 47 26.79	71 32 48.6	1.82	16.23	20.24	3.17	4.99	1.20
1 47 7.83	71 32 41.5	1.92	16.33	20.45	3.41	4.67	1.13
1 46 48.12	71 32 41.5	1.88	16.37	20.35	3.29	4.85	1.17
1 46 25.38	71 32 44.9	1.78	16.19	20.15	3.08	5.13	1.24
1 46 10.97	71 32 41.1	1.78	16.16	20.17	3.10	5.09	1.23
1 45 55.05	71 32 48.1	1.80	16.13	20.22	3.15	4.99	1.20
1 45 32.3	71 32 43.9	1.80	15.99	20.25	3.18	4.90	1.18
1 45 13.35	71 32 43.3	1.81	16.06	20.26	3.19	4.90	1.18
1 44 55.14	71 32 49.9	1.83	16.14	20.29	3.23	4.87	1.17
1 44 32.4	71 32 45.3	1.92	16.44	20.41	3.36	4.76	1.15
1 49 16.55	71 31 15.5	1.95	16.69	20.42	3.38	4.81	1.16
1 48 59.13	71 31 16.3	1.88	16.33	20.37	3.32	4.80	1.16
1 48 42.47	71 31 16.9	1.76	16.18	20.11	3.04	5.20	1.25
1 48 24.3	71 31 17.5	1.76	15.91	20.19	3.11	4.98	1.20
1 48 3.85	71 31 14.4	1.74	15.95	20.12	3.04	5.11	1.23
1 47 44.92	71 31 11.1	1.90	15.92	20.50	3.48	4.46	1.08
1 47 25.99	71 31 18.6	1.96	16.18	20.59	3.58	4.41	1.06
1 47 10.09	71 31 11.5	1.94	16.53	20.45	3.41	4.72	1.14
1 46 51.16	71 31 7.9	1.86	16.65	20.24	3.17	5.12	1.24
1 46 31.47	71 31 18.6	1.82	16.55	20.16	3.09	5.22	1.26
1 46 10.27	71 31 18.3	1.80	16.34	20.18	3.10	5.13	1.24
1 45 55.88	71 31 21.7	1.81	16.09	20.26	3.20	4.90	1.18
1 45 33.91	71 31 28.4	1.84	15.97	20.37	3.32	4.69	1.13
1 45 14.99	71 31 20.6	1.87	16.00	20.43	3.39	4.60	1.11
1 44 53.81	71 31 9	1.87	16.18	20.38	3.33	4.73	1.14
1 44 35.63	71 31 11.8	1.86	16.58	20.26	3.19	5.07	1.22
1 49 39.02	71 29 30	1.83	16.57	20.19	3.11	5.19	1.25
1 49 19.37	71 29 38.2	1.84	16.17	20.30	3.24	4.86	1.17
1 49 1.98	71 29 38.9	1.80	15.91	20.28	3.21	4.83	1.16
1 48 40.82	71 29 43.3	1.76	15.83	20.20	3.13	4.93	1.19
1 48 23.43	71 29 43.9	1.68	15.72	20.03	2.95	5.19	1.25
1 48 4.51	71 29 37.2	1.81	15.69	20.36	3.31	4.63	1.12
1 47 46.37	71 29 33.9	1.86	15.82	20.45	3.41	4.52	1.09
1 47 27.47	71 29 41.3	1.90	16.08	20.48	3.45	4.55	1.10
1 47 9.32	71 29 48.7	1.84	16.45	20.23	3.17	5.06	1.22
1 46 48.15	71 29 45.1	1.84	16.45	20.24	3.18	5.05	1.22
1 46 31.51	71 29 48.6	1.81	16.53	20.14	3.06	5.26	1.27
1 46 10.33	71 29 48.3	1.74	15.92	20.13	3.05	5.09	1.23
1 45 50.66	71 29 55.2	1.75	15.91	20.16	3.08	5.03	1.21
1 45 34.03	71 29 47.6	1.76	15.93	20.18	3.10	5.01	1.21
1 45 12.1	71 29 46.9	1.91	16.11	20.49	3.46	4.54	1.10
1 44 56.23	71 29 42.7	1.92	16.41	20.42	3.38	4.73	1.14
1 44 38.08	71 29 45.5	1.89	16.71	20.28	3.22	5.06	1.22

continued on next page

Table 24 – continued from previous page

R.A.(J2000) hh mm ss	Dec.(J2000) dd mm ss	$F(60)$ (MJy)	$F(100)$ (MJy)	$T_{\rm d}$ (K)	$B(\nu,T)$ $(\times10^{-16})$ Js^{-2}	$M_{\rm d}$ $(\times10^{27})$ kg	$A_{\rm V}$ $(\times10^{-5})$ mag
1 49 37.32	71 28 10.9	1.82	16.19	20.25	3.18	4.97	1.20
1 49 16.93	71 28 11.9	1.78	15.75	20.27	3.21	4.78	1.15
1 48 58.05	71 28 12.7	1.76	15.72	20.23	3.16	4.85	1.17
1 48 41.44	71 28 16.9	1.65	15.67	19.97	2.89	5.29	1.28
1 48 21.8	71 28 10.3	1.67	15.56	20.07	2.98	5.08	1.23
1 48 2.17	71 28 10.8	1.62	15.62	19.92	2.83	5.37	1.30
1 47 44.04	71 28 11.1	1.74	15.76	20.19	3.11	4.94	1.19
1 47 22.9	71 28 18.6	1.71	15.84	20.09	3.01	5.13	1.24
1 47 7.79	71 28 15.1	1.73	15.88	20.12	3.04	5.09	1.23
1 46 48.16	71 28 15.1	1.72	15.97	20.06	2.98	5.23	1.26
1 46 29.27	71 28 22.2	1.65	15.74	19.96	2.87	5.35	1.29
1 46 11.15	71 28 18.4	1.59	15.64	19.83	2.74	5.57	1.34
1 45 50.01	71 28 14.4	1.60	15.59	19.87	2.78	5.47	1.32
1 45 28.85	71 28 21	1.69	15.77	20.06	2.98	5.16	1.24
1 45 12.98	71 28 24.1	1.81	15.95	20.30	3.24	4.79	1.16
1 44 53.36	71 28 16.2	1.83	16.23	20.27	3.21	4.94	1.19
1 44 35.22	71 28 22.6	1.83	16.60	20.17	3.10	5.22	1.26
1 49 55.2	71 26 36.3	1.85	16.33	20.28	3.22	4.95	1.19
1 49 35.6	71 26 41	1.85	16.00	20.37	3.32	4.70	1.13
1 49 15.99	71 26 38.3	1.75	15.69	20.22	3.15	4.86	1.17
1 48 54.9	71 26 53.6	1.60	15.68	19.85	2.76	5.55	1.34
1 48 39.05	71 26 50.6	1.66	15.60	20.01	2.93	5.20	1.25
1 48 20.95	71 26 51.1	1.63	15.56	19.96	2.88	5.28	1.27
1 48 2.08	71 26 40.8	1.62	15.41	19.96	2.87	5.23	1.26
1 47 42.48	71 26 48.4	1.62	15.41	19.97	2.89	5.20	1.25
1 47 26.64	71 26 48.6	1.63	15.44	19.99	2.90	5.19	1.25
1 47 9.29	71 26 48.7	1.63	15.41	20.00	2.92	5.15	1.24
1 46 45.15	71 26 41.5	1.62	15.37	19.98	2.89	5.18	1.25
1 46 30.07	71 26 48.6	1.59	15.28	19.94	2.85	5.23	1.26
1 46 6.68	71 26 48.3	1.58	15.28	19.89	2.80	5.32	1.28
1 45 55.37	71 26 51.7	1.64	15.44	20.01	2.92	5.15	1.24
1 45 33.48	71 26 58.3	1.71	15.44	20.18	3.11	4.84	1.17
1 45 16.89	71 26 54.2	1.67	15.67	20.04	2.96	5.16	1.25
1 44 56.53	71 26 53.5	1.66	15.80	19.97	2.88	5.35	1.29
1 44 39.18	71 26 52.8	1.86	16.33	20.32	3.26	4.88	1.18
1 44 17.31	71 26 48.1	1.92	16.64	20.37	3.32	4.88	1.18
1 50 17.54	71 25 57.7	1.97	16.50	20.50	3.48	4.63	1.12
1 49 56.5	71 25 17	1.82	16.22	20.25	3.18	4.97	1.20
1 49 36.16	71 25 14.5	1.80	15.92	20.28	3.22	4.82	1.16
1 49 20.36	71 25 22.5	1.67	15.87	19.99	2.90	5.33	1.29
1 49 0.01	71 25 19.8	1.70	15.59	20.12	3.04	5.01	1.21
1 48 41.92	71 25 13.3	1.76	15.56	20.28	3.22	4.72	1.14
1 48 25.36	71 25 17.4	1.67	15.37	20.10	3.02	4.97	1.20
1 48 2	71 25 14.4	1.59	15.18	19.95	2.86	5.17	1.25
1 47 47.69	71 25 18.3	1.59	15.20	19.95	2.86	5.17	1.25
1 47 26.6	71 25 18.6	1.58	15.20	19.92	2.83	5.24	1.26
1 47 6.26	71 25 11.5	1.56	15.17	19.87	2.78	5.32	1.28
1 46 48.18	71 25 18.7	1.59	15.20	19.96	2.88	5.15	1.24
1 46 30.85	71 25 18.6	1.61	15.14	20.03	2.95	5.01	1.21
1 46 10.51	71 25 21.9	1.65	15.25	20.09	3.01	4.93	1.19
1 45 50.93	71 25 18	1.68	15.28	20.15	3.08	4.84	1.17
1 45 31.35	71 25 13.9	1.62	15.38	19.98	2.89	5.19	1.25
1 45 15.53	71 25 13.4	1.59	15.52	19.86	2.77	5.46	1.32
1 44 58.95	71 25 20	1.67	15.76	20.01	2.93	5.25	1.27
1 44 35.62	71 25 8.2	1.78	16.09	20.18	3.11	5.05	1.22
1 44 16.78	71 25 10.9	1.86	16.61	20.25	3.18	5.09	1.23
1 50 34.62	71 23 40.9	1.96	16.51	20.50	3.47	4.64	1.12
1 50 15.07	71 23 42.2	1.88	16.25	20.37	3.32	4.77	1.15
1 49 53.25	71 23 40	1.76	16.03	20.15	3.07	5.08	1.23
1 49 36.71	71 23 48.1	1.69	16.05	19.98	2.89	5.42	1.31
1 49 17.15	71 23 45.5	1.72	15.66	20.15	3.07	4.97	1.20
1 49 3.6	71 23 42.5	1.78	15.71	20.28	3.22	4.76	1.15
1 48 40.29	71 23 50.5	1.75	15.55	20.25	3.19	4.75	1.15
1 48 20.72	71 23 44	1.73	15.29	20.28	3.22	4.63	1.12
1 48 4.16	71 23 33.6	1.63	15.29	20.03	2.95	5.06	1.22
1 47 43.86	71 23 44.7	1.54	15.11	19.84	2.75	5.36	1.29
1 47 24.3	71 23 37.8	1.53	15.13	19.82	2.72	5.41	1.31
1 47 6.25	71 23 41.5	1.56	15.11	19.89	2.80	5.26	1.27
1 46 48.94	71 23 52.3	1.60	15.14	20.01	2.92	5.05	1.22
1 46 31.64	71 23 48.6	1.69	15.23	20.19	3.12	4.76	1.15
1 46 8.32	71 23 44.7	1.67	15.27	20.13	3.05	4.88	1.18
1 45 52.52	71 23 44.4	1.62	15.37	19.99	2.90	5.16	1.24
1 45 32.2	71 23 51.1	1.59	15.58	19.85	2.76	5.50	1.33
1 45 12.65	71 23 43.3	1.63	15.65	19.93	2.84	5.38	1.30
1 44 53.09	71 23 46.2	1.66	15.91	19.93	2.84	5.46	1.32
1 44 36.57	71 23 31	1.82	16.19	20.25	3.19	4.95	1.19
1 44 15.48	71 23 44.4	1.81	16.39	20.17	3.10	5.16	1.24

continued on next page

Table 24 – continued from previous page

R.A.(J2000) hh mm ss	Dec.(J2000) dd mm ss	$F(60)$ (MJy)	$F(100)$ (MJy)	$T_{\rm d}$ (K)	$B(\nu,T)$ $(\times10^{-16})$ Js^{-2}	$M_{\rm d}$ $(\times10^{27})$ kg	$A_{\rm V}$ $(\times10^{-5})$ mag
1 50 53.1	71 22 2.3	2.02	16.70	20.58	3.56	4.57	1.10
1 50 32.82	71 22 3.8	1.96	16.39	20.53	3.51	4.56	1.10
1 50 14.82	71 22 15.9	1.80	16.19	20.21	3.14	5.02	1.21
1 49 54.51	71 22 6.3	1.71	15.93	20.05	2.96	5.24	1.26
1 49 37.99	71 22 10.8	1.75	15.76	20.19	3.12	4.93	1.19
1 49 19.21	71 22 8.2	1.77	15.69	20.28	3.22	4.76	1.15
1 49 0.44	71 22 19.8	1.78	15.39	20.39	3.34	4.49	1.08
1 48 39.39	71 22 6.2	1.72	15.45	20.22	3.15	4.78	1.15
1 48 23.61	71 22 6.7	1.71	15.34	20.22	3.15	4.75	1.14
1 48 3.33	71 22 14.4	1.66	15.26	20.12	3.04	4.90	1.18
1 47 46.06	71 22 14.7	1.60	15.36	19.93	2.84	5.28	1.27
1 47 25.02	71 22 18.6	1.54	15.19	19.83	2.73	5.42	1.31
1 47 6.99	71 22 7.9	1.62	15.17	20.04	2.95	5.01	1.21
1 46 48.96	71 22 15.1	1.66	15.31	20.10	3.02	4.95	1.19
1 46 30.92	71 22 25.8	1.65	15.28	20.09	3.01	4.94	1.19
1 46 12.14	71 22 11.2	1.63	15.67	19.93	2.84	5.38	1.30
1 45 51.11	71 22 14.4	1.68	15.77	20.02	2.94	5.24	1.26
1 45 33.07	71 22 17.5	1.70	15.99	20.02	2.93	5.31	1.28
1 45 15.79	71 22 13.4	1.73	16.13	20.06	2.98	5.29	1.27
1 44 55.52	71 22 9.1	1.81	16.18	20.24	3.18	4.96	1.20
1 44 35.99	71 22 4.6	1.79	16.27	20.16	3.09	5.14	1.24
1 44 15.68	71 22 18	1.80	16.40	20.16	3.09	5.17	1.25
1 43 59.94	71 22 2.7	1.80	16.58	20.11	3.03	5.33	1.29
1 50 51.33	71 20 43.2	2.03	16.71	20.59	3.59	4.54	1.10
1 50 33.3	71 20 37.4	1.90	16.44	20.37	3.32	4.83	1.17
1 50 14.54	71 20 35.1	1.82	15.93	20.33	3.27	4.75	1.15
1 49 55.8	71 20 43.4	1.79	15.54	20.37	3.32	4.57	1.10
1 49 37.04	71 20 40.9	1.72	15.41	20.24	3.17	4.74	1.14
1 49 16.03	71 20 41.9	1.72	15.30	20.25	3.18	4.68	1.13
1 48 58.02	71 20 39.1	1.72	15.30	20.25	3.19	4.68	1.13
1 48 40.76	71 20 43.3	1.73	15.37	20.26	3.19	4.70	1.13
1 48 20.49	71 20 29.6	1.67	15.42	20.10	3.02	4.97	1.20
1 48 0.99	71 20 37.2	1.66	15.38	20.08	3.00	5.01	1.21
1 47 43.73	71 20 33.9	1.61	15.44	19.94	2.85	5.29	1.28
1 47 22.73	71 20 34.2	1.61	15.32	19.97	2.88	5.19	1.25
1 47 5.47	71 20 34.3	1.70	15.33	20.19	3.12	4.80	1.16
1 46 48.22	71 20 45.1	1.66	15.48	20.05	2.97	5.09	1.23
1 46 27.2	71 20 48.6	1.69	15.65	20.08	2.99	5.10	1.23
1 46 10.7	71 20 48.3	1.70	16.07	19.99	2.90	5.40	1.30
1 45 50.45	71 20 37.2	1.76	16.39	20.07	2.98	5.36	1.29
1 45 33.92	71 20 51.2	1.92	16.49	20.40	3.36	4.79	1.16
1 45 14.42	71 20 47	2.03	16.62	20.62	3.62	4.48	1.08
1 44 54.91	71 20 46.2	1.95	16.65	20.44	3.40	4.77	1.15
1 44 38.42	71 20 38.3	1.84	16.44	20.23	3.16	5.07	1.22
1 44 15.9	71 20 44.4	1.80	16.36	20.15	3.08	5.18	1.25
1 43 59.4	71 20 39.9	1.72	16.45	19.96	2.87	5.58	1.35
1 43 42.15	71 20 35.2	1.77	16.75	19.99	2.90	5.63	1.36
1 50 49.56	71 19 24.2	2.17	16.65	20.91	3.98	4.08	0.98
1 50 32.28	71 19 11	1.95	16.23	20.55	3.53	4.48	1.08
1 50 12.03	71 19 5.2	1.88	15.61	20.54	3.52	4.32	1.04
1 49 56.33	71 19 17	1.74	15.26	20.32	3.26	4.56	1.10
1 49 35.34	71 19 14.6	1.71	15.04	20.29	3.23	4.54	1.09
1 49 17.35	71 19 15.5	1.68	15.13	20.20	3.12	4.72	1.14
1 48 59.37	71 19 16.2	1.68	15.28	20.15	3.08	4.84	1.17
1 48 41.39	71 19 20.5	1.68	15.43	20.11	3.03	4.96	1.20
1 48 20.4	71 19 17.6	1.67	15.68	20.02	2.93	5.22	1.26
1 48 0.17	71 19 21.6	1.65	15.65	19.99	2.90	5.26	1.27
1 47 42.18	71 19 14.8	1.68	15.57	20.08	3.00	5.06	1.22
1 47 26.45	71 19 15	1.71	15.57	20.16	3.09	4.92	1.19
1 47 6.96	71 19 11.5	1.70	15.56	20.12	3.04	4.98	1.20
1 46 48.23	71 19 11.5	1.68	15.61	20.06	2.98	5.10	1.23
1 46 29.49	71 19 22.2	1.69	15.90	20.02	2.93	5.29	1.28
1 46 11.5	71 19 22	1.84	16.23	20.29	3.23	4.90	1.18
1 45 51.28	71 19 14.4	1.90	16.77	20.28	3.22	5.07	1.22
1 45 31.79	71 19 13.9	2.09	16.98	20.64	3.65	4.54	1.09
1 45 13.8	71 19 16.9	2.09	17.04	20.63	3.64	4.57	1.10
1 44 55.06	71 19 19.8	2.12	16.95	20.71	3.73	4.43	1.07
1 44 35.56	71 19 29.8	1.84	16.62	20.19	3.12	5.20	1.25
1 44 18.35	71 19 14.5	1.78	16.45	20.10	3.02	5.32	1.28
1 43 58.86	71 19 17	1.75	16.40	20.04	2.95	5.42	1.31
1 43 40.15	71 19 8.7	1.70	16.63	19.86	2.77	5.85	1.41
1 43 26.63	71 19 18.6	1.76	16.69	20.00	2.91	5.59	1.35
1 51 7.93	71 17 41.9	2.25	16.75	21.05	4.17	3.91	0.94
1 50 51.48	71 17 46.8	2.19	16.38	21.02	4.13	3.87	0.93
1 50 32.77	71 17 44.6	2.10	15.66	21.04	4.16	3.67	0.89
1 50 11.78	71 17 35.2	1.82	15.37	20.48	3.45	4.34	1.05
1 49 53.07	71 17 32.8	1.79	14.98	20.52	3.49	4.18	1.01

continued on next page

Table 24 – continued from previous page

R.A.(J2000) hh mm ss	Dec.(J2000) dd mm ss	$F(60)$ (MJy)	$F(100)$ (MJy)	$T_{\rm d}$ (K)	$B(\nu,T)$ $(\times10^{-16})$ Js^{-2}	$M_{\rm d}$ $(\times10^{27})$ kg	$A_{\rm V}$ $(\times10^{-5})$ mag
1 49 36.65	71 17 51.7	1.67	14.97	20.23	3.17	4.61	1.11
1 49 13.45	71 17 52.8	1.61	14.99	20.05	2.97	4.92	1.19
1 48 58.48	71 17 53.5	1.65	15.32	20.06	2.98	5.01	1.21
1 48 40.51	71 17 54.1	1.74	15.56	20.22	3.15	4.81	1.16
1 48 16.55	71 17 47.7	1.67	15.75	20.01	2.92	5.25	1.27
1 47 59.35	71 17 55.3	1.72	15.69	20.15	3.07	4.98	1.20
1 47 44.37	71 17 51.9	1.69	15.63	20.09	3.01	5.07	1.22
1 47 24.16	71 17 45	1.63	15.55	19.97	2.89	5.25	1.27
1 47 4.7	71 17 48.7	1.64	15.59	19.98	2.89	5.26	1.27
1 46 45.99	71 17 48.7	1.60	15.66	19.85	2.76	5.54	1.34
1 46 28.03	71 17 52.2	1.72	15.96	20.09	3.00	5.18	1.25
1 46 12.31	71 17 52	1.83	16.37	20.23	3.16	5.04	1.22
1 45 51.35	71 17 51.6	1.93	16.78	20.36	3.31	4.95	1.19
1 45 31.89	71 17 54.7	2.02	17.01	20.49	3.46	4.79	1.16
1 45 16.93	71 17 50.6	2.04	17.14	20.50	3.48	4.80	1.16
1 44 55.97	71 17 49.9	2.03	17.04	20.51	3.48	4.77	1.15
1 44 35.77	71 17 45.4	1.83	16.60	20.18	3.11	5.21	1.26
1 44 17.05	71 17 48.1	1.72	16.36	19.98	2.89	5.51	1.33
1 44 0.58	71 17 50.7	1.69	16.23	19.93	2.84	5.58	1.35
1 43 41.14	71 17 42.3	1.72	16.14	20.03	2.94	5.35	1.29
1 43 21.66	71 17 48.2	1.75	16.51	20.01	2.93	5.50	1.33
1 51 27.77	71 16 6.6	2.06	16.58	20.70	3.71	4.35	1.05
1 51 8.31	71 16 57.4	2.13	16.02	21.01	4.12	3.79	0.91
1 50 48.15	71 16 2.7	2.01	15.82	20.80	3.85	4.01	0.97
1 50 33.22	71 16 11	2.04	15.59	20.93	4.01	3.79	0.91
1 50 10.78	71 16 5.3	1.86	15.45	20.55	3.54	4.26	1.03
1 49 56.6	71 16 9.8	1.81	15.25	20.49	3.46	4.29	1.04
1 49 33.42	71 16 7.5	1.71	15.20	20.25	3.19	4.65	1.12
1 49 15.5	71 16 15.5	1.68	15.38	20.14	3.07	4.89	1.18
1 48 56.05	71 16 5.6	1.67	15.58	20.05	2.97	5.11	1.23
1 48 38.86	71 16 6.2	1.64	15.64	19.96	2.87	5.32	1.28
1 48 19.44	71 16 14	1.68	15.71	20.04	2.96	5.18	1.25
1 48 0.76	71 16 25.2	1.71	15.67	20.12	3.04	5.03	1.21
1 47 42.06	71 16 11.2	1.59	15.55	19.87	2.78	5.45	1.32
1 47 24.13	71 16 11.4	1.57	15.58	19.79	2.70	5.62	1.36
1 47 5.44	71 16 0.7	1.52	15.53	19.67	2.58	5.86	1.41
1 46 46.01	71 16 15.1	1.61	15.80	19.84	2.75	5.60	1.35
1 46 27.32	71 16 11.4	1.67	16.00	19.94	2.85	5.48	1.32
1 46 10.13	71 16 18.3	1.72	16.12	20.04	2.96	5.31	1.28
1 45 47.7	71 16 25.1	1.83	16.40	20.22	3.15	5.07	1.22
1 45 31.27	71 16 13.9	1.81	16.87	20.06	2.98	5.53	1.33
1 45 14.07	71 16 16.9	1.84	16.98	20.10	3.02	5.47	1.32
1 44 53.9	71 16 12.6	1.84	16.82	20.14	3.06	5.36	1.29
1 44 35.94	71 16 19	1.77	16.56	20.03	2.95	5.47	1.32
1 44 18.01	71 16 18.1	1.65	16.20	19.85	2.76	5.73	1.38
1 43 58.59	71 16 9.8	1.70	16.07	20.00	2.91	5.38	1.30
1 43 41.4	71 16 8.7	1.75	16.09	20.12	3.04	5.16	1.24
1 43 19.71	71 16 14.5	1.77	16.37	20.10	3.02	5.28	1.27
1 43 0.3	71 16 5.8	1.79	16.63	20.06	2.98	5.45	1.31
1 51 29.61	71 14 22	2.03	16.39	20.67	3.68	4.35	1.05
1 51 8.01	71 14 34.7	1.88	15.91	20.48	3.45	4.50	1.08
1 50 50.11	71 14 39.7	2.02	15.72	20.84	3.90	3.94	0.95
1 50 30.72	71 14 44.7	1.98	15.85	20.71	3.73	4.14	1.00
1 50 13.55	71 14 45.9	1.97	15.73	20.73	3.75	4.09	0.99
1 49 53.4	71 14 47.1	1.87	16.25	20.36	3.31	4.78	1.15
1 49 34.72	71 14 41	1.89	16.17	20.43	3.39	4.65	1.12
1 49 16.07	71 14 49.1	1.81	16.26	20.22	3.15	5.03	1.21
1 48 56.65	71 14 39.1	1.73	16.10	20.07	2.99	5.25	1.27
1 48 40.23	71 14 43.3	1.68	15.87	19.99	2.91	5.32	1.28
1 48 18.58	71 14 36.8	1.60	15.67	19.85	2.75	5.55	1.34
1 48 1.41	71 14 37.2	1.62	15.68	19.89	2.80	5.46	1.32
1 47 42.74	71 14 26.8	1.62	15.60	19.91	2.82	5.39	1.30
1 47 24.09	71 14 45	1.59	15.46	19.89	2.80	5.38	1.30
1 47 4.69	71 14 48.7	1.62	15.58	19.92	2.83	5.37	1.30
1 46 46.77	71 14 41.5	1.63	15.69	19.91	2.82	5.42	1.31
1 46 23.63	71 14 52.1	1.66	15.88	19.95	2.86	5.41	1.30
1 46 8.7	71 14 41.1	1.67	16.11	19.93	2.84	5.53	1.33
1 45 47.05	71 14 44.3	1.71	16.39	19.94	2.85	5.61	1.35
1 45 30.62	71 14 51.1	1.73	16.63	19.94	2.85	5.69	1.37
1 45 12.71	71 14 43.3	1.81	16.78	20.08	3.00	5.45	1.31
1 44 53.31	71 14 42.6	1.83	16.62	20.17	3.09	5.24	1.26
1 44 32.4	71 14 45.2	1.78	16.27	20.14	3.06	5.18	1.25
1 44 18.21	71 14 48.1	1.72	16.06	20.05	2.97	5.27	1.27
1 43 59.53	71 14 54.3	1.76	16.00	20.16	3.09	5.06	1.22
1 43 40.13	71 14 49.5	1.80	16.08	20.23	3.16	4.96	1.20
1 43 22.25	71 14 37.4	1.76	16.43	20.04	2.95	5.42	1.31
1 43 2.8	71 14 50.4	1.80	16.68	20.09	3.00	5.41	1.31

continued on next page

Table 24 – continued from previous page

R.A.(J2000) hh mm ss	Dec.(J2000) dd mm ss	$F(60)$ (MJy)	$F(100)$ (MJy)	T_d (K)	$B(\nu,T)$ $(\times10^{-16})$ Js^{-2}	M_d $(\times10^{27})$ kg	A_V $(\times10^{-5})$ mag
1 51 24.14	71 13 17.7	2.07	16.73	20.68	3.69	4.42	1.07
1 51 6.97	71 13 11.9	2.01	16.48	20.60	3.59	4.47	1.08
1 50 49.86	71 13 24.1	2.05	16.26	20.75	3.78	4.19	1.01
1 50 31.92	71 13 11	2.07	16.58	20.71	3.73	4.34	1.05
1 48 55.77	71 13 23.6	1.74	16.75	19.93	2.84	5.76	1.39
1 48 37.87	71 13 17	1.72	16.26	20.00	2.92	5.44	1.31
1 48 21.46	71 13 13.9	1.73	15.96	20.09	3.01	5.17	1.25
1 48 0.6	71 13 21.6	1.66	15.79	19.97	2.88	5.35	1.29
1 47 44.19	71 13 14.7	1.69	15.61	20.09	3.01	5.06	1.22
1 47 21.82	71 13 15	1.70	15.56	20.14	3.06	4.96	1.20
1 47 3.18	71 13 15.1	1.72	15.90	20.08	3.00	5.17	1.25
1 46 44.55	71 13 18.7	1.76	16.08	20.13	3.06	5.13	1.24
1 46 31.13	71 13 18.6	1.75	16.20	20.09	3.01	5.25	1.27
1 46 9.49	71 13 32.7	1.70	16.61	19.85	2.76	5.87	1.42
1 45 31.47	71 13 28.3	1.78	16.73	20.02	2.94	5.55	1.34
1 45 11.34	71 13 27.6	1.81	16.58	20.14	3.06	5.28	1.27
1 44 51.21	71 13 23.3	1.78	16.45	20.09	3.01	5.33	1.29
1 44 31.84	71 13 15.2	1.77	16.09	20.15	3.08	5.10	1.23
1 44 16.95	71 13 7.2	1.78	16.03	20.21	3.14	4.98	1.20
1 43 59.79	71 13 13.5	1.80	16.01	20.24	3.18	4.91	1.18
1 43 39.67	71 13 8.6	1.76	16.37	20.07	2.99	5.34	1.29
1 43 21.76	71 13 14.6	1.79	16.72	20.05	2.97	5.49	1.32
1 48 23.59	71 11 43.9	1.81	16.25	20.22	3.15	5.03	1.21
1 48 4.23	71 11 48	1.78	16.08	20.19	3.12	5.02	1.21
1 47 42.63	71 11 37.6	1.78	15.66	20.29	3.23	4.72	1.14
1 47 21.79	71 11 41.4	1.88	16.23	20.39	3.34	4.73	1.14
1 47 6.15	71 11 45.1	1.84	16.36	20.26	3.20	4.98	1.20
1 44 56.59	71 11 53.5	1.79	16.63	20.08	3.00	5.41	1.31
1 44 32.04	71 11 41.6	1.75	16.28	20.06	2.98	5.33	1.28
1 44 17.91	71 11 33.7	1.70	16.24	19.96	2.87	5.52	1.33
1 43 58.54	71 11 36.2	1.74	16.43	19.99	2.91	5.51	1.33
1 43 42.87	71 11 49.6	1.80	16.61	20.09	3.01	5.39	1.30
1 48 16.05	71 10 24.9	1.86	16.71	20.22	3.15	5.17	1.25
1 47 59.68	71 10 14.5	1.84	16.66	20.19	3.12	5.21	1.26
1 44 3.18	71 10 28.1	1.83	16.75	20.13	3.05	5.35	1.29

Table 25: The Database of far infrared cavity CASKK2 nearby to the AGB star AGB0409+6105 located with in G143+07. The first two columns represent position of the pixels with in the cavity. The next two columns give values of relative flux density at 60 μm and 100 μm that have obtained after processing the FITS image using ALADIN 2.5 software. The calculated values of dust color temperature (in K), Planck function and dust mass for 100 μm and visual extinction (in mag) of the corresponding pixels,respectively.

R.A.(J2000) hh mm ss	Dec.(J2000) dd mm ss	$F(60)$ (MJy)	$F(100)$ (MJy)	T_d (K)	$B(\nu,T)$ $(\times10^{-16})$ Js^{-2}	M_d $(\times10^{27})$ kg	A_V $(\times10^{-5})$ mag
04 08 12.22	+61 29 49.9	2.4893	20.878	20.51	3.54	0.96	1.38
04 08 00.65	+61 29 56.8	2.3009	20.858	20.17	3.15	1.08	1.55
04 07 48.08	+61 30 00.0	2.271	20.847	20.12	3.10	1.10	1.58
04 07 35.50	+61 30 06.7	2.2471	20.889	20.07	3.04	1.12	1.62
04 07 23.92	+61 30 17.1	2.3218	20.868	20.21	3.20	1.07	1.54
04 08 24.32	+61 28 16.5	2.4744	20.784	20.50	3.54	0.96	1.38
04 08 11.76	+61 28 19.8	2.4235	20.523	20.47	3.49	0.96	1.38
04 08 01.20	+61 28 26.8	2.3039	20.45	20.26	3.26	1.02	1.48
04 07 48.63	+61 28 40.8	2.2411	20.534	20.13	3.10	1.08	1.56
04 07 35.06	+61 28 40.3	2.2052	20.565	20.05	3.02	1.11	1.60
04 07 22.99	+61 28 43.4	2.2501	20.419	20.17	3.15	1.06	1.52
04 07 09.41	+61 28 53.6	2.3189	20.722	20.24	3.22	1.05	1.51
04 08 34.39	+61 26 46.6	2.3248	20.878	20.21	3.20	1.06	1.53
04 08 24.35	+61 26 53.7	2.3727	20.555	20.37	3.38	0.99	1.43
04 08 11.79	+61 27 00.6	2.4235	20.262	20.52	3.56	0.93	1.34
04 07 58.23	+61 27 07.5	2.2172	20.095	20.18	3.16	1.04	1.50
04 07 47.19	+61 27 00.0	2.1245	20.064	20.00	2.97	1.10	1.59
04 07 33.62	+61 27 10.3	2.1514	19.98	20.07	3.04	1.07	1.54
04 07 23.07	+61 27 13.4	2.2022	19.834	20.20	3.19	1.02	1.46
04 07 09.50	+61 27 23.6	2.1843	20.241	20.08	3.05	1.08	1.56
04 06 57.44	+61 27 33.7	2.1962	20.69	20.01	2.98	1.13	1.63
04 08 36.42	+61 25 16.7	2.2381	20.523	20.13	3.10	1.08	1.56
04 08 22.37	+61 25 20.1	2.3159	20.387	20.30	3.30	1.01	1.45
04 08 10.83	+61 25 27.0	2.2949	19.917	20.36	3.37	0.97	1.39
04 07 58.79	+61 25 23.1	2.1156	19.834	20.03	3.00	1.08	1.55
04 07 44.73	+61 25 33.5	2.0438	19.792	19.90	2.86	1.13	1.63
04 07 32.19	+61 25 33.0	2.1126	19.656	20.06	3.03	1.06	1.52
04 07 20.13	+61 25 46.9	2.1455	19.656	20.13	3.10	1.03	1.49
04 07 07.59	+61 25 49.9	2.1724	20.053	20.10	3.07	1.07	1.54

continued on next page

Table 25 – continued from previous page

R.A.(J2000) hh mm ss	Dec.(J2000) dd mm ss	$F(60)$ (MJy)	$F(100)$ (MJy)	$T_{\rm d}$ (K)	$B(\nu, T)$ $(\times 10^{-16})$ Js^{-2}	$M_{\rm d}$ $(\times 10^{27})$ kg	A_V $(\times 10^{-5})$ mag
04 06 55.03	+61 26 00.0	2.1305	20.743	19.88	2.83	1.19	1.72
04 08 58.50	+61 23 25.2	2.3248	20.795	20.23	3.22	1.05	1.52
04 08 47.97	+61 23 39.6	2.1753	20.387	20.03	3.00	1.11	1.60
04 08 33.93	+61 23 46.6	2.3009	20.398	20.27	3.26	1.02	1.47
04 08 21.90	+61 23 53.7	2.277	20.189	20.27	3.26	1.01	1.46
04 08 10.87	+61 23 53.4	2.2261	20.074	20.20	3.18	1.03	1.48
04 07 58.84	+61 23 53.1	2.0797	19.844	19.96	2.92	1.11	1.60
04 07 43.29	+61 24 03.4	2.0557	19.74	19.93	2.89	1.11	1.60
04 07 30.75	+61 24 06.6	2.1425	19.74	20.11	3.08	1.05	1.51
04 07 19.21	+61 24 13.3	2.2142	19.959	20.20	3.18	1.02	1.48
04 07 06.67	+61 24 23.4	2.1455	20.189	20.02	2.98	1.10	1.59
04 08 58.50	+61 21 58.8	2.2112	20.513	20.08	3.05	1.10	1.58
04 08 46.48	+61 22 09.5	2.1992	20.387	20.08	3.05	1.09	1.57
04 08 34.46	+61 22 05.8	2.3488	20.461	20.34	3.35	1.00	1.44
04 08 21.43	+61 22 12.9	2.3278	20.398	20.32	3.32	1.00	1.44
04 08 08.91	+61 22 19.8	2.283	20.262	20.26	3.26	1.02	1.46
04 07 57.38	+61 22 30.3	2.0976	20.064	19.95	2.91	1.13	1.62
04 07 43.85	+61 22 29.9	2.1245	19.917	20.03	3.00	1.08	1.56
04 07 28.82	+61 22 36.5	2.1783	19.876	20.15	3.12	1.04	1.50
04 07 20.30	+61 22 43.3	2.283	20.137	20.29	3.29	1.00	1.44
04 07 05.76	+61 22 53.4	2.2202	20.701	20.06	3.02	1.12	1.61
04 09 47.03	+61 20 03.1	2.4325	20.837	20.42	3.43	0.99	1.43
04 09 09.51	+61 20 28.8	2.3099	20.837	20.19	3.18	1.07	1.54
04 08 57.00	+61 20 28.8	2.2232	20.419	20.12	3.09	1.08	1.55
04 08 44.99	+61 20 35.9	2.1992	20.481	20.06	3.03	1.10	1.59
04 08 33.48	+61 20 39.4	2.3547	20.701	20.31	3.30	1.02	1.47
04 08 19.96	+61 20 53.6	2.3697	20.45	20.38	3.40	0.98	1.42
04 08 08.44	+61 20 57.0	2.1783	20.293	20.06	3.03	1.09	1.58
04 07 55.43	+61 20 56.6	2.1215	20.032	20.00	2.97	1.10	1.59
04 07 41.41	+61 21 07.0	2.1634	19.708	20.15	3.13	1.03	1.48
04 07 28.89	+61 21 10.1	2.1425	19.698	20.11	3.09	1.04	1.50
04 07 16.87	+61 21 16.8	2.2411	20.001	20.24	3.23	1.01	1.46
04 07 03.84	+61 21 26.9	2.1873	20.419	20.05	3.02	1.10	1.59
04 10 13.48	+61 18 25.2	2.3488	20.555	20.32	3.33	1.01	1.45
04 09 59.48	+61 18 22.0	2.3667	20.471	20.38	3.38	0.99	1.42
04 09 46.49	+61 18 29.5	2.3607	20.617	20.33	3.34	1.01	1.45
04 09 31.00	+61 18 40.6	2.3637	20.764	20.31	3.31	1.02	1.48
04 09 11.00	+61 18 51.6	2.2501	20.795	20.09	3.06	1.11	1.60
04 08 58.00	+61 18 51.6	2.1455	20.544	19.94	2.91	1.15	1.66
04 08 44.50	+61 18 55.1	2.2142	20.607	20.06	3.03	1.11	1.60
04 08 33.00	+61 19 09.4	2.3338	20.628	20.28	3.28	1.03	1.48
04 08 16.99	+61 19 12.8	2.3069	20.429	20.27	3.27	1.02	1.47
04 08 05.99	+61 19 23.3	2.1305	20.126	20.00	2.96	1.11	1.60
04 07 54.48	+61 19 23.0	2.1126	19.781	20.04	3.00	1.07	1.55
04 07 43.48	+61 19 26.3	2.0707	19.374	20.04	3.01	1.05	1.51
04 07 28.96	+61 19 43.7	2.0886	19.364	20.08	3.05	1.04	1.49
04 07 16.96	+61 19 36.0	2.0049	19.395	19.90	2.86	1.11	1.59
04 07 04.95	+61 19 46.2	1.9152	19.677	19.66	2.61	1.23	1.77
04 06 52.43	+61 19 56.3	1.9929	20.44	19.66	2.62	1.27	1.83
04 10 22.41	+61 16 54.8	2.3069	20.534	20.25	3.24	1.03	1.49
04 10 10.42	+61 16 44.5	2.3129	20.419	20.29	3.28	1.02	1.46
04 09 57.94	+61 16 52.0	2.3787	20.346	20.42	3.44	0.96	1.39
04 09 46.46	+61 17 06.7	2.3667	20.617	20.34	3.35	1.00	1.45
04 09 31.97	+61 17 07.0	2.3876	20.847	20.33	3.34	1.02	1.47
04 09 08.49	+61 17 25.2	2.2351	20.868	20.05	3.02	1.13	1.63
04 08 56.50	+61 17 21.6	2.1664	20.669	19.96	2.92	1.15	1.66
04 08 42.01	+61 17 21.5	2.2232	20.575	20.09	3.06	1.10	1.58
04 08 29.02	+61 17 43.0	2.3039	20.367	20.28	3.28	1.01	1.46
04 08 17.53	+61 17 39.2	2.2471	20.231	20.20	3.19	1.04	1.49
04 08 06.53	+61 17 53.3	2.1455	19.907	20.08	3.05	1.07	1.54
04 07 53.54	+61 17 53.0	2.0946	19.573	20.05	3.01	1.06	1.53
04 07 42.53	+61 18 10.6	2.0468	19.311	20.01	2.97	1.06	1.53
04 07 29.53	+61 18 10.1	1.969	19.217	19.87	2.82	1.11	1.60
04 07 18.04	+61 18 13.2	1.7955	18.987	19.54	2.50	1.24	1.78
04 07 03.53	+61 18 23.3	1.7866	19.301	19.46	2.42	1.30	1.87
04 06 53.53	+61 18 26.3	1.8763	19.74	19.56	2.52	1.28	1.84
04 06 40.53	+61 18 25.5	1.9869	20.356	19.67	2.62	1.27	1.82
04 10 23.84	+61 15 14.0	2.3278	20.607	20.28	3.27	1.03	1.48
04 10 08.37	+61 15 25.3	2.3368	20.45	20.32	3.33	1.00	1.45
04 09 57.89	+61 15 25.6	2.3637	20.481	20.37	3.38	0.99	1.43
04 09 44.92	+61 15 25.9	2.3847	20.68	20.36	3.37	1.00	1.44
04 09 33.94	+61 15 40.5	2.4176	20.889	20.38	3.39	1.01	1.45
04 09 06.49	+61 15 48.0	2.2411	20.889	20.06	3.03	1.13	1.62
04 08 55.01	+61 15 51.6	2.2142	20.628	20.06	3.03	1.11	1.60
04 08 41.53	+61 16 05.9	2.3039	20.513	20.25	3.24	1.03	1.49
04 08 29.05	+61 16 02.2	2.3009	20.231	20.30	3.30	1.00	1.44
04 08 17.56	+61 16 09.2	2.262	20.314	20.21	3.20	1.04	1.49

continued on next page

Table 25 – continued from previous page

R.A.(J2000) hh mm ss	Dec.(J2000) dd mm ss	$F(60)$ (MJy)	$F(100)$ (MJy)	$T_{\rm d}$ (K)	$B(\nu,T)$ $(\times10^{-16})$ Js^{-2}	$M_{\rm d}$ $(\times10^{27})$ kg	A_V $(\times10^{-5})$ mag
04 08 06.07	+61 16 16.1	2.1932	20.022	20.14	3.12	1.05	1.51
04 07 52.09	+61 16 19.3	2.1574	19.698	20.14	3.12	1.03	1.48
04 07 41.10	+61 16 29.8	2.0288	19.489	19.93	2.89	1.10	1.58
04 07 28.11	+61 16 36.5	1.963	19.05	19.89	2.85	1.09	1.57
04 07 16.61	+61 16 53.9	1.7716	18.831	19.52	2.48	1.24	1.78
04 07 03.61	+61 17 04.1	1.7537	19.04	19.44	2.41	1.29	1.86
04 06 53.12	+61 17 03.5	1.8613	19.426	19.59	2.55	1.24	1.79
04 06 38.13	+61 17 09.8	1.9301	19.949	19.63	2.59	1.26	1.81
04 06 26.63	+61 17 19.8	2.1245	20.868	19.84	2.80	1.22	1.75
04 10 32.24	+61 13 40.0	2.3458	20.868	20.25	3.24	1.05	1.51
04 10 20.29	+61 13 54.9	2.3129	20.753	20.22	3.20	1.06	1.52
04 10 07.82	+61 13 51.7	2.3817	20.534	20.39	3.40	0.99	1.42
04 09 55.36	+61 14 06.5	2.4475	20.669	20.48	3.51	0.96	1.39
04 09 42.39	+61 14 03.2	2.4265	20.68	20.44	3.46	0.98	1.41
04 09 32.42	+61 14 10.6	2.4295	20.753	20.43	3.45	0.98	1.41
04 09 19.45	+61 14 14.3	2.4086	20.795	20.38	3.39	1.00	1.44
04 09 05.99	+61 14 18.0	2.2261	20.732	20.06	3.03	1.12	1.61
04 08 55.01	+61 14 25.2	2.2321	20.565	20.11	3.08	1.09	1.57
04 08 40.54	+61 14 35.9	2.3488	20.492	20.34	3.34	1.00	1.44
04 08 28.07	+61 14 50.2	2.3637	20.471	20.37	3.38	0.99	1.42
04 08 18.09	+61 14 50.0	2.3607	20.555	20.35	3.35	1.00	1.44
04 08 03.12	+61 14 53.3	2.2531	20.325	20.19	3.18	1.04	1.50
04 07 52.64	+61 14 53.0	2.268	19.938	20.31	3.30	0.98	1.42
04 07 40.16	+61 15 06.9	2.1634	19.687	20.16	3.14	1.02	1.48
04 07 26.68	+61 15 20.8	1.9989	19.311	19.91	2.87	1.10	1.58
04 07 15.19	+61 15 23.9	1.8793	19.05	19.71	2.67	1.17	1.68
04 07 02.21	+61 15 26.8	1.8823	19.27	19.67	2.63	1.20	1.72
04 06 48.23	+61 15 33.2	1.9331	19.813	19.67	2.62	1.23	1.78
04 06 36.74	+61 15 46.9	1.9989	20.743	19.62	2.57	1.31	1.89
04 10 31.17	+61 12 06.5	2.3189	20.743	20.23	3.22	1.05	1.52
04 10 20.21	+61 12 10.5	2.3547	20.607	20.32	3.33	1.01	1.46
04 10 08.26	+61 12 14.5	2.4086	20.555	20.43	3.45	0.97	1.40
04 09 53.81	+61 12 22.1	2.4774	20.429	20.58	3.64	0.92	1.32
04 09 43.35	+61 12 33.2	2.4594	20.45	20.55	3.59	0.93	1.34
04 09 29.90	+61 12 37.0	2.4086	20.607	20.42	3.44	0.98	1.41
04 09 18.94	+61 12 44.3	2.2919	20.659	20.20	3.18	1.06	1.53
04 09 03.99	+61 12 48.0	2.2052	20.669	20.03	3.00	1.12	1.62
04 08 54.02	+61 12 44.4	2.2471	20.649	20.12	3.09	1.09	1.57
04 08 40.06	+61 13 02.3	2.3667	20.575	20.35	3.36	1.00	1.44
04 08 26.60	+61 13 09.3	2.3727	20.732	20.33	3.33	1.01	1.46
04 08 16.63	+61 13 12.8	2.3039	20.805	20.19	3.17	1.07	1.54
04 08 02.67	+61 13 19.6	2.2919	20.69	20.19	3.17	1.06	1.53
04 07 51.70	+61 13 30.1	2.3069	20.555	20.25	3.24	1.04	1.49
04 07 39.23	+61 13 36.9	2.277	20.293	20.25	3.24	1.02	1.47
04 07 27.26	+61 13 32.8	2.1365	20.032	20.03	3.00	1.09	1.57
04 07 13.79	+61 13 39.4	2.1275	20.043	20.01	2.98	1.10	1.58
04 07 03.31	+61 13 49.7	2.1066	20.335	19.91	2.87	1.16	1.67
04 06 51.33	+61 14 07.0	2.1305	20.701	19.88	2.84	1.19	1.71
04 10 31.60	+61 10 40.1	2.286	20.628	20.19	3.18	1.06	1.53
04 10 18.16	+61 10 44.2	2.3218	20.44	20.30	3.30	1.01	1.46
04 10 06.72	+61 10 51.8	2.3936	20.408	20.44	3.46	0.96	1.39
04 09 53.77	+61 10 55.7	2.3936	20.189	20.48	3.51	0.94	1.35
04 09 42.83	+61 11 14.0	2.3697	20.168	20.45	3.47	0.95	1.37
04 09 27.39	+61 11 10.6	2.2471	20.22	20.21	3.19	1.03	1.49
04 09 16.43	+61 11 14.3	2.2291	20.314	20.15	3.13	1.06	1.53
04 09 05.48	+61 11 18.0	2.2232	20.502	20.10	3.07	1.09	1.57
04 08 52.53	+61 11 28.8	2.286	20.659	20.19	3.17	1.06	1.53
04 08 41.57	+61 11 39.5	2.4026	20.795	20.37	3.38	1.00	1.45
04 07 25.82	+61 12 28.0	2.3189	20.868	20.21	3.19	1.07	1.54
04 10 42.96	+61 08 55.2	2.2381	20.816	20.07	3.04	1.12	1.61
04 10 31.53	+61 09 06.5	2.2351	20.241	20.18	3.16	1.05	1.51
04 10 19.59	+61 09 14.1	2.2561	20.053	20.26	3.25	1.01	1.45
04 10 06.17	+61 09 21.8	2.3039	19.896	20.38	3.39	0.96	1.38
04 09 52.74	+61 09 29.4	2.2411	19.886	20.27	3.26	1.00	1.44
04 09 40.80	+61 09 40.4	2.1514	19.886	20.09	3.06	1.06	1.53
04 09 28.36	+61 09 40.6	2.1305	19.959	20.04	3.00	1.08	1.56
04 09 15.92	+61 09 51.5	2.1185	20.043	19.99	2.96	1.11	1.59
04 09 04.98	+61 09 58.8	2.1753	20.387	20.03	3.00	1.11	1.60
04 08 52.04	+61 10 06.0	2.289	20.701	20.18	3.17	1.07	1.54
04 10 39.40	+61 07 32.5	2.1903	20.837	19.97	2.93	1.16	1.67
04 10 29.47	+61 07 40.2	2.1514	20.189	20.03	2.99	1.10	1.59
04 10 17.04	+61 07 44.2	2.1694	19.667	20.17	3.15	1.02	1.47
04 10 04.12	+61 07 41.1	2.1395	19.311	20.19	3.17	0.99	1.43
04 09 51.70	+61 07 52.2	2.0916	19.51	20.05	3.02	1.05	1.52
04 09 41.76	+61 08 03.2	2.0647	19.635	19.97	2.94	1.09	1.57
04 09 27.34	+61 08 10.6	2.0498	19.708	19.93	2.89	1.11	1.60
04 09 16.41	+61 08 17.9	2.0677	19.876	19.93	2.89	1.12	1.62

continued on next page

Table 25 – continued from previous page

R.A.(J2000) hh mm ss	Dec.(J2000) dd mm ss	$F(60)$ (MJy)	$F(100)$ (MJy)	$T_{\rm d}$ (K)	$B(\nu,T)$ $(\times10^{-16})$ Js^{-2}	$M_{\rm d}$ $(\times10^{27})$ kg	A_V $(\times10^{-5})$ mag
04 09 03.48	+61 08 32.4	2.1932	20.147	20.12	3.09	1.06	1.53
04 08 50.55	+61 08 28.8	2.3189	20.669	20.25	3.24	1.04	1.50
04 10 41.31	+61 05 58.8	2.1903	20.596	20.02	2.99	1.13	1.62
04 10 27.91	+61 06 10.2	2.1245	19.949	20.03	2.99	1.09	1.57
04 10 15.50	+61 06 17.9	2.0647	19.395	20.02	2.99	1.06	1.53
04 10 05.07	+61 06 18.2	2.0408	19.061	20.05	3.02	1.03	1.49
04 09 52.65	+61 06 25.8	2.0288	19.301	19.97	2.93	1.07	1.55
04 09 40.23	+61 06 26.0	1.972	19.51	19.81	2.77	1.15	1.66
04 09 27.32	+61 06 40.6	1.978	19.499	19.82	2.78	1.14	1.65
04 09 13.91	+61 06 55.2	2.0438	19.708	19.92	2.87	1.12	1.61
04 09 02.48	+61 06 51.6	2.1753	20.158	20.08	3.05	1.08	1.55
04 08 50.56	+61 06 58.8	2.3637	20.837	20.29	3.29	1.03	1.49
04 10 40.73	+61 04 32.5	2.1185	20.628	19.88	2.83	1.19	1.71
04 10 27.83	+61 04 36.6	2.1544	19.75	20.13	3.10	1.04	1.50
04 10 14.94	+61 04 51.5	2.0797	19.259	20.08	3.05	1.03	1.48
04 10 02.53	+61 04 51.9	2.0797	19.165	20.10	3.08	1.02	1.46
04 09 50.63	+61 05 06.6	2.0109	19.52	19.89	2.85	1.12	1.61
04 09 39.71	+61 05 06.8	1.9541	19.677	19.74	2.69	1.19	1.72
04 09 27.80	+61 05 10.6	1.9421	19.614	19.73	2.68	1.19	1.72
04 09 12.91	+61 05 18.0	2.0767	19.959	19.93	2.89	1.13	1.62
04 09 00.50	+61 05 21.6	2.2561	20.304	20.20	3.19	1.04	1.50
04 10 39.66	+61 03 02.5	2.1753	20.44	20.02	2.99	1.12	1.61
04 10 26.28	+61 03 03.1	2.1753	19.813	20.15	3.13	1.03	1.49
04 10 14.38	+61 03 17.9	2.1514	19.405	20.20	3.18	1.00	1.44
04 10 02.49	+61 03 25.5	2.1873	19.667	20.21	3.19	1.00	1.45
04 09 49.60	+61 03 33.0	2.2142	20.022	20.18	3.17	1.03	1.49
04 09 36.21	+61 03 36.9	2.1096	20.168	19.95	2.91	1.13	1.63
04 09 25.30	+61 03 40.7	2.1066	20.064	19.97	2.93	1.12	1.61
04 09 12.90	+61 03 44.4	2.1903	20.273	20.09	3.06	1.08	1.56
04 09 00.00	+61 03 44.4	2.3069	20.534	20.25	3.24	1.03	1.49
04 10 38.10	+61 01 36.2	2.2172	20.398	20.11	3.09	1.08	1.55
04 10 26.71	+61 01 40.3	2.2202	19.771	20.25	3.24	1.00	1.43
04 10 13.34	+61 01 48.0	2.2531	19.677	20.33	3.34	0.96	1.39
04 10 02.93	+61 01 55.5	2.3218	20.481	20.29	3.29	1.02	1.47
04 09 51.04	+61 01 55.8	2.3189	20.607	20.26	3.25	1.03	1.49
04 09 38.16	+61 02 06.9	2.265	20.534	20.17	3.15	1.06	1.53
04 09 24.29	+61 02 21.5	2.2501	20.314	20.19	3.17	1.04	1.50
04 09 13.38	+61 02 14.4	2.259	20.304	20.21	3.19	1.04	1.49
04 09 00.00	+61 02 28.8	2.3308	20.325	20.34	3.34	0.99	1.43
04 10 37.53	+61 00 09.8	2.2531	20.429	20.17	3.15	1.06	1.52
04 10 24.16	+61 00 10.4	2.2919	20.043	20.33	3.33	0.98	1.42
04 10 12.29	+61 00 18.0	2.3069	20.137	20.34	3.34	0.98	1.42
04 10 00.41	+61 00 25.6	2.3577	20.743	20.30	3.30	1.03	1.48
04 09 49.02	+61 00 33.0	2.286	20.92	20.13	3.11	1.10	1.58
04 09 38.13	+61 00 40.5	2.2351	20.555	20.11	3.09	1.09	1.57
04 09 21.29	+61 00 44.3	2.2082	20.189	20.14	3.11	1.06	1.52
04 09 10.90	+61 00 48.0	2.1724	20.043	20.10	3.07	1.06	1.53
04 08 57.03	+61 00 55.2	2.1455	20.314	19.99	2.95	1.12	1.62
04 10 34.98	+60 58 43.5	2.3817	20.805	20.33	3.33	1.02	1.47
04 10 22.62	+60 58 51.2	2.3966	20.607	20.40	3.41	0.98	1.42
04 10 10.76	+60 59 02.4	2.4325	20.617	20.46	3.49	0.96	1.39
04 09 48.99	+60 59 06.6	2.2142	20.69	20.05	3.01	1.12	1.61
04 09 33.15	+60 59 10.5	2.0976	20.241	19.91	2.87	1.15	1.66
04 09 22.76	+60 59 21.5	2.0856	19.99	19.94	2.90	1.12	1.62
04 09 09.40	+60 59 32.4	2.0677	19.761	19.95	2.91	1.11	1.59
04 08 58.52	+60 59 25.2	2.1036	20.231	19.93	2.89	1.14	1.65
04 08 44.16	+60 59 32.3	2.1634	20.649	19.96	2.92	1.15	1.66
04 09 46.47	+60 57 29.5	2.1932	20.649	20.01	2.98	1.13	1.63
04 09 32.14	+60 57 33.4	2.1365	20.21	20.00	2.96	1.11	1.61
04 09 19.78	+60 57 44.3	2.1036	19.917	19.99	2.95	1.10	1.58
04 09 09.40	+60 57 51.6	2.0617	19.813	19.93	2.89	1.12	1.61
04 08 58.02	+60 57 58.8	2.1185	20.283	19.95	2.91	1.14	1.64
04 09 44.96	+60 56 06.7	2.2471	20.878	20.07	3.04	1.12	1.61
04 09 31.62	+60 56 03.4	2.2291	20.461	20.12	3.10	1.08	1.55
04 09 19.76	+60 56 17.9	2.1066	20.095	19.96	2.92	1.12	1.62
04 09 09.39	+60 56 21.6	2.0856	20.147	19.91	2.87	1.15	1.65
04 08 55.06	+60 56 28.8	2.2142	20.575	20.07	3.04	1.10	1.59
04 09 32.58	+60 54 37.0	2.2531	20.816	20.09	3.07	1.11	1.60
04 09 20.24	+60 54 40.7	2.1275	20.325	19.95	2.92	1.14	1.64
04 09 07.41	+60 54 44.4	2.1006	20.314	19.90	2.86	1.16	1.67
04 08 55.06	+60 55 02.4	2.1873	20.534	20.03	2.99	1.12	1.61
04 08 42.72	+60 54 55.1	2.286	20.753	20.17	3.15	1.08	1.55
04 08 30.37	+60 55 09.4	2.3458	20.638	20.30	3.30	1.02	1.47
04 08 16.05	+60 55 12.8	2.3637	20.805	20.30	3.30	1.03	1.48
04 09 31.57	+60 53 03.4	2.2082	20.753	20.02	2.99	1.13	1.63
04 09 19.24	+60 53 07.1	2.0976	20.44	19.87	2.83	1.18	1.70
04 09 05.43	+60 53 18.0	2.0946	20.21	19.91	2.87	1.15	1.65

continued on next page

Table 25 – continued from previous page

R.A.(J2000) hh mm ss	Dec.(J2000) dd mm ss	$F(60)$ (MJy)	$F(100)$ (MJy)	$T_{\rm d}$ (K)	$B(\nu, T)$ $(\times 10^{-16})$ Js^{-2}	$M_{\rm d}$ $(\times 10^{27})$ kg	$A_{\rm V}$ $(\times 10^{-5})$ mag
04 08 53.09	+60 53 28.8	2.2052	20.283	20.11	3.09	1.07	1.55
04 08 39.77	+60 53 28.7	2.265	20.314	20.22	3.21	1.03	1.49
04 08 29.90	+60 53 39.4	2.277	20.304	20.24	3.23	1.02	1.48
04 08 16.09	+60 53 46.4	2.274	20.273	20.25	3.23	1.02	1.47
04 08 06.22	+60 53 49.7	2.2919	20.45	20.24	3.23	1.03	1.49
04 09 18.24	+60 51 40.7	2.1096	20.335	19.92	2.88	1.15	1.66
04 09 05.91	+60 51 40.8	2.0498	20.22	19.82	2.78	1.19	1.71
04 08 53.10	+60 51 55.2	2.1604	20.084	20.07	3.04	1.08	1.55
04 08 39.79	+60 52 02.3	2.2142	20.064	20.18	3.16	1.04	1.49
04 08 29.43	+60 52 13.0	2.1962	19.771	20.20	3.19	1.01	1.46
04 08 16.12	+60 52 23.6	2.1275	19.687	20.09	3.06	1.05	1.51
04 08 04.28	+60 52 23.3	2.1724	20.001	20.11	3.08	1.06	1.53
04 07 52.94	+60 52 33.8	2.277	20.44	20.22	3.20	1.04	1.50
04 09 28.07	+60 50 17.8	2.286	20.659	20.19	3.17	1.06	1.53
04 09 16.75	+60 50 17.9	2.1425	20.502	19.95	2.91	1.15	1.66
04 09 03.94	+60 50 21.6	2.1395	20.262	19.99	2.95	1.12	1.61
04 08 52.61	+60 50 32.4	2.1783	20.064	20.11	3.08	1.06	1.53
04 08 39.31	+60 50 28.7	2.1664	19.886	20.12	3.10	1.05	1.51
04 08 28.47	+60 50 32.2	2.0916	19.552	20.04	3.01	1.06	1.53
04 08 15.66	+60 50 39.1	2.0019	19.437	19.89	2.85	1.11	1.61
04 08 03.35	+60 50 46.1	2.0288	19.583	19.91	2.87	1.11	1.60
04 07 51.51	+60 51 00.1	2.0797	19.729	19.98	2.95	1.09	1.57
04 07 37.71	+60 51 06.8	2.1783	20.387	20.04	3.01	1.11	1.59
04 09 39.37	+60 48 44.0	2.3189	20.764	20.23	3.21	1.05	1.52
04 09 27.56	+60 48 47.8	2.2291	20.544	20.10	3.08	1.09	1.57
04 09 13.78	+60 48 58.8	2.1604	20.596	19.96	2.92	1.15	1.66
04 09 01.97	+60 48 55.2	2.1843	20.408	20.05	3.01	1.10	1.59
04 08 51.63	+60 48 55.2	2.2501	20.252	20.20	3.19	1.04	1.49
04 08 39.82	+60 49 02.3	2.1903	19.813	20.18	3.16	1.02	1.47
04 08 28.00	+60 49 09.4	2.0557	19.52	19.98	2.94	1.08	1.56
04 08 13.24	+60 49 09.1	1.9989	19.353	19.90	2.86	1.11	1.59
04 08 02.41	+60 49 16.0	1.978	19.447	19.84	2.79	1.14	1.64
04 07 51.08	+60 49 22.9	1.969	19.51	19.80	2.76	1.15	1.66
04 07 38.27	+60 49 33.3	2.0348	20.158	19.80	2.76	1.19	1.72
04 07 25.95	+60 49 50.8	2.28	20.711	20.17	3.14	1.07	1.55
04 09 53.59	+60 46 55.7	2.1903	20.575	20.02	2.99	1.12	1.62
04 09 39.34	+60 47 10.5	2.283	20.502	20.21	3.20	1.05	1.51
04 09 25.08	+60 47 14.3	2.2261	20.461	20.12	3.09	1.08	1.56
04 09 11.80	+60 47 14.4	2.1992	20.617	20.03	3.00	1.12	1.62
04 09 02.46	+60 47 21.6	2.2919	20.607	20.21	3.19	1.05	1.52
04 08 48.69	+60 47 32.4	2.3009	20.419	20.26	3.26	1.02	1.47
04 08 36.39	+60 47 35.9	2.2172	20.126	20.17	3.15	1.04	1.50
04 08 26.55	+60 47 50.1	2.1126	19.74	20.05	3.01	1.07	1.54
04 08 13.27	+60 47 53.5	2.0348	19.729	19.89	2.85	1.13	1.63
04 08 02.45	+60 47 53.2	2.0169	19.761	19.85	2.81	1.15	1.66
04 07 48.18	+60 48 00.0	2.0109	20.273	19.73	2.69	1.23	1.77
04 07 35.88	+60 48 03.2	2.1574	20.45	19.99	2.95	1.13	1.63
04 07 23.08	+60 48 09.8	2.2471	20.764	20.09	3.06	1.11	1.59
04 09 51.58	+60 45 22.2	2.1694	20.575	19.98	2.95	1.14	1.64
04 09 40.78	+60 45 26.0	2.2261	20.408	20.13	3.10	1.07	1.55
04 09 27.02	+60 45 40.6	2.28	20.659	20.18	3.16	1.07	1.54
04 08 35.42	+60 46 20.3	2.3338	20.659	20.28	3.27	1.03	1.49
04 08 24.61	+60 46 16.5	2.2022	20.377	20.09	3.06	1.09	1.57
04 08 11.34	+60 46 16.3	2.0856	20.043	19.93	2.89	1.13	1.63
04 07 59.54	+60 46 26.8	2.0976	20.074	19.95	2.91	1.13	1.62
04 07 47.25	+60 46 37.2	2.1604	20.429	20.00	2.96	1.13	1.62
04 07 35.44	+60 46 40.3	2.2411	20.743	20.09	3.06	1.11	1.60
04 07 25.61	+60 46 47.1	2.289	20.826	20.16	3.14	1.08	1.56
04 10 01.36	+60 43 59.1	2.2202	20.837	20.03	2.99	1.14	1.64
04 09 50.08	+60 44 06.6	2.1425	20.732	19.90	2.86	1.18	1.70
04 09 37.32	+60 44 17.7	2.2321	20.544	20.11	3.08	1.09	1.57
04 09 26.02	+60 44 25.1	2.3129	20.659	20.24	3.23	1.05	1.51
04 08 25.62	+60 44 39.3	2.2471	20.408	20.17	3.15	1.06	1.53
04 08 12.36	+60 44 53.5	2.1305	20.273	19.97	2.93	1.13	1.63
04 08 00.08	+60 44 46.0	2.1813	20.429	20.04	3.00	1.11	1.60
04 07 48.77	+60 45 10.8	2.2291	20.826	20.05	3.01	1.13	1.62
04 09 49.06	+60 42 36.7	2.1962	20.805	19.99	2.95	1.15	1.66
04 09 36.79	+60 42 36.9	2.1903	20.596	20.02	2.99	1.13	1.62
04 09 26.00	+60 42 37.1	2.3248	20.753	20.24	3.23	1.05	1.51
04 08 22.70	+60 43 23.7	2.286	20.847	20.15	3.13	1.09	1.57
04 08 07.98	+60 43 30.6	2.2351	20.764	20.07	3.04	1.11	1.61
04 09 35.29	+60 41 14.1	2.2471	20.826	20.08	3.05	1.11	1.60
04 09 24.51	+60 41 21.5	2.3248	20.858	20.22	3.20	1.06	1.53

Table 26: The Database of far infrared cavity CASKK3 nearby to the AGB star AGB0538+1216 located with in G195-11. The first two columns represent position of the pixels with in the cavity. The next two columns give values of relative flux density at 60 μm and 100 μm that have obtained after processing the FITS image using ALADIN 2.5 software. The calculated values of dust color temperature (in K), Planck function and dust mass for 100 μm and visual extinction (in mag) of the corresponding pixels,respectively.

R.A.(J2000) hh mm ss	Dec.(J2000) dd mm ss	$F(60)$ (MJy)	$F(100)$ (MJy)	$T_{\rm d}$ (K)	$B(\nu,T)$ $(\times10^{-16})$ Js^{-2}	$M_{\rm d}$ $(\times10^{26})$ kg	$A_{\rm V}$ $(\times10^{-5})$ mag
05 35 27.85	12 20 21.3	4.28	23.32	22.60	6.79	1.11	0.81
05 35 21.71	12 20 17.6	4.27	23.40	22.56	6.71	1.12	0.82
05 35 27.86	12 18 36.9	4.31	23.41	22.61	6.82	1.11	0.81
05 35 21.22	12 18 44	4.28	23.36	22.58	6.76	1.11	0.81
05 35 16.07	12 17 14	4.25	23.40	22.54	6.67	1.13	0.82
05 35 8.7	12 17 10.3	4.30	23.40	22.60	6.78	1.11	0.81
05 35 3.3	12 17 6.6	4.29	23.38	22.58	6.76	1.11	0.81
05 34 56.91	12 17 17.3	4.33	23.33	22.65	6.88	1.09	0.80
05 34 51.51	12 17 13.6	4.34	23.15	22.71	7.01	1.07	0.78
05 34 44.63	12 17 24.2	4.42	23.25	22.77	7.13	1.05	0.77
05 35 22.71	12 15 44.1	4.19	23.19	22.51	6.63	1.13	0.82
05 35 15.58	12 15 47.6	4.10	22.97	22.44	6.49	1.14	0.83
05 35 9.44	12 15 43.9	4.11	22.82	22.50	6.60	1.11	0.81
05 35 3.06	12 15 51	4.08	22.60	22.50	6.61	1.10	0.80
05 34 56.92	12 15 50.9	4.10	22.69	22.50	6.61	1.11	0.81
05 34 50.78	12 15 47.2	4.19	22.65	22.63	6.85	1.07	0.78
05 34 45.13	12 15 50.6	4.32	22.77	22.77	7.12	1.03	0.75
05 34 38.5	12 15 50.5	4.38	23.07	22.77	7.13	1.04	0.76
05 35 28.61	12 14 17.7	4.24	23.05	22.60	6.80	1.09	0.80
05 35 21.97	12 14 17.7	4.07	22.86	22.44	6.48	1.14	0.83
05 35 15.59	12 14 21.2	4.00	22.54	22.42	6.45	1.13	0.82
05 35 9.2	12 14 21.1	3.99	22.33	22.45	6.51	1.11	0.81
05 35 3.31	12 14 21	4.04	22.24	22.54	6.68	1.07	0.78
05 34 57.17	12 14 24.5	4.06	22.36	22.53	6.66	1.08	0.79
05 34 51.77	12 14 20.8	4.12	22.37	22.60	6.80	1.06	0.77
05 34 45.14	12 14 27.8	4.22	22.62	22.68	6.95	1.05	0.77
05 34 38.75	12 14 27.7	4.32	22.83	22.76	7.10	1.04	0.76
05 35 58.57	12 12 33.6	4.30	23.32	22.62	6.83	1.10	0.80
05 35 52.18	12 12 33.5	4.28	23.26	22.60	6.80	1.10	0.80
05 35 47.03	12 12 33.5	4.23	23.28	22.54	6.68	1.12	0.82
05 35 40.15	12 12 40.6	4.19	23.13	22.52	6.65	1.12	0.82
05 35 34.26	12 12 44.2	4.19	22.94	22.56	6.72	1.10	0.80
05 35 27.87	12 12 44.1	4.09	22.73	22.49	6.59	1.11	0.81
05 35 21.73	12 12 51.3	4.00	22.73	22.37	6.37	1.15	0.84
05 35 15.84	12 12 47.6	3.99	22.36	22.44	6.49	1.11	0.81
05 35 10.19	12 12 51.1	4.02	21.99	22.57	6.74	1.05	0.77
05 35 3.32	12 12 58.2	4.02	22.15	22.53	6.66	1.07	0.78
05 34 56.93	12 12 58.1	4.06	22.25	22.56	6.72	1.07	0.78
05 34 50.79	12 13 1.6	4.11	22.36	22.59	6.78	1.06	0.78
05 34 44.9	12 13 1.4	4.26	22.54	22.75	7.08	1.03	0.75
05 34 39.01	12 13 4.9	4.34	22.79	22.79	7.16	1.03	0.75
05 34 32.62	12 13 4.8	4.41	23.30	22.75	7.09	1.06	0.77
05 35 58.82	12 11 3.6	4.17	23.00	22.52	6.64	1.12	0.81
05 35 51.94	12 11 7.1	4.19	22.80	22.60	6.80	1.08	0.79
05 35 46.54	12 11 10.7	4.21	22.86	22.61	6.81	1.08	0.79
05 35 39.91	12 11 10.6	4.18	22.69	22.62	6.82	1.07	0.78
05 35 33.77	12 11 14.2	4.12	22.56	22.57	6.73	1.08	0.79
05 35 27.88	12 11 14.1	4.08	22.53	22.52	6.65	1.09	0.80
05 35 21.25	12 11 17.6	3.93	22.50	22.33	6.30	1.15	0.84
05 35 15.85	12 11 17.6	3.96	22.28	22.42	6.45	1.11	0.81
05 35 9.71	12 11 17.5	4.03	22.04	22.57	6.74	1.05	0.77
05 35 2.83	12 11 21	4.08	22.15	22.60	6.80	1.05	0.77
05 34 57.68	12 11 20.9	4.12	22.37	22.61	6.81	1.06	0.77
05 34 51.05	12 11 20.8	4.19	22.49	22.67	6.93	1.05	0.76
05 34 44.17	12 11 24.2	4.32	22.58	22.81	7.21	1.01	0.74
05 34 38.28	12 11 27.7	4.37	22.81	22.82	7.23	1.02	0.74
05 34 32.39	12 11 27.6	4.40	23.14	22.78	7.15	1.04	0.76
05 34 26.25	12 11 31	4.33	23.23	22.67	6.93	1.08	0.79
05 36 47.67	12 9 8.3	4.44	23.30	22.79	7.16	1.05	0.77
05 36 41.53	12 9 11.9	4.41	23.36	22.74	7.06	1.07	0.78
05 36 4.22	12 9 37.2	4.20	23.22	22.52	6.64	1.13	0.82
05 35 57.59	12 9 40.8	4.13	22.90	22.49	6.59	1.12	0.82
05 35 51.7	12 9 40.7	4.14	22.60	22.59	6.77	1.08	0.78
05 35 46.05	12 9 40.7	4.19	22.65	22.64	6.86	1.06	0.78
05 35 39.18	12 9 37	4.07	22.50	22.52	6.63	1.09	0.80
05 35 33.53	12 9 37	4.03	22.19	22.53	6.66	1.07	0.78
05 35 27.64	12 9 40.5	3.97	22.12	22.47	6.55	1.09	0.79
05 35 21.5	12 9 36.9	3.90	22.29	22.33	6.30	1.14	0.83
05 35 15.61	12 9 40.4	3.91	22.12	22.39	6.40	1.11	0.81
05 35 9.71	12 9 47.5	4.06	22.01	22.61	6.82	1.04	0.76

continued on next page

Table 26 – continued from previous page

R.A.(J2000) hh mm ss	Dec.(J2000) dd mm ss	$F(60)$ (MJy)	$F(100)$ (MJy)	$T_{\rm d}$ (K)	$B(\nu,T)$ $(\times10^{-16})$ Js^{-2}	$M_{\rm d}$ $(\times10^{26})$ kg	$A_{\rm V}$ $(\times10^{-5})$ mag
05 35 2.6	12 9 47.4	4.17	22.26	22.69	6.98	1.03	0.75
05 34 56.95	12 9 50.9	4.13	22.47	22.60	6.80	1.06	0.78
05 34 50.57	12 9 40	4.20	22.63	22.65	6.89	1.06	0.77
05 34 43.94	12 9 39.8	4.34	22.69	22.82	7.22	1.01	0.74
05 34 37.8	12 9 46.9	4.31	22.79	22.75	7.08	1.04	0.76
05 34 32.64	12 9 46.8	4.33	22.96	22.74	7.07	1.05	0.76
05 34 26.26	12 9 57.4	4.26	23.12	22.61	6.82	1.09	0.80
05 34 20.86	12 9 53.7	4.30	23.36	22.61	6.80	1.11	0.81
05 36 47.42	12 7 52.7	4.37	23.33	22.70	7.00	1.08	0.78
05 36 41.29	12 7 49.1	4.33	23.13	22.70	6.98	1.07	0.78
05 36 34.17	12 7 49.2	4.20	23.01	22.56	6.71	1.10	0.81
05 36 28.03	12 7 49.2	4.24	23.04	22.60	6.80	1.09	0.80
05 36 22.63	12 7 49.2	4.25	23.18	22.58	6.76	1.10	0.81
05 36 4.46	12 8 3.6	4.14	22.85	22.53	6.66	1.11	0.81
05 35 57.59	12 8 7.2	4.03	22.63	22.43	6.48	1.13	0.82
05 35 51.94	12 8 10.7	4.05	22.45	22.50	6.61	1.09	0.80
05 35 46.05	12 8 10.7	4.11	22.32	22.61	6.82	1.06	0.77
05 35 39.92	12 8 10.6	4.01	22.15	22.52	6.64	1.07	0.78
05 35 33.78	12 8 17.8	3.93	21.88	22.48	6.57	1.07	0.78
05 35 26.91	12 8 14.1	3.98	21.89	22.54	6.67	1.06	0.77
05 35 21.01	12 8 17.6	3.94	22.22	22.42	6.45	1.11	0.81
05 35 14.88	12 8 14	3.94	22.11	22.44	6.49	1.10	0.80
05 35 8.99	12 8 10.3	4.07	22.14	22.59	6.78	1.05	0.77
05 35 2.85	12 8 13.8	4.17	22.36	22.67	6.93	1.04	0.76
05 34 56.47	12 8 17.3	4.16	22.67	22.60	6.79	1.08	0.79
05 34 50.33	12 8 13.6	4.20	22.70	22.64	6.87	1.07	0.78
05 34 43.7	12 8 17	4.33	22.75	22.79	7.16	1.02	0.75
05 34 38.54	12 8 24.1	4.29	22.92	22.69	6.97	1.06	0.77
05 34 32.65	12 8 20.4	4.30	22.97	22.70	6.98	1.06	0.77
05 34 26.03	12 8 23.8	4.24	23.27	22.55	6.69	1.12	0.82
05 34 19.89	12 8 30.9	4.24	23.13	22.59	6.77	1.10	0.80
05 36 41.04	12 6 19.1	4.26	23.15	22.60	6.80	1.10	0.80
05 36 35.15	12 6 26.4	4.15	22.61	22.60	6.79	1.07	0.78
05 36 29.01	12 6 26.4	4.09	22.51	22.54	6.69	1.08	0.79
05 36 22.14	12 6 30	4.09	22.53	22.53	6.67	1.09	0.79
05 36 16.25	12 6 33.6	4.06	22.99	22.39	6.40	1.16	0.84
05 36 10.6	12 6 33.6	4.11	22.71	22.52	6.64	1.10	0.80
05 36 4.47	12 6 33.6	4.07	22.49	22.51	6.63	1.09	0.80
05 35 57.84	12 6 40.8	3.96	22.33	22.41	6.43	1.12	0.82
05 35 52.44	12 6 37.1	4.02	22.14	22.53	6.66	1.07	0.78
05 35 46.3	12 6 44.3	4.05	22.01	22.61	6.81	1.04	0.76
05 35 40.16	12 6 44.2	3.96	22.02	22.48	6.57	1.08	0.79
05 35 33.78	12 6 44.2	3.91	21.87	22.45	6.50	1.08	0.79
05 35 26.91	12 6 40.5	3.93	21.83	22.49	6.59	1.07	0.78
05 35 21.76	12 6 36.9	3.97	22.09	22.48	6.57	1.08	0.79
05 35 15.62	12 6 44	3.98	22.19	22.47	6.55	1.09	0.80
05 35 8.25	12 6 47.5	4.16	22.18	22.71	7.00	1.02	0.74
05 35 3.1	12 7 1.8	4.19	22.34	22.71	7.01	1.03	0.75
05 34 55.98	12 7 1.7	4.16	22.59	22.61	6.82	1.07	0.78
05 34 50.34	12 7 1.6	4.27	22.64	22.74	7.06	1.03	0.75
05 34 43.95	12 6 57.8	4.35	22.78	22.81	7.20	1.02	0.74
05 34 38.55	12 6 57.7	4.35	23.00	22.76	7.10	1.04	0.76
05 34 32.66	12 7 8.4	4.29	22.99	22.68	6.94	1.07	0.78
05 34 26.28	12 7 8.2	4.21	23.32	22.50	6.60	1.14	0.83
05 34 19.65	12 7 11.7	4.22	23.18	22.55	6.69	1.12	0.81
05 36 40.06	12 4 56.3	4.21	23.39	22.48	6.57	1.15	0.84
05 36 34.9	12 5 3.6	4.11	22.64	22.54	6.68	1.09	0.80
05 36 29.01	12 4 56.4	4.09	22.39	22.57	6.74	1.07	0.78
05 36 22.38	12 4 52.8	4.00	22.46	22.44	6.49	1.12	0.81
05 36 16.98	12 4 52.8	3.92	22.54	22.31	6.26	1.16	0.85
05 36 10.11	12 5 7.2	4.00	22.51	22.43	6.47	1.12	0.82
05 36 4.47	12 4 56.4	3.98	22.12	22.49	6.58	1.08	0.79
05 35 58.09	12 4 52.8	3.97	22.03	22.50	6.60	1.08	0.78
05 35 51.7	12 5 3.5	4.04	21.82	22.64	6.87	1.02	0.75
05 35 45.57	12 5 3.5	4.00	21.90	22.57	6.74	1.05	0.76
05 35 39.43	12 5 7	3.96	21.86	22.52	6.65	1.06	0.77
05 35 33.79	12 5 3.4	4.00	21.78	22.59	6.78	1.03	0.75
05 35 28.39	12 5 3.3	3.97	21.86	22.53	6.67	1.06	0.77
05 35 22.01	12 5 10.5	3.98	22.18	22.48	6.56	1.09	0.79
05 35 15.38	12 5 10.4	4.09	22.29	22.59	6.78	1.06	0.77
05 35 7.77	12 5 17.5	4.21	22.27	22.75	7.09	1.01	0.74
05 35 2.13	12 5 13.8	4.22	22.32	22.75	7.10	1.01	0.74
05 34 56.23	12 5 17.3	4.17	22.42	22.66	6.91	1.05	0.76
05 34 50.59	12 5 24.4	4.13	22.58	22.58	6.75	1.08	0.79
05 34 44.21	12 5 31.4	4.33	22.65	22.81	7.20	1.01	0.74
05 34 38.32	12 5 27.7	4.29	22.81	22.72	7.03	1.05	0.76
05 34 32.18	12 5 27.6	4.28	23.00	22.67	6.93	1.07	0.78

continued on next page

Table 26 – continued from previous page

R.A.(J2000) hh mm ss	Dec.(J2000) dd mm ss	$F(60)$ (MJy)	$F(100)$ (MJy)	$T_{\rm d}$ (K)	$B(\nu,T)$ $(\times10^{-16})$ Js^{-2}	$M_{\rm d}$ $(\times10^{26})$ kg	$A_{\rm V}$ $(\times10^{-5})$ mag
05 34 26.05	12 5 27.4	4.22	23.16	22.56	6.71	1.11	0.81
05 34 20.4	12 5 34.5	4.28	23.32	22.59	6.78	1.11	0.81
05 36 34.9	12 3 30	4.22	22.96	22.60	6.79	1.09	0.79
05 36 28.27	12 3 22.8	4.16	22.59	22.61	6.82	1.07	0.78
05 36 22.14	12 3 26.4	4.02	22.47	22.46	6.53	1.11	0.81
05 36 16.98	12 3 30	3.93	22.39	22.36	6.34	1.14	0.83
05 36 9.87	12 3 33.6	3.96	22.28	22.43	6.47	1.11	0.81
05 36 3.98	12 3 33.6	4.00	21.99	22.54	6.68	1.06	0.77
05 35 57.84	12 3 37.2	3.98	21.98	22.52	6.64	1.07	0.78
05 35 51.46	12 3 47.9	4.00	21.87	22.57	6.74	1.05	0.76
05 35 46.31	12 3 40.7	4.05	21.88	22.64	6.87	1.03	0.75
05 35 40.42	12 3 47.8	4.04	21.81	22.63	6.86	1.03	0.75
05 35 34.04	12 3 47.8	4.09	21.71	22.72	7.03	0.99	0.73
05 35 28.39	12 3 51.3	4.04	21.85	22.63	6.85	1.03	0.75
05 35 21.76	12 3 58.5	3.98	22.21	22.46	6.52	1.10	0.80
05 35 15.38	12 3 44	4.09	22.20	22.61	6.82	1.05	0.77
05 35 8.76	12 3 47.5	4.14	22.07	22.71	7.00	1.02	0.74
05 35 2.38	12 3 54.6	4.14	22.13	22.70	6.98	1.02	0.75
05 34 56.24	12 3 50.9	4.10	22.23	22.62	6.84	1.05	0.76
05 34 50.84	12 3 50.8	4.09	22.31	22.59	6.77	1.06	0.77
05 34 44.71	12 3 50.6	4.23	22.58	22.70	6.98	1.04	0.76
05 34 38.57	12 3 57.7	4.27	22.58	22.75	7.09	1.03	0.75
05 34 32.19	12 3 54	4.31	23.02	22.70	6.99	1.06	0.77
05 34 26.79	12 4 8.2	4.29	23.40	22.59	6.77	1.11	0.81
05 36 34.65	12 2 0	4.33	23.06	22.71	7.00	1.06	0.77
05 36 28.03	12 1 49.2	4.21	22.69	22.65	6.88	1.06	0.78
05 36 22.38	12 2 3.6	4.10	22.54	22.55	6.70	1.08	0.79
05 36 16.25	12 2 3.6	3.96	22.54	22.36	6.34	1.15	0.84
05 36 10.11	12 1 52.8	4.00	22.27	22.48	6.57	1.09	0.80
05 36 3.98	12 2 0	4.03	22.11	22.55	6.70	1.06	0.78
05 35 57.84	12 2 3.6	3.98	21.90	22.54	6.69	1.06	0.77
05 35 51.46	12 2 7.1	4.03	21.87	22.61	6.81	1.03	0.75
05 35 45.82	12 2 10.7	4.01	21.97	22.56	6.73	1.05	0.77
05 35 38.95	12 2 10.6	4.02	21.91	22.58	6.76	1.04	0.76
05 35 33.3	12 2 17.8	4.07	21.88	22.66	6.91	1.02	0.74
05 35 27.66	12 2 14.1	4.03	21.78	22.63	6.85	1.02	0.75
05 35 21.28	12 2 10.5	4.02	21.98	22.58	6.75	1.05	0.77
05 35 14.41	12 2 6.8	4.03	21.91	22.60	6.79	1.04	0.76
05 35 8.03	12 2 13.9	4.06	21.63	22.72	7.02	0.99	0.72
05 35 2.14	12 2 10.2	4.07	21.87	22.67	6.93	1.02	0.74
05 34 56.25	12 2 10.1	4.08	21.97	22.65	6.89	1.03	0.75
05 34 50.61	12 2 20.8	4.06	22.11	22.60	6.79	1.05	0.77
05 34 44.23	12 2 20.6	4.24	22.34	22.77	7.12	1.01	0.74
05 34 38.34	12 2 24.1	4.23	22.57	22.71	7.01	1.04	0.76
05 34 31.46	12 2 31.2	4.30	23.04	22.69	6.96	1.07	0.78
05 36 33.92	12 0 30	4.26	22.93	22.66	6.91	1.07	0.78
05 36 28.03	12 0 33.6	4.21	22.63	22.67	6.93	1.05	0.77
05 36 21.65	12 0 37.2	4.14	22.53	22.60	6.79	1.07	0.78
05 36 15.76	12 0 30	4.03	22.42	22.48	6.57	1.10	0.80
05 36 9.13	12 0 26.4	4.05	22.19	22.56	6.71	1.07	0.78
05 36 3.24	12 0 26.4	4.06	22.16	22.58	6.75	1.06	0.77
05 35 57.85	12 0 33.6	4.04	22.13	22.57	6.73	1.06	0.77
05 35 51.22	12 0 33.5	4.19	22.05	22.78	7.14	0.99	0.73
05 35 45.82	12 0 40.7	4.07	21.88	22.66	6.90	1.02	0.75
05 35 39.69	12 0 40.6	4.02	21.86	22.60	6.79	1.04	0.76
05 35 33.31	12 0 44.2	4.03	21.87	22.61	6.82	1.03	0.75
05 35 27.42	12 0 47.7	3.98	21.72	22.59	6.77	1.03	0.75
05 35 21.29	12 0 40.5	4.00	21.70	22.62	6.83	1.02	0.75
05 35 14.66	12 0 47.6	4.00	21.71	22.61	6.82	1.03	0.75
05 35 8.28	12 0 51.1	3.98	21.76	22.58	6.75	1.04	0.76
05 35 1.66	12 0 51	4.07	21.76	22.69	6.97	1.01	0.73
05 34 55.52	12 0 47.3	4.06	21.97	22.63	6.85	1.03	0.75
05 34 50.12	12 0 54.4	4.14	22.10	22.70	6.99	1.02	0.74
05 34 43.99	12 0 50.6	4.21	22.11	22.78	7.15	1.00	0.73
05 34 38.34	12 0 57.7	4.30	22.56	22.80	7.18	1.01	0.74
05 34 31.97	12 1 1.2	4.30	23.18	22.64	6.88	1.09	0.79
05 36 40.29	11 58 56.3	4.28	23.38	22.58	6.76	1.11	0.81
05 36 33.91	11 59 0	4.24	22.70	22.68	6.95	1.05	0.77
05 36 28.03	11 58 56.4	4.17	22.61	22.62	6.84	1.07	0.78
05 36 21.65	11 59 3.6	4.15	22.72	22.56	6.73	1.09	0.79
05 36 16	11 59 3.6	4.07	22.60	22.49	6.58	1.11	0.81
05 36 9.38	11 59 7.2	4.14	22.56	22.58	6.76	1.08	0.78
05 36 1.77	11 59 7.2	4.16	22.51	22.63	6.84	1.06	0.77
05 35 55.88	11 59 10.7	4.14	22.46	22.62	6.82	1.06	0.77
05 35 50.73	11 59 10.7	4.13	22.34	22.63	6.86	1.05	0.77
05 35 45.58	11 59 7.1	4.16	22.18	22.71	7.00	1.02	0.75
05 35 39.69	11 59 14.2	4.09	21.93	22.67	6.93	1.02	0.74

continued on next page

Table 26 – continued from previous page

R.A.(J2000) hh mm ss	Dec.(J2000) dd mm ss	$F(60)$ (MJy)	$F(100)$ (MJy)	$T_{\rm d}$ (K)	$B(\nu,T)$ $(\times10^{-16})$ Js^{-2}	$M_{\rm d}$ $(\times10^{26})$ kg	$A_{\rm V}$ $(\times10^{-5})$ mag
05 35 33.56	11 59 14.2	4.12	21.82	22.74	7.07	0.99	0.73
05 35 28.16	11 59 17.7	4.00	21.64	22.62	6.84	1.02	0.74
05 35 21.78	11 59 10.5	3.99	21.75	22.59	6.78	1.03	0.75
05 35 15.16	11 59 28.4	3.98	21.88	22.54	6.68	1.06	0.77
05 35 8.29	11 59 24.7	4.09	21.68	22.73	7.05	0.99	0.72
05 35 2.4	11 59 28.2	4.12	21.77	22.76	7.10	0.99	0.72
05 34 56.75	11 59 28.1	4.14	21.81	22.77	7.12	0.99	0.72
05 34 49.64	11 59 20.7	4.08	22.06	22.63	6.85	1.04	0.76
05 34 44.49	11 59 20.6	4.20	22.09	22.79	7.16	0.99	0.73
05 34 38.35	11 59 27.7	4.32	22.71	22.78	7.14	1.02	0.75
05 34 32.96	11 59 31.2	4.38	23.41	22.69	6.98	1.08	0.79
05 36 40.04	11 57 19.1	4.37	23.28	22.71	7.01	1.07	0.78
05 36 35.38	11 57 19.2	4.33	23.03	22.71	7.02	1.06	0.77
05 36 27.78	11 57 15.6	4.31	23.04	22.69	6.97	1.07	0.78
05 36 22.14	11 57 30	4.29	23.34	22.59	6.78	1.11	0.81
05 35 57.85	11 57 37.2	4.38	23.20	22.74	7.07	1.06	0.77
05 35 50.98	11 57 29.9	4.35	22.98	22.76	7.11	1.04	0.76
05 35 45.58	11 57 29.9	4.35	22.70	22.82	7.23	1.01	0.74
05 35 38.71	11 57 37	4.22	22.38	22.73	7.05	1.02	0.75
05 35 33.07	11 57 40.6	4.20	21.77	22.85	7.30	0.96	0.70
05 35 28.16	11 57 40.5	4.10	21.68	22.75	7.08	0.99	0.72
05 35 20.56	11 57 44	3.92	21.82	22.48	6.56	1.07	0.78
05 35 14.67	11 57 44	3.97	22.00	22.50	6.60	1.07	0.78
05 35 9.03	11 57 43.9	4.01	21.72	22.62	6.84	1.02	0.75
05 35 3.14	11 57 43.8	4.09	22.04	22.65	6.88	1.03	0.75
05 34 56.76	11 57 43.7	4.18	22.17	22.74	7.07	1.01	0.74
05 34 50.39	11 57 47.2	4.10	22.14	22.64	6.88	1.04	0.76
05 34 44.5	11 57 47	4.24	22.30	22.79	7.16	1.00	0.73
05 34 38.85	11 57 54.1	4.37	23.16	22.74	7.06	1.06	0.77
05 35 45.34	11 56 10.7	4.34	23.00	22.73	7.05	1.05	0.77
05 35 39.45	11 56 7	4.28	22.31	22.82	7.23	0.99	0.73
05 35 33.57	11 56 17.8	4.29	21.91	22.94	7.47	0.95	0.69
05 35 26.94	11 56 14.1	4.10	21.77	22.73	7.05	1.00	0.73
05 35 21.06	11 56 17.7	4.03	21.92	22.60	6.79	1.04	0.76
05 35 14.92	11 56 24.8	4.02	22.12	22.55	6.69	1.07	0.78
05 35 8.79	11 56 17.5	4.09	22.07	22.64	6.86	1.04	0.76
05 35 2.41	11 56 17.4	4.15	22.30	22.66	6.91	1.04	0.76
05 34 56.53	11 56 17.3	4.21	22.49	22.70	6.98	1.04	0.76
05 34 50.39	11 56 17.2	4.25	22.52	22.74	7.07	1.03	0.75
05 34 44.26	11 56 17	4.28	22.61	22.76	7.10	1.03	0.75
05 34 38.13	11 56 31.3	4.43	23.21	22.80	7.19	1.04	0.76
05 35 45.34	11 54 37.1	4.29	23.02	22.68	6.94	1.07	0.78
05 35 39.7	11 54 37	4.19	22.42	22.68	6.95	1.04	0.76
05 35 33.82	11 54 44.2	4.18	21.98	22.78	7.15	0.99	0.72
05 35 27.44	11 54 40.5	4.12	22.07	22.68	6.96	1.02	0.75
05 35 21.06	11 54 44.1	4.18	22.27	22.71	7.01	1.02	0.75
05 35 15.17	11 54 44	4.17	22.51	22.64	6.87	1.06	0.77
05 35 8.06	11 54 51.1	4.15	22.53	22.62	6.83	1.06	0.78
05 35 2.42	11 54 47.4	4.18	22.68	22.61	6.82	1.07	0.78
05 34 56.04	11 54 50.9	4.28	22.77	22.72	7.03	1.04	0.76
05 34 50.4	11 54 50.8	4.29	22.83	22.72	7.02	1.05	0.76
05 34 43.78	11 54 57.8	4.39	22.81	22.85	7.29	1.01	0.74
05 35 50.5	11 53 7.1	4.38	23.40	22.69	6.97	1.08	0.79
05 35 45.1	11 53 14.3	4.25	22.88	22.66	6.91	1.07	0.78
05 35 39.21	11 53 17.8	4.16	22.38	22.65	6.90	1.05	0.76
05 35 33.08	11 53 25	4.17	22.07	22.74	7.07	1.01	0.73
05 35 27.44	11 53 17.7	4.13	22.21	22.66	6.91	1.04	0.76
05 35 21.31	11 53 17.7	4.22	22.51	22.71	7.00	1.04	0.76
05 35 15.18	11 53 17.6	4.26	23.00	22.64	6.86	1.08	0.79
05 35 7.82	11 53 10.3	4.29	23.04	22.66	6.92	1.07	0.78
05 35 1.94	11 53 24.6	4.32	22.99	22.72	7.02	1.06	0.77
05 34 56.05	11 53 24.5	4.30	22.99	22.69	6.97	1.06	0.78
05 34 50.16	11 53 13.6	4.38	23.05	22.78	7.15	1.04	0.76
05 34 44.03	11 53 13.4	4.41	23.09	22.80	7.18	1.04	0.76
05 35 51.24	11 51 44.3	4.37	23.15	22.74	7.07	1.06	0.77
05 35 45.35	11 51 44.3	4.29	22.94	22.70	6.98	1.06	0.77
05 35 39.22	11 51 40.6	4.25	22.49	22.74	7.07	1.02	0.75
05 35 33.33	11 51 44.2	4.25	22.15	22.83	7.24	0.99	0.72
05 35 27.45	11 51 44.1	4.22	22.45	22.72	7.04	1.03	0.75
05 35 21.07	11 51 36.9	4.22	22.95	22.60	6.80	1.09	0.79
05 35 14.2	11 51 44	4.30	23.18	22.65	6.89	1.08	0.79
05 35 2.43	11 51 54.6	4.38	23.25	22.73	7.05	1.06	0.78
05 34 56.79	11 51 54.5	4.39	23.20	22.76	7.10	1.05	0.77
05 34 50.66	11 51 54.4	4.41	23.19	22.78	7.14	1.05	0.76
05 34 44.53	11 51 54.3	4.53	23.16	22.93	7.45	1.00	0.73
05 35 51.24	11 50 17.9	4.37	23.03	22.76	7.11	1.04	0.76
05 35 44.62	11 50 14.3	4.42	22.86	22.87	7.32	1.01	0.73

continued on next page

Table 26 – continued from previous page

R.A.(J2000) hh mm ss	Dec.(J2000) dd mm ss	$F(60)$ (MJy)	$F(100)$ (MJy)	$T_{\rm d}$ (K)	$B(\nu,T)$ $(\times10^{-16})$ Js^{-2}	$M_{\rm d}$ $(\times10^{26})$ kg	$A_{\rm V}$ $(\times10^{-5})$ mag
05 35 38.49	11 50 25	4.28	22.53	22.78	7.14	1.02	0.74
05 35 32.85	11 50 21.4	4.29	22.24	22.86	7.31	0.98	0.72
05 35 26.47	11 50 21.3	4.25	22.51	22.75	7.08	1.02	0.75
05 35 20.34	11 50 14	4.25	22.85	22.66	6.90	1.07	0.78
05 35 14.7	11 50 10.4	4.31	23.36	22.62	6.84	1.10	0.80
05 34 43.8	11 50 24.2	4.58	23.41	22.94	7.46	1.01	0.74
05 35 56.63	11 48 48	4.41	23.32	22.75	7.09	1.06	0.77
05 35 50.26	11 48 55.1	4.43	22.96	22.86	7.31	1.01	0.74
05 35 45.11	11 48 55.1	4.37	22.74	22.84	7.27	1.01	0.73
05 35 38.49	11 48 58.6	4.32	22.53	22.83	7.24	1.00	0.73
05 35 32.85	11 48 55	4.36	22.22	22.95	7.49	0.96	0.70
05 35 26.48	11 48 51.3	4.32	22.69	22.79	7.16	1.02	0.74
05 35 20.1	11 48 58.4	4.27	22.99	22.65	6.90	1.07	0.78
05 35 13.48	11 48 54.8	4.38	23.27	22.72	7.03	1.07	0.78
05 35 56.88	11 47 10.8	4.27	23.00	22.65	6.89	1.08	0.78
05 35 50.51	11 47 17.9	4.42	22.73	22.91	7.40	0.99	0.72
05 35 44.13	11 47 21.5	4.36	22.45	22.89	7.38	0.98	0.72
05 35 38.25	11 47 14.2	4.33	22.43	22.86	7.30	0.99	0.72
05 35 32.86	11 47 10.6	4.41	22.25	23.00	7.60	0.94	0.69
05 35 26.24	11 47 17.7	4.33	22.83	22.77	7.12	1.03	0.75
05 35 20.11	11 47 17.7	4.37	22.92	22.79	7.17	1.03	0.75
05 35 13.98	11 47 21.2	4.42	23.32	22.76	7.11	1.06	0.77
05 36 9.63	11 45 30	4.37	23.30	22.71	7.01	1.07	0.78
05 36 3.26	11 45 44.4	4.27	23.23	22.60	6.78	1.10	0.81
05 35 56.64	11 45 48	4.27	22.73	22.72	7.02	1.04	0.76
05 35 50.51	11 45 40.7	4.34	22.36	22.90	7.38	0.98	0.71
05 35 44.87	11 45 47.9	4.28	22.34	22.82	7.22	1.00	0.73
05 35 38.01	11 45 44.2	4.35	22.43	22.89	7.37	0.98	0.72
05 35 32.86	11 45 51.4	4.41	22.24	23.01	7.62	0.94	0.69
05 35 26.24	11 45 51.3	4.43	22.77	22.91	7.40	0.99	0.72
05 36 15.51	11 44 0	4.27	23.32	22.58	6.75	1.11	0.81
05 36 8.9	11 44 3.6	4.26	23.18	22.60	6.79	1.10	0.80
05 36 2.77	11 44 10.8	4.17	22.81	22.58	6.75	1.09	0.79
05 35 56.15	11 44 18	4.33	22.69	22.80	7.19	1.02	0.74
05 35 50.51	11 44 10.7	4.40	22.35	22.97	7.53	0.96	0.70
05 35 44.63	11 44 10.7	4.31	22.54	22.81	7.21	1.01	0.74
05 35 38.5	11 44 17.8	4.36	22.27	22.94	7.47	0.96	0.70
05 35 33.11	11 44 14.2	4.39	22.27	22.98	7.54	0.95	0.69
05 35 25.51	11 44 14.1	4.37	22.97	22.78	7.15	1.04	0.76
05 36 14.78	11 42 37.2	4.27	23.41	22.56	6.71	1.12	0.82
05 36 9.39	11 42 30	4.26	23.09	22.62	6.84	1.09	0.79
05 36 2.52	11 42 48	4.21	23.03	22.57	6.73	1.10	0.80
05 35 56.64	11 42 33.6	4.33	22.76	22.78	7.15	1.03	0.75
05 35 51	11 42 37.1	4.40	22.73	22.87	7.33	1.00	0.73
05 35 44.88	11 42 44.3	4.36	22.79	22.82	7.22	1.02	0.74
05 35 38.99	11 42 51.5	4.34	22.55	22.85	7.29	1.00	0.73
05 35 32.62	11 42 40.6	4.36	22.22	22.95	7.48	0.96	0.70
05 35 26.49	11 42 58.5	4.33	22.92	22.74	7.07	1.04	0.76
05 35 19.39	11 42 58.5	4.36	23.35	22.68	6.94	1.08	0.79
05 36 14.78	11 41 3.6	4.32	23.38	22.63	6.85	1.10	0.80
05 36 8.65	11 41 3.6	4.36	23.33	22.68	6.95	1.08	0.79
05 36 2.53	11 41 10.8	4.28	23.14	22.63	6.86	1.09	0.79
05 35 55.91	11 41 10.8	4.35	22.94	22.76	7.11	1.04	0.76
05 35 49.78	11 41 14.3	4.44	22.95	22.88	7.35	1.01	0.73
05 35 44.14	11 41 10.7	4.38	22.85	22.83	7.25	1.02	0.74
05 35 38.26	11 41 10.7	4.43	22.83	22.89	7.37	1.00	0.73
05 35 32.63	11 41 21.4	4.35	22.37	22.90	7.39	0.98	0.71
05 35 25.76	11 41 14.1	4.33	22.98	22.73	7.05	1.05	0.77
05 35 20.37	11 41 21.3	4.32	23.41	22.62	6.83	1.10	0.81
05 36 2.04	11 39 40.8	4.42	23.32	22.76	7.11	1.06	0.77
05 35 56.65	11 39 33.6	4.35	23.28	22.69	6.96	1.08	0.79
05 35 51.25	11 39 40.8	4.50	23.14	22.90	7.38	1.01	0.74
05 35 44.88	11 39 37.1	4.47	23.24	22.85	7.28	1.03	0.75
05 35 38.51	11 39 37.1	4.50	23.10	22.91	7.41	1.01	0.73
05 35 31.65	11 39 37	4.40	22.61	22.91	7.40	0.98	0.72
05 35 25.28	11 39 51.3	4.35	23.16	22.72	7.03	1.06	0.77
05 35 19.64	11 39 51.3	4.41	23.36	22.75	7.08	1.06	0.78
05 35 32.39	11 38 10.6	4.55	23.00	23.00	7.60	0.98	0.71
05 35 26.02	11 38 21.3	4.49	23.41	22.83	7.24	1.04	0.76
05 35 31.17	11 36 51.4	4.67	23.34	23.05	7.70	0.98	0.71

Table 27: The Database of far infrared cavity CASKK4 nearby to the AGB star AGB0555+2827 located with in G182+00. The first two columns represent position of the pixels with in the cavity. The next two columns give values of relative flux density at 60 μm and 100 μm that have obtained after processing the FITS image using ALADIN 2.5 software. The calculated values of dust color temperature (in K), Planck function and dust mass for 100 μm and visual extinction (in mag) of the corresponding pixels,respectively.

R.A.(J2000) hh mm ss	Dec.(J2000) dd mm ss	$F(60)$ (MJy)	$F(100)$ (MJy)	$T_{\rm d}$ (K)	$B(\nu,T)$ $(\times10^{-16})$ Js^{-2}	$M_{\rm d}$ $(\times10^{28})$ kg	A_V $(\times10^{-5})$ mag
05 54 56.24	29 17 46.1	1.99	23.16	19.16	2.16	3.11	2.52
05 54 49.36	29 17 46.2	2.11	22.96	19.42	2.39	2.79	2.25
05 54 42.2	29 17 42.7	2.18	23.02	19.56	2.52	2.66	2.15
05 54 36.15	29 17 35.6	2.13	23.05	19.45	2.42	2.78	2.24
05 54 27.62	29 17 35.7	2.10	22.98	19.41	2.38	2.81	2.27
05 54 21.01	29 17 35.8	2.08	23.13	19.34	2.32	2.90	2.34
05 54 14.68	29 17 21.5	2.12	23.18	19.40	2.37	2.84	2.30
05 54 8.08	29 17 21.5	2.14	23.16	19.46	2.42	2.78	2.25
05 54 0.92	29 17 28.7	2.17	23.06	19.52	2.48	2.71	2.19
05 53 54.59	29 17 21.5	2.13	23.01	19.45	2.42	2.77	2.24
05 53 48.27	29 17 14.2	2.21	23.14	19.58	2.54	2.65	2.15
05 55 1.73	29 16 15.9	2.06	23.18	19.31	2.29	2.95	2.38
05 54 55.67	29 16 16.1	1.92	22.93	19.07	2.09	3.20	2.58
05 54 49.62	29 16 16.2	2.01	22.70	19.28	2.26	2.92	2.36
05 54 42.19	29 16 16.3	2.03	22.68	19.32	2.30	2.87	2.32
05 54 35.86	29 16 5.6	2.01	22.79	19.26	2.25	2.95	2.39
05 54 28.16	29 16 2.1	2.12	22.77	19.48	2.45	2.71	2.19
05 54 22.38	29 16 2.2	2.05	23.00	19.31	2.29	2.92	2.36
05 54 14.4	29 15 51.5	2.04	23.05	19.28	2.27	2.96	2.39
05 54 7.8	29 15 47.9	2.07	22.93	19.35	2.33	2.86	2.31
05 54 0.92	29 15 55.1	2.09	22.93	19.39	2.36	2.82	2.28
05 53 53.77	29 15 40.7	2.08	22.81	19.39	2.37	2.81	2.27
05 53 47.72	29 15 51.4	2.16	23.00	19.51	2.47	2.71	2.19
05 53 41.67	29 15 55	2.20	23.02	19.59	2.55	2.63	2.13
05 55 2.81	29 14 45.9	2.05	23.16	19.28	2.27	2.97	2.40
05 54 55.38	29 14 38.9	1.87	22.70	19.00	2.03	3.26	2.63
05 54 49.88	29 14 39	1.90	22.47	19.11	2.12	3.08	2.49
05 54 43.01	29 14 39.1	1.96	22.51	19.21	2.21	2.97	2.40
05 54 35.86	29 14 32.1	2.01	22.47	19.33	2.31	2.83	2.29
05 54 29.53	29 14 28.5	2.08	22.54	19.44	2.41	2.72	2.20
05 54 22.93	29 14 32.2	2.11	22.87	19.44	2.40	2.77	2.24
05 54 15.5	29 14 28.7	2.08	23.01	19.36	2.34	2.86	2.31
05 54 9.18	29 14 17.9	2.06	22.84	19.35	2.33	2.85	2.30
05 54 1.2	29 14 17.9	2.04	22.79	19.33	2.31	2.87	2.32
05 53 55.15	29 14 10.7	2.06	22.82	19.37	2.34	2.83	2.29
05 53 47.45	29 14 7	2.12	22.84	19.46	2.43	2.73	2.21
05 53 41.12	29 13 59.8	2.16	23.00	19.52	2.48	2.70	2.18
05 55 9.12	29 13 12.1	2.00	23.13	19.20	2.19	3.07	2.48
05 55 2.8	29 13 15.9	1.97	22.90	19.17	2.17	3.07	2.48
05 54 56.75	29 13 12.5	1.84	22.49	18.98	2.01	3.25	2.62
05 54 48.77	29 13 9	1.84	22.26	19.03	2.05	3.15	2.55
05 54 42.45	29 13 5.6	1.87	22.23	19.08	2.09	3.09	2.50
05 54 36.67	29 13 5.6	1.98	22.36	19.28	2.27	2.87	2.32
05 54 29.25	29 13 2.1	2.08	22.50	19.45	2.41	2.71	2.19
05 54 23.47	29 12 55	2.09	22.84	19.41	2.38	2.79	2.25
05 54 16.05	29 12 47.9	2.06	23.02	19.32	2.30	2.91	2.35
05 54 8.9	29 12 51.5	2.09	22.88	19.41	2.38	2.79	2.26
05 54 2.3	29 12 47.9	2.01	22.71	19.27	2.26	2.92	2.36
05 53 54.05	29 12 37.1	1.96	22.72	19.19	2.18	3.03	2.45
05 53 48.28	29 12 51.4	2.09	22.81	19.41	2.38	2.78	2.25
05 53 40.3	29 12 40.6	2.19	23.01	19.56	2.52	2.65	2.14
05 55 9.66	29 11 38.5	1.98	22.97	19.18	2.18	3.07	2.48
05 55 2.51	29 11 38.7	1.92	22.64	19.11	2.12	3.11	2.51
05 54 55.64	29 11 42.5	1.80	22.21	18.94	1.98	3.26	2.63
05 54 49.59	29 11 35.4	1.81	21.99	19.01	2.04	3.14	2.54
05 54 42.99	29 11 31.9	1.88	21.92	19.15	2.15	2.96	2.39
05 54 35.29	29 11 32.1	1.90	22.19	19.16	2.16	2.99	2.41
05 54 30.07	29 11 24.9	2.01	22.34	19.35	2.32	2.80	2.26
05 54 23.47	29 11 28.6	2.03	22.77	19.30	2.29	2.90	2.34
05 54 16.32	29 11 21.5	2.05	22.88	19.34	2.32	2.87	2.32
05 54 9.17	29 11 21.5	2.07	22.92	19.36	2.34	2.85	2.30
05 54 2.03	29 11 21.5	1.93	22.76	19.12	2.12	3.12	2.52
05 53 55.15	29 11 17.9	2.00	22.71	19.26	2.25	2.93	2.37
05 53 48.01	29 11 7	2.13	23.00	19.46	2.42	2.76	2.23
05 53 41.41	29 11 7	2.23	23.09	19.63	2.59	2.60	2.10
05 55 17.61	29 10 15.4	1.99	23.04	19.19	2.19	3.06	2.47
05 55 9.92	29 10 15.7	1.96	22.88	19.15	2.15	3.09	2.50
05 55 2.49	29 10 12.3	1.83	22.52	18.95	1.99	3.29	2.66
05 54 55.9	29 10 12.5	1.70	22.08	18.75	1.84	3.50	2.83
05 54 50.12	29 10 1.8	1.77	21.67	18.97	2.01	3.14	2.54

continued on next page

Table 27 – continued from previous page

R.A.(J2000) hh mm ss	Dec.(J2000) dd mm ss	$F(60)$ (MJy)	$F(100)$ (MJy)	$T_{\rm d}$ (K)	$B(\nu,T)$ $(\times10^{-16})$ Js^{-2}	$M_{\rm d}$ $(\times10^{28})$ kg	$A_{\rm V}$ $(\times10^{-5})$ mag
05 54 43.53	29 10 1.9	1.84	21.80	19.10	2.11	3.00	2.42
05 54 35.56	29 9 54.9	1.91	22.05	19.21	2.20	2.92	2.36
05 54 28.96	29 9 55	1.99	22.31	19.30	2.28	2.84	2.30
05 54 21.54	29 9 55	1.98	22.69	19.23	2.22	2.97	2.40
05 54 15.22	29 9 58.7	2.03	22.89	19.30	2.28	2.92	2.36
05 54 9.17	29 9 55.1	2.01	22.90	19.25	2.24	2.98	2.41
05 54 2.3	29 9 51.5	1.93	22.81	19.11	2.12	3.13	2.53
05 53 55.71	29 9 51.5	2.01	22.70	19.28	2.27	2.91	2.36
05 53 48.83	29 9 40.6	2.20	23.01	19.58	2.54	2.64	2.13
05 53 42.79	29 9 55	2.23	23.19	19.60	2.56	2.64	2.13
05 53 34.82	29 9 47.7	2.28	23.16	19.71	2.67	2.53	2.04
05 53 28.22	29 9 29.6	2.25	23.16	19.65	2.60	2.59	2.09
05 53 21.63	29 9 33.1	2.23	23.17	19.61	2.57	2.63	2.12
05 55 18.14	29 8 45.4	1.93	22.86	19.10	2.11	3.15	2.54
05 55 9.07	29 8 42.1	1.86	22.53	19.01	2.03	3.22	2.61
05 55 2.48	29 8 38.7	1.76	22.37	18.84	1.90	3.43	2.77
05 54 56.43	29 8 38.9	1.67	21.74	18.75	1.83	3.45	2.79
05 54 50.39	29 8 42.6	1.74	21.57	18.92	1.96	3.20	2.58
05 54 42.97	29 8 46.3	1.87	21.69	19.17	2.17	2.91	2.35
05 54 36.38	29 8 46.5	1.91	22.10	19.18	2.18	2.95	2.38
05 54 29.78	29 8 35.7	1.93	22.35	19.19	2.19	2.97	2.40
05 54 23.19	29 8 32.2	1.96	22.71	19.18	2.18	3.03	2.45
05 54 15.77	29 8 17.9	1.97	22.93	19.17	2.17	3.07	2.48
05 54 9.45	29 8 25.1	2.00	22.78	19.25	2.24	2.96	2.40
05 54 2.85	29 8 21.5	2.01	22.62	19.30	2.28	2.88	2.33
05 53 55.43	29 8 14.3	2.06	22.60	19.40	2.37	2.78	2.24
05 53 49.39	29 8 21.4	2.17	22.90	19.55	2.51	2.65	2.14
05 53 43.07	29 8 14.2	2.17	23.15	19.52	2.48	2.72	2.20
05 53 37.02	29 8 10.5	2.23	23.10	19.62	2.58	2.61	2.11
05 53 28.51	29 7 56	2.18	23.02	19.55	2.51	2.67	2.16
05 53 21.91	29 7 52.3	2.11	23.14	19.39	2.36	2.85	2.30
05 55 17.03	29 7 11.9	1.89	22.75	19.03	2.05	3.22	2.60
05 55 9.61	29 7 8.5	1.77	22.35	18.86	1.92	3.39	2.74
05 55 3.29	29 7 8.7	1.73	22.26	18.79	1.86	3.47	2.81
05 54 56.42	29 7 23.3	1.63	21.67	18.67	1.77	3.56	2.88
05 54 50.1	29 7 12.6	1.73	21.45	18.93	1.97	3.17	2.56
05 54 43.78	29 7 1.9	1.86	21.72	19.15	2.15	2.93	2.37
05 54 35.82	29 7 9.3	1.94	22.11	19.25	2.24	2.88	2.32
05 54 30.32	29 7 5.7	1.93	22.37	19.19	2.18	2.98	2.41
05 54 22.91	29 6 51.4	1.99	22.69	19.24	2.23	2.96	2.39
05 54 15.21	29 6 47.9	2.02	23.00	19.25	2.24	2.99	2.42
05 54 9.99	29 6 55.1	1.99	22.92	19.20	2.19	3.04	2.46
05 54 2.58	29 6 55.1	1.98	22.62	19.24	2.23	2.94	2.38
05 53 56.81	29 6 40.7	2.08	22.58	19.43	2.40	2.74	2.21
05 53 49.67	29 6 40.6	2.20	22.86	19.61	2.57	2.59	2.10
05 53 43.07	29 6 44.2	2.17	23.01	19.54	2.50	2.68	2.16
05 53 34.83	29 6 29.7	2.22	22.90	19.64	2.59	2.57	2.07
05 53 28.79	29 6 36.8	2.11	22.98	19.42	2.39	2.79	2.26
05 53 21.37	29 6 33.1	2.09	22.98	19.38	2.35	2.84	2.30
05 53 15.33	29 6 25.7	2.13	23.12	19.44	2.41	2.79	2.26
05 53 8.74	29 6 32.8	2.22	23.14	19.60	2.56	2.63	2.13
05 55 17.01	29 5 56.3	1.83	22.62	18.95	1.99	3.31	2.67
05 55 10.42	29 5 42.1	1.76	22.08	18.89	1.94	3.31	2.68
05 55 4.92	29 5 42.3	1.74	22.01	18.85	1.91	3.35	2.71
05 54 57.23	29 5 49.7	1.61	21.56	18.64	1.75	3.58	2.90
05 54 50.37	29 5 46.2	1.75	21.54	18.95	1.99	3.15	2.55
05 54 43.5	29 5 46.3	1.85	21.82	19.11	2.12	2.99	2.42
05 54 37.46	29 5 35.6	1.92	22.10	19.22	2.21	2.91	2.35
05 54 29.49	29 5 46.6	2.01	22.53	19.32	2.30	2.85	2.30
05 54 24	29 5 32.2	2.07	22.80	19.39	2.36	2.81	2.27
05 54 16.04	29 5 32.3	2.09	23.22	19.35	2.33	2.90	2.34
05 54 9.44	29 5 25.1	2.06	23.04	19.33	2.30	2.91	2.35
05 54 2.85	29 5 21.5	2.01	22.67	19.29	2.28	2.90	2.34
05 53 55.44	29 5 21.5	2.11	22.58	19.49	2.45	2.68	2.17
05 53 50.77	29 5 17.9	2.17	22.65	19.59	2.55	2.58	2.09
05 53 42.25	29 5 17.8	2.17	22.84	19.56	2.52	2.63	2.13
05 53 35.39	29 5 17.7	2.20	22.92	19.60	2.56	2.61	2.11
05 53 27.97	29 5 10.4	2.13	22.93	19.46	2.43	2.74	2.22
05 53 21.66	29 4 59.5	2.04	23.05	19.27	2.26	2.97	2.40
05 53 14.79	29 4 48.5	2.12	22.95	19.45	2.42	2.76	2.23
05 53 7.1	29 4 59.1	2.13	23.06	19.45	2.41	2.78	2.25
05 53 1.61	29 4 48.2	2.24	23.17	19.63	2.59	2.60	2.10
05 52 55.3	29 4 48	2.26	23.18	19.66	2.62	2.58	2.08
05 55 17.82	29 4 15.5	1.85	22.64	18.98	2.01	3.27	2.64
05 55 11.23	29 4 15.7	1.80	22.09	18.96	2.00	3.21	2.60
05 55 4.09	29 4 12.3	1.72	21.95	18.82	1.89	3.39	2.74
05 54 57.77	29 4 12.4	1.66	21.70	18.72	1.81	3.48	2.81

continued on next page

Table 27 – continued from previous page

R.A.(J2000) hh mm ss	Dec.(J2000) dd mm ss	$F(60)$ (MJy)	$F(100)$ (MJy)	$T_{\rm d}$ (K)	$B(\nu,T)$ $(\times10^{-16})$ Js^{-2}	$M_{\rm d}$ $(\times10^{28})$ kg	$A_{\rm V}$ $(\times10^{-5})$ mag
05 54 51.73	29 4 12.6	1.75	21.70	18.92	1.97	3.21	2.59
05 54 44.04	29 4 12.7	1.81	21.91	19.03	2.05	3.11	2.51
05 54 38.27	29 4 9.2	1.95	22.14	19.27	2.25	2.86	2.31
05 54 30.86	29 4 5.7	2.08	22.49	19.45	2.42	2.71	2.19
05 54 22.9	29 4 5.8	2.10	23.05	19.40	2.37	2.83	2.28
05 54 17.68	29 4 2.3	2.13	23.32	19.41	2.38	2.85	2.30
05 54 9.99	29 3 51.5	2.13	23.12	19.43	2.40	2.80	2.26
05 54 4.5	29 3 47.9	2.00	22.67	19.27	2.26	2.92	2.36
05 53 57.09	29 3 40.7	2.11	22.46	19.51	2.47	2.64	2.13
05 53 51.05	29 3 40.7	2.18	22.63	19.62	2.57	2.56	2.07
05 53 41.71	29 3 37	2.17	22.76	19.57	2.53	2.62	2.12
05 53 34.02	29 3 36.9	2.16	23.07	19.50	2.46	2.73	2.20
05 53 27.71	29 3 33.2	2.12	23.07	19.43	2.40	2.80	2.26
05 53 21.67	29 3 40.3	2.04	23.02	19.29	2.27	2.95	2.38
05 53 14.81	29 3 29.3	2.07	22.80	19.39	2.36	2.81	2.27
05 53 7.94	29 3 25.6	2.05	22.76	19.36	2.33	2.84	2.29
05 53 2.18	29 3 32.6	2.14	22.78	19.51	2.48	2.68	2.16
05 52 55.31	29 3 32.4	2.24	22.92	19.67	2.62	2.54	2.05
05 55 18.89	29 2 38.2	1.87	22.79	18.99	2.02	3.28	2.65
05 55 11.48	29 2 49.3	1.83	22.42	18.98	2.01	3.24	2.62
05 55 4.35	29 2 42.3	1.77	22.28	18.88	1.93	3.35	2.71
05 54 57.76	29 2 35.2	1.67	22.11	18.68	1.78	3.61	2.92
05 54 50.34	29 2 35.4	1.75	21.95	18.88	1.93	3.31	2.67
05 54 44.58	29 2 31.9	1.82	21.96	19.04	2.06	3.10	2.51
05 54 37.17	29 2 32.1	1.96	22.26	19.27	2.25	2.87	2.32
05 54 31.13	29 2 32.1	2.08	22.54	19.44	2.41	2.72	2.20
05 54 23.17	29 2 21.4	2.07	23.05	19.35	2.33	2.88	2.33
05 54 17.13	29 2 14.3	2.12	23.25	19.40	2.37	2.85	2.31
05 54 10.54	29 2 14.3	2.11	23.02	19.41	2.38	2.81	2.27
05 54 4.23	29 2 10.7	2.01	22.56	19.30	2.29	2.87	2.32
05 53 56.27	29 2 7.1	2.07	22.46	19.43	2.40	2.72	2.20
05 53 50.77	29 2 14.3	2.23	22.74	19.68	2.64	2.50	2.02
05 53 43.36	29 2 3.4	2.16	22.96	19.52	2.48	2.69	2.18
05 53 35.13	29 2 10.5	2.20	23.11	19.57	2.53	2.66	2.15
05 53 29.36	29 2 3.2	2.12	23.23	19.41	2.38	2.84	2.30
05 53 22.23	29 2 6.7	2.03	22.88	19.28	2.27	2.93	2.37
05 53 15.92	29 1 52.2	2.04	22.62	19.36	2.33	2.82	2.28
05 53 9.05	29 1 52	2.05	22.54	19.38	2.35	2.78	2.25
05 53 2.19	29 1 51.8	2.08	22.46	19.45	2.42	2.70	2.18
05 52 55.06	29 1 48	2.15	22.72	19.55	2.51	2.63	2.12
05 55 19.15	29 1 26.2	1.86	23.01	18.94	1.98	3.38	2.73
05 55 11.74	29 1 19.3	1.85	22.62	18.98	2.01	3.28	2.65
05 55 5.7	29 1 15.8	1.91	22.91	19.05	2.07	3.23	2.61
05 54 58.29	29 1 8.8	1.84	22.60	18.96	2.00	3.29	2.66
05 54 51.98	29 1 9	1.83	22.46	18.96	2.00	3.27	2.65
05 54 45.39	29 1 9.1	2.01	22.33	19.35	2.32	2.80	2.26
05 54 37.98	29 0 58.4	2.04	22.46	19.38	2.35	2.78	2.24
05 54 31.94	29 0 58.5	2.09	22.81	19.41	2.38	2.79	2.26
05 54 24.26	29 0 58.6	2.12	23.35	19.38	2.36	2.88	2.33
05 54 16.58	29 1 2.3	2.14	23.39	19.42	2.39	2.85	2.30
05 54 9.99	29 1 2.3	2.11	22.89	19.44	2.41	2.76	2.23
05 54 3.95	29 0 47.9	2.03	22.65	19.33	2.31	2.86	2.31
05 53 57.64	29 0 37.1	2.13	22.72	19.51	2.47	2.67	2.16
05 53 49.41	29 0 40.6	2.30	22.91	19.78	2.74	2.43	1.97
05 53 28.82	29 0 40.4	2.16	23.12	19.49	2.45	2.74	2.22
05 53 21.14	29 0 33.1	2.03	22.93	19.29	2.27	2.93	2.37
05 53 15.65	29 0 32.9	2.00	22.51	19.29	2.28	2.88	2.33
05 53 8.24	29 0 18.4	2.07	22.55	19.42	2.39	2.74	2.21
05 53 1.93	29 0 21.8	2.10	22.69	19.46	2.43	2.72	2.20
05 52 54.8	29 0 25.2	2.07	22.58	19.41	2.38	2.75	2.23
05 52 49.03	29 0 28.6	2.10	23.07	19.39	2.36	2.84	2.30
05 55 25.45	28 59 59.6	1.86	23.17	18.90	1.95	3.46	2.79
05 55 18.59	28 59 49	1.85	23.02	18.92	1.96	3.41	2.76
05 55 10.9	28 59 45.7	1.93	23.01	19.08	2.09	3.20	2.58
05 55 4.87	28 59 38.7	2.04	23.23	19.26	2.25	3.01	2.43
05 54 59.38	28 59 38.8	1.99	23.22	19.15	2.16	3.13	2.53
05 54 52.52	28 59 35.4	2.03	22.89	19.29	2.28	2.93	2.37
05 54 46.21	28 59 35.5	2.06	22.67	19.39	2.36	2.79	2.25
05 54 37.7	28 59 32	2.16	22.84	19.55	2.51	2.65	2.14
05 54 31.12	28 59 42.9	2.18	23.35	19.50	2.46	2.76	2.23
05 54 23.16	28 59 28.6	2.15	23.53	19.41	2.38	2.87	2.32
05 54 16.02	28 59 28.7	2.17	23.75	19.40	2.37	2.91	2.35
05 54 9.99	28 59 28.7	2.12	23.24	19.40	2.37	2.85	2.31
05 54 3.4	28 59 17.9	2.03	22.84	19.31	2.29	2.90	2.35
05 53 56.27	28 59 14.3	2.17	22.96	19.53	2.50	2.68	2.16
05 53 50.78	28 59 17.9	2.30	23.18	19.74	2.69	2.50	2.02
05 53 22.25	28 58 59.5	1.98	23.02	19.18	2.18	3.08	2.49

continued on next page

Table 27 – continued from previous page

R.A.(J2000) hh mm ss	Dec.(J2000) dd mm ss	$F(60)$ (MJy)	$F(100)$ (MJy)	$T_{\rm d}$ (K)	$B(\nu,T)$ $(\times10^{-16})$ Js^{-2}	$M_{\rm d}$ $(\times10^{28})$ kg	$A_{\rm V}$ $(\times10^{-5})$ mag
05 53 15.94	28 58 55.8	2.02	22.62	19.31	2.29	2.87	2.32
05 53 8.81	28 58 59.2	2.06	22.76	19.37	2.34	2.83	2.28
05 53 1.4	28 58 55.4	2.10	22.72	19.44	2.41	2.74	2.22
05 52 54.82	28 58 48	2.10	22.60	19.47	2.43	2.70	2.18
05 52 48.51	28 58 44.2	2.06	22.88	19.34	2.32	2.87	2.32
05 52 42.47	28 58 43.9	2.14	23.18	19.45	2.42	2.79	2.26
05 52 36.44	28 58 36.5	2.24	23.18	19.62	2.58	2.61	2.11
05 55 25.7	28 58 36.8	1.85	23.09	18.90	1.95	3.45	2.79
05 55 19.39	28 58 29.8	1.86	22.88	18.95	1.99	3.34	2.70
05 55 12.26	28 58 26.4	1.92	22.83	19.08	2.09	3.17	2.56
05 55 5.13	28 58 26.7	2.02	22.98	19.26	2.25	2.98	2.41
05 54 57.72	28 58 30.4	2.00	23.15	19.19	2.19	3.08	2.49
05 54 51.68	28 58 19.8	2.01	23.00	19.23	2.22	3.01	2.43
05 54 44.83	28 58 12.7	2.06	22.93	19.33	2.31	2.89	2.33
05 54 38.24	28 58 5.6	2.20	23.13	19.56	2.52	2.67	2.16
05 54 30.84	28 58 12.9	2.23	23.65	19.54	2.50	2.76	2.23
05 54 23.98	28 58 5.8	2.20	23.93	19.43	2.40	2.90	2.35
05 54 18.22	28 57 51.5	2.16	23.97	19.36	2.34	2.99	2.41
05 54 11.08	28 58 5.9	2.13	23.39	19.38	2.36	2.89	2.33
05 54 4.23	28 58 2.3	2.08	22.91	19.38	2.36	2.83	2.29
05 53 56.82	28 57 55.1	2.16	22.97	19.53	2.49	2.68	2.17
05 53 23.08	28 57 36.7	2.05	23.12	19.29	2.27	2.96	2.39
05 53 15.95	28 57 33	2.00	23.01	19.21	2.21	3.03	2.45
05 53 9.09	28 57 25.6	2.03	22.91	19.28	2.27	2.94	2.38
05 53 2.51	28 57 18.2	2.10	22.90	19.42	2.39	2.79	2.26
05 52 54.56	28 57 18	2.12	22.76	19.47	2.44	2.71	2.19
05 52 48.8	28 57 17.8	2.08	22.80	19.40	2.37	2.80	2.26
05 52 42.22	28 57 17.5	2.07	23.04	19.35	2.33	2.88	2.33
05 52 35.63	28 57 17.3	2.25	23.18	19.64	2.60	2.59	2.09
05 55 26.51	28 56 55.9	1.88	23.09	18.95	1.99	3.37	2.73
05 55 20.2	28 56 59.8	1.85	22.93	18.93	1.97	3.38	2.73
05 55 11.42	28 56 56.5	1.83	22.80	18.91	1.96	3.38	2.73
05 55 5.66	28 56 53	1.92	22.70	19.11	2.12	3.12	2.52
05 54 57.98	28 56 49.6	1.88	22.91	18.99	2.02	3.30	2.67
05 54 51.67	28 56 46.2	1.95	22.90	19.14	2.14	3.11	2.51
05 54 44.54	28 56 39.1	2.00	22.87	19.24	2.23	2.98	2.41
05 54 39.06	28 56 39.2	2.13	23.05	19.44	2.41	2.78	2.25
05 54 31.38	28 56 39.3	2.23	23.44	19.56	2.52	2.70	2.18
05 54 25.07	28 56 32.2	2.19	23.77	19.44	2.41	2.87	2.32
05 54 17.12	28 56 32.3	2.09	23.66	19.27	2.26	3.05	2.47
05 54 11.63	28 56 25.1	2.08	23.26	19.33	2.31	2.93	2.37
05 54 3.95	28 56 17.9	2.04	22.86	19.32	2.30	2.89	2.33
05 53 57.64	28 56 25.1	2.13	23.03	19.46	2.42	2.77	2.24
05 53 8.83	28 56 2.8	2.10	23.17	19.37	2.35	2.87	2.32
05 53 3.07	28 55 55.4	2.10	23.05	19.39	2.36	2.84	2.29
05 52 55.12	28 55 55.2	2.12	22.83	19.47	2.43	2.73	2.21
05 52 49.09	28 55 47.8	2.10	22.86	19.43	2.40	2.77	2.24
05 52 42.51	28 55 47.5	2.10	23.09	19.38	2.35	2.86	2.31
05 52 35.11	28 55 43.7	2.18	23.11	19.54	2.50	2.69	2.17
05 55 38.83	28 55 29	1.87	23.18	18.93	1.97	3.42	2.76
05 55 19.08	28 55 37	1.87	23.02	18.95	1.99	3.37	2.72
05 55 11.4	28 55 22.9	1.86	22.88	18.96	1.99	3.34	2.70
05 55 5.65	28 55 19.4	1.93	22.74	19.13	2.13	3.10	2.51
05 54 57.97	28 55 19.6	1.89	22.72	19.04	2.06	3.21	2.60
05 54 51.39	28 55 12.6	1.92	22.88	19.08	2.09	3.18	2.57
05 54 44.26	28 55 12.7	2.02	22.89	19.27	2.26	2.95	2.38
05 54 38.23	28 55 9.2	2.13	23.07	19.45	2.42	2.77	2.24
05 54 32.19	28 55 5.7	2.20	23.22	19.55	2.51	2.69	2.18
05 54 25.89	28 54 58.6	2.14	23.32	19.43	2.40	2.83	2.28
05 54 18.21	28 54 58.7	2.07	23.24	19.30	2.28	2.96	2.39
05 54 10.81	28 54 55.1	2.04	22.88	19.32	2.30	2.90	2.34
05 54 4.23	28 54 51.5	2.01	22.67	19.29	2.28	2.90	2.34
05 53 57.37	28 54 40.7	2.04	22.77	19.33	2.31	2.87	2.32
05 53 51.34	28 54 51.5	2.10	22.95	19.42	2.39	2.80	2.26
05 52 57.61	28 54 18.1	2.12	23.07	19.43	2.40	2.80	2.26
05 52 49.11	28 54 17.8	2.09	23.14	19.36	2.33	2.89	2.33
05 55 38.8	28 53 51.8	1.86	23.11	18.93	1.97	3.41	2.76
05 55 32.5	28 53 55.7	1.84	22.98	18.90	1.95	3.43	2.77
05 55 26.19	28 53 52.4	1.89	23.17	18.97	2.00	3.37	2.72
05 55 18.79	28 53 49	1.86	23.16	18.92	1.96	3.43	2.78
05 55 11.66	28 53 56.5	1.89	22.97	19.00	2.02	3.30	2.67
05 55 5.91	28 53 53	1.93	22.91	19.09	2.10	3.17	2.56
05 54 59.6	28 53 49.6	1.92	22.77	19.09	2.11	3.14	2.54
05 54 52.47	28 53 49.8	1.93	22.84	19.11	2.12	3.13	2.53
05 54 44.8	28 53 42.7	2.01	23.02	19.22	2.21	3.02	2.44
05 54 38.77	28 53 42.8	2.17	23.03	19.53	2.49	2.69	2.17
05 54 32.19	28 53 46.5	2.18	23.16	19.53	2.49	2.71	2.19

continued on next page

Table 27 – continued from previous page

R.A.(J2000) hh mm ss	Dec.(J2000) dd mm ss	$F(60)$ (MJy)	$F(100)$ (MJy)	$T_{\rm d}$ (K)	$B(\nu,T)$ $(\times10^{-16})$ Js^{-2}	$M_{\rm d}$ $(\times10^{28})$ kg	$A_{\rm V}$ $(\times10^{-5})$ mag
05 54 24.79	28 53 35.8	2.15	23.12	19.47	2.44	2.76	2.23
05 54 18.48	28 53 43.1	2.05	23.00	19.31	2.29	2.92	2.36
05 54 11.63	28 53 32.3	1.99	22.74	19.24	2.23	2.97	2.40
05 54 3.4	28 53 25.1	1.99	22.55	19.28	2.26	2.90	2.34
05 53 57.37	28 53 21.5	2.06	22.62	19.40	2.37	2.77	2.24
05 53 50.79	28 53 25.1	2.04	22.80	19.32	2.30	2.88	2.33
05 53 43.94	28 53 25	2.06	23.12	19.30	2.28	2.95	2.38
05 55 33.02	28 52 22.1	1.85	22.99	18.93	1.97	3.40	2.75
05 55 26.45	28 52 26	1.86	23.05	18.94	1.98	3.39	2.74
05 55 19.32	28 52 29.8	1.86	23.02	18.92	1.97	3.40	2.75
05 55 11.65	28 52 30.1	1.92	22.88	19.08	2.09	3.18	2.57
05 55 6.16	28 52 19.4	1.98	22.92	19.18	2.18	3.06	2.47
05 54 59.59	28 52 12.4	1.93	22.95	19.09	2.10	3.18	2.57
05 54 53.28	28 52 12.6	1.93	22.95	19.08	2.10	3.18	2.57
05 54 45.33	28 52 5.5	2.01	23.12	19.22	2.21	3.04	2.46
05 54 38.76	28 52 12.8	2.13	23.11	19.43	2.40	2.80	2.26
05 54 25.6	28 52 9.4	2.14	23.08	19.47	2.44	2.76	2.23
05 54 19.3	28 51 51.4	2.03	23.03	19.27	2.26	2.97	2.40
05 54 11.35	28 51 47.9	1.94	22.70	19.15	2.15	3.07	2.48
05 54 3.68	28 51 51.5	1.96	22.56	19.21	2.20	2.98	2.41
05 53 58.75	28 51 51.5	2.00	22.58	19.28	2.26	2.90	2.35
05 53 50.8	28 51 44.3	2.00	22.70	19.27	2.25	2.93	2.37
05 53 43.95	28 51 40.6	2.05	22.92	19.32	2.30	2.90	2.35
05 55 39.58	28 50 55.4	1.81	23.10	18.82	1.89	3.56	2.88
05 55 33.28	28 51 2.9	1.79	22.98	18.81	1.88	3.56	2.88
05 55 25.88	28 50 59.6	1.86	22.96	18.95	1.99	3.36	2.71
05 55 19.03	28 50 56.2	1.83	22.80	18.92	1.96	3.38	2.73
05 55 12.45	28 50 56.4	1.84	22.68	18.96	2.00	3.30	2.67
05 55 6.42	28 50 42.2	1.88	22.78	19.02	2.04	3.25	2.62
05 54 59.02	28 50 35.2	1.87	23.01	18.95	1.99	3.36	2.72
05 54 53.27	28 50 46.2	1.94	23.05	19.09	2.10	3.19	2.58
05 54 45.87	28 50 42.7	2.01	23.18	19.20	2.19	3.07	2.48
05 54 18.2	28 50 28.7	2.06	23.16	19.30	2.28	2.95	2.39
05 54 11.9	28 50 21.5	2.01	22.91	19.26	2.24	2.97	2.40
05 54 5.32	28 50 25.1	1.96	22.68	19.18	2.18	3.02	2.44
05 53 58.2	28 50 14.3	1.97	22.67	19.22	2.21	2.99	2.41
05 53 50.8	28 50 14.3	2.00	22.77	19.24	2.23	2.96	2.40
05 53 44.5	28 50 7	2.10	22.93	19.41	2.38	2.80	2.26
05 53 37.93	28 50 3.3	2.15	23.17	19.47	2.44	2.76	2.23
05 55 39.83	28 49 36.2	1.85	22.94	18.93	1.97	3.38	2.73
05 55 33.53	28 49 25.7	1.78	22.98	18.79	1.86	3.59	2.90
05 55 26.95	28 49 22.3	1.86	22.82	18.96	1.99	3.33	2.69
05 55 20.38	28 49 15.4	1.86	22.66	18.98	2.02	3.27	2.64
05 55 13.26	28 49 19.2	1.78	22.50	18.85	1.91	3.42	2.77
05 55 7.23	28 49 15.8	1.80	22.65	18.87	1.92	3.43	2.77
05 54 59.83	28 49 5.2	1.84	23.12	18.89	1.94	3.47	2.80
05 54 11.07	28 48 58.7	2.06	23.13	19.31	2.29	2.94	2.38
05 54 5.32	28 49 2.3	1.99	22.93	19.20	2.19	3.04	2.46
05 53 58.47	28 48 47.9	1.97	22.77	19.19	2.18	3.03	2.45
05 53 50.8	28 48 47.9	1.99	22.89	19.21	2.20	3.02	2.44
05 53 45.33	28 48 47.8	2.08	23.01	19.37	2.34	2.86	2.31
05 53 38.2	28 48 47.7	2.15	23.12	19.48	2.45	2.75	2.22
05 53 31.36	28 48 40.4	2.15	23.18	19.47	2.43	2.77	2.24
05 55 46.38	28 48 13.1	1.98	22.98	19.17	2.17	3.07	2.49
05 55 40.09	28 48 13.4	1.85	22.79	18.95	1.99	3.34	2.70
05 55 33.78	28 48 2.9	1.78	22.79	18.81	1.88	3.52	2.85
05 55 27.21	28 47 59.5	1.86	22.80	18.97	2.00	3.31	2.68
05 55 20.63	28 47 45.4	1.78	22.69	18.83	1.89	3.49	2.82
05 55 14.34	28 47 52.8	1.76	22.50	18.82	1.88	3.47	2.81
05 55 6.94	28 47 49.4	1.82	22.81	18.89	1.94	3.41	2.76
05 54 6.14	28 47 25.1	2.02	23.14	19.22	2.21	3.04	2.46
05 53 59.02	28 47 17.9	2.03	23.09	19.26	2.25	2.99	2.42
05 53 51.63	28 47 17.9	2.06	23.16	19.29	2.28	2.96	2.39
05 53 44.51	28 47 21.4	2.01	23.17	19.21	2.20	3.06	2.47
05 53 38.21	28 47 17.7	2.12	23.17	19.40	2.37	2.84	2.29
05 55 53.75	28 46 28.4	1.97	23.18	19.13	2.14	3.16	2.55
05 55 48.82	28 46 43	1.94	22.85	19.12	2.13	3.12	2.52
05 55 40.88	28 46 36.2	1.80	22.74	18.86	1.92	3.45	2.79
05 55 34.58	28 46 36.4	1.77	22.69	18.81	1.88	3.52	2.84
05 55 25.82	28 46 33.2	1.84	22.83	18.94	1.98	3.36	2.71
05 55 20.89	28 46 22.6	1.83	22.80	18.91	1.96	3.38	2.73
05 55 14.05	28 46 26.4	1.81	22.67	18.89	1.94	3.39	2.74
05 55 7.2	28 46 33.8	1.93	23.03	19.08	2.09	3.20	2.59
05 55 48.8	28 45 2.2	2.00	23.02	19.21	2.21	3.04	2.45
05 55 40.31	28 45 9.8	1.97	23.02	19.15	2.15	3.11	2.51
05 55 34.29	28 45 6.4	1.90	23.15	19.00	2.03	3.32	2.68
05 55 27.72	28 44 59.5	1.93	23.17	19.04	2.06	3.27	2.64

continued on next page

Table 27 – continued from previous page

R.A.(J2000) hh mm ss	Dec.(J2000) dd mm ss	$F(60)$ (MJy)	$F(100)$ (MJy)	T_d (K)	$B(\nu,T)$ $(\times10^{-16})$ Js^{-2}	M_d $(\times10^{28})$ kg	A_V $(\times10^{-5})$ mag
05 55 21.69	28 44 56.1	1.88	23.05	18.98	2.01	3.33	2.70
05 55 14.03	28 44 45.6	1.90	22.88	19.04	2.06	3.22	2.61
05 55 13.2	28 43 40.8	1.95	23.16	19.09	2.10	3.21	2.59

Table 28: The Database of far infrared cavity CASKK5 nearby to the AGB star AGB0617-0634 located with in G212-11. The first two columns represent position of the pixels with in the cavity. The next two columns give values of relative flux density at 60 μm and 100 μm that have obtained after processing the FITS image using ALADIN 2.5 software. The calculated values of dust color temperature (in K), Planck function and dust mass for 100 μm and visual extinction (in mag) of the corresponding pixels,respectively.

R.A.(J2000) hh mm ss	Dec.(J2000) dd mm ss	$F(60)$ (MJy)	$F(100)$ (MJy)	T_d (K)	$B(\nu,T)$ $(\times10^{-16})$ Js^{-2}	M_d $(\times10^{26})$ kg	A_V $(\times10^{-5})$ mag
0 6 17 28.78	-6 30 38.4	1.61	15.99	19.80	2.75	2.92	1.37
0 6 17 22.5	-6 30 34.8	1.54	16.04	19.60	2.56	3.15	1.47
0 6 17 28.78	-6 32 12	1.56	15.78	19.72	2.68	2.97	1.39
0 6 17 22.5	-6 32 12	1.50	15.52	19.64	2.60	3.01	1.41
0 6 17 16.46	-6 32 12	1.53	15.81	19.63	2.59	3.08	1.44
0 6 17 34.58	-6 33 38.4	1.64	16.00	19.88	2.83	2.84	1.33
0 6 17 29.02	-6 33 42	1.48	15.40	19.60	2.56	3.03	1.41
0 6 17 22.5	-6 33 38.4	1.43	15.02	19.58	2.54	2.98	1.39
0 6 17 16.22	-6 33 38.4	1.40	15.22	19.43	2.40	3.19	1.49
0 6 17 10.66	-6 33 45.6	1.46	15.61	19.49	2.46	3.20	1.50
0 6 17 4.62	-6 33 38.4	1.52	15.69	19.63	2.58	3.06	1.43
0 6 16 59.06	-6 33 38.4	1.56	16.08	19.65	2.61	3.11	1.45
0 6 17 34.82	-6 35 8.4	1.54	15.89	19.63	2.59	3.09	1.45
0 6 17 28.54	-6 35 8.4	1.39	15.10	19.45	2.41	3.15	1.47
0 6 17 22.74	-6 35 4.8	1.33	14.77	19.34	2.31	3.21	1.50
0 6 17 17.18	-6 35 1.2	1.34	14.74	19.40	2.37	3.14	1.46
0 6 17 10.66	-6 35 1.2	1.35	15.06	19.35	2.32	3.26	1.52
0 6 17 4.38	-6 35 4.8	1.44	15.14	19.57	2.53	3.01	1.41
0 6 16 58.58	-6 35 4.8	1.55	15.54	19.75	2.71	2.89	1.35
0 6 18 5.26	-6 36 45.5	1.53	16.01	19.59	2.55	3.16	1.48
0 6 17 59.22	-6 36 41.9	1.58	16.16	19.67	2.63	3.10	1.45
0 6 17 41.1	-6 36 42	1.61	16.03	19.79	2.75	2.94	1.37
0 6 17 34.82	-6 36 31.2	1.51	15.72	19.61	2.57	3.09	1.44
0 6 17 28.3	-6 36 34.8	1.38	14.99	19.43	2.40	3.15	1.47
0 6 17 22.26	-6 36 38.4	1.31	14.56	19.34	2.31	3.17	1.48
0 6 17 17.42	-6 36 31.2	1.29	14.29	19.37	2.34	3.07	1.44
0 6 17 10.9	-6 36 34.8	1.31	14.66	19.32	2.30	3.21	1.50
0 6 17 4.14	-6 36 34.8	1.41	14.99	19.52	2.48	3.04	1.42
0 6 16 58.82	-6 36 27.6	1.46	15.24	19.59	2.55	3.01	1.40
0 6 16 53.02	-6 36 24	1.52	15.96	19.57	2.53	3.18	1.48
0 6 18 11.06	-6 38 1	1.55	15.95	19.64	2.60	3.09	1.44
0 6 18 4.78	-6 38 1.1	1.46	15.75	19.47	2.44	3.26	1.52
0 6 17 58.98	-6 38 1.1	1.52	15.91	19.58	2.54	3.16	1.48
0 6 17 52.7	-6 38 11.9	1.53	16.10	19.56	2.52	3.22	1.50
0 6 17 46.9	-6 38 11.9	1.51	16.00	19.54	2.50	3.23	1.51
0 6 17 41.34	-6 38 12	1.52	15.71	19.64	2.60	3.05	1.42
0 6 17 35.54	-6 38 8.4	1.45	15.36	19.55	2.51	3.09	1.44
0 6 17 29.26	-6 38 8.4	1.35	14.79	19.41	2.38	3.13	1.46
0 6 17 22.74	-6 38 8.4	1.29	14.35	19.33	2.31	3.13	1.46
0 6 17 17.18	-6 38 12	1.27	14.28	19.29	2.28	3.16	1.48
0 6 17 10.9	-6 38 8.4	1.28	14.55	19.27	2.25	3.25	1.52
0 6 17 4.86	-6 38 4.8	1.34	14.78	19.37	2.35	3.17	1.48
0 6 16 58.58	-6 38 4.8	1.39	14.99	19.46	2.42	3.12	1.46
0 6 16 53.5	-6 38 8.4	1.45	15.63	19.46	2.43	3.24	1.51
0 6 16 47.22	-6 38 8.3	1.52	16.08	19.53	2.50	3.24	1.51
0 6 16 41.42	-6 38 8.3	1.57	16.07	19.67	2.62	3.08	1.44
0 6 16 33.45	-6 38 4.7	1.58	16.02	19.72	2.68	3.01	1.41
0 6 18 10.82	-6 39 38.2	1.52	15.83	19.61	2.57	3.10	1.45
0 6 18 5.27	-6 39 34.7	1.43	15.54	19.44	2.40	3.26	1.52
0 6 17 58.98	-6 39 41.9	1.48	15.69	19.53	2.49	3.17	1.48
0 6 17 52.7	-6 39 38.3	1.50	15.76	19.57	2.53	3.14	1.47
0 6 17 46.9	-6 39 41.9	1.45	15.73	19.45	2.42	3.28	1.53
0 6 17 40.86	-6 39 38.4	1.48	15.43	19.59	2.55	3.05	1.42
0 6 17 34.82	-6 39 38.4	1.44	15.13	19.55	2.51	3.03	1.42
0 6 17 28.78	-6 39 38.4	1.32	14.77	19.33	2.31	3.22	1.50
0 6 17 22.98	-6 39 38.4	1.28	14.39	19.30	2.28	3.17	1.48
0 6 17 17.18	-6 39 42	1.25	14.44	19.20	2.19	3.32	1.55
0 6 17 11.38	-6 39 42	1.26	14.60	19.17	2.17	3.38	1.58
0 6 17 5.1	-6 39 42	1.28	14.77	19.20	2.19	3.39	1.58
0 6 16 58.82	-6 39 45.6	1.36	15.01	19.38	2.35	3.22	1.50
0 6 16 53.26	-6 39 38.4	1.41	15.48	19.41	2.38	3.28	1.53

continued on next page

Table 28 – continued from previous page

R.A.(J2000) hh mm ss	Dec.(J2000) dd mm ss	$F(60)$ (MJy)	$F(100)$ (MJy)	$T_{\rm d}$ (K)	$B(\nu,T)$ $(\times10^{-16})$ Js^{-2}	$M_{\rm d}$ $(\times10^{26})$ kg	A_V $(\times10^{-5})$ mag
0 6 16 47.46	-6 39 41.9	1.45	15.94	19.40	2.37	3.38	1.58
0 6 16 40.45	-6 39 45.5	1.53	15.98	19.60	2.56	3.14	1.47
0 6 16 34.17	-6 39 41.9	1.55	15.97	19.64	2.60	3.09	1.45
0 6 18 11.07	-6 41 8.2	1.52	15.78	19.62	2.57	3.09	1.44
0 6 18 4.79	-6 41 8.3	1.40	15.42	19.38	2.36	3.30	1.54
0 6 17 58.99	-6 41 8.3	1.44	15.53	19.45	2.42	3.23	1.51
0 6 17 52.22	-6 41 4.7	1.49	15.81	19.52	2.48	3.21	1.50
0 6 17 46.42	-6 41 1.2	1.43	15.72	19.40	2.37	3.34	1.56
0 6 17 41.59	-6 41 1.2	1.50	15.53	19.63	2.58	3.03	1.41
0 6 17 35.3	-6 40 57.6	1.49	15.05	19.71	2.67	2.84	1.33
0 6 17 29.75	-6 41 1.2	1.41	14.78	19.58	2.54	2.93	1.37
0 6 17 23.95	-6 41 4.8	1.36	14.52	19.51	2.47	2.96	1.38
0 6 17 17.18	-6 41 1.2	1.33	14.58	19.41	2.38	3.08	1.44
0 6 17 11.62	-6 41 12	1.32	14.69	19.33	2.31	3.21	1.50
0 6 17 4.86	-6 41 12	1.33	14.90	19.33	2.31	3.26	1.52
0 6 16 58.82	-6 41 12	1.40	15.08	19.46	2.43	3.13	1.46
0 6 16 53.5	-6 41 12	1.42	15.40	19.43	2.40	3.23	1.51
0 6 16 46.98	-6 41 8.3	1.46	15.81	19.44	2.41	3.30	1.54
0 6 16 42.14	-6 41 11.9	1.56	16.11	19.64	2.60	3.12	1.46
0 6 16 34.89	-6 41 11.9	1.62	16.12	19.80	2.75	2.95	1.38
0 6 18 11.55	-6 42 38.2	1.52	15.72	19.62	2.58	3.06	1.43
0 6 18 5.51	-6 42 31.1	1.42	15.37	19.45	2.42	3.20	1.49
0 6 17 58.5	-6 42 34.7	1.39	15.40	19.37	2.34	3.31	1.55
0 6 17 52.7	-6 42 34.7	1.44	15.59	19.44	2.41	3.26	1.52
0 6 17 47.15	-6 42 38.3	1.45	15.61	19.46	2.43	3.24	1.51
0 6 17 40.86	-6 42 38.4	1.45	15.49	19.51	2.47	3.15	1.47
0 6 17 35.55	-6 42 38.4	1.48	15.26	19.64	2.60	2.96	1.38
0 6 17 29.02	-6 42 38.4	1.45	14.91	19.66	2.62	2.87	1.34
0 6 17 23.22	-6 42 38.4	1.46	14.73	19.73	2.68	2.77	1.29
0 6 17 16.7	-6 42 42	1.40	14.86	19.52	2.48	3.01	1.41
0 6 17 11.38	-6 42 42	1.40	15.07	19.47	2.44	3.11	1.45
0 6 17 5.1	-6 42 42	1.42	15.19	19.49	2.45	3.12	1.46
0 6 16 58.82	-6 42 45.6	1.46	15.32	19.56	2.52	3.06	1.43
0 6 16 53.02	-6 42 45.6	1.46	15.54	19.51	2.47	3.16	1.48
0 6 16 46.97	-6 42 38.3	1.48	15.87	19.49	2.45	3.26	1.52
0 6 16 40.45	-6 42 34.7	1.54	16.06	19.59	2.55	3.17	1.48
0 6 16 34.41	-6 42 38.3	1.57	16.11	19.66	2.61	3.10	1.45
0 6 18 10.59	-6 44 15.4	1.52	15.86	19.60	2.56	3.12	1.46
0 6 18 4.55	-6 44 15.5	1.44	15.48	19.48	2.44	3.19	1.49
0 6 17 58.99	-6 44 11.9	1.39	15.40	19.37	2.34	3.31	1.55
0 6 17 52.47	-6 44 8.3	1.42	15.52	19.42	2.39	3.28	1.53
0 6 17 47.63	-6 44 11.9	1.42	15.61	19.38	2.35	3.34	1.56
0 6 17 41.35	-6 44 12	1.47	15.61	19.53	2.49	3.15	1.47
0 6 17 35.31	-6 44 8.4	1.52	15.45	19.71	2.66	2.92	1.37
0 6 17 29.27	-6 44 8.4	1.48	15.14	19.68	2.63	2.89	1.35
0 6 17 23.47	-6 44 8.4	1.48	14.98	19.71	2.66	2.83	1.32
0 6 17 17.18	-6 44 12	1.42	15.17	19.49	2.46	3.11	1.45
0 6 17 10.9	-6 44 12	1.44	15.38	19.49	2.45	3.16	1.47
0 6 17 5.34	-6 44 8.4	1.46	15.45	19.54	2.50	3.11	1.45
0 6 16 59.78	-6 44 1.2	1.50	15.48	19.63	2.59	3.01	1.41
0 6 16 53.26	-6 44 4.8	1.51	15.64	19.63	2.58	3.05	1.42
0 6 16 47.22	-6 44 1.1	1.51	15.86	19.56	2.52	3.16	1.48
0 6 16 41.9	-6 44 1.1	1.59	15.94	19.75	2.70	2.97	1.39
0 6 16 35.62	-6 43 57.5	1.57	16.13	19.65	2.60	3.12	1.46
0 6 18 5.28	-6 45 49.1	1.46	15.67	19.49	2.45	3.22	1.50
0 6 17 59.23	-6 45 52.7	1.44	15.48	19.48	2.45	3.19	1.49
0 6 17 52.71	-6 45 52.7	1.48	15.54	19.56	2.52	3.11	1.45
0 6 17 46.67	-6 45 45.5	1.49	15.65	19.58	2.54	3.11	1.45
0 6 17 41.35	-6 45 45.6	1.56	15.78	19.72	2.68	2.97	1.39
0 6 17 35.07	-6 45 45.6	1.54	15.65	19.69	2.65	2.98	1.39
0 6 17 29.75	-6 45 42	1.57	15.39	19.84	2.79	2.77	1.30
0 6 17 23.22	-6 45 42	1.54	15.36	19.78	2.73	2.83	1.32
0 6 17 16.7	-6 45 34.8	1.50	15.56	19.61	2.57	3.05	1.42
0 6 17 11.14	-6 45 42	1.48	15.55	19.57	2.53	3.10	1.45
0 6 17 5.1	-6 45 38.4	1.48	15.53	19.56	2.52	3.10	1.45
0 6 16 58.81	-6 45 38.4	1.49	15.58	19.59	2.55	3.08	1.44
0 6 16 52.77	-6 45 27.6	1.52	15.59	19.68	2.63	2.98	1.39
0 6 16 47.21	-6 45 27.5	1.53	15.88	19.62	2.58	3.10	1.45
0 6 16 41.65	-6 45 27.5	1.61	16.00	19.78	2.74	2.94	1.37
0 6 16 35.37	-6 45 31.1	1.58	16.11	19.67	2.63	3.08	1.44
0 6 18 4.79	-6 47 8.3	1.47	15.86	19.47	2.43	3.28	1.53
0 6 17 58.75	-6 47 8.3	1.46	15.59	19.52	2.48	3.17	1.48
0 6 17 52.95	-6 47 11.9	1.49	15.64	19.56	2.52	3.12	1.46
0 6 17 46.43	-6 47 8.3	1.55	15.78	19.68	2.64	3.01	1.41
0 6 17 41.35	-6 47 1.2	1.55	15.86	19.67	2.63	3.04	1.42
0 6 17 34.58	-6 47 8.4	1.57	15.84	19.72	2.68	2.98	1.39
0 6 17 28.78	-6 47 12	1.59	15.68	19.83	2.79	2.83	1.32

continued on next page

Table 28 – continued from previous page

R.A.(J2000) hh mm ss	Dec.(J2000) dd mm ss	$F(60)$ (MJy)	$F(100)$ (MJy)	$T_{\rm d}$ (K)	$B(\nu,T)$ $(\times10^{-16})$ Js^{-2}	$M_{\rm d}$ $(\times10^{26})$ kg	A_V $(\times10^{-5})$ mag
0 6 17 23.47	-6 47 8.4	1.56	15.62	19.76	2.72	2.89	1.35
0 6 17 17.18	-6 47 12	1.56	15.68	19.75	2.71	2.92	1.36
0 6 17 11.38	-6 47 1.2	1.52	15.57	19.66	2.61	3.00	1.40
0 6 17 5.1	-6 47 12	1.51	15.64	19.61	2.57	3.06	1.43
0 6 17 0.02	-6 47 15.6	1.44	15.51	19.47	2.44	3.20	1.50
0 6 16 53.5	-6 47 12	1.49	15.60	19.58	2.54	3.09	1.44
0 6 16 47.21	-6 46 57.5	1.54	15.82	19.65	2.60	3.06	1.43
0 6 16 41.41	-6 47 11.9	1.61	16.02	19.79	2.75	2.93	1.37
0 6 16 35.13	-6 47 4.7	1.60	16.03	19.76	2.72	2.97	1.39
0 6 18 4.8	-6 48 41.9	1.44	15.98	19.35	2.33	3.46	1.61
0 6 17 59	-6 48 38.3	1.44	15.58	19.46	2.43	3.23	1.51
0 6 17 52.95	-6 48 34.7	1.45	15.63	19.48	2.44	3.22	1.51
0 6 17 47.39	-6 48 34.7	1.44	15.78	19.40	2.37	3.35	1.57
0 6 17 41.84	-6 48 42	1.50	15.80	19.56	2.52	3.15	1.47
0 6 17 35.31	-6 48 42	1.59	15.88	19.77	2.73	2.93	1.37
0 6 17 30.23	-6 48 42	1.57	15.90	19.71	2.67	3.00	1.40
0 6 17 24.19	-6 48 42	1.56	16.02	19.67	2.62	3.08	1.44
0 6 17 16.46	-6 48 34.8	1.56	15.97	19.67	2.63	3.06	1.43
0 6 17 11.62	-6 48 38.4	1.55	15.74	19.71	2.67	2.97	1.39
0 6 17 5.82	-6 48 42	1.52	15.82	19.61	2.57	3.10	1.45
0 6 16 59.54	-6 48 34.8	1.49	15.64	19.58	2.54	3.11	1.45
0 6 16 53.49	-6 48 42	1.50	15.71	19.58	2.54	3.12	1.46
0 6 16 47.21	-6 48 41.9	1.56	15.96	19.67	2.62	3.06	1.43
0 6 16 41.89	-6 48 34.7	1.56	15.96	19.67	2.62	3.06	1.43
0 6 16 35.61	-6 48 38.3	1.58	15.86	19.74	2.70	2.96	1.38
0 6 16 28.6	-6 48 45.4	1.54	16.06	19.59	2.55	3.17	1.48
0 6 18 4.8	-6 50 8.3	1.46	15.98	19.40	2.37	3.39	1.58
0 6 17 59.48	-6 50 1.1	1.40	15.49	19.37	2.34	3.33	1.56
0 6 17 53.68	-6 50 4.7	1.39	15.60	19.31	2.29	3.43	1.60
0 6 17 47.88	-6 50 4.7	1.40	15.73	19.30	2.28	3.47	1.62
0 6 17 41.84	-6 50 1.2	1.51	15.85	19.56	2.52	3.16	1.48
0 6 17 35.31	-6 50 8.4	1.60	15.90	19.79	2.75	2.91	1.36
0 6 17 29.75	-6 50 1.2	1.59	16.05	19.74	2.69	3.00	1.40
0 6 17 23.22	-6 50 4.8	1.58	16.13	19.68	2.64	3.08	1.44
0 6 17 17.42	-6 50 8.4	1.56	16.14	19.64	2.59	3.13	1.46
0 6 17 11.14	-6 50 4.8	1.54	16.04	19.61	2.57	3.14	1.47
0 6 17 5.82	-6 50 4.8	1.56	16.03	19.65	2.61	3.09	1.44
0 6 16 59.05	-6 50 8.4	1.52	15.89	19.60	2.56	3.13	1.46
0 6 16 53.49	-6 50 15.6	1.56	15.84	19.71	2.67	2.99	1.40
0 6 16 47.93	-6 50 4.7	1.56	16.09	19.65	2.61	3.11	1.45
0 6 16 41.41	-6 50 4.7	1.55	15.98	19.66	2.61	3.08	1.44
0 6 16 36.09	-6 50 8.3	1.52	15.70	19.63	2.59	3.06	1.43
0 6 16 29.56	-6 50 4.6	1.50	15.75	19.57	2.53	3.13	1.46
0 6 16 22.31	-6 50 8.2	1.50	15.91	19.52	2.48	3.23	1.51
0 6 18 5.53	-6 51 41.9	1.46	16.00	19.39	2.36	3.41	1.59
0 6 17 59.24	-6 51 38.3	1.43	15.64	19.42	2.39	3.30	1.54
0 6 17 53.2	-6 51 27.5	1.40	15.63	19.34	2.32	3.40	1.59
0 6 17 46.91	-6 51 27.5	1.44	15.83	19.39	2.36	3.37	1.58
0 6 17 41.35	-6 51 34.8	1.53	15.83	19.63	2.58	3.09	1.44
0 6 17 34.59	-6 51 31.2	1.63	16.01	19.85	2.80	2.88	1.34
0 6 16 59.29	-6 51 45.6	1.56	16.10	19.64	2.60	3.12	1.46
0 6 16 53.73	-6 51 45.6	1.56	15.95	19.67	2.62	3.06	1.43
0 6 16 47.21	-6 51 38.3	1.56	16.08	19.65	2.61	3.11	1.45
0 6 16 41.41	-6 51 27.5	1.51	15.94	19.55	2.51	3.20	1.50
0 6 16 34.88	-6 51 23.9	1.56	15.70	19.74	2.70	2.93	1.37
0 6 16 29.32	-6 51 38.2	1.58	15.70	19.80	2.76	2.87	1.34
0 6 16 22.79	-6 51 38.2	1.51	15.91	19.56	2.52	3.18	1.49
0 6 18 5.77	-6 53 11.8	1.47	16.02	19.42	2.39	3.37	1.57
0 6 17 59.49	-6 53 4.7	1.44	15.69	19.41	2.38	3.32	1.55
0 6 17 53.44	-6 53 11.9	1.43	15.75	19.37	2.34	3.38	1.58
0 6 17 46.43	-6 53 4.7	1.48	15.91	19.47	2.43	3.29	1.54
0 6 17 41.11	-6 53 4.8	1.56	16.01	19.65	2.61	3.09	1.44
0 6 16 52.77	-6 53 12	1.55	16.16	19.60	2.56	3.19	1.49
0 6 16 47.69	-6 53 8.3	1.53	16.02	19.59	2.55	3.17	1.48
0 6 16 41.65	-6 53 1.1	1.49	15.91	19.51	2.47	3.24	1.51
0 6 16 34.63	-6 53 8.3	1.56	15.76	19.73	2.69	2.95	1.38
0 6 16 29.8	-6 53 8.2	1.60	15.87	19.79	2.74	2.91	1.36
0 6 16 23.52	-6 52 57.4	1.57	16.08	19.67	2.63	3.08	1.44
0 6 18 5.29	-6 54 38.2	1.51	16.05	19.53	2.49	3.24	1.51
0 6 17 59.73	-6 54 34.7	1.52	15.84	19.61	2.56	3.11	1.45
0 6 17 53.2	-6 54 31.1	1.50	15.86	19.55	2.51	3.18	1.49
0 6 17 47.88	-6 54 34.7	1.53	16.02	19.57	2.53	3.18	1.49
0 6 17 42.08	-6 54 31.2	1.60	16.16	19.73	2.68	3.03	1.42
0 6 16 47.45	-6 54 31.1	1.56	15.97	19.68	2.63	3.05	1.43
0 6 16 41.89	-6 54 38.3	1.49	15.84	19.52	2.48	3.21	1.50
0 6 16 35.6	-6 54 34.7	1.54	15.78	19.66	2.62	3.03	1.42
0 6 16 29.31	-6 54 34.6	1.61	15.97	19.79	2.75	2.92	1.37

continued on next page

Table 28 – continued from previous page

R.A.(J2000) hh mm ss	Dec.(J2000) dd mm ss	$F(60)$ (MJy)	$F(100)$ (MJy)	$T_{\rm d}$ (K)	$B(\nu,T)$ $(\times10^{-16})$ Js^{-2}	$M_{\rm d}$ $(\times10^{26})$ kg	A_V $(\times10^{-5})$ mag
0 6 17 59.49	-6 56 15.5	1.60	16.02	19.76	2.72	2.97	1.39
0 6 17 53.69	-6 56 11.9	1.54	16.10	19.58	2.54	3.19	1.49
0 6 17 47.16	-6 56 15.5	1.53	16.16	19.55	2.51	3.25	1.52
0 6 16 53.73	-6 56 8.4	1.59	16.16	19.71	2.67	3.05	1.42
0 6 16 47.2	-6 56 1.1	1.54	15.80	19.67	2.63	3.03	1.42
0 6 16 41.4	-6 56 15.5	1.48	15.78	19.51	2.47	3.22	1.50
0 6 16 36.08	-6 56 11.9	1.52	15.95	19.59	2.54	3.16	1.47
0 6 17 53.45	-6 57 49.1	1.49	16.16	19.44	2.41	3.37	1.58
0 6 17 47.4	-6 57 49.1	1.55	16.16	19.61	2.57	3.17	1.48
0 6 16 53.49	-6 57 31.1	1.56	15.97	19.68	2.64	3.05	1.42
0 6 16 47.44	-6 57 31.1	1.56	15.73	19.73	2.69	2.95	1.38
0 6 16 41.64	-6 57 27.5	1.48	15.72	19.52	2.48	3.19	1.49
0 6 16 35.84	-6 57 38.3	1.52	15.91	19.59	2.55	3.14	1.47
0 6 17 46.92	-6 59 1.1	1.47	16.08	19.42	2.39	3.39	1.58
0 6 16 53.73	-6 59 1.1	1.55	15.76	19.69	2.64	3.00	1.40
0 6 16 47.44	-6 59 4.7	1.53	15.72	19.66	2.62	3.02	1.41
0 6 16 41.64	-6 59 11.9	1.54	15.82	19.66	2.62	3.05	1.42
0 6 16 35.59	-6 59 11.9	1.58	16.00	19.71	2.66	3.02	1.41
0 6 17 46.44	-7 0 38.3	1.44	16.16	19.31	2.29	3.55	1.66
0 6 17 40.88	-7 0 34.7	1.57	16.10	19.66	2.62	3.10	1.45
0 6 16 59.29	-7 0 31.2	1.56	16.16	19.63	2.59	3.14	1.47
0 6 16 54.45	-7 0 27.5	1.55	15.76	19.69	2.64	3.00	1.40
0 6 16 48.65	-7 0 23.9	1.52	15.67	19.64	2.59	3.04	1.42
0 6 16 41.88	-7 0 23.9	1.57	15.85	19.72	2.68	2.98	1.39
0 6 16 35.83	-7 0 23.9	1.62	16.02	19.82	2.77	2.91	1.36
0 6 17 47.41	-7 1 53.9	1.44	16.16	19.32	2.30	3.54	1.65
0 6 17 41.6	-7 1 57.5	1.55	16.10	19.61	2.57	3.16	1.48
0 6 17 0.01	-7 2 1.2	1.60	16.05	19.74	2.70	2.99	1.40
0 6 16 53.48	-7 2 4.7	1.52	15.80	19.62	2.58	3.09	1.44
0 6 16 47.92	-7 1 53.9	1.53	15.58	19.68	2.64	2.97	1.39
0 6 16 42.12	-7 1 57.5	1.54	15.92	19.63	2.59	3.09	1.45
0 6 16 35.59	-7 1 57.5	1.53	16.08	19.57	2.53	3.21	1.50
0 6 17 0.49	-7 3 34.8	1.58	16.15	19.69	2.65	3.07	1.44
0 6 16 54.45	-7 3 34.7	1.54	15.88	19.63	2.59	3.09	1.44
0 6 16 47.92	-7 3 31.1	1.50	15.80	19.57	2.53	3.15	1.47
0 6 16 41.87	-7 3 31.1	1.55	15.91	19.67	2.63	3.05	1.42
0 6 16 35.59	-7 3 34.7	1.55	15.99	19.65	2.61	3.09	1.44
0 6 16 59.04	-7 5 15.5	1.55	16.16	19.61	2.57	3.17	1.48
0 6 16 53.24	-7 5 8.3	1.55	16.00	19.63	2.59	3.11	1.45
0 6 16 47.19	-7 5 11.9	1.55	16.00	19.64	2.59	3.11	1.45
0 6 16 41.63	-7 5 11.9	1.56	16.02	19.67	2.62	3.08	1.44
0 6 16 35.83	-7 5 11.8	1.52	16.04	19.55	2.51	3.22	1.50

Table 29: The Database of far infrared cavity CASKK6 nearby to the AGB star AGB0619-0558 located with in G212-11. The first two columns represent position of the pixels with in the cavity. The next two columns give values of relative flux density at 60 μm and 100 μm that have obtained after processing the FITS image using ALADIN 2.5 software. The calculated values of dust color temperature (in K), Planck function and dust mass for 100 μm and visual extinction (in mag) of the corresponding pixels,respectively.

R.A.(J2000) hh mm ss	Dec.(J2000) dd mm ss	$F(60)$ (MJy)	$F(100)$ (MJy)	$T_{\rm d}$ (K)	$B(\nu,T)$ $(\times10^{-16})$ Js^{-2}	$M_{\rm d}$ $(\times10^{26})$ kg	A_V $(\times10^{-5})$ mag
0 6 21 19.91	-5 33 52	1.28	13.99	19.42	2.39	2.95	1.38
0 6 21 20.4	-5 35 18.4	1.29	13.94	19.46	2.43	2.89	1.35
0 6 21 37.76	-5 36 59.2	1.25	14.04	19.32	2.30	3.08	1.44
0 6 21 31.97	-5 36 55.6	1.17	13.96	19.09	2.10	3.35	1.56
0 6 21 27.15	-5 36 55.6	1.19	13.92	19.14	2.15	3.27	1.53
0 6 21 20.88	-5 37 10	1.27	13.76	19.46	2.43	2.86	1.33
0 6 21 14.13	-5 37 2.8	1.27	14.03	19.36	2.34	3.03	1.41
0 6 21 38.73	-5 38 25.6	1.21	13.89	19.24	2.23	3.14	1.47
0 6 21 32.94	-5 38 22	1.18	13.85	19.14	2.14	3.26	1.52
0 6 21 25.94	-5 38 18.4	1.14	13.79	19.03	2.05	3.38	1.58
0 6 21 21.36	-5 38 25.6	1.21	13.65	19.30	2.28	3.01	1.41
0 6 21 14.61	-5 38 29.2	1.25	13.92	19.34	2.32	3.02	1.41
0 6 20 57.25	-5 38 29.2	1.21	14.02	19.20	2.20	3.22	1.50
0 6 21 38.73	-5 39 51.9	1.16	13.76	19.10	2.11	3.28	1.53
0 6 21 32.21	-5 39 52	1.14	13.60	19.08	2.09	3.27	1.53
0 6 21 26.19	-5 39 55.6	1.16	13.65	19.13	2.14	3.22	1.50
0 6 21 21.12	-5 39 55.6	1.19	13.73	19.22	2.21	3.13	1.46
0 6 21 15.33	-5 39 59.2	1.23	13.77	19.31	2.29	3.03	1.42
0 6 21 8.58	-5 40 2.8	1.24	14.02	19.28	2.26	3.12	1.46
0 6 21 3.03	-5 39 59.2	1.24	14.04	19.27	2.26	3.13	1.46
0 6 20 56.76	-5 39 52	1.20	13.83	19.21	2.20	3.16	1.48
0 6 21 43.79	-5 41 18.3	1.26	13.90	19.37	2.34	2.99	1.39

continued on next page

Table 29 – continued from previous page

R.A.(J2000) hh mm ss	Dec.(J2000) dd mm ss	$F(60)$ (MJy)	$F(100)$ (MJy)	$T_{\rm d}$ (K)	$B(\nu,T)$ $(\times10^{-16})$ Js^{-2}	$M_{\rm d}$ $(\times10^{26})$ kg	A_V $(\times10^{-5})$ mag
0 6 21 38	-5 41 21.9	1.16	13.57	19.15	2.15	3.18	1.48
0 6 21 32.46	-5 41 22	1.16	13.57	19.13	2.14	3.20	1.49
0 6 21 26.91	-5 41 25.6	1.14	13.61	19.06	2.08	3.30	1.54
0 6 21 20.64	-5 41 25.6	1.13	13.62	19.05	2.07	3.32	1.55
0 6 21 15.57	-5 41 25.6	1.21	13.85	19.25	2.24	3.12	1.46
0 6 21 9.06	-5 41 22	1.22	13.92	19.25	2.24	3.13	1.46
0 6 21 3.27	-5 41 29.2	1.27	13.88	19.42	2.39	2.93	1.37
0 6 20 57.49	-5 41 29.2	1.24	13.90	19.31	2.29	3.06	1.43
0 6 21 50.31	-5 43 6.3	1.33	13.94	19.56	2.52	2.78	1.30
0 6 21 44.52	-5 42 59.1	1.20	13.68	19.25	2.23	3.08	1.44
0 6 21 38.25	-5 42 55.5	1.12	13.45	19.06	2.08	3.26	1.52
0 6 21 32.7	-5 42 59.2	1.07	13.43	18.89	1.94	3.48	1.63
0 6 21 26.67	-5 42 59.2	1.11	13.53	19.01	2.03	3.35	1.56
0 6 21 20.64	-5 42 48.4	1.15	13.61	19.11	2.12	3.24	1.51
0 6 21 15.09	-5 42 55.6	1.20	13.74	19.22	2.21	3.13	1.46
0 6 21 8.82	-5 43 2.8	1.22	13.92	19.25	2.24	3.13	1.46
0 6 21 3.76	-5 42 55.6	1.25	13.90	19.35	2.33	3.01	1.41
0 6 20 56.76	-5 42 55.6	1.28	14.00	19.41	2.38	2.96	1.38
0 6 21 49.34	-5 44 25.5	1.26	13.97	19.37	2.34	3.01	1.40
0 6 21 44.28	-5 44 18.3	1.17	13.55	19.18	2.17	3.14	1.47
0 6 21 38.25	-5 44 18.3	1.05	13.41	18.84	1.90	3.56	1.66
0 6 21 32.94	-5 44 22	1.03	13.49	18.74	1.83	3.72	1.74
0 6 21 27.39	-5 44 29.2	1.08	13.52	18.88	1.93	3.53	1.65
0 6 21 20.88	-5 44 25.6	1.17	13.52	19.21	2.20	3.09	1.44
0 6 21 14.85	-5 44 25.6	1.19	13.72	19.20	2.19	3.15	1.47
0 6 21 9.79	-5 44 14.8	1.17	14.05	19.06	2.08	3.40	1.59
0 6 21 3.27	-5 44 14.8	1.25	13.98	19.33	2.31	3.05	1.43
0 6 20 57.73	-5 44 14.8	1.29	14.03	19.43	2.40	2.94	1.37
0 6 21 49.59	-5 45 44.7	1.24	13.92	19.29	2.28	3.08	1.44
0 6 21 44.52	-5 45 44.7	1.16	13.51	19.15	2.15	3.16	1.48
0 6 21 38.97	-5 45 44.7	1.07	13.52	18.87	1.92	3.54	1.65
0 6 21 32.94	-5 45 52	1.05	13.49	18.79	1.86	3.64	1.70
0 6 21 27.64	-5 45 55.6	1.07	13.56	18.83	1.90	3.60	1.68
0 6 21 20.4	-5 45 52	1.17	13.54	19.20	2.20	3.10	1.45
0 6 21 15.33	-5 45 48.4	1.20	13.79	19.23	2.22	3.13	1.46
0 6 21 9.55	-5 45 59.2	1.25	14.03	19.29	2.27	3.11	1.45
0 6 21 3.27	-5 45 59.2	1.29	13.99	19.44	2.41	2.92	1.36
0 6 21 50.07	-5 47 18.3	1.22	13.90	19.24	2.23	3.14	1.46
0 6 21 43.8	-5 47 18.3	1.21	13.46	19.34	2.32	2.92	1.36
0 6 21 38.49	-5 47 18.3	1.13	13.48	19.06	2.08	3.27	1.53
0 6 21 32.46	-5 47 14.8	1.06	13.49	18.82	1.89	3.60	1.68
0 6 21 27.64	-5 47 11.2	1.06	13.54	18.81	1.87	3.64	1.70
0 6 21 21.12	-5 47 14.8	1.15	13.60	19.09	2.11	3.25	1.52
0 6 21 14.85	-5 47 25.6	1.18	13.71	19.18	2.18	3.17	1.48
0 6 21 10.27	-5 47 25.6	1.26	13.99	19.35	2.33	3.03	1.41
0 6 21 3.76	-5 47 14.8	1.29	14.03	19.43	2.40	2.95	1.38
0 6 21 51.04	-5 48 44.7	1.22	13.81	19.28	2.27	3.07	1.43
0 6 21 44.77	-5 48 44.7	1.20	13.48	19.31	2.29	2.96	1.38
0 6 21 38.74	-5 48 51.9	1.17	13.43	19.22	2.21	3.06	1.43
0 6 21 33.19	-5 48 52	1.09	13.49	18.95	1.98	3.42	1.60
0 6 21 26.92	-5 48 48.4	1.04	13.48	18.75	1.83	3.70	1.73
0 6 21 21.13	-5 48 52	1.12	13.39	19.06	2.08	3.25	1.52
0 6 21 15.58	-5 48 55.6	1.19	13.54	19.27	2.25	3.03	1.41
0 6 21 10.03	-5 48 48.4	1.15	13.90	19.03	2.06	3.40	1.59
0 6 21 3.52	-5 48 52	1.22	13.97	19.23	2.22	3.17	1.48
0 6 21 51.77	-5 50 25.5	1.19	13.73	19.21	2.20	3.14	1.47
0 6 21 44.77	-5 50 18.3	1.18	13.30	19.30	2.28	2.93	1.37
0 6 21 38.74	-5 50 18.3	1.11	13.16	19.11	2.12	3.13	1.46
0 6 21 32.95	-5 50 29.2	1.05	13.18	18.88	1.93	3.43	1.60
0 6 21 27.16	-5 50 25.6	0.99	13.14	18.67	1.77	3.73	1.74
0 6 21 22.09	-5 50 25.6	1.03	13.20	18.80	1.87	3.55	1.66
0 6 21 16.3	-5 50 25.6	1.12	13.41	19.05	2.07	3.27	1.53
0 6 21 9.31	-5 50 18.4	1.15	13.71	19.09	2.10	3.29	1.54
0 6 21 3.03	-5 50 14.8	1.17	13.91	19.10	2.11	3.32	1.55
0 6 22 2.62	-5 51 44.6	1.19	14.00	19.14	2.14	3.29	1.53
0 6 21 56.83	-5 51 41	1.20	13.98	19.17	2.17	3.25	1.52
0 6 21 51.77	-5 51 41.1	1.14	13.60	19.08	2.09	3.27	1.53
0 6 21 45.01	-5 51 48.3	1.10	13.09	19.09	2.10	3.13	1.46
0 6 21 39.95	-5 51 51.9	1.06	12.89	19.01	2.04	3.19	1.49
0 6 21 33.43	-5 51 48.4	1.00	12.94	18.76	1.84	3.54	1.65
0 6 21 27.88	-5 51 55.6	0.94	12.87	18.56	1.70	3.82	1.78
0 6 21 21.37	-5 51 48.4	0.98	12.92	18.71	1.81	3.60	1.68
0 6 21 15.1	-5 51 37.6	1.10	13.31	19.01	2.04	3.29	1.53
0 6 21 9.79	-5 51 52	1.16	13.62	19.13	2.13	3.21	1.50
0 6 21 3.76	-5 51 55.6	1.14	13.81	19.01	2.03	3.42	1.60
0 6 22 3.11	-5 53 21.8	1.19	13.96	19.14	2.14	3.28	1.53
0 6 21 56.35	-5 53 11.1	1.21	13.98	19.19	2.19	3.22	1.50

continued on next page

Table 29 – continued from previous page

R.A.(J2000) hh mm ss	Dec.(J2000) dd mm ss	$F(60)$ (MJy)	$F(100)$ (MJy)	$T_{\rm d}$ (K)	$B(\nu,T)$ $(\times10^{-16})$ Js^{-2}	$M_{\rm d}$ $(\times10^{26})$ kg	$A_{\rm V}$ $(\times10^{-5})$ mag
0 6 21 50.56	-5 53 14.7	1.16	13.52	19.17	2.17	3.14	1.47
0 6 21 44.77	-5 53 18.3	1.08	12.95	19.06	2.08	3.14	1.47
0 6 21 39.46	-5 53 18.3	1.03	12.77	18.92	1.96	3.28	1.53
0 6 21 34.16	-5 53 25.6	0.98	12.75	18.74	1.82	3.52	1.64
0 6 21 27.4	-5 53 25.6	0.90	12.75	18.45	1.62	3.97	1.85
0 6 21 21.85	-5 53 18.4	0.92	12.88	18.47	1.63	3.97	1.85
0 6 21 15.82	-5 53 22	1.06	13.19	18.93	1.97	3.37	1.57
0 6 21 9.79	-5 53 14.8	1.11	13.46	19.00	2.03	3.34	1.56
0 6 21 3.51	-5 53 22	1.08	13.72	18.83	1.89	3.65	1.70
0 6 22 4.08	-5 54 37.4	1.21	13.95	19.20	2.19	3.21	1.50
0 6 21 56.6	-5 54 41	1.16	13.94	19.05	2.07	3.40	1.59
0 6 21 49.6	-5 54 37.5	1.12	13.45	19.04	2.06	3.28	1.53
0 6 21 44.77	-5 54 44.7	1.06	12.89	19.00	2.03	3.20	1.49
0 6 21 40.19	-5 54 44.7	1.02	12.75	18.89	1.94	3.31	1.54
0 6 21 33.19	-5 54 52	0.95	12.78	18.64	1.75	3.67	1.71
0 6 21 28.13	-5 54 41.2	0.88	12.86	18.32	1.53	4.24	1.98
0 6 21 21.37	-5 54 37.6	0.93	12.85	18.54	1.68	3.86	1.80
0 6 21 15.58	-5 54 41.2	1.06	13.20	18.92	1.96	3.39	1.58
0 6 21 10.03	-5 54 41.2	1.08	13.38	18.93	1.97	3.41	1.59
0 6 21 3.76	-5 54 48.4	1.04	13.67	18.71	1.80	3.82	1.78
0 6 20 57	-5 54 44.8	1.11	13.95	18.88	1.93	3.64	1.70
0 6 22 3.6	-5 56 14.6	1.21	13.94	19.21	2.20	3.19	1.49
0 6 21 56.84	-5 56 11	1.16	13.80	19.08	2.10	3.31	1.55
0 6 21 50.81	-5 56 14.7	1.06	13.41	18.86	1.92	3.53	1.65
0 6 21 46.22	-5 56 14.7	1.08	13.09	19.01	2.04	3.23	1.51
0 6 21 40.43	-5 56 18.3	1.04	12.97	18.90	1.95	3.35	1.56
0 6 21 33.92	-5 56 11.2	1.00	13.02	18.75	1.83	3.58	1.67
0 6 21 27.4	-5 56 18.4	0.97	13.06	18.62	1.73	3.79	1.77
0 6 21 21.37	-5 56 14.8	0.99	12.97	18.71	1.80	3.62	1.69
0 6 21 16.06	-5 56 22	1.07	13.17	18.96	2.00	3.32	1.55
0 6 21 9.79	-5 56 14.8	1.08	13.47	18.92	1.97	3.45	1.61
0 6 21 3.76	-5 56 18.4	1.04	13.65	18.73	1.82	3.78	1.77
0 6 20 58.21	-5 56 22	1.09	13.91	18.83	1.90	3.69	1.73
0 6 22 8.43	-5 57 41	1.26	14.04	19.33	2.31	3.06	1.43
0 6 22 3.6	-5 57 41	1.22	13.87	19.26	2.24	3.11	1.45
0 6 21 55.4	-5 57 41.1	1.12	13.81	18.96	2.00	3.48	1.63
0 6 21 50.57	-5 57 41.1	1.13	13.59	19.04	2.06	3.32	1.55
0 6 21 45.98	-5 57 41.1	1.13	13.41	19.11	2.12	3.19	1.49
0 6 21 40.68	-5 57 41.1	1.11	13.38	19.03	2.06	3.28	1.53
0 6 21 33.68	-5 57 41.2	1.07	13.46	18.86	1.92	3.53	1.65
0 6 21 27.4	-5 57 44.8	1.07	13.33	18.91	1.96	3.43	1.60
0 6 21 21.61	-5 57 44.8	1.07	13.14	18.96	1.99	3.32	1.55
0 6 21 16.06	-5 57 41.2	1.12	13.28	19.09	2.10	3.18	1.48
0 6 21 9.79	-5 57 52	1.10	13.48	18.96	1.99	3.40	1.59
0 6 21 4.24	-5 57 48.4	1.07	13.66	18.81	1.88	3.66	1.71
0 6 20 57.96	-5 57 37.6	1.12	13.86	18.92	1.97	3.55	1.66
0 6 22 2.64	-5 59 21.8	1.26	13.91	19.38	2.36	2.97	1.39
0 6 21 57.33	-5 59 21.8	1.18	13.96	19.12	2.12	3.31	1.55
0 6 21 50.81	-5 59 18.3	1.16	13.74	19.09	2.10	3.29	1.54
0 6 21 45.99	-5 59 7.5	1.19	13.73	19.19	2.18	3.17	1.48
0 6 21 39.47	-5 59 14.7	1.19	13.57	19.24	2.23	3.06	1.43
0 6 21 33.44	-5 59 14.8	1.15	13.72	19.06	2.08	3.32	1.55
0 6 21 27.89	-5 59 22	1.08	13.54	18.88	1.93	3.53	1.65
0 6 21 21.61	-5 59 14.8	1.10	13.33	19.03	2.05	3.27	1.53
0 6 21 14.86	-5 59 18.4	1.13	13.42	19.10	2.11	3.20	1.50
0 6 21 9.55	-5 59 18.4	1.10	13.45	18.97	2.01	3.37	1.57
0 6 21 3.76	-5 59 14.8	1.10	13.64	18.94	1.98	3.47	1.62
0 6 20 57.72	-5 59 14.8	1.12	13.80	18.96	2.00	3.48	1.62
0 6 20 51.69	-5 59 14.8	1.15	14.04	18.98	2.01	3.51	1.64
0 6 22 8.67	-6 0 48.2	1.40	14.01	19.75	2.71	2.61	1.22
0 6 22 2.16	-6 0 44.6	1.27	14.00	19.37	2.34	3.01	1.40
0 6 21 57.33	-6 0 41	1.18	13.98	19.10	2.11	3.34	1.56
0 6 21 50.81	-6 0 41.1	1.17	13.89	19.09	2.10	3.33	1.55
0 6 21 45.02	-6 0 37.5	1.20	13.91	19.17	2.17	3.23	1.51
0 6 21 40.2	-6 0 41.1	1.21	13.81	19.23	2.22	3.13	1.46
0 6 21 33.2	-6 0 34	1.17	13.92	19.08	2.09	3.35	1.56
0 6 21 27.41	-6 0 41.2	1.13	13.71	18.99	2.02	3.41	1.59
0 6 21 21.61	-6 0 37.6	1.10	13.52	18.95	1.99	3.42	1.60
0 6 21 15.1	-6 0 41.2	1.19	13.54	19.26	2.25	3.03	1.42
0 6 21 10.03	-6 0 37.6	1.17	13.62	19.16	2.16	3.18	1.48
0 6 21 4.24	-6 0 41.2	1.11	13.72	18.93	1.97	3.50	1.63
0 6 20 58.21	-6 0 52	1.12	13.87	18.94	1.98	3.53	1.65
0 6 22 9.4	-6 2 14.6	1.30	13.98	19.47	2.43	2.89	1.35
0 6 22 3.12	-6 2 7.4	1.24	14.01	19.28	2.27	3.11	1.45
0 6 21 39.96	-6 2 11.1	1.25	13.95	19.32	2.30	3.06	1.43
0 6 21 33.68	-6 2 14.8	1.19	14.00	19.14	2.14	3.29	1.54
0 6 21 27.41	-6 2 25.6	1.16	13.84	19.06	2.08	3.35	1.56

continued on next page

Table 29 – continued from previous page

R.A.(J2000) hh mm ss	Dec.(J2000) dd mm ss	$F(60)$ (MJy)	$F(100)$ (MJy)	T_d (K)	$B(\nu,T)$ $(\times10^{-16})$ Js^{-2}	M_d $(\times10^{26})$ kg	A_V $(\times10^{-5})$ mag
0 6 21 21.13	-6 2 22	1.19	13.65	19.21	2.20	3.12	1.46
0 6 21 16.06	-6 2 22	1.21	13.66	19.28	2.26	3.04	1.42
0 6 21 10.03	-6 2 18.4	1.21	13.75	19.28	2.26	3.06	1.43
0 6 21 4.24	-6 2 11.2	1.10	13.79	18.89	1.94	3.58	1.67
0 6 20 58.45	-6 2 22	1.12	13.89	18.92	1.97	3.56	1.66
0 6 20 51.93	-6 2 14.8	1.12	14.04	18.90	1.95	3.63	1.69
0 6 22 9.4	-6 3 44.6	1.19	13.95	19.13	2.14	3.28	1.53
0 6 21 27.65	-6 3 52	1.19	13.95	19.15	2.16	3.26	1.52
0 6 21 22.58	-6 3 41.2	1.21	13.76	19.27	2.26	3.07	1.43
0 6 21 16.31	-6 3 41.2	1.24	13.85	19.33	2.31	3.03	1.41
0 6 21 9.31	-6 3 41.2	1.22	13.79	19.29	2.27	3.06	1.43
0 6 21 3.03	-6 3 41.2	1.13	13.86	18.97	2.00	3.48	1.63
0 6 20 57.48	-6 3 37.6	1.14	13.94	18.97	2.01	3.50	1.63
0 6 22 10.13	-6 5 7.4	1.20	13.95	19.17	2.17	3.24	1.51
0 6 21 27.65	-6 5 14.8	1.21	13.87	19.23	2.22	3.15	1.47
0 6 21 21.86	-6 5 14.8	1.22	13.75	19.28	2.27	3.05	1.43
0 6 21 15.82	-6 5 22	1.16	13.77	19.10	2.11	3.29	1.53
0 6 21 9.07	-6 5 22	1.20	13.75	19.24	2.23	3.11	1.45
0 6 21 3.76	-6 5 7.6	1.14	13.82	19.01	2.04	3.42	1.60
0 6 20 57.48	-6 5 7.6	1.12	13.92	18.91	1.96	3.58	1.67
0 6 21 28.13	-6 6 37.6	1.23	13.92	19.27	2.26	3.10	1.45
0 6 21 21.86	-6 6 41.2	1.18	13.72	19.17	2.17	3.19	1.49
0 6 21 16.07	-6 6 37.6	1.16	13.68	19.10	2.11	3.26	1.52
0 6 21 9.31	-6 6 34	1.14	13.79	19.01	2.04	3.40	1.59
0 6 21 3.76	-6 6 34	1.15	13.91	19.02	2.04	3.43	1.60
0 6 20 57.96	-6 6 41.2	1.16	13.97	19.05	2.07	3.40	1.59
0 6 21 28.14	-6 8 4	1.20	13.80	19.21	2.20	3.15	1.47
0 6 21 21.86	-6 8 7.6	1.18	13.64	19.19	2.19	3.14	1.47
0 6 21 16.55	-6 8 14.8	1.15	13.67	19.08	2.10	3.28	1.53
0 6 21 10.03	-6 8 7.6	1.16	13.82	19.07	2.09	3.34	1.56
0 6 21 4.24	-6 7 56.8	1.18	13.93	19.11	2.12	3.30	1.54
0 6 21 28.14	-6 9 26.8	1.19	13.81	19.17	2.17	3.21	1.50
0 6 21 21.38	-6 9 37.6	1.18	13.63	19.19	2.19	3.14	1.47
0 6 21 15.58	-6 9 34	1.11	13.68	18.96	1.99	3.45	1.61
0 6 21 10.51	-6 9 34	1.16	13.81	19.10	2.11	3.30	1.54
0 6 21 4.48	-6 9 37.6	1.20	13.92	19.18	2.18	3.22	1.50
0 6 21 27.41	-6 11 0.4	1.19	13.97	19.15	2.15	3.27	1.53
0 6 21 22.1	-6 11 11.2	1.19	13.68	19.23	2.22	3.10	1.45
0 6 21 16.31	-6 11 0.4	1.19	13.65	19.22	2.21	3.11	1.45
0 6 21 10.27	-6 11 7.6	1.20	13.79	19.22	2.21	3.14	1.46
0 6 21 4.24	-6 11 7.6	1.19	13.83	19.17	2.17	3.22	1.50
0 6 21 22.1	-6 12 37.6	1.26	13.73	19.42	2.39	2.90	1.35
0 6 21 15.1	-6 12 37.6	1.22	13.63	19.32	2.30	2.99	1.40
0 6 21 10.27	-6 12 26.8	1.21	13.76	19.27	2.26	3.07	1.43
0 6 21 4	-6 12 30.4	1.16	13.87	19.07	2.09	3.35	1.56
0 6 21 21.62	-6 14 4	1.24	13.86	19.31	2.29	3.05	1.42
0 6 21 15.59	-6 14 14.8	1.25	13.73	19.40	2.38	2.91	1.36
0 6 21 10.76	-6 14 7.6	1.27	13.90	19.41	2.38	2.94	1.37
0 6 21 4.72	-6 14 11.2	1.18	13.95	19.10	2.11	3.33	1.56
0 6 21 16.31	-6 15 37.6	1.30	13.92	19.50	2.47	2.84	1.33
0 6 21 10.03	-6 15 37.6	1.26	13.96	19.35	2.33	3.02	1.41
0 6 21 4	-6 15 34	1.21	14.02	19.19	2.19	3.22	1.51
0 6 21 15.1	-6 17 7.6	1.32	14.00	19.52	2.48	2.84	1.33
0 6 21 21.62	-6 18 44.8	1.18	14.02	19.08	2.09	3.38	1.58
0 6 21 16.07	-6 18 44.8	1.27	14.03	19.37	2.34	3.01	1.41

Table 30: The Database of far infrared cavity CASKK7 nearby to the AGB star AGB0712-1720 located with in G229-03. The first two columns represent position of the pixels with in the cavity. The next two columns give values of relative flux density at 60 μm and 100 μm that have obtained after processing the FITS image using ALADIN 2.5 software. The calculated values of dust color temperature (in K), Planck function and dust mass for 100 μm and visual extinction (in mag) of the corresponding pixels,respectively.

R.A.(J2000) hh mm ss	Dec.(J2000) dd mm ss	$F(60)$ (MJy)	$F(100)$ (MJy)	T_d (K)	$B(\nu,T)$ $(\times10^{-16})$ Js^{-2}	M_d $(\times10^{27})$ kg	A_V $(\times10^{-5})$ mag
07 06 30.74	-17 12 13.7	1.05	12.78	18.99	2.02	2.15	1.49
07 06 24.46	-17 12 6.4	1.00	13.01	18.75	1.83	2.42	1.67
07 06 36.52	-17 13 36.5	1.07	13.09	18.99	2.02	2.20	1.52
07 06 31.49	-17 13 43.7	1.02	12.69	18.91	1.96	2.20	1.52
07 06 24.71	-17 13 43.6	0.96	12.75	18.68	1.78	2.43	1.68
07 06 19.18	-17 13 43.6	0.91	12.93	18.43	1.61	2.74	1.89
07 06 12.14	-17 13 36.3	0.92	12.93	18.49	1.65	2.67	1.85
07 06 37.77	-17 15 13.7	1.03	13.04	18.85	1.91	2.32	1.61
07 06 30.73	-17 15 13.6	0.97	12.58	18.75	1.84	2.33	1.61

continued on next page

Table 30 – continued from previous page

R.A.(J2000) hh mm ss	Dec.(J2000) dd mm ss	$F(60)$ (MJy)	$F(100)$ (MJy)	$T_{\rm d}$ (K)	$B(\nu,T)$ $(\times10^{-16})$ Js^{-2}	$M_{\rm d}$ $(\times10^{27})$ kg	$A_{\rm V}$ $(\times10^{-5})$ mag
07 06 24.7	-17 15 13.6	0.86	12.49	18.35	1.55	2.74	1.89
07 06 18.67	-17 15 13.5	0.83	12.61	18.22	1.46	2.93	2.02
07 06 11.88	-17 15 20.7	0.88	12.77	18.36	1.56	2.79	1.93
07 06 5.35	-17 15 17	0.96	12.76	18.66	1.76	2.46	1.70
07 06 59.57	-17 15 13.3	1.10	13.00	19.11	2.12	2.09	1.44
07 06 37.26	-17 16 47.3	1.03	13.00	18.87	1.93	2.29	1.58
07 06 30.73	-17 16 43.6	0.96	12.63	18.70	1.80	2.39	1.65
07 06 25.2	-17 16 50.8	0.85	12.39	18.34	1.54	2.73	1.89
07 06 18.16	-17 16 47.1	0.80	12.35	18.14	1.42	2.97	2.05
07 06 12.38	-17 16 47.1	0.81	12.56	18.15	1.42	3.01	2.08
07 06 5.85	-17 16 43.4	0.91	12.57	18.53	1.67	2.56	1.77
07 06 0.07	-17 16 43.3	1.08	12.77	19.11	2.12	2.05	1.42
07 06 53.53	-17 16 39.6	1.16	13.08	19.28	2.27	1.96	1.36
07 06 37.01	-17 18 13.7	1.01	12.96	18.82	1.89	2.34	1.61
07 06 30.98	-17 18 17.2	0.98	12.66	18.79	1.87	2.31	1.60
07 06 24.44	-17 18 13.6	0.91	12.41	18.59	1.72	2.46	1.70
07 06 17.66	-17 18 17.1	0.84	12.39	18.29	1.51	2.79	1.93
07 06 12.38	-17 18 13.5	0.84	12.59	18.26	1.49	2.88	1.99
07 06 6.09	-17 18 20.6	0.86	12.68	18.32	1.53	2.82	1.95
07 06 0.31	-17 18 24.1	1.07	12.87	19.05	2.07	2.12	1.46
07 06 53.78	-17 18 20.4	1.20	13.01	19.45	2.42	1.83	1.26
07 06 37.26	-17 19 40.1	1.00	12.98	18.75	1.84	2.41	1.66
07 06 29.97	-17 19 43.6	1.02	12.85	18.86	1.92	2.28	1.57
07 06 23.94	-17 19 40	0.94	12.51	18.67	1.77	2.40	1.66
07 06 17.9	-17 19 47.1	0.90	12.55	18.51	1.66	2.58	1.78
07 06 12.12	-17 19 50.7	0.88	12.82	18.33	1.54	2.84	1.96
07 06 5.33	-17 19 57.8	0.90	12.99	18.37	1.56	2.83	1.95
07 06 59.8	-17 19 46.9	1.11	13.06	19.11	2.12	2.10	1.45
07 06 37.76	-17 21 17.3	0.98	13.00	18.67	1.78	2.49	1.72
07 06 30.47	-17 21 17.2	1.01	12.95	18.81	1.88	2.34	1.62
07 06 24.94	-17 21 17.2	0.99	12.62	18.83	1.89	2.27	1.57
07 06 17.65	-17 21 17.1	0.92	12.71	18.52	1.67	2.60	1.79
07 06 11.86	-17 21 20.7	0.92	12.92	18.49	1.65	2.67	1.85
07 06 5.58	-17 21 17	0.87	13.07	18.23	1.47	3.03	2.09
07 06 43.29	-17 22 40.1	0.95	13.15	18.52	1.66	2.69	1.86
07 06 37.01	-17 22 36.5	0.98	12.95	18.70	1.80	2.45	1.69
07 06 30.72	-17 22 40	1.01	12.95	18.81	1.88	2.34	1.62
07 06 25.44	-17 22 40	1.05	12.81	18.99	2.02	2.16	1.49
07 06 18.65	-17 22 47.1	0.93	12.86	18.55	1.69	2.60	1.79
07 06 12.61	-17 22 47.1	0.94	13.03	18.53	1.67	2.65	1.83
07 06 51.09	-17 24 10.1	1.04	13.14	18.86	1.92	2.33	1.61
07 06 43.54	-17 24 17.3	1.03	13.06	18.83	1.90	2.34	1.62
07 06 37	-17 24 13.7	0.93	13.05	18.48	1.64	2.71	1.87
07 06 31.47	-17 24 10	0.99	12.90	18.74	1.82	2.41	1.66
07 06 24.68	-17 24 13.6	1.01	12.77	18.84	1.90	2.28	1.58
07 06 19.4	-17 24 13.5	0.97	12.87	18.66	1.77	2.48	1.71
07 06 11.6	-17 24 20.7	0.95	13.09	18.53	1.67	2.66	1.84
07 06 55.87	-17 25 47.3	1.02	13.00	18.83	1.89	2.34	1.61
07 06 50.33	-17 25 47.3	1.01	12.96	18.82	1.89	2.34	1.61
07 06 43.79	-17 25 43.7	0.96	12.82	18.64	1.75	2.49	1.72
07 06 37.5	-17 25 43.7	0.89	12.86	18.36	1.56	2.81	1.94
07 06 31.72	-17 25 47.2	0.89	12.73	18.43	1.60	2.71	1.87
07 06 24.93	-17 25 47.2	0.98	12.78	18.73	1.82	2.39	1.65
07 06 18.89	-17 25 54.3	0.94	12.74	18.60	1.72	2.52	1.74
07 06 11.85	-17 25 50.7	0.92	13.01	18.47	1.63	2.72	1.88
07 06 56.12	-17 27 17.3	0.96	12.91	18.64	1.75	2.50	1.73
07 06 48.82	-17 27 20.9	0.89	12.57	18.46	1.63	2.63	1.82
07 06 44.04	-17 27 13.7	0.91	12.47	18.57	1.70	2.49	1.72
07 06 37.5	-17 27 24.5	0.84	12.42	18.30	1.51	2.79	1.93
07 06 30.96	-17 27 20.8	0.87	12.48	18.40	1.59	2.68	1.85
07 06 24.92	-17 27 17.2	0.91	12.56	18.54	1.68	2.55	1.76
07 06 19.39	-17 27 17.1	0.93	12.51	18.62	1.73	2.46	1.70
07 06 12.6	-17 27 20.7	0.91	12.82	18.46	1.63	2.68	1.85
07 07 6.56	-17 27 13.4	0.92	13.05	18.43	1.60	2.77	1.92
07 06 2.41	-17 28 43.7	0.98	12.87	18.73	1.82	2.41	1.66
07 06 55.62	-17 28 47.3	0.89	12.40	18.49	1.64	2.57	1.78
07 06 50.08	-17 28 47.3	0.81	12.24	18.23	1.47	2.83	1.96
07 06 44.29	-17 28 47.3	0.85	12.11	18.41	1.59	2.59	1.79
07 06 37.5	-17 28 43.7	0.83	12.23	18.32	1.53	2.73	1.88
07 06 31.21	-17 28 43.6	0.89	12.34	18.50	1.65	2.54	1.75
07 06 25.17	-17 28 43.6	0.93	12.55	18.64	1.75	2.44	1.69
07 06 18.38	-17 28 43.5	0.96	12.35	18.80	1.87	2.24	1.55
07 06 12.34	-17 28 50.7	0.90	12.66	18.48	1.64	2.63	1.81
07 06 5.8	-17 28 47	0.93	12.96	18.51	1.66	2.65	1.83
07 06 59.26	-17 28 50.5	1.00	13.15	18.70	1.79	2.49	1.72
07 06 1.91	-17 30 10.1	0.96	12.61	18.72	1.81	2.37	1.64
07 06 56.37	-17 30 10.1	0.82	11.97	18.35	1.55	2.63	1.82

continued on next page

Table 30 – continued from previous page

R.A.(J2000) hh mm ss	Dec.(J2000) dd mm ss	$F(60)$ (MJy)	$F(100)$ (MJy)	$T_{\rm d}$ (K)	$B(\nu,T)$ $(\times10^{-16})$ Js^{-2}	$M_{\rm d}$ $(\times10^{27})$ kg	$A_{\rm V}$ $(\times10^{-5})$ mag
07 06 50.08	-17 30 10.1	0.72	11.88	17.91	1.28	3.17	2.19
07 06 44.04	-17 30 24.5	0.77	11.89	18.17	1.43	2.83	1.95
07 06 38.25	-17 30 2.9	0.84	12.15	18.39	1.58	2.62	1.81
07 06 30.7	-17 30 6.4	0.88	12.29	18.50	1.65	2.53	1.75
07 06 24.92	-17 30 13.6	0.96	12.45	18.77	1.85	2.29	1.58
07 06 18.88	-17 30 9.9	0.95	12.37	18.74	1.82	2.31	1.59
07 06 12.33	-17 30 9.9	0.87	12.49	18.38	1.57	2.70	1.87
07 05 6.55	-17 30 17	0.88	12.73	18.38	1.57	2.76	1.91
07 07 59.25	-17 30 13.3	0.95	12.99	18.57	1.70	2.60	1.80
07 07 8.45	-17 31 43.7	0.99	12.87	18.77	1.85	2.37	1.64
07 06 1.66	-17 31 43.7	0.91	12.39	18.58	1.71	2.47	1.71
07 06 55.62	-17 31 43.7	0.78	11.88	18.19	1.44	2.80	1.93
07 06 49.58	-17 31 50.9	0.66	11.66	17.70	1.16	3.41	2.36
07 06 43.29	-17 31 47.3	0.71	11.80	17.90	1.27	3.15	2.18
07 06 37.25	-17 31 40.1	0.78	12.00	18.15	1.42	2.87	1.98
07 06 29.7	-17 31 32.8	0.83	12.22	18.32	1.53	2.72	1.88
07 06 24.66	-17 31 40	0.88	12.19	18.53	1.67	2.48	1.71
07 06 17.36	-17 31 39.9	0.88	12.23	18.53	1.67	2.49	1.72
07 06 12.08	-17 31 39.9	0.85	12.25	18.39	1.58	2.65	1.83
07 05 05.03	-17 31 39.8	0.83	12.52	18.22	1.46	2.91	2.01
07 05 58.99	-17 31 36.1	0.85	12.70	18.25	1.49	2.91	2.01
07 05 54.46	-17 31 43.2	1.06	12.83	19.00	2.03	2.15	1.48
07 07 46.66	-17 31 46.6	1.15	13.00	19.29	2.27	1.95	1.35
07 07 14.25	-17 33 13.6	0.97	12.94	18.64	1.75	2.51	1.73
07 07 07.45	-17 33 20.9	0.92	12.53	18.57	1.70	2.51	1.73
07 06 01.66	-17 33 10.1	0.90	12.24	18.58	1.71	2.43	1.68
07 06 54.86	-17 33 13.7	0.81	11.87	18.32	1.53	2.64	1.83
07 06 49.83	-17 33 6.5	0.67	11.71	17.74	1.18	3.37	2.33
07 06 43.54	-17 33 13.7	0.70	11.80	17.83	1.24	3.25	2.24
07 06 37.75	-17 33 17.3	0.66	11.84	17.65	1.14	3.54	2.45
07 06 30.95	-17 33 13.6	0.70	11.99	17.80	1.22	3.36	2.32
07 06 25.66	-17 33 17.2	0.77	12.13	18.06	1.37	3.02	2.08
07 06 17.86	-17 33 17.1	0.85	12.09	18.44	1.61	2.56	1.76
07 06 12.32	-17 33 13.5	0.88	12.10	18.56	1.69	2.44	1.68
07 06 05.78	-17 33 20.6	0.79	12.39	18.07	1.37	3.07	2.12
07 05 00.24	-17 33 13.3	0.80	12.41	18.12	1.40	3.01	2.08
07 05 54.2	-17 33 24	0.95	12.52	18.72	1.81	2.36	1.63
07 05 47.65	-17 33 23.9	1.08	12.71	19.12	2.13	2.04	1.41
07 07 41.61	-17 33 23.7	1.08	13.03	19.04	2.06	2.15	1.49
07 07 15.26	-17 34 43.6	1.00	12.76	18.81	1.88	2.31	1.60
07 07 8.96	-17 34 40.1	0.87	12.33	18.42	1.60	2.62	1.81
07 06 1.41	-17 34 43.7	0.87	12.20	18.47	1.63	2.55	1.76
07 06 55.62	-17 34 43.7	0.81	11.94	18.29	1.51	2.68	1.85
07 06 49.33	-17 34 36.5	0.76	11.67	18.15	1.42	2.80	1.93
07 06 42.53	-17 34 32.9	0.70	11.73	17.87	1.26	3.18	2.20
07 06 36.74	-17 34 40.1	0.71	11.94	17.87	1.26	3.23	2.23
07 06 31.7	-17 34 40	0.73	12.00	17.91	1.28	3.20	2.21
07 06 24.4	-17 34 32.8	0.82	12.17	18.28	1.50	2.76	1.90
07 06 18.61	-17 34 32.7	0.91	12.07	18.67	1.77	2.32	1.60
07 06 11.31	-17 34 36.3	0.90	12.02	18.64	1.75	2.34	1.61
07 05 4.76	-17 34 43.4	0.78	12.30	18.08	1.38	3.03	2.09
07 05 59.73	-17 34 32.5	0.79	12.34	18.10	1.39	3.02	2.08
07 05 54.44	-17 34 54	0.83	12.34	18.26	1.49	2.82	1.95
07 05 48.15	-17 34 46.7	0.96	12.46	18.74	1.83	2.32	1.60
07 07 40.85	-17 34 35.7	0.99	12.88	18.77	1.85	2.38	1.64
07 07 28.1	-17 36 20.7	1.03	13.14	18.82	1.89	2.37	1.64
07 07 21.55	-17 36 6.4	1.07	12.99	19.00	2.03	2.18	1.51
07 07 15.01	-17 36 17.2	1.03	12.75	18.92	1.97	2.20	1.52
07 07 8.21	-17 36 10.1	0.93	12.37	18.66	1.77	2.38	1.64
07 06 2.42	-17 36 13.7	0.86	12.28	18.40	1.59	2.64	1.82
07 06 55.62	-17 36 10.1	0.84	11.85	18.48	1.64	2.47	1.70
07 06 50.84	-17 36 6.5	0.76	11.64	18.16	1.43	2.77	1.91
07 06 44.79	-17 36 2.9	0.72	11.83	17.94	1.30	3.11	2.15
07 06 38.25	-17 36 2.9	0.78	12.09	18.14	1.42	2.90	2.01
07 06 31.2	-17 36 13.6	0.77	12.25	18.06	1.37	3.04	2.10
07 06 25.41	-17 36 10	0.82	12.38	18.24	1.48	2.85	1.97
07 06 18.86	-17 36 13.5	0.92	12.25	18.68	1.78	2.34	1.61
07 06 12.31	-17 36 9.9	0.93	12.09	18.77	1.85	2.23	1.54
07 05 6.52	-17 36 6.2	0.81	12.28	18.20	1.46	2.87	1.98
07 05 58.97	-17 36 16.9	0.82	12.34	18.25	1.48	2.83	1.96
07 05 52.92	-17 36 16.8	0.90	12.39	18.53	1.67	2.52	1.74
07 05 47.89	-17 36 20.3	0.95	12.51	18.70	1.79	2.37	1.64
07 05 40.59	-17 36 16.5	0.99	12.78	18.79	1.86	2.33	1.61
07 07 35.55	-17 36 20	1.00	13.12	18.72	1.81	2.46	1.70
07 07 28.11	-17 37 47.1	1.09	13.10	19.05	2.07	2.16	1.49
07 07 21.56	-17 37 40	1.07	12.90	19.03	2.06	2.14	1.47
07 07 14.76	-17 37 43.6	1.03	12.76	18.91	1.96	2.22	1.53

continued on next page

Table 30 – continued from previous page

R.A.(J2000) hh mm ss	Dec.(J2000) dd mm ss	$F(60)$ (MJy)	$F(100)$ (MJy)	$T_{\rm d}$ (K)	$B(\nu,T)$ $(\times10^{-16})$ Js^{-2}	$M_{\rm d}$ $(\times10^{27})$ kg	$A_{\rm V}$ $(\times10^{-5})$ mag
07 07 8.21	-17 37 47.3	0.94	12.35	18.72	1.81	2.33	1.61
07 06 1.92	-17 37 43.7	0.88	12.25	18.50	1.65	2.53	1.75
07 06 56.88	-17 37 40.1	0.84	11.94	18.45	1.62	2.51	1.73
07 06 51.09	-17 37 43.7	0.80	11.71	18.33	1.54	2.59	1.79
07 06 43.53	-17 37 43.7	0.76	12.04	18.08	1.38	2.98	2.06
07 06 37.24	-17 37 40.1	0.82	12.31	18.22	1.47	2.86	1.97
07 06 30.69	-17 37 50.8	0.81	12.45	18.17	1.43	2.96	2.04
07 06 24.9	-17 37 40	0.83	12.49	18.25	1.49	2.86	1.98
07 06 18.1	-17 37 39.9	0.93	12.37	18.67	1.77	2.38	1.64
07 06 12.06	-17 37 39.9	0.98	12.25	18.91	1.96	2.13	1.47
07 05 5.51	-17 37 32.6	0.89	12.35	18.52	1.67	2.52	1.74
07 05 59.21	-17 37 39.7	0.87	12.39	18.41	1.59	2.65	1.83
07 05 53.67	-17 37 39.6	0.89	12.42	18.50	1.65	2.56	1.77
07 05 47.63	-17 37 50.3	0.97	12.58	18.77	1.85	2.32	1.60
07 07 41.08	-17 37 46.5	1.02	12.79	18.88	1.93	2.26	1.56
07 07 26.6	-17 39 6.3	1.12	13.14	19.13	2.13	2.10	1.45
07 07 20.56	-17 39 13.6	1.08	12.91	19.07	2.08	2.11	1.46
07 07 13.76	-17 39 24.4	1.06	12.72	19.04	2.06	2.10	1.45
07 07 8.72	-17 39 24.5	0.90	12.56	18.51	1.66	2.57	1.78
07 06 3.18	-17 39 20.9	0.92	12.46	18.62	1.74	2.44	1.69
07 06 56.38	-17 39 10.1	0.90	12.12	18.64	1.75	2.35	1.62
07 06 50.33	-17 39 6.5	0.82	11.99	18.32	1.53	2.66	1.84
07 06 43.78	-17 39 6.5	0.77	12.22	18.07	1.37	3.03	2.09
07 06 38.24	-17 39 13.7	0.85	12.51	18.32	1.53	2.78	1.92
07 06 31.95	-17 39 17.2	0.82	12.56	18.16	1.43	2.99	2.07
07 06 25.65	-17 39 10	0.84	12.71	18.22	1.46	2.96	2.04
07 06 17.84	-17 39 20.7	0.96	12.33	18.81	1.87	2.24	1.55
07 06 12.05	-17 39 17.1	0.98	12.31	18.89	1.94	2.16	1.49
07 05 6.76	-17 39 13.4	0.93	12.41	18.66	1.77	2.39	1.65
07 05 59.71	-17 39 13.3	0.86	12.53	18.35	1.55	2.75	1.90
07 05 52.4	-17 39 9.5	0.90	12.70	18.45	1.62	2.67	1.85
07 5 47.62	-17 39 9.4	1.00	12.74	18.84	1.90	2.28	1.58
07 07 41.32	-17 39 9.3	1.03	12.90	18.90	1.95	2.26	1.56
07 07 21.32	-17 40 36.4	1.09	12.89	19.09	2.11	2.08	1.44
07 07 14.51	-17 40 40	1.06	12.79	19.04	2.06	2.11	1.46
07 07 8.47	-17 40 40.1	0.94	12.58	18.66	1.77	2.43	1.68
07 06 2.93	-17 40 43.7	0.95	12.44	18.71	1.81	2.34	1.62
07 06 56.38	-17 40 50.9	0.96	12.33	18.79	1.86	2.25	1.56
07 06 50.58	-17 40 36.5	0.89	12.30	18.55	1.69	2.48	1.71
07 06 43.53	-17 40 40.1	0.84	12.49	18.27	1.50	2.84	1.96
07 06 38.75	-17 40 47.3	0.84	12.65	18.21	1.46	2.95	2.03
07 06 30.94	-17 40 54.4	0.82	12.65	18.16	1.43	3.01	2.08
07 06 26.15	-17 40 43.6	0.85	12.65	18.27	1.50	2.87	1.98
07 06 18.59	-17 40 50.7	0.91	12.50	18.57	1.70	2.50	1.73
07 06 12.55	-17 40 39.9	0.97	12.43	18.81	1.88	2.25	1.56
07 05 06.0	-17 40 43.4	0.91	12.41	18.60	1.72	2.46	1.70
07 05 58.95	-17 40 46.9	0.88	12.74	18.37	1.56	2.78	1.92
07 07 53.66	-17 40 36	0.95	12.99	18.58	1.71	2.59	1.79
07 07 27.87	-17 42 20.7	1.04	12.99	18.88	1.94	2.28	1.58
07 07 21.82	-17 42 10	1.10	12.75	19.19	2.18	1.99	1.37
07 07 15.02	-17 42 17.2	1.10	12.70	19.21	2.20	1.96	1.35
07 07 9.73	-17 42 17.2	1.01	12.64	18.91	1.96	2.20	1.52
07 06 03.68	-17 42 17.3	0.93	12.40	18.65	1.76	2.40	1.66
07 06 56.88	-17 42 17.3	0.96	12.61	18.71	1.80	2.38	1.64
07 06 49.32	-17 42 13.7	0.95	12.53	18.70	1.79	2.38	1.64
07 06 43.03	-17 42 6.5	0.91	12.65	18.52	1.67	2.59	1.79
07 06 37.48	-17 42 6.5	0.86	12.67	18.32	1.53	2.82	1.95
07 06 31.69	-17 42 13.6	0.88	12.62	18.39	1.58	2.72	1.88
07 06 24.64	-17 42 17.2	0.88	12.61	18.40	1.59	2.71	1.87
07 06 18.09	-17 42 13.5	0.92	12.67	18.56	1.70	2.54	1.76
07 06 11.54	-17 42 9.9	0.95	12.61	18.68	1.78	2.41	1.66
07 06 6.5	-17 42 17	0.95	12.65	18.68	1.78	2.42	1.67
07 07 0.2	-17 42 6.1	0.97	12.97	18.64	1.75	2.52	1.74
07 07 28.38	-17 43 54.3	0.97	12.78	18.70	1.80	2.42	1.67
07 07 20.32	-17 43 47.2	1.06	12.61	19.09	2.10	2.05	1.41
07 07 15.02	-17 43 36.4	1.06	12.58	19.08	2.09	2.05	1.41
07 07 10.24	-17 43 43.6	1.01	12.56	18.93	1.97	2.17	1.50
07 06 2.68	-17 43 36.5	0.98	12.52	18.80	1.87	2.28	1.57
07 06 57.14	-17 43 40.1	0.98	12.63	18.79	1.86	2.31	1.60
07 06 50.08	-17 43 43.7	1.02	12.63	18.93	1.97	2.18	1.51
07 06 44.29	-17 43 40.1	0.97	12.65	18.73	1.82	2.36	1.63
07 06 37.73	-17 43 43.7	0.87	12.59	18.37	1.57	2.74	1.89
07 06 29.92	-17 43 43.6	0.88	12.70	18.38	1.57	2.75	1.90
07 06 24.63	-17 43 54.4	0.86	12.73	18.28	1.50	2.88	1.99
07 06 18.33	-17 43 43.5	0.97	12.85	18.68	1.78	2.45	1.69
07 06 12.29	-17 43 47.1	1.03	12.87	18.90	1.95	2.25	1.55
07 07 5.23	-17 43 43.4	1.10	13.05	19.09	2.10	2.11	1.46

continued on next page

Table 30 – continued from previous page

R.A.(J2000) hh mm ss	Dec.(J2000) dd mm ss	$F(60)$ (MJy)	$F(100)$ (MJy)	T_d (K)	$B(\nu,T)$ $(\times10^{-16})$ Js^{-2}	M_d $(\times10^{27})$ kg	A_V $(\times10^{-5})$ mag
07 07 28.13	-17 45 20.7	0.99	12.91	18.73	1.82	2.42	1.67
07 07 21.58	-17 45 20.8	1.01	12.68	18.90	1.95	2.22	1.53
07 07 14.52	-17 45 13.6	1.07	12.78	19.08	2.09	2.08	1.44
07 07 9.23	-17 45 13.6	1.07	12.71	19.11	2.11	2.05	1.41
07 06 2.93	-17 45 10.1	1.04	12.81	18.94	1.98	2.20	1.52
07 06 57.14	-17 45 10.1	1.04	12.91	18.91	1.96	2.24	1.55
07 06 50.08	-17 45 13.7	1.06	12.75	19.06	2.07	2.09	1.45
07 06 44.54	-17 45 13.7	0.95	12.59	18.67	1.78	2.41	1.67
07 06 37.73	-17 45 13.7	0.83	12.60	18.22	1.47	2.93	2.02
07 06 31.68	-17 45 13.6	0.92	12.75	18.52	1.67	2.60	1.80
07 07 24.88	-17 45 17.2	0.92	12.94	18.47	1.63	2.70	1.86
07 07 20.83	-17 46 47.2	1.03	13.01	18.87	1.93	2.30	1.59
07 07 15.54	-17 46 32.8	1.09	13.00	19.08	2.10	2.11	1.46
07 07 8.48	-17 46 43.7	1.13	13.07	19.18	2.18	2.04	1.41
07 06 2.93	-17 46 47.3	1.09	13.13	19.02	2.05	2.18	1.51
07 06 56.63	-17 46 36.5	1.08	13.05	19.03	2.06	2.16	1.49
07 06 50.08	-17 46 36.5	1.06	12.80	19.03	2.05	2.13	1.47
07 06 43.02	-17 46 40.1	0.93	12.68	18.58	1.71	2.52	1.74
07 06 37.48	-17 46 47.3	0.88	12.67	18.38	1.57	2.75	1.90
07 06 31.68	-17 46 43.6	0.88	12.79	18.34	1.55	2.82	1.94
07 06 25.13	-17 46 40	0.90	13.07	18.36	1.55	2.86	1.98
07 06 56.63	-17 48 13.7	1.07	13.06	18.99	2.02	2.20	1.52
07 06 50.08	-17 48 6.5	1.01	12.84	18.85	1.91	2.29	1.58
07 06 43.27	-17 48 6.5	0.93	12.72	18.58	1.71	2.53	1.75
07 06 37.22	-17 47 59.3	0.87	12.77	18.30	1.52	2.87	1.98
07 06 30.42	-17 48 6.4	0.85	12.90	18.21	1.46	3.00	2.08
07 06 25.38	-17 47 59.2	0.87	13.08	18.22	1.46	3.04	2.10
07 06 57.39	-17 49 47.3	1.03	12.91	18.88	1.94	2.27	1.57
07 06 50.33	-17 49 32.9	0.97	12.82	18.70	1.80	2.43	1.68
07 06 44.28	-17 49 36.5	0.99	12.65	18.80	1.87	2.30	1.59
07 06 38.23	-17 49 47.3	0.94	12.75	18.59	1.71	2.53	1.75
07 07 30.92	-17 49 40	0.86	12.95	18.23	1.47	3.00	2.07
07 06 3.44	-17 51 17.3	1.13	13.11	19.19	2.19	2.04	1.41
07 06 56.38	-17 51 17.3	0.97	12.84	18.69	1.79	2.45	1.69
07 06 50.58	-17 51 17.3	0.96	12.69	18.71	1.80	2.40	1.66
07 06 44.53	-17 51 10.1	0.96	12.58	18.72	1.81	2.36	1.63
07 06 37.98	-17 51 17.3	0.96	12.86	18.66	1.77	2.48	1.71
07 07 30.92	-17 51 2.8	0.92	13.01	18.44	1.61	2.74	1.89
07 06 2.69	-17 52 47.3	1.19	13.12	19.37	2.34	1.91	1.32
07 06 55.88	-17 52 43.7	1.00	12.88	18.79	1.86	2.36	1.63
07 06 51.59	-17 52 47.3	0.95	12.64	18.65	1.76	2.45	1.69
07 06 43.52	-17 52 40.1	0.97	12.51	18.79	1.86	2.28	1.58
07 06 36.97	-17 52 47.3	0.97	12.84	18.67	1.78	2.46	1.70
07 07 30.41	-17 52 40	0.95	13.06	18.54	1.68	2.65	1.83
07 06 2.69	-17 54 17.3	1.14	13.09	19.23	2.22	2.01	1.39
07 06 57.14	-17 54 13.7	1.02	12.87	18.87	1.92	2.28	1.58
07 06 51.59	-17 54 10.1	0.94	12.62	18.65	1.76	2.44	1.69
07 06 43.77	-17 54 13.7	0.93	12.61	18.62	1.74	2.47	1.71
07 07 37.72	-17 54 6.5	0.93	12.97	18.50	1.65	2.67	1.84
07 06 2.44	-17 55 47.3	1.06	13.14	18.92	1.97	2.28	1.57
07 06 56.38	-17 55 43.7	1.04	13.00	18.88	1.93	2.29	1.58
07 06 50.08	-17 55 40.1	1.00	12.76	18.83	1.89	2.29	1.58
07 06 45.29	-17 55 47.3	1.00	12.77	18.81	1.88	2.32	1.60
07 07 38.73	-17 55 50.9	0.98	13.05	18.67	1.77	2.51	1.73
07 06 2.94	-17 57 13.7	1.07	13.14	18.95	1.99	2.25	1.55
07 06 51.34	-17 57 2.9	1.03	12.96	18.86	1.92	2.30	1.59
07 06 43.52	-17 57 10.1	1.06	13.05	18.94	1.98	2.24	1.55

Table 31: The Database of far infrared cavity CASKK8 nearby to the AGB star AGB1105-5451 located with in G229-03. The first two columns represent position of the pixels with in the cavity. The next two columns give values of relative flux density at 60 μm and 100 μm that have obtained after processing the FITS image using ALADIN 2.5 software. The calculated values of dust color temperature (in K), Planck function and dust mass for 100 μm and visual extinction (in mag) of the corresponding pixels,respectively.

R.A.(J2000) hh mm ss	Dec.(J2000) dd mm ss	$F(60)$ (MJy)	$F(100)$ (MJy)	T_d (K)	$B(\nu,T)$ $(\times10^{-16})$ Js^{-2}	M_d $(\times10^{27})$ kg	A_V $(\times10^{-5})$ mag
11 5 4.24	-54 4 3.7	3.22	19.66	22.01	5.72	4.68	0.81
11 4 53.2	-54 3 58.6	3.18	19.45	21.99	5.69	4.66	0.80
11 4 42.77	-54 3 53.4	3.16	19.46	21.96	5.64	4.70	0.81
11 4 33.57	-54 3 53.5	3.18	19.17	22.07	5.82	4.48	0.77
11 4 23.75	-54 3 58.9	3.18	19.06	22.10	5.89	4.41	0.76
11 4 11.49	-54 3 58.9	3.16	19.06	22.07	5.82	4.46	0.77
11 4 2.9	-54 3 48.1	3.14	19.08	22.02	5.74	4.52	0.78

continued on next page

Table 31 – continued from previous page

R.A.(J2000) hh mm ss	Dec.(J2000) dd mm ss	$F(60)$ (MJy)	$F(100)$ (MJy)	$T_{\rm d}$ (K)	$B(\nu,T)$ $(\times10^{-16})$ Js^{-2}	$M_{\rm d}$ $(\times10^{27})$ kg	$A_{\rm V}$ $(\times10^{-5})$ mag
11 3 50.63	-54 3 53.3	3.18	19.24	22.04	5.78	4.53	0.78
11 5 13.47	-54 5 19.1	3.14	19.64	21.88	5.50	4.86	0.84
11 5 4.27	-54 5 24.7	2.96	18.96	21.76	5.32	4.85	0.84
11 4 53.22	-54 5 25	2.96	18.70	21.83	5.43	4.69	0.81
11 4 44.01	-54 5 25.2	2.93	18.62	21.80	5.38	4.71	0.81
11 4 32.96	-54 5 25.3	3.01	18.64	21.93	5.60	4.54	0.78
11 4 21.92	-54 5 36.1	3.03	18.51	22.00	5.71	4.41	0.76
11 4 12.1	-54 5 30.7	3.02	18.55	21.97	5.66	4.46	0.77
11 4 4.12	-54 5 30.7	3.00	18.49	21.95	5.62	4.48	0.77
11 3 53.07	-54 5 30.6	3.04	19.04	21.88	5.51	4.71	0.81
11 3 43.86	-54 5 19.7	3.15	19.84	21.85	5.46	4.95	0.85
11 5 23.95	-54 6 56	3.14	19.44	21.93	5.59	4.73	0.82
11 5 12.89	-54 6 50.9	2.92	18.91	21.71	5.23	4.92	0.85
11 5 3.68	-54 6 35	2.81	18.63	21.60	5.05	5.02	0.87
11 4 53.24	-54 6 51.4	2.79	18.32	21.64	5.12	4.87	0.84
11 4 43.41	-54 6 51.5	2.82	18.16	21.74	5.28	4.69	0.81
11 4 31.75	-54 6 57	2.89	18.34	21.80	5.38	4.64	0.80
11 4 21.92	-54 7 2.5	2.97	18.58	21.87	5.49	4.61	0.80
11 4 11.48	-54 6 46.3	2.95	18.48	21.87	5.50	4.58	0.79
11 4 2.88	-54 6 51.7	2.94	18.46	21.86	5.48	4.59	0.79
11 3 52.44	-54 7 7.8	2.98	18.72	21.86	5.48	4.65	0.80
11 3 40.77	-54 6 46	3.08	19.31	21.87	5.50	4.78	0.83
11 5 45.5	-54 8 16.1	3.33	19.61	22.19	6.03	4.42	0.76
11 5 34.43	-54 8 27.4	3.20	19.37	22.04	5.77	4.57	0.79
11 5 23.99	-54 8 22.3	3.03	18.93	21.88	5.51	4.68	0.81
11 5 12.31	-54 8 22.7	2.91	18.39	21.82	5.42	4.62	0.80
11 5 3.71	-54 8 23	2.78	18.09	21.69	5.19	4.74	0.82
11 4 53.88	-54 8 12.4	2.72	18.09	21.57	5.01	4.91	0.85
11 4 42.81	-54 8 17.9	2.78	17.95	21.72	5.24	4.66	0.81
11 4 34.21	-54 8 28.8	2.82	18.20	21.72	5.25	4.72	0.81
11 4 23.15	-54 8 28.9	2.93	18.39	21.86	5.48	4.57	0.79
11 4 12.7	-54 8 23.5	3.02	18.96	21.86	5.47	4.72	0.81
11 4 2.26	-54 8 28.9	3.00	18.77	21.88	5.51	4.64	0.80
11 3 51.81	-54 8 34.1	2.94	18.69	21.79	5.36	4.74	0.82
11 3 41.98	-54 8 34	3.00	18.92	21.84	5.44	4.74	0.82
11 3 32.15	-54 8 23	3.07	19.37	21.84	5.44	4.85	0.84
11 3 20.47	-54 8 33.5	3.10	19.63	21.82	5.41	4.94	0.85
11 3 1.42	-54 8 27.4	3.09	19.79	21.76	5.32	5.07	0.88
11 2 50.97	-54 8 27	3.02	19.76	21.67	5.16	5.22	0.90
11 2 40.52	-54 8 26.6	3.03	19.77	21.68	5.18	5.20	0.90
11 6 4.6	-54 9 36.1	3.35	19.83	22.16	5.99	4.51	0.78
11 5 54.14	-54 9 31.3	3.26	19.47	22.12	5.92	4.48	0.77
11 5 43.7	-54 9 48	3.20	19.00	22.14	5.95	4.35	0.75
11 5 33.86	-54 9 53.8	3.08	18.72	22.02	5.75	4.43	0.77
11 5 22.79	-54 9 54.2	2.93	18.62	21.80	5.38	4.71	0.81
11 5 12.96	-54 9 59.9	2.88	18.03	21.88	5.50	4.46	0.77
11 5 3.73	-54 9 49.3	2.81	17.91	21.79	5.36	4.55	0.79
11 4 53.9	-54 9 54.9	2.75	17.70	21.73	5.26	4.58	0.79
11 4 42.83	-54 9 49.7	2.70	17.85	21.60	5.06	4.81	0.83
11 4 33.61	-54 9 44.4	2.76	17.69	21.75	5.29	4.55	0.79
11 4 23.15	-54 9 44.5	2.86	18.09	21.83	5.42	4.54	0.78
11 4 12.7	-54 9 49.9	3.07	18.70	22.01	5.72	4.45	0.77
11 4 2.25	-54 10 0.7	3.03	18.96	21.89	5.52	4.68	0.81
11 3 51.79	-54 10 6	2.90	18.63	21.75	5.30	4.79	0.83
11 3 41.34	-54 10 5.8	2.88	18.59	21.72	5.25	4.82	0.83
11 3 31.5	-54 10 11	2.93	18.88	21.73	5.26	4.89	0.84
11 3 21.66	-54 10 10.7	2.95	19.03	21.72	5.25	4.93	0.85
11 3 12.44	-54 10 5.1	2.97	19.33	21.69	5.19	5.07	0.88
11 3 0.75	-54 10 10	2.91	19.14	21.63	5.10	5.11	0.88
11 2 52.15	-54 10 9.7	2.84	19.04	21.54	4.96	5.23	0.90
11 2 43.53	-54 10 9.2	2.86	19.19	21.54	4.97	5.26	0.91
11 2 32.47	-54 10 3.2	2.96	19.80	21.56	4.99	5.41	0.93
11 6 16.35	-54 11 7.2	3.37	19.75	22.21	6.07	4.43	0.77
11 6 5.28	-54 11 13.3	3.27	19.52	22.12	5.91	4.49	0.78
11 5 54.21	-54 11 13.9	3.20	19.36	22.05	5.79	4.55	0.79
11 5 43.75	-54 11 25.3	3.13	18.90	22.05	5.80	4.43	0.77
11 5 33.91	-54 11 31	3.01	18.38	22.00	5.70	4.39	0.76
11 5 24.69	-54 11 25.9	2.89	18.22	21.84	5.44	4.56	0.79
11 5 13.61	-54 11 37.1	2.87	17.88	21.90	5.53	4.40	0.76
11 5 4.38	-54 11 48.1	2.86	17.59	21.96	5.64	4.25	0.73
11 4 53.31	-54 11 43	2.73	17.45	21.77	5.32	4.47	0.77
11 4 44.08	-54 11 26.9	2.65	17.38	21.65	5.13	4.61	0.80
11 4 35.46	-54 11 32.4	2.65	17.59	21.59	5.04	4.76	0.82
11 4 22.54	-54 11 37.9	2.81	17.88	21.79	5.36	4.55	0.78
11 4 13.93	-54 11 27.1	2.99	18.27	22.00	5.70	4.36	0.75
11 4 2.24	-54 11 32.4	2.95	18.58	21.85	5.46	4.63	0.80
11 3 52.39	-54 11 37.8	2.85	18.53	21.70	5.21	4.84	0.84

continued on next page

Table 31 – continued from previous page

R.A.(J2000) hh mm ss	Dec.(J2000) dd mm ss	$F(60)$ (MJy)	$F(100)$ (MJy)	$T_{\rm d}$ (K)	$B(\nu,T)$ $(\times10^{-16})$ Js^{-2}	$M_{\rm d}$ $(\times10^{27})$ kg	$A_{\rm V}$ $(\times10^{-5})$ mag
11 3 41.32	-54 11 48.4	2.81	18.42	21.66	5.14	4.88	0.84
11 3 30.86	-54 11 37.4	2.80	18.42	21.63	5.10	4.92	0.85
11 3 21.63	-54 11 26.3	2.87	18.77	21.65	5.14	4.97	0.86
11 3 11.17	-54 11 26	2.84	18.82	21.60	5.06	5.07	0.87
11 2 59.49	-54 11 25.6	2.88	19.03	21.61	5.07	5.11	0.88
11 2 51.48	-54 11 36	2.83	18.79	21.59	5.04	5.08	0.88
11 2 38.56	-54 11 35.4	2.86	18.90	21.61	5.07	5.07	0.88
11 2 30.57	-54 11 35	2.90	19.23	21.59	5.04	5.20	0.90
11 2 22.57	-54 11 18.4	2.99	19.83	21.59	5.05	5.35	0.92
11 6 13.97	-54 12 50	3.40	19.80	22.24	6.13	4.40	0.76
11 6 5.97	-54 12 50.4	3.24	19.43	22.09	5.86	4.52	0.78
11 5 53.66	-54 12 56.5	3.16	19.29	22.01	5.72	4.59	0.79
11 5 44.42	-54 12 56.9	3.11	19.28	21.93	5.58	4.70	0.81
11 5 35.19	-54 13 2.8	3.08	18.57	22.07	5.82	4.34	0.75
11 5 24.11	-54 13 8.5	2.90	18.00	21.92	5.57	4.40	0.76
11 5 11.8	-54 13 3.5	2.89	17.78	21.97	5.65	4.29	0.74
11 5 3.18	-54 13 3.8	2.79	17.57	21.85	5.46	4.38	0.76
11 4 54.56	-54 13 9.3	2.79	17.47	21.88	5.51	4.32	0.75
11 4 42.24	-54 12 37.2	2.65	17.22	21.70	5.21	4.50	0.78
11 4 34.24	-54 13 4.2	2.61	17.46	21.56	4.99	4.77	0.82
11 4 22.55	-54 13 9.7	2.72	17.82	21.64	5.12	4.74	0.82
11 4 12.69	-54 13 9.7	2.85	18.31	21.75	5.30	4.70	0.81
11 4 3.46	-54 12 58.8	2.92	18.48	21.82	5.40	4.66	0.80
11 3 52.99	-54 12 58.8	2.82	18.35	21.68	5.18	4.83	0.83
11 3 43.14	-54 13 9.4	2.82	18.59	21.61	5.08	4.99	0.86
11 3 31.45	-54 13 3.7	2.82	18.38	21.67	5.17	4.84	0.84
11 3 21.6	-54 12 47.3	2.81	18.38	21.66	5.15	4.86	0.84
11 3 10.52	-54 13 3.1	2.85	18.44	21.71	5.23	4.80	0.83
11 3 0.05	-54 13 2.8	2.89	18.74	21.70	5.21	4.89	0.85
11 2 50.19	-54 13 2.3	2.93	18.97	21.71	5.23	4.94	0.85
11 2 39.73	-54 13 7.3	2.89	19.00	21.63	5.11	5.07	0.87
11 2 30.5	-54 12 56.1	2.90	18.95	21.67	5.16	4.99	0.86
11 2 21.88	-54 12 55.6	2.97	19.22	21.70	5.22	5.01	0.87
11 2 11.41	-54 13 0.3	2.99	19.72	21.62	5.09	5.28	0.91
11 6 5.42	-54 14 27.6	3.40	19.68	22.28	6.20	4.32	0.75
11 5 54.33	-54 14 28.3	3.34	19.59	22.20	6.06	4.40	0.76
11 5 44.47	-54 14 18	3.22	19.48	22.05	5.80	4.57	0.79
11 5 35.24	-54 14 29.1	3.10	19.21	21.93	5.59	4.68	0.81
11 5 24.76	-54 14 29.5	3.04	18.62	21.99	5.68	4.46	0.77
11 5 12.44	-54 14 24.5	2.83	18.02	21.80	5.37	4.57	0.79
11 5 3.82	-54 14 35.5	2.81	17.61	21.88	5.50	4.36	0.75
11 4 53.96	-54 14 30.4	2.76	17.48	21.83	5.42	4.39	0.76
11 4 44.11	-54 14 30.5	2.71	17.43	21.75	5.29	4.49	0.77
11 4 35.48	-54 14 25.2	2.64	17.59	21.57	5.00	4.79	0.83
11 4 23.78	-54 14 25.3	2.75	17.92	21.68	5.18	4.71	0.81
11 4 12.08	-54 14 36.1	2.79	18.30	21.65	5.13	4.85	0.84
11 4 3.45	-54 14 25.3	2.82	18.32	21.69	5.20	4.80	0.83
11 3 54.21	-54 14 19.8	2.79	18.55	21.58	5.03	5.02	0.87
11 3 43.74	-54 14 25	2.87	18.59	21.70	5.21	4.85	0.84
11 3 33.27	-54 14 24.8	2.89	18.79	21.69	5.20	4.92	0.85
11 3 19.72	-54 14 29.9	2.89	18.54	21.75	5.29	4.78	0.82
11 3 9.24	-54 14 24.1	2.91	18.56	21.79	5.35	4.72	0.82
11 3 0	-54 14 29.1	2.97	18.63	21.87	5.49	4.62	0.80
11 2 51.38	-54 14 23.3	2.96	19.03	21.75	5.29	4.90	0.85
11 2 41.52	-54 14 28.4	2.95	19.29	21.65	5.14	5.11	0.88
11 2 30.44	-54 14 27.9	2.95	19.23	21.68	5.19	5.05	0.87
11 2 21.19	-54 14 21.9	2.99	19.09	21.78	5.34	4.87	0.84
11 2 11.34	-54 14 26.7	3.03	19.49	21.74	5.28	5.03	0.87
11 2 0.86	-54 14 31.4	2.96	19.85	21.53	4.95	5.46	0.94
11 5 55.62	-54 16 0	3.39	19.72	22.25	6.15	4.37	0.75
11 5 44.52	-54 15 55	3.34	19.67	22.18	6.02	4.45	0.77
11 5 34.66	-54 15 55.6	3.28	19.46	22.15	5.97	4.44	0.77
11 5 26.04	-54 15 55.8	3.15	18.98	22.07	5.82	4.44	0.77
11 5 14.94	-54 16 1.6	2.96	18.45	21.89	5.53	4.55	0.79
11 5 5.69	-54 15 51.1	2.85	17.87	21.87	5.49	4.43	0.77
11 4 53.99	-54 15 56.8	2.89	17.87	21.93	5.60	4.35	0.75
11 4 43.51	-54 15 56.9	2.86	17.77	21.92	5.57	4.35	0.75
11 4 33.65	-54 15 51.6	2.85	17.98	21.84	5.45	4.49	0.78
11 4 24.4	-54 15 57.1	2.83	18.04	21.79	5.36	4.58	0.79
11 4 13.92	-54 15 57.1	2.87	18.39	21.77	5.32	4.71	0.81
11 4 2.21	-54 16 2.5	2.88	18.74	21.68	5.18	4.93	0.85
11 3 52.96	-54 16 2.4	2.91	18.67	21.76	5.31	4.79	0.83
11 3 42.49	-54 16 2.2	2.86	18.87	21.62	5.08	5.06	0.87
11 3 32.01	-54 15 56.6	2.93	18.74	21.77	5.33	4.79	0.83
11 3 20.29	-54 16 12.5	3.01	18.74	21.90	5.55	4.60	0.79
11 3 10.44	-54 15 45.2	3.07	18.69	22.01	5.72	4.45	0.77
11 2 59.34	-54 16 0.9	3.02	18.80	21.91	5.56	4.60	0.79

continued on next page

Table 31 – continued from previous page

R.A.(J2000) hh mm ss	Dec.(J2000) dd mm ss	$F(60)$ (MJy)	$F(100)$ (MJy)	$T_{\rm d}$ (K)	$B(\nu,T)$ $(\times10^{-16})$ Js^{-2}	$M_{\rm d}$ $(\times10^{27})$ kg	$A_{\rm V}$ $(\times10^{-5})$ mag
11 2 51.95	-54 15 55.2	2.98	18.74	21.86	5.47	4.67	0.81
11 2 41.46	-54 16 5.6	2.96	19.04	21.75	5.29	4.90	0.85
11 2 30.36	-54 16 10.5	2.92	19.12	21.66	5.15	5.05	0.87
11 2 21.12	-54 15 53.6	2.95	19.18	21.69	5.20	5.02	0.87
11 2 10.64	-54 15 58.5	3.01	19.22	21.77	5.32	4.92	0.85
11 2 0.17	-54 16 8.5	3.01	19.75	21.64	5.11	5.26	0.91
11 6 4.94	-54 17 25.9	3.40	19.77	22.26	6.16	4.37	0.75
11 5 55.06	-54 17 10.2	3.32	19.74	22.14	5.94	4.52	0.78
11 5 42.73	-54 17 21.6	3.29	19.59	22.12	5.92	4.50	0.78
11 5 34.71	-54 17 21.9	3.20	19.32	22.06	5.82	4.52	0.78
11 5 24.85	-54 17 27.7	3.12	19.06	22.00	5.71	4.55	0.78
11 5 14.36	-54 17 33.5	2.95	18.65	21.82	5.41	4.69	0.81
11 5 4.49	-54 17 12.1	2.92	18.40	21.85	5.46	4.59	0.79
11 4 55.24	-54 17 28.5	2.90	17.94	21.94	5.60	4.36	0.75
11 4 45.37	-54 17 28.7	2.96	18.18	21.97	5.66	4.38	0.76
11 4 33.04	-54 17 28.8	3.00	18.13	22.05	5.80	4.26	0.73
11 4 23.79	-54 17 28.9	3.05	18.62	22.00	5.70	4.44	0.77
11 4 13.92	-54 17 23.5	3.00	18.75	21.88	5.51	4.64	0.80
11 4 2.82	-54 17 28.8	3.03	18.95	21.88	5.50	4.69	0.81
11 3 52.33	-54 17 34.1	2.97	19.11	21.75	5.29	4.92	0.85
11 3 43.7	-54 17 12.4	2.90	19.00	21.66	5.14	5.03	0.87
11 3 31.98	-54 17 17.6	2.85	18.80	21.61	5.07	5.05	0.87
11 3 21.49	-54 17 28.1	3.01	18.72	21.91	5.56	4.59	0.79
11 3 11.62	-54 17 27.8	3.11	18.74	22.07	5.83	4.38	0.76
11 3 0.53	-54 17 22	3.11	18.97	22.00	5.71	4.52	0.78
11 2 51.27	-54 17 21.6	3.01	18.94	21.85	5.46	4.72	0.82
11 2 41.41	-54 17 21.2	2.99	18.75	21.86	5.48	4.66	0.81
11 2 31.53	-54 17 31.5	2.98	18.84	21.82	5.41	4.74	0.82
11 2 20.43	-54 17 25.4	2.94	19.09	21.70	5.22	4.98	0.86
11 2 9.95	-54 17 24.7	2.97	19.30	21.69	5.20	5.06	0.87
11 2 0.08	-54 17 24.1	3.02	19.36	21.75	5.30	4.97	0.86
11 6 7.46	-54 18 52.1	3.38	19.66	22.25	6.14	4.36	0.75
11 5 55.12	-54 18 52.9	3.28	19.55	22.13	5.93	4.49	0.77
11 5 42.78	-54 18 53.3	3.23	19.48	22.06	5.80	4.57	0.79
11 5 35.37	-54 18 53.7	3.12	19.19	21.96	5.64	4.63	0.80
11 5 24.27	-54 18 54.1	2.97	18.91	21.79	5.37	4.80	0.83
11 5 13.78	-54 19 5.3	2.89	18.75	21.70	5.21	4.90	0.85
11 5 3.91	-54 19 5.5	2.91	18.69	21.75	5.30	4.81	0.83
11 4 54.65	-54 18 54.9	2.96	18.57	21.87	5.49	4.61	0.80
11 4 42.92	-54 18 55.1	2.96	18.32	21.94	5.61	4.45	0.77
11 4 33.05	-54 18 55.2	3.05	18.61	22.00	5.72	4.43	0.77
11 4 23.79	-54 19 11.5	3.05	18.62	22.00	5.71	4.44	0.77
11 4 13.3	-54 19 0.7	3.04	19.08	21.86	5.47	4.75	0.82
11 4 3.43	-54 19 6.1	2.99	19.12	21.77	5.33	4.89	0.84
11 3 52.93	-54 19 11.4	2.93	19.15	21.66	5.15	5.06	0.87
11 3 42.44	-54 19 11.2	2.78	19.00	21.44	4.81	5.38	0.93
11 3 32.57	-54 19 0.2	2.78	18.98	21.46	4.84	5.34	0.92
11 3 21.46	-54 19 0	2.98	18.97	21.79	5.35	4.83	0.83
11 3 10.35	-54 19 10.4	3.10	19.03	21.98	5.67	4.57	0.79
11 3 0.47	-54 18 53.7	3.11	19.07	21.98	5.67	4.58	0.79
11 2 51.21	-54 18 58.9	2.98	19.07	21.77	5.32	4.88	0.84
11 2 41.96	-54 19 9.2	2.95	18.77	21.79	5.37	4.76	0.82
11 2 30.84	-54 19 14	2.90	18.46	21.80	5.37	4.68	0.81
11 2 21.6	-54 18 51.9	2.89	18.71	21.70	5.22	4.88	0.84
11 2 9.25	-54 19 1.9	2.92	19.20	21.63	5.11	5.12	0.88
11 2 1.23	-54 19 1.3	3.04	19.62	21.73	5.27	5.07	0.88
11 1 50.74	-54 18 55.3	3.13	19.61	21.88	5.50	4.86	0.84
11 6 7.53	-54 20 18.5	3.39	19.22	22.38	6.38	4.11	0.71
11 5 56.42	-54 20 13.8	3.27	19.26	22.19	6.03	4.35	0.75
11 5 44.68	-54 20 19.6	3.25	19.14	22.18	6.02	4.33	0.75
11 5 34.81	-54 20 20.1	3.14	18.91	22.07	5.84	4.41	0.76
11 5 23.69	-54 20 15.1	2.98	18.62	21.88	5.51	4.61	0.80
11 5 15.05	-54 20 20.8	2.85	18.40	21.73	5.26	4.76	0.82
11 5 4.55	-54 20 21.1	2.89	18.61	21.73	5.26	4.82	0.83
11 4 52.2	-54 20 21.3	2.98	18.84	21.83	5.43	4.73	0.82
11 4 45.41	-54 20 16.1	3.05	19.11	21.88	5.50	4.73	0.82
11 4 33.06	-54 20 16.2	3.06	19.07	21.90	5.54	4.69	0.81
11 4 23.8	-54 20 21.7	3.06	19.17	21.87	5.49	4.75	0.82
11 4 11.44	-54 20 16.3	3.00	19.07	21.79	5.36	4.84	0.84
11 4 2.18	-54 20 27	2.94	19.17	21.67	5.17	5.05	0.87
11 3 52.92	-54 20 27	2.87	19.11	21.57	5.01	5.19	0.90
11 3 41.8	-54 20 21.4	2.78	19.09	21.42	4.78	5.44	0.94
11 3 33.16	-54 20 15.8	2.75	19.13	21.36	4.69	5.55	0.96
11 3 22.04	-54 20 31.7	2.84	19.25	21.48	4.87	5.38	0.93
11 3 10.93	-54 20 31.4	2.97	19.33	21.68	5.18	5.08	0.88
11 2 59.81	-54 20 25.5	3.06	19.17	21.88	5.50	4.74	0.82
11 2 51.17	-54 20 14.4	2.93	19.02	21.70	5.21	4.97	0.86

continued on next page

Table 31 – continued from previous page

R.A.(J2000) hh mm ss	Dec.(J2000) dd mm ss	$F(60)$ (MJy)	$F(100)$ (MJy)	$T_{\rm d}$ (K)	$B(\nu,T)$ $(\times10^{-16})$ Js^{-2}	$M_{\rm d}$ $(\times10^{27})$ kg	$A_{\rm V}$ $(\times10^{-5})$ mag
11 2 40.05	-54 20 30.1	2.82	18.81	21.56	4.99	5.13	0.89
11 2 30.17	-54 20 13.4	2.79	18.58	21.57	5.01	5.05	0.87
11 2 21.53	-54 20 23.7	2.74	18.43	21.53	4.95	5.07	0.88
11 2 9.8	-54 20 17.6	2.84	19.14	21.52	4.92	5.29	0.91
11 6 26.76	-54 21 54.6	3.54	19.77	22.46	6.53	4.12	0.71
11 6 18.1	-54 21 38.9	3.42	19.35	22.39	6.40	4.12	0.71
11 6 6.36	-54 21 28.8	3.36	18.89	22.42	6.46	3.98	0.69
11 5 57.1	-54 21 40.2	3.27	18.77	22.33	6.28	4.07	0.70
11 5 45.97	-54 21 40.6	3.22	18.83	22.22	6.09	4.21	0.73
11 5 35.47	-54 21 46.5	3.13	18.67	22.12	5.92	4.30	0.74
11 5 26.21	-54 21 57.7	2.98	18.35	21.95	5.63	4.44	0.77
11 5 15.7	-54 21 58.1	2.88	18.04	21.87	5.48	4.48	0.77
11 5 3.34	-54 21 47.5	2.83	18.13	21.76	5.32	4.64	0.80
11 4 55.93	-54 21 47.7	2.91	18.72	21.75	5.29	4.82	0.83
11 4 44.81	-54 21 58.7	3.04	19.06	21.87	5.49	4.72	0.82
11 4 36.16	-54 21 53.4	3.15	19.35	21.98	5.67	4.64	0.80
11 4 25.03	-54 21 53.5	3.03	19.04	21.86	5.48	4.73	0.82
11 4 12.68	-54 21 58.9	2.95	18.68	21.83	5.42	4.70	0.81
11 4 3.41	-54 21 53.4	2.90	18.78	21.72	5.24	4.88	0.84
11 3 54.76	-54 21 58.8	2.88	18.93	21.63	5.11	5.05	0.87
11 3 43.64	-54 22 4	2.77	18.91	21.45	4.82	5.34	0.92
11 3 33.13	-54 21 58.4	2.80	19.21	21.44	4.80	5.45	0.94
11 3 23.25	-54 21 42	2.91	19.32	21.59	5.04	5.22	0.90
11 3 13.36	-54 21 52.4	2.89	19.58	21.49	4.89	5.46	0.94
11 3 1	-54 21 52	2.93	19.53	21.58	5.02	5.30	0.91
11 2 52.35	-54 21 46.3	2.92	19.37	21.60	5.05	5.22	0.90
11 2 41.85	-54 21 45.7	2.83	19.06	21.52	4.93	5.27	0.91
11 2 31.97	-54 21 56.1	2.82	19.16	21.47	4.86	5.36	0.93
11 2 20.84	-54 21 44.6	2.73	18.72	21.44	4.81	5.30	0.92
11 2 11.57	-54 21 44	2.83	19.21	21.49	4.88	5.36	0.92
11 6 27.46	-54 23 37.1	3.39	19.73	22.25	6.15	4.37	0.75
11 6 16.95	-54 23 26.9	3.35	19.16	22.34	6.30	4.14	0.71
11 6 5.82	-54 23 27.6	3.26	18.91	22.26	6.16	4.18	0.72
11 5 55.93	-54 23 44.4	3.25	18.73	22.30	6.24	4.09	0.71
11 5 46.65	-54 23 17.9	3.22	18.67	22.27	6.18	4.11	0.71
11 5 38	-54 23 29	3.10	18.66	22.08	5.85	4.35	0.75
11 5 25.01	-54 23 24.1	3.02	18.28	22.05	5.79	4.30	0.74
11 5 12.64	-54 23 24.5	2.86	17.93	21.88	5.50	4.44	0.77
11 5 5.23	-54 23 19.3	2.76	17.72	21.75	5.29	4.56	0.79
11 4 55.33	-54 23 19.5	2.82	18.13	21.75	5.30	4.66	0.80
11 4 45.44	-54 23 25.1	3.00	18.81	21.86	5.48	4.67	0.81
11 4 33.7	-54 23 25.2	3.08	18.94	21.97	5.66	4.56	0.79
11 4 25.04	-54 23 36.1	3.02	18.68	21.94	5.60	4.54	0.78
11 4 13.29	-54 23 30.7	2.97	18.35	21.93	5.60	4.46	0.77
11 4 4.02	-54 23 25.2	2.91	17.97	21.95	5.63	4.35	0.75
11 3 52.89	-54 23 9	2.85	18.40	21.73	5.26	4.77	0.82
11 3 43	-54 23 19.6	2.89	18.72	21.71	5.24	4.87	0.84
11 3 33.72	-54 23 24.9	2.99	19.15	21.76	5.31	4.91	0.85
11 3 21.35	-54 23 29.9	3.01	19.44	21.72	5.24	5.05	0.87
11 3 12.08	-54 23 24.2	2.97	19.37	21.68	5.18	5.09	0.88
11 3 1.58	-54 23 23.8	2.96	19.59	21.60	5.05	5.28	0.91
11 2 50.44	-54 23 28.7	2.94	19.37	21.63	5.10	5.17	0.89
11 2 41.78	-54 23 33.8	2.90	19.38	21.55	4.98	5.30	0.92
11 2 31.89	-54 23 44	2.88	19.14	21.58	5.02	5.19	0.90
11 2 20.76	-54 23 43.4	2.86	19.63	21.43	4.80	5.57	0.96
11 2 10.26	-54 23 15.8	2.91	19.45	21.55	4.98	5.32	0.92
11 7 38.91	-54 20 11.2	3.50	19.66	22.43	6.47	4.14	0.71
11 7 28.42	-54 20 17.6	3.36	19.65	22.23	6.10	4.39	0.76
11 7 17.92	-54 20 18.8	3.34	19.63	22.19	6.04	4.43	0.76
11 7 8.04	-54 20 8.7	3.36	19.82	22.18	6.02	4.48	0.77
11 7 40.26	-54 21 21.4	3.46	19.51	22.41	6.44	4.12	0.71
11 7 27.91	-54 21 44.1	3.36	19.48	22.27	6.18	4.29	0.74
11 7 19.26	-54 21 44.9	3.34	19.50	22.23	6.11	4.35	0.75
11 7 6.91	-54 21 51.3	3.41	19.64	22.31	6.25	4.28	0.74
11 7 39.78	-54 23 14.7	3.39	19.48	22.31	6.25	4.24	0.73
11 7 28.04	-54 23 21.2	3.32	19.29	22.25	6.15	4.27	0.74
11 7 18.77	-54 23 22.1	3.33	19.50	22.21	6.08	4.37	0.75
11 7 10.1	-54 23 17.5	3.37	19.55	22.26	6.16	4.32	0.75
11 6 58.97	-54 23 7.7	3.40	19.69	22.27	6.18	4.34	0.75
11 7 38.66	-54 24 46.7	3.34	19.75	22.16	5.98	4.49	0.78
11 7 29.39	-54 24 47.4	3.31	19.26	22.25	6.15	4.26	0.74
11 7 18.87	-54 24 59.4	3.44	19.33	22.43	6.46	4.07	0.70
11 7 8.36	-54 24 49.5	3.46	19.45	22.43	6.47	4.09	0.71
11 6 59.08	-54 24 50.2	3.37	19.55	22.26	6.16	4.32	0.75
11 6 50.42	-54 24 50.9	3.35	19.53	22.23	6.11	4.35	0.75
11 6 36.19	-54 24 41.3	3.32	19.74	22.14	5.95	4.52	0.78
11 6 27.53	-54 24 41.9	3.28	19.69	22.09	5.86	4.57	0.79

continued on next page

Table 31 – continued from previous page

R.A.(J2000) hh mm ss	Dec.(J2000) dd mm ss	$F(60)$ (MJy)	$F(100)$ (MJy)	$T_{\rm d}$ (K)	$B(\nu,T)$ $(\times10^{-16})$ Js^{-2}	$M_{\rm d}$ $(\times10^{27})$ kg	$A_{\rm V}$ $(\times10^{-5})$ mag
11 6 15.77	-54 24 48.1	3.19	19.35	22.03	5.76	4.58	0.79
11 6 7.12	-54 24 43.2	3.20	18.83	22.19	6.04	4.24	0.73
11 5 56.61	-54 24 59.8	3.20	18.87	22.19	6.03	4.26	0.74
11 5 47.32	-54 24 44.1	3.13	18.68	22.12	5.92	4.30	0.74
11 5 37.42	-54 24 44.6	3.11	18.61	22.10	5.89	4.31	0.74
11 5 26.28	-54 24 45.1	2.96	18.14	21.99	5.69	4.34	0.75
11 5 15.16	-54 24 50.9	2.90	17.94	21.93	5.60	4.37	0.75
11 5 5.26	-54 24 56.5	2.81	17.76	21.82	5.41	4.47	0.77
11 4 56.59	-54 24 45.9	2.84	18.03	21.81	5.38	4.56	0.79
11 4 44.22	-54 24 51.5	2.89	18.36	21.80	5.38	4.65	0.80
11 4 34.32	-54 24 51.6	3.00	18.64	21.92	5.57	4.55	0.79
11 4 21.95	-54 25 2.5	2.97	18.72	21.84	5.45	4.68	0.81
11 4 15.76	-54 24 51.7	2.95	18.49	21.87	5.49	4.58	0.79
11 4 4.63	-54 24 57.1	2.95	18.46	21.89	5.52	4.56	0.79
11 3 53.49	-54 24 57	2.91	18.10	21.91	5.56	4.43	0.77
11 3 43.59	-54 25 7.6	2.91	18.54	21.79	5.36	4.71	0.81
11 3 33.69	-54 25 2	2.98	18.87	21.82	5.41	4.75	0.82
11 3 21.94	-54 24 45.5	3.10	19.48	21.86	5.48	4.84	0.84
11 3 12.66	-54 24 56.1	3.07	19.58	21.79	5.35	4.98	0.86
11 3 2.15	-54 24 55.6	3.02	19.43	21.74	5.28	5.01	0.87
11 2 50.39	-54 25 0.6	3.00	19.56	21.67	5.17	5.16	0.89
11 2 39.87	-54 25 0.1	2.98	19.20	21.73	5.27	4.96	0.86
11 2 31.2	-54 25 5	3.02	19.37	21.76	5.31	4.97	0.86
11 2 20.7	-54 24 53.6	3.02	19.48	21.72	5.25	5.05	0.87
11 2 10.8	-54 24 53	3.05	19.71	21.72	5.25	5.11	0.88
11 7 29.51	-54 26 13.9	3.36	19.33	22.30	6.23	4.23	0.73
11 7 18.36	-54 26 9.6	3.51	19.08	22.61	6.81	3.82	0.66
11 7 8.46	-54 26 21.4	3.49	19.16	22.55	6.69	3.90	0.67
11 6 59.79	-54 26 11.2	3.33	19.27	22.28	6.19	4.24	0.73
11 6 51.13	-54 26 17.4	3.14	19.19	22.00	5.71	4.57	0.79
11 6 37.51	-54 26 13.1	3.14	19.05	22.03	5.75	4.51	0.78
11 6 27.6	-54 26 13.7	3.03	19.18	21.83	5.42	4.82	0.83
11 6 17.7	-54 26 14.4	2.97	19.22	21.72	5.24	5.00	0.86
11 6 7.8	-54 26 9.5	3.04	19.13	21.86	5.47	4.76	0.82
11 5 56.04	-54 26 15.4	3.12	18.91	22.03	5.76	4.47	0.77
11 5 47.99	-54 26 15.9	3.18	18.96	22.12	5.92	4.36	0.75
11 5 36.23	-54 26 27.3	3.03	18.77	21.93	5.60	4.57	0.79
11 5 25.71	-54 26 11.4	3.01	18.28	22.04	5.77	4.31	0.74
11 5 15.81	-54 26 22.6	2.85	18.07	21.82	5.41	4.55	0.79
11 5 7.14	-54 26 33.7	2.86	17.99	21.85	5.45	4.49	0.78
11 4 54.14	-54 26 17.8	2.88	18.04	21.87	5.48	4.48	0.77
11 4 44.24	-54 26 34.1	2.96	18.32	21.93	5.59	4.46	0.77
11 4 35.57	-54 26 34.2	2.91	18.43	21.82	5.41	4.64	0.80
11 4 25.05	-54 26 28.9	2.97	18.54	21.89	5.53	4.57	0.79
11 4 13.29	-54 26 34.3	2.93	18.63	21.80	5.38	4.72	0.81
11 4 4	-54 26 39.7	2.94	18.66	21.80	5.38	4.73	0.82
11 3 54.1	-54 26 28.8	3.01	18.56	21.95	5.62	4.50	0.78
11 3 42.33	-54 26 34	3.00	18.45	21.96	5.64	4.46	0.77
11 3 32.43	-54 26 33.8	3.05	19.08	21.88	5.51	4.72	0.81
11 3 23.15	-54 26 28.2	3.13	19.48	21.91	5.55	4.78	0.83
11 3 11.38	-54 26 22.4	3.17	19.86	21.88	5.51	4.91	0.85
11 3 1.48	-54 26 27.4	3.10	19.74	21.79	5.36	5.02	0.87
11 2 51.58	-54 26 26.9	3.10	19.68	21.81	5.39	4.97	0.86
11 2 41.67	-54 26 26.6	3.04	19.78	21.68	5.18	5.20	0.90
11 2 29.91	-54 26 25.9	3.04	19.66	21.71	5.23	5.12	0.88
11 2 20.63	-54 26 20.2	3.04	19.71	21.71	5.23	5.13	0.89
11 2 10.73	-54 26 24.7	3.10	19.77	21.79	5.36	5.03	0.87
11 7 38.9	-54 27 39.4	3.28	19.51	22.13	5.94	4.48	0.77
11 7 30.23	-54 27 34.9	3.23	19.26	22.13	5.93	4.43	0.76
11 7 19.08	-54 27 41.3	3.39	18.90	22.47	6.56	3.92	0.68
11 7 9.18	-54 27 42.1	3.41	18.77	22.54	6.69	3.82	0.66
11 6 59.27	-54 27 37.7	3.18	18.88	22.14	5.95	4.32	0.75
11 6 48.74	-54 27 43.9	3.04	19.00	21.89	5.53	4.68	0.81
11 6 38.84	-54 27 50.1	2.99	18.75	21.87	5.49	4.65	0.80
11 6 28.3	-54 27 45.4	2.99	18.70	21.88	5.50	4.63	0.80
11 6 16.54	-54 27 46.1	2.91	18.67	21.75	5.30	4.80	0.83
11 6 7.25	-54 27 46.7	2.98	18.98	21.79	5.37	4.82	0.83
11 5 57.96	-54 27 58	3.08	19.11	21.93	5.58	4.66	0.80
11 5 47.43	-54 27 47.8	3.19	19.09	22.10	5.88	4.42	0.76
11 5 36.9	-54 27 48.2	3.18	18.88	22.15	5.96	4.31	0.74
11 5 23.9	-54 27 54.1	2.96	18.40	21.90	5.55	4.52	0.78
11 5 15.23	-54 28 5.2	2.88	18.12	21.86	5.47	4.51	0.78
11 5 7.17	-54 27 54.6	2.90	18.19	21.86	5.48	4.52	0.78
11 4 55.4	-54 27 54.9	2.97	18.24	21.97	5.65	4.39	0.76
11 4 45.49	-54 28 0.5	2.95	18.27	21.94	5.60	4.44	0.77
11 4 34.34	-54 27 55.2	2.91	18.31	21.85	5.46	4.56	0.79
11 4 24.43	-54 27 55.3	2.90	18.32	21.83	5.42	4.60	0.80

continued on next page

Table 31 – continued from previous page

R.A.(J2000) hh mm ss	Dec.(J2000) dd mm ss	$F(60)$ (MJy)	$F(100)$ (MJy)	$T_{\rm d}$ (K)	$B(\nu,T)$ $(\times10^{-16})$ Js^{-2}	$M_{\rm d}$ $(\times10^{27})$ kg	A_V $(\times10^{-5})$ mag
11 4 13.9	-54 27 55.3	2.92	18.52	21.82	5.41	4.67	0.81
11 4 4.61	-54 27 49.9	2.93	18.75	21.76	5.31	4.80	0.83
11 3 54.08	-54 28 0.6	2.96	18.86	21.79	5.35	4.80	0.83
11 3 41.69	-54 28 0.4	3.05	18.89	21.92	5.58	4.61	0.80
11 3 33.02	-54 28 0.2	3.07	18.72	22.00	5.71	4.46	0.77
11 3 22.49	-54 28 10.7	3.10	19.40	21.88	5.51	4.80	0.83
11 3 12.58	-54 27 54.2	3.14	19.62	21.88	5.50	4.85	0.84
11 3 0.81	-54 28 10.1	3.17	19.80	21.89	5.53	4.88	0.84
11 2 50.28	-54 27 58.8	3.12	19.80	21.80	5.38	5.01	0.87
11 2 39.75	-54 27 58.3	3.08	19.79	21.75	5.29	5.10	0.88
11 2 29.84	-54 28 3.2	3.02	19.85	21.64	5.11	5.29	0.91
11 2 19.31	-54 27 51.8	3.06	19.82	21.70	5.22	5.17	0.89
11 2 8.18	-54 27 40.1	3.13	19.82	21.81	5.40	5.00	0.86
11 7 48.33	-54 29 15.6	3.45	19.79	22.33	6.28	4.29	0.74
11 7 38.39	-54 29 0.4	3.25	18.90	22.25	6.14	4.19	0.72
11 7 27.25	-54 29 7	3.18	18.80	22.16	5.99	4.27	0.74
11 7 19.18	-54 29 2.3	3.23	18.72	22.27	6.19	4.12	0.71
11 7 9.28	-54 29 14	3.24	18.56	22.32	6.27	4.03	0.70
11 6 59.98	-54 28 58.5	3.09	18.49	22.11	5.89	4.27	0.74
11 6 49.44	-54 29 5	3.06	18.60	22.03	5.76	4.40	0.76
11 6 38.3	-54 29 22	3.03	18.77	21.93	5.59	4.57	0.79
11 6 27.14	-54 29 6.4	2.94	18.46	21.86	5.48	4.59	0.79
11 6 17.85	-54 29 12.5	2.92	18.20	21.90	5.54	4.47	0.77
11 6 7.93	-54 29 13.1	2.96	18.46	21.90	5.54	4.54	0.78
11 5 56.78	-54 29 13.8	3.08	18.90	21.98	5.67	4.54	0.78
11 5 45.62	-54 29 19.7	3.25	19.16	22.17	6.01	4.34	0.75
11 5 36.95	-54 29 14.7	3.20	18.91	22.16	5.99	4.30	0.74
11 5 25.79	-54 29 15.1	3.08	18.56	22.06	5.82	4.34	0.75
11 5 15.88	-54 29 20.8	2.86	18.31	21.76	5.31	4.69	0.81
11 5 7.2	-54 29 21.1	2.88	18.29	21.81	5.38	4.63	0.80
11 4 55.42	-54 29 26.7	2.94	18.36	21.88	5.51	4.54	0.78
11 4 44.89	-54 29 10.7	2.98	18.42	21.94	5.60	4.48	0.77
11 4 35.59	-54 29 16.2	2.89	18.23	21.83	5.42	4.58	0.79
11 4 25.68	-54 29 5.5	2.84	18.36	21.71	5.24	4.77	0.82
11 4 15.14	-54 29 5.5	2.82	18.48	21.65	5.14	4.89	0.85
11 4 4.61	-54 29 21.7	2.85	18.69	21.64	5.13	4.96	0.86
11 3 52.83	-54 29 21.5	2.96	18.93	21.78	5.34	4.83	0.83
11 3 42.92	-54 29 21.4	3.03	19.01	21.86	5.47	4.73	0.82
11 3 32.38	-54 29 21.1	3.12	18.98	22.02	5.75	4.50	0.78
11 3 23.08	-54 29 26.4	3.07	19.04	21.92	5.58	4.65	0.80
11 3 12.54	-54 29 31.4	3.02	19.25	21.79	5.35	4.90	0.85
11 3 2.62	-54 29 25.7	3.14	19.53	21.90	5.54	4.80	0.83
11 2 49.61	-54 29 14.3	3.12	19.97	21.77	5.33	5.10	0.88
11 2 40.93	-54 29 19.4	3.06	19.79	21.72	5.25	5.13	0.89
11 2 29.78	-54 29 18.7	3.00	19.67	21.65	5.14	5.21	0.90
11 2 20.48	-54 29 18.3	3.01	19.67	21.67	5.17	5.18	0.90
11 2 7.47	-54 29 12.1	3.20	19.77	21.94	5.61	4.80	0.83
11 7 50.31	-54 30 30.9	3.29	19.46	22.16	5.99	4.42	0.76
11 7 40.38	-54 30 15.8	3.15	18.74	22.14	5.95	4.29	0.74
11 7 29.22	-54 30 27.8	3.13	18.28	22.22	6.09	4.09	0.71
11 7 19.91	-54 30 34.1	3.13	18.35	22.21	6.07	4.12	0.71
11 7 10.62	-54 30 29.6	3.14	18.36	22.22	6.10	4.10	0.71
11 6 59.46	-54 30 35.7	3.05	18.34	22.08	5.84	4.28	0.74
11 6 49.54	-54 30 36.6	3.02	18.49	22.00	5.70	4.42	0.76
11 6 39.01	-54 30 42.9	3.02	18.46	22.00	5.70	4.41	0.76
11 6 28.47	-54 30 54.5	3.03	18.41	22.03	5.75	4.36	0.75
11 6 18.55	-54 30 49.7	2.97	18.22	21.97	5.66	4.38	0.76
11 6 6.76	-54 30 34.2	2.94	18.27	21.92	5.57	4.47	0.77
11 5 58.7	-54 30 50.9	3.06	18.74	21.99	5.69	4.48	0.77
11 5 46.91	-54 30 35.2	3.12	18.98	22.02	5.74	4.50	0.78
11 5 38.23	-54 30 35.6	3.25	19.08	22.20	6.06	4.29	0.74
11 5 26.46	-54 30 52.3	3.14	18.72	22.11	5.90	4.32	0.75
11 5 15.91	-54 30 52.6	3.03	18.47	22.01	5.72	4.39	0.76
11 5 7.23	-54 30 47.4	2.91	18.45	21.81	5.39	4.66	0.80
11 4 54.83	-54 30 53.1	2.91	18.54	21.78	5.35	4.72	0.82
11 4 46.14	-54 30 47.9	2.94	18.57	21.83	5.42	4.67	0.81
11 4 36.23	-54 30 58.8	2.96	18.43	21.90	5.54	4.53	0.78
11 4 23.2	-54 30 48.1	2.86	18.24	21.79	5.36	4.63	0.80
11 4 14.52	-54 30 48.1	2.84	18.43	21.70	5.21	4.82	0.83
11 4 3.98	-54 30 48.1	2.80	18.66	21.57	5.01	5.07	0.88
11 3 52.81	-54 30 53.3	2.89	18.85	21.68	5.18	4.96	0.86
11 3 42.27	-54 30 58.6	3.06	19.06	21.90	5.55	4.68	0.81
11 3 32.97	-54 30 47.6	3.09	19.06	21.95	5.62	4.62	0.80
11 3 23.67	-54 30 58.2	3.04	18.83	21.93	5.59	4.59	0.79
11 3 11.88	-54 31 3.2	2.93	18.82	21.75	5.30	4.83	0.83
11 3 1.96	-54 30 57.4	2.96	19.11	21.73	5.26	4.95	0.85
11 2 52.66	-54 31 2.4	3.08	19.58	21.79	5.36	4.97	0.86

continued on next page

Table 31 – continued from previous page

R.A.(J2000) hh mm ss	Dec.(J2000) dd mm ss	$F(60)$ (MJy)	$F(100)$ (MJy)	$T_{\rm d}$ (K)	$B(\nu,T)$ $(\times10^{-16})$ Js^{-2}	$M_{\rm d}$ $(\times10^{27})$ kg	$A_{\rm V}$ $(\times10^{-5})$ mag
11 2 39.64	-54 31 1.8	3.01	19.74	21.65	5.13	5.24	0.90
11 2 29.71	-54 30 56	2.94	19.51	21.59	5.05	5.26	0.91
11 2 22.27	-54 30 55.5	2.93	19.42	21.59	5.04	5.24	0.91
11 2 9.88	-54 30 49.3	3.02	19.71	21.67	5.17	5.20	0.90
11 8 0.35	-54 32 6.9	3.40	19.64	22.29	6.22	4.30	0.74
11 7 50.42	-54 31 57.6	3.22	19.21	22.12	5.92	4.42	0.76
11 7 39.88	-54 31 58.4	3.06	18.82	21.96	5.64	4.55	0.78
11 7 29.33	-54 31 59.7	3.09	18.57	22.09	5.86	4.32	0.75
11 7 21.27	-54 32 0.3	3.06	18.02	22.18	6.02	4.08	0.70
11 7 7.63	-54 32 12.2	3.04	18.19	22.10	5.88	4.21	0.73
11 7 0.18	-54 32 13	3.04	18.21	22.10	5.88	4.22	0.73
11 6 49.64	-54 32 19.3	3.05	18.43	22.05	5.79	4.33	0.75
11 6 39.1	-54 32 20	3.06	18.57	22.04	5.77	4.38	0.76
11 6 27.31	-54 32 26.2	3.01	18.39	21.99	5.69	4.40	0.76
11 6 17.38	-54 32 27	3.00	18.29	22.00	5.71	4.36	0.75
11 6 7.45	-54 32 22.2	3.01	18.30	22.02	5.74	4.34	0.75
11 5 57.52	-54 32 11.9	3.00	18.59	21.92	5.57	4.54	0.78
11 5 48.21	-54 32 23.2	3.10	18.94	21.99	5.69	4.53	0.78
11 5 38.28	-54 32 23.6	3.15	19.03	22.05	5.80	4.47	0.77
11 5 25.88	-54 32 29.4	3.20	18.81	22.19	6.04	4.24	0.73
11 5 17.81	-54 32 18.9	3.15	18.69	22.15	5.97	4.27	0.74
11 5 7.26	-54 32 30.1	3.04	18.49	22.03	5.76	4.37	0.76
11 4 56.09	-54 32 35.7	3.03	18.70	21.95	5.62	4.53	0.78
11 4 48.03	-54 32 25.1	3.02	18.67	21.95	5.62	4.52	0.78
11 4 35.62	-54 32 30.6	3.00	18.74	21.88	5.50	4.64	0.80
11 4 25.07	-54 32 25.3	2.98	18.57	21.89	5.52	4.58	0.79
11 4 14.52	-54 32 19.9	2.95	18.46	21.88	5.51	4.56	0.79
11 4 4.59	-54 32 14.5	2.93	18.66	21.78	5.35	4.75	0.82
11 3 53.42	-54 32 25.1	2.93	18.79	21.75	5.30	4.83	0.83
11 3 44.11	-54 32 30.4	3.00	18.83	21.86	5.47	4.68	0.81
11 3 33.56	-54 32 35.6	3.03	18.79	21.92	5.58	4.59	0.79
11 3 23.01	-54 32 35.4	3.00	18.62	21.92	5.58	4.54	0.78
11 3 11.22	-54 32 45.7	2.91	18.49	21.80	5.38	4.68	0.81
11 3 2.54	-54 32 18.4	2.89	18.81	21.68	5.19	4.94	0.85
11 2 52.61	-54 32 34.3	2.97	19.06	21.75	5.29	4.91	0.85
11 2 40.2	-54 32 28.2	3.03	19.42	21.76	5.31	4.98	0.86
11 2 29.65	-54 32 16.9	3.00	19.35	21.72	5.25	5.02	0.87
11 2 22.2	-54 32 32.7	2.88	19.33	21.54	4.95	5.31	0.92
11 2 9.8	-54 32 15.9	2.95	19.48	21.61	5.07	5.24	0.90
11 8 1.73	-54 33 28	3.42	19.43	22.38	6.37	4.15	0.72
11 7 50.55	-54 33 34.5	3.23	18.79	22.25	6.14	4.17	0.72
11 7 41.26	-54 33 35.7	3.12	18.85	22.06	5.81	4.42	0.76
11 7 31.32	-54 33 42.1	3.09	18.99	21.97	5.67	4.56	0.79
11 7 20.77	-54 33 37.5	3.12	18.59	22.12	5.92	4.28	0.74
11 7 9.6	-54 33 33.2	3.07	18.09	22.18	6.03	4.09	0.71
11 7 0.3	-54 34 1	3.06	18.31	22.11	5.90	4.23	0.73
11 6 48.5	-54 33 51.1	3.13	18.65	22.13	5.93	4.29	0.74
11 6 39.81	-54 33 57.3	3.13	18.81	22.08	5.85	4.38	0.76
11 6 28.63	-54 33 58	3.11	18.59	22.10	5.89	4.30	0.74
11 6 18.07	-54 34 4.1	3.07	18.33	22.11	5.89	4.24	0.73
11 6 8.14	-54 33 59.3	3.08	18.30	22.14	5.96	4.18	0.72
11 5 58.21	-54 34 5.3	3.07	18.43	22.09	5.87	4.28	0.74
11 5 47.03	-54 33 44.2	3.06	18.53	22.05	5.79	4.36	0.75
11 5 37.72	-54 34 6.2	3.14	18.92	22.07	5.83	4.42	0.76
11 5 27.16	-54 33 55.9	3.14	18.80	22.11	5.89	4.35	0.75
11 5 15.99	-54 33 56.2	3.14	18.57	22.17	6.00	4.22	0.73
11 5 7.29	-54 33 56.4	3.12	18.61	22.13	5.93	4.28	0.74
11 4 54.88	-54 34 7.5	3.05	18.47	22.05	5.79	4.34	0.75
11 4 46.18	-54 33 46.1	3.10	18.64	22.08	5.84	4.34	0.75
11 4 34.38	-54 33 57	3.04	18.48	22.02	5.75	4.38	0.76
11 4 24.45	-54 34 2.5	3.00	18.62	21.91	5.56	4.56	0.79
11 4 13.89	-54 33 57.1	2.97	18.46	21.91	5.55	4.53	0.78
11 4 5.2	-54 33 51.7	3.00	18.64	21.92	5.57	4.56	0.79
11 3 52.78	-54 33 51.5	2.98	18.70	21.86	5.47	4.66	0.80
11 3 43.47	-54 34 7.6	2.96	18.64	21.85	5.45	4.66	0.80
11 3 34.15	-54 34 2	2.93	18.54	21.82	5.40	4.68	0.81
11 3 22.36	-54 34 7.1	2.96	18.45	21.89	5.53	4.54	0.78
11 3 11.18	-54 34 6.7	2.96	18.63	21.85	5.45	4.65	0.80
11 3 1.25	-54 34 6.4	2.97	18.74	21.84	5.45	4.68	0.81
11 2 51.31	-54 34 11.4	2.98	19.17	21.74	5.28	4.94	0.85
11 2 41.38	-54 33 54.8	3.09	19.24	21.90	5.54	4.73	0.82
11 2 32.06	-54 33 59.8	2.99	19.32	21.72	5.24	5.02	0.87
11 2 22.13	-54 33 42.9	2.94	19.27	21.65	5.14	5.11	0.88
11 2 11.59	-54 33 42.4	2.98	19.43	21.67	5.17	5.12	0.88
11 8 9.95	-54 34 53.3	3.47	19.65	22.39	6.39	4.19	0.72
11 8 0.64	-54 35 10.6	3.34	19.28	22.29	6.22	4.22	0.73
11 7 50.69	-54 35 1.1	3.18	18.72	22.19	6.03	4.23	0.73

continued on next page

Table 31 – continued from previous page

R.A.(J2000) hh mm ss	Dec.(J2000) dd mm ss	$F(60)$ (MJy)	$F(100)$ (MJy)	$T_{\rm d}$ (K)	$B(\nu,T)$ $(\times10^{-16})$ Js^{-2}	$M_{\rm d}$ $(\times10^{27})$ kg	$A_{\rm V}$ $(\times10^{-5})$ mag
11 7 41.39	-54 35 12.7	3.15	18.51	22.20	6.05	4.16	0.72
11 7 29.58	-54 35 19.3	3.11	18.88	22.02	5.75	4.47	0.77
11 7 19.64	-54 35 4.1	3.09	18.90	22.00	5.70	4.51	0.78
11 7 9.08	-54 35 15.8	3.11	18.52	22.13	5.93	4.25	0.73
11 7 0.38	-54 35 16.6	3.15	18.45	22.22	6.09	4.13	0.71
11 6 48.59	-54 35 17.5	3.23	18.86	22.22	6.10	4.21	0.73
11 6 38.02	-54 35 7.5	3.30	19.12	22.27	6.18	4.21	0.73
11 6 29.33	-54 35 13.6	3.24	18.93	22.23	6.11	4.22	0.73
11 6 17.53	-54 35 19.7	3.16	18.46	22.23	6.10	4.12	0.71
11 6 8.84	-54 35 36.5	3.15	18.19	22.29	6.22	3.98	0.69
11 5 57.03	-54 35 31.7	3.14	18.17	22.27	6.17	4.01	0.69
11 5 47.09	-54 35 32.2	3.11	18.39	22.16	5.99	4.18	0.72
11 5 37.77	-54 35 27.2	3.08	18.49	22.08	5.85	4.30	0.74
11 5 27.21	-54 35 33.1	3.06	18.49	22.06	5.81	4.33	0.75
11 5 16.64	-54 35 33.4	3.06	18.29	22.11	5.89	4.23	0.73
11 5 5.45	-54 35 17.5	3.03	18.23	22.07	5.83	4.26	0.73
11 4 55.52	-54 35 28.5	3.07	18.43	22.09	5.87	4.27	0.74
11 4 45.58	-54 35 7.1	3.01	18.17	22.07	5.82	4.25	0.73
11 4 35.02	-54 35 34.2	3.05	18.34	22.08	5.85	4.27	0.74
11 4 25.08	-54 35 28.9	3.00	18.26	22.01	5.72	4.34	0.75
11 4 14.51	-54 35 28.9	3.06	18.57	22.04	5.77	4.38	0.76
11 4 3.95	-54 35 23.5	3.08	18.55	22.07	5.83	4.33	0.75
11 3 54.01	-54 35 28.8	3.04	18.61	21.99	5.69	4.45	0.77
11 3 43.45	-54 35 28.6	2.95	18.45	21.88	5.50	4.57	0.79
11 3 34.13	-54 35 17.6	2.89	18.33	21.82	5.41	4.62	0.80
11 3 21.71	-54 35 17.3	2.91	18.37	21.84	5.44	4.60	0.79
11 3 11.15	-54 35 17	3.01	18.82	21.89	5.53	4.64	0.80
11 3 1.83	-54 35 11.2	3.09	19.27	21.90	5.54	4.74	0.82
11 2 50.64	-54 35 10.8	3.11	19.35	21.90	5.54	4.76	0.82
11 2 41.94	-54 35 26.6	3.12	19.52	21.88	5.50	4.83	0.83
11 2 32	-54 35 31.5	3.07	19.36	21.84	5.44	4.85	0.84
11 2 21.43	-54 35 30.8	2.96	19.44	21.64	5.11	5.18	0.89
11 8 21.89	-54 36 29.2	3.29	19.63	22.12	5.91	4.52	0.78
11 8 11.94	-54 36 30.3	3.16	19.09	22.05	5.80	4.48	0.77
11 8 2	-54 36 31.5	3.09	18.93	21.99	5.69	4.53	0.78
11 7 52.06	-54 36 27.3	3.10	18.76	22.04	5.78	4.42	0.76
11 7 42.1	-54 36 28.3	3.08	18.54	22.08	5.84	4.32	0.75
11 7 31.54	-54 36 18.6	3.07	18.69	22.02	5.75	4.43	0.76
11 7 19.11	-54 36 30.7	3.05	18.87	21.94	5.60	4.59	0.79
11 7 9.81	-54 36 42.1	3.11	19.08	21.98	5.68	4.58	0.79
11 6 59.23	-54 36 37.8	3.19	19.21	22.08	5.84	4.48	0.77
11 6 50.53	-54 36 33	3.37	19.35	22.31	6.25	4.21	0.73
11 6 39.97	-54 36 33.8	3.45	19.24	22.47	6.54	4.01	0.69
11 6 28.78	-54 36 34.5	3.32	18.90	22.35	6.33	4.06	0.70
11 6 18.23	-54 36 46.1	3.13	18.44	22.19	6.03	4.16	0.72
11 6 8.9	-54 36 46.7	3.15	18.21	22.28	6.21	4.00	0.69
11 5 57.71	-54 36 47.4	3.22	18.35	22.35	6.33	3.95	0.68
11 5 46.52	-54 36 58.7	3.20	18.33	22.33	6.30	3.96	0.68
11 5 36.57	-54 36 59.1	3.14	18.46	22.19	6.03	4.17	0.72
11 5 27.25	-54 36 48.7	3.10	18.27	22.19	6.03	4.13	0.71
11 5 17.3	-54 36 59.8	3.03	18.08	22.13	5.92	4.16	0.72
11 5 6.73	-54 36 54.7	3.00	18.01	22.08	5.84	4.20	0.72
11 4 55.54	-54 37 5.7	2.96	18.16	21.98	5.68	4.35	0.75
11 4 45.6	-54 36 55.1	3.00	18.24	22.01	5.73	4.33	0.75
11 4 35.65	-54 37 6	2.98	18.11	22.03	5.76	4.28	0.74
11 4 25.7	-54 37 0.7	3.03	18.20	22.08	5.85	4.24	0.73
11 4 13.89	-54 36 49.9	3.09	18.41	22.13	5.93	4.23	0.73
11 4 4.57	-54 36 49.9	3.14	18.76	22.11	5.89	4.33	0.75
11 3 54	-54 36 55.2	3.07	18.60	22.03	5.77	4.39	0.76
11 3 42.81	-54 36 49.6	2.98	18.34	21.96	5.64	4.42	0.76
11 3 34.1	-54 36 54.8	2.90	18.34	21.82	5.41	4.62	0.80
11 3 22.29	-54 36 59.9	2.99	18.59	21.91	5.55	4.56	0.79
11 3 14.21	-54 36 54.3	3.13	19.01	22.03	5.76	4.49	0.78
11 3 0.54	-54 36 32.2	3.22	19.62	22.01	5.72	4.67	0.81
11 2 32.56	-54 36 47.1	3.14	19.77	21.85	5.45	4.94	0.85
11 2 22	-54 36 41.2	3.06	19.58	21.77	5.33	5.00	0.86
11 8 22.65	-54 37 50	3.26	19.51	22.11	5.89	4.51	0.78
11 8 12.09	-54 38 2	3.01	18.65	21.94	5.60	4.53	0.78
11 8 2.76	-54 37 57.6	3.04	18.59	22.00	5.70	4.44	0.77
11 7 51.58	-54 38 9.8	3.12	18.70	22.09	5.87	4.34	0.75
11 7 40.37	-54 38 0.2	3.12	18.79	22.07	5.83	4.39	0.76
11 7 32.28	-54 37 44.9	3.11	18.62	22.09	5.87	4.32	0.75
11 7 19.85	-54 38 7.7	3.11	18.83	22.05	5.79	4.43	0.76
11 7 10.53	-54 38 13.9	3.13	19.16	21.99	5.69	4.58	0.79
11 6 59.34	-54 38 20.3	3.19	19.49	22.00	5.71	4.65	0.80
11 6 50.01	-54 38 15.6	3.29	19.61	22.13	5.93	4.50	0.78
11 6 38.18	-54 38 11.2	3.32	19.37	22.24	6.13	4.30	0.74

continued on next page

Table 31 – continued from previous page

R.A.(J2000) hh mm ss	Dec.(J2000) dd mm ss	$F(60)$ (MJy)	$F(100)$ (MJy)	$T_{\rm d}$ (K)	$B(\nu,T)$ $(\times10^{-16})$ Js^{-2}	$M_{\rm d}$ $(\times10^{27})$ kg	$A_{\rm V}$ $(\times10^{-5})$ mag
11 6 26.36	-54 37 55.9	3.24	18.78	22.27	6.18	4.14	0.71
11 6 15.81	-54 38 28.8	3.13	18.38	22.20	6.05	4.14	0.71
11 6 6.47	-54 38 13.3	3.17	18.40	22.25	6.15	4.07	0.70
11 5 58.39	-54 38 19	3.22	18.65	22.28	6.19	4.10	0.71
11 5 47.82	-54 38 19.6	3.28	18.93	22.30	6.23	4.14	0.71
11 5 36.62	-54 38 25.5	3.23	18.66	22.28	6.19	4.10	0.71
11 5 24.8	-54 38 15.1	3.18	18.61	22.22	6.09	4.16	0.72
11 5 16.71	-54 38 26.1	3.04	18.19	22.11	5.89	4.20	0.73
11 5 4.89	-54 38 10.3	2.98	17.93	22.08	5.84	4.18	0.72
11 4 54.32	-54 38 32.1	2.95	18.01	22.00	5.71	4.29	0.74
11 4 44.99	-54 38 21.5	2.95	18.22	21.95	5.63	4.41	0.76
11 4 35.66	-54 38 32.4	2.99	18.18	22.02	5.73	4.32	0.75
11 4 25.71	-54 38 16.3	3.05	18.17	22.12	5.92	4.18	0.72
11 4 14.51	-54 38 21.7	3.10	18.42	22.13	5.94	4.22	0.73
11 4 3.94	-54 38 27	3.14	18.74	22.12	5.92	4.31	0.74
11 3 53.98	-54 38 27	3.14	18.83	22.09	5.87	4.37	0.75
11 3 44.03	-54 38 10.6	3.03	18.66	21.96	5.65	4.50	0.78
11 3 34.08	-54 38 32	3.03	18.65	21.96	5.64	4.50	0.78
11 3 21.01	-54 38 20.9	3.10	19.04	21.97	5.66	4.58	0.79
11 3 12.93	-54 38 20.6	3.21	19.55	22.01	5.73	4.65	0.80
11 8 21.58	-54 39 32.7	3.22	19.55	22.02	5.75	4.63	0.80
11 8 12.23	-54 39 28.4	3.09	19.20	21.91	5.55	4.71	0.81
11 8 2.28	-54 39 34.9	3.07	18.89	21.96	5.65	4.55	0.79
11 7 52.33	-54 39 36.3	3.13	18.85	22.07	5.83	4.40	0.76
11 7 40.51	-54 39 37.4	3.20	19.01	22.15	5.96	4.34	0.75
11 7 32.42	-54 39 43.7	3.26	18.97	22.25	6.15	4.20	0.73
11 7 21.21	-54 39 39.2	3.24	18.81	22.26	6.15	4.16	0.72
11 7 10.63	-54 39 34.9	3.22	19.04	22.17	6.00	4.32	0.75
11 7 0.07	-54 39 52.1	3.28	19.51	22.13	5.94	4.48	0.77
11 6 48.24	-54 39 47.6	3.27	19.63	22.10	5.87	4.55	0.79
11 6 40.15	-54 39 53.6	3.26	19.19	22.18	6.03	4.33	0.75
11 6 28.33	-54 39 38.3	3.17	18.72	22.18	6.02	4.24	0.73
11 6 15.88	-54 39 55.2	3.14	18.48	22.19	6.03	4.17	0.72
11 6 7.16	-54 39 50.4	3.18	18.64	22.21	6.08	4.18	0.72
11 5 58.45	-54 39 56.3	3.37	18.94	22.42	6.46	3.99	0.69
11 5 48.49	-54 39 35.2	3.34	19.25	22.29	6.22	4.21	0.73
11 5 36.67	-54 40 2.7	3.41	19.21	22.42	6.45	4.06	0.70
11 5 25.46	-54 39 41.5	3.32	18.77	22.40	6.42	3.98	0.69
11 5 17.37	-54 39 58	3.17	18.70	22.18	6.02	4.23	0.73
11 5 5.55	-54 40 9.1	3.01	18.26	22.04	5.78	4.30	0.74
11 4 54.96	-54 39 47.7	2.93	18.11	21.94	5.61	4.40	0.76
11 4 46.25	-54 39 42.5	2.97	18.22	21.97	5.66	4.38	0.76
11 4 35.05	-54 39 58.8	2.95	18.37	21.90	5.55	4.51	0.78
11 4 23.84	-54 40 9.7	2.94	18.48	21.85	5.46	4.61	0.80
11 4 13.89	-54 40 9.7	3.12	18.69	22.10	5.88	4.33	0.75
11 4 2.68	-54 39 42.6	3.14	18.72	22.13	5.92	4.30	0.74
11 3 53.35	-54 39 47.9	3.12	19.07	21.99	5.69	4.56	0.79
11 3 43.38	-54 40 9.4	3.08	18.92	21.98	5.67	4.54	0.78
11 3 34.05	-54 39 53.1	3.13	19.12	22.00	5.70	4.57	0.79
11 3 23.47	-54 39 47.3	3.21	19.57	22.01	5.72	4.66	0.80
11 8 11.78	-54 41 16.5	3.14	19.66	21.88	5.51	4.86	0.84
11 8 1.17	-54 40 50.8	3.10	19.53	21.84	5.44	4.89	0.84
11 7 51.23	-54 41 8.1	3.15	19.09	22.04	5.78	4.49	0.78
11 7 40.02	-54 41 14.8	3.26	19.08	22.22	6.09	4.27	0.74
11 7 30.04	-54 40 59.6	3.30	19.31	22.21	6.08	4.33	0.75
11 7 20.08	-54 41 5.8	3.39	19.24	22.38	6.39	4.10	0.71
11 7 11.36	-54 41 6.6	3.39	19.40	22.33	6.29	4.20	0.73
11 7 0.77	-54 41 2.1	3.35	19.56	22.23	6.11	4.36	0.75
11 6 49.56	-54 41 8.7	3.28	19.63	22.10	5.89	4.54	0.78
11 6 40.23	-54 41 14.6	3.24	19.45	22.09	5.86	4.52	0.78
11 6 29.02	-54 41 15.5	3.27	19.05	22.24	6.13	4.23	0.73
11 6 19.68	-54 41 10.7	3.22	18.72	22.25	6.14	4.15	0.72
11 6 7.22	-54 41 11.4	3.42	18.90	22.52	6.64	3.88	0.67
11 5 56.64	-54 41 17.4	3.46	18.96	22.56	6.73	3.84	0.66
11 5 47.3	-54 41 17.8	3.50	19.24	22.54	6.68	3.92	0.68
11 5 36.71	-54 41 18.2	3.50	19.33	22.52	6.64	3.97	0.68
11 5 24.26	-54 41 13.3	3.47	19.16	22.52	6.64	3.93	0.68
11 5 17.41	-54 41 24.3	3.25	18.86	22.26	6.16	4.17	0.72
11 5 4.95	-54 41 24.7	3.08	18.60	22.06	5.81	4.36	0.75
11 4 54.99	-54 41 30.3	2.92	18.32	21.87	5.49	4.54	0.78
11 4 44.4	-54 41 25.1	2.92	18.21	21.89	5.52	4.49	0.78
11 4 36.3	-54 41 19.8	2.90	18.36	21.82	5.42	4.62	0.80
11 4 25.72	-54 41 25.3	2.95	18.64	21.82	5.41	4.69	0.81
11 4 14.51	-54 41 25.3	3.06	18.97	21.92	5.58	4.63	0.80
11 4 3.92	-54 41 25.2	3.18	18.98	22.11	5.90	4.38	0.76
11 3 55.2	-54 41 25.2	3.20	19.21	22.08	5.85	4.47	0.77
11 3 43.99	-54 41 30.4	3.17	19.42	21.99	5.70	4.64	0.80

continued on next page

Table 31 – continued from previous page

R.A.(J2000) hh mm ss	Dec.(J2000) dd mm ss	$F(60)$ (MJy)	$F(100)$ (MJy)	$T_{\rm d}$ (K)	$B(\nu,T)$ $(\times10^{-16})$ Js^{-2}	$M_{\rm d}$ $(\times10^{27})$ kg	$A_{\rm V}$ $(\times10^{-5})$ mag
11 3 34.65	-54 41 3.2	3.14	19.74	21.85	5.45	4.93	0.85
11 8 10.66	-54 42 26.9	3.27	19.74	22.06	5.81	4.62	0.80
11 8 2.57	-54 42 28	3.22	19.45	22.06	5.81	4.56	0.79
11 7 50.73	-54 42 45.3	3.11	19.14	21.96	5.64	4.62	0.80
11 7 41.99	-54 42 35.4	3.14	18.62	22.15	5.97	4.25	0.73
11 7 29.55	-54 42 36.7	3.26	18.91	22.27	6.18	4.17	0.72
11 7 20.21	-54 42 48.4	3.31	19.35	22.22	6.10	4.32	0.75
11 7 10.85	-54 42 38.5	3.35	19.52	22.24	6.14	4.33	0.75
11 7 0.25	-54 42 39.4	3.35	19.85	22.15	5.96	4.54	0.78
11 6 49.04	-54 42 34.8	3.36	19.76	22.20	6.05	4.44	0.77
11 6 37.82	-54 42 46.5	3.31	19.68	22.13	5.94	4.51	0.78
11 6 28.47	-54 42 36.4	3.23	19.35	22.09	5.87	4.49	0.78
11 6 19.76	-54 42 37.1	3.34	19.20	22.32	6.26	4.17	0.72
11 6 9.16	-54 42 43	3.44	19.33	22.42	6.46	4.07	0.70
11 5 57.32	-54 42 38.3	3.57	19.32	22.62	6.83	3.85	0.66
11 5 47.35	-54 42 49.6	3.56	19.48	22.56	6.72	3.95	0.68
11 5 37.38	-54 42 39.2	3.60	19.73	22.56	6.72	4.00	0.69
11 5 28.04	-54 43 1.2	3.56	19.58	22.54	6.68	3.99	0.69
11 5 18.07	-54 42 56.2	3.42	19.27	22.42	6.45	4.07	0.70
11 5 4.36	-54 42 51.1	3.27	18.86	22.29	6.22	4.13	0.71
11 4 56.88	-54 42 45.9	3.12	18.83	22.05	5.80	4.42	0.76
11 4 46.91	-54 42 51.5	3.08	18.42	22.10	5.88	4.27	0.74
11 4 35.69	-54 43 2.4	3.04	18.17	22.11	5.90	4.19	0.72
11 4 25.1	-54 42 51.7	3.16	18.57	22.20	6.06	4.17	0.72
11 4 15.75	-54 42 40.9	3.20	19.03	22.13	5.94	4.36	0.75
11 4 3.91	-54 42 51.7	3.22	19.40	22.07	5.83	4.53	0.78
11 3 53.94	-54 42 40.8	3.28	19.61	22.11	5.90	4.52	0.78
11 8 2.71	-54 44 15.9	3.24	19.43	22.09	5.86	4.52	0.78
11 7 52.73	-54 44 0.8	3.12	18.86	22.05	5.79	4.43	0.77
11 7 43.38	-54 44 1.8	3.11	18.68	22.08	5.85	4.35	0.75
11 7 30.27	-54 43 57.8	3.21	18.72	22.24	6.12	4.16	0.72
11 7 20.93	-54 44 9.3	3.25	19.17	22.18	6.01	4.34	0.75
11 7 10.32	-54 44 5	3.37	19.53	22.27	6.18	4.30	0.74
11 6 58.48	-54 44 5.8	3.44	19.69	22.34	6.30	4.26	0.73
11 6 49.14	-54 44 12.2	3.43	19.76	22.30	6.24	4.32	0.75
11 6 39.16	-54 44 2.1	3.42	19.41	22.37	6.37	4.15	0.72
11 6 29.18	-54 44 2.8	3.34	19.37	22.27	6.18	4.27	0.74
11 6 18.58	-54 44 3.5	3.30	19.30	22.21	6.08	4.32	0.75
11 6 8.6	-54 43 58.8	3.45	19.37	22.43	6.47	4.08	0.70
11 5 59.87	-54 43 59.2	3.51	19.35	22.53	6.66	3.96	0.68
11 5 46.17	-54 44 21.5	3.56	19.32	22.62	6.82	3.85	0.67
11 5 36.81	-54 44 11	3.49	19.46	22.47	6.55	4.05	0.70
11 5 28.08	-54 44 16.8	3.46	19.76	22.35	6.32	4.26	0.73
11 5 14.98	-54 44 17.2	3.45	19.59	22.38	6.38	4.18	0.72
11 5 6.26	-54 44 22.9	3.35	19.45	22.26	6.17	4.29	0.74
11 4 55.03	-54 44 12.3	3.28	19.06	22.26	6.16	4.21	0.73
11 4 45.68	-54 44 12.5	3.18	18.95	22.12	5.92	4.36	0.75
11 4 33.83	-54 44 18	3.25	18.90	22.25	6.14	4.19	0.72
11 4 24.48	-54 44 12.7	3.33	19.12	22.31	6.25	4.17	0.72
11 4 15.13	-54 44 18.1	3.37	19.67	22.23	6.12	4.38	0.76
11 7 52.85	-54 45 32.7	3.11	19.17	21.96	5.64	4.63	0.80
11 7 40.38	-54 45 39.3	3.10	18.96	21.99	5.70	4.53	0.78
11 7 30.39	-54 45 24.2	3.18	19.04	22.09	5.87	4.42	0.76
11 7 21.66	-54 45 25	3.27	19.23	22.20	6.05	4.33	0.75
11 6 49.22	-54 45 22.3	3.53	19.74	22.45	6.51	4.13	0.71
11 6 28.63	-54 45 39.9	3.45	19.45	22.41	6.44	4.11	0.71
11 6 18.04	-54 45 40.6	3.32	19.13	22.30	6.23	4.18	0.72
11 6 8.68	-54 45 41.3	3.43	18.91	22.53	6.65	3.87	0.67
11 5 58.07	-54 45 41.9	3.51	19.23	22.56	6.72	3.90	0.67
11 5 48.09	-54 45 37	3.57	19.39	22.61	6.81	3.88	0.67
11 5 38.1	-54 45 32.1	3.53	19.32	22.56	6.72	3.91	0.68
11 5 27.5	-54 45 59.4	3.48	19.40	22.47	6.54	4.04	0.70
11 5 16.26	-54 45 38.2	3.47	19.75	22.36	6.34	4.24	0.73
11 5 7.53	-54 45 43.8	3.42	19.46	22.37	6.36	4.16	0.72
11 4 56.3	-54 45 54.9	3.34	19.36	22.27	6.18	4.27	0.74
11 4 44.45	-54 45 49.7	3.32	19.30	22.25	6.14	4.28	0.74
11 4 33.84	-54 45 39	3.34	19.51	22.22	6.09	4.36	0.75
11 4 23.86	-54 45 28.3	3.40	19.78	22.24	6.13	4.39	0.76
11 7 52.37	-54 47 9.8	3.17	19.63	21.93	5.59	4.78	0.83
11 7 41.77	-54 47 5.5	3.14	19.33	21.96	5.63	4.67	0.81
11 7 31.78	-54 47 12	3.20	19.17	22.10	5.88	4.44	0.77
11 7 23.63	-54 46 51.1	3.27	19.58	22.11	5.89	4.53	0.78
11 6 20.61	-54 47 12.4	3.40	19.38	22.36	6.34	4.17	0.72
11 6 9.99	-54 47 7.7	3.39	19.29	22.36	6.34	4.14	0.72
11 5 57.5	-54 47 13.7	3.48	19.14	22.54	6.68	3.90	0.67
11 5 47.52	-54 47 3.4	3.59	19.48	22.61	6.81	3.90	0.67
11 5 28.16	-54 46 58.9	3.64	19.80	22.61	6.81	3.96	0.68

continued on next page

Table 31 – continued from previous page

R.A.(J2000) hh mm ss	Dec.(J2000) dd mm ss	$F(60)$ (MJy)	$F(100)$ (MJy)	$T_{\rm d}$ (K)	$B(\nu,T)$ $(\times10^{-16})$ Js^{-2}	$M_{\rm d}$ $(\times10^{27})$ kg	$A_{\rm V}$ $(\times10^{-5})$ mag
11 5 15.68	-54 47 10	3.59	19.72	22.55	6.71	4.00	0.69
11 4 56.95	-54 47 21.3	3.45	19.61	22.36	6.35	4.21	0.73
11 4 46.34	-54 47 10.7	3.44	19.62	22.35	6.33	4.22	0.73
11 6 9.44	-54 48 44.9	3.39	19.45	22.32	6.27	4.22	0.73
11 5 58.2	-54 48 50.9	3.44	19.50	22.38	6.38	4.17	0.72

Appendix B

Publications

(A) **International Journals**

(1) **A study of four low latitude (|l|<10°) far infrared cavities**. Journal of Astrophysics and Astronomy (Springer), **40**, 16 (2019)

(2) **Study of Dusty Environment around a Carbon-rich AGB Star in Far Infrared Maps at Latitude 15°.** International Journal of Applied Physics (IJAP), **8**(1), 92 (2017)

(3) **A Study of Dusty Environment at Far Infrared IRAS Map Around the Mass-Losing Carbon-rich AGB Star at Latitude -53°.** International Journal of Applied Physics (IJAP), **9**(1), 24 (2018)

(4) **A Study of Dusty Environment at Far Infrared IRAS Map Around the Mass Losing Carbon-rich AGB Star at Latitude -59.6°.** International Journal of Multidisciplinary Research Review (IJMDRR), **1**(35), 45 (January, 2018)

(5) **Interaction Between C-rich AGB Star and the Interstellar Medium in Far Infrared Maps at 16° Latitude.** Research Highlights (A Multidisciplinary Quarterly International Referred Research Journal) **4**(4), 85 (2017)

(B) **National Journals**

(1) **A Study of Dust Structure around AGB Star in 60 and 100 μm IRAS Survey at Latitude 54.68°.** Journal of Nepal Physical Society (JNPS), **4**(1), 67 (2017)

(2) **Far Infrared Cavity of a Post C-rich AGB Star under IRAS Survey.** BIBECHANA, **15**, 90 (2018)

(3) **Study of Far Infrared Cavity around a Post AGB Star Under IRAS Survey at galactic Latitude -3°.** BIBECHANA, **16**, 23 (2019)

Appendix C

Participation in Conferences

(A) **International**

(1) Oral presentation on the topic **"A Study of Materials in the Far Infrared Sky at Latitude -53°" (ICMRT, July 10-11, 2017, Ballavgarh India)**

(B) **National**

(1) Oral presentation on the topic **"A Study of Dusty Environment at Far Infrared IRAS Map Around the Mass -Losing Carbon-rich AGB Star at Latitude -59.6°" (ICPSM-2017, September 2-3, Kathmandu)**

(2) Oral presentation on the topic "Study of Dusty Environment of a Far Infrared Cavity at 60 μm and 100 μm IRAS map around the Carbon-rich AGB Star at Galactic Latitude 8.6°" (ICEP, May 29-31, 2018, Kathmandu, Nepal)

J. Astrophys. Astr. (2019) 40:16
https://doi.org/10.1007/s12036-019-9578-1

A study of four low-latitude ($|l| < 10°$) far-infrared cavities

A. K. GAUTAM and B. ARYAL*

Central Department of Physics, Tribhuvan University, Kirtipur, Nepal.
*Corresponding author. E-mail: aryalbinil@gmail.com

MS received 17 October 2018; accepted 11 January 2019; published online 19 March 2019

Abstract. We present dust color temperature, dust mass, planck function and visual extinction distributions in the four low-latitude ($| l | < 10°$) far-infrared cavities namely FIC01+55, FIC05+28, FIC06−05 and FIC06−01 which are found to be located within 0.5° far-infrared loops G128−03, G182+00, G212−11 and G214−01, respectively. These cavities are located within 3° of AGB stars ABG01+55, AGB05+28, AGB06−05 and PAGB181, respectively. The dust color temperature of the core region is found to lie in the range 18.4 ± 1.2 to 26.2 ± 1.7K. The product of dust color temperature and visual extinction is found to be consistent. The contour maps showed that the low temperature region have greater mass density. The distribution of planck function along major and minor diameters is found to be sinusoidal, suggesting oscillation in the grain temperature distribution.

Keywords. ISM—AGB—DUST—IRAS.

1. Introduction

The surroundings of an AGB star is a natural laboratory in which one can study its effect in the interstellar medium. The study of interaction between AGB wind and the ambient interstellar medium can reveal the process of cavity formation. A complete catalog of AGB stars in IRAS PSC was developed by Suh and Kwon (2009, 2011). Using all sky database of IRAS, Wood *et al.* (1994) studied the images of nearby 100 dark molecular clouds at 60 μm and 100 μm wavelengths. They calculated optical depth, visual extinction of dust and hence proposed an empirical formula relating them.

Kiss *et al.* (2004) and Koenyves *et al.* (2007) investigated 462 far-infrared loops at 60 and 100 μm IRAS map and studied their luminosity distributions. They concluded that these structures might be formed by high pressure events (e.g., AGB wind) in the past. Odenwald and Rickard (1987) and Odenwald (1988) recorded 15 high Galactic latitude clouds in the 100 μm IRAS maps and studied their far-IR properties. Weinberger and Armsdorfer (2004) found a very large (∼ 9°) jet like structures in the far-infrared. They concluded that the structure might form because of the interactions of the wind of the AGB stars with ambient matter. Aryal *et al.* (2010) found two giant bipolar dust emission structures centred on PN NGC 1514 at FIR wavelengths. In another work, Aryal *et al.* (2009) noticed that the PN NGC 2899 is located at the center of a huge quadrupolar cavity, whose directions of axes coincide with the directions of the main axes of the optical PN. Aryal and Weinberger (2006) detected a new infrared nebula (R.A. = 08^h27^m, Dec. = $+25°54'$(J2000)), suggested that the pulsar PSR B0823+26 might be responsible for its shaping.

Jha *et al.* (2017) studied dust color temperature and dust mass distributions in four low-latitude ($l \leq 20°$) far infrared loops (G007+18, G143+07, G214−01 and G323−02) located nearby pulsars. They concluded that these loops might be formed due to the high pressure events occurred in the past (e.g., supernova explosion). The dust color temperature of these loops are found to lie in the range 19.4 ± 1.2 to 25.3 ± 1.7K. In another study, Jha and Aryal (2018) calculated dust color temperature of two far-infrared cavities using AKARI and IRIS maps. Interestingly, they found that the longer wavelength AKARI map gives larger values of dust color temperature than that of the shorter wavelength IRIS maps.

Here we studied the dust color temperature and extinction distributions in the cavity located nearby

AGB stars. In addition, the distribution of Planck function was studied. Finally, we drew conclusions regarding the nature of FIR spectral distribution of cavities. A selection procedure of four far-infrared cavity candidates are described in Section. 2. A description of dust color temperatures, dust mass and visual extinction is given in Section 3. Our result will be presented in Section 4. Finally, we summarize our conclusions in Section 5.

2. Far infrared cavities

Suh and Kwon (2009) presented infrared two-colour diagrams for 3003 O-rich, 1168 C-rich, 362 S-type and 35 silicate carbon stars in our Galaxy. We performed systematic search to find far-infrared cavities around 1168 C-rich AGB stars at 60 and 100 μm IRIS maps using Sky View Virtual Observatory (http://skyview.gsfc.nasa.gov/current/) and selected 4 far infrared cavities for the study on the basis of following selection criteria: (1) the core region of the cavity should have flux minima at 100 μm IRIS maps, (2) the major diameter should be $> 0.5°$, (3) the region should lie in the Galactic plane ($-10° < b < 10°$), and (4) the region should lie within far-infrared loops (Kiss *et al.* 2004; Koenyves *et al.* 2007; KK-loop hereafter). The database of 4 far-infrared (FIR) cavities is listed in Table 1.

Figure 1 shows relative positions of the far-infrared cavities and nearby AGB star with their proper motion (represented by an arrow). The cavity FIC06−01 is the distant (6.1 kpc) and FIC06−55 is the nearby (0.5 kpc). These cavities are found to be located within 0.5° from the centre of KK-loops namely G128−03, G182+00, G212−11 and G214−01 (Kiss *et al.* 2004; Koenyves *et al.* 2007), respectively. In all FIR maps (Figures. 2a, 4a, 6a, 8a), KK-loop centres are represented by symbol '+') are shown. The size of these loops

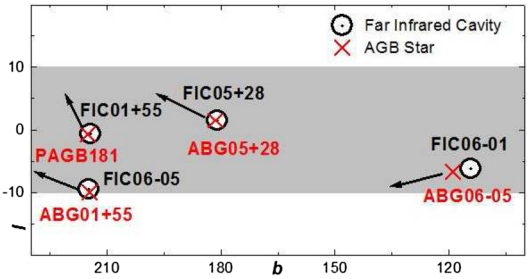

Figure 1. Position of the four FIR cavities (dotted hollow circle) and nearby AGB star (cross). The radius of the hollow circle is 5°, where KK-loops (Kiss *et al.* 2004; Koenyves *et al.* 2007) are found to be located. The name of the far-infrared cavities and AGB stars are shown. The arrows represent proper motions of the AGB star. The direction of proper motion suggests that the AGB star might have passed through the far-infrared cavities.

are $3.6° \times 3.2°$, $4.7° \times 4.1°$, $8.4° \times 7.1°$, $2.1° \times 2.0°$, respectively (Kiss *et al.* 2004; Koenyves *et al.* 2007). The nearby AGB stars (Table 1) are well within the far-infrared loops.

In the raw IRAS image, point sources appear elongated, along the scan direction. The point spread function (PSF) of an IRAS source can be determined by studying geometry of the scans covering the source. Therefore, we used IRIS maps (Miville-Deschnes and Lagache 2005) which are available through the IRSA interface (NASA/IPAC Infrared Science Archive). IRIS maps benefit from better zodiacal emission subtraction, calibration and zero level compatible with COBE/DIRBE, and better destriping. IRIS maps keep the full ISSA resolution, including calibrated point sources. In addition, diffuse emission calibration at scales smaller than 1° was corrected for the variation of the IRAS detector responsivity with scale and brightness.

For the background subtraction, we adopted the method used in Aryal *et al.* (2010). We used the surrounding region where flux density is minimum as a

Table 1. The database of four low-latitude ($|l| < 10°$) far-infrared cavities.

FIC	α(J2000) (deg)	δ(J2000) (deg)	D (kpc)	a (pc)	b (pc)	Nearby AGB
FIC01+55	$01^h35^m19^s$	$+55°39'19''$	1.9[1]	10.2	5.5	ABG01+55
FIC05+28	$05^h54^m04^s$	$+28°52'38''$	3.8[2]	43.1	26	AGB05+28
FIC06−55	$06^h21^m05^s$	$-05°38'31''$	0.5[3]	6.3	2.3	AGB06−05
FIC06−01	$06^h51^m54^s$	$-01°35'43''$	6.1[4]	103.2	33.1	PAGB181

The first column lists the name of the cavity (FIChh+dd). The second and third columns give positions. The next three columns list the derived distance (D), major (a) and minor (b) diameters of cavities. The last column lists the name of nearest AGB star from the cavity centre.
[1]: Garmany and Stencel (1992), [2]: Preite-Martinez (1988), [3]: Blitz *et al.* (1982), [4]: Szczerba *et al.* (2007)

reference. After making a histogram, average value of flux density was determined, and later it was subtracted from each pixel. The foreground emission was subtracted by considering the flux density contributed by the IRAS point sources. The errors given with dust color temperature and the mass are mainly due to the variation in the background and foreground subtraction. The background correction was made in both 60 and 100 μm IRIS maps. We used ALADIN2.5 software to get the values of flux density from FITS image of the region of interest. The FITS images of FIR cavities are downloaded from SkyView Virtual Observatory (http://skyview.gsfc.nasa.gov/current/).

In the present work we studied dust color temperature, dust mass, visual extinction and Planck function distributions. Finally, nature of FIR spectral distribution will be discussed.

3. Methods

The method of calculation for the dust color temperature and dust mass is described in Jha *et al.* (2017). Here we briefly describe the methods for calculating optical thickness and hence visual extinction using 100 μm IRIS maps.

3.1 *Dust color temperature*

The dust color temperature of all pixels of selected four FIR cavities were calculated using 60 and 100 μm IRIS flux densities. For this, we followed the method proposed by Wood *et al.* (1994), and later it was improved by Arce and Goodman (1999), Dupac *et al.* (2003), Schnee *et al.* (2005). They derived an expression for dust color temperature T_d as

$$T_d = \frac{-96}{ln\{R \times 0.6^{(3+\beta)}\}}, R = \frac{F(60\mu m)}{F(100\mu m)} \quad (1)$$

Here the value of β depends on dust, grain properties (e.g., composition, size, compactness, structure, etc). Its value is zero for a perfect blackbody. The amorphous layer-lattice matter and crystalline dielectrics have β = 1 and 2, respectively.

3.2 *Dust mass and visual extinction*

For the calculation of dust mass we first obtained the value of flux density (F_λ) at 100 μm maps. The dust masses are estimated using (Hildebrand 1983)

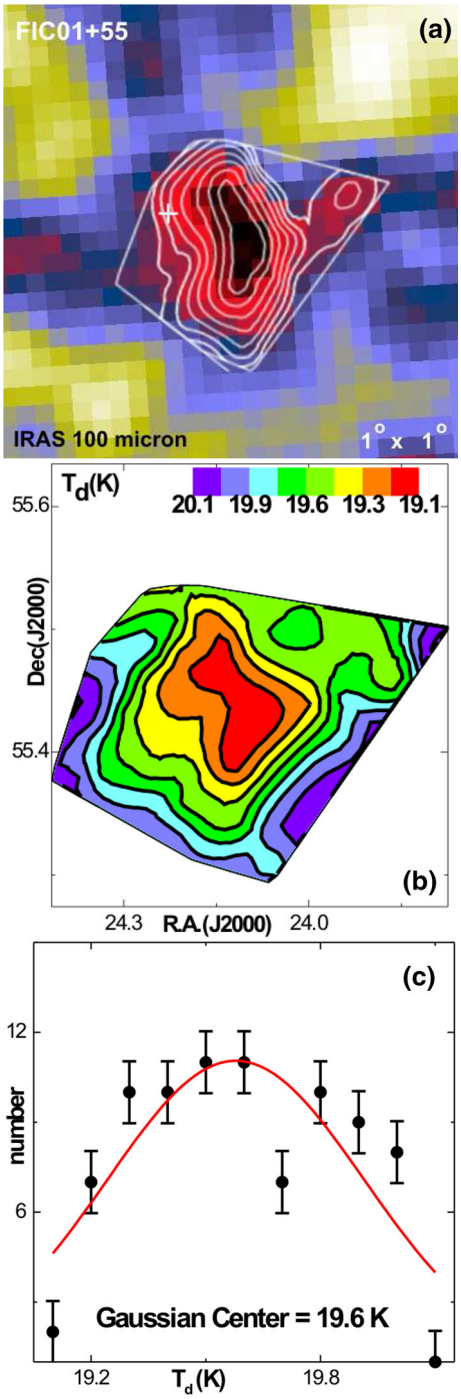

Figure 2. (a) 100 μm IRIS map of the far-infrared cavity FIC01+55 centered at (a) RA ($J2000$) = $01^h35^m19^s$, Dec ($J2000$) = $55°39'19''$. The contours and image size are shown. The IRIS contours represent 12.4, 12.6, 12.8, 12.9, 13.1, 13.2, 13.4 and 13.6 MJy sr^{-1}. The symbol '+' represents the position of the centre of KK-loop G128−03 (Kiss *et al.* 2004; Koenyves *et al.* 2007). The dust color temperature contour map (b) and distribution (c) are shown. The color bars (b) and Gaussian fit (c) can be seen. The error bars represent standard error ($\pm 1\sigma$) of the distribution.

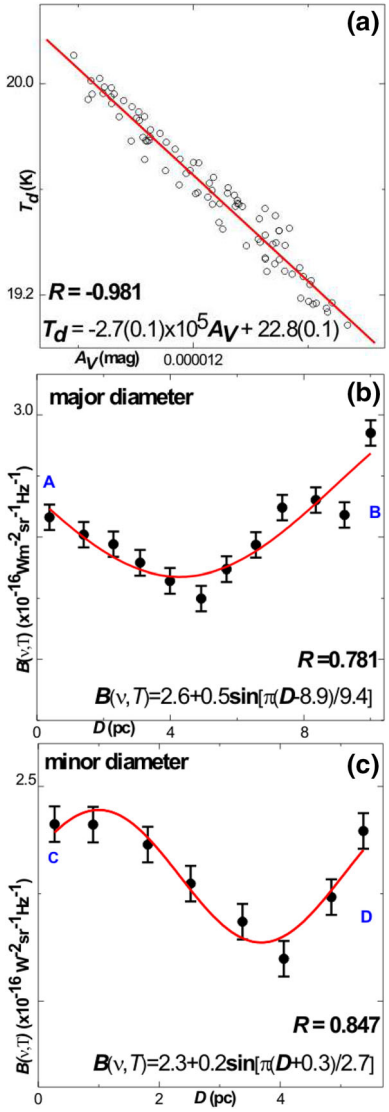

Figure 3. (a) The variation of visual extinction (A_V) with dust color temperature (T_d) in the cavity FIC01+55. The best fit equation is given (error in parentis). The distribution of Planck function along the major (b) and minor diameter (c) of the cavity. The positions A → B and C → D represent north–south and east–west directions in the cavity. The Planck function distribution shows sinusoidal like function, related to the grain temperature distribution. The sinusoidal equation and regression coefficient (R) are shown. The error bars represent standard error ($\pm 1\sigma$) of the distribution.

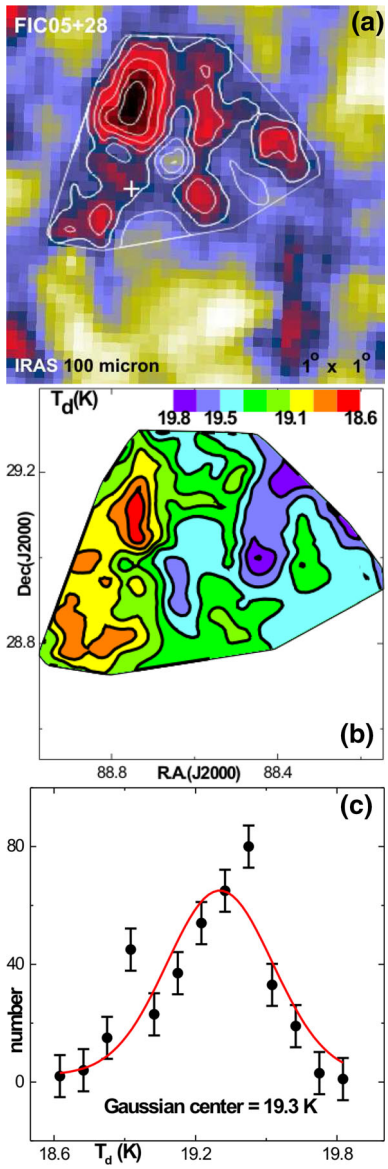

Figure 4. (a) 100 μm IRIS map of the far-infrared cavity FIC05+28 centered at (a) RA ($J2000$) = $05^h54^m04^s$, Dec (J2000) = $28°52'38''$. The contours and image size are shown. The IRAS contours represent 21.5, 21.8, 22.1, 22.4, 22.7, 23.0, 23.3 and 23.7 MJy sr^{-1}. The symbol '+' represents the position of the centre of KK-loop G182+00 (Kiss *et al.* 2004; Koenyves *et al.* 2007). The dust color temperature contour map (b) and distribution (c) are shown. The color bars (b) and Gaussian fit (c) can be seen. The error bars represent standard error ($\pm 1\sigma$) of the distribution.

$$M_{dust} = \frac{4}{3}\frac{a\rho}{Q_\nu}\left[\frac{F_\lambda D^2}{B(\nu, T)}\right] \quad (2)$$

where a, ρ and Q_ν represent grain size, grain density and grain emissivity. The grains with radii 0.01–0.30 μm radiate a spectrum characteristic of thermal emission at the temperature 15–20 K for grains in the diffuse interstellar medium (Draine 2001). This accounts for nearly all of the emission at $\lambda > 60\,\mu$m. Young *et al.* (1993) estimated the values of grain emissivity and weighted grain size at 100 μm by interpolating the data tabulated by Draine (1987). Therefore we adopted Young *et al.* (1993) and used the following values: weighted grain size (a) = 0.1 μm, grain density (ρ) =

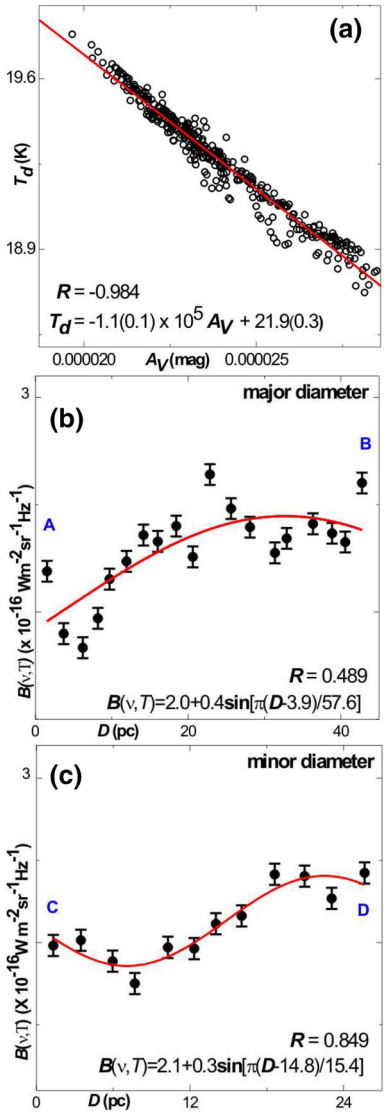

Figure 5. (a) The variation of visual extinction (A_V) with dust color temperature (T_d) in the cavity FIC05+28. The best fit equation is given. The distribution of Planck function along the major (b) and minor diameters (c) of the cavity. The positions A → B and C → D represent north–south and east–west directions in the cavity. The Planck function shows sinusoidal like distribution, related to the grain temperature. The sinusoidal equation and regression coefficient (R) are shown. The error bars represent standard error ($\pm 1\sigma$) of the distribution.

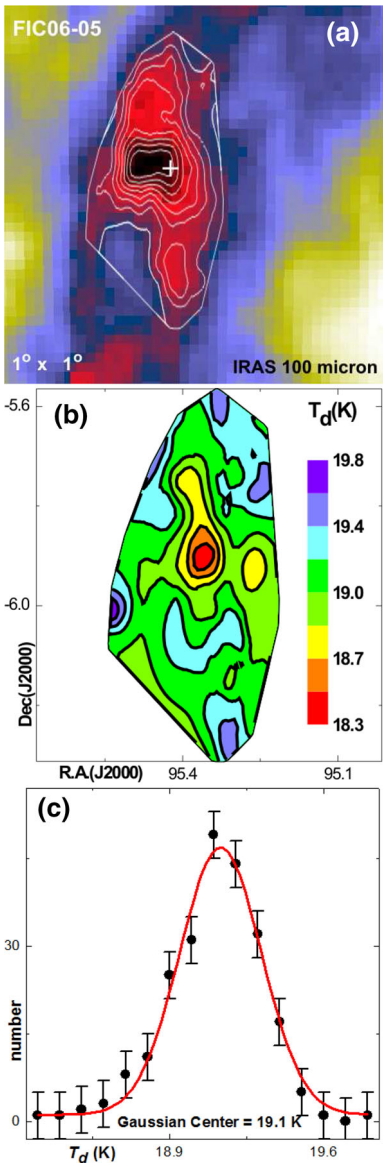

Figure 6. (a) IRIS 100 μm map of the far-infrared cavity FIC06−05 centered at (a) RA ($J2000$) = $06^h21^m05^s$, Dec ($J2000$) = $-05°38'31''$. The contours and image size are shown. The IRAS contours represent 12.7, 12.9, 13.1, 13.2, 13.4, 13.6, 13.7 and 13.9 MJy sr^{-1}. The symbol '+' represents the position of the centre of KK-loop G212−11 (Kiss *et al.* 2004; Koenyves *et al.* 2007). The dust color temperature contour map (b) and distribution (c) are shown. The color bars (b) and Gaussian fit (c) can be seen. The error bars represent standard error ($\pm 1\sigma$) of the distribution.

3 000 kg m^{-3}, grain emissivity (Q_ν) = 0.0010 (for 100 μm) (Young *et al.* 1993). For 100 μm wavelength, the expression for the dust mass (3) reduces to

$$M_{dust} = 0.40 \left[\frac{F_\lambda D^2}{B(\lambda, T)} \right] \tag{3}$$

The Planck function $B(\lambda, T)$ was calculated using dust color temperature of each pixels. We used the known distance (D) to calculate dust mass of the cavity. Optical depth for 100 μm wavelength (Wood *et al.* 1994) is given by

$$\tau_{100} = \frac{F_\lambda(100\mu m)}{B_\lambda(100\mu m, T_d)} \tag{4}$$

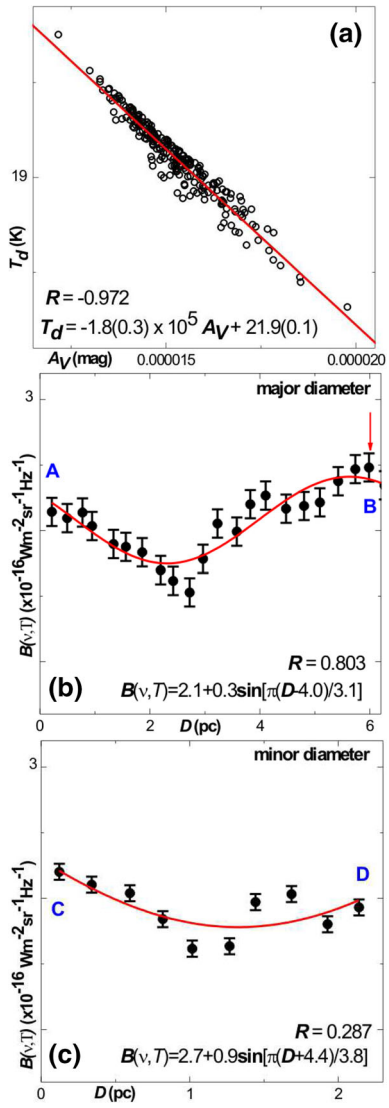

Figure 7. (a) The variation of visual extinction (A_V) with dust color temperature (T_d) in the cavity FIC06−05. The best fit equation is shown (error in parentis). The distribution of Planck function along the major (b) and minor diameter (c) of the cavity. The positions A → B and C → D represent north–south and east–west directions in the cavity. The Planck function distribution shows sinusoidal nature, related to the grain temperature. The sinusoidal equations (b,c) and regression coefficients (R) are shown. The error bars represent standard error ($\pm 1\sigma$) of the distribution.

An empirical formula between visual extinction and optical depth at 100 μm, given by Wood *et al.* (1994) is given by

$$A_V = 15.078\left(1 - e^{\frac{-\tau_{100}}{641.3}}\right) \quad (5)$$

Using the values of flux densities and Planck functions of each pixels, we can calculate visual extinction (A_V) of each pixel of the cavity.

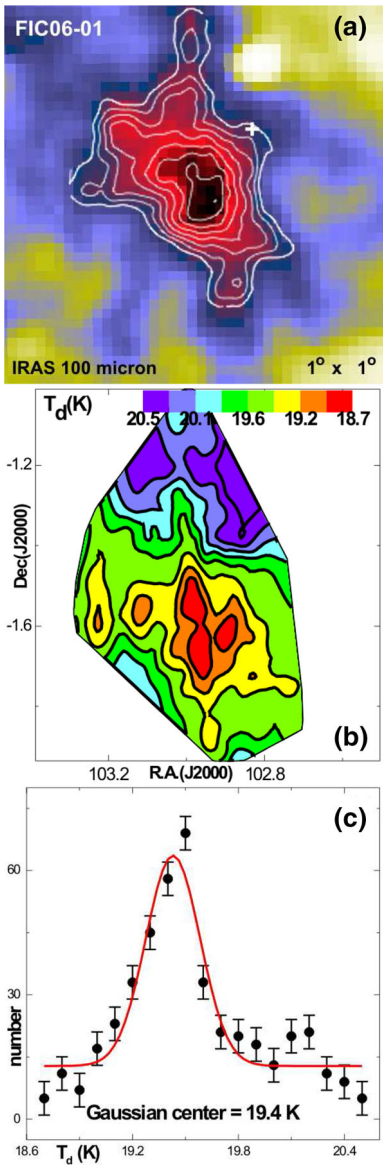

Figure 8. (a) 100 μm IRIS map of the far-infrared cavity FIC06−01 centered at (a) RA ($J2000$) = $06^h51^m54^s$, Dec (J2000) = $-01°35'43''$. The contours and image size are shown. The IRAS contours represent 16.7, 17.1, 17.4, 17.8, 18.1, 18.5, 18.8 and 19.2 MJy sr^{-1}. The symbol '+' represents the position of the centre of KK-loop G214−01 (Kiss *et al.* 2004; Koenyves *et al.* 2007). The dust color temperature contour map (b) and distribution (c) are shown. The color bars (b) and Gaussian fit (c) can be seen. The error bars represent standard error ($\pm 1\sigma$) of the distribution.

4. Results and discussion

We describe the physical properties of four FIR cavity candidates and compare it with the published works.

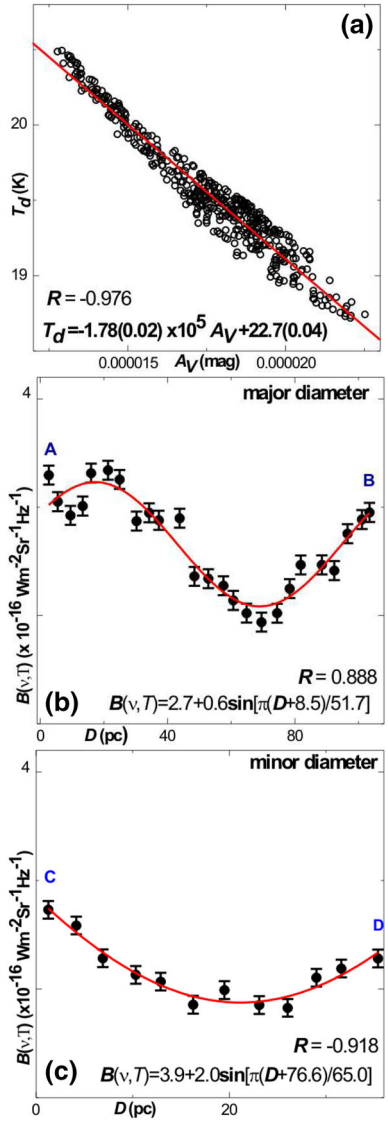

Figure 9. (a) Visual extinction (A_V) versus dust color temperature (T_d) in the cavity FIC06−01. The distribution of Planck function along the major (b) and minor diameter (c) of the cavity. The positions A → B and C → D represent north–south and east–west directions in the cavity. The Planck function distribution shows sinusoidal like function, related to the grain temperature distribution. The sinusoidal equations (b,c) and regression coefficients (R) are shown. The error bars represent standard error ($\pm 1\sigma$) of the distribution.

4.1 *FIC01+55*

Figure 2a shows the cavity FIC01+55 at 100 μm IRIS map. Using Equation (1), the dust color temperature (T_d) is calculated and found to lie in the range 19.1 ± 1.2 K to 20.1 ± 1.3 K. In the dust color temperature map (Figure 2b), the central region shows north–south elongation representing region of temperature minima. The lower temperature region is found to be massive than that of the higher temperature region. Using Equation (3), dust mass of the region is calculated. It is about $0.0038 M_\odot$.

Figure 2c shows dust color temperature distribution in the cavity. This distribution is found to be deviated from the Gaussian. A positive skewness and a significant dip at ∼ 19.7K suggest the influence of external sources (nearby AGB?) in the cavity formation. Interestingly, a very good correlation between the visual extinction (A_V) and the dust color temperature is noticed (Figure 3a). A linear relationship between the visual extinction and dust color temperature is found. Figure 3b and c show the variation of Planck function along the major and minor diameters of the cavity passing through flux minima at 100 μm. The Planck function is found to be non-uniform along the diameters. Interestingly, a very good agreement is noticed when fitting sinusoidal distribution. This oscillation is probably related to the grain temperature distribution.

4.2 *FIC05+28*

A cone-shaped structure with a well defined minima at northern part of the cavity can be seen in Figure 4a. In dust color map (Figure 4b) a good agreement can be seen: lower the dust color temperature higher the dust mass. The dust color temperature distribution (Figure 4c) do not agree with Gaussian fit, indicating a disturbance due to external cause (AGB wind?). A very good linear relationship between the dust color temperature and visual extinction is noticed (Figure 5a).

Similar to the cavity FIC01+55, the distribution of Planck function along the major and minor diameters in the cavity FIC05+28 is found to be sinusoidal (Figure 5b, c).

4.3 *FIC06−05*

An oval-shaped north–south elongated FIR cavity with a well defined flux minima at the central region is found nearby AGB star AGB06−05 (Figure 6a). Similar to the previous two cavities, low temperature region is found to be massive (Figure 6b). A good agreement with Gaussian distribution is noticed in the dust color temperature distribution (Figure 6c), advocating a stable and self-evolving FIR cavity. This nature is supported by the T_d versus A_V plot (Figure 7a).

In the Planck function distributions along the diameters, a continuous decrease and then increase can be seen (Figure 7c, d). A very good agreement is noticed when fitting sinusoidal distribution. This suggests the

Table 2. Properties of four low-latitude ($| l | < 10°$) far-infrared cavities.

Cavity Name	T_d (K)	$M_d(M_\odot)$	KK-loop[1] Name	T_d (K)
FIC01+55	19.1 ± 1.2	0.00380	G128−03	42.2 ± 3.1
FIC05+28	18.6 ± 1.1	0.02970	G182+00	38.6 ± 2.6
FIC06−55	18.3 ± 1.2	0.00033	G212−11	54.1 ± 4.0
FIC06−01	20.5 ± 1.3	0.05600	G214−01	46.7 ± 3.8

The first column represents the name of the FIR cavities as in Table 1. The next two columns give dust color temperature and dust mass of the cavity. Last two columns list the name of the KK-loops[1] and their dust color temperature. ([1]: Kiss *et al.* 2004; Koenyves *et al.* 2007)

Table 3. The first column lists the name of the cavity. Values of offset (B_0), amplitude (A), phase shift (D_c) and period (w) of sinusoidal Planck function distribution (equation 10) are given in 2–5 (along major diameter) and 7–10 columns (along minor diameter), respectively.

FIC	B_0	A	D_c	w	R	B_0	A	D_c	w	R
FIC01+55	2.6	0.5	8.9	9.4	0.781	2.3	0.2	−0.3	2.7	0.847
FIC05+28	2.0	0.4	3.9	57.6	0.489	2.1	0.3	14.8	15.4	0.849
FIC06−55	2.1	0.3	4.0	3.1	0.802	2.7	0.9	−4.4	3.8	0.287
FIC06−01	2.7	0.6	−8.5	51.7	0.888	3.9	2.0	−76.6	65.0	0.918

The columns 6 and 11 show the values of coefficient of regression (R) for respective fittings.

existence of well defined and stable flux minima in the cavity.

4.4 *FIC06−01*

A cloud-like irregularly shaped cavity having a strong minima nearly at the central region is seen in Figure 8a. In the dust color map (Figure 8b), similar to the previous three FIR cavities: lower temperature region is found to be massive. A Gaussian-like T_d distribution with positive skewness (Figure 8c) suggest the effect of nearby AGB wind.

A very good agreement between the dust color temperature and visual extinction is noticed (Figure 9a). In the Planck function distributions with diameters (Figure 9b,c), a decrease and then increase is noticed, suggesting a sinusoidal nature. This distribution should be related to the grain temperature distribution.

4.5 *Discussion*

The best fit lines between the T_d and A_V for FIR cavities FIC01+55, FIC05+28, FIC06−05 and FIC06−01 (Figures 3a, 5a, 7a, 9a) are found to be

$$T_d = -2.7 \times 10^5 A_V + 22.8 \quad (6)$$

$$T_d = -1.1 \times 10^5 A_V + 21.9 \quad (7)$$

$$T_d = -1.8 \times 10^5 A_V + 21.9 \quad (8)$$

$$T_d = -1.8 \times 10^5 A_V + 22.7 \quad (9)$$

respectively. Taking log and solving this, it is found the product of dust color temperature and visual extinction of these cavities give nearly a similar value ($\sim 10^{-5}$). This value should be calculated for other KK-loops (Jha *et al.* 2017; Jha and Aryal 2017) in the future.

We have used the data provided by Kiss *et al.* (2004) and Koenyves *et al.* (2007) to calculate the dust color temperature of KK-loops. Our FIR cavities lies at the core part of the KK-loops G128−03, G182+00, G212−11 and G214−01. The dust color temperature of the outer region of our cavities are found to be greater than 38K (last column of Table 2). An offset of more than 20K suggests that the loop is dynamically active: the core part is much cooler than that of its surrounding region. Since the observed distribution of Planck function is found to be fluctuating or non-uniform along both major and minor diameters, we assume sinusoidal distribution as

$$B(\lambda, T) = B_0 + A sin\left(\pi \frac{D - D_c}{w}\right) \quad (10)$$

where B_0, A, D_c and w represent offset, amplitude ($A > 0$), phase shift and period, respectively. In all 4 cavities, the values of B_0, A, D_c and w for major and minor diameters are given in Table 3.

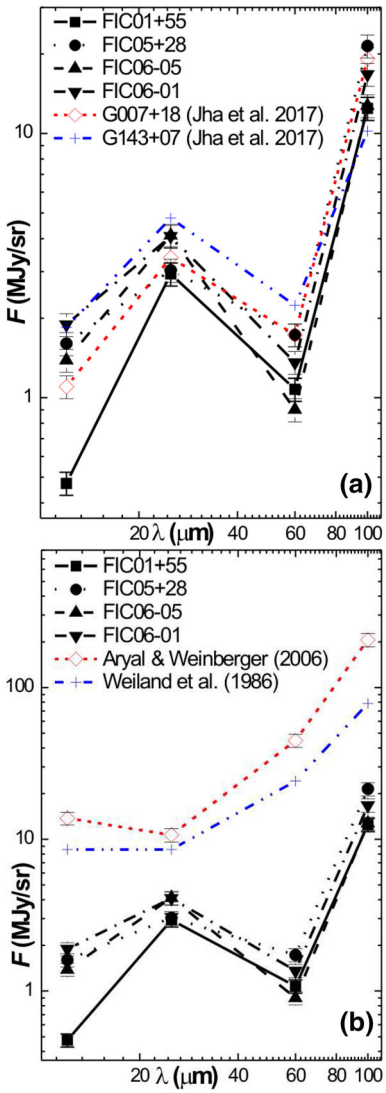

Figure 10. FIR spectral distributions of the cavity. A comparison with the far-infrared cavity G007+08 and G143+07 (Jha *et al.* 2017) (a) and with MBM 20 "cirrus cloud" (position no. 1 from Table 1, Weiland *et al.* 1986) and Skeleton Nebula (Aryal and Weinberger 2006) can be seen (b). All intensities were background subtracted and color-corrected for 240 K blackbody emission. The spectra were rescaled by dividing the intensities for the Skeleton Nebula and MBM 20 by 4.5 and 13.0, respectively.

Interestingly, the distribution of Planck function is found to be sinusoidal along major and minor diameters of the cavity (see Figures 3b, c, 5b, c, 7b, c and 9b, c). The amplitude and period of oscillation of dust/grain is found to be maximum in the cavity FIC06−01. It is minimum along the minor diameter of the cavity FIC01+55. Distant cavity (FIC06−01) showed a large value of phase shift in the oscillation. The offset in the Planck function is almost constant in all cavities.

Figure 10 shows the FIR spectral distributions of all four cavities. In all cavities, a significant rise from 12 μm to 25 μm and then a fall from 25 μm to 60 μm is noticed (Figure 10a). When comparing with the cavities studied by Jha et al (2017a), a similar trend is noticed (Figure 10a). We have compared FIR spectral distribution with skeleton nebula (Aryal and Weinberger 2006) and MBM cloud (Weiland *et al.* 1986). A continuous rise with different slope is noticed for these nebula. In other words, four FIR cavities emit less radiation at 60 μm wavelengths than that of the nebula. This suggests that the deficiency of materials (dust and grain) in the cavity. These materials are expected to be swept away from the cavity due to AGB wind.

5. Conclusions

We present physical properties of four cavities at far-infrared (60 μm and 100 μm) IRIS maps, located nearby AGB stars. The dust color temperature, dust mass, visual extinction and Planck function along the diameters are studied. We conclude our results as follows:

1. The values of dust color temperature is found to lie in the range 18.4 ± 1.2 to 26.2 ± 1.7K. An offset of $\sim$ 20K is found when comparing with the dust color temperature of core region and its surroundings. The dust color maps compliments the dust mass maps in all four FIR cavities. The minimum temperature region is found to be elongated along north–south direction at the 100 μm flux maxima in all four FIR cavities.
2. A very good correlation is noticed between the visual extinction and dust color temperature. It is found that the rate of decrease of dust color temperature with visual extinction is almost identical ($-2.2 \pm 0.5 \times 10^5$ K/mag) in all four FIR cavities. The product of dust color temperature and visual extinction is found to lie in the range 0.2 to 8.0 ($\times 10^{-5}$).
3. A sinusoidal distribution of Planck function along the major and minor diameters is noticed in all cavities. This oscillation should be related to the grain temperature distributions in the cavity.
4. In FIR spectral distribution, flux density is found to be minimum at 60 μm in all four cavities than 25 μm and 100 μm IRAS bands.

The superposition and possible interaction of these loops with the AGB stars (or other sources?) will be studied in the future. In addition, the amount of expelled mass from the central region will be calculated in

order to estimate the energy required for the structure formation.

Acknowledgements

We are indebted to the referee for his/her constructive criticism and useful comments. We acknowledge SIMBAD, Sky View Virtual Observatory, IRAS survey and GIRL catalog. One of the authors (AKG) acknowledges Central Department of Physics, Tribhuvan University, Nepal for all kinds of support for his Ph.D. work.

References

Arce H. G., Goodman A. A. 1999, ApJ, 517, 264
Aryal B., Weinberger R. 2006, AandA, 44, 1, 213
Aryal B., Rajbahak C., Weinberger R. 2009, ApandSS, 323, 323
Aryal B., Rajbahak C., Weinberger R. 2010, MNRAS, 402, 1307
Blitz L., Fich M., Stark A. A. 1982, Astrophys. J. Suppl. Ser., 49, 183
Draine B. T. 2001, Encyclopedia of Astronomy and Astrophysic, IOP Publishing and MacMillan, 1266
Draine B. T. 1987, unpublished suppliment to Draine and Lee (1984)
Dupac X., Bernard J.-P., Boudet N., Giard M., Lamarre J.-M. *et al.* 2003, AandA, 404, L11
Garmany C. D., Stencel R. E. 1992, Astron. Astrophys., Suppl. Ser., 94, 211
Hildebrand R. H. 1983, Q. Jl. R. Astr. Soc., 24, 267
Jha A. K., Aryal B., Weinberger R., 2017, RMxAA, 53, 467
Jha A. K., Aryal B. 2018, J. Astrophys. Astron., 39, 2, 7
Kiss CS., Mor A., Tth L. V. 2004, AandA, 418, 131
Koenyves V., Kiss Cs., Mor A., Kiss Z. T., Tth L. V. 2007, AandA, 463, 3, 1227
Miville-Deschnes M., Lagache G. 2005, ApJS, 157, 302
Odenwald S. F. 1988, ApJ, 325, 320
Odenwald S. F. and Rickard L. J. 1987, ApJ, 318, 702
Preite-Martinez A. 1988, *Astron. Astrophys. Suppl. Ser.*, 76, 317
Schnee, S. L., Ridge, N. A., Goodman, A. A., Jason G. L. 2005, ApJ, 634, 442
Suh K., Kwon Y. 2009, J. Kor. Astronom. Soc., 42, 4, 81
Suh K., Kwon Y. 2011, MNRAS, 417, 4, 3047
Szczerba R., Sidmiak N., Stasinska G., Borkowski J. 2007, AandA, 469, 2, 799
Weiland J. L., Blitz L., Dwek E., Hauser M. G., Magnani, L., and Rickard L. J. 1986, ApJ, 306, L101
Weinberger R., and Armsdorfer B. 2004, AandA, 416, L27
Wood D., Myers P., Daugherty D. 1994, ApJS, 95, 2, 457
Young K., Phillips T. G., and Knapp, G. R. 1993, ApJ, 409, 725

ISST Journal of Applied Physics, Vol. 8 No. 1, (January - June 2017), p.p. 92-96
ISSN No. 0976-903X © Intellectuals Society for Socio-Techno Welfare

STUDY OF DUSTY ENVIRONMENT AROUND A CARBON-RICH AGB STAR IN FAR INFRARED MAPS AT LATITUDE 15^0

A. Gautam and B. Aryal
Central Department of Physics, T.U., Kirtipur, Nepal
E-mail: arjungautamnpj@gmail.com, baryal@tucdp.edu.np

ABSTRACT

This paper discusses the physical properties of the dusty environment around the AGB star located at R.A. (J2000) =06^h 09^m 03^s and Dec (J2000) =14^o 46' 00", in the far infrared (60 and 100μm) IRAS maps. A cavity like structure (major diameter ~ 35.04 pc & minor diameter ~12.44 pc) is found to lie at R.A. (J2000)= 06^h 09^m 55.9^s and DEC (J2000) = 14^o 46' 10.4", located at a distance ~ 3.65 kpc from the star. We studied the distribution of flux density, dust color temperature and dust mass in the cavity. The dust color temperature is found to lie in the range 21.5 K to 23.2 K which shows the cavity is isolated and independently evolved. A possible explanation of the results will be discussed.

Keywords : *AGB Stars, Dust temperature, Dust mass, S-process, Excess mass.*

1. INTRODUCTION

Asymptotic giant branch (AGB) stars are the final nuclear burning stage of low- and intermediate-mass stars driven by nuclear burning. This phase of evolution is characterized by two nuclear burning shell of hydrogen and helium where hydrogen burning shell lies below the convective envelope and helium burning shell lies above the electron-degenerate core of carbon and oxygen, or for the most massive AGB stars a core of oxygen, neon, and magnesium [1: 435]. The AGB phase is obtained by evolving low and intermediate mass stars and limit of mass of stars are defined by the development of electron degenerate core after leaving the MS. In case of intermediate mass stars, they ignite their He-cores under non-degenerate conditions but in case of AGB phase, they are characterized by an electron degenerate core of C and O.

Mass range of each class is determined by different burning and mixing processes in the stars. In case of thermally pulsating AGB phase low and intermediate mass stars are able to form C-rich stars and produce heavy elements through s-process. Similarly hot-bottom burning (HBB), massive and AGB stars remain O-rich and only super AGB stars are massive enough to ignite C [2: 822].

He-core burning phase is about 10 times shorter than the H-core burning shell so that the He-core burning leaves a C/O core behind that is surrounded by both a hydrogen and helium burning shell. For low and intermediate mass stars, carbon doesn't ignite and C/O core contracts and becomes electron degenerate. During the early AGB phase, the abundance of He in the centre goes to zero where He-burning continues in a shell around a degenerate C-O core. In the meantime, the H- layer around the helium shell expands and cools sufficiently so that hydrogen burning shell is extinguished. Convective envelope sets in and moves inwards and second dredge-up takes place. He shell is the main source for nuclear production so that it burns outward and reaches the hydrogen shell. In case of thermally pulsating AGB phase, helium shell becomes thin and remains thermally unstable as a result thermal pulses are produced. In each thermal pulse, luminosity of helium shell nearly approaches $10^8 L_{SUN}$[3: 515].The production of such high luminosity in helium shell is called He shell flash or thermal pulse which is used to expand the outer layers. Such strong expansion drives the H shell cooler and less dense as a result H shell is extinguished. The inner edge of deep convective envelope can then move inward and mix to the surface products of internal nucleosynthesis. This mixing process which occurs periodically after each TP is known as third dredge-up which is the mechanism for producing carbon stars. During TP-AGB phase, main dominant source of nuclear energy is the hydrogen shell. Thermally pulsating AGB phase is the phase after the first thermal pulse to the time when the star ejects its envelope.

In this paper, we study the physical properties of far infrared cavity, that we investigated during a systematic search on IRAS maps, located close to a carbon-rich AGB star (AGB 06+14) at 15^o latitude. In section 2, we describe

methods of calculation. A brief description of the result and discussion will be given in the section 3. Finally, we conclude our results in the section 4.

2. METHODS

We investigated a cavity-like structure in both 60 and 100 micron IRAS maps around a AGB star. We briefly describe a method for calculation of dust color temperature and dust mass of the dusty environment around carbon-rich Asymptotic Giant Branch named AGB06+14.

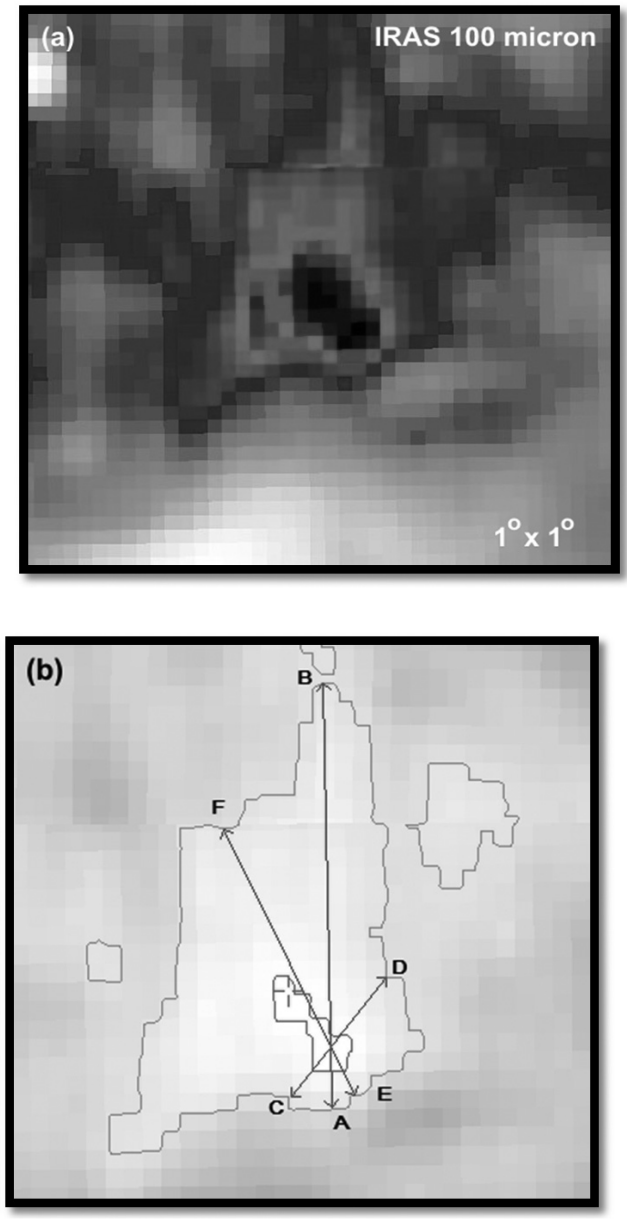

Fig. 1. IRAS 100 μm far infrared image of the core region of AGB 06+14 centered at R.A. (J2000) = 06^{h}09^{m}55.9^s, Dec. (J2000) = 14^{0}46'10.4" (a). Contour map of the cavity where major (AB), minor (CD) diameters (b).

2.1. Dust Color Temperature Estimation

Dust color temperature was calculated by Schnee et al. [4: 442] from the IRAS 60 μm and 100 μm flux densities. If we know the ratio of flux densities at 60 μm and 100 μm, the temperature contribution due to dust can be calculated. By using modified power law of spectral emissivity index, dust color temperature T_d in each pixel of a far infrared image can be obtained by assuming that the dust in a single beam is isothermal and that the observed ratio of 60 μm to 100 μm emission is due to black body radiation from dust grains at T_d. The flux density of emission at a wavelength λ_i is given by

$$F_i = \left[\frac{2h}{\lambda_i^3 \left(e^{\frac{h}{\lambda_i k T_d}} - 1 \right)} \right] N_d \alpha \lambda_i^{-\beta} \Omega_i \qquad (1)$$

where β is the spectral emissivity index, N_d is the column density of dust grains, α is a constant i.e. free parameter which relates the flux with the optical depth of the dust, and Ω_i is the solid angle subtended at λ_i by the detector. In Dupac et al. [5: L11], we have

$$\beta = \frac{1}{\delta + wT_d} \qquad (2)$$

which is used to describe the observed inverse relationship between temperature and emissivity spectral index. With the assumptions that the dust emission is optically thin at 60 μm and 100 μm and that Ωω Ω100 (true for IRAS image), we can write the ratio, R, of the flux densities at 60 μm and 100 μm as

$$R = 0.6^{-(3+\beta)} \quad \frac{e^{144/T_d} - 1}{e^{240/T_d} - 1} \qquad (3)$$

The spectral emissivity index (β) depends on dust grain properties like composition, size, and compactness. For a pure blackbody would have β = 0, the amorphous layer-lattice matter has β ~ 1, and the metals and crystalline dielectrics have β ~ 2 which isused in our calculations.

For a smaller value of T_d, 1 can be dropped from both numerator and denominator of Eq. (3) and it takes the form

$$R == 0.6^{-(3+\beta)} \quad \frac{e^{144/T_d}}{e^{240/T_d}} \tag{4}$$

Taking natural logarithm on both sides of Eq. (4) and solving it, we find the expression for the temperature as

$$T_d = \frac{-96}{\ln\{R \times 0.6^{(3+\beta)}\}} \tag{5}$$

where R is given by

$$R = \frac{F(60\mu m)}{F(100\mu m)} \tag{6}$$

F(60 μm) and F(100 μm) are the flux densities in 60 μm and 100 μm respectively and Eq. (5) can be used for calculation of the dust grain temperature.

2.2. Dust Mass Estimation

Dust mass is another important physical quantity which is useful to analysis the cavity structure. Dust masses are estimated from the infrared background corrected flux densities at 100 μm image. The distance of the structure was provided in catalog of far infrared loops in the galaxy [6: 1227]. We are calculating dust mass following the analysis of [7: L23]. The infrared flux density can be measured from IRAS Sky View virtual images and the images from the Groningen using ALADIN2.5. The resulting dust mass depends on the physical and chemical properties of the dust grains, the adopted dust color temperature and the distance to the object. The final expression for the dust mass can be written as:

$$M_{dust} = \frac{4a\rho}{3Q_v}\left|\frac{S_v D^2}{B(\nu, T)}\right| \tag{7}$$

where, a = weighted grain size, ρ = grain density, Q_v = grain emissivity, S_v = flux density measured from the image (IRAS 100 μm image), D = distance of the structure. The Planck's function B(ν, *T)*, which is the function of the temperature and the frequency and given by the expression:

$$B(\nu, T) = \frac{2h\nu^3}{C^2}\left[\frac{2hc}{e^{\frac{h\nu}{kT}} - 1}\right] \tag{8}$$

where, h = Planck's constant, c = velocity of light, ν = frequency at which the emission is observed, T = the average temperature of the region. The values of various parameters we use in the calculation of the dust mass in our region of interest are as follows: a = 0.1 μm [8: 725], ρ = 1000 Kg m^{-3} [8: 725], Qv = 0.0010 for 100 μm and 0.0046 for 60 μm respectively [8: 725].

Using these values the expression (7) takes the form:

$$M_{dust} = 0.4\left[\frac{S_v D^2}{B(\nu, T)}\right] \tag{9}$$

We use equation (9) to calculate dust mass of the cavity.

3. RESULT AND DISCUSSION

3.1 Structure: Contour Maps

While going through the systematic search on IRAS maps, we discovered an isolated cavity in the 100 μm and 60 μm at R.A. (J2000) = $06^h\ 09^m\ 55.9^s$ and Dec. (J2000) = 14^o 46' 10.4". With the help of the software ALADIN2.5, we have studied physical properties (size, dust color temperature, dust mass, etc) of the cavity. We selected contour level in such a way that it circles the cavity. The major axis, minor axis and line passing through minimum temperature and minimum flux are shown in the fig.1(b).

3.2 Distribution of Flux Density

By using ALADIN 2.5 software, the values of flux densities at 60μm and 100μm have measured. The flux density distribution within the contour of the region of interest has studied. We plotted a graph between flux at 100μm and 60μm with the help of ORIGIN 5.0 which is shown in fig.2(a). From the linear fit, slope of the line was 0.29. The linear equation of the fitted line is, *y = -3.56+0.29x*. Using the slope of best fitted plot, dust color temperature is calculated as 25.3 K.

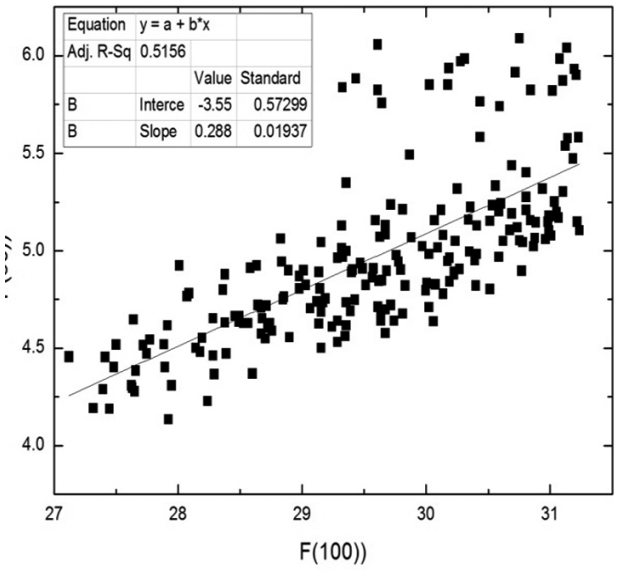

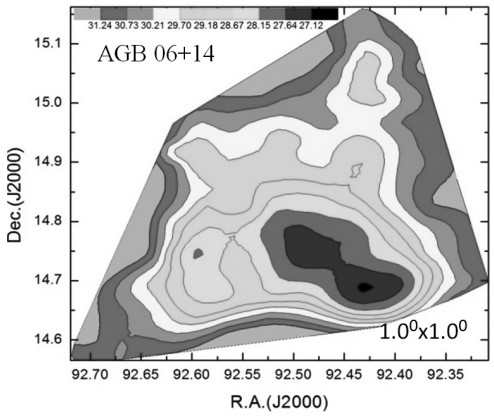

Fig.2(a): The 100µm verses 60µm flux density in the region of interest and 2(b) Contour map at 100µm flux density where the AGB star is located at the center R.A. (J2000) = $06^h09^m55.9^s$, Dec. (J2000) = $14^0$46'10.4."

Again distribution of flux at 100µm of the pixels within the contour level with right ascension (R.A.) and declination (Dec.) are plotted by using ORIGIN 8.0 and the graph is shown in fig.2(b). Graph shows that all the fluxes from minimum to maximum lie within the contour level. Most of the maximum flux regions lie at the boundary.

2.3. Dust color Temperature and its Variation

Using the method of [4: 442], we calculated dust color temperature of each pixel inner the outer isocontour in the region of interest. We use the IRAS 100 µm and 60 µm FITS images downloaded from the IRAS server [1]. For the calculation of temperature we choose the value of β = 2 following the explanation given by [5: L11]. Variation of temperature with corresponding R.A.(J2000) and Dec. (J2000) are plotted by using ORIGIN 8.0 and the graph is shown in figure 3(a). Graph shows that temperature distributions are in separate cluster but minimum temperature region is little bit shifted from minimum flux density which is unusual behaviour. Such type of nature is obtained due to external factors.

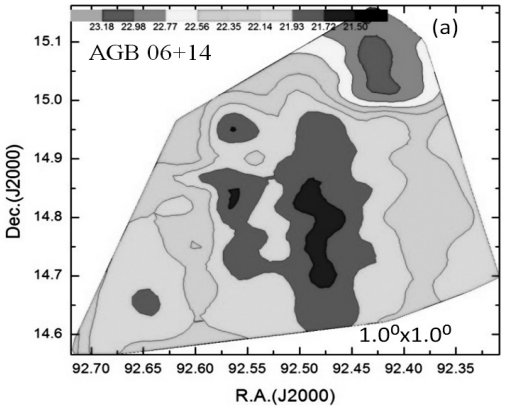

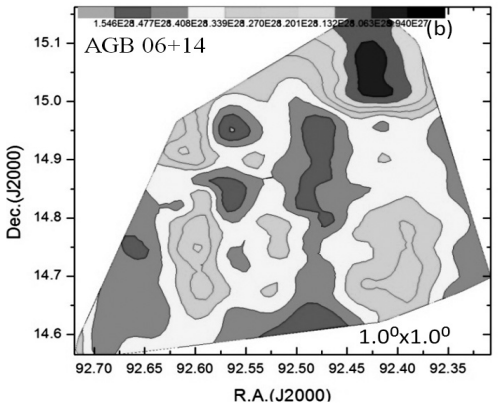

Fig. 3: Dust color temperature (a) and dust mass (b) contour maps. The field is centered at R.A. (J2000)= 06^h 09^m 55.9^s and Dec. (J2000) = 14^o 46' 10.4". The contour levels are shown.

The region in which minimum and maximum temperature is found in the range of 21.5K to 23.2K with an offset temperature of dust 1.7K. Such a low offset temperature variation shows that there is symmetric outflow or symmetric distribution of density and temperature. It further suggests that our structure is not independently evolved or the role of discrete point sources in the field of cavity is important for the structure destruction mechanism. The cavity may be in thermally pulsating phase. The dust temperature less than 20 K represents the interstellar cirrus cloud. Thus our far infrared dust structure (i.e. cavity) is not a cirrus cloud. Another region of cloud fulfills the criteria of Cirrus clod. When this result is compared with the result obtained in [9: 5] where temperature variation is 20K to 22K so our result is also comparable with that result.

2.4. Size of the Structure

Major and minor diameter of the structure can be easily calculated by using a simple expression i.e., L = R × θ, where R = 3.65 kpc is the distance of the structure and θ = pixel size (in radian). After calculation the major and minor diameter of the cavity region are found to be 35.04 pc and 12.44 pc respectively. Thus, the size of the structure is 35.04 pc × 12.43 pc .

2.5. Dust Mass Estimation and its variation

For the calculation of dust mass, we need the distance to the region of interest. The distance of the structure is 3.65 kpc [10: 1227]. By using the temperature of each pixel and corresponding distance of the structure, we calculated mass of each pixel. Average mass of each pixel is $1.3x10^{28}$ kg and total mass of the structure is 2.8×10^{30} kg i.e $0.014M_{sun}$. But mass of dust obtained around white dwarf WD 1003-44 in [9: 5] is $0.08M_{SUN}$. It means mass of dust around AGB Star is less than White Dwarf.

Distribution of dust mass of the pixels within the selected contour level with R.A. (J2000) and Dec.(J2000) are plotted in contour map by using ORIGIN 8.0. Graph obtained is shown in fig.3(b) which shows that minimum mass region lie at the maximum temperature region in the selected contour which is the general trend.

2.6. Calculation of Excess Mass

For the calculation of excess mass, we have drawn two circles i.e. inner and outer circle with the help of software Aladin V8.0. Circle through major diameter is supposed as outer circle and the circle through minor diameter is supposed as inner diameter of the interested region. With the help of those circles we have calculated excess mass.

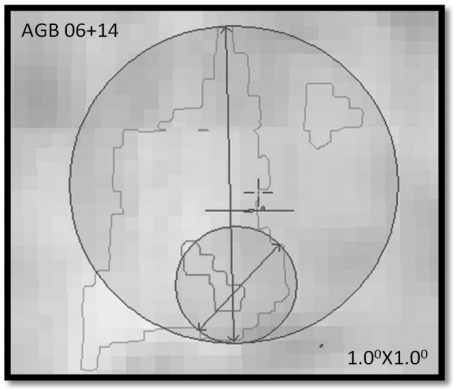

Figure 4: The inner and outer circle drawn in the structure at the center R..A.(J2000)= 06^h 09^m 55.9^s and Dec. (J2000)= 14^o 46' 10.4" for calculation of excess mass.

From the calculation total mass of the inner circle was found to be 7.4 x 10^{29} kg and the total mass of outer circle including inner circle was 5.4 x 10^{30} kg . So the mass deficit in the inner pixel which was blown away by the AGB star is 4.7 x 10^{30} kg i.e. 1.6 M_{SUN}.

4. CONCLUSION

The physical properties of the cavity-like structure that we investigated while searching a effect of AGB wind around carbon-rich AGB stars. A study of flux density and dust color temperature maps dust color temperature, mass of dust, mass deficit of the cavity was calculated. Our conclusions are as follows:

- The major and minor diameter of the cavity like structure was found to be 35.04 pc and 12.44 pc respectively.
- The maximum temperature 23.2K was found at R.A.(J2000) = 92.43^0 & Dec.(J2000) = 15.08^0 and minimum temperature 21.5K was found at R.A.(J2000) = 92.43^0 & Dec.(J2000) = 15.08^0 with offset of 1.7K. The small value of dust color temperature in the cavity suggests a continuous process by which cavity is supposed to be formed. Low offset in the temperature hints that there is symmetric outflow or symmetric distribution of density and temperature.
- In general, minimum flux and minimum temperature lie at same point in the pixel but in this case minimum temperature is shifted which may be due to external factors, possibly wind emitted from the AGB star. Similarly maximum temperature and minimum mass region lie at same region which is normal behavior.
- The total mass of the inner circled cavity was 7.4 x 10^{29}Kg and that of the outer circle including inner circle was 5.4 × 10^{30} kg . The mass deficit of the structure was 4.7 × 10^{30} kg i.e. 1.6 M_{SUN}.

We intend to study the role of cabon-rich AGB star to form the far-infrared cavity in the future.

5. ACKNOWLEDGEMENTS

We are grateful to the Department of Astro-Particle Physics, Innsbrck University, specially to Prof. R. Weinberger for invoking us to work on dusty environments around AGB stars. This research has made use of SkyView Virtual Observatory and NASA/IPAC Extragalactic Database (NED).

REFERENCES

[1] F. Herwig. "Evolution of Asymptotic Giant Branch Stars". ARAA, vol. 43, pp435, 2005

[2] L. Seiss and M. L. Pumo."Evolutionary Properties of Massive AGB Stars". Mem.S.A.It, vol. 77, pp 822, 2006

[3] A.I. Karakas, J.C. Lattanzio and O.R. Pols. "Parameterising the third dredge- up in asymptotic giant branch stars". Astron. Soc. Aust., vol. 19, pp515, 2002

[4] S.L. Schnee, N. A. Ridge, A.A. Goodman, G. L. Jason." A Complete Look at the Use of IRAS Emission Maps to Estimate Extinction and Dust Temperature". APJ, vol.634, pp442, 2005

[5] X. Dupac, J.P. Bernard, N. Boudet, M. Giard, J.M. Lamarre, C. Meny, F. Pajot, I. Ristorcelli, G. Serra, B. Stepnik, J.P. Torre. "Inverse Temperature Dependance of the Dust Submillimeter Spectral Index". A&A, vol.404, ppL11, 2003

[6] S.L. Schnee, N. A. Ridge, A.A. Goodman, G. L. Jason. "A Complete Look at the Use of IRAS Emission Maps to Estimate Extinction and Dust Temperature". APJ, vol.634, pp442, 2005

[7] K. W. Suh &Y. J. Kwon. "A Catalog of AGB Stars in IRAS PSC". JKAS, vol.42, pp81, 2009

[8] K. Young, T.G. Phillips, G.R. Knapp." Circumstellar Shells Resolved in IRAS Survey Data II. Analysis". ApJ, vol. 409, pp.725, 1993

[9] B. Aryal, R. Weinbergerr. "Dust structure around White Dwarf WD 1003-44 in 60 and 100 μm Iras Survey". The Himalayan Physics, vol. II, pp.5, 2011

[10] V. Konyves, Cs. Kiss, A. Moor, Z.T. Kiss, and L.V. Toth. «Catalog of Far- Infrared Loops in the Galaxy». A&A, vol. 463, pp1227, 2007.

ISST Journal of Applied Physics, Vol. 9 No. 1, (January - June 2018), p.p. 24-26
ISSN No. 0976-903X © Intellectuals Society for Socio-Techno Welfare

A STUDY OF DUSTY ENVIRONMENT AT FAR INFRARED IRAS MAP AROUND THE MASS-LOSING CARBON-RICH AGB STAR AT LATITUDE -53^{O}

A.K. Gautam and B. Aryal
Central Department Physics, Tribhuvan University, Kirtipur, Kathmandu, Nepal
E-mail : arjungautamnpj@gmail.com, baryal@tucdp.edu.np

MS Received from International Conference on Materials Research and Technology (ICMRT-2017)
at Aggarwal College, Ballabhgarh, Faridabad (Haryana) on 10-11 July 2017

ABSTRACT

In this paper, we discuss about the physical properties of the dusty environment around the mass losing AGB star located at R.A. (J2000) = 09^{h} 39^{m} 07^{s} and Dec (J2000) = -52^{o} 49' 00", in the far infrared IRAS maps. A cavity like structure (major diameter ~ 1.55 pc & minor diameter ~0.61 pc) is found to lie at R.A. (J2000)= 09^{h} 40^{m} 50,63^{s} and DEC (J2000) = -52^{o} 48' 32", located at a distance ~ 265 pc from the star. We studied the distribution of flux density, dust color temperature, dust mass and outflow mass in the cavity. The dust color temperature is found to lie in the range 22.3K to 22.6 K which shows the cavity is isolated and independently evolved. Such a low offset temperature variation shows that there is symmetric outflow. The cavity may be in thermally pulsating phase. A possible explanation of the results will be discussed.

Keywords: *AGB Stars, dust temperature, dust mass, s-process, excess mass*

1. INTRODUCTION

Asymptotic giant branch (AGB) stars are the final nuclear burning stage of low- and intermediate-mass stars driven by nuclear burning. This phase of evolution is characterized by two nuclear burning shell of hydrogen and helium where hydrogen burning shell lies below the convective envelope and helium burning shell lies above the electron-degenerate core of carbon and oxygen, or for the most massive AGB stars a core of oxygen, neon, and magnesium (Herwig 2005). This AGB stage is characterized by low surface effective temperatures (below 3000K) and intense mass loss (from10^{-7} to 10^{-4} $M_{\odot}$yr^{-1}) (Seiss et al.2006). When the gas temperature drops to the sublimation temperature range, heavy elements in the mass outflow from a central star will condense to form dust. Dusty circumstellar envelopes will format the distance of several stellar radii .Dust grains in the envelopes absorb stellar radiation and re-emit infrared radiation so AGB stars are important infrared sources . The mass loss process plays an important role in the evolution of AGB stars. It affects the lifetime of the AGB phase and the core-mass of the subsequent post-AGB stars. Statistics of a large sample of AGB stars would help to constrain the evolution of dust envelope. There are two main types of AGB stars: the O-rich with C/O < 1 and mainly silicate-type grains in the outflow, and C-rich with C/O > 1 and mainly carbonaceous grains in the envelopes. Due to different dust compositions of these two types of AGB stars, different infrared spectral features are obtained which can be used to distinguish the two groups of the stellar objects.

He-core burning phase is about 10 times shorter than the H-core burning shell so that the He-core burning leaves a C/O core behind that is surrounded by both a hydrogen and helium burning shell. For low and intermediate mass stars, carbon doesn't ignite and C/O core contracts and becomes electron degenerate. During the early AGB phase, the abundance of He in the centre goes to zero where He-burning continues in a shell around a degenerate C-O core. In the meantime, the H- layer around the helium shell expands and cools sufficiently so that hydrogen burning shell is extinguished. Convective envelope sets

in and moves inwards and second dredge-up takes place. He shell is the main source for nuclear production so that it burns outward and reaches the hydrogen shell. In case of thermally pulsating AGB phase, helium shell becomes thin and remains thermally unstable as a result thermal pulses are produced. In each thermal pulse, luminosity of helium shell nearly approaches $10^8 L_\odot$ (Karakas 2002). The production of such high luminosity in helium shell is called He shell flash or thermal pulse which is used to expand the outer layers. Such strong expansion drives the H shell cooler and less dense as a result H shell is extinguished. The inner edge of deep convective envelope can then move inward and mix to the surface products of internal nucleosynthesis. This mixing process which occurs periodically after each TP is known as third dredge-up which is the mechanism for producing carbon stars. During TP-AGB phase, main dominant source of nuclear energy is the hydrogen shell. Thermally pulsating AGB phase is the phase after the first thermal pulse to the time when the star ejects its envelope.

In this paper, we study the physical properties of far infrared cavity, that we investigated during a systematic search on IRAS maps, located close to a carbon-rich AGB star (AGB 09-52) at -52.8^o latitude. In section 2, we describe methods of calculation. A brief description of the result and discussion will be given in the section 3. Finally, we conclude our results in the section 4.

2. METHODS

We investigated a cavity-like structure in both 60 and 100 micron IRAS maps around a AGB star. We briefly describe a method for calculation of dust color temperature and dust mass of the dusty environment around carbon-rich Asymptotic Giant Branch named AGB09-52.

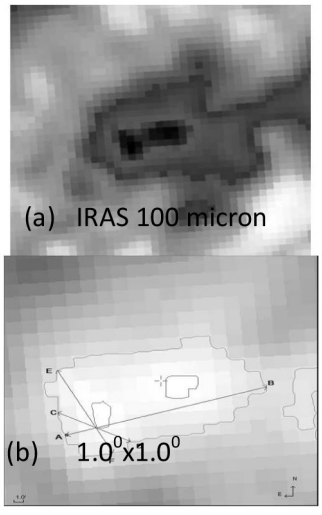

Fig. 1. (a) IRAS 100 µm and 60 µm far infrared image of the core region of AGB 09-52 centered at R.A. (J2000) = 09^h 40^m 50.63^s, Dec. (J2000) = -52^0 48' 32" and (b) Contour map of the cavity where major diameter (AB), minor diameter (CD) and diameter between minimum flux &minimum temperature.

2.1. Dust Color Temperature Estimation

Schnee et al.(Schnee et al. 2005) calculated dust color temperature by using the IRAS 60 µm and 100 µm flux densities. From modified power law of spectral emissivity index, the flux density of emission at a wavelength λ_i is given by

$$F_i = \left[\frac{2hc}{\lambda_i^3 \left(e^{\frac{hc}{\lambda_i kT_d}} \right) - 1} \right] N_d \alpha \lambda_i^{-\beta} \Omega_i \quad \ldots (1)$$

where β is the spectral emissivity index, N_d is the column density of dust grains, α is a constant i.e. free parameter which relates the flux with the optical depth of the dust, and Ω_i is the solid angle subtended at λ_i by the detector. In Dupac et al. 2003, there is an inverse relationship between temperature and emissivity spectral index. we have

With the assumptions that the dust emission is optically thin at 60 µm and 100 µm and that Ωω Ω100 (true for IRAS image), we can write the ratio, R, of the flux densities at 60 µm and 100 µm as

$$R = 0.6^{-(3+\beta)} \quad \frac{e^{144/T_d} - 1}{e^{240/T_d} - 1} \quad \ldots (3)$$

The spectral emissivity index (β) depends on dust grain properties like composition, size, and compactness. For a pure blackbody would have β = 0, the amorphous layer-lattice matter has β ~ 1, and the metals and crystalline dielectrics have β ~ 2 which is used in our calculations.

For a smaller value of T_d, 1 can be dropped from both numerator and denominator of Eq. (3) and it takes the form

$$R == 0.6^{-(3+\beta)} \quad \frac{e^{144/T_d}}{e^{240/T_d}} \quad \ldots (4)$$

$$\text{where , } R = \frac{F(60\mu m)}{F(100\mu m)}$$

Taking natural logarithm on both sides of Eq. (4) and solving it, we find the expression for the temperature as

$$\ln(R) = \ln 0.6^{-(3+\beta)} [144/T_d - 240/T_d]$$

$$= \ln 0.6^{-(3+\beta)} [-96/T_d]$$

$$T_d = \frac{-96}{\ln\{R \times 0.6^{(3+\beta)}\}} \quad \ldots (5)$$

F(60 μm) and F(100 μm) are the flux densities in 60 μm and 100 μm respectively and Eq. (5) can be used for calculation of the dust grain temperature.

2.2. Dust Mass Estimation

Dust mass is another important dust property which is useful to analysis the cavity structure. To calculate dust mass, we need the known distance of the loops which was provided in catalog of far infrared loops in the galaxy (Konyves et al. 2007).

For the calculation of dust mass, we first obtained the value of flux density (S_ν) at 100 μm maps.

The dust mass is estimated using (Hildebrand 1983),

$$M_{dust} = \frac{4a\rho}{3Q_\nu}\left|\frac{S_\nu D^2}{B(\nu, T)}\right| \quad \ldots(7)$$

where, weighted grain size (a) = 0.1 μm, grain density (ρ) = 3000 kg m^{-3}, grain emissivity (Q_ν) = 0.0010 (for 100 μm) (Young et al. 1993).

The Planck's function B(ν, *T)*, which is the function of temperature and frequency and is given by the expression:

$$B(\nu,T) = \frac{2hc}{\lambda^3}\left(\frac{1}{e^{\frac{hc}{\lambda kT}} - 1}\right) \quad \ldots (8)$$

where, h = Planck's constant, c = velocity of light, ν = frequency at which the emission is observed, T = the average temperature of the region.

For 100 μm wavelength, the expression for the dust mass (8) reduces to,

$$M_{dust} = 0.4\left[\frac{S_\nu D^2}{B(\nu, T)}\right] \quad \ldots(9)$$

We use equation (9) to calculate dust mass of the cavity

3. Result and Discussion

3.1 Structure: Contour Maps

While going through the systematic search on IRAS maps, we discovered an isolated cavity in the 100 μm and 60 μm at R.A. (J2000) = $09^h\ 40^m\ 50.63^s$ and Dec. (J2000) = $-52^o\ 48'\ 32''$. With the help of the software ALADIN2.5, we have studied physical properties (size, dust color temperature, dust mass, etc) of the cavity. We selected contour level in such a way that it circles the cavity. The major axis, minor axis and line passing through minimum temperature and minimum flux are shown in the fig.1(b).

3.2 Distribution of Flux Density

By using ALADIN 2.5 software, the values of flux densities at 60μm and 100μm have measured. The flux density distribution within the contour of the region of interest has studied. We plotted a graph between flux at 100μm and 60μm with the help of ORIGIN 5.0 which is shown in fig.2(a). From the linear fit, slope of the line was 0.29. The linear equation of the fitted line is, y=-1.1+0.2x. Using the slope of best fitted plot, dust color temperature is found as 23 K which is nearly similar with our calculated value.

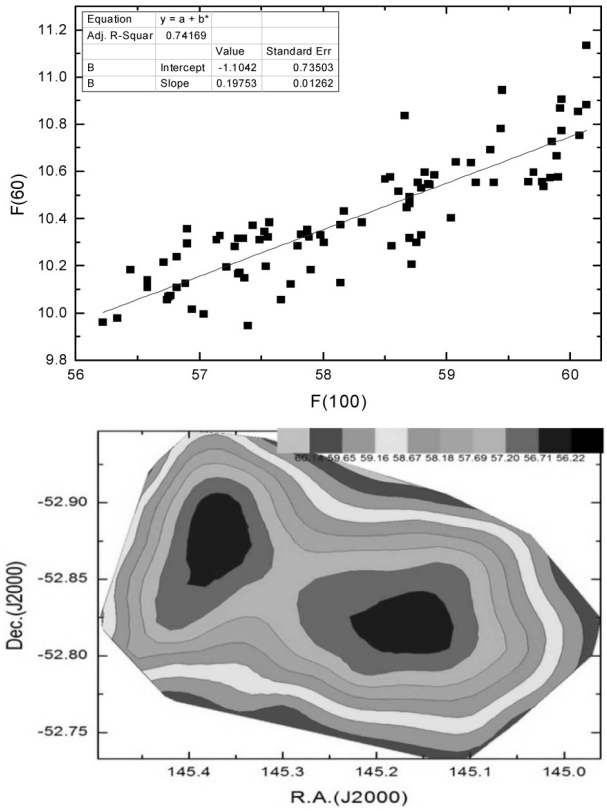

Fig.2(a) The 100μm verses 60μm flux density in the region of interest and 2(b) Contour map at 100μm flux density where the AGB star is located at the center R.A. (J2000) = $09^h\ 40^m\ 50.63^s$, Dec. (J2000) = $-52^0\ 48'\ 32''$.

Again distribution of flux at 100μm of the pixels within the contour level with right ascension (R.A.) and declination (Dec.) are plotted by using ORIGIN 8.0 and the graph is shown in fig.2(b). Graph shows that all the fluxes from minimum to maximum lie within the contour level. Most of the maximum flux regions lie at the boundary.

2.3. Dust color Temperature and its Variation

Using the method of Schnee at. al.(2005), we calculated dust color temperature of each pixel inner the outer isocontour in the region of interest. We use the IRAS 100 μm and 60 μm FITS images downloaded from the IRAS server . For the calculation of temperature we choose the value of β = 2 following the explanation given by (Dupac at.al. 2003). Variation of temperature with corresponding R.A.(J2000) and Dec.(J2000) are plotted by using ORIGIN 8.0 and the graph is shown in figure 3(a). Graph shows that temperature distributions are in separate cluster but minimum temperature region is little bit shifted from minimum flux density which is unusual behaviour. Such type of nature is obtained due to external factors.

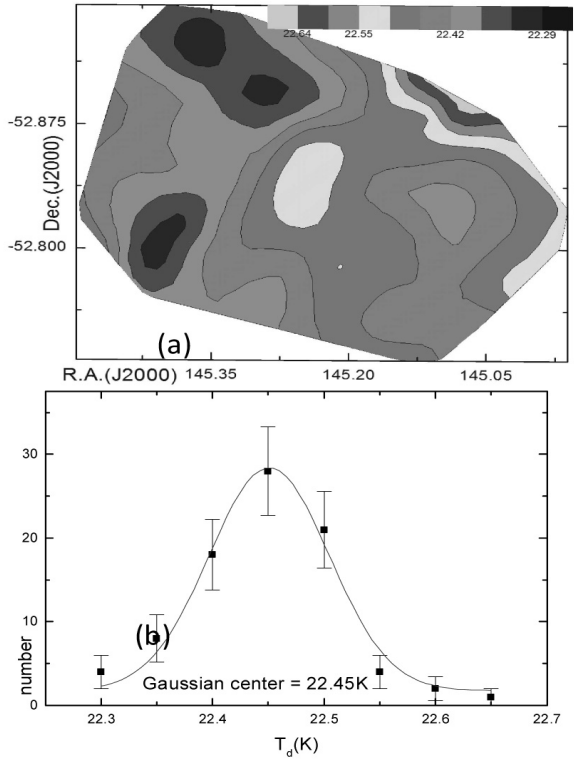

Fig. 3: (a) Contour map of dust color temperature and (b) Gaussian fit between dust color temperature and number of pixels. The field is centered at R.A.(J2000)=09^h 40^m 50.63^s and Dec.(J2000)=-52^o 48' 32".

The region in which minimum and maximum temperature is found in the range of 22.3K to 22.6K with an offset temperature of dust 0.3K. Such a low offset temperature variation shows that there is symmetric outflow or symmetric distribution of density and temperature. It further suggests that particles are independently vibrating. The cavity may be in thermally pulsating phase. When this result is compared with the result obtained in (Aryal et al. 20011) where temperature variation is 20K to 22K so our result is also comparable with that result. In the contour map, minimum flux and minimum temperature region are shifted which is due to some external factors possibly due to AGB wind. There is good agreement in case of temperature in the Gaussian fit with offset 1.21 K.

2.4. Size of the Structure

Major and minor diameter of the structure can be easily calculated by using a simple expression i.e., L = R × θ, where R = 265 pc is the distance of the structure and θ = pixel size (in radian). After calculation the major and minor diameter of the cavity region are found to be 1.55 pc and 0.61 pc respectively. Thus, the size of the structure is 1.55 pc × 0.61 pc .

2.5. Dust Mass Estimation and its variation

For the calculation of dust mass, we need the distance to the region of interest. The distance of the structure is 265 pc (Konyves et al. 2007). By using the temperature of each pixel and corresponding distance of the structure, we calculated mass of each pixel. Average mass of each pixel is 1.3x10^{26} kg and total mass of the structure is 1.1 x 10^{28} kg i.e 0.0055M$_\odot$. But mass of dust obtained around white dwarf WD 1003-44 in (Aryal et al. 2011) is 0.08M$_\odot$. It means mass of dust around AGB Star is less than White Dwarf.

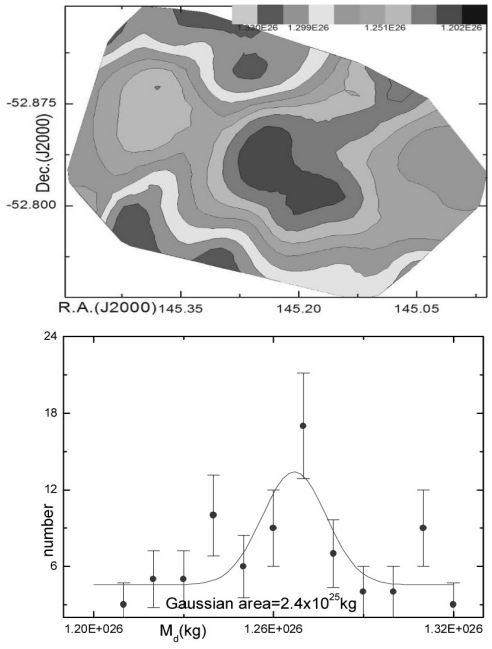

Fig.4: (a) contour map of dust mass and (b)Gaussian fit between mass and number of pixels. The field is centered at R.A.(J2000)= 09^h 40^m 50.63^s and Dec. (J2000) = -52^o 48' 32".

Distribution of dust mass of the pixels within the selected contour level with R.A. (J2000) and Dec.(J2000) are

plotted in contour map by using ORIGIN 8.0. Graph obtained is shown in fig.4(a) which shows that minimum mass region didn't lie at the maximum temperature region in the selected contour which is unusual trend and is possibly due to AGB wind. There is no good agreement in case of dust mass where offset mass is 4.56 kg.

2.6. Calculation of Excess Mass

For the calculation of excess mass, we have drawn two circles i.e. inner and outer circle with the help of software Aladin V8.0. Circle through major diameter is supposed as outer circle and the circle through minor diameter is supposed as inner diameter of the interested region. With the help of those circles we have calculated excess mass.

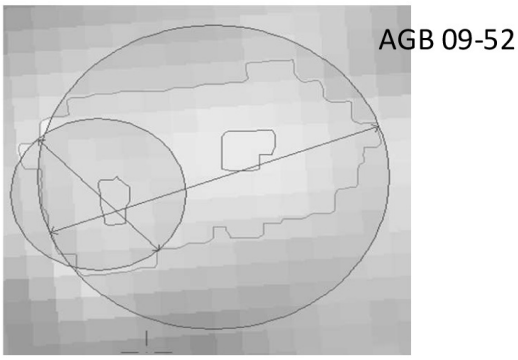

Figure 4: The inner and outer circle drawn in the structure at the center R..A.(J2000)= 09^h 40^m 50.63^s and Dec. (J2000)= -52^o 48' 32" for calculation of excess mass.

From the calculation total mass of the inner circle was found to be 4.4 x 10^{27} kg and the total mass of outer circle including inner circle was 1.8 x 10^{28} kg . So the mass deficit in the inner pixel which was blown away by the AGB star is 1.36 x 10^{28} kg i.e. 0.007 $M_{\odot}$.

4. CONCLUSION

The physical properties of the cavity-like structure that we investigated while searching a effect of AGB wind around carbon-rich AGB stars. A study of flux density and dust color temperature maps mass of dust, mass deficit of the cavity was calculated. Our conclusions are as follows:

- The major and minor diameter of the cavity like structure was found to be 1.55 pc and 0.61 pc respectively.
- The maximum temperature 22.6K was found at R.A.(J2000) = 145.12^0 & Dec.(J2000) = -52.90^0 and minimum temperature 22.3K was found at R.A.(J2000) = 145.36^0 & Dec.(J2000) = -52.92^0 with offset of 0.3 K. The small value of dust color temperature in the cavity suggests a continuous process by which cavity is supposed to be formed.
- In general, minimum flux and minimum temperature lie at same point in the pixel but in this case minimum temperature is shifted which may be due to external factors, possibly wind emitted from the AGB star. Similarly maximum temperature and minimum mass region didn't lie at same region which isn't normal behavior.
- Total mass of inner circled cavity was 4.4 x 10^{27} Kg and that of the outer circle including inner circle was 1.8 × 10^{28} kg . The mass deficit of the structure was 1.36 × 10^{28} kg i.e. 0.007 $M_{\odot}$.

We intend to study the role of cabon-rich AGB star to form the far-infrared cavity in the future.

ACKNOWLEDGEMENTS

We are grateful to the Department of Astro-Particle Physics, Innsbrck University, specially to Prof. R. Weinberger for invoking us to work on dusty environments around AGB stars. This research has made use of SkyView Virtual Observatory, Aladin v2.5 and NASA/IPAC Extragalactic Database (NED). One of the authors (AKG) acknowledges Central Department of Physics, T.U., Nepal for providing various support of Ph.D.

REFERENCES

[1] Aryal, B. & Weinberger, R. (2011). Dust structure around White Dwarf WD 1003-44 in 60 and 100μm Iras Survey. The Himalayan Physics, II, .5-10.

[2] Dupac, X., Bernard,J.P., Boudet, N., Giard, M., Lamarre, J.M., Meny, C., Pajot, F., Ristorcelli, I., Serra, G., Stepnik, B. & Torre, J.P. (2003). Inverse Temperature Dependance of the Dust Submillimeter Spectral Index. Astronomy & Astrophysics, 404, L11-L15.

[3] Herwig,F., (2005). Evolution of Asymptotic Giant Branch Stars. Annu.Rev.Astron.Astrophysics,43, 435-479.

[4] Hildebrand, R.H. (1983). The determination of cloud mass and dust characteristics from sub millimeter thermal emission. Royal Astronomical Society, 24, 267-282.

[5] Karakas, A.I., Lattanzio, J.C. & Pols, O.R., (2002). Parameterising the third dredge- up in asymptotic giant branch stars. Astron. Soc. Aust., 19, 515-38.

[6] Konyves, V., Kiss, Cs., Moor, A., Kiss, Z.T., & Toth, L.V.,(2007). Catalog of Far- Infrared Loops in the Galaxy. Astronomy & Astrophysics, 463,1227-1234.

[7] Schnee, S.L., Ridge, N.A., Goodman, A.A. & Jason, G.L.(2005). A Complete Look at the Use of IRAS Emission Maps to Estimate Extinction and Dust Temperature. The Astrophysical Journal, 634, 442-450.

[8] Seiss, L. & Pumo, M.L., (2006). Evolutionary Properties of Massive AGB Stars. Memorie della Societa Astronomica Italiana, 77, 822-827.

[9] Suh, K.W & Kwon,Y.J. (2009). A Catalog of AGB Stars in IRAS PSC. Journal of the Korean Astronomical Sociaty, 42, 81-91.

[10] Young, K., Phillips, T.G. & Knapp, G.R. (1993). Circumstellar Shells Resolved in IRAS Survey Data II. Analysis. Astrophysical Journal, 409, 725-738.

Research Paper
Impact Factor: 4.164
Refereed Journal

IJMDRR
E- ISSN –2395-1885
ISSN -2395-1877

A STUDY OF DUSTY ENVIRONMENT AT FAR INFRARED IRAS MAP AROUND THE MASS -LOSING CARBON-RICH AGB STAR AT LATITUDE -59.6^{o}

A.K. Gautam B. Aryal
Central Department of Physics, T.U., Kirtipur,Nepal.

Abstract
This paper discusses the physical properties of the dusty environment around the mass losing AGB star located at R.A. (J2000) =10h 25m 08s and Dec (J2000) =-59o 33' 00", in the far infrared (60 and 100μm) IRAS maps. A cavity like structure (major diameter ∼ 2.3 pc & minor diameter ∼0.21 pc) is found to lie at R.A. (J2000) = 10h 26m 54.73s and DEC (J2000) = -59o 18' 22.5", located at a distance ∼ 305 pc from the star. By using contour map diagram, we studied the distribution of flux density, dust color temperature, dust mass and outflow mass in the cavity. The dust color temperature is found to lie in the range 23.9 K to 25.1 K which shows the cavity is isolated and independently evolved. Such a low offset temperature variation shows that the star is in thermal equilibrium and its life is long. Dust particles are less interacting and mean free path is large. The cavity may be in thermally pulsating phase. A possible explanation of the results will be discussed.

Key Words: AGB Stars, Dust Color Temperature, Dust Mass and Excess Mass.

Introduction

The evolution of star that follows core helium burning depends strongly on the stellar mass. The mass determines how high the central temperature and the degree of degeneracy when heavier nuclear fuels are ignited. When the central helium supply is exhausted, helium will continue to burn in a shell, while the hydrogen burning shell is extinguished. In the HR diagram the star will move towards lower effective temperature and higher luminosity. This phase is quite similar to the red giant phase of low-mass stars, although the temperatures are slightly hotter. For this reason it is known as the asymptotic giant branch, AGB.
Asymptotic giant branch (AGB) stars are the final nuclear burning stage of low- and intermediate-mass stars driven by nuclear burning. This phase of evolution is characterized by two nuclear burning shells of hydrogen and helium where hydrogen burns shell lies below the convective envelope and helium burning shell lies above the electron-degenerate core of carbon and oxygen, or for the most massive AGB stars a core of oxygen, neon, and magnesium [1: 435]. This AGB stage is characterized by low surface effective temperatures (below 3000K) and intense mass loss (from10−7 to 10−4 M yr−1) [2: 822]. When the gas temperature drops to the sublimation temperature range, heavy elements in the mass outflow from a central star will condense to form dust. Dusty circumstellar envelopes will format the distance of several stellar radii .Dust grains in the envelopes absorb stellar radiation and re-emit infrared radiation so AGB stars are important infrared sources. The mass loss process plays an important role in the evolution of AGB stars. It affects the lifetime of the AGB phase and the core-mass of the subsequent post-AGB stars. Statistics of a large sample of AGB stars would help to constrain the evolution of dust envelope. There are two main types of AGB stars: the O-rich with C/O < 1 and mainly silicate-type grains in the outflow, and C-rich with C/O > 1 and mainly carbonaceous grains in the envelopes [1:435]. Due to different dust compositions of these two types of AGB stars, different infrared spectral features are obtained which can be used to distinguish the two groups of the stellar objects. Most of the carbon compounds such as aromatic hydrocarbon, benzene, methane, etc. are responsible for biological life so carbon- rich AGB stars are preferred in our research work.

He-core burning phase is about 10 times shorter than the H-core burning shell so that the He-core burning leaves a C/O core behind that is surrounded by both a hydrogen and helium burning shell. For low and intermediate mass stars, carbon doesn't ignite and C/O core contracts and becomes electron degenerate. During the early AGB phase, the abundance of He in the centre goes to zero where He-burning continues in a shell around a degenerate C-O core. In the meantime, the H- layer around the helium shell expands and cools sufficiently so that hydrogen burning shell is extinguished. Convective envelope sets in and moves inwards and second dredge-up takes place. He shell is the main source for nuclear production so that it burns outward and reaches the hydrogen shell. In case of thermally pulsating AGB phase, helium shell becomes thin and remains thermally unstable as a result thermal pulses are produced. In each thermal pulse, luminosity of helium shell nearly approaches 108L [3: 515].The production of such high luminosity in helium shell is called He shell flash or thermal pulse which is used to expand the outer layers. Such strong expansion drives the H shell cooler and less dense as a result H shell is extinguished. The inner edge of deep convective envelope can then move inward and mix to the surface products of internal nucleosynthesis. This mixing process which occurs periodically after each TP is known as third dredge-up which is the mechanism for producing carbon stars. During TP-AGB phase, main dominant source of nuclear energy is the hydrogen shell. Thermally pulsating AGB phase is the phase after the first thermal pulse to the time when the star ejects its envelope.

In this paper, we study the physical properties of far infrared cavity, that we investigated during a systematic search on IRAS maps, located close to a carbon-rich AGB star (AGB 09-52) at -52.8o latitude. In section 2, we describe methods of calculation. A brief description of the result and discussion will be given in the section 3. Finally, we conclude our results in the section 4.

Methods

We investigated a cavity-like structure in both 60 and 100 micron IRAS maps around a AGB star. We briefly describe a method for calculation of dust color temperature and dust mass of the dusty environment around carbon-rich Asymptotic Giant Branch named AGB10-59.

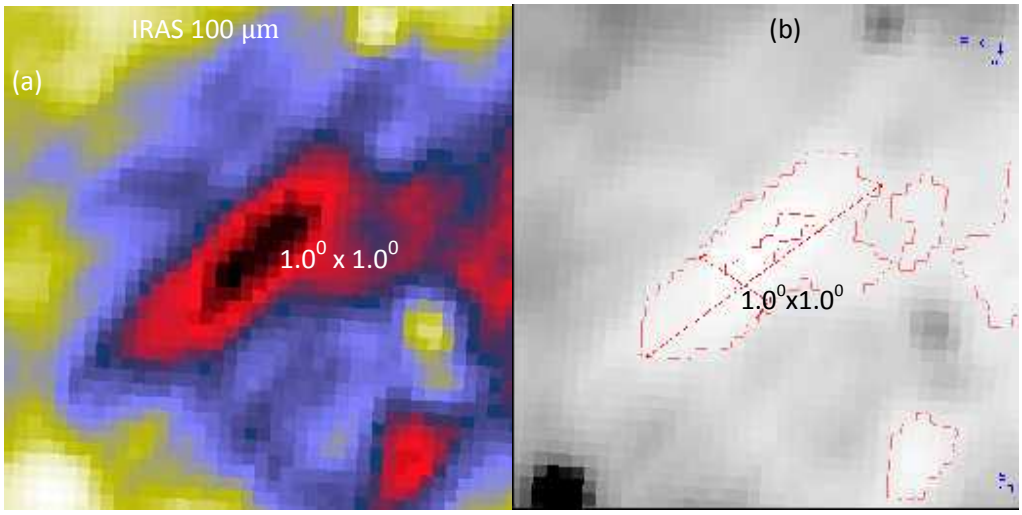

Fig. 1. (a) IRAS 100 µm and 60 µm far infrared image of the core region of AGB 10-59 centered at R.A. (J2000) = 10h 26m 54.73s, Dec. (J2000) = -590 18' 22.5" and (b) Contour map of the cavity where major diameter (AB), minor diameter (CD) and diameter between minimum flux &minimum temperature.

Dust Color Temperature Estimation

Schnee et al. [4: 442] derived an expression to calculate dust color temperature. The flux density of emission at a wavelength λi is given by

$$Fi = \left[\frac{2hc}{a_i^3 \left(e^{\frac{hc}{a_i kT_d}} - 1 \right)} \right] Nd\ \alpha\ \lambda i\text{-}\beta\ \Omega i \qquad \ldots (1)$$

where β is the spectral emissivity index, Nd is the column density of dust grains, α is a constant i.e. free parameter which relates the flux with the optical depth of the dust, and Ωi is the solid angle subtended at λi by the detector. In Dupac et al. [5: L11], there is an inverse relationship between temperature and emissivity spectral index. we have

With the assumptions that the dust emission is optically thin at 60 µm and 100 µm and that Ωω Ω100 (true for IRAS image), we can write the ratio, R, of the flux densities at 60 µm and 100 µm as

$$R = 0.6-(3+\beta)\ \frac{e^{144/T_d} - 1}{e^{240/T_d} - 1} \qquad \ldots (3)$$

The spectral emissivity index (β) depends on dust grain properties like composition, size, and compactness. For a pure blackbody would have β = 0, the amorphous layer-lattice matter has β ~ 1, and the metals and crystalline dielectrics have β ~ 2 which is used in our calculations.

For a smaller value of Td, 1 can be dropped from both numerator and denominator of Eq. (3) and it takes the form

$$R == 0.6-(3+\beta) \frac{e^{144/T_d}}{e^{240/T_d}} \quad \ldots (4)$$

$$\text{Where } R = \frac{F(60\mu m)}{F(100\mu m)}$$

Taking natural logarithm on both sides of Eq. (4) and solving it, we find the expression for the temperature as

$\ln(R)=\ln 0.6-(3+\beta)\ [144/Td-240/Td]$

$= \ln 0.6-(3+\beta)[-96/Td]$

$$Td = \frac{-96}{\ln\{R \times 0.6(3+\beta)\}} \quad \ldots (5)$$

F(60 µm) and F(100 µm) are the flux densities in 60 µm and 100 µm respectively and Eq. (5) can be used for calculation of the dust grain temperature.

Dust Mass Estimation

Dust mass is another important physical quantity which is useful to analysis the cavity structure. We need the known distance of the loops to calculate its dust mass which was provided in catalog of far infrared loops in the galaxy [6: 1227].

For the calculation of dust mass, we first obtained the value of flux density (Sν) at 100 µm maps.

The dust mass is estimated using [7: 267],

$$M = \frac{4ar}{3Qn}\left|\frac{SnD2}{B(n, T)}\right| \quad \ldots(7)$$

where, weighted grain size (a) = 0.1 µm, grain density (ρ) = 3000 kg m-3, grain emissivity (Qν) = 0.0010 (for 100 µm) [8: 725].

The Planck's function B(ν, T), which is the function of temperature and frequency and is given by the expression:

$$B(\quad T) = \frac{2hc}{l3}\left(\frac{1}{\frac{hc}{elkT}-1}\right) \ldots (8)$$

Where, h = Planck's constant, c = velocity of light, ν = frequency at which the emission is observed, T = the average temperature of the region.

For 100 µm wavelength, the expression for the dust mass (8) reduces to,

$$Mdust = 0.4\left[\frac{SnD2}{B(n, T)}\right] \quad \ldots (9)$$

We use equation (9) to calculate dust mass of the cavity

Result and Discussion

Structure: Contour Maps

While going through the systematic search on IRAS maps, we discovered an isolated cavity in the 100 µm and 60 µm at R.A. (J2000) = 10h 26m 54.73s and Dec. (J2000) = -59o 18' 22.5". With the help of the software ALADIN2.5, we have studied physical properties (size, dust color temperature, dust mass, etc) of the cavity. We selected contour level in such a way that it circles the cavity. The major axis, minor axis and line passing through minimum temperature and minimum flux are shown in the fig.1(b).

Distribution of Flux Density

By using ALADIN 2.5 software, the values of flux densities at 60µm and 100µm have measured. The flux density distribution within the contour of the region of interest has studied. We plotted a graph between flux at 100µm and 60µm with the help of ORIGIN 5.0 which is shown in fig.2(a). From the linear fit, slope of the line was 0.21. The linear equation of the fitted line is,

y=-7.5+0.21x. Using the slope of best fitted plot, dust color temperature is found as 23.3 K which is nearly similar with our calculated value.

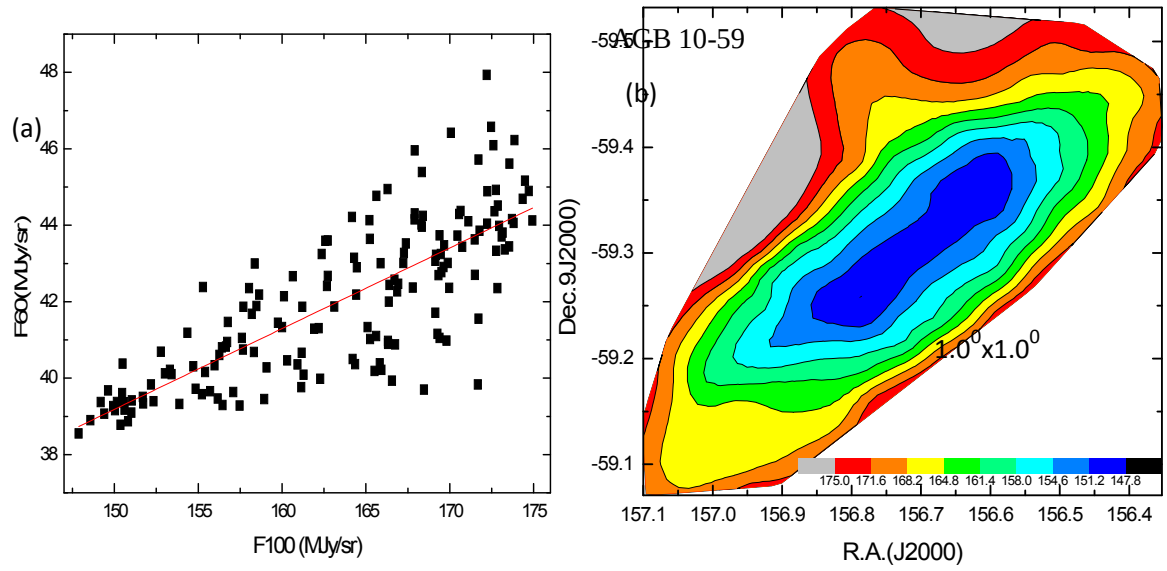

Fig.2(a) The 100µm verses 60µm flux density in the region of interest and 2(b) Contour map at 100µm flux density where the AGB star is located at the center R.A. (J2000) = 10h 26m 54.73s, Dec. (J2000) = -590 18' 22.5".

Again distribution of flux at 100µm of the pixels within the contour level with right ascension (R.A.) and declination (Dec.) are plotted by using ORIGIN 8.0 and the graph is shown in fig.2 (b). Graph shows that all the fluxes from minimum to maximum lie within the contour level. Most of the maximum flux regions lie at the boundary.

Dust Color Temperature and Its Variation

Using the method of [4: 442], we calculated dust color temperature of each pixel inner the outer isocontour in the region of interest. We use the IRAS 100 µm and 60 µm FITS images downloaded from the IRAS. For the calculation of temperature we choose the value of β = 2 following the explanation given by [5: L11]. Variation of temperature with corresponding R.A.(J2000) and Dec.(J2000) are plotted by using ORIGIN 8.0 and the graph is shown in figure 3(a). Graph shows that temperature distributions are in separate cluster but minimum temperature region is little bit shifted from minimum flux density which is unusual behaviour. Such type of nature is obtained due to external factors.

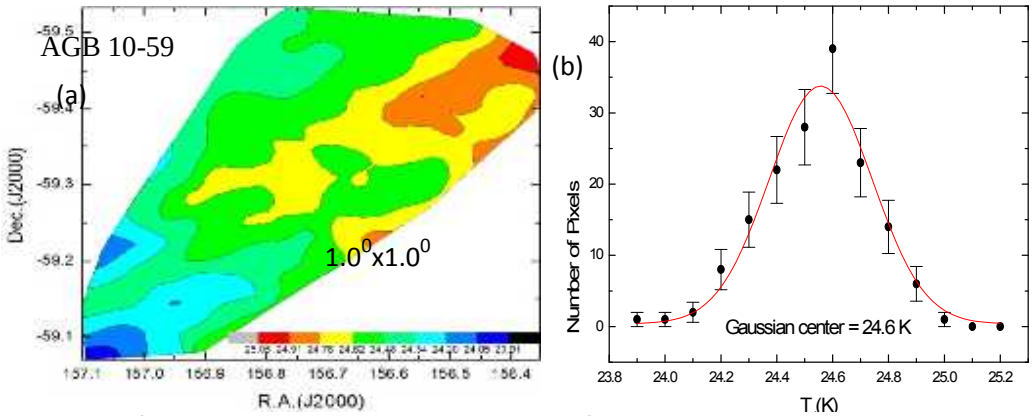

Fig. 3: (a) Contour map of dust color temperature and (b) Gaussian fit between dust color temperature and number of pixels. The field is centered at R.A.(J2000)= 10h 26m 54.73s and Dec. (J2000) = -59o 18' 22.5".

The region in which minimum and maximum temperature is found in the range of 23.9 K to 25.1 K with an offset temperature of dust 1.2 K. Such a low offset temperature variation shows that there is symmetric outflow or symmetric distribution of density and temperature. When this result is compared with the result obtained in [9: 5] where temperature variation is 20K to 22K so our result is also comparable with that result. In the contour map, minimum flux and minimum temperature region are shifted which is due to some external factors possibly due to AGB wind. There is good agreement in case of temperature in the Gaussian fit with offset 0.4 K.

Size of the Structure

Major and minor diameter of the structure can be easily calculated by using a simple expression i.e., $L = R \times \theta$, where R = 305 pc is the distance of the structure and θ = pixel size (in radian). After calculation the major and minor diameter of the cavity region are found to be 2.3 pc and 0.21 pc respectively. Thus, the size of the structure is 2.3 pc × 0.21 pc .

Dust Mass Estimation and its variation

For the calculation of dust mass, we need the distance to the region of interest. The distance of the structure is 305 pc [6: 1227]. By using the temperature of each pixel and corresponding distance of the structure, we calculated mass of each pixel. Average mass of each pixel is 2.7x1026 kg and total mass of the structure is 4.4 x 1028 kg i.e 0.02M . But mass of dust obtained around white dwarf WD 1003-44 in [9: 5] is 0.08M . It means mass of dust around AGB Star is less than White Dwarf.

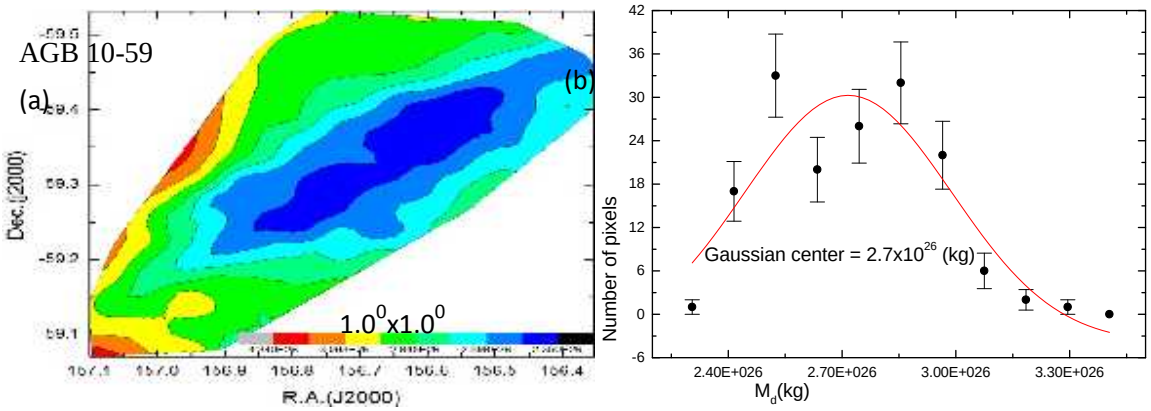

Fig.4: (a) contour map of dust mass and (b) Gaussian fit between mass and number of pixels. The field is centered at R.A.(J2000)= 10h 26m 54.73s and Dec. (J2000) = -59o 18’ 22.5”.

Distribution of dust mass of the pixels within the selected contour level with R.A. (J2000) and Dec.(J2000) are plotted in contour map by using ORIGIN 8.0. Graph obtained is shown in fig.4 (a) which shows that minimum mass region didn't lie at the maximum temperature region in the selected contour which is unusual trend and is possibly due to AGB wind. There is no good agreement in case of dust mass where offset mass is -3.9 kg.

Calculation of Excess Mass

For the calculation of excess mass, we have drawn two circles i.e. inner and outer circle with the help of software Aladin V8.0. Circle through major diameter is supposed as outer circle and the circle through minor diameter is supposed as inner diameter of the interested region. With the help of those circles we have calculated excess mass.

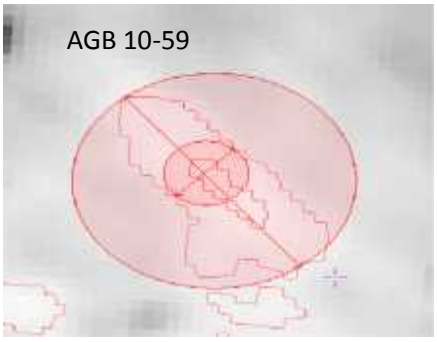

Figure 5: The inner and outer circle drawn in the structure at the center R..A.(J2000)= 10h 26m 54.73s and Dec. (J2000)= -59o 18' 22.5" for calculation of excess mass.

From the calculation total mass of the inner circle was found to be 9.7 x 1027 kg and the total mass of outer circle including inner circle was 1.2 x 1029 kg . So the mass deficit in the inner pixel which was blown away by the AGB star is 1.1 x 1029 kg i.e. 0.06 M .

Conclusion

The physical properties of the cavity-like structure that we investigated while searching around carbon-rich AGB stars. A study of flux density and dust color temperature maps mass of dust; mass deficit of the cavity was calculated. Our conclusions are as follows:

1. The major and minor diameter of the cavity like structure was found to be 1.55 pc and 0.61 pc respectively.
2. The maximum temperature 23.9 K was found at R.A.(J2000) = 145.120 & Dec.(J2000) = -59.070 and minimum temperature 25.1 K was found at R.A.(J2000) = 145.360 & Dec.(J2000) = -59.470 with offset of 1.2 K.. Low offset in the temperature hints that there is symmetric outflow or symmetric distribution of density and temperature.
3. In general, minimum flux and minimum temperature lie at same point in the pixel but in this case minimum temperature is shifted which may be due to external factors, possibly wind emitted from the AGB star. Similarly maximum temperature and minimum mass region didn't lie at same region which isn't normal behavior.
4. Average mass of dust in each pixel is 2.7x1026 kg.
5. Total mass of inner circled cavity was 9.7 x 1027 kg and that of the outer circle including inner circle was 1.2 × 1029 kg . The mass deficit of the structure was 1.1 × 1029 kg i.e. 0.06 M.

We intend to study the role of cabon-rich AGB star to form the far-infrared cavity in the future.

Acknowledgements

1. We are grateful to the Department of Astro-Particle Physics, Innsbrck University, specially to Prof. R. Weinberger for invoking us to work on dusty environments around AGB stars. This research has made use of SkyView Virtual Observatory, Aladin v2.5 and NASA/IPAC Extragalactic Database (NED). One of the authors (AKG) acknowledges Central Department of Physics, T.U., Nepal for providing various support of Ph.D.

References

1. F. Herwig. "Evolution of Asymptotic Giant Branch Stars". ARAA, vol. 43, pp435, 2005.
2. L. Seiss and M. L. Pumo."Evolutionary Properties of Massive AGB Stars". Mem.S.A.It, vol. 77, pp 822, 2006.
3. A.I. Karakas, J.C. Lattanzio and O.R. Pols. "Parameterising the third dredge- up in asymptotic giant branch stars". Astron. Soc. Aust., vol. 19, pp515, 2002.
4. S.L. Schnee, N. A. Ridge, A.A. Goodman, G. L. Jason." A Complete Look at the Use of IRAS Emission Maps to Estimate Extinction and Dust Temperature". APJ, vol.634, pp442, 2005.
5. X. Dupac, J.P. Bernard, N. Boudet, M. Giard, J.M. Lamarre, C. Meny, F. Pajot, I. Ristorcelli, G. Serra, B. Stepnik, J.P. Torre. "Inverse Temperature Dependance of the Dust Submillimeter Spectral Index". A&A, vol.404, ppL11, 2003.
6. V. Konyves, Cs. Kiss, A. Moor, Z.T. Kiss, and L.V. Toth. "Catalog of Far- Infrared Loops in the Galaxy". A&A, vol. 463, pp1227, 2007.
7. R.H. Hildebrand."The determination of cloud mass and dust characteristics from sub millimeter thermal emission". Q.Jl.R.astr. obs.ser, vol.24, pp267, 1983.
8. K. Young, T.G. Phillips, G.R. Knapp." Circumstellar Shells Resolved in IRAS Survey Data II. Analysis". ApJ, vol. 409, pp.725, 1993.
9. B. Aryal, R. Weinbergerr. "Dust structure around White Dwarf WD 1003-44 in 60 and 100 μm Iras Survey". The Himalayan Physics, vol. II, pp.5, 2011.

Interaction between C- Rich AGB Star and the Interstellar Medium in Far Infrared Maps at 16^0 Latitude

A. K. Gautam and B. Aryal*

Abstract

This paper discusses the physical properties of the dusty environment around the AGB star located at R.A. (J2000) =06^h 31^m 05^s and Dec.(J2000) = 16^0 06′ 00″ in the far infrared (60 and 100μm) IRAS maps. A cavity like structure (major diameter ~ 3.57 pc & minor diameter ~1.19 pc) is found to lie at the center R.A.(J2000)= 06^h 32^m 38.12^s and Dec.(J2000)= 15^0 59′ 47.9 ″ located at a distance ~ 310 pc (5) from the star. We studied the flux density variation and the temperature variation about major diameter, minor diameter and the distance between minimum temperature and minimum flux region within the structure. Mass profile of each pixel of the structure was calculated by using these temperature. We also calculated the speed of sound and wind velocity of the structure which is required to estimate energy of the structure.

Key-words : AGB Star, interstellar medium, flux density, dust color temperature, mass of dust, AGB wind speed

1. Introduction

AGB stars are low and intermediate mass stars driven by nuclear which happens when the star leaves the main sequence through red giant and passed the horizontal branch . AGB stars are the main distributors of dust into the interstellar medium due to their high mass loss rates in combination with an effective dust condensation. It is therefore important to understand the dust formation process and sequence in their extended atmosphere. The interaction between wind and its surroundings in the interstellar medium (ISM) provides a laboratory to study the behavior of dust particles. Actually Asymptotic giant branch (AGB) stars are the final evolution stage of low- and intermediate-mass stars driven by nuclear burning. This phase of evolution is characterized by nuclear burning of hydrogen and helium in thin shells on top of the electron-degenerate core of carbon and oxygen, or for the most massive AGB stars a core of oxygen, neon, and magnesium.(Herwig 2005)

He-core burning phase is about 10 times shorter than the H-core burning shell so that the He-core burning leaves a C/O core behind that is surrounded by both a hydrogen and helium burning shell. For low and intermediate mass stars, carbon doesn't ignite and C/O core contracts and becomes electron degenerate. During the early AGB phase, the abundance of He in the centre goes to zero where He-burning continues in a shell around a degenerate C-O core. In the meantime, the H- layer around the helium shell expands and cools sufficiently so that hydrogen burning shell is extinguished. Convective envelope sets in and moves inwards and second dredge-up takes place. He shell is the main source for nuclear production so that it burns outward and reaches the hydrogen shell. In case of thermally pulsating AGB phase, helium shell becomes thin and remains thermally unstable as a result thermal pulses are produced. In each thermal pulse, luminosity of helium shell

* Central Department of Physics, T.U., Kirtipur, Kathmandu, Nepal, E-mail: arjungautamnpj@gmail.com and baryal@tucdp.edu.np

nearly approaches $10^8 L\odot$ (Karakas et al. 2002).The production of such high luminosity in helium shell is called He shell flash or thermal pulse which is used to expand the outer layers. Such strong expansion drives the H shell cooler and less dense as a result H shell is extinguished. The inner edge of deep convective envelope can then move inward and mix to the surface products of internal nucleosynthesis. This mixing process which occurs periodically after each TP is known as third dredge-up which is the mechanism for producing carbon stars. During TP-AGB phase, main dominant source of nuclear energy is the hydrogen shell. Thermally pulsating AGB phase is the phase after the first thermal pulse to the time when the star ejects its envelope.

According to model calculations, thermal-pulse AGB evolution is strongly mass dependent. For example dredge-up efficiency, the s process, C-star formation, or hot-bottom burning are strongly correlated with specific initial mass ranges. Therefore different evolutionary properties of AGB stars can be classified according to mass. Generally stars are broadly distinguished by their initial masses as massive, intermediate, and low-mass stars. Here low-mass stars may be designated to have $M < 1.8\ M\odot$ (depending on overshoot mixing), ignite He-core burning under degenerate conditions in a flash, and end their lives as white dwarfs. Intermediate-mass stars ignite He in the non degenerate core and end their lives as white dwarfs, and massive stars are those massive enough to explode as a supernova. This classification is not useful for thermal pulse AGB stars. Low-mass AGB stars do not experience hot-bottom burning, whereas massive AGB stars do. Those intermediate-mass stars that can ignite carbon and have a sub-Chandrasekhar H-free core after the second dredge-up are super AGB stars. Some of these may core collapse into a neutron star; some will evolve into the most massive white dwarfs with ONeMg cores. Thus, all massive AGB stars have initially intermediate-mass stars as progenitors, and some low mass and some intermediate-mass stars become low-mass AGB stars. The stars of very low mass may never reach the AGB. The most massive intermediate-mass stars may become super-AGB stars.

The spectra of AGB stars fall into very characteristic groups: the oxygen-rich stars, with spectra dominated by oxygen-containing molecules such as TiO, carbon-rich stars with spectra dominated by molecules containing carbon (e.g. CN, C_2), and rarer stars in between with $C/O \approx 1$ (S stars). Examples of these spectra are shown in Fig. 1(Wood ,2010). The existence of these stars indicates that the products of helium burning in the interior of the star are being brought to the stellar surface. The pulsations are first seen with very small amplitude and short period at low luminosities. The pulsations grow in amplitude with increasing luminosity up to amplitudes in bolometric magnitude of $\sim$1 mag. and periods typically of 500- 1000 days. This large amplitude pulsation has a major consequence - it causes a very large increase in the mass loss rate, so that essentially all the envelope outside the nuclear burning core is lost. The star then evolves from the AGB through the post-AGB phase to the planetary nebula phase and ultimately to the white dwarf stage. During the planetary nebular phase, the envelope material lost in the AGB stellar wind is illuminated by energetic photons from the remnant star, thus creating the glowing planetary nebula.

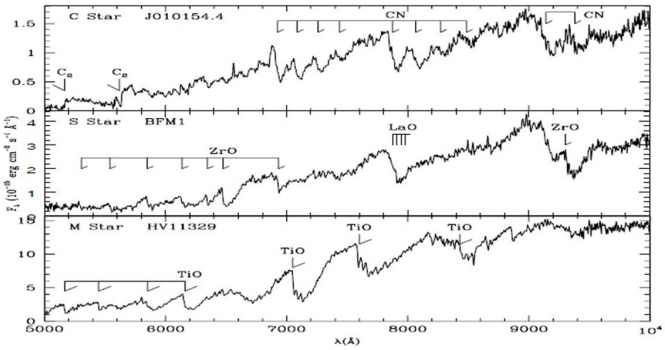

Fig. 1. The distinctive spectra of an M star, an S star and a C star. The sequence M→S→C corresponds to a change from C/O < 1 to C/O ~ 1 to C/O > 1. M stars have spectra dominated by molecules containing oxygen (e.g. TiO, VO) while C star spectra are dominated by molecules containing carbon (e.g. CN, C_2). Some of the stronger bands are marked on the figure(Wood, 2010).

In this paper, we study the physical properties of far infrared cavity, that we investigated during a systematic search on IRAS maps, located close to a carbon-rich AGB star (AGB 06+16) at 16.1° latitude. In section 2, we describe methods of calculation. A brief description of the result and discussion will be given in the section 3. Finally, we conclude our results in the section 4.

2. Methods

In this paper, we study the far infra red cavity located close to the Carbon-rich AGB star at 16.1^0 and briefly we describe the method of calculation for dust color temperature, dust mass, wind speed, energy estimation of the selected dusty loop under IRAS survey.

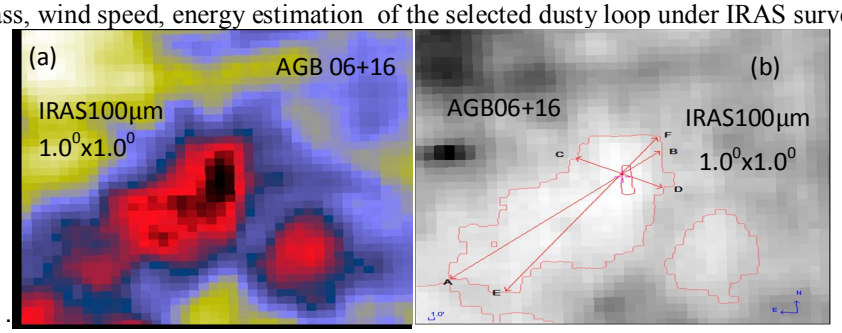

Fig.2(a): IRAS 100μm far infrared image of the core region of AGB 06+16 centered at R.A.(J2000)= 06h 32m 38.12s and Dec.(J2000)= 15◦ 59 m 47.9 s , (b)Contour map with major axis AB, minor axis CD, line joining between minimum temperature and minimum flux EF where size of the field is shown.

2.1 Flux Density

To calculate temperature and mass of each pixel due to the contribution of dust, we need flux density of all pixel lying inside the outermost contour i.e. isoconter level 38 at 60 μm and 100 μm respectively. It is done by using software Aladin v2.5.

2.2 Dust Color Temperature

For the calculation of dust color temperature, we adopt the method proposed by Schnee et al. (2005) and Dupac et al. (2003). According to Schnee et al. (2005), dust color temperature of the emission at a wavelength λ_i is given by

$$T_d = \frac{-96}{\ln\{R \times 0.6^{(3+\beta)}\}} \qquad \text{.....(1)}$$

where , $R = \frac{F(60\ \mu m)}{F(100\ \mu m)}$

F(60 μm) and F(100 μm) are the flux densities in 60 μm and 100 μm respectively and Eq. (1) is used for calculation of the dust color temperature. The spectral emissivity index (β) depends on dust grain properties like composition, size, and compactness. For a pure blackbody would have $\beta = 0$, the amorphous layer-lattice matter has $\beta \sim 1$, and the metals and crystalline dielectrics have $\beta \sim 2$ which is used in our calculations.

2.3 Planck's Function

The value of Planck's function depends on the wavelength (frequency), and hence the temperature. Finally it is used to calculate dust mass. In 1900, Planck proposed a relation which is named as Planck's function. According to him, the Planck's function is given by

$$B(\nu,T) = \frac{2hc}{\lambda^3}\left(\frac{1}{e^{\frac{hc}{\lambda kT}} - 1}\right) \qquad \text{.....(2)}$$

where, h = Planck's constant, c = velocity of light, ν = frequency at which the emission is observed,

λ = wavelength of the radiation and T = temperature of each pixel.

2.4 Dust Mass

For the calculation of dust mass, first we need the value of flux density (F_ν) at 100 μm maps and we use the expression given by Hildebrand (1983),

$$M_{dust} = \frac{4a\rho}{3Q_\nu}\left|\frac{S_\nu D^2}{B(\nu, T)}\right| \qquad \text{..... (3)}$$

where, weighted grain size (a) = 0.1 μm, grain density (ρ) = 3000 kg m^{-3}, grain emissivity (Q_ν) = 0.0010 (for 100 μm) [11: 725]. So the equation (3) reduces to

$$M_{dust} = 0.4\left[\frac{S_\nu D^2}{B(\nu, T)}\right] \qquad \text{.....(4)}$$

We use equation (4) to calculate dust mass of the cavity.

3 Result and Discussion:

3.1 Structure: Contour Maps

While going through the systematic search on IRAS maps, we discovered an isolated cavity in the 100 μm and 60 μm at R.A. (J2000) = $06^h\ 31^m\ 05^s$ and Dec. (J2000) = 16^o 06' 06". With the help of the software ALADIN2.5, we have studied physical properties (size, dust color temperature, dust mass, etc) of the cavity. We selected contour level in such a way that it circles the cavity. The major axis, minor axis and line passing through minimum temperature and minimum flux are shown in the fig.2(b).

3.2 Distribution of Flux Density

By using ALADIN 2.5 software, the values of flux densities at 60μm and 100μm have measured. The flux density distribution within the contour of the region of interest has

studied. We plotted a graph between flux at 100µm and 60µm with the help of ORIGIN 5.0 which is shown in fig.2(a). From the linear fit, slope of the line was 0.18. The linear equation of the fitted line is, *y =-0.9+0.18x*. Using the slope of best fitted plot, dust color temperature is calculated as 22.6 K.

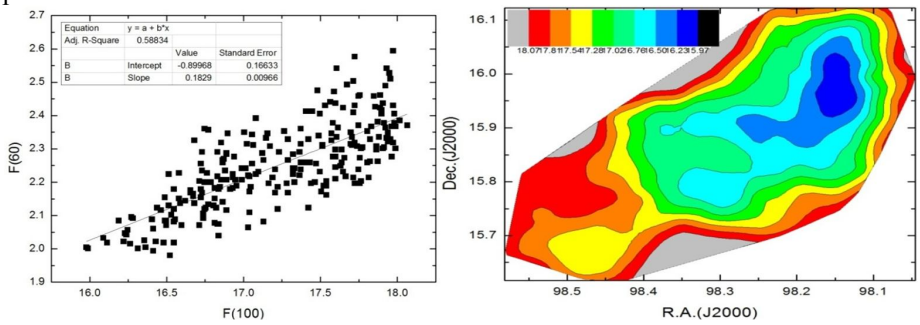

(a) (b)

Fig.3(a) The 100µm verses 60µm flux density in the region of interest and 3(b) Contour map at 100µm flux density where the AGB star is located at the center R.A. (J2000) = $06^h\,32^m\,38.12^s$, Dec. (J2000) = 15^0 59' 47.9."

Again distribution of flux at 100µm of the pixels within the contour level with right ascension (R.A.) and declination (Dec.) are plotted by using ORIGIN 8.0 and the graph is shown in fig.3(b). Graph shows that all the fluxes from minimum to maximum lie within the contour level. Most of the maximum flux regions lie at the boundary.

3.3. Dust color Temperature and its Variation

Using the method of Schnee et al. (2005) ,we calculated dust color temperature of each pixel inside the outer isocontour 38 in the region of interest. We use the IRAS 100 µm and 60 µm FITS images downloaded from the IRAS server. For the calculation of temperature, we choose the value of β = 2 following the explanation given by Dupac et al. (2003). Variation of temperature with corresponding R.A.(J2000) and Dec.(J2000) are plotted by using ORIGIN 8.0 and the graph is shown in figure 3(a). Graph shows that temperature distributions are in separate cluster but minimum temperature region is little bit shifted from minimum flux density which is unusual behaviour. Such type of nature is obtained due to external factors.

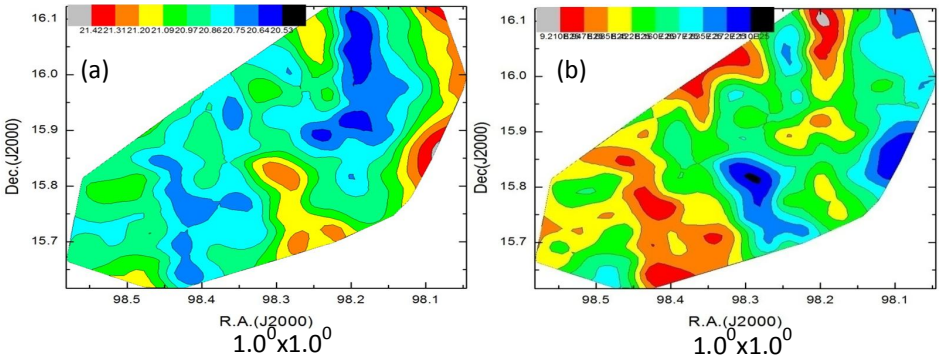

Fig. 4: Dust color temperature (a) and dust mass (b) contour maps. The field is centered at R.A. (J2000) = $06^h\,32^m\,38.12^s$, Dec. (J2000) = 15^0 59' 47.9." The contour levels are shown.

The region in which minimum and maximum temperature is found in the range of 20.5K to 21.4K with an offset temperature of dust 0.9K. Such a low offset temperature variation shows that there is symmetric outflow or symmetric distribution of density and temperature. It further suggests that our structure is not independently evolved or the role of discrete point sources in the field of cavity is important for the structure destruction mechanism. The cavity may be in thermally pulsating phase. The dust temperature less than 20 K represents the interstellar cirrus cloud. Thus our far infrared dust structure (i.e. cavity) is not a cirrus cloud. Another region of cloud fulfills the criteria of Cirrus clod. When this result is compared with the result obtained in Aryal et al.(2011) where temperature variation is 20K to 22K so our result is also comparable with that result.

3.4 Size of the Structure

To measure the major and minor diameter for each FITS image, we used a simple expression for the calculation, $L = R \times \theta$, where R = 310pc is the distance of the structure from us provided by Weinberger (5) and θ = pixel size (in radian). After calculation the major and minor diameter of the cavity region are 3.57 pc and 1.19 pc respectively at contour level 38 in the 100 μm image. Thus, the size of the structure is 3.57 pc × 1.19 pc .

3.5 Dust Mass Estimation

For the calculation of dust mass, we need the distance to the region of interest. The distance of the structure provided by Weinberger (2014) is 310 pc. By using the temperature of each pixel and corresponding distance of the structure, we calculated mass of each pixel. Average mass of each pixel is 8.22 x 10^{25} kg and total mass of the structure is 2.06 x 10^{28} kg.

3.7 AGB Wind Speed

The wind velocity was calculated by the relation given in Mattsson et al. (2010).

$$u_{out}^2 = \frac{2}{\gamma - 1} u_s^2 + (\Gamma - 1) u_{esc}^2$$

where u_{out} is the dust velocity, u_s is the velocity of the sound, u_{esc} is the escape velocity, γ is the polytropic index of the system and Γ is defined by,

$$\Gamma = \frac{kL_*}{4\pi cGM_*}$$

For the AGB star we can assume that the $\frac{L_*}{M_*}$ is $10^3 \frac{L_\odot}{M_\odot}$ to $10^4 \frac{L_\odot}{M_\odot}$.

The value of k is the opacity of the medium which is 0.1 m^2Kg^{-1} for the 100 μm emitter dust,(Ossenkopf . et al. 1994).

Using solar Luminosity to be 3.846 × 10^{26} W and the solar mass 2 × 10^{30} Kg we get the value of Γ to be 0.076 to 0.765 which tends the second term of the wind velocity equation negative, which was expected result because of the gravitational term which have to reduce the outer wind velocity.

Now we calculate the escape velocity of the structure using the diameter of the inner circle.

$$u_{esc} = \sqrt{\frac{4GM}{d_1}}$$

here d1 is the diameter of the inner circle which was calculated as 1.19 pc , M is the mass inside inner circle which was calculated as 8.148x10^{27} and gives the value of the escape velocity to be

$$u_{esc}^2 = 0.59\ m^2/s^2$$

$$u_{esc} = 0.768\ m/s$$

Velocity of the sound in that structure can be defined as the velocity of the dust having that temperature. We assume that kinetic energy of the dust is equal to the thermal energy i.e.

$$K_B T_{ave} = \frac{1}{2} m_d u_s^2$$

The average temperature of the structure is 20.91 K and m_d is the mass of the dust structure which was assumed to 10^4 m_p, (m_p is mass of the proton which is equal to 1.67×10^{-27}kg) this gives the value

$$u_s^2 = 34.55\ m^2 s^{-2}$$

$$u_s = 5.87\ m/s$$

This gives the wind velocity as

$$u_{out}^2 = \frac{2}{g-1} u_s^2 - 0.84$$

to

$$u_{out}^2 = \frac{2}{g-1} u_s^2 - 0.43$$

The value of the polytropic index is assumed to be 1.5 in The AGB star. This make the range of the dust velocity as,

$$u_{out}^2 = 192.05 - 0.84 = 191.25$$

to

$$u_{out}^2 = 192.05 - 0.43 = 191.62$$

Thus

$$u_{out} = 13.83\ m/s \text{ to } 13.84\ m/s, \text{ i.e } 13.84\ m/s$$

When analyzing the u_{out} equation for the compact AGB star we can assume the polytropic index of it to be ~ 1:1. Then the speed for the proton can have the value of $3{:}09 \times 10^3\ ms^{-1}$.

3.8 Energy Estimation

The energy estimated by considering that energy that was required to pull that excess mass by that velocity using the classical mass energy relation

$$E = \frac{1}{2} M_{deficit} u_{out}^2$$

Here $M_{deficit}$ is the mass deficit per pixel as we already calculated $M_{deficit}$ is 4.7×10^{28} Kg and the $u_{out}^2 = 191.62\ m^2 s^2$, we get the required energy for the structure formation as

$E = 4.5 \times 10^{30}$ J

4. Conclusions

We present physical properties of a dusty loop at far infrared (60 μm and 100 μm) IRAS maps located within 1^0 radius. The dust color temperature, dust mass, excess mass and inclination angle of the core region of the loop are studied . We conclude our results as follows:

- The major and minor diameter of the cavity like structure is found to be 3.57 pc and 1.19 pc respectively.
- The maximum and minimum flux was found to be at R.A. 06h 33m 49.4s DEC +15◦ 34m 37.6s & R.A. 06h 32m 36,6s DEC +15◦ 49m 47s , maximum and minimum temperature is at R.A. 06h 32m 22.1s DEC 15◦ 50m 51s & at R.A. 06h 32m 49.1s DEC 15◦ 55m 17s respectively.
- The region in which minimum and maximum temperature is found in the range of 20.53K to 21.42 K with an offset temperature of dust 0.89 K . Such low offset temperature variation shows that there is symmetric outflow or symmetric distribution of density and temperature.
- The flux and the temperature variation does not fit the Gaussian variation it mean the cavity prefer polytropic behavior.
- The total mass of the inner circled cavity was 5.54×10^{27} Kg, the average mass of the inner circle was 8.148×10^{25} Kg and that of the outer circle including inner was 4.709×10^{28} Kg and 8.44×10^{25} Kg respectively. The mass deficit per pixel of the structure was 4.7×10^{28} Kg i.e. 0.0236 M$\odot$.
- The wind speed of the structure was found to be 13.84 m/s and energy of the structure was found to be 4.5×10^{30} J.

Acknowledgements

We are grateful to the Department of Astro-Particle Physics, Innsbrck University, specially to Prof. R. Weinberger for invoking us to work on dusty environments around AGB stars. This research has made use of SkyView Virtual Observatory and NASA/IPAC Extragalactic Database (NED). One of the authors (AKG) acknowledges Central Department of Physics, T.U., Nepal for providing various support of Ph.D.

References

Aryal B., Rajbahak C. and Weinberger R. (2010). MNRAS 402 : 1307
Aryal B. and Weinberger R. (2006). A&A 446 :213
Aryal B.,and Weinberger R. (2011) . " The Himalayan Physics, vol. II : pp.5
Dupac X., Bernard J.P., Boudet N., Giard M., Lamarre J.M., Meny C., Pajot F., Ristorcelli I., Serra G., Stepnik B. and Torre J.P. (2003). A & A 404 : L11
Herwig F. (2005) . A & A 43 : 435
Hildebrand R. (1983). Q Jl R. astr. Soc. 24: 267
Karakas A.I., Lattanzio C.J. and Pols O.R.,(2002). Astron. Soc. Aust. 19 :515
Lagadec E., Mekarnia D., de Freitas Pacheco J. A. and Dougados C. (2005) . A & A 433 :553
Mattsson L., Wahlin R. & Hoefner S. (2010) . A&A 509 : A14
Meaburn J., Redman M.P., Connor O., Holloway A.J. and Bryce M. (2000). MNRAS 312 : 23
Ossenkopf V., and Henning T. (1994). A&A 291 : 943
Schnee S.L., Ridge N.A., Goodman A.A. and Jason G.L. (2005). APJ 634 : 442
Suh K.W. and Kwon Y.J. (2011). MNRAS 417 : 3047
Weinberger R. (2014). Private Communication
Wood P.R. (2010) . SAIt 81 : 883
Young K., Phillips T.G. and Knapp G.R. (1993). Apj 409, 725

JNPS **4** *(1), 67-77 (2017)*
ISSN: 2392-473X

Research Article

A Study of Dust Structure around AGB Star in 60 and 100 μm IRAS Survey at Latitude 54.68°

Arjun Kumar Gautam[1], and Binil Aryal[2,*]
[1]*Department of Physics, Bhaktapur Multiple Campus, Bhaktapur, Nepal*
[2]*Central Department of Physics, Tribhuvan University, Kirtipur, Nepal*
[*]*Corrosponding Email: baryal@gmail.com*

ABSTRACT

We have studied about the evolution of Asymptotic Giant Branch (AGB) stars, mass losses from them and a systematic search of AGB stars in J2000 coordinate system provided by K. W. Shu & Y. J. Kwon (2011) of dust structure in the far infrared range (100 μm and 60 μm). For dust structure IRAS survey was performed using Sky View virtual Observatory. The FITS images downloaded from sky view was processed using software Aladin v 2.5. A cavity like structure (major diameter∼1.93 pc & minor diameter∼ 0.89 pc) lies in the coordinate of R. A. (J2000) 04h 15m 03s and DEC (J2000) 54d 41m 00s was found at the distance∼ 240 pc. We studied the flux density variation and the temperature variation about major diameter, minor diameter and the distance between minimum temperature and minimum flux within the structure. We observed the variation of the temperature is 20.53 K to 21.09 K, with the offset of about 0.56 K, which show the cavity is independently evolved. The mass profile of each pixel of the structure was also calculated using this temperature.

Keywords: AGB Stars, Low and intermediate mass stars, Dredge-up, Thermal pulse, Nucleosynthesis, S-process, Mass loss, Excess mass.

INTRODUCTION

Low-to-intermediate mass stars end their life on the asymptotic giant branch (AGB) star. AGB stars are the main distributors of dust into the interstellar medium due to their high mass loss rates in combination with an effective dust condensation. It is therefore important to understand the dust formation process and sequence in their extended atmosphere. The interaction between wind and its surroundings in the interstellar medium (ISM) provides a laboratory to study the behavior of dust particles. Actually Asymptotic Giant Branch (AGB) stars are the final evolution stage of low- and intermediate-mass stars driven by nuclear burning. This phase of evolution is characterized by nuclear burning of hydrogen and helium in thin shells on top of the electron-degenerate core of carbon and oxygen, or for the most massive super AGB stars a core of oxygen, neon, and magnesium. In particular, the recurrent thermonuclear flashes that induce a complex series of convective mixing events provide a rich environment for nuclear production. The nucleosynthesis in AGB stars plays an important role for our understanding of the origin of the elements. AGB stars are the major contributors to the integral luminosity of intermediate-age stellar systems.

The spectra of AGB stars fall into very characteristic groups: the oxygen-rich stars, with spectra dominated by oxygen-containing molecules such as TiO, carbon-rich stars with spectra dominated by molecules containing carbon (e.g. CN, C_2), and rarer stars in between with C/O ≈ 1 (S stars). Examples of these spectra are shown in figure 1. The existence of these stars indicates that the products of helium burning in the interior of the star are being brought to the stellar surface. Any theory of AGB evolution must be able to explain this. While changes due to nuclear processes in the stellar interior occur on timescales of $\sim 10^5$ years, the outer envelopes of AGB stars pulsate on timescales of ∼10-1000 days. The pulsations are first seen with very small amplitude and short period at low luminosities. The pulsations grow in amplitude with increasing luminosity up to amplitudes in bolometric magnitude of ∼1 mag. and periods typically of 500- 1000 days. This large amplitude pulsation has a major consequence - it causes a very large increase in the mass loss rate, so that essentially

the entire envelope outside the nuclear burning core is lost. The star then evolves from the AGB through the post-AGB phase to the planetary nebula phase and ultimately to the white dwarf stage. During the planetary nebular phase, the envelope material lost in the AGB stellar wind is illuminated by energetic photons from the remnant star, thus creating the glowing planetary nebula.

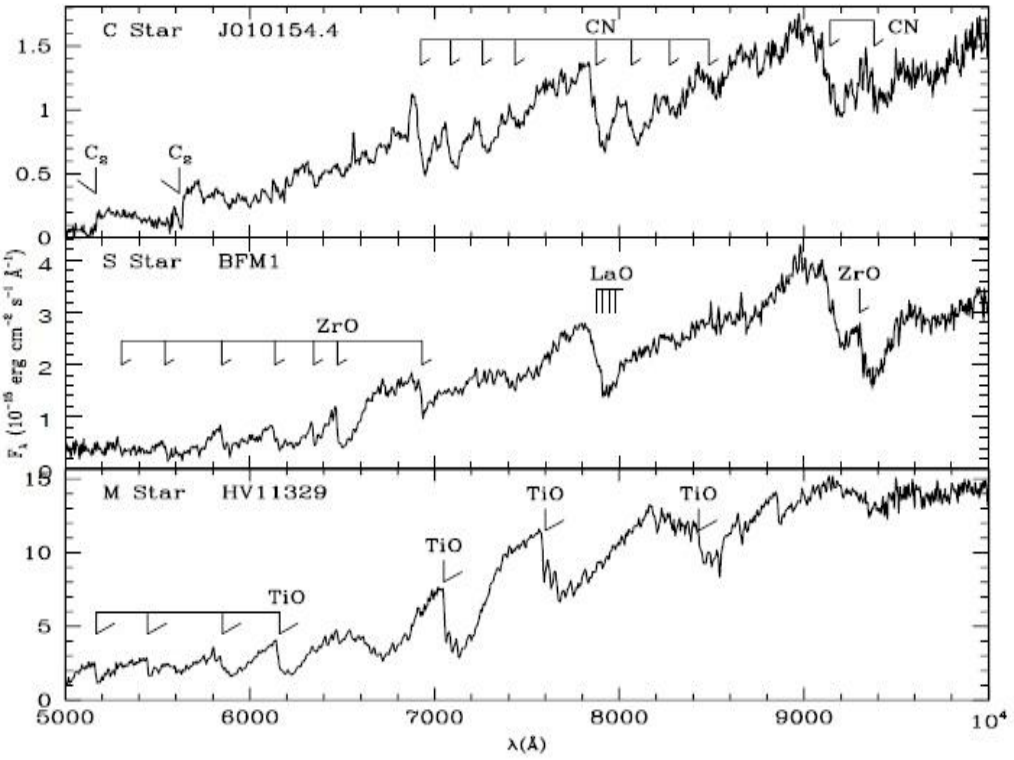

Fig.1. The distinctive spectra of an M star, an S star and a C star. The sequence M→S→C corresponds to a change from C/O < 1 to C/O ∼ 1 to C/O > 1. M stars have spectra dominated by molecules containing oxygen (e.g. TiO, VO) while C star spectra are dominated by molecules containing carbon (e.g. CN, C_2). Some of the stronger bands are marked on the figure {source: P. R.Wood, SAIt 81,883 (2010)}.

In the remainder of this article, we will discuss the interior nuclear evolution of AGB stars, mass loss from them, estimation of dust color temperature, dust mass, excess mass, etc.

THE EVOLUTION OF AGB STARS

AGB stars have large, low density convective envelopes of radius several hundred R_{sun} surrounding a dense, electron-degenerate core of carbon and oxygen. Between the envelope and the core are hydrogen and helium burning shells, whose typical energy production can be seen as a function of time in figure 2. In the early AGB phase, following exhaustion of helium in the core, the H and He shells burn smoothly, but the He shell soon becomes unstable and starts a series of thermal relaxation cycles. The He burning shell is effectively dormant for about 80% of the time, but at the end of each dormant period, it ignites furiously (but hydrostatically), reaching peak energy generation rates of $\sim 10^8$ L_{sun} in the more massive cores. After several hundred years, the helium shell drops back to burning at a rate roughly in equilibrium with the surface luminosity of the star, taking over from the H burning shell as the main energy source. Over the next ∼20% of the shell flash cycle, the He burning shell burning rate gradually declines, while the H burning shell rate increases to again become the dominant energy source, so that a new shell flash cycle begins.

The duration of a shell flash cycle, like most properties of the nuclear burning core, depends mostly on the core mass (Wood & Zarro, 1981; Boothroyd & Sackmann, 1988a). For a 1 M_{sun} AGB star with a typical core of mass ∼0.6 M_{sun} the cycle length is $\sim 10^5$ years, while for an AGB star of initial mass more than ∼ 5 M_{sun} and a core mass of 0.9 M_{sun}, the cycle length is $\sim 10^4$ years.

A very important aspect of AGB evolution is mass loss. The loss of essentially all the hydrogen-rich envelope is what terminates AGB evolution and leaves a compact remnant star that evolves through the parts of the HR diagram occupied by post-AGB stars, planetary nebular nuclei and white dwarfs (figure 1). Figure 2 shows the typical evolution of the mass loss rate and the mass in a 1 M_{sun} AGB star - many more examples are given in Vassiliadis & Wood (1993). It is particularly notable that mass tends to be ejected in multiple stages, which coincide with the brighter parts of the shell flash cycle when the H-burning shell is active. The mass loss process in AGB stars is discussed further in the next section of this paper.

The large energy release at a helium shell flash and its subsequent transport by convection leads to mixing processes that bring nuclear burning products, especially carbon and s-process elements, to the stellar surface: this process causes the transformation of AGB stars from oxygen-rich M stars to carbon stars with C/O > 1. The material ejected from AGB stars is a major source of enrichment of the interstellar medium in ^{12}C and heavy s-process elements.

A general overview of the mixing processes is shown in figure 3. When the He shell ignites and releases a large amount of energy, the resulting temperature gradient is sufficient to drive convective energy transport, creating the Inter shell Convective Zone. This zone carries the carbon produced by He burning outward, but not to the convective envelope, so that carbon is not directly mixed to the stellar surface. However, when the energy dumped into the He burning zone finally escapes from the core into the envelope, after the Intershell Convective Zone has disappeared, the envelope convection moves inward in mass and dredges up carbon rich material within the mass region previously occupied by the Intershell Convective Zone. This process is called the Third Dredge-Up and is the mechanism by which carbon stars are formed.

Another important nuclear process that occurs in AGB stars is s-process nucleosynthesis, wherein heavy elements are created by the addition of neutrons to relatively abundant nuclei, such as those in the Fe-peak. For the process to occur, a source of neutrons is required. These neutrons come from two sources in AGB stars: the reactions $^{12}C(p,\gamma)\ ^{13}N(\beta^+\nu)\ ^{13}C(\alpha,n)\ ^{16}O$ and $^{14}N(\alpha,\gamma)\ ^{18}F(\beta^+\nu)\ ^{18}O(\alpha,\gamma)\ ^{22}Ne(\alpha,n)\ ^{25}Mg$. The first set of reactions need to occur in a region with a restricted number of protons, so that the ^{13}C is not converted to ^{14}N by proton absorption as would be the case with the CNO cycle operating in a H-rich region. Furthermore, the temperature needs to be higher than that in the vicinity of the H-burning shell if the reaction $^{13}C(\alpha,n)\ ^{16}O$ is to occur. The first condition (low H abundance) occurs in the partial mixing region left at the bottom of the H-rich convective envelope by third dredgeup (the light grey region in figure 3). The details of the amount of mixing here are very uncertain, but some sort of semi-convection seems to be involved (Hollowell and Iben, 1988). Because of the uncertainties in current evolution models, most nucleosynthesis calculations treat the amount of mixing (size of the "convective pocket") as a free parameter. The second condition (sufficiently high temperatures) was found by Straniero, *et al*. (1995) to exist in the convective pocket between He shell flashes. Although the reaction rates are slow, there is sufficient time for the s-process to occur in this interval. At the next He shell flash, s-process elements so produced are engulfed by the new inter shell convection zone and then partially dredged-up to the stellar surface by the subsequent third dredge-up event. Other s-process elements remain in the convective pocket at the base of the third dredge-up zone, ready to be further enhanced with neutrons in the next inter-flash interval.

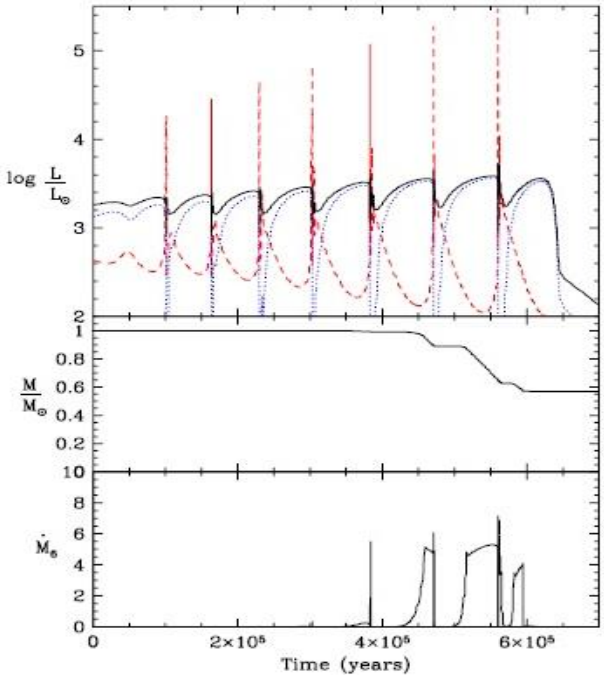

Fig. 2. The variation of L, LH (dotted line), LHe (dashed line), M and M˙ with time for a 1 M AGB star. This solar metallicity model is from the calculations of Vassiliadis & Wood (1993).

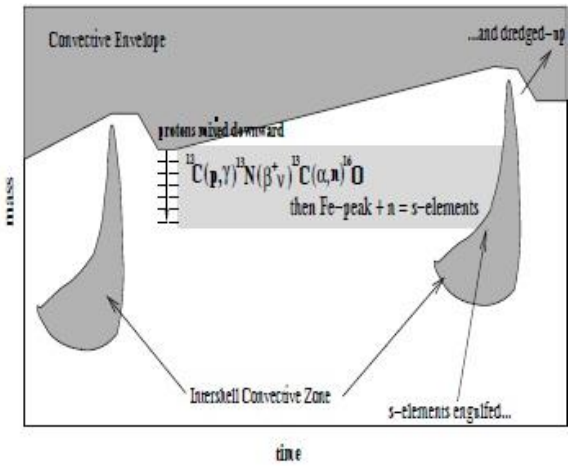

Fig. 3. A schematic diagram showing the positions of convection regions (dark grey) in the (mass fraction, time) plane. The light grey area is the region in which s-process nucleosynthesis occurs between He shell flashes. From Lattanzio & Wood (2004).

The second set of neutron-producing reactions also contribute to s-process nucleosynthesis. ^{14}N left over form the CNO cycle is readily burnt to ^{22}Ne soon after He burning shell ignition. However, the final reaction $^{22}Ne(\alpha,n)^{25}Mg$ requires temperatures near 3×10^{8} K, and is important mainly in the intershell convection zone of the more massive cores of the more massive AGB stars (Hollowell and Iben, 1988).

A consistent problem with all studies of mixing in AGB stars is our lack of knowledge of convective processes, especially the amount of overshoot occurring at the edges of convective regions. Convection is usually treated by the mixing length theory, and it is well known that the adopted mixing length significantly affects the amount of dredge-up (Wood, 1981; Boothroyd and Sackmann, 1988b; Lattanzio, 1989). Increasing the mixing-length enhances dredge-up. Attempts are now being been made to study mixing in AGB stars by using multi-dimensional fluid dynamics (Herwig *et al*., 2006), rather than simple theories like the mixing-length theory. Much work remains to be done in this area.

The problems with numerical simulations of AGB stars has led to the creation of synthetic models of AGB evolution in which various aspects of the evolution, such as the amount of dredge-up at each helium shell flash and the minimum core mass at which dredge-up occurs, are treated as free parameters (Marigo and Girardi, 2007). The parameters of these models are then calibrated against observational data, such as the luminosities of carbon stars in the LMC (Large Magellanic Cloud) and SMC (Small Magellanic Cloud). The synthetic model calculations are useful when wide areas of parameter space (initial M and abundance) are to be explored.

MASS LOSS FROM AGB STARS

For a star to have a wind, there must be an outward force that provides momentum and energy input, accelerating the surface layers to velocities larger than the escape velocity. This may be realized in various ways, including the scattering of UV radiation by resonance line opacity in hot stars, the generation of magneto-acoustic waves above the photosphere in red giants, or the absorption of photons by dust grains in the outer atmospheres of the coolest and most luminous stars (Lamers and Cassinelli, 1999). Mass-loss dominates an AGB star's evolution and fate. It is clear from observations of Mira and OH/IR stars that mass-loss rates increase exponentially along the AGB until they reach super-wind values of $\sim 10^{-5} - 10^{-4}$ M_{sun} yr^{-1} (Willson, 2000; Olofsson, 2003).

Combining theoretical efforts and empirical evidence, a reasonable scenario takes form in which mass-loss on the AGB can be divided into three regimes: an initial period before the onset of the dust-driven wind (designated as "pre-dust mass-loss"); a subsequent phase characterised by an exponential increase of mass-loss driven by the combined action of dust and pulsation (designated as "dust-driven mass-loss"); and a final brief regime with high mass-loss (designated as "super-wind mass-loss").

In our scheme, the phase of pre-dust mass-loss (with rate $\dot{M}_{pre\text{-}dust}$) is thought to apply to the early stages on the AGB in which either dust has not yet formed in the outermost atmospheric layers, or if present in some small amount, is unable to generate an outflow. In these conditions a likely wind mechanism could be related to a strong flux of pressure waves or Alfven waves able to cause the spillover of the extended and highly turbulent chromospheres typical of red giants. The same mechanism might be at work during both the ascent along the RGB and the early stages of the AGB (Schroder and Cuntz, 2005; Cranmer and Saar, 2011).

In stellar evolutionary calculations a frequent choice to describe mass-loss during the early phases is the classical Reimers (1975) law, a simple

scaling relation of stellar parameters based on observations of few red giants and supergiants. The Reimers relation is commonly multiplied by an efficiency parameter η_R, whose value is calibrated such that it recovers the observed morphology of horizontal branch stars in Galactic Globular clusters. The calibration however, still depends on the residual envelope mass left over from the RGB (Renzini and Fusi Pecci, 1988).

More recently Schroder and Cuntz (2005) proposed a modified version of the Reimers (1975) law, in which additional dependencies on the effective temperature and surface gravity follow from a physically-motivated consideration of the mechanical flux responsible for the wind. The role of the chromosphere in driving mass-loss in lateK to early-M giants is supported by the analysis McDonald and van Loon, (2007) of the Hα and infrared calcium triplet lines in a sample of red giant stars hosted in Galactic globular clusters. Similarly to the Reimers relation, the Schroder and Cuntz (2005) formula also needs an efficiency parameter η_{SC} to be specified.

Novel efforts to model stellar winds from red giants were carried out by Cranmer and Saar (2011). A selfconsistent and more detailed theoretical approach is developed to follow the generation of energy flux due to magneto hydrodynamic turbulence from subsurface convection zones to its eventual dissipation and escape through the stellar wind. One major difference is that, while in Schroder & Cuntz (2005) the mass-loss rate is assumed to scale linearly with the photospheric mechanical energy flux (F_M) of Alfven waves ($\dot{M}_{pre\text{-}dust} \propto F_M$), the analysis of Cranmer and Saar (2011) yields a higher dependence ($\dot{M}_{pre\text{-}dust} \propto F_M^{12/7}$). Analytic models for magnetic wave generation indicate that the mechanical energy flux scales as $F_M \propto T_{eff}^{7.5}$ (Musielak and Rosner, 1988). Hence, considering that the mass-loss rate is proportional to the surface-integrated mechanical energy flux, $L_M = 4\pi R^2 F_M$, and expressing the stellar radius R with the Stefan-Boltzmann law for a black body, we eventually obtain a significantly steeper dependence of the mass-loss rate on the effective temperature,

$\dot{M}_{pre\text{-}dust} \propto T_{eff}^{3.5}$ (Schroder and Cuntz, 2005) and

$\dot{M}_{pre\text{-}dust} \propto T_{eff}^{8.86}$ (Cranmer and Saar,2011).

Following the pre-dust phase of mass-loss, as the star climbs the AGB at increasing luminosity, suitable conditions can be met in the cool atmosphere for stellar winds to be generated through a different intervening mechanism. The most plausible hypothesis resides in the momentum input when the stellar radiation field is absorbed (or scattered) by dust grains and transferred to the gas via collisions. This wind is enhanced by pulsations that shock the envelope and periodically levitate matter up to regions where dust can more efficiently condense (Gustafsson and Hofner, 2003). Observationally there is a clear correlation, though with a large scatter, between the mass-loss rate (here designated with $\dot{M}_{dust}$) and the pulsation period P of AGB variables, such that $\dot{M}_{dust}$ is seen to increase exponentially with the period (Vassiliadis and Wood, 1993).

Finally, close to tip of the TP-AGB, the mass-loss rates almost level out to $10^{-5} - 10^{-4} M_{sun}\ yr^{-1}$ of the so-called super-wind phase ($\dot{M}_{SW}$), corresponding to the condition in which the maximum momentum of the radiation field is transferred to the stellar atmosphere.

Within this framework, the mass-loss prescriptions adopted in the TP-AGB stellar models computed for this study are as follows. For the dust driven wind phase we adopt a formula similar to Bedijn (1988), which predicts an exponential increase of mass-loss $\dot{M}_{dust} \propto \exp(R^a M^b)$ dependent on stellar parameters derived from models of periodic shocked atmospheres. Coefficients a and b are calibrated on a sample of Galactic Mira stars (Marigo *et al*., 2013; Nanni *et al*., 2013, and Kalirai *et al*., 2014).

For the super-wind phase we adopt the formalism of Vassiliadis and Wood (1993), in which the mass-loss rate, $\dot{M}_{SW}$, is proportional to the ratio of the stellar luminosity to the terminal velocity of the gas, which itself scales linearly with the pulsation period. In practice as soon as $P > 500 - 600$ days the super-wind regime is expected to set in.

We keep the same prescriptions for $\dot{M}_{dust}$ and $\dot{M}_{SW}$ and vary only the $\dot{M}_{pre\text{-}dust}$. For the mass-loss rates $\dot{M}_{pre\text{-}dust}$ before the onset of dust-driven winds we consider four options:

- $\dot{M}^{\eta=0}_{\text{pre-dust}}$: no mass-loss before the possible onset of the dust-driven wind, $\dot{M}_{\text{pre-dust}} = 0$;
- $\dot{M}^{\text{R75}}_{\text{pre-dust}}$: the traditional Reimers (1975), mass-loss $\dot{M}_{\text{pre-dust}} = 4 \times 10^{-13} \eta_R$ L/ gR $= 4\text{x}10^{-13} \eta_R$LR/M with the efficiency parameter $\eta_R = 0.4$;
- $\dot{M}^{\text{SC05}}_{\text{pre-dust}}$: the original Schroder & Cuntz (2005) law $\dot{M}_{\text{pre-dust}} = 10^{-14}\ \eta_{SC}$ LR/ M $\left\{\frac{T_{\text{eff}}}{4000\text{K}}\right\}^{3.5} \left\{1 + \frac{1}{4300\ \text{g}}\right\}$ with the efficiency parameter $\eta_{SC} = 8.0$;
- $\dot{M}^{\text{MSC05}}_{\text{pre-dust}}$: a modified version of the Schroder & Cuntz (2005) scaling relation $\dot{M}_{\text{pre-dust}} = 10^{-12}\ \eta_{mSC}$ LR/ M $\left\{\frac{T_{\text{eff}}}{4000\text{K}}\right\}^{8.9} \left\{1 + \frac{1}{4300\ \text{g}}\right\}$

in which, for the reasons explained above, the power-law dependence on the effective temperature is steepened; here the efficiency parameter is set to $\eta_{mSC} = 0.4$.

In all formulas the mass-loss rate is given in M_{sun} yr^{-1}, the effective temperature T_{eff} is in Kelvin, the stellar radius R, luminosity L, the mass M, and surface gravity g are expressed in solar units.

Finally, we caution the reader that our modified Schroder and Cuntz relation, with $\eta_{mSC} = 0.4$, set for the early stages of the TP-AGB, may be too efficient to be extended to lower luminosities of RGB stars based on a quick comparison to the measured mass-loss rates of the sample, collected by Cranmer and Saar (2011), that includes metal poor RGB stars with and effective temperatures in the range 3800-5800 K, as a function of the luminosity.

DATA REDUCTION

Each pixels of the FITS image of our region of interest are analyzed using software Aladin v2.5 which is one of the handy and extensively used software in the data reduction processes. This software is designed to reduce and analyze the data collected from the ground based and space telescopes covering all wavelength regions. Information regarding the energy spectrum, relative flux density with coordinate of each pixel, different types of contour maps, longitude and the latitude of the desired structure can be obtained by using software .5 Contour Map.

We intend to study the isolated cavity structure at 60 μm and 100 μm. We adopt the method of drawing contours at different levels so that we can separate the region of maximum and minimum flux density. The best contour level of the selected FITS image is chosen in between 1 to 38.

We are interested in these maxima to study the flux density within the region because our focus is on the temperature profile and the mass distribution of the dust within the isolated structure. We are interested to study the temperature and mass profile of isolated structure and possibility of star formation in this region. The contour picture is shown in figure1.

FLUX DENSITY VARIATION

To calculate temperature and mass of each pixel due to the contribution of dust, we need flux density of all pixel lying inside the outermost contour i.e. isoconter level 40 at 60 μm and 100 μm respectively. It is done by using Aladin v2.5 to evaluate Variation of flux density with distance along major diameter (AB), minor diameter CD and the distance between minimum temperature and minimum flux density (EF).

DUST COLOR TEMPERATURE ESTIMATION

Adopting the similar method as that of Schnee *et al*. (2005) the dust temperature was calculated from the IRAS 60 μm and 100 μm flux densities (Dupac, 2003). By knowing the ratio of flux densities at 60 μm and 100 μm, the temperature contribution due to dust color can be calculated. The dust temperature T_d in each pixel of a FIR image can be obtained by assuming that the dust in a single beam is isothermal and that the observed ratio of 60 μm to 100 μm emission is due to black body radiation from dust grains at T_d, modified by a power law of spectral emissivity index. The flux density of emission at a wavelength λ_i is given by

$$F_i = \left[\frac{2hc}{\lambda_i^3\left(e^{\frac{hc}{\lambda_i kT_d}}\right) - 1}\right] N_d\, \alpha\, \lambda_i^{-\beta}\, \Omega_i \qquad (1)$$

where β is the spectral emissivity index, N_d is the column density of dust grains, α is a constant which relates the flux with the optical depth of the dust, and Ω_i is the solid angle subtended at λ_i by the detector. We use the equation following Dupac *et al*. (2003).

$$\beta = \frac{1}{\delta + wT_d} \quad (2)$$

to describe the observed inverse relationship between temperature and emissivity spectral index.

With the assumptions that the dust emission is optically thin at 60 μm and 100 μm and that Ωω~ Ω100 (true for IRAS image), we can write the ratio, R, of the flux densities at 60 μm and 100 μm as

$$R = 0.6^{-(3+\beta)} \quad \frac{e^{144/T_d} - 1}{e^{240/T_d} - 1} \quad (3)$$

The value of β depends on dust grain properties like composition, size, and compactness. For reference, a pure blackbody would have β = 0, the amorphous layer-lattice matter has β ~ 1, and the metals and crystalline dielectrics have β ~ 2.

For a smaller value of T_d, 1 can be dropped from both numerator and denominator of Eq. (3) and it takes the form

$$R = 0.6^{-(3+\beta)} \frac{e^{144/T_d}}{e^{240/T_d}} \quad (4)$$

Taking natural logarithm on both sides of Eq. (4) , we find the expression for the temperature as

$$T_d = \frac{-96}{\ln\{R \times 0.6^{(3+\beta)}\}} \quad (5)$$

where R is given by

$$R = \frac{F(60\mu m)}{F(100\mu m)} \quad (6)$$

F(60 μm) and F(100 μm) are the flux densities in 60 μm and 100 μm respectively. One can use Eq. (5) for the determination of the dust grain temperature.

DUST MASS ESTIMATION

Further analysis of the structure needs the mass of the structure. Dust masses are estimated from the infrared background corrected flux densities at 100 μm image. The distance of the structure was provided by Weinberger (2014). We are calculating dust mass following the analysis of Meaburn *et al*. (2000). The infrared flux can be measured from IRAS Sky View images and images from the Groningen using ALADIN2.5. The resulting dust mass depends on the physical and chemical properties of the dust grains, the adopted dust temperature and the distance to the object. The final expression for the dust mass can be written as:

$$M_{dust} = \frac{4\rho\rho}{3Q_n} \left| \frac{S_n D^2}{B(\nu, T)} \right| \quad (7)$$

where, a = weighted grain size , ρ = grain density, Q_ν = grain emissivity

$S_\nu = f \times MJy/Str \times 5.288 \times 10^{-9}$ where, 1 MJy/Str = 1×10^{-20} Kg s^{-2} and f = relative flux density measured from the image (IRAS 100 μm image).

D = distance of the structure

B(ν, T) = Planck's function, which is the function of the temperature and the frequency and given by the expression:

$$B(\nu, T) = \frac{2h\nu^3}{C^2} \left[\frac{2hc}{e^{\frac{h\nu}{kT}} - 1} \right] \quad (8)$$

where, h = Planck's constant, c = velocity of light

ν = frequency at which the emission is observed, T = the average temperature of the region

Value of various parameters we use in the calculation of the dust mass in our region of interest are as follows:

a = 0.1 μm (Young *et al*., 1993)

ρ = 1000 Kg m^{-3} (Young *et al*., 1993)

Qν = 0.0010 for 100 μm and 0.0046 for 60 μm respectively (Young *et al*., 1993).

Using these values the expression (7) takes the form:

$$M_{dust} = 0.4 \left[\frac{S\nu D^2}{B(\nu, T)} \right] \quad (9)$$

We use the above equation for the calculation of the dust mass.

RESULTS AND DISCUSSION

Structure: Contour Maps

While going through the systematic search we discovered an isolated cavity in the spectrum of the 100 μm and 60 μm at the R.A. 04h 15m 03s and DEC 54° 41 m 00 s. With the help of the software ALADIN2.5, we have drawn the contour maps to distinguish the minimum flux region in the field of the interest. We select the contour level at 40 and major axis, minor axis and line passing through minimum temperature and minimum flux was drawn which was shown in the Fig 4. While drawing the major axis and the minor axis we should pass it through the minimum flux pixel.

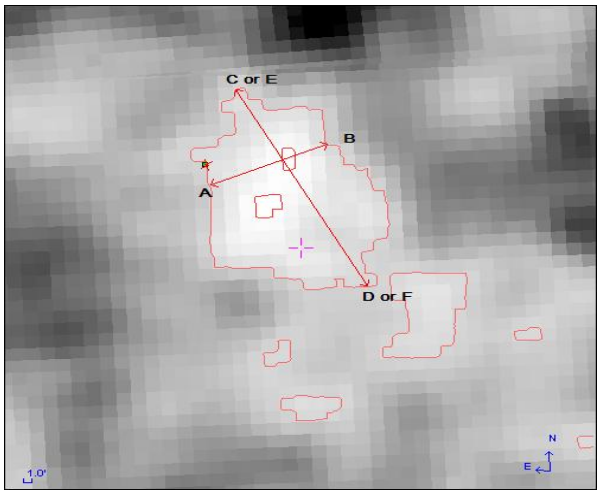

Fig. 4. The image of IRAS survey of the R.A. 04h 15m 03s and DEC 54◦ 41 m 00 s at the contour level 1-40 with major axis AB, minor axis CD, line joining minimum temperature and minimum flux EF.

This gives the distance of major diameter of the structure is 1.93 pc and minor diameter of the structure is 0.89 pc, whose calculation is shown latter.

FLUX DENSITY VARIATION

By using the ALADIN 2.5 software, flux density variation of the region of interest is studied. We obtained the graph of flux density variation along the major axis, minor axis and line joining the minimum temperature region and minimum flux region considering R.A. 04h 15m 03 s and DEC 54◦ 41m 00 s as center. We plotted it with the help of the ORIGIN5.0 for the polynomial fit of the data as in figure 5(a).

The polynomial equation of the fitted line is,

S_v =36.21 -25.77d +113.47 d^2-220.70 d^3+197.45 d^4-81.32 d^5 +12.57 d^6

Similarly the variation of flux density along minor diameter is plotted as in figure 5(b).

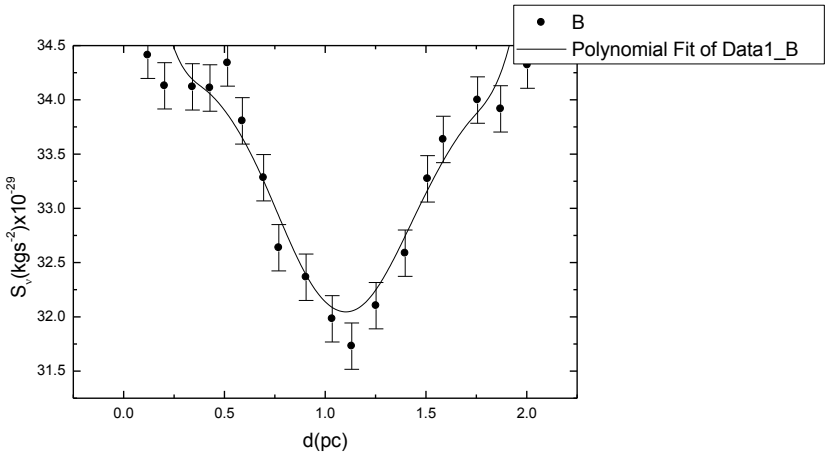

(a)

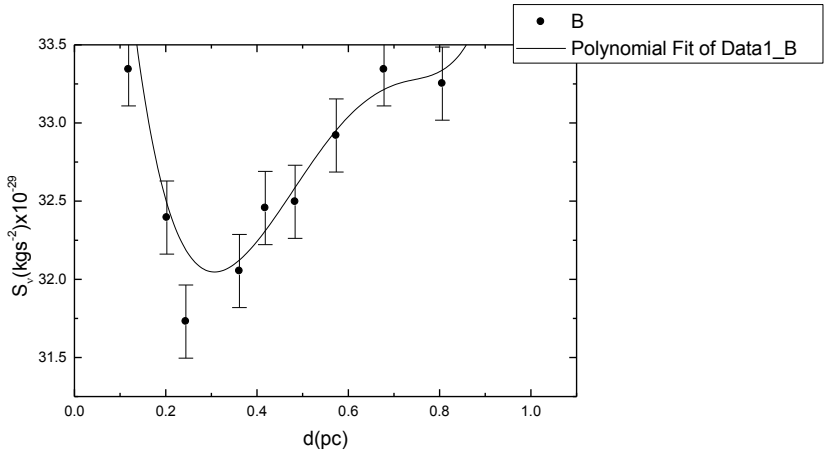

(b)

Fig. 5. Best fit polynomial showing the variation of flux density along (a) major diameter and (b) minor diameter of isocontour level 1-40. The distribution of flux density along major and minor diameters with distance of AGB star AGB 04153, +5441 and standard error of the distribution $\pm\sigma/\sqrt{n}$.

The polynomial equation of the fitted line is,
S_v=38.21-65.39d+265.19d^2-574.09d^3+777.16d^4-615.19d^5+209.22d^6

Then we studied the variation of flux density with the distance along the line joining the minimum flux and minimum temperature. But in this case major diameter and line joining between minimum flux and minimum temperature coincides.

DUST COLOR TEMPERATURE VARIATION

Using the method of Schnee *et al*. (2005), we calculated dust color temperature of each pixel inside the outer isocontour 40 in the region of interest. We use the IRAS 100 μm and 60 μm FITS images downloaded from the IRAS server (Web, 2014). For the calculation of temperature we choose the value of β = 2 following the explanation given by Dupac *et al*. (2003). The region with minimum and maximum temperature is found to lie in the range of 20.53 K to 21.09. So offset temperature is 0.56 K. It means for low temperature variation, there is symmetric outflow or symmetric distribution of density and temperature. Variation of temperature along major diameter AB with distance is shown in figure 7.

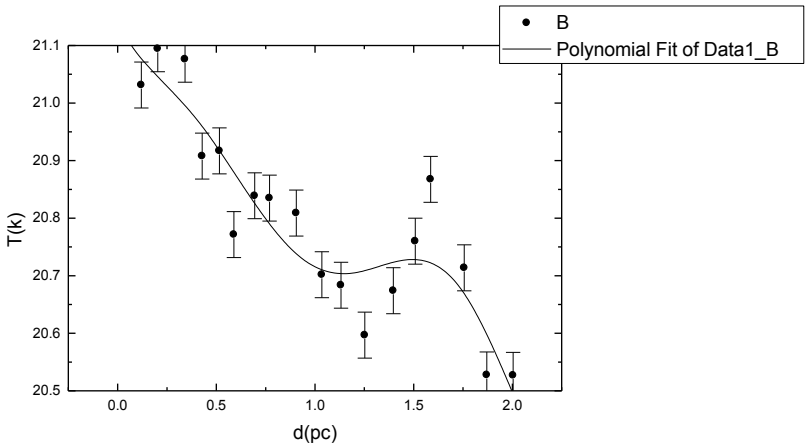

Fig. 7. Showing the variation of dust temperature with distance along major diameter AB of isocontour level 1-40 of the same AGB star. The solid circle with $\pm\sigma/\sqrt{n}$ error bar represents the standard error of the distribution. The solid curve represents the best fit polynomial (6^{th} order polynomial).

The polynomial equation of the fitted line is,
T=21.10-0.41d+1.64d^2-5.42d^3+6.20d^4-2.87d^5+0.46d^6

Variation of dust temperature along minor diameter CD with distance is shown in figure 8.

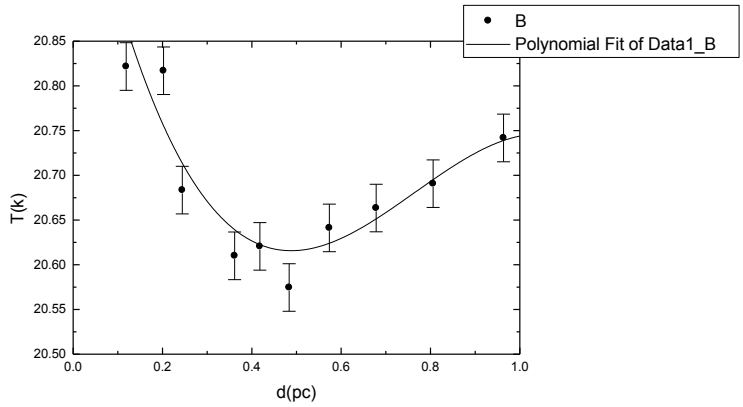

Fig. 8. Showing the variation of dust temperature with distance along minor diameter CD of isocontour level 1-40 of the same AGB star. The solid circle with $\pm\sigma/\sqrt{n}$ error bar represents the standard error of the distribution. The solid curve represents the best fit polynomial (3^{rd} order polynomial).

The polynomial equation of the fitted line is,

$T=21.08- 2.32d+ 3.52d^2- 1.53d^3$.

Similarly major diameter and line joining between minimum temperature and minimum flux is same so the variation of dust temperature along line joining between minimum temperature and minimum flux EF with distance is already shown in figure 7.

The region in which minimum and maximum temperature is found in the range of 20.53K to 21.09 K with an offset temperature of dust 0.56 K . Such low offset temperature variation shows that there is symmetric outflow or symmetric distribution of density and temperature. It further suggests that our structure is not independently evolved or the role of discrete point sources in the field of cavity is important for the structure destruction mechanism. The cavity may be in thermally pulsating phase. The dust color temperature less than 20 K represents the interstellar cirrus cloud. Thus our far infrared dust structure (i.e. Cavity) is not a cirrus cloud. Another region of cloud fulfill the criteria of Cirrus clod.

SIZE OF THE STRUCTURE

To measure the major and minor diameter for each FITS image, we used a simple expression for the calculation, $L = R \times \theta$, where R = 240pc is the distance of the structure from us provided by Weinberger (5) and θ = pixel size (in radian). After calculation the major and minor diameter of the cavity region are 1.93 pc and 0.89 pc respectively at contour level 40 in the 100 μm image. Thus, the size of the structure is 1.93 pc × 0.89 pc .

DUST MASS ESTIMATION

For the calculation of dust mass, we need the distance to the region of interest. The distance of the structure provided by Weinberger (2014) is 240 pc. By using the temperature of each pixel and corresponding distance of the structure, we calculated mass of each pixel. Average mass of each pixel is $1.006x10^{26}$ kg and total mass of the structure is $1.438x10^{28}$ kg.

CALCULATION OF EXCESS MASS

For calculation of excess mass, we have drawn two circles i.e. inner and outer circle with the help of software Aladin v8.0. Circle through major diameter is supposed as outer circle and the circle through minor diameter is supposed as inner diameter of the interested region. With the help of those circles we have calculated excess mass

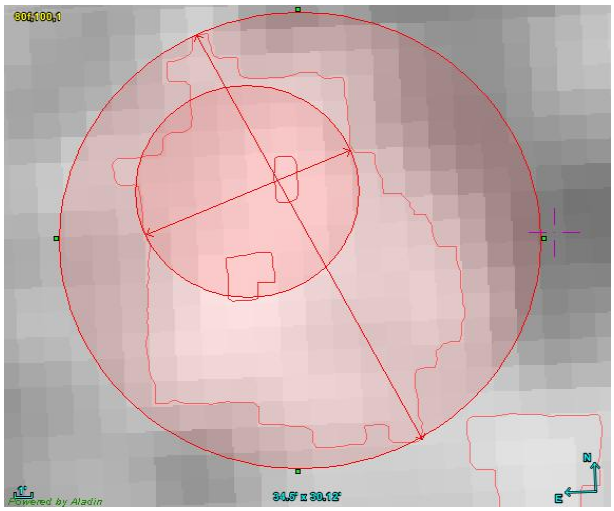

Fig. 9. Showing the inner circle and outer circle drawn in the structure for calculation of excess mass.

From the calculation total mass of the inner circle was found to be $6.054x10^{27}$ kg and average mass of inner circle was $1.009x10^{26}$ kg. Similarly the total mass of outer circle including inner circle was $2.699x\ 10^{28}$ kg and the average mass was $1.03x\ 10^{26}$ kg. So the total mass deficit in the inner pixel which was blown away by the AGB star is $2.094x\ 10^{28}$ kg i.e.o.0105 M_{sun}.

CONCLUSIONS

A systematic search of dust structure in the far infrared (100 μm and 60 μm) IRAS survey was performed using Sky View Virtual Observatory to find an isolated new cavity. We searched for the all C-rich AGB star surrounding in our galaxy, we found an isolated cavity like structure having cavity at both 60 μm and 100 μm wavelength at the center R.A. 04d 15m 03s and DEC 54◦ 41m 00s. The distance of the structure was found to be 240 pc[5]. The software ALADIN 2.5 is used for the data reduction and ORIGIN 5.0 for the plotting graphs. The physical properties of the structure, a study of flux density and temperature variation, dust color temperature, mass of dust, mass deficit per pixel of the cavity was calculated. The conclusions drawn from the present calculations are as follows:

- The major and minor diameter of the cavity like structure is found to be 1.93 pc and 0.89 pc respectively.

- The maximum and minimum flux was found to be at R.A. 04h 14m 14.9s DEC +54◦ 37m 01s & R.A. 04h 15m 10.9s DEC +54◦ 51m 08s, maximum and minimum temperature is at R.A. 04h 14m 25.2s DEC +54◦ 38m 03s & at R.A. 04h 15m 46.1s DEC +55◦ 00m 07s respectively.
- The region in which minimum and maximum temperature is found in the range of 20.53K to 21.09 K with an offset temperature of dust 0.56 K which shows that the cavity is independently evolved. Such low offset temperature variation shows that there is symmetric outflow or symmetric distribution of density and temperature.
- The total mass of the inner circled cavity was 6.054×10^{27} Kg, the average mass of the inner circle was 1.009×10^{26} Kg and that of the outer circle including inner was 2.699×10^{28} Kg and 1.03×10^{26} Kg respectively. The total mass deficit of the structure was 2.094×10^{28} Kg i.e. 0.0105 M_{sun}.

REFERENCES

Aryal B., and Weinberger R. (2006). A & A **446**:213.

Aryal B.; Rajbahak C., and Weinberger R. (2010). MNRAS **402**:1307.

Dupac X.; Bernard J. P.; Boudet N.; Giard M.; Lamarre J. M.; Meny C. *et al*. (2003). A & A **404**.

Herwig F. (2005). A & A **43**:435.

Hollowell, D., and Iben, I. (1988). Jr. APJL, **333**:25.

Lagadec E.; Mekarnia D.; de Freitas Pacheco J. A., and Dougados C. (2005). A & A **433**:553.

Marigo P. and Girardi L. (2007). A & A **469**:239.

Meaburn J.; Redman M. P.; Connor O.; Holloway A. J., and Bryce M. (2000). MNRAS **312**:23.

Reimers D. (1975). Problems in Stellar Atmospheres and Envelopes, eds. Bascheck, B.; Kegel W. H., and Traving, G. (springer: Berlin), p.229

Renzini A., and Fusi Pecci F. (1988). ARA & A **26**:199.

Schnee S. L. (2006). Gas and Dust in the Molecular Cloud: Density, Temperature and Velocity Structure, Ph.D. Thesis, Harward University, Cambridge Massachusetts.

Schnee, S. L.; Ridge N. A.; Goodman A. A., and Jason G. L. (2005). APJ, **634:**442.

Schroder K. P., and Cuntz M. (1993). APJL **630**:73.

Suh K. W., and Kwon Y. J. (2011). MNRAS **417**: 3047.

Vassiliadis E., and Wood P. R. (1993). APJ **413**:641.

Web (2014). http://skyview.gsfc.nasa.gov/current/cgi/query.pl

Weinberger R. (2014). Private Communication.

Wood P. R. (2010). SAIt **81**:883.

Young K.; Phillips T. G., and Knapp G. R. (1993). APJ **409**:725.

BIBECHANA
A Multidisciplinary Journal of Science, Technology and Mathematics
ISSN 2091-0762 (Print), 2382-5340 (0nline)
Journal homepage: http://nepjol.info/index.php/BIBECHANA
Publisher: Research Council of Science and Technology, Biratnagar, Nepal

Far infrared cavity of a post C-rich AGB star under IRAS survey

A.K. Gautam*, B. Aryal

Central Department of Physics, T.U., Kirtipur,Nepal
*Email: arjungautamnpj@gmail.com

Article history: Received 26 October, 2017; Accepted 03 December, 2017
DOI: http://dx.doi.org/10.3126/bibechana.v15i0.18506

Abstract

In this paper, we discuss about the physical properties of the dusty environment around the mass losing carbon rich post AGB star located at R.A. (J2000) =06 h 53m 01s and Dec (J2000) =-02º 16' 00", in the far infrared IRAS maps. A cavity like structure (major diameter ~ 103.3 pc & minor diameter ~33.1 pc) is found to lie at R.A. (J2000)= 06 h 51 m 54.02 s and DEC (J2000) = -01º 35' 43", located at a distance ~ 6.11 kpc from the star. We studied the distribution of flux density, dust color temperature, dust mass in the cavity. The dust color temperature is found to lie in the range 18.7 K to 20.5 K which shows the cavity is isolated and independently evolved. Such a low offset temperature variation shows that there is symmetric outflow or symmetric distribution of density and temperature. It further suggests that our structure is bigger in size and is far away from the far infrared loops(KK loops). The cavity may be in thermally pulsating phase. A possible explanation of the results will be discussed.

Keywords: AGB stars; Post AGB Stars; Dust color temperature; Dust mass.

1. Introduction

Asymptotic giant branch (AGB) stars are the final nuclear burning stage of low- and intermediate-mass stars driven by nuclear burning. This phase of evolution is characterized by two nuclear burning shell of hydrogen and helium where hydrogen burning shell lies below the convective envelope and helium burning shell lies above the electron-degenerate core of carbon and oxygen, or for the most massive AGB stars a core of oxygen, neon, and magnesium [1]. This AGB stage is characterized by low surface effective temperatures (below 3000K) and intense mass loss (from10^{-7} to 10^{-4} $M_{\odot}yr^{-1}$) [2]. When the gas temperature drops to the sublimation temperature range, heavy elements in the mass outflow from a central star will condense to form dust . Dusty circumstellar envelopes will format the distance of several stellar radii. Dust grains in the envelopes absorb stellar radiation and re-emit infrared radiation so AGB stars are important infrared sources . The mass loss process plays an important role in the evolution of AGB stars . It affects the lifetime of the AGB phase and the core-mass of the subsequent post-AGB stars. Statistics of a large sample of AGB stars would help to constrain the evolution of dust envelope.

There are two main types of AGB stars: the O-rich with C/O < 1 and mainly silicate-type grains in the outflow, and C-rich with C/O > 1 and mainly carbonaceous grains in the envelopes. Due to different dust compositions of these two types of AGB stars, different infrared spectral features are obtained which can be used to distinguish the two groups of the stellar objects . Most of the carbon compounds such as aromatic hydrocarbon, benzene, methane, etc. are responsible for biological life so carbon- rich AGB stars are preferred in our research work.

He-core burning phase is about 10 times shorter than the H-core burning shell so that the He-core burning leaves a C/O core behind that is surrounded by both a hydrogen and helium burning shell. For low and intermediate mass stars, carbon doesn't ignite and C/O core contracts and becomes electron degenerate. During the early AGB phase, the abundance of He in the centre goes to zero where He-burning continues in a shell around a degenerate C-O core. In the meantime, the H- layer around the helium shell expands and cools sufficiently so that hydrogen burning shell is extinguished. Convective envelope sets in and moves inwards and second dredge-up takes place. He shell is the main source for nuclear production so that it burns outward and reaches the hydrogen shell. In case of thermally pulsating AGB phase, helium shell becomes thin and remains thermally unstable as a result thermal pulses are produced. In each thermal pulse, luminosity of helium shell nearly approaches $10^8 L_\odot$[3].The production of such high luminosity in helium shell is called He shell flash or thermal pulse which is used to expand the outer layers. Such strong expansion drives the H shell cooler and less dense as a result H shell is extinguished. The inner edge of deep convective envelope can then move inward and mix to the surface products of internal nucleosynthesis. This mixing process which occurs periodically after each TP is known as third dredge-up which is the mechanism for producing carbon stars. During TP-AGB phase, main dominant source of nuclear energy is the hydrogen shell. Thermally pulsating AGB phase is the phase after the first thermal pulse to the time when the star ejects its envelope.

At the end of the TP-AGB, the envelope mass is strongly reduced down to 0.05 $M_\odot$ due to the strong mass loss. The star now evolves towards high temperatures at an almost constant luminosity . This is because the surface layer is gradually heating up due to the proximity of the stable burning thin H-shell which produces the luminosity. The star has now entered the post-asymptotic giant branch (post-AGB) phase.

The material expelled away from the system during the AGB stage forms a slowly expanding circumstellar shell [4]. When the mass of the hydrogen-rich envelope drops to $\approx 10^{-3} M_\odot$, it starts to contract at a constant luminosity. This contraction phase causes an increase in effective temperature and at the same time leads to a radiatively driven wind which can compress the circumstellar shell and may result in ionization of the circumstellar material. In other words, the star may become hot enough to ionize its circumstellar material, observable as a planetary nebula (PN), in a few hundred years [5]. The star at this stage is known as a post-AGB star. These have luminosity classes ranging from I (supergiant) to III (giant) with spectral types from B to K. Typical post-AGB stars are expected to have luminosities around 10^3–10^4 $L_\odot$ [6]. Masses of these objects are in the range $0.6 M_\odot$ – 1 $M_\odot$. The star leaves the AGB with T_{eff}< 5000 K . When it reaches T_{eff}> 30,000, it may ionize the remnant nebula.

In this paper, we study the physical properties of a far infrared cavity, that we investigated during a systematic search on IRAS maps, located close to a carbon-rich post AGB star (PAGB 06-02) at -1.3° latitude. In section 2, we describe methods of calculation. A brief description of the result and discussion will be given in the section 3. Finally, we conclude our results in the section 4.

2. Methods

We investigated a cavity-like structure in both 60 and 100 micron IRAS maps around a PAGB star. Fig.1(a), and 1(b) are cavity images at 60 and 100 μm whereas 1(c) is its contour map. We briefly describe a method for calculation of dust color temperature and dust mass of the dusty environment around carbon-rich post Asymptotic Giant Branch named PAGB06-02.

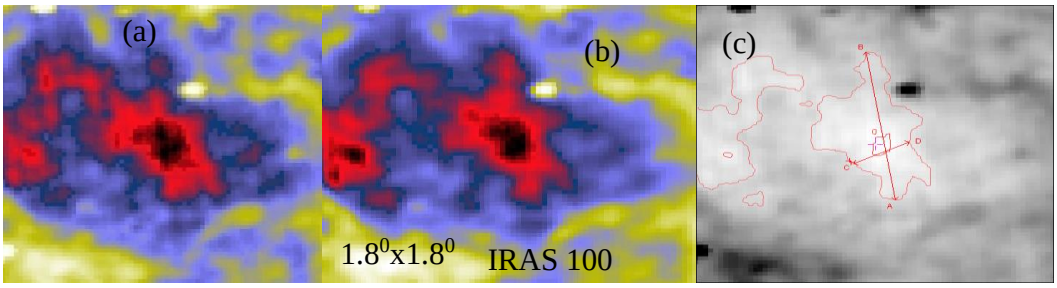

Fig. 1: (a) and (b) IRAS 60 μm and 100 μm far infrared image of the core region of AGB 06-02 centered at R.A. (J2000) = 06h 51m 54.02s, Dec. (J2000) = -01^0 35' 43" and (c) Contour map of the cavity where major diameter (AB) and minor diameter (CD) passing through minimum flux.

2.1. Dust Color Temperature Estimation

By using the IRAS 60 μm and 100 μm flux densities, Schnee et al.[7] calculated dust color temperature. The flux density of emission at a wavelength λ_i is given by

$$F_i = \left[\frac{2hc}{\lambda_i^3 \left(e^{\frac{hc}{\lambda_i k T_d}} \right) - 1} \right] N_d \alpha \lambda_i^{-\beta} \Omega_i \qquad (1)$$

where β is the spectral emissivity index, N_d is the column density of dust grains, α is a constant i.e. free parameter which relates the flux with the optical depth of the dust, and Ω_i is the solid angle subtended at λ_i by the detector. In Dupac et al. [8], there is an inverse relationship between temperature and emissivity spectral index. We have with the assumptions that the dust emission is optically thin at 60 μm and 100 μm and that Ωω∼ Ω100 (true for IRAS image), we can write the ratio, R, of the flux densities at 60 μm and 100 μm as

$$R = 0.6^{-(3+\beta)} \frac{e^{144/T_d} - 1}{e^{240/T_d} - 1} \qquad (2)$$

The spectral emissivity index (β) depends on dust grain properties like composition, size, and compactness. For a pure blackbody would have β = 0, the amorphous layer-lattice matter has β ∼ 1, and the metals and crystalline dielectrics have β ∼ 2 which is used in our calculations. For a smaller value of T_d, 1 can be dropped from both numerator and denominator of Eq. (2) and it takes the form

$$R == 0.6^{-(3+\beta)} \frac{e^{144/T_d}}{e^{240/T_d}} \qquad (3)$$

where , $R = \frac{F(60\mu m)}{F(100\mu m)}$

Taking natural logarithm on both sides of Eq. (3) and solving it, we find the expression for the temperature as

$$\ln(R) = \ln 0.6^{-(3+\beta)} [144/T_d - 240/T_d]$$
$$= \ln 0.6^{-(3+\beta)} [-96/T_d]$$
$$T_d = \frac{-96}{\ln\{R \times 0.6^{(3+\beta)}\}} \qquad (4)$$

F(60 μm) and F(100 μm) are the flux densities in 60 μm and 100 μm respectively and Eq. (5) can be used for calculation of the dust grain temperature.

2.2. Dust Mass Estimation

Dust mass is another important physical quantity which is useful to analysis the cavity structure. We need the known distance of the loops to calculate its dust mass which was provided in catalog of far infrared loops in the galaxy [9].

For the calculation of dust mass, we first obtained the value of flux density (S_ν) at 100 μm maps.

The dust mass is estimated using [10],

$$M_{dust} = \frac{4a\rho}{3Q_n}\left|\frac{S_n D^2}{B(n, T)}\right| \quad (5)$$

where, weighted grain size (a) = 0.1 μm, grain density (ρ) = 3000 kg m^{-3}, grain emissivity (Q_ν) = 0.0010 (for 100 μm) [11].

The Planck's function B(ν, *T)*, which is the function of temperature and frequency and is given by the expression:

$$B(\nu, T) = \frac{2hc}{\lambda^3}\left(\frac{1}{e^{\frac{hc}{lkT}} - 1}\right) \quad (6)$$

where, h = Planck's constant, c = velocity of light, ν = frequency at which the emission is observed, T = the average temperature of the region.

For 100 μm wavelength, the expression for the dust mass (5) reduces to,

$$M_{dust} = 0.4\left[\frac{S_\vartheta D^2}{B(\vartheta, T)}\right] \quad (7)$$

We use equation (7) to calculate dust mass of the cavity.

3. Result and Discussion

3.1 Structure: Contour Maps

While going through the systematic search on IRAS maps, we discovered an isolated cavity in the 100 μm and 60 μm at R.A. (J2000) = $06^h\ 51^m\ 54.02^s$ and Dec. (J2000) = $-01^o\ 35'\ 43''$. With the help of the software ALADIN2.5, we have studied physical properties (size, dust color temperature, dust mass, etc) of the cavity. We selected contour level in such a way that it circles the cavity. The major axis, minor axis and line passing through minimum temperature and minimum flux are shown in the Fig.1(b).

3.2 Flux Density and its Variation

By using ALADIN 2.5 software, the values of flux densities at 60μm and 100μm have measured. The flux density distribution within the contour of the region of interest has studied. We plotted a graph between flux at 100μm and 60μm with the help of ORIGIN 5.0 which is shown in Fig.2(a). From the linear fit, slope of the line was 0.25. The linear equation of the fitted line is, y=-2.87+0.25x. Using the slope of best fitted plot, dust color temperature is found as 24.4 K which is slightly more than our calculated value.

Again distribution of flux at 100μm of the pixels within the contour level with right ascension (R.A.) and declination (Dec.) are plotted by using ORIGIN 8.0 and the graph is shown in Fig.2(b). Graph shows that all the fluxes from minimum to maximum lie within the contour level. Most of the maximum flux regions lie at the boundary.

3.3. Dust color Temperature and its Variation

Using the method of [7], we calculated dust color temperature of each pixel inner the outer isocontour in the region of interest. We use the IRAS 100 μm and 60 μm FITS images downloaded from the IRAS

server. For the calculation of temperature we choose the value of β = 2 following the explanation given by [8]. Variation of temperature with corresponding R.A.(J2000) and Dec.(J2000) are plotted by using ORIGIN 8.0 and the graph is shown in Fig. 3(a). Graph shows that temperature distributions are in separate cluster but minimum temperature region is little bit shifted from minimum flux density which is unusual behaviour. Such type of nature is obtained due to external factors.

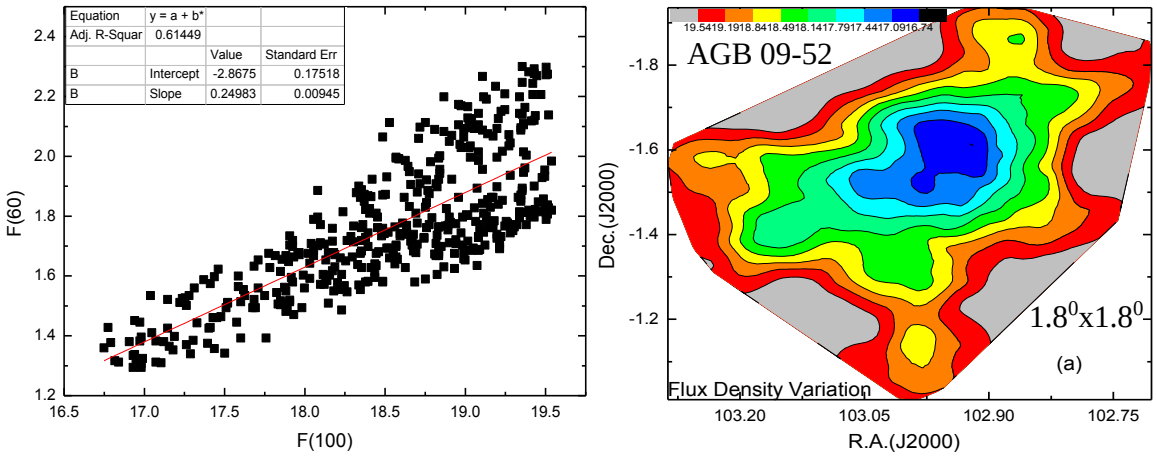

Fig.2: (a) The 100μm verses 60μm flux density in the region of interest and 2(b) Contour map at 100μm flux density where the AGB star is located at the center R.A. (J2000) = $06^h\,51^m\,54.02^s$, Dec. (J2000) = $-01^0\,35'\,43''$.

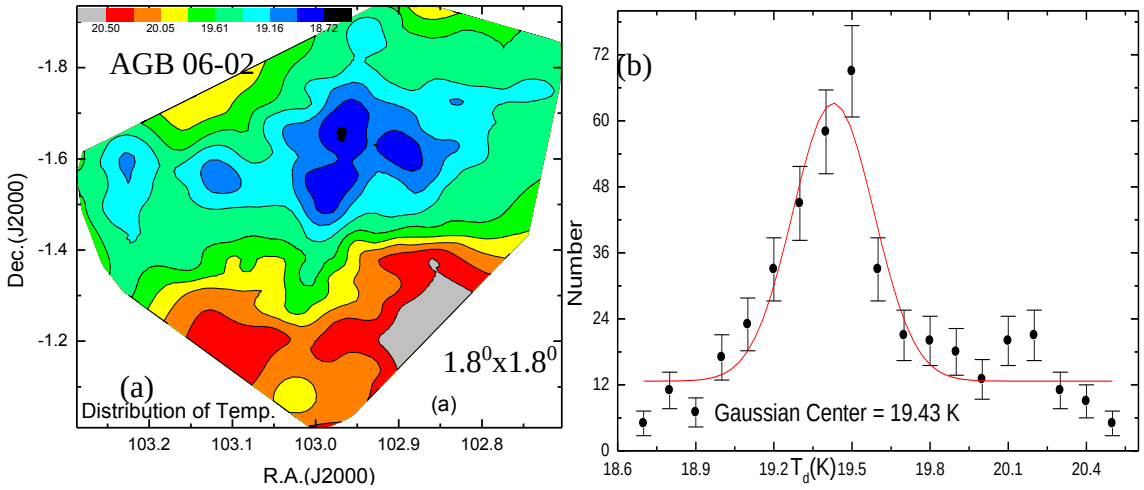

Fig. 3: (a) Contour map of dust color temperature and (b) Gaussian fit between dust color temperature and number of pixels. The field is centered at R.A.(J2000)= $06^h\,51^m\,54.02^s$ and Dec. (J2000) = $-01^o\,35'\,43''$.

The region in which minimum and maximum temperature is found in the range of 18.7K to 20.5K with an offset temperature of dust 1.8K. Such a low offset temperature variation shows that there is symmetric outflow or symmetric distribution of density and temperature. It further suggests that particles are independently vibrating . The cavity may be in thermally pulsating phase. When this result is compared with the result obtained in [12] where temperature variation is 20K to 22K so our result is also

comparable with that result. In the contour map, minimum flux and minimum temperature region are shifted which is due to some external factors possibly due to AGB wind. There is no good agreement in case of temperature in the Gaussian fit (Fig. 3b) with offset 12.69 K.

3.4 Size of the Structure

Major and minor diameter of the structure can be easily calculated by using a simple expression i.e., L = R × θ, where R = 6.11kpc is the distance of the structure [9] and θ = pixel size (in radian). After calculation the major and minor diameter of the cavity region are found to be 103.3 pc and 33.1 pc respectively. Thus, the size of the structure is 103.3 pc × 33.1 pc.

3.5 Dust Mass Estimation and its variation

For the calculation of dust mass, we need the distance to the region of interest. The distance of the structure is 6.11kpc [9]. By using the temperature of each pixel and corresponding distance of the structure, we calculated mass of each pixel. Average mass of each pixel is 5.6×10^{28} kg and total mass of the structure is 2.5×10^{31} kg i.e $12.6 M_{\odot}$. But mass of dust obtained around white dwarf WD 1003-44 in [12, 5] is $0.08 M_{\odot}$. It means mass of dust around AGB Star is less than White Dwarf.

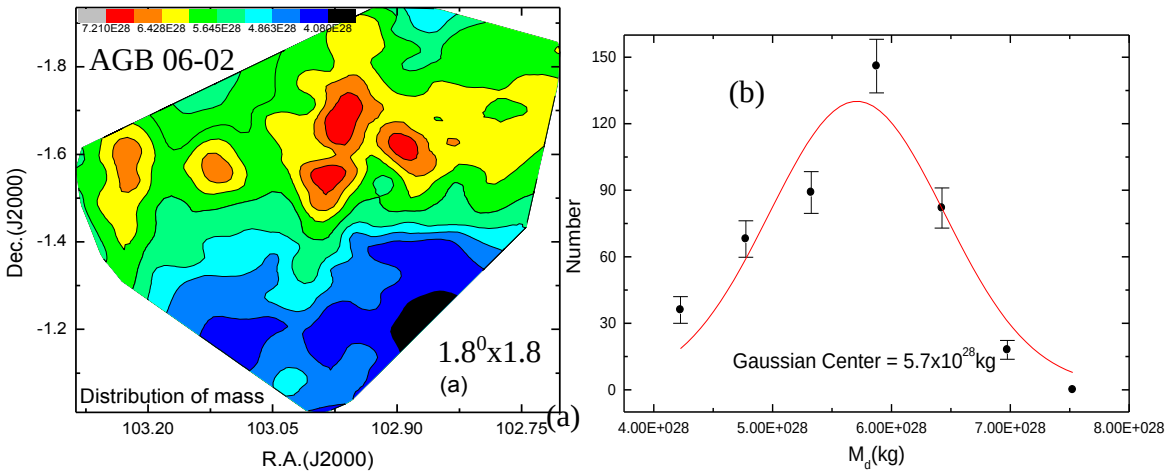

Fig.4: (a) contour map of dust mass and (b)Gaussian fit between mass and number of pixels. The field is centered at R.A.(J2000)= $06^h\ 51^m\ 54.02^s$ and Dec. (J2000) = $-01^0\ 35'\ 43''$.

Distribution of dust mass of the pixels within the selected contour level with R.A. (J2000) and Dec.(J2000) are plotted in contour map by using ORIGIN 8.0. Graph obtained is shown in Fig.4(a) which shows that minimum mass region didn't lie at the maximum temperature region in the selected contour which is unusual trend and is possibly due to AGB wind. There is around good agreement in case of dust mass where offset mass is 1.6 kg. Graph 4(b) is the Gaussian fit between mass and number of pixels where offset mass is 1.6 kg.

4. Conclusion

The physical properties of the cavity-like structure that we investigated while searching an effect of AGB wind around carbon-rich AGB stars. A study of flux density and dust color temperature maps mass of dust was calculated. Our conclusions are as follows:

- The major and minor diameter of the cavity like structure was found to be 103.3 pc and 33.1 pc respectively.

- The maximum temperature 20.5K was found at R.A.(J2000) = 102.85^0 & Dec.(J2000) = -1.36^0 and minimum temperature 18.7K was found at R.A.(J2000) = 102.98^0 & Dec.(J2000) = -1.55^0 with offset of 1.8K. The small value of dust color temperature in the cavity suggests a continuous process by which cavity is supposed to be formed. Low offset in the temperature hints that there is symmetric outflow or symmetric distribution of density and temperature.
- In general, minimum flux and minimum temperature lie at same point in the pixel and in this case nearly normal condition is achieved. Similarly maximum temperature and minimum mass region lie nearly at same region which is normal behavior.
- Average mass of each pixel is $5.6x10^{28}$kg and total mass of the cavity is $2.5x10^{31}$kg.
  We intend to study the role of cabon-rich PAGB star to form the far-infrared cavity in the future.

Acknowledgements

We are grateful to the Department of Astro-Particle Physics, Innsbrck University, specially to Prof. R. Weinberger for invoking us to work on dusty environments around AGB stars. This research has made use of SkyView Virtual Observatory, Aladin v2.5 and NASA/IPAC Extragalactic Database (NED). One of the authors (AKG) acknowledges Central Department of Physics, T.U., Nepal for providing various support of Ph.D.

References

[1] F. Herwig, Evolution of Asymptotic Giant Branch Stars, ARAA, 43 (2005) 435. doi.org/10.1146/annurev.astro.43.072103.150600.

[2] Kyung-Won Suh, Astrophysics of dusty stellar winds from AGB stars, Journal of the Korean astrophysical Society 47(2014) 219-233. doi.org/10.5303/JKAS.2014.47.6.219.

[3] A.I. Karakas, J.C. Lattanzio and O.R. Pols, Parameterising the third dredge- up in asymptotic giant branch stars, Astron. Soc. Aust. 19 (200) 515.

[4] Jr. Icko Iben and A.Renzini, Asymptotic giant branch evolution and beyond, Annual review of Astronomy and Astrophysics 21(1983) 271.

[5] R.D. Oudmaizer, A search for hot- post AGB stars in the IRAS point source catalog, Astronomy and Astrophysics 306 (1996) 823.

[6] T. Blocker, Stellar evolution of low-and intermediate mass stars II. Post AGB evolution, Astronomy and Astrophysics 299 (1995) 755.

[7] S.L. Schnee, N. A. Ridge, A.A. Goodman, G. L. Jason, A Complete Look at the Use of IRAS Emission Maps to Estimate Extinction and Dust Temperature, APJ .634 (2005) 442. doi.org/10.1086/511054.

[8] X. Dupac, J.P. Bernard, N. Boudet, M. Giard, J.M. Lamarre, C. Meny, F. Pajot, I. Ristorcelli, G. Serra, B. Stepnik, J.P. Torre,Inverse Temperature Dependance of the Dust Submillimeter Spectral Index, A&A, 404 (2003) L11. doi.org/10.1051/0004-6361:200030575.

[9] R. Szczerba, N. Siodmiak, G. Stasinska and J.Borkowski, An evolutionary catalogue of galactic post-AGB and related objects, Astronomy and astrophysics 469 (2007) 799. doi.org / 10.1051/0004-6361:20067035.

[10] R.H. Hildebrand, The determination of cloud mass and dust characteristics from sub millimeter thermal emission, Q.Jl.R.astr. obs.ser 24 (1983) 267.

[11] K. Young, T.G. Phillips, G.R. Knapp, Circumstellar Shells Resolved in IRAS Survey Data II. Analysis, ApJ, 409 (1993) 725.

[12] B. Aryal, R. Weinbergerr., Dust structure around White Dwarf WD 1003-44 in 60 and 100 μm Iras Survey". The Himalayan Physics II (2011) 5.

BIBECHANA
A Multidisciplinary Journal of Science, Technology and Mathematics
ISSN 2091-0762 (Print), 2382-5340 (0nline)
Journal homepage: http://nepjol.info/index.php/BIBECHANA
Publisher: Research Council of Science and Technology, Biratnagar, Nepal

Study of far infrared cavity around a post AGB star under IRAS survey at galactic latitude -3^0

A. K. Gautam[*], B. Aryal[**]
Central Department of Physics, T.U., Kirtipur,Nepal
Email: arjungautamnpj@gmail.com[*], baryal@tucdp.edu.np[**]
Article history: Received 20 February, 2018; Accepted 3 September, 2018
DOI: http://dx.doi.org/10.3126/bibechana.v16i0.20960

Abstract

A systematic search of dust structure in the far infrared (100 μm and 60 μm) under Infrared Astronomical Satellite (IRAS) survey was performed using Sky View virtual Observatory. In order to find the possible candidate of cavity structure not yet studied, we used SIMBAD database to locate discrete sources in the region. A new relatively symmetric spherical cavity like structure (size: 44.4 pc x 19.4 pc) at R.A.(J2000) =08^h 03^m 01.65^s, Dec.(J2000) = -36^0 35' 47.9" was found at the distance of about 2800 pc. In this article, we have calculated dust color temperature, dust mass and size. We also studied the flux density variation and then calculated temperature and mass profile of the dust of p-AGB star using data reduction software Aladin2.5 and Aladin8.0. We have studied a cavity like structure centered at R.A.(J2000) = 08^h 04^m 07.21^s, Dec.(J2000) = -37^0 11' 48.0". The dust color temperature is found to lie in the range 21.6 ± 0.09 K to 22.5 ± 0.05 K with an offset of 0.9 K. Such low off set suggests that the post AGB is in local thermodynamic equilibrium. The total mass of the dust in the cavity structure is found about 5.93 x 10^{25} Kg (0.00003M⊙)

Keywords: AGB Stars; dust color temperature; dust mass; post AGB star; inclination angle.

1. Introduction

Low-to-intermediate mass stars end their life on the asymptotic giant branch (AGB) star. AGB stars are the main distributors of dust into the interstellar medium due to their high mass loss rates in combination with an effective dust condensation. It is therefore important to understand the dust formation process and sequence in their extended atmosphere [1]. An evolutionary phase in which the star sheds most of its mantle into the circumstellar environment through a stellar wind. This stellar wind expands at relatively low velocities and enriches the interstellar medium with elements newly made in the stellar interior. The physical processes controlling the gas and dust chemistry in the outflow, as well as the driving mechanism of the wind itself, are poorly understood and constitute the broader context. When helium in the core is used up, energy production shifts to helium burning in a

shell. The outer layers of the star expand. The star evolves towards the early-asymptotic giant branch (AGB) and becomes a red-giant for the second time. The expansion of the outer layer extinguishes the hydrogen-burning shell in the intermediate-mass stars, which causes the convective envelope to move inward for a second time. This second dredge-up brings the hydrogen burning products, mainly helium and nitrogen, to the surface but it does not occur in low mass stars since the hydrogen-burning shell is not extinguished.

Following the helium exhaustion in the shell, the hydrogen-burning shell takes over until enough helium has been produced. When the helium shell is sufficiently massive, it will re-ignite and new helium-burning will control the evolution. The helium-burning shell is known to be thermally unstable and it undergoes thermal pulses recurrently. This is the thermally-pulsing AGB (TP-AGB) phase, characterised by two nuclear burning shells surrounding an electron-degenerate carbon-oxygen core and a deep convective envelope. According to [1], thermal pulses may occur in both low- and intermediate mass stars and huge amounts of energy are released. This allows envelope convection to penetrate to the inter-shell region and mix carbon and oxygen enriched material to the surface (third dredge-up). It is important to note that mixing events occurring during these thermal pulses are responsible for the transport of carbon and s-process elements to the surface [2]. It is also equally important to note that observed abundances of post-AGB stars are mostly determined during this stage of mixing episodes driven by consecutive thermal pulses.

During AGB evolution, the helium-burning shell is thermally unstable and causes energy bursts called thermal pulses or flashes repeating apparently every 105 years leading to the development of a convective zone in the shell (3). The phase where hydrogen-shell burning dominates is known as the "inter-pulse phase" which is interrupted by the helium-shell instabilities. The thermal pulse drives a convection zone between the helium and hydrogen burning shells. The fusion products of the helium-burning shell including 12C and some 16O are mixed throughout this region. Once a thermal pulse has occurred, a huge amount of energy is released.

Low to intermediate-mass stars cross the HR diagram horizontally from the tip of the asymptotic giant branch (AGB) to the planetary nebula (PN) region after they terminate a rapid mass-loss phase. This transition phase is called post-AGB phase of evolution. From an analysis of the IRAS point source catalog, several post-AGB stars have been identified [4, 5]. The spectral energy distribution (SED) of post-AGB stars is double peaked. One peak is at far-infrared wavelengths due to the cold dust shell (100-200 K) and the other peak is at shorter wavelengths, optical or near-infrared, from the obscured central star. The cold dust-shell was observed by IRAS. Most of the post-AGB stars, proto-planetary nebulae (PPNe) and PNe were found within the IRAS color box defined by $F(12\ \mu m)/F(25\ \mu m) < 0.3$ and $F(25\ \mu m)/F(60\ \mu m) > 0.3$ [6].

In this paper, we study the physical properties of a far infrared cavity, that we investigated during a systematic search on IRAS maps, located close to a carbon-rich post AGB star (PAGB 08-36) at -3o galactic latitude. In section 2, we describe methods of calculation. A brief description of the result and discussion will be given in the section 3. Finally, we conclude our results in the section 4.

2. Methods

We investigated a cavity-like structure in both 60 and 100 micron IRAS maps around a p-AGB star. Fig.1(a), and 1(b) are cavity images at 60 and 100 μm whereas 1(c) is its contour map. We briefly

describe a method for calculation of dust color temperature and dust mass of the dusty environment around carbon-rich post Asymptotic Giant Branch named p-AGB08-36[7].

2.1 Dust Color Temperature

For the calculation of dust color temperature, we adopt the method proposed by Schnee et al. (2005) [8] and Dupac et al. (2003)[9]. According to Schnee et al. (2005)[8], dust color temperature of the emission at a wavelength λi is given by

$$T_d = \frac{-96}{\ln\{R \times 0.6^{(3+\beta)}\}} \quad (1)$$

where , $R = \frac{F(60\ \mu m)}{F(100\ \mu m)}$

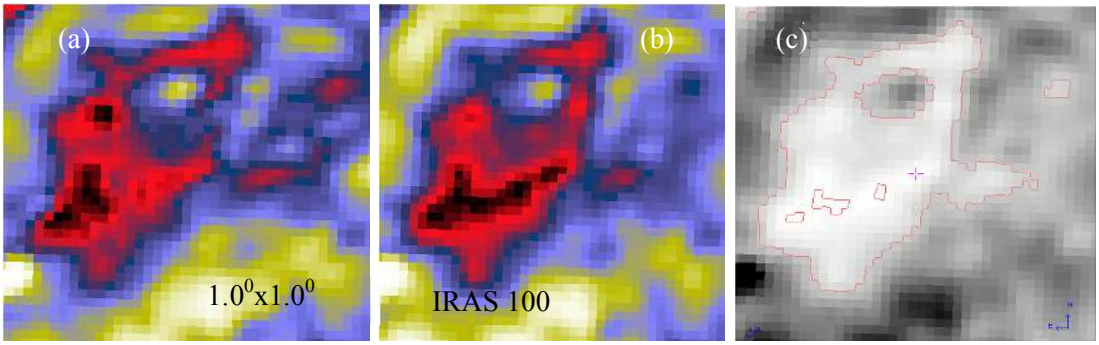

Fig. 1: (a) & (b) IRAS 60 μm and 100 μm far infrared image of the core region of AGB 08-36 centered at R.A. (J2000)= 08^h 04^m 07.21^s and Dec.(J2000) = -37^0 11' 48.0", and (c) Contour map of the cavity where contour level is 1-50.

F(60 μm) and F(100 μm) are the flux densities in 60 μm and 100 μm respectively and Eq. (1) is used for calculation of the dust color temperature. The spectral emissivity index (β) depends on dust grain properties like composition, size, and compactness. For a pure blackbody would have β = 0, the amorphous layer-lattice matter has β ~ 1, and the metals and crystalline dielectrics have β ~ 2 which is used in our calculations.

2.2 Planck's Function

The value of Planck's function depends on the wavelength (frequency), and hence the temperature. Finally it is used to calculate dust mass. In 1900, Planck proposed a relation which is named as Planck's function. According to him, the Planck's function is given by

$$B(\vartheta, T) = \frac{2hc}{\lambda^3}\left[\frac{1}{e^{\frac{hc}{\lambda KT}}-1}\right] \quad (2)$$

where, h = Planck's constant, c = velocity of light, ν = frequency at which the emission is observed, λ = wavelength of the radiation and T = temperature of each pixel.

2.3 Dust Mass

For the calculation of dust mass, first we need the value of flux density (Fν) at 100 μm maps and we use the expression given by Hildebrand (1983)[10],

$$M_{dust} = \frac{4a\rho}{3Q_v}\left|\frac{S_v D^2}{B(v,T)}\right| \quad (3)$$

where, weighted grain size (a) = 0.1 μm, grain density (ρ) = 3000 kg m^{-3}, grain emissivity (Qv) = 0.0010 (for 100 μm) [11]. So the equation (3) reduces to

$$M_{dust} = 0.4\left|\frac{S_v D^2}{B(v,T)}\right| \quad (4)$$

We use equation (4) to calculate dust mass of the cavity.

2.4. Inclination angle

The long axis of KK-loops can be assumed to be inclined by a certain angle with respect to the plane of the sky. The inclination angle i (angle between the line-of-sight and the normal vector of the plane of the loops) can be estimated using Holmberg (1946) [12] formula:

$$Cos^2 i = \frac{\frac{b^2}{a^2} - q^2}{1 - q^2} \quad (5)$$

where b/a is the measured axial ratio and q is the intrinsic flatness of the cavity. We use the value of intrinsic flatness q = 0.33 as suggested by Holmberg (1946) for oblate spheroid structure.

3. Results and Discussion

3.1 Structure: Contour Maps

While going through the systematic search on IRAS maps, we found an isolated cavity in the 100 μm and 60 μm at R.A. (J2000)= 08^h 04^m 07.21^s and Dec.(J2000) = -37^0 11' 48.0". With the help of the software ALADIN2.5, we have studied physical properties (size, dust color temperature, dust mass, etc) of the cavity. We selected contour level in such a way that it circles the cavity. The contour map in the contour level 1-50 is shown in the fig.1(c).

3.2 Flux Density and its Variation

By using ALADIN 2.5 software, the values of flux densities at 60μm and 100μm have measured. The flux density distribution within the contour of the region of interest has studied. We plotted a graph between flux at 100μm and 60μm with the help of ORIGIN 5.0 which is shown in fig.2(a). From the linear fit, slope of the line was 0.2. The linear equation of the fitted line is, y= -1.9 + 0.2x. Using the slope of best fitted plot, dust color temperature is found as 23 K which is slightly more than our calculated value.

Again distribution of flux at 100μm of the pixels within the contour level with right ascension (R.A.) and declination (Dec.) are plotted by using ORIGIN 8.0 and the graph is shown in fig.2(b). Graph shows that all the fluxes from minimum to maximum lie within the contour level. Most of the maximum flux regions lie at the boundary.

3.3. Dust color Temperature and its Variation

Using the method of [8], we calculated dust color temperature of each pixel inner the outer isocontour in the region of interest. We use the IRAS 100 μm and 60 μm FITS images downloaded from the IRAS server. For the calculation of temperature we choose the value of β = 2 following the explanation given by [9]. Variation of temperature with corresponding R.A.(J2000) and Dec.(J2000) are plotted by using ORIGIN 8.0 and the graph is shown in figure 3(a). Graph shows that temperature distributions are in separate cluster but minimum temperature region is little bit shifted from minimum flux density which is unusual behaviour. Such type of nature is obtained due to external factors. Graph 3(b) is the Gaussian fit between dust color temperature and number of pixels with

offset temperature 0.98 K. This Gaussian fit more or less follow the Gaussian distribution with positive skewness.

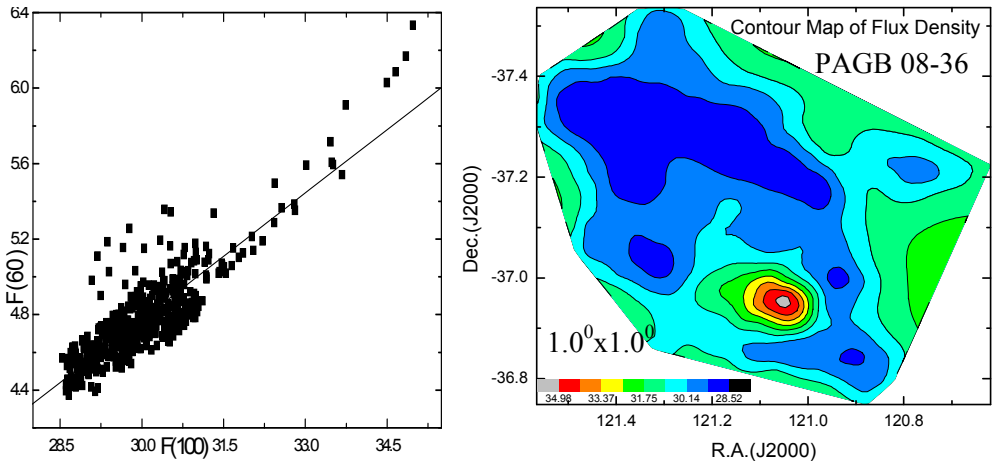

Fig.2(a): The 100µm verses 60µm flux density in the region of interest and 2(b) Contour map at 100µm flux density where the AGB star is located at the center R.A. (J2000)= 08^h 04^m 07.21^s and Dec.(J2000) = -37^0 11' 48.0".

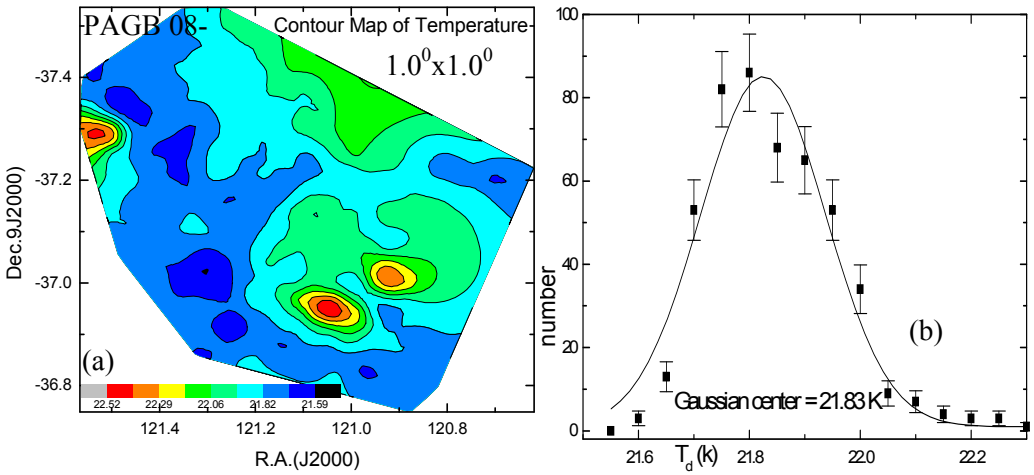

Fig. 3: (a) Contour map of dust color temperature and (b) Gaussian fit between dust color temperature and number of pixels. The field is centered at R.A. (J2000)= 08^h 04^m 07.21^s and Dec.(J2000) = -37^0 11' 48.0".

The region in which minimum and maximum temperature is found in the range of 21.6 K to 22.5 K with an offset temperature of dust 0.9 K. It suggests that particles are independently vibrating . The cavity may be in thermally pulsating phase. When this result is compared with the result obtained in [13] where temperature variation is 20K to 22 K so our result is also comparable with that result. In the contour map, minimum flux and minimum temperature region are shifted which is due to some

external factors possibly due to AGB wind. There is good agreement in case of temperature in the Gaussian fit with offset 0.98 K.

3.4. Size of the Structure

Major and minor diameter of the structure can be easily calculated by using a simple expression i.e., L = R × θ, where R = 2.8 kpc is the distance of the structure [7] and θ = pixel size (in radian). After calculation the major and minor diameter of the cavity region are found to be 44.4 pc and 19.4 pc respectively. Thus, the size of the structure is 44.4 pc × 19.4 pc.

3.5. Dust Mass Estimation and its variation

For the calculation of dust mass, we need the distance to the region of interest. The distance of the structure is 2.8 kpc [7]. By using the temperature of each pixel and corresponding distance of the structure, we calculated mass of each pixel. Average mass of each pixel is 8.7 x 10^{27} kg and total mass of the structure is 4.3 x 1030 kg i.e 2.16 $M_{\odot}$.. But mass of dust obtained around white dwarf WD 1003-44 in [12] is 0.08 $M_{\odot}$.. It means mass of dust around AGB Star is less than White Dwarf.

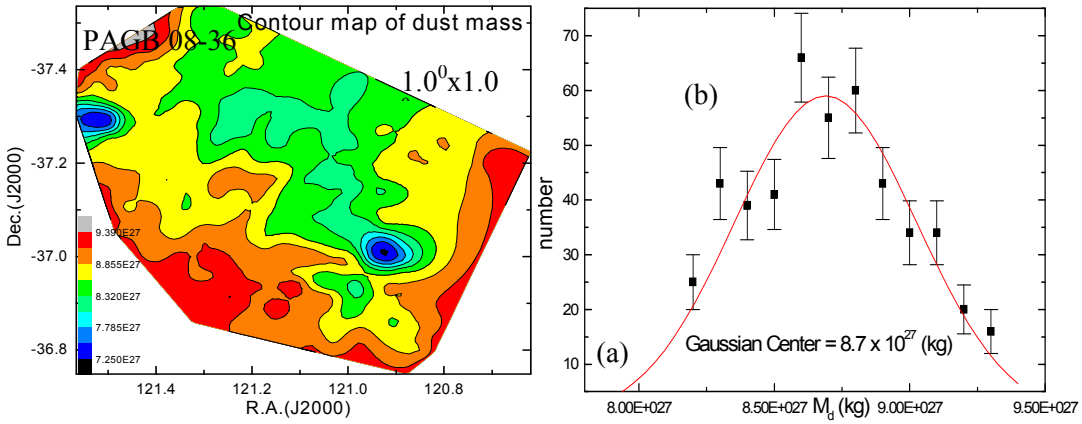

Fig.4: (a) Contour map of dust mass and (b) Gaussian fit between mass and number of pixels. The field is centered at R.A. (J2000)= 08^{h} 04^{m} 07.21^{s} and Dec.(J2000) = -37^{0} 11' 48.0".

Distribution of dust mass of the pixels within the selected contour level with R.A. (J2000) and Dec.(J2000) are plotted in contour map by using ORIGIN 8.0. Graph obtained is shown in fig.4(a) which shows that minimum temperature region is massive which suggests that it follows cosmological principle means distribution of dust mass is homogeneous and isotropy. Graph 4(b) is the Gaussian fit between mass and number of pixels with standard error ±σ. Fitted Gaussian fit of dust mass follow the Gaussian distribution and suggests symmetric behaviour.

4. Conclusion

The physical properties of the cavity-like structure that we investigated while searching an effect of AGB wind around carbon-rich AGB stars. A study of flux density and dust color temperature maps, mass of dust, size of the cavity and inclination angle was calculated. Our conclusions are as follows:

- The major and minor diameter of the cavity like structure was found to be 44.4 pc and 19.4 pc respectively so size of the cavity is 44.4 pc x 19.4 pc.

- The maximum temperature 22.5±0.05K was found at R.A.(J2000) = 121.040 & Dec.(J2000) = -36.940 and minimum temperature 21.6±0.09 K was found at R.A.(J2000) = 121.290 & Dec.(J2000) = -36.980 with offset of 0.9K. The small value of dust color temperature in the cavity suggests a continuous process by which cavity is supposed to be formed. Low offset in the temperature hints that there is symmetric outflow or symmetric distribution of density and temperature.
- In general, minimum flux and minimum temperature lie at same point in the pixel and in this case nearly normal condition is achieved. Similarly maximum temperature and minimum mass region lie nearly at same region which is normal behavior. It means their distribution follow cosmological principle
- Average mass of each pixel is 8.7 x 10^{27} kg and total mass of the cavity is 4.3 x 10^{30} kg.
- The inclination angle (i) of the cavity is found to be and 840 suggesting that the cavity will be in face-on (i = 0◦) when it is rotated through 60 from northern to southern direction (it is assumed that the cavity is in the sky plane).

We intend to study the role of cabon-rich PAGB star to form the far-infrared cavity in the future.

Acknowledgements

We are grateful to the Department of Astro-Particle Physics, Innsbrck University, specially to Prof. R. Weinberger for invoking us to work on dusty environments around AGB stars. This research has made use of SkyView Virtual Observatory, Aladin v2.5 and NASA/IPAC Extragalactic Database (NED). One of the authors (AKG) acknowledges Central Department of Physics, T.U., Nepal for providing various support of Ph.D.

References

[1] F. Herwig, Evolution of Asymptotic Giant Branch Stars. ARAA 43 (2005) 435. doi.org/10.1146/annurev.astro.43.072103.150600.

[2] Jr. Icko Iben and A.Renzini, Asymptotic giant branch evolution and beyond, Annual review of Astronomy and Astrophysics 21 (983) 271.

[3] A. I. Karakas, J. C. Lattanzio and O. R. Pols, Parameterising the third dredge- up in asymptotic giant branch stars, Astron. Soc. Aust. 19 (2002) 515.

[4] M. Pathasarathy & S. R. Pottasch, The infrared (IRAS) excess in HD161796 and related stars, A & A 154 (1986) L16.

[5] S. R. Pottasch, C. bignell, R. Olling & Zijlstra, Planetary nebula near the galactic plane, A & A 225 (1989) 521.

[6] W.E.C.J. Van der Veen & H.J. Habing, The IRAS two color diagram as a tool for studying late stages of stellar evolution, A & A 194 (1988) 125.

[7] R. Szczerba, N. Siodmiak, G. Stasinska and J.Borkowski, An evolutionary catalogue of galactic post-AGB and related objects, Astronomy and astrophysics 469 (2007) 799. doi.org / 10.1051/0004-6361:20067035.

[8] S. L. Schnee, N. A. Ridge, A. A. Goodman, G. L. Jason, A Complete Look at the Use of IRAS Emission Maps to Estimate Extinction and Dust Temperature, APJ 634 (2005) 442. doi.org/10.1086/511054.

[9] X. Dupac, J. P. Bernard, N. Boudet, M. Giard, J. M. Lamarre, C. Meny, F. Pajot, I. Ristorcelli, G. Serra, B. Stepnik, J. P. Torre, Inverse Temperature Dependance of the Dust Submillimeter Spectral Index, A&A, .404 (2003) L11. doi.org/10.1051/0004-6361:200030575.

[10] R. H. Hildebrand, The determination of cloud mass and dust characteristics from sub millimeter thermal emission, Q.Jl.R.Astr. Obs.ser 24 (1983) 267.

[11] K. Young, T. G. Phillips, G. R. Knapp, Circumstellar Shells Resolved in IRAS Survey Data II Analysis, ApJ 409 (1993) 725.

[12] Erik Holmberg, Investigations of the systematic errors in the apparent diameters of the nebulae, MeLus, 117 (1946) 3H.

[13] B. Aryal, R. Weinberger, Dust structure around White Dwarf WD 1003-44 in 60 and 100 μm Iras Survey, The Himalayan Physics II (2011) 5.

International Conference on Materials Research and Technology (ICMRT-2017)

July 10-11, 2017

Certificate

AWARDED TO

Prof./Dr./Mr./Ms. Arjun Kumar Gautam

of Tribhuvan University, Nepal

For Participating / Presenting Paper / Invited Talk / Chairing Session

Titled A Study of Materials in the Far Infrared Sky At Lattitude -53°

Organized by

FACULTY OF SCIENCE

AGGARWAL COLLEGE BALLABGARH, FARIDABAD (HARYANA), INDIA

A Post Graduate Co-educational College Accredited 'A' Grade (CGPA: 3.40) by NAAC

College with Potential for Excellence (CPE) Status by UGC

In Association with

INDIAN SOCIETY OF ANALYTICAL SCIENTISTS - DELHI CHAPTER

Dr. Ajit Singh Yadav
Organising Secretary

Dr. Krishan Kant
Principal & Convener

TRANSFORMING HARYANA - PROGRESSING HARYANA

DHE, Haryana

Indian Council of Social Science Research

ST. XAVIER'S COLLEGE

The Physics department of St. Xavier's College, Kathmandu would like to award this certificate to

ARJUN K. GAUTAM

for his presentation on

A STUDY OF DUSTY ENVIRONMENT AT FAR INFRARED IRAS MAP AROUND THE MASS -LOSING CARBON-RICH AGB STAR AT GALACTIC LATITUDE -59.6^0

in the

International Conference on Physics of Space and Materials

held on September 2-3, 2017.

MR. DRABINDRA PANDIT
HEAD OF DEPARTMENT
PHYSICS

PROF. DR JIBA RAJ POKHAREL
VICE CHANCELLOR
NAST
CHIEF GUEST

FR. JIJU VARGHESE
PRINCIPAL

ST. XAVIER'S | COLLEGE | KATHMANDU

INTERNATIONAL CONFERENCE ON
EXPLORATIONS IN PHYSICS (ICEP-2018)

29-31 May, 2018, Kathmandu, Nepal

Arjun Kumar Gautam

Bhaktapur Multiple Campus, Tribhubhan University, Nepal

Contributed an oral presentation entitled

Study of Dusty Environment of a Far Infrared Cavity at 60 μm and 100 μm IRAS map around the Carbon-rich AGB Star at Galactic Latitude 8.6^0

during the conference

Chief Guest
Prof. Dr. Jiba Raj Pokharel
Vice Chancellor, NAST

Campus Chief
Rajesh Mahaju
Amrit Campus

SOC Chair
Assoc. Prof. Dr. Leela Pradhan Joshi
Amrit Campus